Optimalisatie van de verstijverconfiguratie van axiaal samengedrukte stalen silo's op lokale steunpunten

Optimisation of the Stiffening Configuration of Axially Compressed Steel Silos on Local Supports

Arne Jansseune

Promotoren: prof. dr. ir. -architect J. Belis, prof. dr. ir. W. De Corte
Proefschrift ingediend tot het behalen van de graad van
Doctor in de Ingenieurswetenschappen: Bouwkunde

Vakgroep Bouwkundige Constructies
Voorzitter: prof. dr. ir. L. Taerwe

Vakgroep Industriële Technologie en Constructie
Voorzitter: prof. dr. M. Vanhaelst

Faculteit Ingenieurswetenschappen en Architectuur
Academiejaar 2014 - 2015

UNIVERSITEIT GENT

ISBN 978-90-8578-811-9
NUR 955
Wettelijk depot: D/2015/10.500/55

Supervisors

Professor Jan Belis
Professor Wouter De Corte

Examination committee

Professor Jan Belis	Ghent University
Professor Wouter De Corte	Ghent University
Professor Wim De Waele (secretary)	Ghent University
Professor emeritus Guy Lagae	Ghent University
Professor Bert Snijder	Eindhoven University of Technology, Eindhoven
Professor Luc Taerwe (chairman)	Ghent University
Professor Wim Van Paepegem	Ghent University

Research Institute

Research Lab
Department of Industrial Technology and Construction
Faculty of Engineering and Architecture
Ghent University
Valentin Vaerwyckweg 1
B-9000 Ghent
Belgium

Financial support

Research Fund of the University College Ghent and Ghent University

Dankwoord

Dit doctoraatsproefschrift is het resultaat van een zes jaar lang lopend onderzoek naar het bezwijkgedrag van lokaal ondersteunde stalen silo's. Gedurende die periode deed ik er alles aan om, voor dit specifiek domein binnen de bouwkunde, het inzicht te verhogen om zo het ontwerp ervan op termijn te verbeteren. Het spreekt voor zich dat dit onderzoek en dit doctoraatsproefschrift, waarop ik best wel trots ben, niet alleen door mezelf tot stand is gekomen! Integendeel, heel wat mensen hebben hun steentje bijgedragen waarvoor ik hen via deze weg uitdrukkelijk en vooral oprecht wil bedanken voor hun steun.

Laat ik starten met het bedanken van mijn promotoren. Wouter en Jan, dank jullie wel ! Als ervaren gidsen op vlak van bouwkundige constructies hebben jullie het door mij bewandelde pad mee helpen uitstippelen en had ik, dankzij jullie advies en tips, (bijna) geen moment waarop ik verdwaald gelopen ben. Wat ik regelmatig ervoer was, doordat ik zó dicht met mijn neus op het onderzoek zat, dat ik voor de hand liggende zaken rondom mij uit het oog verloor. Op dat moment wezen jullie mij daarop en kon ik daar mee aan de slag. Verder apprecieer ik jullie eerlijke, waardevolle en opbouwende commentaren. Daarom herhaal ik het nogmaals, dank jullie wel dat jullie in mijn team zaten !

Het feit dat ik dit doctoraat gestart ben, heb ik in grote mate te danken aan Wesley Vanlaere. Hij heeft mij destijds als dagelijkse begeleider van mijn masterproef de vraag gesteld of ik interesse had in doctoreren, mij overtuigd en uiteindelijk ook stappen ondernomen om een doctoraatsvoorstel in te dienen, samen met Wouter De Corte en Rudy Van Impe (mijn voormalige promotor). Dat voorstel verdedigde ik met succes, waardoor ik na het afstuderen meteen aan de slag kon als onderzoeksassistent. Wesley en Rudy, dank jullie wel om mij te lanceren en begeleiden gedurende de eerste jaren van mijn doctoraat.

Voor het experimentele luik van dit onderzoek wil ik absoluut Dennis Elias en Eric Vonck in de bloemetjes zetten. Dankzij jullie ervaring in het vervaardigen van silo's en bereidwillige medewerking ben ik er in geslaagd om met succes echte silo's kapot te drukken.

Tevens wil ik ook de leden van de examencommissie bedanken: Luc Taerwe, Bert Snijder, Guy Lagae, Wim Van Paepegem, Wim De Waele, Jan Belis en Wouter De Corte. Jullie wierpen een kritische blik op mijn werk wat leidde tot een verdere verbetering van de kwaliteit van dit werk. Ik waardeer jullie inspanning ten zeerste.

Tijdens deze ontdekkingstocht had ik het geluk om in een bijzonder aangename sfeer te mogen werken, wat echt wel bevorderlijk is daar je al snel heel wat uren doorbrengt op het werk. Dankzij de vele aanmoedigingen en de collegialiteit had ik nooit het gevoel dat ik er alleen voor stond. De vele leuke en ontspannende gesprekken, de "korte" pauzes in de koffiecorner waarin veel gelachen werd, de etentjes, de uitstapjes, de studiereizen, enz. hebben allemaal bijgedragen tot dit resultaat. Om dat verband aan te tonen is geen wetenschappelijk onderzoek nodig. Daarom dank ik de bouwkunde (zowel huidige als voormalige collega's) voor de vele leuke momenten. De groep met de jonge collega's (definitieve oplevering 1985 en later) zag ik de voorbije zes jaar niet alleen groeien in aantal, maar ook hechter worden. Dank jullie wel daarvoor: Peter, Sara, Lieve, Tanja, Sara, Leo, Anthony, Maarten, Kizzy, Sven, Koos, Hanne, Charlotte en Céline. De andere collega's beginnen nu alvast schrik te krijgen dat ik hen vergeet. Niets is minder waar: dank jullie wel Dirk, Frank, Greet, Hilde, Ignaas, Jeroen, Kathleen, Kristof, Lucien, Marc, Marc, Marijke, Patrick, Rik, Tom, Veerle, Wouter, ... Ook de collega's van Labo Modelonderzoek (o.a. Wesley, Rudy, Jan, Delphine, Didier, Christel, Eric en Dennis) zou ik graag willen bedanken. En om volledig te zijn breid ik de groep uit naar alle personeelsleden van het P-gebouw en de vakgroep.

Voorts wil ik alle studenten van de opleiding industrieel ingenieur bouwkunde bedanken. Als assistent kreeg ik de kans om mijn doctoraat af en toe (de ene periode al wat meer dan de andere) langs de kant te schuiven en in te staan voor de begeleiding van diverse berekenings- en ontwerpvakken, bachelor- en masterproeven. Het lesgeven en de band met de studenten ervaar ik dan ook als positief en als meerwaarde voor het doctoraat.

Last but not least, ze hebben er lang moeten op wachten, wil ik ook mijn familie en vrienden bedanken. Op café met vrienden, een barbecue, een fietsweekendje of andere sportieve momenten, of gewoonweg thuis met de dichte familie, allemaal leuke ontspannende momenten die ik heb mogen meemaken tijdens het doctoreren. Tot slot wil ik mijn ouders bedanken omdat ze me de kans gaven om te studeren en zo mezelf te ontplooien. Kathleen, Ignace en broer Hannes, dank jullie wel voor jullie onvoorwaardelijke steun! Zonder jullie was ik nooit zo ver geraakt.

Arne Jansseune

Diksmuide, 26 mei 2015

Table of contents

List of symbols and abbreviations

Roman alphabet

A	Area of cross-section	mm²
A_{shell}	Cross-section of the shell wall	mm²
A_{stif}	Cross-section of the longitudinal stiffener / engaged column	mm²
C	Rotational spring stiffness	kNm/rad
C	Load magnifying factor	-
C_{0p}	Patch load solid reference factor	-
d_c	Internal diameter of the circular cross-section of the barrel	m
d_{stif}	Circumferential width of the longitudinal stiffener / engaged column	mm
d_{stif}^{sup}	Circumferential width of the top of the longitudinal stiffener	mm
E	Young's modulus	N / mm²
e	Eccentricity	m
F	Force	kN
F_{cip}	Improved estimate of the plastic failure load from a Convergende Indicator Plot	kN
F_{cr} / F_{LBA}	Elastic critical failure load from a linear elastic bifurcation analysis	kN
F_{GMNA}	Failure load from a geometrically and materially non-linear analysis without imperfections	kN
F_{GMNIA}	Failure load from a geometrically and materially non-linear analysis with imperfections	kN
F_{gn} / F_{GNIA}	Failure load from a geometrically non-linear elastic analysis with imperfections	kN
F_{ms}	Upper bound estimate of the plastic failure load from a Modified Southwell plot	kN
F_{pl} / F_{MNA}	Plastic failure load or failure load from a small displacement theory materially non-linear analysis	kN
F_u	Failure load	kN
g	Gravity acceleration	m / s²
h or h_c	Cylinder height	m
h_{free}	Free height below the hopper	m

h_{hop}	Hopper height	m
h_{stif}^{inf}	Free height of the engaged column	m
h_{stif}^{sup}	Height over which the longitudinal stiffener / engaged column is attached to the cylindrical barrel	m
I	Second moment of area of cross-section	cm^4
I_{stif}	Moment of inertia of the longitudinal stiffener / engaged column	cm^4
K	Lateral pressure ratio	-
k	Calibration factor	-
k'	Modified value of the calibration factor	-
l_{gx}	Gauge length	m
$\Delta l_{\text{initial}}$	Initial increment in arc length	
$l_{initial}$	Maximum arc length	
l_{min}	Minimum arc length	
l_{period}	Total arc length scale factor	
n_{sup}	Number of discrete supports	-
p	Pressure	MPa
p_h	Frictional traction on the silo wall	MPa
p_p	Patch load pressure (normal on the silo wall)	MPa
p_w	Normal pressure on the silo wall	MPa
q	Uniform line load	kN / m
Q	(meridional compression) fabrication quality parameter	-
R	Cylinder radius	m
r	Effective radius of curvature	m
r_{hop}	Radius of the circular opening at the bottom of the conical hopper	m
r_{roof}	Radius of the circular opening at the top of the conical roof	m
s	Scaling factor	-
s	Height of the patch load	m
t	Cylinder thickness	mm
t	Time	s
t_{hop}	Hopper thickness	mm
t_{lr}	Lower ring thickness	mm
t_{roof}	Roof thickness	mm
t_{stif}	Stiffener / column thickness	mm
t_{ur}	Upper ring thickness	mm
U_{0x}	Dimple parameter	-
$U_{0,max}$	Dimple tolerance parameter	-

U_n	Dimple imperfection amplitude parameter	-
U_R	Out-of-roundness parameter	-
$U_{R,max}$	Out-of-roundness tolerance parameter	-
U_R	Displacement along the radial direction (local cylindrical coordinate system)	mm
U_T	Displacement along the circumferential direction (local coordinate system)	mm
U_X	Displacement along the X direction (global coordinate system)	mm
U_Y	Displacement along the Y direction (global coordinate system)	mm
U_Z	Displacement along the Z direction (global coordinate system)	mm
V	Volume	m^3
w_{lr}	Radial width of the lower ring	mm
w_{stif}	Radial width of the longitudinal stiffener / engaged column	mm
w_{stif}^{sup}	Radial width of the top of the longitudinal stiffener	mm
w_{ur}	Radial width of the upper ring	mm
Δw_{0x}	Maximal measured depth of the initial dimple	m

Greek alphabet

α	Elastic imperfection reduction factor	-
α_0	Unpressurized value of the imperfection reduction factor	-
α_p	Pressurized value of the imperfection reduction factor	-
α_{roof}	Angle of the roof with respect to the horizontal	°
β	Plastic range factor	-
β_{early}	Lower limit of the plastic range factor for early yielding	-
β_{late}	Upper limit of the plastic range factor for late yielding	-
β_{hop}	Angle of the hopper with respect to the vertical	°
γ	Bulk unit weight	kN / m^3
γ	Partial factor	-
Δ	Increment	variable
δ	Deviation of the imperfection shell wall and is measured perpendicular to the middle surface of the perfect shell	mm
ε	Strain	-
ε_e	Engineering strain	-
ε_t	True strain	-
ε_t^{el}	True elastic strain	-
ε_t^{pl}	True plastic strain	-
η	Interaction exponent	-
η_0	Squash limit interaction exponent	-

η_P	Plastic limit interaction exponent	-
θ	Circumferential angle	°
λ	Relative slenderness of the structure	-
λ_0	Squash limit relative slenderness	-
λ_b	Linear elastic bending half wavelength	mm
λ_{cl}	Half-wavelength of the square chequer-board pattern	mm
λ_P	Plastic limit relative slenderness	-
$\Delta\lambda_{initial}$	Initial load increment	kN
μ	Wall friction coefficient	-
μ_{sup}	Degree of support along the circumference	- or %
ν	Coefficient of Poisson	-
ρ	Density	kg / m³
σ	Stress	N / mm²
σ_e	Engineering stress	N / mm²
σ_t	True stress	N / mm²
σ_x	Meridional membrane stress	N / mm²
σ_y	Yield stress	N / mm²
σ_θ	Circumferential membrane stress	N / mm²
τ	Shear stress	N / mm²
$\tau_{x\theta}$	Membrane shear stress	N / mm²
φ_i	Effective angle of internal friction	°
φ_r	Angle of repose	°
φ_R	Rotation about the radial axis (local cylindrical coordinate system)	-
φ_T	Rotation about the circumferential axis (local coordinate system)	-
φ_w	Wall friction angle	°
φ_Z	Rotation about the meridional axis (local coordinate system)	-
χ	Dimensionless resistance or strength	-
χ_0	Dimensionless resistance or strength when λ=0	-
ω	Convergence parameter in a CIP plot	-

Other symbols

$\emptyset$	Diameter	m
$\emptyset_{max}$	Maximal measured internal diameter	m
$\emptyset_{min}$	Minimal measured internal diameter	m
$\emptyset_{nom}$	Nominal internal diameter	m

Subscripts

E	Value arising from design actions
F	Actions
M	Material
R	Resistance
Abq	Abaqus
bif	Bifurcation
cr	Critical
$corr$	Corrected
d	Design
e	Emptying
e	Engineering
eff	Effective
el	Elastic
$el-pl$	Elasto-plastic
eq	Equivalent
f	Filling
fit	Fitting
hop	Hopper
i	Inlet
k	Characteristic
l	Lower
lim	Limit
lr	Lower ring
max	Maximum
$meas$	Measured
min	Minimum
o	Outlet
pl	Plastic
r or rad	Radial direction
r	Ring
ref	Reference
req	Required

$roof$	Roof
$stif$	Stiffener / engaged column
sup	Support
t	True
u	Ultimate
u	Upper
ur	Upper ring
x	Meridional direction
y	Yield
z	Axial direction
θ	Circumferential direction

Superscripts

inf	Inferior
sup	Superior

Abbreviations

AAC	Action Assessments Class
CC	Consequence Class
Cla	Clamped support
DOF	Degree of freedom
EC	Engaged column
ECCS	European Convention for Constructional Steelwork
Exp	Experimental
GMNA	Geometrically and materially non-linear analysis without imperfections
GMNIA	Geometrically and materially non-linear analysis with imperfections
GNA	Geometrically non-linear elastic analysis without imperfections
GNIA	Geometrically non-linear elastic analysis with imperfections
LA	Linear elastic shell analysis
LBA	Linear elastic bifurcation analysis
LBM	Linear buckling mode of the perfect shell
LPF	Load proportionality factor
MNA	Small displacement theory materially non-linear analysis
NBM	Non-linear buckling mode of the perfect shell
Pin	Pinned support
PC	Partially clamped support
PDS	Post-buckling deformed shapes of the perfect shell
RC	Reliability class
WD	Weld depression

Conventions

Sign conventions

Radial displacements are positive/negative when they are outwardly/inwardly oriented relative to the perfect silo wall. Compressive stresses are negative, tensile stresses positive.

Directions and coordinate systems

A single curved shell surface is defined by three main **directions** as shown in Fig 0-1 (a).

- Radial direction
- Vertical or meridional or axial direction
- Circumferential direction

The **global coordinate system** is a right-handed Cartesian coordinate system. Its origin coincides with the centre of the circular lower edge of the silo and has the following axes (See Fig 0-1 (b)).

- X: Global X-Coordinate
- Y: Global Y-Coordinate
- Z: Global Z-coordinate

A **local coordinate system** is a cylindrical coordinate system which is defined in each point of the shell surface and has the following axes (See Fig 0-1 (c)).

- R: Local radial coordinate, perpendicular to the shell surface (out-of-plane)
- θ: Local circumferential coordinate, tangential to the shell surface (in-plane)
- Z: Local axial coordinate, tangential to the shell surface (in-plane)

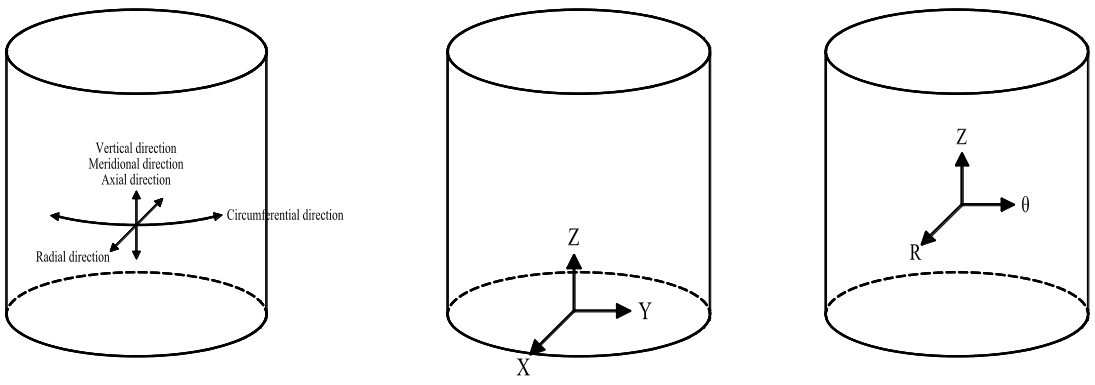

(a) Main directions. (b) Global coordinate system. (c) Local coordinate system.

Fig 0-1 Directions and coordinate systems.

Summary

Introduction and scope

Nowadays, silos have become an essential link in many applications because large volumes of (dry) powdered, granular, and bulk materials can be easily stored on a relatively limited floor space. Ranging from agriculture to food processing, from mining to industrial processing... all these sectors need to **temporarily store bulk solids** between different stages of all kinds of manufacturing processes and between manufacturing process and transportation, or vice versa.

In practice, most metal silos have **a circular planform** and are placed **in elevated position**. The elevated position frequently is preferred because of the necessity to discharge the silo contents (by gravity) into a transporting system. To facilitate the emptying process, sufficient space must be provided under the silo by means of **local supports**, either by columns or by an elevated floor system. In addition, this work focuses on **steel** silos with a **flat wall**.

Given that such silo structures are discretely supported and are for the most part exposed to vertical compressive pressures caused by friction between the bulk material and the silo wall, axial peak stresses are locally introduced in the silo wall above the discrete supports. These disadvantageous stress concentrations cause premature failure of the silo structure, either by **plastic yielding, by elastic buckling, or a combination of both phenomena**.

In this work, the failure behaviour is investigated for two types of locally supported cylindrical steel silos. For the first configuration, the cylindrical barrel is stiffened with **U-shaped longitudinal stiffeners** above the column supports, combined with a transition ring stiffener and an intermediate ring stiffener. The second configuration consists of rectangular shaped supporting **columns** which **are engaged** along a specific distance to the external side of the shell wall, without the presence of ring stiffeners. While the first type is used for intermediate to large silos and the second type for lighter silos, both configurations have in common that, along the attached height of the longitudinal stiffener/engaged column, the ground reaction force is transferred more gradually into the silo wall by shear. Consequently, the axial stresses are better distributed in circumferential direction and the disadvantageous stress concentrations are reduced, resulting in a much higher load level at the moment of failure.

Problem statement

The design of axially compressed cylindrical steel walls is governed by the **buckling limit state** (for relatively thin-walled silos) and the **plastic limit state** (for relatively thick-walled silos). However, not in the relevant European normative documents (EN 1993-1-6, 2007; EN 1993-4-1, 2007) nor in the recommendations of the European Convention for Constructional Steelwork (ECCS, 2008), there are currently calculation rules available for the design of locally supported stiffened cylindrical steel silos subjected to meridional compression. These documents only provide a general applicable framework and methodology with general concepts, rules, guidelines, and commentary. The design methods are (1) the stress design approach, (2) the MNA/LBA approach, and (3) the GMNIA approach.

For the first method, the elasto-plastic strength is estimated by using stresses. When high stress gradients and stress concentrations occur in the structure, as is here the case, **much too conservative** predictions are obtained, making this method not suitable to use.

For the second method, two relatively simple numerical shell analyses (i.e. MNA and LBA) must be performed from which the elasto-plastic strength can be estimated on the basis of interaction (or buckling) parameters. However, these **interaction parameters** for meridional compression are currently **missing** in the normative document for locally supported stiffened cylindrical steel silos (EN 1993-1-6, 2007). Instead, the Eurocode proposes that the designer (1) makes an own appropriate conservative choice for the interaction parameters (by comparing the current problem with similar buckling problems), (2) switches to the more complex GMNIA approach (i.e. the third method), or (3) uses the default interaction parameters mentioned in the Eurocode for uniformly compressed unstiffened cylindrical steel silos (EN 1993-1-6, 2007; ECCS, 2008). In other words, none of the proposed alternatives seem to provide a satisfactory answer to the lack of interaction parameters.

A GMNIA calculation must be performed for the third method. This type of shell analysis is **relatively complex**, because the failure behaviour is influenced by geometric and material non-linearity and by geometrical (equivalent) imperfections. Furthermore, during the entire design process, **several important decisions** have to be taken such as the choice of an appropriate imperfection shape, the failure criterion, etc. However, the Eurocode and the ECCS documents only give general rules and guidelines to make an appropriate choice for these decisions. Consequently, the results largely depend on the designer decisions.

To conclude, the elasto-plastic strength estimate (and its conservatism) largely depends on the decisions and the effort of the design. Both depend, among other things, on the designer and on the method to follow, which is in turn related to the size (expressed in tonnes) and the complexity of the silo.

Experimental research and validation

For the above mentioned configurations of locally supported steel barrels, a FEM model was developed in Abaqus. Before this numerical model can be used with sufficient reliability for the prediction of the elasto-plastic failure load, the **numerical model is validated against experimental results** from destructive tests on scale models.

For the validation, geometrically and materially non-linear shell calculations (GMNIA) were performed of a 360 degrees model taking into account the real material behaviour (tensile tests), the real imperfections of the silo wall (imperfection scans), the connection of the bolted steel plate, and the real supporting boundary conditions.

By comparing the numerical results with the experimental results, it can be stated that after all a satisfying agreement was obtained and that the validation of the numerical model was successful.

Numerical research: parametric studies

The numerical study consisted of three mains parts: a mesh study, several parametric studies to explore the influence of boundary conditions and geometrical parameters, and an imperfection sensitivity study. Below, these parts will now be described.

Firstly, the **mesh study** confirmed the suitability of the **S8R5** shell element and demonstrated that a doubling of the default mesh size leads to minor changes in failure load (less than 1%). In other words, the results of the mesh convergence study exhibited **convergence** for the default mesh density. This combination of element type and mesh size was used for all subsequent numerical parametric studies.

Secondly, the influence of all boundary conditions and many geometrical parameters was investigated on the failure behaviour and load. Given the symmetrical nature of the cylinder (i.e. the geometry, the loading, and the imperfections), **symmetry** was applied to reduce the size of the model in circumferential direction. Furthermore, **boundary conditions** are imposed on the top edge, the lower edge, and the local supports of the cylindrical barrel to model the connection with the structure with its environment: the conical roof, the conical hopper, and the supporting columns/foundation, respectively. At first instance, **all geometrical parameters** were one by one investigated for their effects on the failure behaviour and load: the geometry of the cylindrical barrel, the U-shaped longitudinal stiffeners, the ring stiffeners, the engaged columns, etc. In this way, more insight was gained into the failure behaviour of locally supported silos. Afterwards, an **optimisation study** was performed to determine the most optimal configuration of U-shaped longitudinal stiffeners and engaged columns, which corresponds to the largest ratio of the failure load to the material added. For the first configuration, a relatively high and thin U-shaped longitudinal stiffener

with a large developed length (large circumferential width and smaller radial width) is preferred to maximally distribute the axial stresses in circumferential direction and consequently to maximise the failure load. For the second configuration, an intermediately high (the attached height is just below the critical height) relatively thin engaged column with a large developed length is preferred to maximise the failure load. Depending on the silo thickness and the column height, a larger or a smaller ratio of the radial width to the circumferential width is the best solution. For most cases, a large ratio of the radial width to the circumferential width is more suitable because of the increased moment of inertia of the column cross-section relative to the shell wall. For thick-walled silos combined with short columns, a square column is preferred with a relatively small eccentricity.

Finally, an **imperfection sensitivity study** was performed to investigate the influence of geometrical equivalent imperfections to the failure behaviour and load, because the elasto-plastic buckling load of a perfect structure is significantly reduced by the presence of small geometric and material imperfections in the cylindrical barrel, which cannot be avoided in practice. Different shapes (linear and non-linear buckling modes, post-buckling deformed shapes, and weld depressions), orientations (inwardly and outwardly oriented), and equivalent amplitudes (quality class A, B, and C) were considered in this study.

For the final study or the design rule study, a range was defined for all geometrical parameters and an inward weld depression type A with half-wavelength equal to linear elastic bending half-wavelength was picked out based on the results of the above parametric studies.

Numerical research: design rule study

For the final study, **capacity curves** were developed for a wide range of geometries using different types of shell analyses (i.e. LBA, MNA, GN(I)A, GMN(I)A) and an inward weld depression type A as imperfection shape. The relative slenderness of the structure was varied by changing the yield stress from very small to very large values.

Firstly, **all points with realistic yield stresses** (i.e. 235; 355; 460; 690; 960MPa) were plotted in a traditional χ- λ diagram (i.e. large scattered cloud of points) and compared with the current buckling curves for meridional compression mentioned in the Eurocode (EN 1993-1-6, 2007). This comparison revealed that a relatively good agreement was found between the smallest values of the dimensionless strength χ from the calculated dataset (calculated for locally supported silos) and the estimated characteristic/design values of the dimensionless strength χ (based on the buckling parameters in the Eurocode for uniformly supported silos, taking into account a partial coefficient on the resistance γ_{M1} of 1.10). Furthermore, a number of sets of interaction parameters were determined for which the corresponding interaction curves are fitting better to the lower bound of the scatter than the current interaction curves. However, all proposals have in common that, for most cases, a relatively **conservative result** is obtained for the strength χ (and thus load). This is the main disadvantage of the approach of

a **lower bound**.

Secondly, for each **individual capacity curve**, the interaction parameters (i.e. α_x, $\lambda_{x,0}$, β_x, and η_x) were determined which best approximate the shape of the capacity curve. A linearly varying interaction exponent η_x, combined with a squash limit slendernesses $\lambda_{x,0}$ which can be both negative and positive, results in the best agreement between the fitting capacity curve and the calculated capacity curve. The next step was to develop rules for the prediction of these interaction parameters as a function of the geometry. However, due to the large scatter and the (mixed) influence of different geometrical parameters, it is **not evident to predict the interaction parameters** (for meridional compression) by relating them to the geometrical parameters of a locally supported stiffened cylindrical steel silos and the adopted quality tolerance class.

Samenvatting

Inleiding en scope

Tegenwoordig zijn silo's alom aanwezig in allerlei toepassingen omdat grote volumes (droge) poedervormige, granulaire en bulkmaterialen relatief eenvoudig kunnen opgeslaan worden op een relatief beperkte (grond)oppervlakte. Zowel in de landbouw en de voedingsindustrie, als in de mijnbouw en industriële processen, heel wat van deze sectoren hebben de behoefte om **(bulk)materialen tijdelijk op te slaan** tussen verschillende stappen van het productieproces en tussen de productie en het transport, of omgekeerd.

In de praktijk hebben de meeste metalen silo's een **cirkelvormige doorsnede** en wordt de silo in een **verhoogde positie** geplaatst. Deze verhoogde positie krijgt dikwijls de voorkeur om de inhoud van de silo te kunnen ledigen in een transportsysteem. Om dit proces te vergemakkelijken moet er voldoende ruimte voorzien worden onder de silo door middel van **lokale steunpunten**, ofwel door steunkolommen ofwel door een verhoogd vloersysteem. Bijkomend worden in dit werk enkel silo's bestudeerd met een **vlakke stalen wand**.

Aangezien zulke silo's lokaal ondersteund zijn en ze voornamelijk belast worden door verticale drukspanningen ten gevolge van wrijving tussen het bulkmateriaal en de silowand, zullen er boven de discrete steunpunten lokaal hoge spanningspieken voorkomen. Deze spanningsconcentraties zijn nadelig en leiden tot vroegtijdig bezwijken van de silo door **plastisch vloeien, elastisch knikken of een combinatie van beide fenomenen**.

In dit werk wordt het bezwijkgedrag bestudeerd voor twee verschillende types van lokaal ondersteunde cilindervormige silo's. Bij de eerste configuratie wordt boven elke steunkolom een **U-vormige langsverstijver** aangebracht, in combinatie met een boven- en een onderring. Bij de tweede configuratie worden de **rechthoekige steunkolommen** langs de buitenzijde van de schaalwand **doorgetrokken** over een bepaalde afstand en worden er geen bijkomende ringverstijvers aangebracht. Het eerste type wordt gebruikt bij middelmatig grote tot grote silo's, terwijl het tweede type gebruikt wordt bij lichtere silo's. De manier waarop de beide types de steunpuntskracht overdragen naar de silowand is gelijkaardig: langs de hoogte waarop de langsverstijver/doorlopende steunkolom verbonden is met de schaalwand wordt de steunpuntsreactie via schuifspanningen geleidelijk overgedragen naar de schaalwand. Op die manier worden de axiale spanningen beter gespreid in de omtreksrichting van de schaalwand en worden de spanningsconcentraties sterk gereduceerd. Hierdoor kunnen veel hogere belastingsniveaus opgenomen worden door de schaalwand vooraleer bezwijken optreedt.

Probleemstelling

Het ontwerp van axiaal samengedrukte cilindervormige stalen silowanden wordt beheerst door de **knikgrenstoestand** (bij relatief dunwandige silo's) en de **plastische grenstoestand** (bij relatief dikwandige silo's). Het probleem is echter dat noch in de Europese normdocumenten (EN 1993-1-6, 2007; EN 1993-4-1, 2007) noch in de aanbevelingen van de European Convention for Constructional Steelwork (ECCS, 2008) rekenregels zijn opgenomen voor het ontwerp van lokaal ondersteunde verstijfde cilindervormige stalen silo's onderworpen aan meridionale samendrukking. Deze documenten geven enkel een algemeen geldend kader en methodologie met de uitwerking van algemene concepten, regels, richtlijnen en commentaar. De ontwerpmethodes zijn (1) de methode op basis van spanningen, (2) de MNA/LBA methode en (3) de GMNIA methode.

Voor de eerste methode wordt de elasto-plastische sterkte geschat op basis van spanningen. Bij structuren met hoge spanningsgradiënten en -concentraties, zoals hier het geval is, leidt deze methode tot **bijzonder conservatieve voorspellingen**. Bijgevolg is deze methode minder geschikt om te gebruiken.

Voor de tweede methode volstaat het om twee relatief eenvoudig numerieke schaalberekeningen (MNA en LBA) uit te voeren van waaruit de elasto-plastische sterkte kan voorspeld worden door gebruik te maken van **interactie- of knikparameters**. Deze parameters voor meridionale samendrukking zijn **momenteel niet beschikbaar in de Eurocode** voor lokaal ondersteunde verstijfde cilindervormige stalen silo's (EN 1993-1-6, 2007). In plaats daarvan stelt de Eurocode voor aan de ontwerper om ofwel (1) zelf een geschikte en conservatieve inschatting te maken van de interactieparameters (door het ontwerp te vergelijken met gelijkaardige ontwerpen), (2) over te schakelen naar de complexere GMNIA methode (= methode 3) of (3) om de standaardinteractieparameters uit de Eurocode te gebruiken voor uniform samengedrukte onverstijfde cilindervormige stalen silo's (EN 1993-1-6, 2007; ECCS, 2008). Met andere woorden, geen van de voorgestelde alternatieven lijkt een bevredigend antwoord te bieden op het ontbreken van interactieparameters.

Een GMNIA berekening moet uitgevoerd worden bij de derde ontwerpmethode. Dergelijke schaalberekening is **relatief complex** omdat het bezwijkgedrag beïnvloed wordt door geometrische en materiaal niet-lineariteit en door geometrische (equivalente) imperfecties. Bovendien moet de ontwerper tijdens het ontwerpen **verschillende belangrijke beslissingen** nemen, zoals de keuze van een geschikte imperfectievorm, een bezwijkcriterium, enz. Daar in de Eurocode en de aanbevelingen van de ECCS enkel algemene regels en richtlijnen verschaft worden om een geschikte keuze te maken voor de beslissingen, zullen de resultaten sterk afhangen van de beslissingen van de ontwerper.

Samengevat, de inschatting van de elasto-plastische sterkte (en het conservatisme van de

voorspelling) hangt grotendeels af van de genomen beslissingen en de inspanningen tijdens het onwerp. Beiden hangen af van zowel de ontwerper als van de ontwerpmethode, welke op hun beurt afhangen van de grootte (uitgedrukt in ton) en de complexiteit van de silo.

Experimenteel onderzoek en validatie

Voor de hierboven vermelde configuraties van lokaal ondersteunde stalen silo's werd een eindige elementenmodel opgesteld in Abaqus. Vooraleer het model als voldoende betrouwbaar kan bestempeld worden voor de voorspelling van de elasto-plastische bezwijkbelasting, dient het **numeriek model gevalideerd te worden met experimentele resultaten** afkomstig van destructieve proeven op schaalmodellen.

Voor deze validatie worden geometrisch en materiaal niet-lineaire schaalberekeningen (GMNIA) uitgevoerd op een 360° model. Dit model houdt verder ook rekening met het werkelijke materiaalgedrag (trekproeven), de werkelijke imperfecties van de schaalwand (scans van het schaaloppervlak), de verbinding met de geboute staalplaat en de werkelijke steunpuntsrandvoorwaarden.

Bij het vergelijken van de numerieke met de experimentele resultaten werd er vastgesteld dat de overeenstemming bevredigend was en de validatie van het numeriek model geslaagd.

Numeriek onderzoek: parameterstudies

Het numeriek onderzoek bestaat uit drie grote delen: een meshstudie, verschillende parameterstudies die de invloed onderzoeken van de randvoorwaarden en de geometrische parameters en tot slot een imperfectiegevoeligheidsstudie. Deze zullen hieronder één voor één behandeld worden.

Als eerste werd er een **meshstudie** uitgevoerd. Deze studie bevestigde de geschiktheid van het **S8R5** schaalelement en toonde aan dat een verdubbeling van de standaard meshgroottes leidde tot minieme wijzigingen van de bezwijkbelasting (minder dan 1%). Met andere woorden, de resultaten van de meshconvergentiestudie vertoonden **convergentie** voor de standaardmeshdensiteit. Deze combinatie van elementtype en meshdensiteit werd dan ook gebruikt voor alle daaropvolgende numerieke parameterstudies.

Vervolgens werd de invloed van alle randvoorwaarden en de geometrische parameters onderzocht op het bezwijkgedrag en -belasting. Daar de cilinder als axisymmetrisch kan beschouwd worden (zowel de geometrie, de belasting als de imperfecties), werd er **symmetrie** toegepast in de omtreksrichting van het model. Verder werden er **randvoorwaarden** gekoppeld aan de boven- en onderrand van de silo en t.p.v. de lokale steunpunten. Op die manier werd de verbinding met de niet-gemodelleerde omgeving in rekening gebracht, namelijk de verbinding met het conisch dak, de conische trechter en de steunkolommen/fundering. Daarna werd het bezwijkbedrag onderzocht door **alle**

geometrische parameters één voor één te variëren. Op die manier werd inzicht verkregen naar het bezwijkgedrag bij dergelijke lokaal ondersteunde silo's. Op basis hiervan kon vervolgens een **optimalisatiestudie** uitgevoerd worden om de meest optimale configuratie te bepalen voor de U-vormige langsverstijvers en de doorlopende steunkolommen. De meest optimale configuratie wordt gekenmerkt door een zo hoog mogelijke verhouding van de bezwijkbelasting op de toegevoegde hoeveelheid materiaal. Bij de eerste configuratie gaat de voorkeur naar een relatief hoge en dunwandige U-vormige langsverstijver met een grote ontwikkelde lengte (grote omtreksbreedte en beperkte radiale breedte) om de spanningen maximaal te spreiden in omtreksrichting en zo de bezwijkbelasting maximaal te verhogen. Bij de tweede configuratie gaat de voorkeur naar een middelmatig hoge (bevestigde hoogte net onder de kritieke hoogte) en dunne doorlopende kolom met een grote ontwikkelde lengte om de bezwijkbelasting maximaal te verhogen. De beste oplossing voor de verhouding van de radiale breedte op de omtreksbreedte hangt af van de silodikte en de kolomhoogte. Meestal is een grote verhouding van de radiale breedte op de omtreksbreedte het meest geschikt, door het grotere traagheidsmoment van de dwarsdoorsnede t.o.v. de schaalwand. Bij dikwandige silo's gecombineerd met korte kolommen, krijgt een vierkante kolom met een relatief beperkte excentriciteit de voorkeur.

Tot slot werd er een **imperfectiegevoeligheidsstudie** uitgevoerd om de invloed van geometrische equivalente imperfecties op het bezwijkgedrag en -belasting te bestuderen. Deze studie is belangrijk omdat de elasto-plastische knikbelasting van een perfecte structuur sterk gereduceerd wordt door de aanwezigheid van kleine geometrische en materiaal imperfecties in de schaalwand, dewelke in de praktijk niet te vermijden zijn. In deze studie werden verschillende imperfectievormen (lineaire en niet-lineaire knikmodes, vervormingspatronen na bezwijken en lasimperfecties), oriëntaties (inwaarts en uitwaarts georiënteerd) en equivalente amplitudes (kwaliteitsklasses A, B en C) beschouwd.

Voor de ontwerpregelstudie werd op basis van de resultaten van de hierboven besproken parameterstudies voor elke geometrische parameter een range vastgelegd en werd een inwaartse lasimperfectie type A als imperfectievorm gekozen met als halve golflengte de lineaire elastische halve buigingsgolflengte.

<u>Numeriek onderzoek: ontwerpregelstudie</u>

Voor de ontwerpregelstudie werden **capaciteitscurves** opgesteld voor een groot aantal geometrieën met behulp van verschillende types van schaalberekeningen (LBA, MNA, GN(I)A, GMN(I)A) en een inwaartse lasimperfectie type A als imperfectievorm. De relatieve slankheid werd gevarieerd door het veranderen van de vloeigrens van heel kleine tot heel grote waarden.

Als eerste werden **alle punten met realistische vloeigrenzen** (235; 355; 460; 690; 960MPa) als een puntenwolk geplot in een χ- λ diagram om vervolgens te kunnen vergelijken met de

huidige knikkrommes voor axiale samendrukking vermeld in de Eurocode (EN 1993-1-6, 2007). Deze vergelijking bracht aan het licht dat een relatief goede overeenstemming gevonden wordt tussen de kleinste waarden van de dimensieloze sterkte χ uit de berekende dataset (berekend voor lokaal ondersteunde silo's) en de geschatte karakteristieke waarde / rekenwaarde van de dimensieloze sterkte χ (op basis van de knikparameters in de Eurocode voor uniform ondersteunde silo's, rekening houdend met een partiële veiligheidscoëfficiënt op de weerstand γ_{M1}van 1.10). Verder werden er ook een aantal sets van knikparameters afgeleid welke beter fitten aan de ondergrens van de puntenwolk dan de huidige knikkrommes. Al deze voorstellen hebben gemeen dat voor de meeste gevallen **relatief conservatieve resultaten** verkregen worden voor de sterkte χ (en dus ook de belasting), wat meteen ook het belangrijkste nadeel is van de benadering met een **ondergrens**.

Ten tweede werden de interactieparameters (α_x, $\lambda_{x,0}$, β_x en η_x) bepaald voor **elke individuele capaciteitscurve** waarbij de parameters genomen worden die de vorm van de berekende curve het best benaderen. De beste overeenstemming tussen de gefitte en de berekende capaciteitscurves werd bekomen door gebruik te maken van een lineair variërende interactie-exponent η_x in combinatie met een grensslankheid $\lambda_{x,0}$ (grens waarbij het materiaal wordt opgestuikt en geen knik optreedt) die zowel negatief als positief kan zijn. De volgende stap was het ontwikkelen van regels om de interactieparameters te kunnen voorspellen in functie van de geometrie. Door de grote spreiding en de (gecombineerde) invloed van heel wat geometrische parameters, is het **niet evident om de interactieparameters** (voor meridionale samendrukking) **te voorspellen** door ze te relateren aan de geometrische parameters van een lokaal ondersteunde verstijfde cilindervormige stalen silo en de gekozen tolerantie kwaliteitsklasse.

CHAPTER 1

Problem statement and scope of the thesis

1 Introduction

When was the last time you saw a silo in the landscape?

Probably, it was today. Whether you were driving through an industrial park, a port, a city, or the countryside, silos are placed everywhere (industrial sites, construction sites, farms, etc.) for the temporary storage of a wide range of bulk solids and liquids. Silos are not a recent discovery. On the contrary, silos were used throughout history by different cultures for the same reason they are used nowadays. An astounding example can be admired in Raqchi (Peru, South America) dating from the Inca culture ($1438 - 1533$) (See Fig. 1-1). To gain control over the expanding Inca empire (up to $2000000 km^2$ in 1527) and its neighbours, the Incas started in mid-fifteenth century with the construction of an extensive network of Inca roads (called Capaq Ñan in Quechua). In approximately 125 years, the Incas built a 40000 kilometre long road system. At different locations, control points were constructed for defensive, administrative, religious, and commercial purposes. For the last two purposes, in each provincial centre, hundreds of circular storehouses or Qullqas were built row after row out of fieldstones from the nearby mountains. These 10 metre diameter structures were used for the storage of food and grains, such as corn and quinoa.

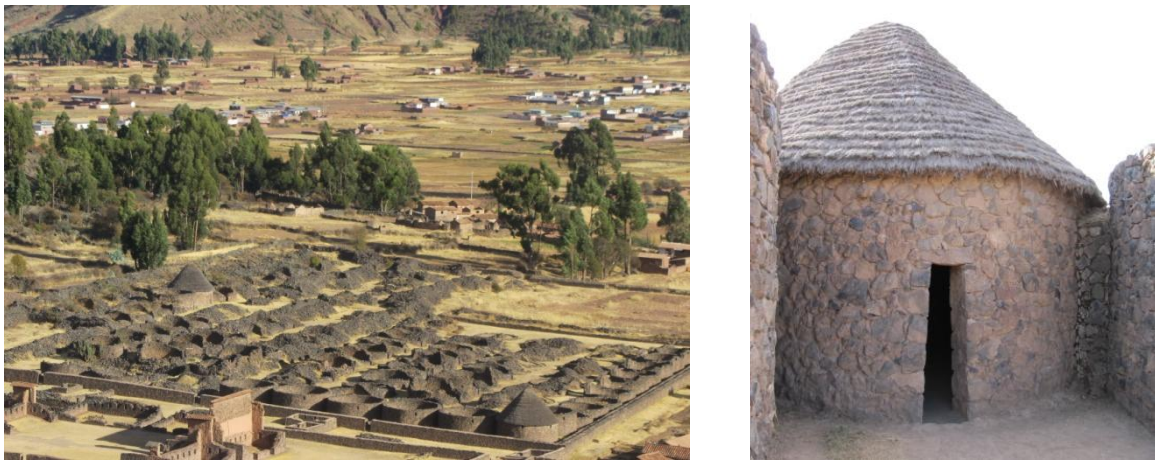

Fig. 1-1 Inca silos.

Nowadays, silos have become an essential component in many applications since they have some important advantages. Indeed, upward silos require less floor space compared to the large volume of stored material (See Fig. 1-2). Frequently, cylindrical barrels are placed at a larger height to be able to easily discharge the silo contents into a transport system. More information about this subject is given later in this work.

Fig. 1-2 Silo battery.

As shown in Fig. 1-3, they are used during different stages of all kinds of manufacturing processes, both for short and for long periods. First, they are found along important trade routes for the supply and distribution of bulk solids, waiting for further transportation by train, ship, or truck. Second, they are used as buffer or as intermediate storage between successive transports and production processes, ranging from large (petro)chemical companies to small concrete plants. Other applications of silos are the mixing (of two or more different components) or the homogenizing (to make uniform in consistency) of bulk solids.

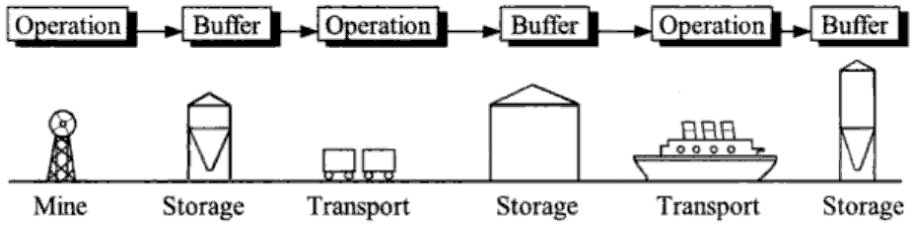

Fig. 1-3 Application of silos (Rotter, 2001a).

To conclude, silos are used for a wide range of applications, for example in mining, chemical processing, food processing, agriculture, etc. Consequently, the contents of the silo also vary strongly. Generally, a silo contains (dry) powdered and granular materials and bulk materials, such as ores, coal, gravel, sand, pellets, cement, lime, ash, seed, grains, sugar, flour, etc.

2 Scope of the thesis

The silo structure itself can be found in a variety of shapes, dimensions, and materials. The most widely used cross-sections are circular and rectangular. The capacity of a silo varies from a few tons up to more than a thousand tonnes. They are fabricated from a wide range of materials such as concrete, steel, stainless steel, carbon steel, aluminium, plastics (e.g. polyethylene), etc.

This work focuses on one specific category of silos:

- Locally or discretely supported silo;
- Flat steel wall;
- Circular cross-section;
- Storage of bulk solids.

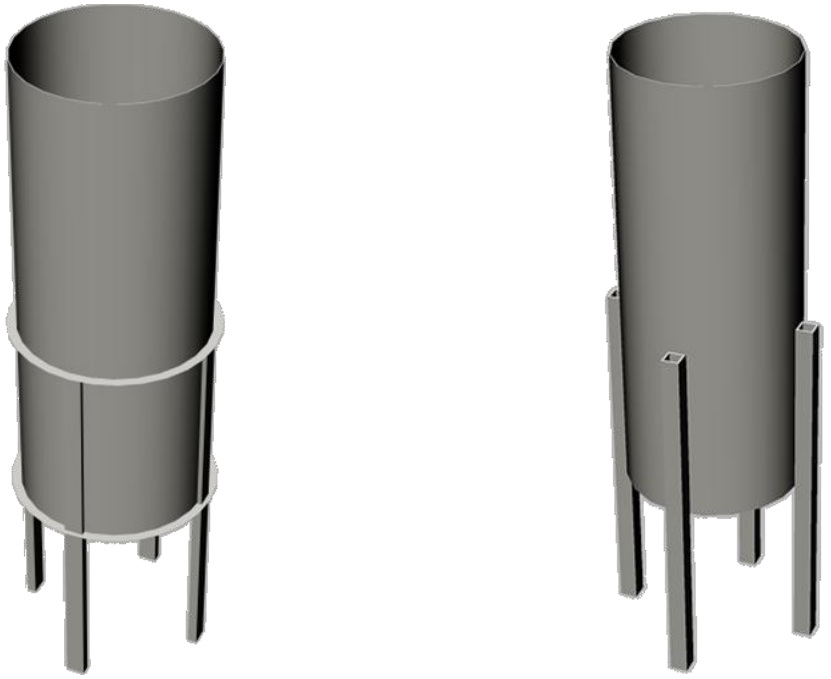

(a) Type 1 - U-shaped longitudinal and ring stiffeners. (b) Type 2 - Engaged columns.

Fig. 1-4 Configurations investigated here.

Two types of locally supported cylindrical steel structures are considered. The first type is a barrel stiffened with U-shaped stiffeners above the column supports, in combination with a lower and an upper ring (See Fig. 1-4 (a)). This type is used for intermediate to large silos, while the second type is used for lighter structures. The latter consists of rectangular shaped supporting columns which are engaged along a specific distance to the external side of the shell wall, without the presence of ring stiffeners (See Fig. 1-4 (b)).

3 Problem statement

When a metal silo structure is filled with bulk solids, the shell wall is mainly subjected to vertical (compressive) pressures which are caused by friction between the bulk material and the silo wall. As a result of this force introduction in the shell wall, the decisive design state for such a structure is the **buckling limit state** (and to a lesser extent the **plastic limit state** for very thick-walled silos). However, for the assessment of the buckling limit state of axially compressed **locally supported stiffened** cylindrical steel silos, there are **currently no calculation rules available** in the relevant Eurocode (EN 1993-1-6, 2007). The European standard only provides a general applicable framework and methodology with general concepts, rules, and guidelines for the design of metal shell structures. Supplementary to and compatible with the rules given in the Eurocode, the recommendations of the European Convention for Constructional Steelwork contain a full commentary on these rules (ECCS, 2008). Where possible, explanatory material, worked examples, and additional rules are provided in the ECCS document.

Regardless of the method used, the designer has to make several important decisions during the entire design process. These decisions have a significant impact on the design, and can lead to a very safe (conservative) buckling strength as well as to an unsafe buckling strength. In other words, very different results can be obtained due to the designer decisions and the design effort (i.e. the detail of the calculations). Both depend, among other things, on the method to follow, which is in turn related to the size (expressed in tonnes) and the complexity of the silo (i.e. the supporting and the loading conditions). Three methods are described in the Eurocode: (1) the stress design approach, (2) the MNA/LBA approach, and (3) the GMNIA approach. For structures with high stress gradients, such as locally supported and stiffened silos are, the first method leads to much too conservative results, making this method less appropriate. The second and third approach are better methods, because more economical results are obtained due to the use of more accurate numerical analyses.

For the designer, both methods have their pros and cons. The GMNIA approach is the most extensive and complex method of the two, because of the complexity of the numerical simulations. Indeed, a GMNIA shell calculation is a geometrically and materially non-linear shell analysis taking into account imperfections. Furthermore, a large number of decisions has to be taken, such as the choice of an appropriate imperfection shape, failure criterion, etc. In contrast, only two relatively simple numerical calculations must be executed for the MNA/LBA approach, respectively a materially non-linear analysis MNA and a linear perturbation analysis LBA. Consequently, this method is much easier to perform. However, due to **a lack of buckling parameters** available, the designer must either (1) make an appropriate conservative choice for the buckling parameters (by comparing the current problem with similar buckling problems), (2) switch to the more complex GMNIA approach, or (3) use the default and much too conservative interaction parameters mentioned in the

Eurocode for **unstiffened** cylindrical steel silos subjected to **uniform axial compression** (EN 1993-1-6, 2007; ECCS, 2008).

Despite the existence of a fully developed framework for the design of metal silos, the use of the simplest MNA/LBA approach is curbed due to a lack of buckling parameters. As a consequence, the complex GMNIA approach is generally required to obtain sufficiently accurate results.

4 Objectives

At first instance, this work seeks to **investigate and understand the elasto-plastic failure behaviour** (i.e. elastic buckling and/or plastic yielding) of the above mentioned types of locally supported cylindrical steel silos subjected to axial compression. This objective will be achieved by means of **numerical simulations** with the finite element package Abaqus. For these simulations, a validated numerical finite element model is used, which is **validated against experimental results on scale models**.

However, the investigation is complicated by **a wide range of parameters which are affecting the buckling strength**, making it challenging to fully understand the behaviour. Indeed, the elasto-plastic behaviour is influenced by many geometrical parameters, the material behaviour, the boundary conditions, etc. Furthermore, a silo structure exhibits a strong non-linear behaviour before, during, and after failure: both material non-linearity (plasticity) as well as geometrical non-linearity (pre-buckling deformations) play an important role. Secondly, the buckling strength is further reduced by the presence of unavoidable deviations relative to the perfect silo geometry and other types of geometric imperfections (e.g. variations in nominal thickness) and material imperfections (such as variations of the material properties, residual stresses (near welds), etc.). In practice, it is difficult to estimate these imperfections accurately during the design stage. Hence, in the Eurocode, the possibility exists to replace the influence of all kinds of imperfections by "equivalent" geometric imperfections. However, it remains very difficult to make an appropriate choice for the set of parameters that define the (equivalent) imperfection: a shape, a location, an amplitude (related to the fabrication tolerance quality class), and an orientation have to be chosen. Finally, there are different buckling criteria available and a wide range of shell analyses, each with their characteristics, importance, and meaning. To conclude, since the elasto-plastic behaviour is influenced by a large number of parameters and the different parameters affect each other's influence to the failure behaviour, it becomes more difficult to explore the failure behaviour of the complete spectrum of silos and to map the influence of all parameters to the failure behaviour.

Afterwards, an attempt is made to **deduce new interaction parameters** and to formulate a design rule. In this way, we aim to fill the gap of the available buckling parameters, as this

would promote and support the use of the easiest MNA/LBA approach in the future.

5 Structure of the thesis

After the current introductory **Chapter 1**, a state-of-the-art is presented in **Chapter 2** on all aspects that are covered in this work. First, general information is given about silos and its supporting arrangements, the failure behaviour in shell structures, and the design procedure. The emphasis of the design procedure is on the plastic limit state (LS1) and the buckling state (LS4), according to (EN 1993-1-6, 2007). Next, a few fundamental aspects are described in detail that are inextricably involved in the design of an axially compressed silo: geometric and material non-linearity, imperfections, and loading conditions. In the last part, more detailed information is given about supporting and stiffening configurations in practice.

Chapter 3 describes the determination of the geometry of the scale models, the fabrication of the scale models, and the experimental setup. Subsequently, a full description is given of the finite element model and the finite element software Abaqus.

The experimental results are presented and discussed in **Chapter 4**, and the results are used for the validation of the numerical model.

Chapter 5 addresses the extensive numerical research, which is the main part of this work. Using the validated numerical model, different parametric studies are conducted to investigate the influence of most parameters on the failure behaviour of the structure. At the end of each parametric study, a range is defined for each parameter for the final study.

Chapter 6 is the final study and deals with the determination of new buckling parameters of capacity curves calculated for a wide range of geometries and different quality classes. Furthermore, the dataset is compared with the lower bound estimate given in the Eurocode (EN 1993-1-6, 2007).

Finally, the entire structure of this work is illustrated in Fig. 1-5 in the form of a flow chart.

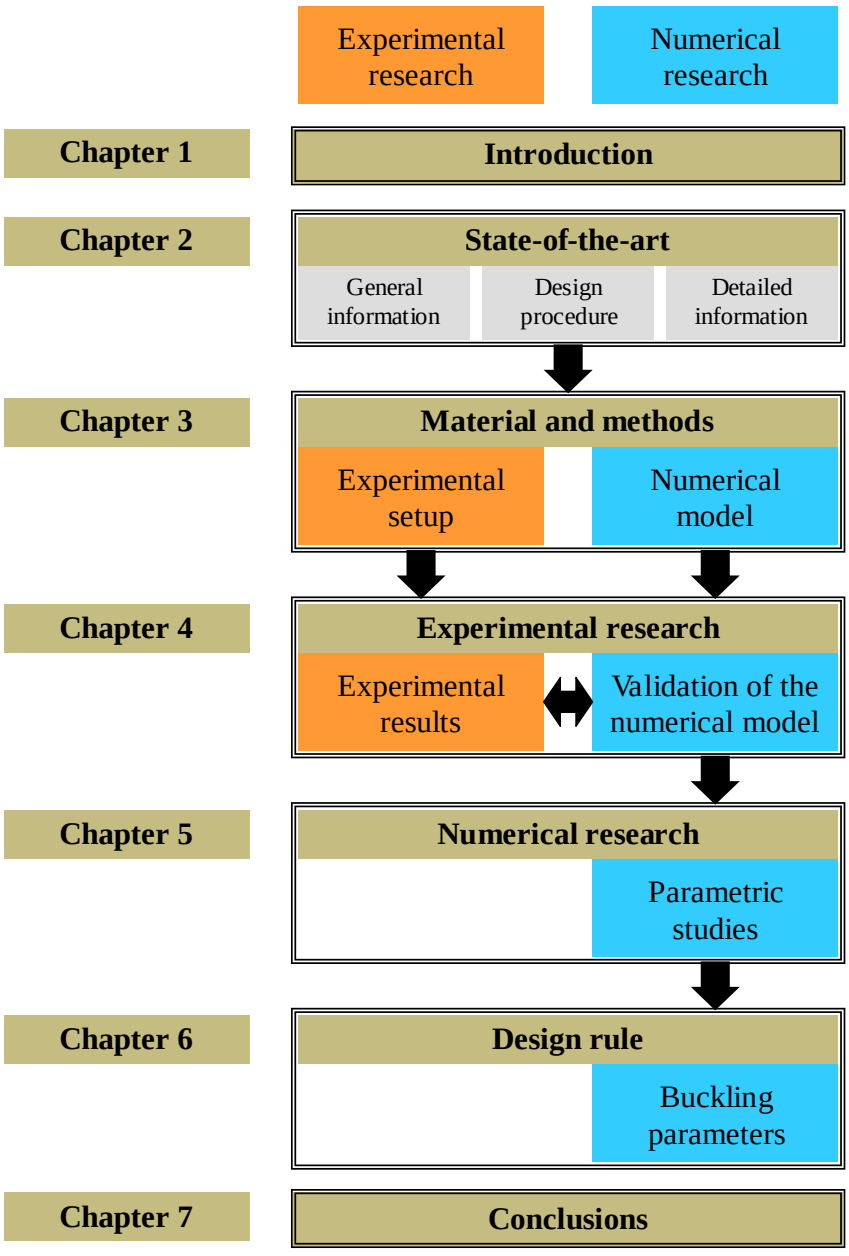

Fig. 1-5 Flow chart of PhD thesis.

CHAPTER 2

State-of-the-art

In this chapter, a state-of-the-art is given on locally supported cylindrical steel silos (used for the storage of bulk solids) and their design. In the first part, a general introduction is given on the different types of silos and supporting arrangements, the failure behaviour and the general design procedure. Subsequently, the methodology and the requirements are discussed in detail for the design of axially compressed cylindrical steel walls against the ultimate limit states: (1) plastic limit and (2) buckling. For metal silos subjected to axial compression, these limit states are decisive for the design process. The second part covers some particularly important issues, such as the influence of geometric and material non-linearity to the buckling strength, the challenging task to choose a disadvantageous imperfection, and the loading conditions due to the bulk solids. In the third and last part, a detailed overview is given on supporting and stiffening configurations in practice.

PART I.

1 Silos and supporting arrangements

The content of the silo

For different industries, steel silos are used for the storage (both for short and long period) of a wide range of bulk solids (such as grain, seed, coal, lime, and many other granular or powdery material) during different stages of the manufacturing process. The reason why in this work only silos are investigated for the storage of solids are the differences in loading conditions, behaviour between the content and the silo wall, and design requirements compared to silos filled with liquids. Below, a brief explanation is given of the different behaviour between solids and liquids.

When considering the resistance of a cylinder against compressive buckling, a rule of thumb is that a pressurized cylinder is more resistant than an unpressurized one. This difference cannot be ignored and is more important for bulk solids than for liquids or gases.

A solid will exert a normal pressure and frictional traction on the silo wall. Moreover, these components are often asymmetric in circumferential direction during the lifetime of a silo, for example due to eccentric filling or discharge. Before and during buckling, the normal pressure

will increase when the wall deforms inwardly and decrease in outward direction, which is an important restriction. In contrast, liquids (or gases) will exert only a normal pressure on the silo wall, which is symmetrical in circumferential direction. As the silo wall deforms, this pressure remains unchanged.

From this, it can be decided that the (failure) behaviour is significantly different between a silo filled with solids and liquids.

The silo and its components

Why steel silos? (versus concrete silos)

- Geometry Steel silos can be less tall, but can have larger diameters compared to concrete silos.
- Design Concrete silos have relatively thick walls and are weakly reinforced. As a consequence, the dominating factor of the design process is the normal pressure of the bulk solids to the concrete wall. In contrast, much thinner metal silo walls are sensitive to buckling and the compressive stresses mainly caused by solid friction against the silo wall (Rotter, 2001a).
- Manufacturing Steel silos are manufactured in a factory, which benefits the quality control of the entire production process and the quality of all parts. Furthermore, there are fewer uncertainties which could delay the manufacturing process, such as the weather conditions and the concrete delivery on the site.
- Construction A lower bearing capacity is required for the lighter steel silos. As a consequence, the foundation can be established lighter and cheaper, and a smaller bearing capacity of the soil is required. One of the main advantages associated with steel structures is the relatively simple erection and the large speed of construction (e.g. no placement of formworks or rebar).
- Cost The storage capacity per euro generally is larger for steel silos.

In practice, steel silos mostly have a circular cross-section and may be ground-supported (Fig. 2-1 (a)) or placed in elevated position (Fig. 2-1 (b)). Typically, an elevated silo is preferred with a hopper under it because of the necessity to discharge the content by gravity flow into trains, trucks, or other conveying systems (See Section 7.1). To facilitate the emptying process, sufficient space must be provided under the silo by means of local supports, either by columns or by an elevated floor system.

A typical elevated silo consists of a conical roof, a cylindrical barrel (i.e. the main part), a conical hopper, and a supporting arrangement. A stiffening ring is usually provided at the transition, which is the junction between the vertical wall and the hopper.

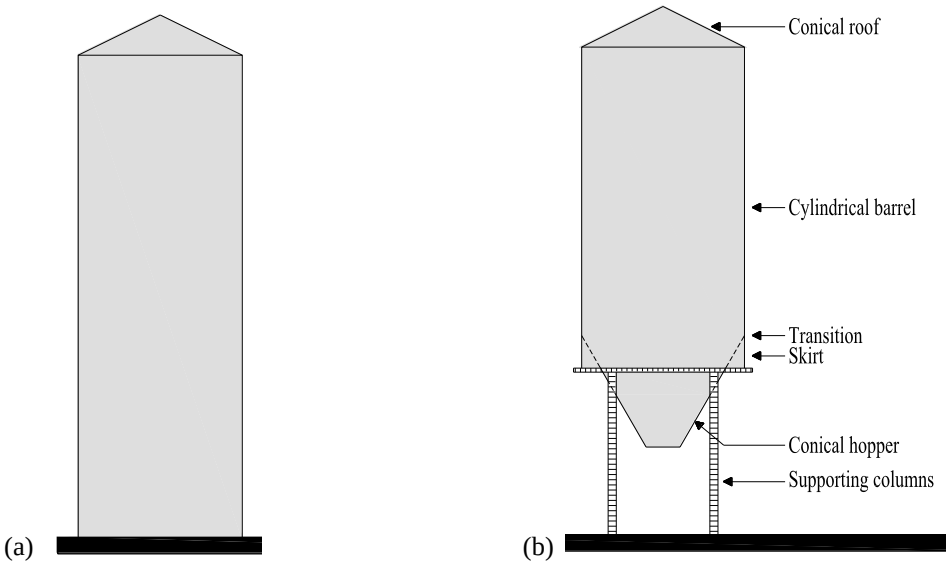

Fig. 2-1 Ground-supported silo (a) versus elevated silo (b).

Steel silos are manufactured in a typical way. At first instance, a bending machine is used to give the flat steel panels a curvature in one direction (See Fig. 2-2 (a)). Afterwards, the cylindrical barrel is usually fabricated by welding together a large number of curved panels by many short meridional welds (panel → circular strakes) and continuous circumferential welds (circular strakes → cylindrical barrel) (See Fig. 2-2 (b)). Other possibilities are bolting, riveting, or screwing the individual panels. These connection methods are less commonly used and will not be discussed in this work.

(a) Bending machine. (b) Silo with patterned welds.

Fig. 2-2 Fabrication of a welded steel silo.

Furthermore, since the shell wall is composed of horizontal strokes, it is possible to gradually decrease the wall thickness of the strokes in upward direction (depending on the stresses). In this way, a more economical solution can be obtained, especially compared to a(n) (un)stiffened silo wall with a constant thickness over its entire height.

Supporting arrangements

In practice, many different variants are possible to support an elevated silo structure. A frequently used method is the use of a limited number of columns (with a limited circumferential width). In such cases, the total load of the silo has to be transferred to a limited number of supports, causing locally high axial compressive stress concentrations in the silo wall above the supports. These increased stresses may lead to premature failure of the silo due to excessive yielding and/or local buckling in the regions above the supports if not designed properly.

The choice for the supporting arrangement depends largely on the magnitude of the local support forces which are introduced into the lower edge of the shell wall. In the classification below, a distinction is made between light silos (Fig. 2-3) and medium to heavy silos (Fig. 2-4).

A first solution is to terminate the columns below the transition junction (See Fig. 2-3 (a) and (b)). The difference between these unstiffened silos is the silo wall thickness: the first alternative has a constant wall thickness, while the second alternative has an increased wall thickness at the bottom course. Other possibilities are the engagement of the supporting columns over a short distance (See Fig. 2-3 (c)) or the connection of the columns by means of brackets to the cylindrical silo wall (See Fig. 2-3 (d)) (Rotter, 2001a; 2004).

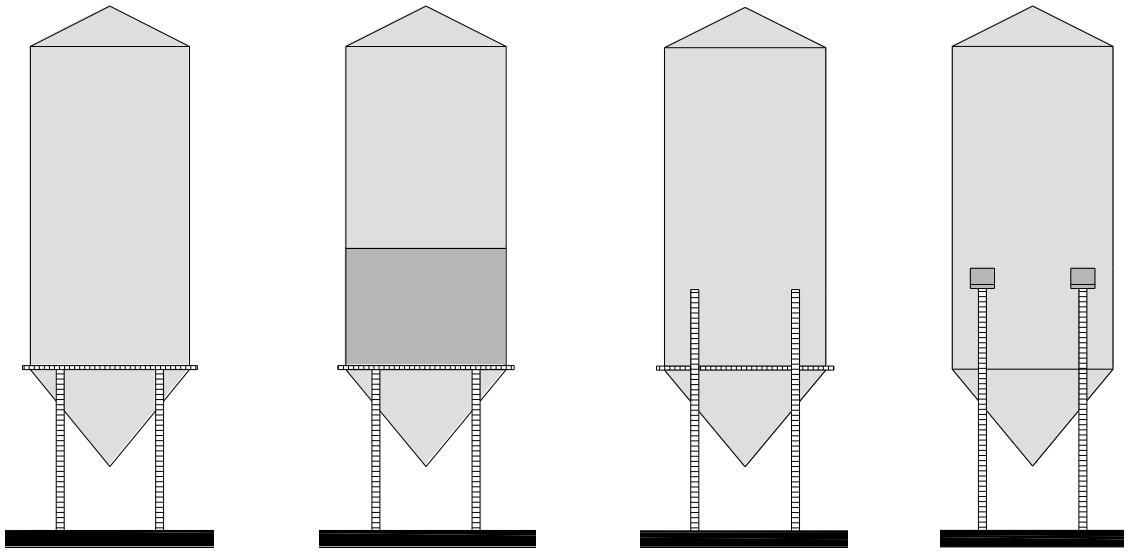

(a) Terminating columns with ring.

(b) Terminating columns with ring and increased wall thickness at the bottom.

(c) Engaged columns.

(d) Bracket supported silo.

Fig. 2-3 Supporting arrangements for locally supported light silos.

For such light silos, a traditional supporting ring beam is too expensive and a simple transition ring may be sufficient (Brown and Nielsen, 1998).

For the medium to heavy silos, either a stiff ring beam can be provided at the lower edge (See Fig. 2-4 (a)) (Topkaya and Rotter, 2011), a double ring can be provided just above the supporting columns (Topkaya and Rotter, 2013) (See Fig. 2-4 (b)), columns or stiffeners can be extended to the eaves (See Fig. 2-4 (c)), or partial-height longitudinal stiffeners can be used above the local supports, whether or not in combination with an upper ring stiffener (See Fig. 2-4 (d)) (Rotter, 2001a).

For the first alternative, Topkaya developed a ring beam stiffness criterion to determine which ring beam stiffness is necessary to reduce the peak stresses above the discrete supports and to redistribute the axial membrane stresses in circumferential direction to achieve a particular degree of uniformity. To reach that goal, the ring beam should be much stiffer than the shell wall, which also has a relatively large stiffness in its own plane (Rotter, 1985a; Topkaya and Rotter, 2011). For the second alternative, the same author determined the ideal location of the secondary or intermediate ring stiffener (i.e. its height) to create a situation where the axial membrane stresses are completely uniformly distributed in circumferential direction (Topkaya and Rotter, 2013). The last alternative owes its outstanding characteristics to the combined performance of the stiffener and the silo wall: the stiffeners carry a significant part of the vertical load (depending on the relative stiffnesses of the stiffeners and the silo wall), and are restrained against buckling by their attachment to the silo wall, resulting in an economic alternative for locally supported steel silos (Rotter, 2011).

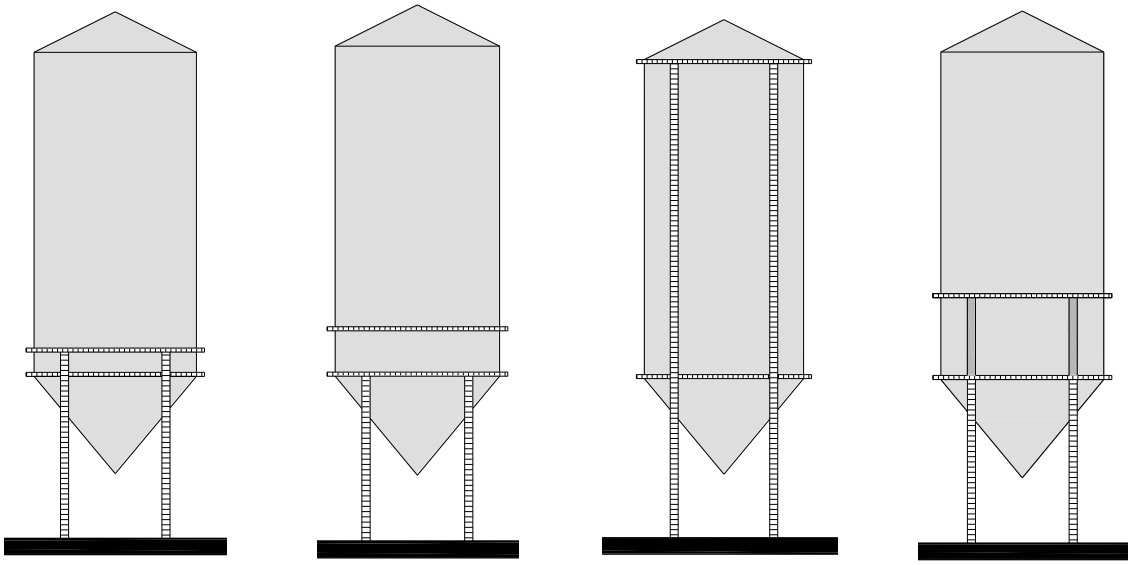

(a) Columns to bottom + heavy ring beam.

(b) Columns to bottom + double ring.

(c) Columns or stiffeners to eaves.

(d) Columns to bottom + partial-height longitudinal stiffeners + double ring.

Fig. 2-4 Supporting arrangements for locally supported medium to heavy silos.

In Fig. 2-5, several alternatives of the connection between the supporting column and the bottom of the cylindrical barrel are displayed for larger silos (Rotter, 2001a). The supporting

column can be placed eccentrically or concentrically relative to the silo wall, and can be engaged to the silo wall (a), to the skirt (b) or can terminate beneath the skirt (c).

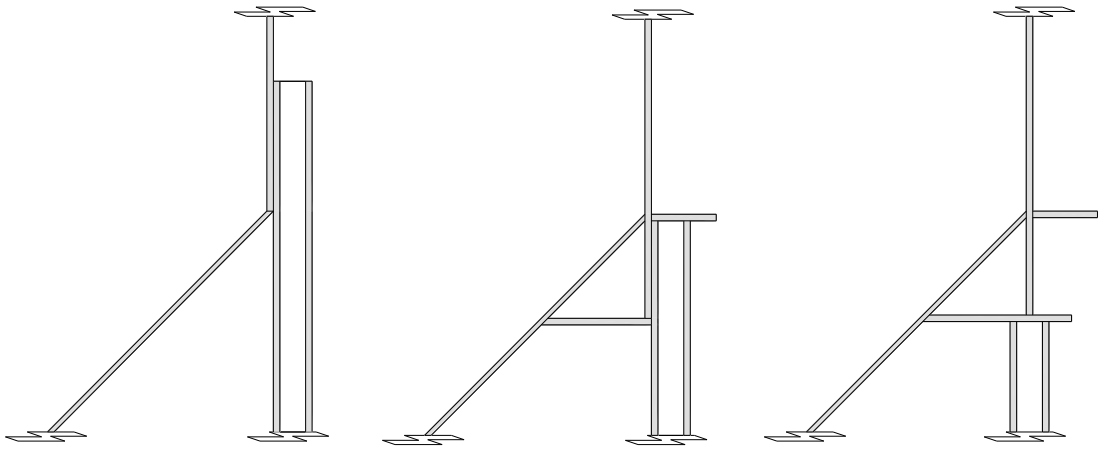

(a) Eccentric column engaged to silo wall.

(b) Triangular box with eccentric column engaged to skirt.

(c) Triangular box with concentric column beneath skirt.

Fig. 2-5 Connection between the supporting column and the silo wall.

It is important to mention that in practice there are much more configurations than those presented in Fig. 2-3, Fig. 2-4, and Fig. 2-5. In Sections 8 and 9 of this chapter, more detailed information is given about practical supporting and stiffening configurations. Therefore, it was at the beginning of the research necessary to define a limited number of configurations to be able to examine their behaviour in detail.

In this work, the buckling behaviour of two of the above mentioned alternatives will be investigated: (1) a light silo with engaged columns ((See Fig. 2-3 (c)) and (2) a medium-heavy silo stiffened with U-shaped partial-height longitudinal stiffeners above each supporting column and ring stiffeners (See Fig. 2-4 (d)). The second configuration arises from earlier research conducted by Vanlaere, in which the failure behaviour was investigated of axially compressed steel silos on local supports stiffened with two rectangular shaped partial-height longitudinal stiffeners above each supporting column and ring stiffeners (Vanlaere, 2006). Both configurations have the same goal to gradually transfer the ground reaction force into the silo wall by shear, spreading the load better in circumferential direction, reducing the peak stresses near the supports.

A simplified illustration of this concept is displayed in Fig. 2-6. Along the attached height of the column/stiffener, the ground reaction force disperses into the silo wall in a zone defined by a 30° slope to the vertical (Brown and Nielsen, 1998). At the bottom of this region, very high stresses can be found within a relatively small region (i.e. the support width). In contrast, much smaller stresses can be found over a relatively wide zone as one looks higher.

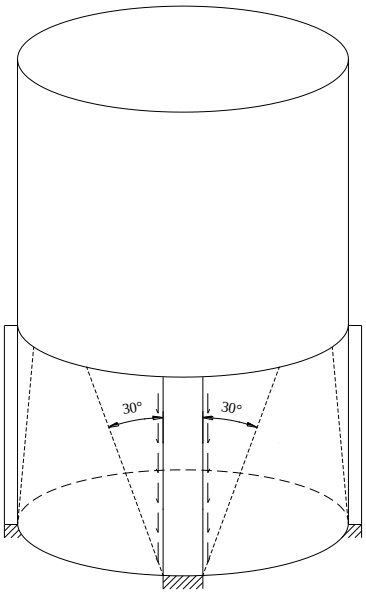

Fig. 2-6 Simple representation of the transfer of the ground reaction force from an engaged column to the silo wall by shear (Brown and Nielsen, 1998).

To conclude, by assisting with the introduction of local loads, the yielding and buckling resistance can be improved by adding a minimum amount of material in the region of elevated stresses, more specifically in the vicinity above the local supports. While engaged columns are an economical way for smaller silo structures, stringer stiffeners will be used for larger silos.

2 Failure behaviour in shells

Silo failures

Compared to other industrial structures, silos fail relatively frequently, resulting in a local damage or a complete structural collapse. This can be attributed to the lack of structural redundancy and alternative paths for the redistribution of stresses within the structure after a local failure occurs (Dogangun, 2009). Such event not only involves the loss of contained material, but also considerable expenses (e.g. cleanup, replacement costs, adjacent facilities, etc.) and possible injury or loss of life. Each year, hundreds of agricultural and industrial silos, bins, and hoppers show some degree of failure, caused by shortcomings in design, construction, usage, and/or maintenance (Carson, 2001). Possible causes of failure due to design errors of the cylindrical barrel are a wrong estimate of the material properties and/or flow properties (e.g. load variations during filling and emptying of the silo contents), poorly chosen design criteria or procedure, etc. (Carson, 2001).

Table 2-1 gives an overview of the most important losses of function in silos (Rotter, 2001a). During the design process, these issues should already be taken into account to prevent them. Firstly, arching or bridging (i.e. the formation of a cohesive arch above the outlet opening),

ratholing (i.e. the formation of a stable hole over the entire silo height in cohesive bulk solids), and incomplete cleanout should be prevented to avoid the flow ceases (See Fig. 2-10). Secondly, disturbing noises and unacceptable vibrations (i.e. silo shaking, quaking, and honking), caused by the discharge process, should also be avoided. Thirdly, segregation of the solids should be prevented for some bulk solids. At last, but most important for this work, collapse of the structure should be taken into account during the design. The failure conditions for collapse can develop by too high pressures in the silo wall mainly due to the geometrical conditions (e.g. local supports) or due to operating conditions (e.g. eccentric discharge). In what follows, the failure conditions for collapse will be discussed: (1) the plastic limit state and (2) buckling.

Table 2-1 Overview loss of function (Rotter, 2001a).

LOSS OF FUNCTION	CAUSES
Arching and ratholing	Solids properties + wall properties
Shaking, quaking, and honking	Solids properties + wall properties + flow pattern (during discharge)
Segregation	Solids properties + filling method + flow pattern (during discharge)
Collapse	Solids during filling, storage, and emptying ⇒ pressures on silo walls ⇒ stresses in silo structure ⇒ failure conditions

Ultimate limit states

According to (EN 1993-1-6, 2007), four different ultimate limit states must be verified during design of steel shells: (1) plastic limit, (2) cyclic plasticity, (3) buckling, and (4) fatigue. In this part, the first and the third state of loss of structural integrity will be discussed in detail, because these pertain to the scope of this work. In addition to plastic yielding and pure elastic buckling, a combination of these phenomena is also possible, which is called elasto-plastic buckling. The structural behaviour (before, during, and after failure) is affected by many factors, such as the geometry, the loading conditions, the boundary conditions, the material properties, and the (geometric) imperfections (ECCS, 2008).

Plastic limit state

The plastic limit is defined as "*The ultimate limit state where the structure develops zones of yielding in a pattern in such a way that its stability to resist increased loading is deemed to be exhausted. It is closely related to a small deflection theory plastic limit load or plastic collapse mechanism.*" (EN 1993-1-6, 2007). For axially compressed silos, possible locations for this failure phenomenon are the engaged columns, the silo wall, or the stringer stiffeners just above the local supports, and the vicinity of the stiffening configuration, since elevated

stresses appear in these regions.

In shells structures, the evaluation of yielding in a specific point can be done by using the 2D yield criterion of Tresca (Tresca, 1864) and von Mises (von Mises, 1913) (See Fig. 2-7). The combination of the axial stress σ_x and the circumferential stress σ_θ must be plotted on the graph and the location of that point must be compared with the yield surface (which depends on the yield stress σ_y) to determine whether or not the structure is yielding in that point. When the importance of material non-linearity increases (i.e. a smaller relative slenderness λ), a larger area must yield before the structure fails.

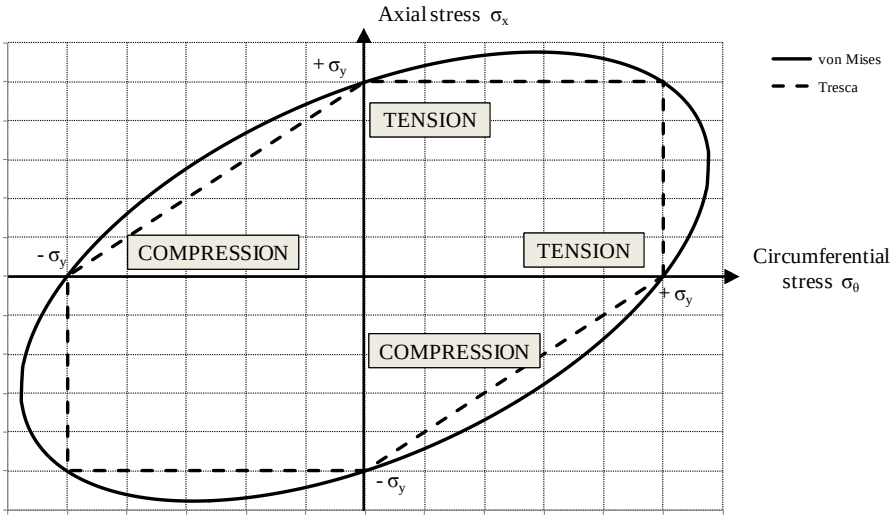

Fig. 2-7 Yielding surface of von Mises (ellipse) and Tresca (hexagon).

Buckling

Buckling is defined as "*The ultimate limit state where the structure suddenly loses its stability under membrane compression and/or shear. It leads either to large displacements or to the structure being unable to support the applied loads.*" (EN 1993-1-6, 2007). For silos subjected to axial compression, this is the most common failure mode due to the high meridional compressive stresses above the local supports and in the vicinity of the stiffening configuration. This failure mode usually controls the design process.

The buckling strength can be related to the elastic critical buckling stress σ_{cr}. This critical stress has been determined by (Timoshenko, 1910) for a perfect isotropic cylindrical shell subjected to a uniform axial compression and with classical boundary conditions and is given by Eq. (2-1). However, in practice, this stress cannot be achieved, but is used as a basis for the evaluation of the buckling strength.

$$\sigma_{cr} = \frac{E}{\sqrt{3 \cdot (1 - \nu^2)}} \cdot \frac{t}{R} = 0.605 \cdot E \cdot \frac{t}{R} \tag{2-1}$$

Where:

σ_{cr} the critical buckling stress [MPa];

E the Young's modulus [MPa];

ν the coefficient of Poisson [-];

t the cylinder thickness [m];

R the cylinder radius [m].

Two types of instability can be distinguished: (1) bifurcation buckling (BIF) and (2) snap-through buckling (ST). In Fig. 2-8, the typical load-displacement response (F versus w) is plotted for both instability phenomena. For both cases, as the load F increases, the stiffness will decrease and a stable non-linear equilibrium path (pre-buckling) is followed until the bifurcation point (BIF) or the limit point (ST) is reached. In this point, either the bifurcation load F_{bif} or the limit load F_{lim} is reached. From this point, the buckling and post-buckling behaviour is different and, therefore, will be discussed separately.

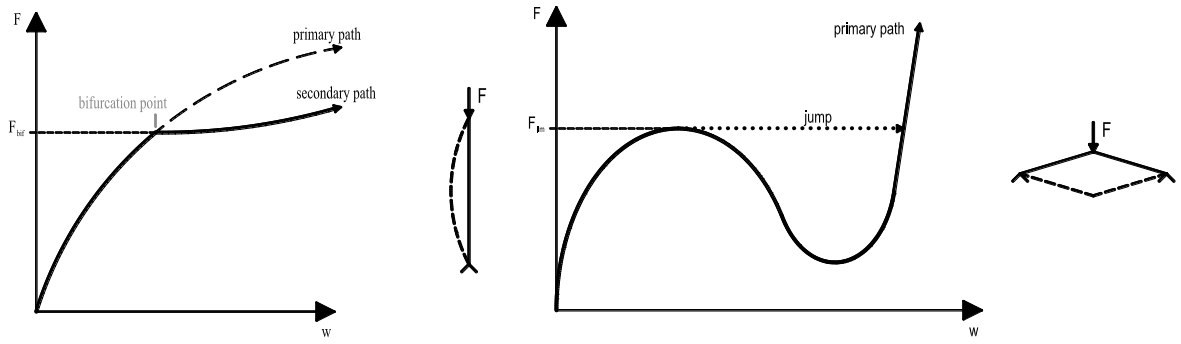

(a) Bifurcation buckling. (b) Snap-through buckling.

Fig. 2-8 Typical load-displacement response.

A bifurcation point is a point where two (or more) equilibrium paths intersect each other (See Fig. 2-8 (a)). In this point, the primary path becomes unstable, and the secondary path may be followed. After bifurcation, the post-buckling deformations (i.e. the buckling mode) are growing faster and are usually rather different from the pre-buckling deformations. In Fig. 2-9, the external load F is plotted against a post-buckling deformation w_b for the different types of bifurcation: (a) asymmetric, (b) stable symmetric, and (c) unstable symmetric bifurcation, depending on whether the secondary paths are stable (solid line) or unstable (dashed line). An unstable secondary equilibrium path corresponds with a structure which is sensitive to geometric imperfections, resulting in a larger reduction in buckling strength (ECCS, 2008). Axially compressed cylinders (whether or not stiffened) frequently exhibit compound or multi-modal bifurcation (i.e. several bifurcation buckling modes occur at the same critical load) and the post-buckling behaviour is influenced by the interaction between the potential buckling modes (ECCS, 2008). Additionally, such structures usually have an

increased sensitivity to small geometric imperfections (ECCS, 2008).

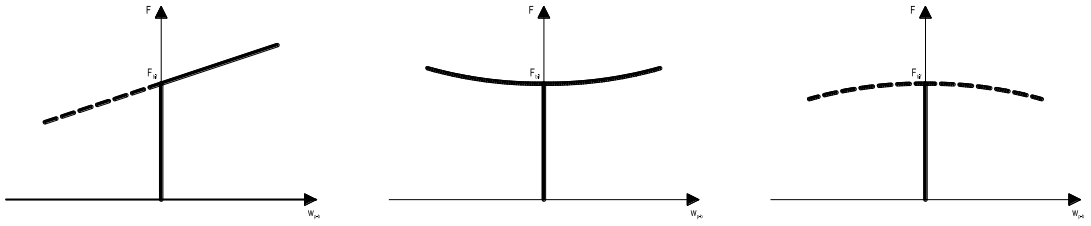

(a) Asymmetric. (b) Stable symmetric. (b) Unstable symmetric.

Fig. 2-9 Bifurcation types.

At a snap-through point (See Fig. 2-8 (b)), the equilibrium path becomes unstable and the post-buckling deformations (i.e. the buckling mode) are growing very fast. In the load-displacement diagram, a dynamic jump occurs from the limit point to a stable rising equilibrium path. The deformations after the jump usually have the inverted shape of the original structure. Under certain conditions, snap-through buckling can be found in cylinders (ECCS, 2008).

To conclude, the (im)perfect elasto-plastic buckling strength is defined as the lowest buckling load determined by the following criteria: (1) the limit load (snap-through), (2) the bifurcation load, and (3) a load below the limit and bifurcation load corresponding with a maximum tolerable deformation (EN 1993-1-6, 2007). In this work, only criteria (1) and (2) will be used. For completeness, a word is given about the definition of the maximum tolerable deformation of the third criterion, which is thus not taken into account here. Generally, an overall displacement is no concern for the designer neither the owner of a silo. In contrast, local deviations of the shell surface are visible and do cause concern. Such deviations are best represented by the rate of change of the normal displacement of the shell surface, which is characterised by the local rotation β of the deformed shell surface relative to the original surface (=dw/ds) (ECCS, 2008). In this document, a value $\beta = 0{,}1$radians is recommended.

Bending stresses

For elastic instability, bending stresses can lead to minor changes in the predicted buckling strength (Rotter, 1987). In certain circumstances (e.g. where the stresses are comparable with the yield stress), bending stresses can cause early yield on one surface of the shell wall, resulting in a significant reduction of the failure load (Rotter, 1987). Bending stresses can be caused by thermal gradients, boundary compatibility, shell junctions (barrel-hopper), eccentricities and steps in the shell middle surface (e.g. near weld depressions), non-uniform pressures (asymmetrical in circumferential direction) and local loads (due to eccentric filling and discharging) (ECCS, 2008).

3 General design procedure

The procedures for the design of a silo for the storage of bulk solids consists of the following steps (Roberts, 1994; Rotter, 2001a):

1) Determination of the properties of the bulk solids;
2) Determination of the silo geometry;
3) Assessment of the loading conditions;
4) Design.

Below, these four steps will be discussed in detail.

STEP 1 - Determination of the properties of the bulk solids

During the lifetime of a silo, the properties of the bulk solids vary within time. Reasons for this variability of the material properties are the variability of the material itself (e.g. modifications in the composition of the material due to segregation, filling and emptying operations, etc.) and the variability of the source of origin. Consequently, all material properties have their own statistical distribution of probability of occurrence during the silo lifetime, and can be defined in terms of a mean value and a standard deviation. To take this variability into consideration, the Eurocode uses characteristic values of the material properties. The lower and upper characteristic values are taken as the 10 and the 90 percentile values and correspond with a lifetime occurrence of respectively 10% and 90%. These values can be calculated as the mean of a normal distribution minus or plus 1.28 times the standard deviation. In Table 2-2, the characteristic values of the properties of frequently used bulk solids are displayed (EN 1991-4, 2006). These values should be used with care, because of the absence of certain assumptions. The values and their application concerning the determination of the silo geometry (i.e. step 2), the loading conditions (i.e. step 3), and the ultimate limit states (i.e. step 4) will now be discussed one by one. The influence of the material parameters to other factors (such as arching, ratholing, etc.) are not discussed here because this is beyond the scope of this work. For this purpose, reference is made to (Rotter, 2001a).

Bulk unit weight γ

The bulk unit weight γ is obtained by multiplying the bulk density ρ (mass per unit volume) and the gravity acceleration g. The value for the density is an average value, because, for some materials, the density may vary within a silo due to the filling process.

The lower characteristic value γ_l (i.e. loosely packed material) will be used for the calculation for the storage volume, while the upper characteristic value γ_u (i.e. the densely packed

material) will be used for all load calculations and the ultimate limit states (EN 1991-4, 2006).

For some materials, the lower and upper characteristic value of the bulk unit weight differ strongly. In mixture of particles with a broad range of densities, it is possible that, due to segregation or the filling process, the silo is mainly filled with particles of the highest density (Rotter, 2001a). For such bulk solids, it is important that a realistic assessment is made for the maximum bulk density γ_u.

Table 2-2 Characteristic values of the bulk solid properties (EN 1991-4, 2006).

Material	Unit weight γ [kN/m³]		Angle of repose φ_r [°]	Effective angle of internal friction φ_i [°]		Lateral pressure ratio K [-]		Wall friction coefficient μ [-]				Patch load solid reference factor C_{0p} [-]
								Wall type D1	Wall type D2	Wall type D3		
	Lower γ_l	Upper γ_u		Mean φ_{im}	Factor a_φ	Mean K_m	Factor a_k	Mean μ_m	Mean μ_m	Mean μ_m	Factor a_μ	
Default material	6	22	40	35	1.30	0.50	1.50	0.32	0.39	0.50	1.40	1.0
Aggregate	17	18	36	31	1.16	0.52	1.15	0.39	0.49	0.59	1.12	0.4
Alumina	10	12	36	30	1.22	0.54	1.20	0.41	0.46	0.51	1.07	0.5
Barley	7	8	31	28	1.14	0.59	1.11	0.24	0.33	0.48	1.16	0.5
Cement	13	16	36	30	1.22	0.54	1.20	0.41	0.46	0.51	1.07	0.5
Cement clinker	15	18	47	40	1.20	0.38	1.31	0.46	0.56	0.62	1.07	0.7
Coal	7	10	36	31	1.16	0.52	1.15	0.44	0.49	0.59	1.12	0.6
Coal powdered	6	8	34	27	1.26	0.58	1.20	0.41	0.51	0.56	1.07	0.5
Coke	6.5	8	36	31	1.16	0.52	1.10	0.49	0.54	0.59	1.12	0.6
Flour	6.5	7	45	42	1.06	0.36	1.11	0.24	0.33	0.48	1.16	0.6
Flyash	8	15	41	35	1.16	0.46	1.20	0.51	0.62	0.72	1.07	0.5
Iron ore pellets	19	22	36	31	1.16	0.52	1.15	0.49	0.54	0.59	1.12	0.5
Lime hydrated	6	8	34	27	1.26	0.58	1.20	0.36	0.41	0.51	1.07	0.6
Limestone powder	11	13	36	30	1.22	0.54	1.20	0.41	0.51	0.56	1.07	0.5
Maize	7	8	35	31	1.14	0.53	1.14	0.22	0.36	0.53	1.24	0.9
Phosphate	16	22	34	29	1.18	0.56	1.15	0.39	0.49	0.54	1.12	0.5
Potatoes	6	8	34	30	1.12	0.54	1.11	0.33	0.38	0.48	1.16	0.5
Sand	14	16	39	36	1.09	0.45	1.11	0.38	0.48	0.57	1.16	0.4
Slag clinkers	10.5	12	39	36	1.09	0.45	1.11	0.48	0.57	0.67	1.16	0.6
Soya beans	7	8	29	25	1.16	0.63	1.11	0.24	0.38	0.48	1.16	0.5
Sugar	8	9.5	38	32	1.19	0.50	1.20	0.46	0.51	0.56	1.07	0.4
Wheat	7.5	9	34	30	1.12	0.54	1.11	0.24	0.38	0.57	1.16	0.5

Angle of repose φ_r

The angle of repose φ_r is the steepest angle relative to the horizontal plane to which a bulk solid can be poured onto a flat rough surface without slumping. This angle is used for the determination of the "equivalent" horizontal surface of the conical pile. The vertical position of the equivalent surface is used as reference level for the calculation of the silo pressures.

Effective angle of internal friction φ_i

The angle of internal friction is the angle at which the bulk material will slip on its own surface. For cohesive materials, an additional force is necessary to promote slip. The proportion due to cohesion is particularly important at small normal pressures. The "effective" angle of friction φ_i takes this effect into account and is consequently slightly larger than the initial loading angle of friction. This parameter controls the failure of the solid (i.e. the point at which the solid starts to flow) and is used for the assessment of flow blockages and flow channel geometries. Its influence on the silo pressures on the vertical cylindrical barrel is given in Table 2-3: the upper characteristic value $\varphi_{i,u}$ should be used for the determination of minimum normal pressures (Eq. (2-3)), the lower characteristic value $\varphi_{i,l}$ for the maximum frictional tractions (Eq. (2-2)) (EN 1991-4, 2006).

$$\varphi_{i,l} = \varphi_{im}/a_\varphi \tag{2-2}$$

$$\varphi_{i,u} = \varphi_{im} \cdot a_\varphi \tag{2-3}$$

Lateral pressure ratio K

The lateral pressure ratio K (in the vertical-walled section of the silo) is defined as the ratio of the horizontal stress in the solid near the wall and the mean vertical stress (i.e. the average value over the entire silo cross-section at a given level). This ratio influences the silo pressures (See. Eq. (2-53)), especially in the case of squat silos. This is a silo with an aspect ratio $0.4 < h_c/d_c \leq 2.0$ (in which h_c corresponds with the height of the cylindrical barrel from the transition to the equivalent surface, and d_c is the internal diameter of the circular cross-section). Its influence on the silo pressures on the vertical cylindrical barrel is given in Table 2-3: the lower characteristic value K_l should be used for the determination of minimum normal pressures (Eq. (2-4)), the upper characteristic value K_u for the maximum frictional tractions (Eq. (2-5)) (EN 1991-4, 2006).

$$K_l = K_m/a_k \tag{2-4}$$

$$K_u = K_m \cdot a_k \tag{2-5}$$

Wall friction coefficient μ

The wall friction coefficient μ is related to the wall friction angle φ_w (Eq. (2-6)) and is a measure for the friction between the bulk solid and the silo wall. The angle φ_w corresponds with the angle at which the bulk material will slip on a sloping surface of material such as in the silo wall. In Table 2-2, the wall friction angle φ_w is given for three categories of walls: D1 (polished), D2 (smooth), and D3 (rough).

$$\mu = tan(\varphi_w) \tag{2-6}$$

The wall friction is important for the determination of the pressures of the bulk solids on the silo wall (See. Eqs. (2-50) to (2-53)). Its influence on the silo pressures on the vertical cylindrical barrel is given in Table 2-3: the upper characteristic value μ_u should be used for determining both minimum normal pressures and maximum frictional tractions (Eq. (2-8)) (EN 1991-4, 2006).

$$\mu_l = \mu_m / a_\mu \tag{2-7}$$

$$\mu_u = \mu_m \cdot a_\mu \tag{2-8}$$

Patch load solid reference factor C_{0p}

During discharge of a silo, the bulk solids will cause increased presssures on the silo wall, both symmetrical and unsymmetrical. These components are respectively relatively independent and quite dependent of the solid being stored. This material dependency of the unsymmetrical pressures is represented by the patch load solid reference factor C_{0p}. However, this method does not reflect the real behaviour. In practice, the pressure is rather redistributed around the circumference than an overall symmetrical increase of pressure.

Table 2-3 Characteristic values of bulk solid properties to be used for different loading conditions on the (vertical) cylindrical silo wall (EN 1991-4, 2006).

LOADING CONDITION	EFFECTIVE ANGLE OF INTERNAL FRICTION φ_i	LATERAL PRESSURE RATIO K	WALL FRICTION COEFFICIENT μ
Minimum normal pressure	Upper	Lower	Upper
Maximum frictional traction	Lower	Upper	Upper

STEP 2 - Determination of the silo geometry

Determination of the volume

The storage volume is calculated on the basis of the desired storage capacity (expressed in tonnes) and the lower characteristic value γ_l. By using the bulk unit weight of loosely packed material, the calculated volume is always on the conservative side for the storage of the desired mass.

Prevent stoppages

To guarantee that the flow does never become arrested, the outlet dimensions must be determined. Three types must be considered: (a) ratholing, (b) arching or bridging, and (c) incomplete clean-out (See Fig. 2-10).

A rathole is an empty flow channel above the outlet opening (See Fig. 2-10 (a)). At the moment a stable rathole develops, the solid material in the rathole has been discharged, while the material besides the rathole is arrested. The formation of a stable rathole is restricted to funnel flow silos containing cohesive material and cannot form in mass flow. Bridging or arching is the formation of an arch-shaped obstruction above the outlet opening (See Fig. 2-10 (b)). Two types of arching can be distinguished: (1) mechanical arching (due to interlocking between large particles) and (2) cohesive arching (particles bond together as a result of compressive stresses). To prevent both ratholing and arching, the diameter of the outlet opening should be chosen large enough.

A "self-cleaning" silo is a silo in which all material discharges under gravity flow. When this is not the case, incomplete discharge should be prevented because (1) a quantity of dead material remains in the silo and (2) the silo capacity reduces (See Fig. 2-10 (c)). To prevent incomplete discharge, without mechanical aids, the hopper half angle β_{hop} (indicated in Fig. 2-11 (a)) should be small enough and the opening large enough.

Determination of the flow pattern

The flow patterns during discharge can be classified into three categories: (a) mass flow, (b) mixed flow, and (c) pipe flow (See Fig. 2-11). The latter two are also known as funnel flow. The mass flow is a flow pattern in which all solid material is in motion in every point within the silo during discharge, including along the walls of the cylindrical barrel and the conical hopper (See Fig. 2-11 (a)). In contrast, the funnel flow pattern exhibits a more erratic behaviour in time and in place: some material falls in the vertical flow channel (in the middle/near the wall) located above the outlet opening (concentric/eccentric outlet), while the rest of the material remains stationary. The point to which the flow channel extends is the vertical silo walls in the case of mixed flow (See Fig. 2-11 (b)) and the top surface for pipe

flow (See Fig. 2-11 (c)). In contrast to mass flow, the particles of the material slide on themselves rather than the silo wall. If the outlet opening is placed eccentrically, a channel of flowing solids can develop against one part of the silo wall, inducing an asymmetrical pattern of normal pressures to the silo wall. The choice for one of these modes depends on many factors. An overview of the main characteristics of mass and funnel flow are given in Table 2-4. For certain bulk materials and processes, a particular feature (e.g. the maintenance of the homogeneity of the solid material) during the residence time in the silo is crucial, while it is less for others.

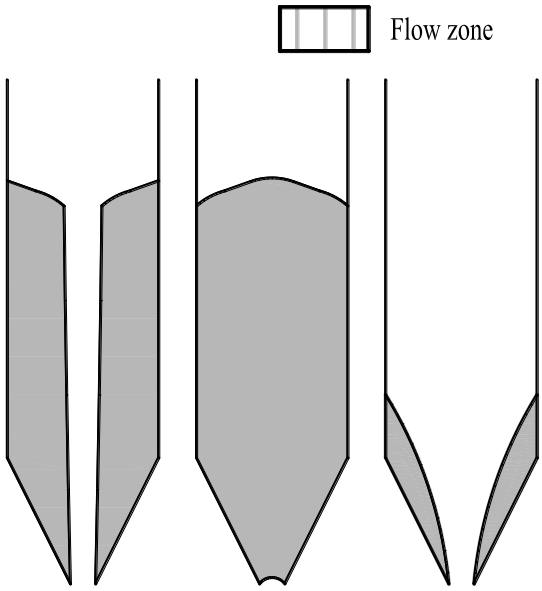

(a) Ratholing. (b) Bridging. (c) Incomplete cleanout.

Fig. 2-10 Flow stoppages.

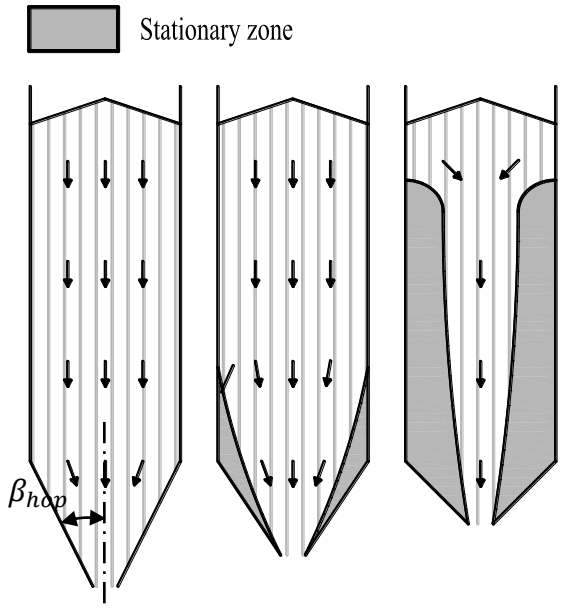

(a) Mass flow. (b) Mixed flow. (c) Pipe flow.

Fig. 2-11 Concentric flow patterns.
((b) and (c) are also known as funnel flow)

The choice for a specific flow pattern is also important for the design engineer, because the flow pattern strongly influences the pressure distribution on the silo walls (i.e. Step 3), and consequently the design of the structure in the ultimate limit states (i.e. Step 4).

However, it is difficult to predict the flow pattern with certainty, because it is affected by the characteristics of the silo geometry (shape of the cross-section), the hopper (steepness, smoothness and transition with the cylindrical barrel), the stored material (internal friction, friction material-wall, and height to diameter ratio), and the filling process (influencing the distribution of the densities and the particle orientations) (Rotter, 2001a; Nielsen, 1983; Nielsen, 1998).

Table 2-4 Mass flow versus funnel flow (Rotter, 2001a).

	MASS FLOW	FUNNEL FLOW
FLOW	Uniform	Non-uniform
RESIDENCE TIME	Relatively short period First-in, first-out	Prolonged time is possible First-in, last-out
SEGREGATION	No	Yes
DISCHARGE RATE	Good controllable, without large fluctuations	Less controllable, large fluctuations are possible
	• Steep hopper • Small wall friction • Large outlet opening	• Less steep hopper
CAPACITY	Decreased capacity within a given space	Increased capacity within a given space
DROP HEIGHTS	Larger ==> higher impact on the hopper ==> particle breakage or damage?	Smaller
WEAR	More solid sliding against the wall ==> increased wear	Less solid sliding against the wall ==> decreased wear

STEP 3 - Assessment of the loading conditions

The loading conditions from the stored bulk solids are discussed in Section 7 of this chapter. In this investigation, a uniform line load will be applied at the top edge of the cylindrical barrel. In this way, the silo wall is subjected to meridional compression. Due to the silo geometry, more specifically the local supports and the stiffening configuration (See Sections 1, 8 and 9 of this chapter), high compressive stresses will develop above the discrete supports and in the vicinity of the stringer stiffeners, while in other regions the compressive stresses will be relatively small. As a consequence of these elevated stresses, the structure is susceptible for failure by plastic yielding, elastic buckling, or a combination of both.

STEP 4 - Design

Because of the importance of this step, a separate section will be dedicated to the extensive discussion of the structural analysis of the silo, according to (EN 1993-1-6, 2007) and (EN 1993-4-1, 2007). The reader is referred to Section 4 of this chapter.

Example

In this paragraph, the four steps to be followed are illustrated for a cylindrical barrel with representative dimensions and a constant storage volume V. Through this initial dimensioning example, the reader gets an idea of the order of magnitude in dimensions, applied and resistance loads, etc.

Step 1 - Determination of the properties of the bulk solids

All bulk materials from Table 2-2 are considered to demonstrate the influence of the bulk density/weight to the design process. It is expected that a larger load requires an increased silo thickness and/or an alternative stiffener configuration.

Step 2 - Determination of the silo geometry

The dimensions (i.e. R and h) and the storage volume V of the cylindrical barrel are constant. The silo thickness t, which is assumed to be constant over the entire height of the barrel, is the unknown parameter of interest. Furthermore, three different locally supported cylindrical barrels are considered: an unstiffened cylindrical barrel, a cylindrical barrel with engaged columns, and a stringer-stiffened cylindrical barrel (a "stringer" stiffener is a synonym for a stiffener that follows the meridian of a shell). Table 2-5 gives an overview of all dimensions of the structure, including the stiffening configuration. The symbols mentioned in this table can be found in Fig. 3-21 for the cylindrical barrel, in Fig. 3-22 for the U-shaped stiffeners, in Fig. 3-25 for the engaged supporting columns, and in Fig. 3-28 for the ring stiffeners.

Table 2-5 Geometry of the example.

	CASE 1 UNSTIFFENED	CASE 2 ENGAGED COLUMNS	CASE 3 U-SHAPED STRINGER STIFFENERS
CYLINDRICAL BARREL	$R = 2.0m$ $R/t = [100; 200; 250; 333.3; 500; 666.6; 1000]$ $h/R = 10.0$		
SUPPORT	$n_{sup} = 4$ $d_{sup}/R = 0.20$		
ENGAGED COLUMNS / STRINGER STIFFENERS	/	$d_{stif}/R = d_{sup}/R$ $w_{stif}/d_{stif} = 100\%$ $t_{stif}/t = max.$ $h_{stif}^{sup}/R = 1.0$ $h_{stif}^{inf}/R = 4.0$	$d_{stif}/R = d_{sup}/R$ $w_{stif}/d_{stif} = 25\%$ $t_{stif}/t = max.$ $h_{stif}^{sup}/R = 1.0$ /
RING STIFFENERS	/	/	$t_{ur}/t = max.$ $w_{ur}/R = 0.10$ $t_{lr}/t = max.$ $w_{lr}/R = 0.20$

Step 3 - Assessment of the loading conditions

The characteristic value of the applied load was taken equal to the compressive vertical force F_{Sk} (Eqs. (2-9) and (2-55)) at a depth H (i.e. at the bottom of the silo) of a completely filled

slender silo, using the upper characteristic values of the bulk unit weight γ_u (densely packed material), the wall friction coefficient μ_u^{D3}, and the lateral pressure ratio K_u (EN 1991-4, 2006). This set of parameters corresponds with the most unfavourable situation with regard to the vertical weight. This force F_{Sk} is smaller than the total weight of the silo contents (i.e. $\gamma_u \cdot V$). The design load is obtained using Eq. (2-10).

$$F_{Ek} = F_{Sk}(H) \tag{2-9}$$

$$F_{Ed} = F_{Ek} \cdot \gamma_F \tag{2-10}$$

Where:

F_{Ek} the characteristic value of the applied load [kN];

F_{Ed} the design value of the applied load [kN];

γ_u the upper characteristic bulk unit weight [kN/m³];

V the storage volume [m³];

γ_F the partial factor on acting loads [-].

The partial safety factor for variable fixed acting loads γ_F is taken equal to 1.5. This corresponds with "normal" solids (not toxic, corrosive, or dangerous) which have an unfavourable effect (EN 1991-4, 2006).

Step 4 - Design

The buckling strength verification requires that the design value of the applied load F_{Ed} should be equal to or smaller than the design value of the resistance F_{Rd} (Eq. (2-11)). The latter value is obtained by dividing the characteristic value of the resistance F_{Rk} to the partial safety factor γ_{M1}(Eq. (2-12)). The partial safety factor on the resistance γ_{M1} is taken equal to 1.1 (EN 1993-4-1, 2007).

$$F_{Ed} \leq F_{Rd} \tag{2-11}$$

$$F_{Rd} = \frac{F_{Rk}}{\gamma_{M1}} \tag{2-12}$$

Where:

F_{Ed} the design value of the applied load [kN];

F_{Rd} the design value of the resistance load [kN];

F_{Rk} the characteristic value of the applied load [kN];

γ_{M1} the partial factor on the resistance [-].

For the determination of the characteristic value of resistance F_{Rk}, two design methods have been used: (1) design by global numerical MNA/LBA analysis and (2) design by global numerical analysis GMN(I)A. The design procedure for both methods is explained in respectively Section 4.4.2 and Section 4.4.3 *of this chapter. For the MNA/LBA approach, the current design rule with the buckling parameters for meridional compression was used (See Section 4.2.4). In addition, following assumptions are made:

- In Abaqus, the total weight of the bulk material is distributed as a uniform line load q on the upper edge of the cylindrical barrel, subjecting the structure to meridional compression. This way of loading application is similar to the loading conditions of this research. The choice for this loading condition is explained in Section 7 of this chapter;
- An ideal elasto-plastic material behaviour is used with a Young's modulus $E = 210GPa$, a coefficient of Poisson $\nu = 0.3$, and a yield stress σ_y of $235MPa$;
- Imperfections are ignored for simplicity of this illustrative example, because the choice of a suitable imperfection pattern (shape/orientation/location) requires an entire study of its own (See Section 6 of this chapter).

The results of this initial dimensioning exercise are displayed in Fig. 2-12. The main conclusions of this exploratory investigation are:

- For all cases, the design curve of buckling loads using the MNA/LBA approach is systematically slightly lower (and thus more conservative) than the curve corresponding with GMNA buckling loads obtained with Abaqus;
- The failure load strongly increases as the silo wall thickness increases (i.e. a decreasing radius-to-thickness ratio R/t) or when the unstiffened silo is converted into a stiffened silo;
- The distribution on the points of design loads F_{Ed} is attributable to the difference in density between the solid materials. If the capacity of the cylindrical barrel remains constant (i.e. a constant volume), a more dense material will correspond with a larger design load and consequently the required silo wall thickness $(R/t)_{req}$ increases as the buckling strength verification is applied (Eq. (2-11));
- When imperfections would be included, the curves of resistance load will shift downward and the required thickness of the silo wall will increase further (i.e. decreasing radius-to-thickness ratio R/t);
- In Fig. 2-12 (d), the total required silo wall thickness t_{req} is plotted against the stiffening configurations for all solid materials. Clearly, a downward trend can be observed in order of appearance: an unstiffened silo, a silo with engaged columns,

and a silo with U-shaped longitudinal and ring stiffeners. In other words, by adding a minimum amount of material to the engaged columns or the U-shaped stiffeners, the needed silo wall thickness strongly decreases and the material use is more optimised.

Table 2-6 provides an overview of the magnitude of the design load F_{Ed} and the required silo wall thickness t_{req}. For example for soya beans, the necessary silo wall decrease is equal to 11.4mm for the unstiffened barrel, 4.7mm for the barrel with engaged columns, and 3.8mm for the barrel stiffened with U-shaped longitudinal stiffeners.

Table 2-6 Order of magnitude of the design load and the silo wall thickness.

		ALL SOLID MATERIALS	SOYA BEANS
F_{Ed}		± 2230 - 7000kN	2334kN
t_{req}	Unstiffened	11.2 - >40.0mm	11.4mm
	Engaged columns	4.6 - 9.2mm	4.7mm
	U-shaped stiffeners	3.7 - 6.8mm	3.8mm

For this example, the total material consumption of the three alternatives is calculated in Table 2-7 (the material of the supporting columns below the lower edge of the barrel is neglected since this value is similar for all alternatives). It appears that the total amount of material of the barrel with engaged columns is equal to 51.7% of the amount of material of the unstiffened barrel, for the barrel with U-shaped and ring stiffeners, the same percentage is only 41.6%. Economically, the additional cost of the welding connections will certainly be recovered by the strong reduction of material usage and corresponding cost.

Table 2-7 Total material consumption.

	CASE 1- UNSTIFFENED	CASE 2 - ENGAGED COLUMNS	CASE 3 - U-SHAPED LONGITUDINAL AND RING STIFFENERS
Barrel	2.865m³	1.181m³	0.955m³
Engaged columns		0.301m³	
U-shaped stiffeners			0.091m³
Upper ring			0.049m³
Lower ring			0.096m³
Sum	2.865m³	1.482m³	1.191m³

In practice, other scenarios must also be considered and explored during the design of a

cylindrical barrel, such as multiple smaller silos (instead of one large silo) and the use of high strength steels.

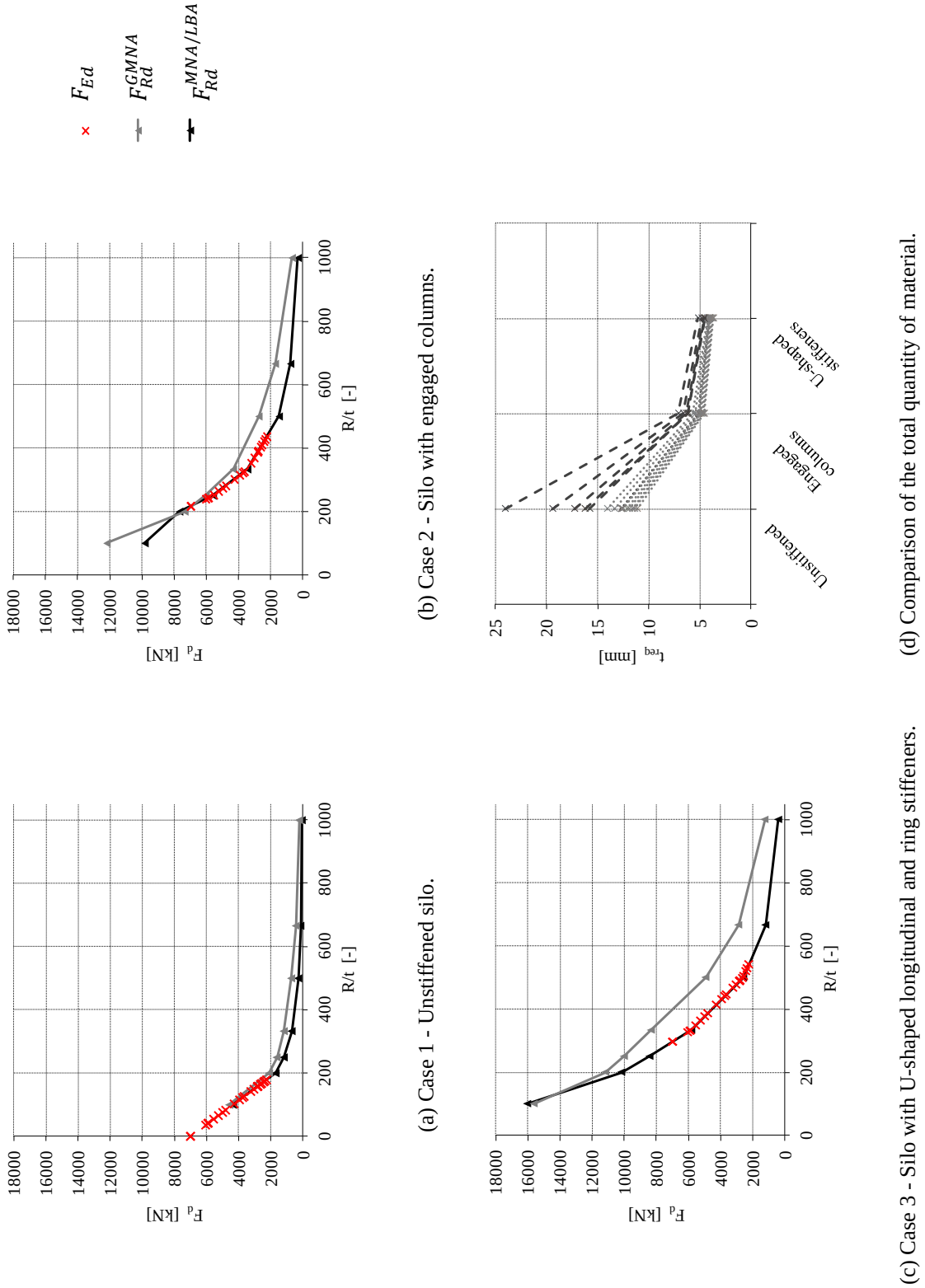

(a) Case 1 - Unstiffened silo. (b) Case 2 - Silo with engaged columns. (c) Case 3 - Silo with U-shaped longitudinal and ring stiffeners. (d) Comparison of the total quantity of material.

Fig. 2-12 Results initial design buckling limit state.

4 Design procedure of axially compressed cylindrical steel walls for LS1 (plastic limit state) and LS4 (buckling)

In practice, steel silos are used for many different applications, with widely varying bulk solids, different industries and process stages. Furthermore, steel silos exhibit a great diversity of shapes, sizes (from a tonne to many thousands of tonnes), stiffening and supporting arrangements, etc. As a result, a flexible and extensible framework is needed for the assessment of the structural integrity.

This section starts with a description of the structural Consequence Classes of silos (abbreviated as CC), which determine the design effort. Next, the concept of capacity curves (similar to "column curves") is explained and the buckling parameters of the current design rule are presented. Afterwards, the importance of the different shell calculation types is clarified. Last but not least, the design procedures of the Eurocode standards are discussed for two ultimate limit states: (1) plastic limit state and (2) buckling.

4.1 Structural reliability classes of silos

The design effort and the corresponding procedures depend on the structural Consequence Class to which the silo belongs. The classification of silos into Consequence Classes is presented in Table 2-8 and depends on the size (expressed in tonnes) and the complexity of the silo (i.e. the supporting and the loading conditions). The requirements for the design of a large complex silo are more extensive compared to a small simple silo, because of the increased risk of malfunction, the higher impact of economic and social consequences, or the increased environmental consequences of the former (See Table 2-9). In other words, the design effort is much higher when the risk of failure and the relating consequences are larger.

Table 2-8 Classification of Consequence Classes of silos (EN 1993-4-1, 2007).

CONSEQUENCE CLASS	DESCRIPTION
CC 1	Silos with capacity between **10 and 100 tonnes** (*).
CC 2	All silos covered by Eurocode 3 Part 4.1 and not placed in another class.
CC 3	• Ground supported silos or silos on a complete skirt extending to the ground with capacity in excess of 5000 tonnes. • **Discretely supported silos** with capacity in excess of **1000 tonnes**. • Silos with capacity in excess of **200 tonnes** in which any of the following design situations occur: (a) eccentric discharge, (b) patch loading, or (c) asymmetrical filling.

(*) Silos with capacity less than 10 tonnes are not covered by (EN 1993-4-1, 2007).

Table 2-9 Consequence and Reliability Classes.

CONSEQUENCE CLASS	RELIABILITY CLASS	DESCRIPTION
CC 1	RC 1	Small risk or negligible impact
CC 2	RC 2	Average risk or considerable impact
CC 3	RC 3	High risk or high impact

As already mentioned, the design effort and the level of accuracy during the design depend on the Consequence Class of the silo. In Table 2-10, a description is given of the permitted methods of analysis and requirements of geometrical imperfections in the shell wall (EN 1993-4-1, 2007). A validated numerical model is obligatory for all silos in CC 3 and silos under non-symmetrical actions or supports in CC 2.

Table 2-10 Design effort depending on the Consequence Classes (EN 1993-4-1, 2007).

	CC 1	CC 2	CC 3
DETERMINATION OF PRIMARY STRESSES	Membrane theory	Membrane theory under conditions of axisymmetric actions and support	/
LOCAL BENDING EFFECTS	Factors and simplified expressions	Bending theory elastic expressions under conditions of axisymmetric actions and support	/
DETERMINATION OF INTERNAL FORCES AND MOMENTS	/	Validated numerical model	Validated numerical model
GEOMETRIC IMPERFECTIONS IN THE SHELL	• Satisfy the limitations defined in (EN 1993-1-6, 2007) • Need to be included where a GNIA or GMNIA analysis is used		
	/	• Measurement is required to ensure that the assumed fabrication tolerance quality has been achieved	

Remark A higher Consequence Class may always be adopted than that required.

4.2 Concept of capacity curves and current design rule

A capacity curve for shell structures (e.g. locally supported silos) presents the complete failure behaviour of a structure in one single curve, ranging from pure plastic yielding to an interaction between plasticity and stability to pure elastic buckling (Rotter, 2002). Furthermore, it brings together the results from different kinds of finite element analyses (i.e. GMN(I)A, GN(I)A, MNA, and LBA load). In this way, the characteristic load of a real

(im)perfect silo derived from a GMN(I)A calculation (i.e. the most complex and accurate analysis) has not been studied separately. In contrast, the GMNIA load is related to simpler calculations such as MNA, GN(I)A, and LBA calculations, allowing an easy and meaningful interpretation of issues such as the influence of material non-linearity (i.e. yielding), geometric non-linearity (i.e. pre-buckling deformations), and geometric imperfections on the buckling load.

To conclude, a capacity curve is a simplified representation of the compressive resistance of a (shell) structure, despite its complex behaviour. The concept of capacity curves is incorporated in the design procedure of the European standard (EN 1993-1-6, 2007).

4.2.1 General versus modified capacity curve

Two types of capacity curves can be distinguished: a general capacity curves (Fig. 2-13 (a)) and a modified capacity curve (Fig. 2-13 (b)).

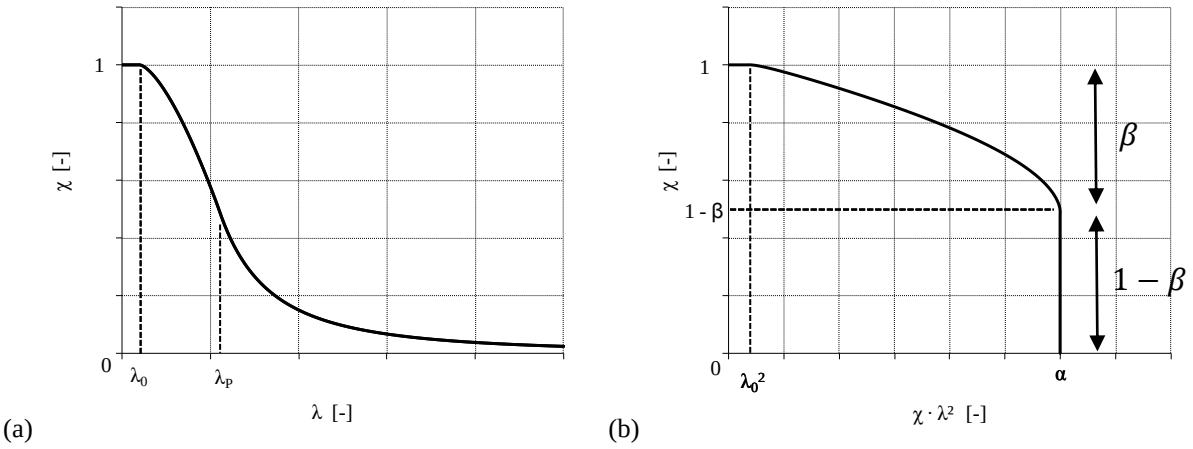

Fig. 2-13 General capacity curve (a) versus modified capacity curve (b).

General capacity curve

In a general or traditional capacity curve, the dimensionless strength parameter χ is plotted against the relative slenderness of the structure λ (Fig. 2-13 (a)). Both parameters are defined in Eq. (2-13) and Eq. (2-14). The dimensionless strength parameter χ is equal to the ratio of the characteristic failure load F to the plastic limit load F_{pl}. The relative slenderness of the structure λ is equal to the square root of the ratio of the plastic limit load F_{pl} (pure material failure) and the elastic limit load F_{cr} (pure elastic buckling). As a consequence, the relative slenderness is a measure between these two limiting cases.

$$\chi = \frac{F}{F_{pl}} \tag{2-13}$$

$$\lambda = \sqrt{\frac{F_{pl}}{F_{cr}}} \tag{2-14}$$

Where:

χ the dimensionless strength parameter [-];

λ the relative slenderness of the structure [-];

F the failure load of a GMN(I)A calculation [kN];

F_{pl} the plastic limit load (i.e. the maximum load of a MNA calculation) [kN];

F_{cr} the elastic limit load (i.e. the first eigenvalue of a LBA calculation) [kN].

The capacity curve describes the failure behaviour from a fully plastic collapse (i.e. the first section: $\lambda \leq \lambda_0$), to an interaction of plastic collapse and elasto buckling (i.e. the second section: $\lambda_0 < \lambda < \lambda_P$) to pure elastic buckling (i.e. the third section: $\lambda_P \leq \lambda$) (See Fig. 2-13 (a)). As can be seen in this figure, the squash limit and the plastic limit relative slenderness (i.e. λ_0 and λ_P) correspond with the transition slendernesses between the three sections. The squash limit relative slenderness λ_0 coincides with the point where stability reduces the resistance for the first time. As the slenderness λ increases further, the reduction of the resistance χ due to stability will increase more and more. The plastic limit relative slenderness λ_P can be calculated using Eq. (2-15) and is the maximum slenderness at which plasticity influences the resistance χ.

$$\lambda_P = \sqrt{\frac{\alpha}{1-\beta}} \tag{2-15}$$

Where:

λ_P the plastic limit relative slenderness [-];

α the elastic imperfection reduction factor [-];

β the plastic range factor [-].

The shape of the capacity curve is described in (EN 1993-1-6, 2007) and the value of the dimensionless strength χ in each of the above mentioned sections can be calculated by

$$\chi = 1.0 \qquad \text{when } \lambda \leq \lambda_0 \tag{2-16}$$

$$\chi = 1 - \beta \cdot \left(\frac{\lambda - \lambda_0}{\lambda_P - \lambda_0}\right)^{\eta} \qquad \text{when } \lambda_0 < \lambda < \lambda_P \tag{2-17}$$

$$\chi = \frac{\alpha}{\lambda^2} \qquad \text{when } \lambda_P \leq \lambda \tag{2-18}$$

Where:

λ_0 the squash limit relative slenderness [-];

η the interaction exponent [-].

In the first section (i.e. small values of the slenderness $\lambda \leq \lambda_0$), failure occurs due to plastic yielding alone (without interaction of elastic buckling). The strength is equal to the plastic limit load F_{pl} (MNA load) and the dimensionless strength χ is equal to one (Eq. (2-16)). In the second section (i.e. intermediate values of the slenderness $\lambda_0 < \lambda < \lambda_P$), plasticity and stability interact with each other and the dimensionless strength parameter χ decreases as the slenderness λ increases as a consequence of stability (Eq. (2-17)). Within the range of elasto-plastic buckling, the dimensionless strength χ and the shape of the capacity curve depend on the plastic range factor β and the interaction exponent η. The value $1 - \beta$ corresponds with the resistance where plasticity reduces the resistance for the first time (See Fig. 2-13 (b)). The interaction exponent η describes the rate of change of resistance with the relative slenderness λ. This parameter will decrease as the plasticity has a stronger effect. In the third section (i.e. large values of the slenderness $\lambda_P \leq \lambda$), failure occurs due to elastic stability alone (without interaction of plastic yielding). The strength is equal to the GN(I)A failure load. The dimensionless strength χ decreases further as the slenderness λ increases (Eq. (2-18)) and depends on the elastic imperfection reduction factor α. This factor is defined in Eq. (2-19) and accounts for two effects: (1) geometric non-linearity (i.e. changes of geometry) and (2) geometric imperfections.

$$\alpha = \frac{F_{gn}}{F_{cr}} \tag{2-19}$$

Where:

F_{gn} the failure load of a GN(I)A calculation [kN];

F_{cr} the elastic limit load (i.e. the first eigenvalue of a LBA calculation) [kN].

The main drawbacks of a traditional representation of the capacity curve are (1) the difficulty

in determining the transition between the second and third section accurately, and (2) the inaccurate representation of the third section. As a consequence, the parameters α and β can be extracted with difficulty. Furthermore, due to the small values of the resistance χ in the elastic part, a large error on the prediction of α or β is hardly visible in the capacity curve. For slender structures such as thin-walled silos, this is a serious disadvantage.

Modified capacity curve

A modified capacity curve is similar to a traditional capacity curve, except that another parameter is plotted on the horizontal axis, namely the product of the dimensionless strength χ and the square of the slenderness λ (Fig. 2-13 (b)), which is defined as

$$\chi \cdot \lambda^2 = \frac{F}{F_{pl}} \cdot \frac{F_{pl}}{F_{cr}} = \frac{F}{F_{cr}} \tag{2-20}$$

Where:

F the failure load of a GMN(I)A calculation [kN];

F_{pl} the plastic limit load (i.e. the maximum load of a MNA calculation) [kN];

F_{cr} the elastic limit load (i.e. the first eigenvalue of a LBA calculation) [kN].

In this way, the elastic part of the curve is depicted as a vertical line with length equal to $1-\beta$. Furthermore, the line intersects the horizontal axis at the value equal to the elastic imperfection reduction factor α. In contrast to a traditional capacity curve, the parameters α and β can be extracted easily.

4.2.2 Changing the slenderness

For the determination of the complete capacity curve, the slenderness of the structure λ should be varied from very small values ($\lambda \approx 0$) to large values ($\lambda \geq \lambda_P$). In the past, the slenderness of other structures was varied by assuming constant material properties and changing the geometry of the structure. For axially compressed cylindrical shells, a possible solution would be to vary the radius-to-thickness ratio R/t. However, by changing one geometrical parameter of the silo, the influence of geometric non-linearity (i.e. pre-buckling deformations) and the imperfection sensitivity to the failure behaviour will change and consequently also the elastic imperfection reduction factor α. As a consequence, it is not possible to find a unique value of α (Doerich and Rotter, 2011b).

For axially compressed cylindrical shells, the only way to obtain a wide range of slendernesses is to keep all geometrical parameters constant and to change the yield stress σ_y from very small values (low slenderness) to large values (high slenderness), including

unrealistic values (Doerich and Rotter, 2011b). This technique was firstly proposed by (Rotter, 2003).

4.2.3 Constant versus varying interaction exponent

The interaction exponent η describes the rate of change of resistance with the relative slenderness λ and influences the shape of the elasto-plastic part of the capacity curve. The interaction exponent η can either have a constant value or can vary linearly with the slenderness λ.

Constant interaction exponent

In Fig. 2-14, the capacity curve is depicted with variable constant interaction exponent η. If η is smaller than the unity, the capacity curve has not the desired shape (i.e. convex side facing down). If η is equal to the unity, which corresponds with the default value, the elasto-plastic curve is a straight line. If η is larger than the unity, the elasto-plastic part is a curve with the convex curve facing upwards. Consequently, the first condition is that the interaction exponent η must be equal or greater than the unity.

When we take a closer look at Fig. 2-14, we can see that the elasto-plastic part with $\eta = 2$ exceeds the elastic curve. However, this situation is not possible, because the elastic limit corresponds with the maximum buckling resistance without the (disadvantageous) interaction of plasticity. In other words, Eq. (2-21) must always be satisfied over the entire elasto-plastic range.

$$\chi_{EL-PL} \leq \chi_{EL} \qquad \text{when } \lambda_0 \leq \lambda \leq \lambda_P \tag{2-21}$$

The above mentioned restriction translates into two new conditions at $\lambda = \lambda_P$: (1) the slope of the elasto-plastic part must be equal to or smaller than the slope of the elastic part (Eq. (2-22)) and (2) the curvature of the elasto-plastic part must be equal to or smaller than the curvature of the elastic part (Eq. (2-23)) (Doerich and Rotter, 2011b).

$$\chi'_{EL-PL} \leq \chi'_{EL} \qquad \text{when } \lambda = \lambda_P \tag{2-22}$$

$$\chi''_{EL-PL} \leq \chi''_{EL} \qquad \text{when } \lambda = \lambda_P \tag{2-23}$$

Based on the slope restriction (i.e. Eq. (2-22)), a maximum value of the plastic range factor β (or a minimum for $1 - \beta$) can be determined by

$$\beta \leq \beta_{max} = \frac{2 \cdot (\lambda_P - \lambda_0)}{\eta \cdot \lambda_P + 2 \cdot (\lambda_P - \lambda_0)} \tag{2-24}$$

In Fig. 2-15, the minimum value of $1 - \beta$ is plotted as a function of the interaction

exponent η, and for different combinations of α and λ_0. For example, if $\eta = 1$ and $\lambda_0 = 0.0$, the value $1 - \beta$ must be larger than $1/3$, which means that structures where plasticity affects the buckling strength at loads lower than $1/3$ of the plastic limit load cannot be presented well if the interaction exponent η is constant (Doerich and Rotter, 2011b). Furthermore, the restriction becomes more severe (i.e. an increase of the minimum value of $1 - \beta$) as η or λ_0 increase or as α decreases.

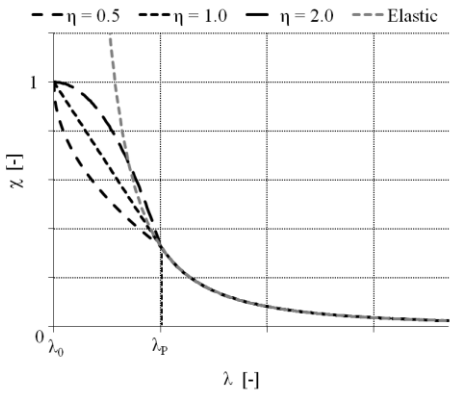

Fig. 2-14 Capacity curve with varying interaction exponent η.

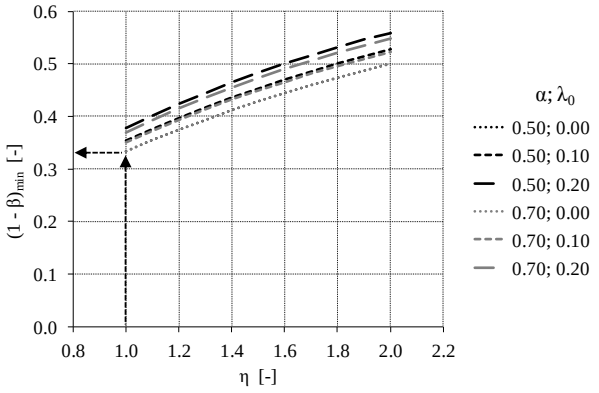

Fig. 2-15 Minimum value for $1 - \beta$ as a function of $\eta, \alpha, and\ \lambda_0$ (i.e. Eq. (2-24)).

Linear varying interaction exponent

Since many structures exist where plasticity affects the buckling strengths at relatively small load levels, a possible solution to circumvent the restriction on the plastic range factor β is to vary the interaction exponent η linearly with the slenderness λ (Eq. (2-25)) (Doerich and Rotter, 2011b). This can lead to a much better fit of the capacity curve where local high stress concentrations arise (Doerich, 2007).

$$\eta(\lambda) = \frac{\eta_0 \cdot (\lambda_P - \lambda) + \eta_P \cdot (\lambda - \lambda_0)}{(\lambda_P - \lambda_0)} \qquad \text{when } \lambda_0 \le \lambda \le \lambda_P \qquad (2\text{-}25)$$

Where:

$\eta(\lambda)$ the interaction exponent at λ [-];

η_0 the squash limit interaction exponent at λ_0 [-];

η_P the plastic limit interaction exponent at λ_P [-];

λ_0 the squash limit relative slenderness [-];

λ_P the plastic limit relative slenderness [-].

Equations Eq. (2-22) and Eq. (2-23) are still present. Instead of restricting the plastic range factor β (if the interaction exponent η is constant), the squash limit and plastic limit

interaction exponents will be determined on the basis of restriction of both the slope (Eq. (2-26)) and the curvature (Eq. (2-27)) when $\lambda = \lambda_p$.

$$\eta_P \leq 2 \cdot \left(\frac{1-\beta}{\beta}\right) \cdot \left(1 - \frac{\lambda_0}{\lambda_P}\right) \tag{2-26}$$

$$\eta_0 \leq 3 \cdot \left(\frac{1-\beta}{\beta}\right) \cdot \left(1 - \frac{\lambda_0}{\lambda_P}\right)^2 + \frac{1}{2} \cdot \eta_P \cdot (1 + \eta_P) \tag{2-27}$$

Additionally, less critical restrictions can be applied when plasticity only interacts with stability at small slendernesses (i.e. a small value of λ_P or a large value of $1 - \beta$) or when plasticity interacts with stability until relatively large slendernesses (i.e. a large value of λ_P or a small value of $1 - \beta$). The curvature at $\lambda = \lambda_P$ is restricted to a negative curvature in the first case or to a positive curvature in the second case (See Fig. 2-16) (Doerich and Rotter, 2011b), resulting in respectively Eq. (2-28) and Eq. (2-29).

$$\eta_0 < \eta_0^{lim} \tag{2-28}$$

$$\eta_0 > \eta_0^{lim} \tag{2-29}$$

$$\eta_0^{lim} = \frac{1}{2} \cdot \eta_P \cdot (1 + \eta_P) \tag{2-30}$$

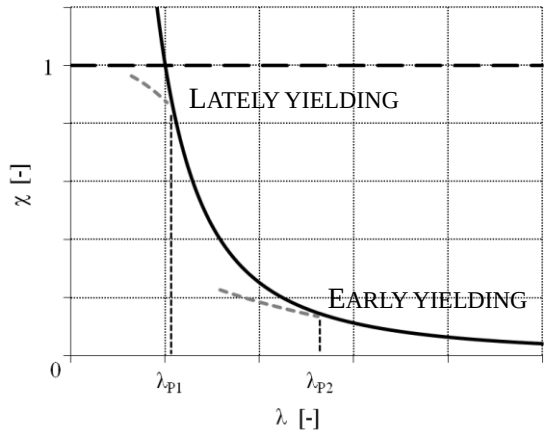

Fig. 2-16 Negative curvature in λ_{P1} (lately yielding) or positive curvature in λ_{P2} (early yielding).

4.2.4 Current design rule

In the Eurocode (EN 1993-1-6, 2007), there are currently no values available for the buckling parameters (i.e. α, β, λ_0, and η) of axially compressed **locally supported stiffened** cylindrical steel silos. If a designer wants to estimate the elasto-plastic buckling strength of such a structure, the designer should make an appropriate choice for the buckling parameters and apply the MNA/LBA approach (See Section 4.4.2) (EN 1993-1-6, 2007; ECCS, 2008). These interaction parameters must be conservatively and carefully estimated based on the

designer's best estimate by comparing the current problem with similar buckling problems, taking into account as much as possible relevant information such as geometry, boundary conditions, loading pattern, dominant stress pattern, influence of imperfection sensitivity and geometric non-linearity, expected (post-)buckling behaviour, etc. (ECCS, 2008). However, if these parameters cannot be estimated with confidence, the designer should perform an advanced GMNIA calculation (i.e. the GMNIA approach and will be described in Section 4.2.3), whether or not combined with a test programme (EN 1993-1-6, 2007; ECCS, 2008). If this latter scenario is not possible either, then the default values of the buckling parameters for axial compression in the Eurocode should be taken into account, applying the MNA/LBA approach (See Section 4.4.2) (EN 1993-1-6, 2007; ECCS, 2008).

These buckling parameters are determined for **unstiffened** cylindrical steel silos subjected to **uniform axial compression** and are rather conservative, because these values are derived as a lower bound empirical fit to a wide scatter of experimental data. For most other shell buckling problems, it is assumed that these buckling parameters are safe, because it is not imaginable that shell structures are more imperfection sensitive than an unstiffened circular cylinder under axial compression (ECCS, 2008). These values are determined for structures which fail by elastic buckling and are sensitive to imperfections. In structures where extensive yielding develops before buckling occurs (and which are consequently less sensitive to imperfections), the plastic range factor β_x is not always on the safe side (ECCS, 2008).

At first instance, the meridional elastic imperfection reduction factor α_x must be determined. For structures which are susceptible for geometric non-linearity and imperfections, the value α_x is very important. Eq. (2-31) presents the expression of the determination of the meridional elastic imperfection reduction factor α_x and accounts for the amplitude Δw_k of the geometric imperfection (Rotter, 1998). In this way, the calculation of the buckling strength takes into account the disadvantageous effect of the imperfection amplitude (Koiter, 1945; Yamaki, 1984; Rotter, 2004).

$$\alpha_x = \frac{0.62}{1 + 1.91 \cdot (\Delta w_k / t)^{1.44}} \tag{2-31}$$

Where:

- α_x the meridional elastic imperfection reduction factor [-];
- Δw_k the characteristic imperfection amplitude [m];
- t the cylinder thickness [m].

The characteristic imperfection amplitude Δw_k is related to the quality of fabrication (by defining a quality parameter Q - see Table 2-11) and the radius-to-thickness ratio R/t (Eq. (2-32)) (Rotter, 1985b; 1998).

$$\Delta w_k/_t = \frac{1}{Q} \cdot \sqrt{\frac{R}{t}} \tag{2-32}$$

Where:

Δw_k the characteristic imperfection amplitude [m];

Q the meridional compression fabrication quality parameter [-];

R the cylinder radius [m];

t the cylinder thickness [m].

Table 2-11 Values of the fabrication quality parameter Q (EN 1993-4-1, 2007).

FABRICATION TOLERANCE QUALITY CLASS	DESCRIPTION	Q [-]
Class A	Excellent quality	40
Class B	High quality	25
Class C	Normal quality	16

In Fig. 2-17, the meridional elastic factor α_x is plotted. Clearly, the value of α_x decreases as the radius-to-thickness ratio R/t increases, because the imperfection sensitivity of thin-walled structures is higher. Of course, the value α_x decreases when the quality of fabrication is worse.

The squash limit relative slenderness $\lambda_{x,0}$, the plastic range factor β_x, and the interaction exponent η_x should be taken as:

$$\lambda_{x,0} = 0.20 \tag{2-33}$$

$$\beta_x = 0.60 \tag{2-34}$$

$$\eta_x = 1.0 \tag{2-35}$$

These values are calibrated against a wide range of experimental data of uniformly compressed cylinders (ECCS, 2008).

Based on these four buckling parameters and the expressions describing the shape of the interaction curves (i.e. Eqs. (2-16) to (2-18)), the buckling curves can be determined for the three fabrication quality classes. These curves are presented in Fig. 2-18 for a radius-to-thickness ratio R/t of 1000 and can be used for the design of shell structures under axial compression using the MNA/LBA approach considered in the Eurocode (EN 1993-1-6, 2007).

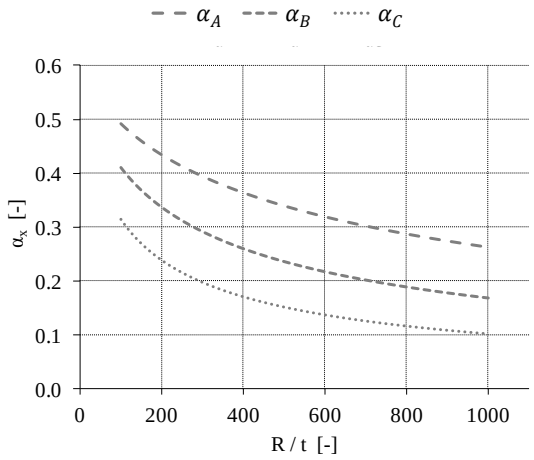

Fig. 2-17 The meridional elastic imperfection reduction factor α_x as a function of the radius-to-thickness ratio R/t and related to the fabrication tolerance quality class.

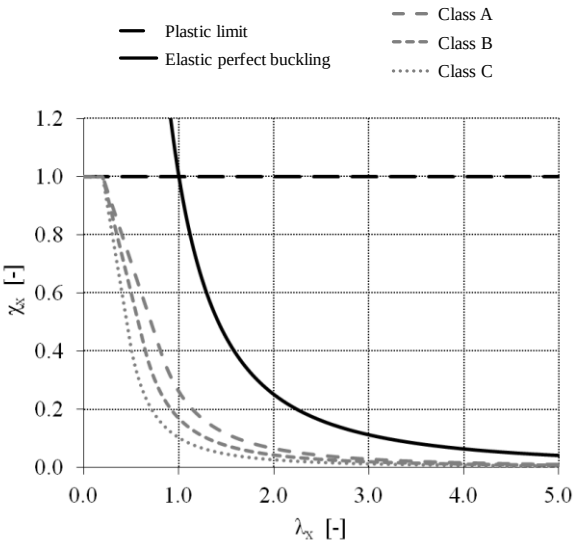

Fig. 2-18 Design curves for buckling of cylindrical silos under axial compression ($R/t = 1000$).

4.2.5 Fitting design rules

Because of the absence of a design rule for stiffened cylindrical silos (See Section 4.2.4), a proposal for a new design rule will be made for locally supported cylindrical steel silos with U-shaped stringer stiffeners or engaged columns (in Chapter 6 - Design rule). For a wide range of geometries, capacity curves will be determined of both the perfect silo and the imperfect silo (with quality class A, B, and C), resulting in four interaction curves for each geometry.

Afterwards, the combination of the four buckling parameters will be determined for each capacity curve according to the best-fitting principle of the shape of the curve. However, it is important to know that the quality of the estimate of the buckling resistance is not equally sensitive for all buckling parameters. The elastic imperfection reduction factor α is the most important parameter, while the value of β, λ_0, and η are less important (ECCS, 2008), at least for the estimate of the elastic buckling resistance.

4.3 Rules for the plastic limit state assessment

The plastic limit load can be obtained by using a MNA calculation. In such calculation, a small displacement theory has been adopted and the stress-strain relationship of steel is treated as an ideal elasto-plastic material behaviour (See Section 4.5). However, it is rather difficult to determine the exact plastic limit load corresponding with the asymptotic plateau, because the fully plastic mechanism is reached very gradually. For design calculations, this is less important since a lower load is a conservative estimate of the real plastic limit load. In

contrast, when in future research new interaction parameter sets are developed for other shell conditions (as is the case here), it is important to precisely estimate the asymptotic plateau load (ECCS, 2008).

In real structures, the above defined plastic limit load can be increased further by two phenomena: (1) strain hardening and (2) geometric hardening (i.e. the change in shape has a (de)stabilising effect). However, these phenomena are difficult to quantify.

In structures with high stress gradients and locally high stress peaks, the use of a linear elastic shell bending theory analysis (LA) is not recommended to obtain a lower bound estimate of the true plastic limit load. The reason for discouraging this method is the much too conservative lower bound when for example the first yield criterion has been applied. For similar locally supported structures, the lower bound prediction using a LA analysis was between 15% and 20% of the true value for a typical bracket supported cylindrical shell, depending on the failure criteria (Doerich et al., 2005). Therefore, the plastic limit load will in this work always be assessed using a more precise MNA calculation.

4.4 Rules for the buckling limit state assessment

For the design of the buckling limit state and thus the assessment of the buckling resistance, three approaches can be applied. In the following sections, these methods will be discussed in depth one for one.

1) Buckling stresses;

2) MNA/LBA approach;

3) GMNIA approach.

Choice for one of these approaches

The first method is the easiest approach and uses simplified expressions for the buckling resistance. When no expressions are available for the buckling resistance or when the designer believes that the use of hand calculations results in much too conservative buckling resistances (e.g. in structures with high stress gradients), the second and third method are better (less conservative) approaches to verify the buckling strength. When applying these methods, more accurate numerical analyses are performed (instead of conservative hand calculations) which lead typically to more economic results. For the second method, only two relatively simple calculations (LBA and MNA) must be performed, while for the third method different (non-)linear calculations (LBA, MNA, GNA, GMNA, and several GMNIA) must be performed. Appendix A contains detailed information about shell analysis (EN 1993-1-6, 2007). Another difference between these methods is the way of evaluating the structure. For the first method, each component of the structure is considered separately, while the whole

structure is considered in once for the second/third method. Finally, Table 2-12 gives an overview between the input (hand calculation or numerical analyses) and the output (accuracy and conservatism of the results) for the three methods.

Table 2-12 Comparison between the available approaches.

	BUCKLING STRESSES	MNA/LBA	GMNIA
HAND CALCULATION	Yes	Yes	No
NUMERICAL ANALYSES	No	LBA MNA	LBA MNA GNA GMNA Several GMNIA
ACCURACY AND CONSERVATISM - FOR STRUCTURES WITH HIGH STRESS GRADIENTS	Small accuracy Conservative	Moderate accuracy Less conservative	High accuracy Less conservative

Individual loadings versus load cases

When non-linear or LBA calculations must be performed (i.e. method 2 and 3), the superposition principle of actions is not valid. Therefore several load cases must be considered with a complete combination of loadings. For the assessment of the buckling limit state, these load combinations should be considered which induce compressive forces in the shell rather than tensile forces or bending moments (ECCS, 2008).

In general, each load case consists of a set of design loads and is a combination of different concentrated loads, line loads, distributed loads, and pressures. Consequently, it is not possible to express the moment of elasto-plastic buckling as one failure load. Instead, a dimensionless resistance R has been used for each load pattern. The magnitude of the loads at the moment of failure is obtained by multiplying the dimensionless resistance R of the load pattern with the corresponding design loads.

In this contribution, only one loading condition will be considered, namely a uniform compression load on the upper edge. Therefore, all resistance values R of a set of design loads will always be replaced by forces F.

4.4.1 Buckling stresses

This method is the traditional procedure that may be found in most literature of shell buckling design until the introduction of (EN 1993-1-6, 2007) and is based on a membrane theory or a linear bending theory (LA). However, this method leads to the least accurate results compared to the other methods, especially for shells with non-uniform stress patterns. The reason for

this inaccuracy will be explained further.

In general, the elastic stress values (acting stress values), the elastic critical buckling stresses (resistance stress values), and the interaction parameters (α, β, λ_0, and η) can be calculated by hand using simplified formulas and/or diagrams. Another possibility to determine the elastic critical buckling stresses is by means of a LBA calculation.

For the buckling strength verification, all membrane stress components (i.e. meridional compression, circumferential compression, and shear) are checked individually. At the end of the procedure, an additional interaction check must be performed on a set of membrane stress components that are present in each point of the shell or on a set of maximum membrane stress components that are present in different points of the shell.

According to this approach, a structure under a complex stress pattern is designed as a structure under a uniform stress pattern with a constant stress value equal to the key value of the membrane stress in the variable stress field. The key value is defined as the maximum (compressive) values at any point of the shell. Consequently, in structures with highly non-uniform stress patterns (as is the case in locally supported stiffened silos), this simplified design method is rather conservative. Indeed, by using the stresses at individual points, the strength may be underestimated significantly because for the formation of a buckle, a region with comparable high stresses is needed comparable with the size of the buckle (ECCS, 2008).

4.4.2 MNA/LBA approach

The MNA/LBA approach is a mix of numerical and hand calculations. The elastic limit load F_{cr} and plastic limit load F_{pl} are determined with great accuracy by means of two relatively simple numerical calculations (respectively with a LBA and a MNA calculation), while the rest of the calculations are done by hand. In *Fig. 2-19*, the complete design scheme of the MNA/LBA approach is presented. The approach consists of three main steps: (1) the determination of the acting load, (2) the determination of the resistance load, and (3) the buckling strength verification.

Firstly, the characteristic value F_{Ek} and the design value F_{Ed} of the acting load must be determined. A possible method for calculating this force is considered in the design example in Section 3 - General design procedure.

Secondly, the design value of the elasto-plastic buckling load F_{Rd} must be determined.

- LBA calculation to determine the elastic limit load F_{cr} of the perfect shell (See Appendix A);
- MNA calculation to determine the plastic limit load F_{pl} of the perfect shell (See

Sections 4.3 and Appendix A);

- Calculation of the relative slenderness λ (Eq. (2-14));
- Determination of the elasto-plastic interaction parameters (α, β, λ_0 λ_P, and η or η_0/η_P) (Section 4.2.4);
- Calculation of the buckling strength reduction factor χ (Eqs. (2-16) - (2-18)) to take into account geometric non-linearity and imperfections;
- Calculation of the characteristic value of the elasto-plastic buckling load F_{Rk};

$$F_{Rk} = \chi \cdot F_{pl} \tag{2-36}$$

- Calculation of the design value of the elasto-plastic buckling load F_{Rd}.

$$F_{Rd} = F_{Rk}/\gamma_{M1} \tag{2-37}$$

In which the partial factor for resistance to buckling γ_{M1} is equal to 1.1 [-] (EN 1993-4-1, 2007).

Finally, the buckling strength verification must be performed:

$$F_{Ed} \leq F_{Rd} \tag{2-38}$$

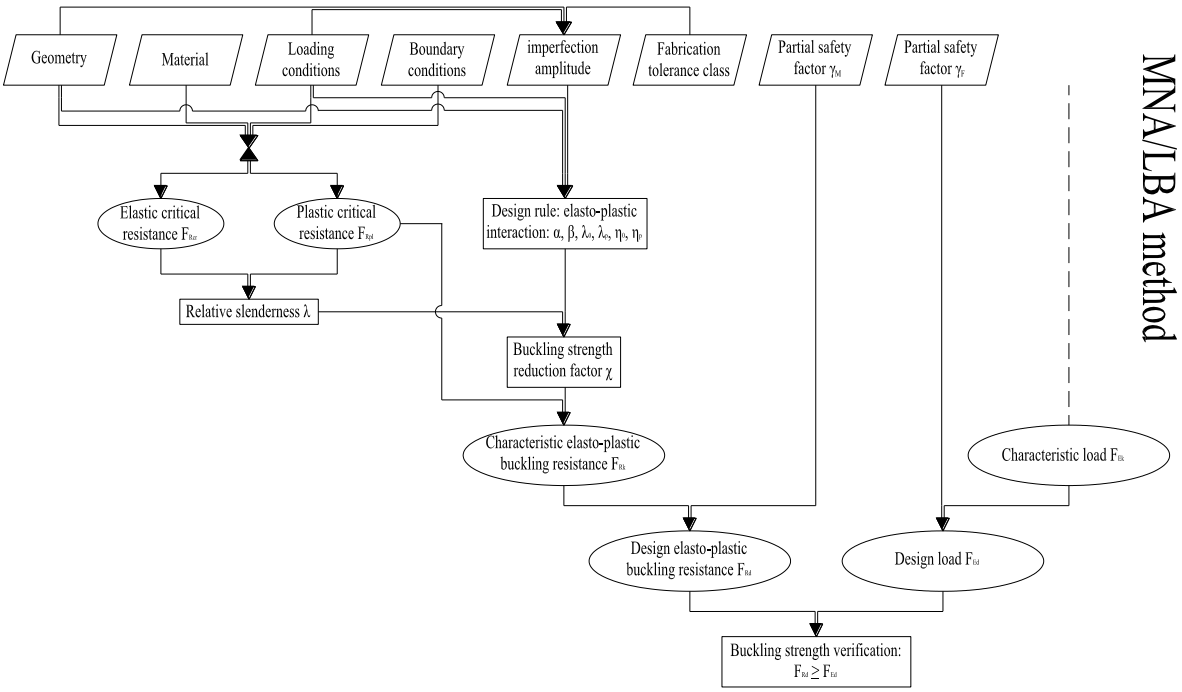

Fig. 2-19 Design scheme of the MNA/LBA procedure.

The accuracy of the estimate of the buckling strength largely depends on the choice of the set of interaction parameters (α, β, λ_0, and η). Currently, only a limited number of (rather

conservative) buckling parameter sets are available for specific combinations of shell geometry (e.g. unstiffened cylindrical steel silos) and loading condition (e.g. pure meridional compression). Therefore, there is currently a need to develop improved sets of interaction parameters for new shell conditions which are calibrated to true MNA calculations (ECCS, 2008). The current approach for the choice of these interaction parameters and the current design rule are discussed in Section 4.2.4.

4.4.3 GMNIA approach

The GMNIA approach is entirely based on the results from numerical calculations. In Fig. 2-20, the complete design scheme of the GMNIA approach is presented. The approach consists of three main steps: (1) the determination of the acting load, (2) the determination of the resistance load, and (3) the buckling strength verification. Steps 1 and 3 are identical to the MNA/LBA approach and are therefore not repeated here (See Section 4.4.2). In contrast, the procedure for the determination of the design value of the elasto-plastic buckling load F_{Rd} (i.e. step 2) is completely different compared to the MNA/LBA approach and is discussed here in detail. The different steps of the extended procedure are listed below.

- LBA calculation to identify the elastic limit load of the perfect shell (See Appendix A);
- MNA calculation to identify the plastic limit load of the perfect shell (See Sections 4.3 and Appendix A);
- GMNA calculation to identify the elasto-plastic limit load of the perfect shell (See Appendix A);
- A series of GMNIA calculation with different imperfections to identify the worst practically relevant imperfection form (See Section 6 for more information concerning this extremely important choice). The failure load corresponding with the latter imperfection form is recognised as the best prediction for the elasto-plastic limit load F_{GMNIA} of the real imperfect shell (See Appendix A);
- A calibration calculation to check the precision of the GMNIA calculation that is being used, because some effects are omitted or simplified in the numerical model (e.g. residual stresses, realistic joint details, etc.). Therefore it is desirable to calibrate the model against experimental results or standard problems for which the solution is known. It should be noted that hand calculation predictions are not adequate for the calibration.

  The calibration factor k is defined as the ratio of the known test result $F_{test,known}^{check}$ or the known characteristic value $F_{k,known}^{check}$ and the result of the current numerical model F_{GMNIA}^{check}.

$$k = \frac{F_{test,known}^{check}}{F_{GMNIA}^{check}} \quad or \quad \frac{F_{k,known}^{check}}{F_{GMNIA}^{check}} \tag{2-39}$$

The value of k should fulfil the following condition.

$$0.8 < k < 1.2 \tag{2-40}$$

- Calculation of the characteristic value of the elasto-plastic buckling load F_{Rk};

$$F_{Rk} = k' \cdot F_{GMNIA} \tag{2-41}$$

$$k' = min(k; 1.0) \tag{2-42}$$

In which k' is the modified value of the calibration factor [-].

- Calculation of the design value of the elasto-plastic buckling load F_{Rd}.

$$F_{Rd} = F_{Rk}/\gamma_{M1} \tag{2-43}$$

In which the partial factor for resistance to buckling γ_{M1} is equal to 1.1 [-] (EN 1993-4-1, 2007).

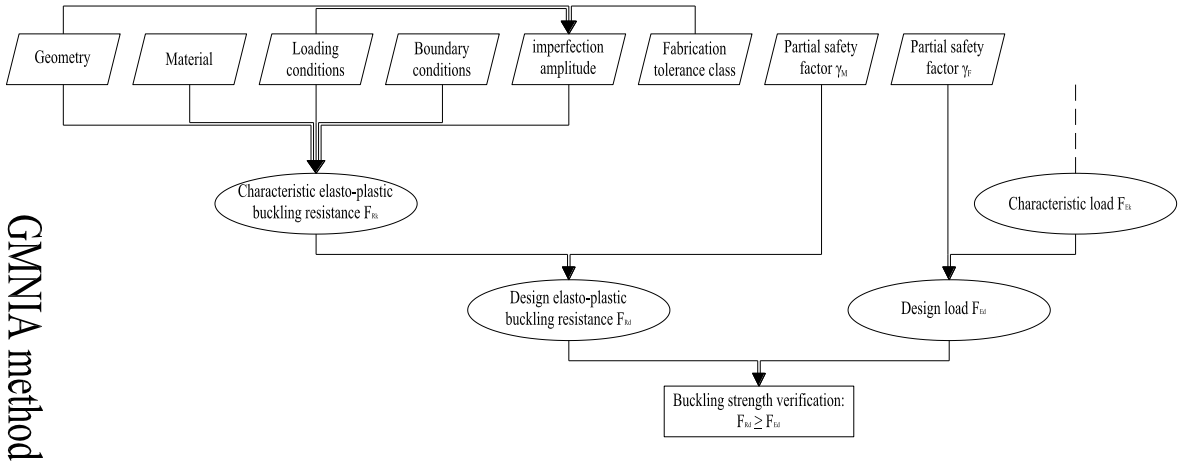

Fig. 2-20 Design scheme of the GMNIA procedure.

The reason why the procedure consists of many different shell calculations is the large number of possible failure phenomena (i.e. plastic yielding, elasto-plastic buckling, or pure elastic buckling - bifurcation or snap-through) and the imperfection sensitivity of the structure for a wide range of imperfections (ECCS, 2008). The first three calculations (i.e. LBA, MNA, and GMNA) are performed as check, in order not to miss the limit state of the perfect structure (respectively elastic, plastic, and elasto-plastic limit state). Furthermore, the performance of a GMNA calculation has a second function: the elasto-plastic strength of the perfect structure is used as reference for all GMNIA calculations to assess the influence of the assumed imperfections.

The conservatism of the GMNIA approach largely depends on the chosen geometric imperfection (i.e. its shape, location, orientation, and amplitude), because imperfections play a significant role in the elasto-plastic buckling load of a real shell structure. In Section 6, the different approaches for the choice of an imperfection are explained in detail.

4.5 Shell analysis

Analysis types in general

Appendix A contains a summary of all shell analysis types and a brief discussion of their usefulness.

Analysis types in this investigation

In Chapter 5 - Parametric study: Numerical research, the influence of the parameters of the silo will be investigated one by one by means of GMNA analyses (the failure load corresponds with the strength of the perfect structure). In some parts, additional analyses (such as GNA and MNA) are performed to estimate the influence of geometric and material non-linearity. In Section 9 of Chapter 5 (Imperfection sensitivity), GMNIA and GMNA analyses are performed to investigate the influence of equivalent geometric imperfections. In Chapter 6 - Design rule, capacity curves will be determined for a wide range of geometries. To conclude, all types of shell analyses from Appendix A will be used in this work (except the first two).

PART II.

5 Geometric and material non-linearity

Geometric non-linearity

The influence of geometric non-linearity (i.e. the changes in geometry or the pre-buckling deformations) can be evaluated by comparing the failure load of a geometrical non-linear analysis without imperfections (GNA) with the (first) eigenvalue of a linear bifurcation analysis (LBA). The ratio of these loads is also known as the elastic (imperfection) reduction factor α of the structure (See Eq. (2-19)). Another method is the comparison of the MNA load with the GMNA load. Geometric non-linearity is increasingly important as the elastic reduction factor α (without imperfections!) decreases or as the difference between the MNA load and the GMNA load increases.

The effect of geometric non-linearity on the buckling behaviour was investigated by (Donnell, 1950; Yamaki, 1984; Doerich, 2008). For a typical axially compressed cylinder, the loss in strength due to geometrical non-linearity only accounts for approximately 8 to 15% (Yamaki, 1984). In contrast to geometric non-linearity, imperfections can decrease the strength up to 80% (Yamaki, 1984; Rotter, 2004). That is the reason why in the past much more research was done on the influence of imperfections than on geometric non-linearity.

First of all, non-linearity in the pre-buckling path often leads to additional destabilising stresses, and as will be explained later, it can decrease the effective yielding stress and the critical buckling stress by flattening of the silo wall.

A key finding from literature is that geometric non-linearity is more severe for asymmetrical loading patterns than for symmetrical loading conditions of uniform compression (Doerich, 2008). In practice, most silo structures are exposed to high local loads from the structure itself (e.g. above local supports or in the vicinity of stiffeners - as in this study), the filling or discharge process (asymmetrical stress distribution due to eccentrically filling/emptying the contents), etc. As a consequence of these local loads, regions with highly non-uniform stresses are introduced in the silo wall. Consequently, these regions are very susceptible to premature failure (plastic yielding and/or elastic buckling). Furthermore, this premature failure is enhanced by the flattening of the silo wall (= pre-buckling deformations) caused by the local compressive loads. In this region, the curvature $1/r$ decreases and the effective radius of curvature r increases, reducing the critical buckling stress σ_{cr} (See Eq. (2-1)) and thus the buckling strength.

The effect of geometric non-linearity to the buckling behaviour was investigated for bracket-supported cylinders by (Doerich, 2008) and for thin cylindrical shells under locally elevated compressive stresses (patch loads) by (Rotter, 2011). Both studies confirm the above statement. For the first study, a reduction of the buckling strength of 33% was obtained for a short narrow bracket, while a tall narrow bracket had a reduction of only 23% (Doerich, 2008). In the second study, the buckling strengths were reduced up to 50% of the linear bifurcation value for very local patch loads (less uniform compression), while for wider patch loads (more uniform compression), the decrease was only 15% (Rotter, 2011). For both studies, the imperfection sensitivity displays the opposite tendency of the geometric non-linearity: while the disadvantageous effect of geometric non-linearity on the buckling strength increases for asymmetrical loadings, the imperfection sensitivity often decreases.

Material non-linearity

The influence of material non-linearity (i.e. the deviation of the real elasto-plastic material behaviour from a purely elastic material behaviour) can be evaluated by comparing the failure load of a material non-linear analysis (MNA) with the (first) eigenvalue of a linear bifurcation analysis (LBA). The square root of the ratio of these loads is also known as the relative slenderness λ of the structure (See Eq. (2-14)). Another method is the comparison of the GNA load with the GMNA load. Material non-linearity is increasingly important as the relative slenderness λ decreases or as the difference between the GNA load and the GMNA load increases.

For a very thin silo (i.e. with a high relative slenderness λ), the structure will fail by pure elastic buckling at a relatively low load level. In this case, the GNA load and the GMNA load will be equal to each other, which means that material non-linearity does not matter. Two scenarios are possible: (1) the material remains fully elastic (i.e. the yield strength has not been reached at any point), or (2) yielding has occurred in a location where it does not influence the buckling conditions. On the other side, an intermediately thick silo (i.e. with an average relative slenderness λ) and a very thick silo (with a low relative slenderness λ) will fail respectively by elasto-plastic buckling at an intermediate load level or by plastic yielding at an increased load level. Such an increased load level of thicker silos corresponds with regions where the stresses locally exceed the yield strength before failure occurs. When the structure fails by pure plastic yielding, the GMNA load is equal to the MNA load. Another finding is that, as the effect of material non-linearity increases, the effect of geometric imperfections will decrease, compared to silos which fail under elastic conditions (ECCS, 2008).

Conclusions

Geometric non-linearity has no effect on the reduction of the failure load of thick-walled silos ($\lambda < \lambda_0$), becomes increasingly important for silos with intermediate thicknesses ($\lambda_0 < \lambda < \lambda_p$), and is of primary importance for the buckling strength of thin-walled silos ($\lambda > \lambda_p$).

Material non-linearity must be taken into account for thick-walled silos ($\lambda < \lambda_0$), becomes less important for silos with intermediate thicknesses ($\lambda_0 < \lambda < \lambda_p$), and has no effect on the buckling strength of thin-walled silos ($\lambda > \lambda_p$).

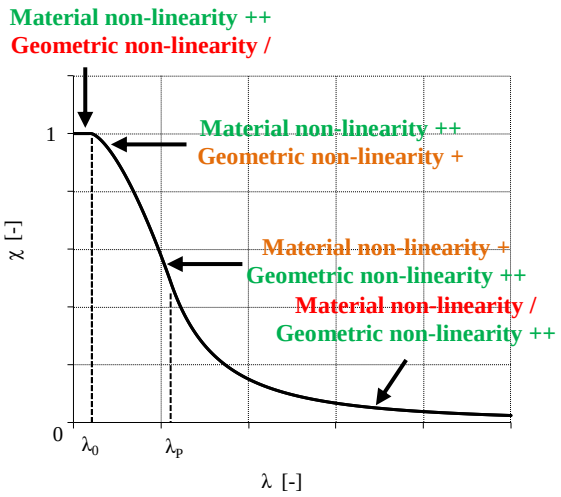

Fig. 2-21 General capacity curve

6 Imperfections

Imperfections simply cannot be avoided in practice and are introduced in the silo wall during different stages of its lifetime: before operational use (i.e. fabrication, manufacture, or erection of the silo), during operational use (e.g. uncontrolled discharge of the silo contents and maintenance), or by time dependent processes (e.g. foundation settlement). Since geometric imperfections have a dominating deleterious effect on the buckling strength of shell structures, it is therefore of vital importance to include small deviations to the nominal surface of the shell wall when predicting the elasto-plastic buckling load of a real structure. Furthermore, "equivalent" geometric imperfections must also take into account the effect of all other imperfections (See paragraph Amplitude in Section 6.2).

6.1 Approaches for the choice of an imperfection shape

Since locally supported thin-walled steel silos subjected to axial compression are highly sensitive to a wide range of imperfections, and the imperfection sensitivity depends on the amplitude of the chosen imperfection, it is very difficult to single out one imperfection shape and amplitude, which is sufficiently disadvantageous for one geometry (as designer during the design process) or for all geometries (as researcher). The latter is necessary if further progress has to be made in the development of design rules. However, it is difficult to select an imperfection shape from previous research, since the imperfection sensitivity depends on the shape of the shell, the corresponding stiffening configuration, and the boundary and loading conditions. Because of the above mentioned reasons, it is an enormous challenge as a designer/researcher to choose one specific imperfection. In general, there are three main philosophies for choosing an imperfection, as described by (Schmidt, 2000) and (Rotter,

2004): (1) the most realistic imperfection shape, (2) the worst imperfection shape, and (3) an equivalent imperfection shape (ECCS, 2008).

Realistic imperfections

The first conceptual approach is to model geometric imperfections **as "realistic" as possible** based on measurements of similar silo structures (full-scale or laboratory shells), while residual stresses and material imperfections are frequently neglected, because of the difficulties to quantify them (ECCS, 2008). Arbocz was probably the first who used such measurements of imperfections in aerospace shells (Arbocz, 1974; Arbocz and Babcock, 1974; Arbocz and Sechler, 1974). Currently, such measurements are only to a limited extent available on large steel silos, because of the cost and the difficulties of its execution and implementation (e.g. define the best-fit surface of the silo wall, Fourier decomposition, etc.). Moreover, it is not obvious to derive a (preferably simple) equivalent geometric imperfection shape in a feasible and repeatable manner for typical civil engineering structures (Arbocz, 1983).

Worst possible imperfections

Searching to **the very "worst possible" geometrical shape** (within a specific range of tolerance) is the second approach, and is intended to provide a safe lower bound for design. This method has been used from the beginning that imperfections were introduced, and can in principle be applied for different shell problems. To find the most severe shape, parametric studies have been done for specific problems (e.g. Greiner and Derler, 1995; Blachut and Jaiswai, 1999). Others used mathematical investigations to deal with this topic (Koiter, 1963; Deml and Wunderlich, 1997). However, nowadays, these attempts are not widely spread in the design stage of shell structures. Furthermore, such methods are difficult to apply due to several inevitable shortcomings: real structures generally do not necessarily have the "worst" mode as geometric imperfection, and the "worst" mode frequently is far from realistic (Rotter, 2004). In other words, it is doubtful that this method provides imperfections which are close enough to real silo structures, and consequently simulate the real imperfection sensitivity and the failure behaviour in practice. Furthermore, underpredictions of the real buckling strength are not economical. In conclusion, this method is less appropriate to determine the buckling strength by numerical simulations with the most severe geometrical imperfection shape.

Simple equivalent imperfections

The third and last approach is the use of **a relatively simple "equivalent" geometric imperfection**. Such a shape might perhaps not be 100% realistic nor is it the most severe possible shape, its main purpose is to sufficiently influence the behaviour of the silo (in an adverse way) to reduce the buckling load. Likely candidates to be used as equivalent shape are shapes which have a certain degree of geometric similarity to either failure patterns (such

as buckling or post-buckling modes) or the fabrication-caused shape deviations (e.g. an axisymmetric weld depression) (ECCS, 2008). These imperfections are modelled as initial shape deviations perpendicular to the middle surface of the perfect silo wall.

Since it is the purpose to develop design rules according to the Eurocode (EN 1993-1-6, 2007; EN 1993-4-1, 2007), the last approach, namely the use of equivalent geometric imperfections, was adopted in the current investigation as prescribed by the requirements of the European normative documents (EN 1993-1-6, 2007). The reason for this choice is simply that, at this moment, the use of "equivalent" imperfections is by far the most suitable approach to predict realistic failure loads by a numerical analysis (ECCS, 2008). Furthermore, the present study takes into account the guidelines and the commentary of the recommendations of the ECCS.

6.2 Equivalent imperfection shapes

Shape

In previous work, different imperfection shapes have been suggested for the use as equivalent geometric imperfection: a linear or non-linear bifurcation buckling mode of the perfect shell (LBM or NBM) (Koiter, 1945; 1963; Danielson, 1974; Brendel and Ramm, 1980; Yamaki, 1984; Combescure, 1986; Speicher and Saal, 1991; Greiner and Derler, 1995; Wunderlich and Albertin, 2000; Guggenberger et al., 2000; Song, 2002; 2004), a post-buckling deformed shape (PDS) (Esslinger and Geier, 1972; Guggenberger, 1998; Guggenberger et al., 2000; Schneider et al., 2001; Song, 2002; 2004), or a combination of (bifurcation) buckling modes. Other studies of measured imperfections pointed out that geometric imperfections are closely related to the fabrication process of the structure (Arcbocz, 1982). A good example are the axisymmetric circumferential welds which are commonly found in silos which are made by welding together circular strakes (Clarke and Rotter, 1988; Ding et al., 1991; Coleman et al., 1992; Song, 2002; 2004). The effect of weld depression(s) on the buckling strength has already extensively been studied by (Bornscheuer and Häfner, 1983; Rotter and Teng, 1989; Teng and Rotter, 1992; Rotter, 1996b, 1997; Ding et al., 1996; Berry, 1997; Berry et al., 2000; Pircher, 2000; Pircher and Bridge, 2001a,b; Pircher et al., 2001). In general, all of the above are good candidates, but none can yet be identified for "universal" application (ECCS, 2008).

Next, since all of the above mentioned shapes seem to be possible candidates as equivalent geometric imperfection, we will have a look at the requirements of the Eurocode (EN 1993-1-6, 2007; ECCS, 2008). At first instance, the Eurocode requires that the imperfection with the "most unfavourable effect" on the failure behaviour/load should be chosen. In other words, a sufficient number of different imperfection patterns should be investigated to identify the most severe one. The main reason why different forms need to be considered is that imperfections of many different shapes and forms are found in real shell structures (ECCS, 2008). First, the eigenmode-affine pattern (i.e. a linear bifurcation mode of the perfect shell) is proposed, unless a different unfavourable pattern could be justified. Furthermore, the

Eurocode recommends the use of realistic unfavourable imperfection shapes, which reflect the constructional detailing (such as axisymmetric weld depressions (WD)) and boundary condition in an adverse way. In contrast, shapes can be excluded from the investigation as they are considered as unrealistic because of the method of fabrication, manufacture, or erection.

In the present study, four alternative imperfection shapes are considered: (1) the linear buckling mode of the perfect shell (LBM); (2) the non-linear buckling mode of the perfect shell (NBM); (3) several post-buckling deformed shapes of the perfect shell (PDS); and (4) the axisymmetric weld depression (WD). The (dis)advantageous effect of all imperfection shapes are always evaluated relative to the same reference resistance. Indeed, the elasto-plastic failure load of an imperfect structure (GMNIA) will always be compared with the elasto-plastic failure load of a perfect silo structure (GMNA) to assess the magnitude of the influence of the considered imperfections. For structures which fail by elastic buckling only, the ratio F_{GMNIA}/F_{GMNA} should be a little higher than the value of the elastic imperfection factor α obtained by hand calculations. When plasticity becomes more important, the ratio F_{GMNIA}/F_{GMNA} will increase (towards one) because thick-walled structures appear to be less severely influenced by imperfections (ECCS, 2008).

Orientation

The Eurocode only gives a general guide on the orientation of equivalent geometric imperfections: the orientation of the maximum initial deviation (perpendicular to the middle surface of the perfect shell) should be chosen unfavourably towards the centre of the shell curvature (EN 1993-1-6, 2007; ECCS, 2008). It is expected that the inward-oriented dents (i.e. the maximum amplitude is oriented towards the centre of the curvature) are generally more disadvantageous, because they reduce the curvature of the shell, resulting in a smaller (buckling) strength (e.g. Teng and Rotter, 1990). However, this rule of thumb is normally valid for shells which fail by elastic buckling, but this is not always the case for thick-walled silos, which fail by plastic yielding. In these, the yield condition is sometimes fulfilled earlier at the centre of an outward dent: axial compression in combination with tension in circumferential direction (Schneider, 2006).

Since the choice for an inward imperfection is not always the most disadvantageous, it is difficult to give a generally applicable guideline. Therefore, in this study, the influence of the orientation is investigated for all imperfection shapes, and both inward deviations and outward deviations are considered, relative to the perfect silo wall.

Amplitude

The amplitude of an equivalent geometric imperfection should be chosen in relation to the fabrication quality of the structure and should include the effects of both geometrical and non-geometrical imperfections. The Eurocode defines three tolerance quality classes: excellent quality (Class A), high quality (Class B), and normal quality (Class C) (EN 1993-1-6, 2007). The reason why the Eurocode defines several fabrication tolerance quality classes is that the reduction of the strength of a perfect geometry largely depends on the amplitude of a bulge. As a result, it is highly valuable to consider different classes of fabrication, and make the failure strength dependent on the quality of fabrication of the silo (ECCS, 2008). Indeed, Class A corresponds with silos with an excellent quality (i.e. smaller imperfections) and will have the largest strength. High and normal quality silos (i.e. medium sized and larger imperfections) are classified in respectively Class B and Class C, and will have smaller strengths compared to Class A silos.

Furthermore, it is important to know that the amplitude of an "equivalent" geometric imperfection is about 60% larger than the standardized values of the dimple tolerance measure, because they additionally must cover the effect of all other types of (non-) geometric, material, and non-measurable imperfections which cannot be avoided in practice (ECCS, 2008), such as deviations from the nominal geometric shape of the middle surface, depressions and irregularities near meridional and circumferential welds, variations in nominal thickness and material properties, weld-induced residual stresses, rolling induced stresses, etc. (EN 1993-1-6, 2007). Other possible negative effects such as ground settlements or flexibilities of connections/supports are not subsumed under the rubric of "imperfections".

In previous research, (Esslinger and Ciprian, 1982) and (Knoedel and Ummenhofer, 1996) estimated the individual contributions of geometrical imperfections (±50%), residual stresses (±10%), and other imperfections (±40%) to the overall effect from imperfections.

Table 2-13 Individual contributions to the overall effect from imperfections.

	ESSLINGER AND CIPRIAN	KNOEDEL AND UMMENHOFER
Geometric imperfections	60%	50%
Residual stresses		10%
Unevenness of the supports and loading imperfection	40%	40%

6.3 Description of the imperfection forms

In this section, a brief outline is given of the four imperfection shapes which are considered here: (1) the linear bifurcation mode (LBM), (2) the non-linear bifurcation mode (NBM), (3) the post-buckling deformed shapes (PDS), and (4) the weld depression (WD).

Type 1 - Linear Bifurcation Mode of the perfect shell or LBM

In previous research, an eigenmode-affine imperfection (i.e. a linear bifurcation mode) of the perfect shell has been commonly used as equivalent imperfection shape. This shape should also be taken into consideration as recommended in the Eurocode (EN 1993-1-6, 2007), unless a different more severe pattern can be justified. In general, a LBM imperfection is a rather severe imperfection (EN 1993-1-6, 2007). The advantage of an eigenmode as imperfection shape is that it is easy to obtain from a linear bifurcation analysis of a perfect geometry (i.e. LBA). In most cases, the first eigenmode, corresponding with the lowest eigenvalue, has been taken. However, it is important to know that higher eigenmodes could be more critical than the first eigenmode (ECCS, 2008).

Type 2 - Non-linear Buckling Mode of the perfect shell or NBM

Compared to a LBM, a non-linear buckling mode or NBM (either the incremental mode at the limit point load or the non-linear bifurcation mode) also considers the influence of geometric non-linearity and thus the pre-buckling deformations. As a result, the shape, the location, and its influence on the failure behaviour may be substantially different from a LBM. Furthermore, such a shape is also easy to obtain from a geometric non-linear analysis of a perfect geometry (i.e. GNA).

Type 3 - Post-buckling Deformed Shapes of the perfect shell or PDS

A post-buckling deformed shape or PDS is a post-buckling deformation pattern which is obtained from the decreasing post-buckling path (i.e. after the limit load) of a geometric and material non-linear analysis of a perfect geometry (i.e. GMNA). However, this pattern changes gradually due to geometric non-linearity, making it difficult to define the shape in a unique and repeatable manner (Yamaki, 1984; Riks et al., 1996; Rotter, 2004). Furthermore, due to a lack of generality, a NBM and a PDS are less applicable as equivalent imperfection shape for all geometries and load cases compared to a LBM (Rotter, 2002).

For practical considerations, the current study is restricted to explore the influence of three different PDS patterns to the failure behaviour, each time after the limit load (similar to Song, 2002; Song, 2004):

- Immediately after the limit load F_{max} (PDS - MAX);
- At the lowest load F_{min} after the limit load (PDS - MIN);

- At the load F_{mid} at approximate halfway between the limit load F_{max} and the lowest load F_{min} (PDS - MID). Since the load increments in Abaqus are dictated by the Riks algorithm, the load F_{mid} was chosen in approximately halfway between F_{min} and F_{max}. However, the deviation between these loads is negligible.

Type 4 - Axisymmetric weld depression or WD

In general, circular steel silos are constructed by welding together many circular panels. First, the panels are connected with short meridional welds to form strakes. The circumferential positions of the meridional welds in one strake are usually offset from those in the adjacent strakes by half a panel width. Subsequently, the strakes are connected with continuous circumferential welds to form the silo. Previous research has demonstrated that, for cylinders under axial compression alone, the circumferential welds lead to a larger reduction of the buckling load compared to meridional welds due to their circumferential nature (Rotter and Teng, 1989; Hübner et al., 2006). This is the reason why in this study (pure axially compressed silos) only continuous circumferential welds have been considered.

At each circumferential welded joint, a weld depression (which is predominantly axisymmetric) is caused by two phenomena. The first reason is **the plate rolling process**. During this process, flat steel plates are rolled into circular strakes, inducing plastic deformations, especially near its circumferential edges. Before welding, the plate near the curved edges is often more slightly inwardly curved than the central part of the plate (Rotter and Teng, 1989). In other words, such curved panels are, in practice, not perfectly cylindrical. Secondly, **weld shrinkage** occurs in the vicinity of the weld joint during cooling, imposing a radial inward force on the shell, causing radial deformations (Rotter and Teng, 1989). These pioneers proposed a well-defined expression for a weld depression, as is presented in Eq. (2-44). In this formula, w is the deviation at a distance x from the centre of the weld depression; δ_{max} is the maximum deviation at the centre of the weld depression; λ is the linear elastic bending half-wavelength (Eq. (2-45)) (Berry et al., 2000); k is a shape factor and depends on the extent to which the deformations are prevented during the cooling process.

$$w = \delta_{max} \cdot e^{-\left(\frac{\pi x}{\lambda}\right)} \cdot \left[cos\left(\frac{\pi x}{\lambda}\right) + k \cdot sin\left(\frac{\pi x}{\lambda}\right)\right] \tag{2-44}$$

$$\lambda = \lambda_b = \sqrt{2} \cdot \lambda_{cl} = 2.44 \cdot \sqrt{R \cdot t} \tag{2-45}$$

Rotter and Teng proposed two extreme shapes, namely a weld depression **type A** ($k = 1$) and a weld depression **type B** ($k = 0$). A type A weld depression (See Fig. 2-22 (a)) is completely rotationally stiff during cooling. This type is formulated according to the linear elastic shell bending theory for long thin-walled cylinders by assuming full meridional moment continuity at the weld. Furthermore, it is expected that this shape is more conservative than a type B weld depression (See Fig. 2-22 (b)). For the latter, the weld depression is completely flexible

(i.e. rotationally free) during cooling and it is assumed that there is no moment continuity in meridional direction at the weld. However, in real structures, the shape lies in between these two extreme cases ($0 < k < 1$) and the flexural yielding is only partially prevented during the cooling process, and there is a certain moment continuity at the weld (Berry et al., 2000; Pircher et al., 2001).

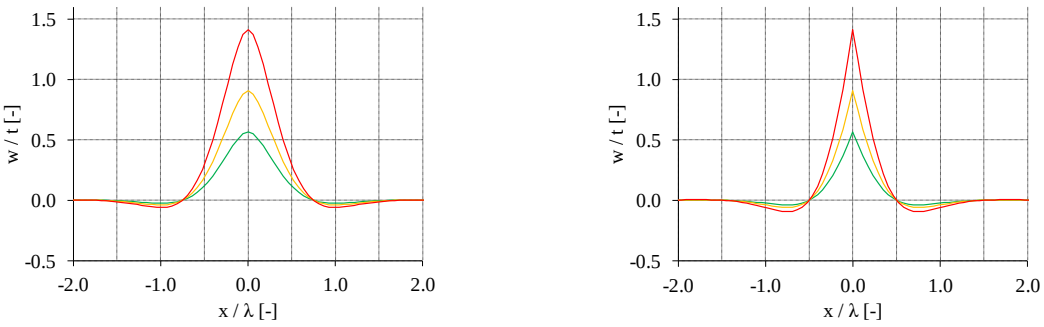

(a) Type A. (b) Type B.

Fig. 2-22 Shape of a weld depression for three fabrication tolerance classes defined in (EN 1993-1-6, 2007) ($R/t = 200$).

An axisymmetric weld depression has several advantages compared to other imperfection shapes. Firstly, it represents a common shape in the real structures, namely a depression in the vicinity of a circumferential weld joint. As proposed in (EN 1993-1-6, 2007), it strongly reflects the fabrication method of the silo structure, in contrast to a LBM, NBM, or PDS. Furthermore, previous research demonstrated that such circumferential welds are characteristic for circular steel silos (Rotter and Teng, 1989). In addition, the proposed formulation (See Eqs. (2-44) - (2-45)) is relatively simple and it can easily be applied in numerical analyses.

Although in principle the weld depression can be placed anywhere along the height of the silo wall, in this study, only those positions are investigated in the region of the silo wall directly above the terminations of the U-shaped longitudinal stiffeners or engaged columns.

Table 2-14 summarizes the chosen set of equivalent imperfection shapes.

6.4 Determination of the amplitude of equivalent imperfection shape

The initial amplitude δ_{max} of the equivalent imperfection (in the beginning of a GMNIA analysis) is the maximum deviation of the imperfection and is measured perpendicularly to the middle surface of the perfect shell. This amplitude is defined in (EN 1993-1-6, 2007) and is equal to the maximum of $\delta_{eq,1}$ (Eq. (2-46)) and $\delta_{eq,2}$ (Eq. (2-47)).

$$\delta_{eq,1} = l_g \cdot U_{n,1} \tag{2-46}$$

$$\delta_{eq,2} = n_i \cdot t \cdot U_{n,2} \quad (2\text{-}47)$$

$$l_g = l_{gx} = 4 \cdot \sqrt{R \cdot t} \quad (2\text{-}48)$$

Where l_g is the relevant gauge length (Eq. (2-48)); R and t are respectively the silo radius and silo wall thickness; n_i is a multiplier to achieve an appropriate tolerance level (a value of 25 is recommended); $U_{n,1}$ and $U_{n,2}$ are the dimple imperfection amplitude parameters, and depend on the fabrication tolerance quality class, as listed in Table 2-15.

Table 2-14 Overview of the different geometrical imperfection shapes.

TYPE	ABBREVIATION	DESCRIPTION	ORIENTATION
Type 1	LBM - INW	Linear bifurcation mode of the perfect shell	Inward
	LBM - OUTW	Linear bifurcation mode of the perfect shell	Outward
Type 2	NBM - INW	Non-linear buckling mode of the perfect shell	Inward
	NBM - OUTW	Non-linear buckling mode of the perfect shell	Outward
Type 3	PDS - MAX - INW	Post-buckling deformed of the perfect shell, immediately after the limit load	Inward
	PDS - MAX - OUTW	Post-buckling deformed of the perfect shell, immediately after the limit load	Outward
	PDS - MID - INW	Post-buckling deformed of the perfect shell, at the load in halfway between the limit load and the lowest load	Inward
	PDS - MID - OUTW	Post-buckling deformed of the perfect shell, at the load in halfway between the limit load and the lowest load	Outward
	PDS - MIN - INW	Post-buckling deformed of the perfect shell, at the lowest load	Inward
	PDS - MIN - OUTW	Post-buckling deformed of the perfect shell, at the lowest load	Outward
Type 4	WD - A - INW	Weld depression type A	Inward
	WD - A - OUTW	Weld depression type A	Outward
	WD - B - INW	Weld depression type B	Inward
	WD - B - OUTW	Weld depression type B	Outward

Table 2-15 Recommended values for the dimple imperfection amplitude parameters (EN 1993-1-6, 2007).

FABRICATION TOLERANCE QUALITY CLASS	DESCRIPTION	$U_{n,1}$ [-]	$U_{n,2}$ [-]
Class A	Excellent quality	0.010	0.010
Class B	High quality	0.016	0.016
Class C	Normal quality	0.025	0.025

When a weld depression is used as equivalent geometrical shape, the calculated value of the amplitude δ_{max} can be entered directly into Eq. (2-44). In contrast, the starting point for a LBM/NBM/PDS imperfection shape is a preceding numerical analysis. In this analysis, the maximum radial deformation δ_{Abq} of the bifurcation/buckling pattern should be found, and this value should be multiplied with a scaling factor s (See Eq. (2-49)) to obtain the desired amplitude δ_{max}. Since the scaling factor s is determined in this study by hand, the use of LBM/NBM/PDS was much more time-consuming compared to a weld depression WD.

$$s = \frac{\delta_{max}}{\delta_{Abq}} \tag{2-49}$$

7 Loading conditions

For the design of silos in the ultimate limit states, different loading conditions must be considered, such as bulk material loadings during filling, storage, and emptying, snow, wind, thermal loads, induced loads (e.g. foundation settlement), and seismic loads (Eurocode 1-4, 2006). In this literature review, only the loading caused by the stored material (e.g. grain and cement) will be discussed.

In general, two major limit states must be considered for the design of cylindrical steel barrels: (1) plasticity due to excessive pressures and (2) pure elastic buckling or elasto-plastic buckling under axial compression. The latter is a serious failure mechanism to fear (Rotter, 1983; 2006; Song et al., 2004), owing to the thin-walled nature of a steel silo and the predominantly vertical loading direction, inducing compressive stresses in the silo wall. These stresses arise from friction of the solids against the wall, from (un)symmetrical pressures during filling and discharge, and from wind loadings.

The pressures on the silo caused by bulk solids wall will always be considered under full conditions, because generally in this state the largest stresses occur (EN 1991-4, 2006). In what follows, the pressures will be discussed for the vertical wall of "slender" cylindrical silos. In (EN 1991-4, 2006), a slender silo has an aspect ratio h_c/d_c larger than or equal to 2.0 (in which h_c corresponds with the height of the cylindrical barrel from the transition to the equivalent surface, and d_c is the internal diameter of the circular cross-section).

7.1 Filling - discharge - feeding

Before proceeding to the detailed discussion of the calculation of the silo wall pressures exerted by the bulk solids during filling and discharge of the contents of the silo, these terms are clarified first.

The **filling** of a silo can be achieved mechanically (e.g. belt conveyers) and/or pneumatically (e.g. pneumatic filling system in the roof or the bulk truck) by providing an opening at the top of the cylindrical barrel or in the silo roof.

During **emptying** the silo, the bulk solids are flowing (by gravity or by discharge aids) from larger to smaller cross-sections in the direction of the discharge system, and then out of the silo. During this operation, discharging is the process of movement of the bulk solid in the area of the discharge system, while feeding is the process to provide and control the flow of bulk solids out of the silo in a reproducible and regulatory way (Brown and Nielsen, 1998).

The **discharge system** consists of discharge elements (devices and machines to which the solids are flowing freely; example of sub functions are shut-off and feeding) and discharge aids (aids, devices, and machines to permit, improve, and maintain the solid flow under conditions where gravity cannot be achieved). For discharge element and aids, four different principles can be distinguished: (1) mechanically: the bulk solids are conveyed by rotating or translatory elements (e.g. screws and scrapers) (example in Fig. 2-23 (a)); (2) oscillatory: vibrators influence the internal friction or the wall friction of the bulk solids (example in Fig. 2-23 (b)); (3) pneumatically: energy is applied to the bulk solids by gas (or air) reducing the internal friction or the wall friction of the bulk solids; (4) statically: the flow profile is changed by fixtures, such as lining and cone (example in Fig. 2-23 (c)) (Brown and Nielsen, 1998). These systems are out of scope of this work.

(a) Screw conveyer.

(b) Pneumatic vibrator on hopper wall.

(c) Cone in cone insert.

Fig. 2-23 Discharge elements and aids.

The **feeding** of the contents is controlled by measuring the feed rate using volumetric and/or gravimetrical (mass flow) measuring instruments.

7.2 Action assessments classes in silos

For the assessment of the actions in silos, the design effort and the level of rigour depend on the reliability of the structural arrangement. The classification of silos into Action Assessments Classes (abbreviated as AAC) is listed in Table 2-16 and depends on the size (expressed in tonnes) and the eccentricity during discharge. The requirements for the determination of the loadings are more extensive for a large complex silo compared to a small simple silo, because of the increased risk of malfunction, the higher impact of economic and social consequences, or the increased environmental consequences of a large complex silo (See Table 2-9).

Table 2-16 Classification of Action Assessment Classes of silos (EN 1991-4, 2006).

ACTION ASSESSMENT CLASS	DESCRIPTION
AAC 1	Silos with capacity below **100 tonnes**.
AAC 2	All silos covered by Eurocode 1 Part 4 and not placed in another class.
AAC 3	• Silos with capacity in excess of **10000 tonnes**. • Silos with capacity in excess of **1000 tonnes** in which any of the following design situations occur: (a) eccentric discharge $e_0/d_c > 0.25$, (b) squat silos with top surface eccentricity $e_t/d_c > 0.25$

Remark A higher Action Assessment Class may always be adopted than that required.

7.3 Pressures on vertical walls of slender silos during storage

In the case a silo is filled with granular solid material (after filling/during storage), the wall pressures are often relatively close to those of the Janssen theory (Janssen, 1895; Rotter, 2001a). The pressures acting on the silo wall can be divided into two components: frictional traction p_{wf} (vertical) and normal pressure p_{hf} (horizontal) (See Fig. 2-24). The first is the result of friction between the stored solid and the wall, subjecting the silo to meridional axial compression. The pressures, which can be calculated by using the formulas (2-50) to (2-53) (EN 1991-4, 2006) at any depth z, and their distribution are depicted in Fig. 2-24. These stresses are uniformly distributed

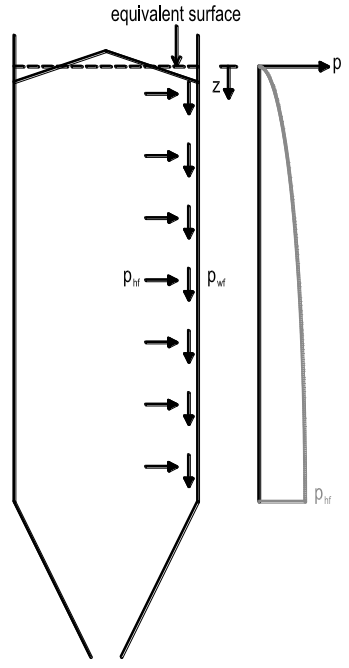

Fig. 2-24 Symmetrical wall pressures during storage.

around the complete circumference of the silo.

$$p_{h0} = \gamma_u \cdot K \cdot z_0 = \frac{\gamma_u}{\mu} \cdot \frac{A}{U} = \frac{\gamma_u}{\mu} \cdot \frac{R}{2} \tag{2-50}$$

$$p_{hf}(z) = p_{h0} \cdot \left(1 - e^{-z/z_0}\right) \tag{2-51}$$

$$p_{wf}(z) = \mu \cdot p_{hf}(z) \tag{2-52}$$

$$z_0 = \frac{1}{K \cdot \mu} \cdot \frac{A}{U} = \frac{1}{K \cdot \mu} \cdot \frac{R}{2} \tag{2-53}$$

Where:

p_{h0} the wall pressure at infinite depth [MPa];

p_{hf} the characteristic value of normal pressure acting on the silo wall [MPa];

p_{wf} the characteristic value of frictional traction acting on the silo wall [MPa];

z the distance below the equivalent top surface of the solid (full condition) [m];

z_0 the Janssen reference depth [m];

R the cylinder radius [m];

A the cylinder cross-section [m²];

U the cylinder perimeter [m];

γ_u the upper characteristic value of the bulk unit weight ($= \rho_u \cdot g$) [kN/m³];

μ the characteristic value of the wall friction coefficient [-];

K the characteristic value of the lateral pressure ratio [-].

The total compressive vertical force $F_{Sk}(z)$ in the silo wall at any depth can be calculated by:

$$F_{Sk}(z) = (2\pi R) \cdot \int_0^z p_{wf}(z) \cdot dz \tag{2-54}$$

$$F_{Sk}(z) = (2\pi R) \cdot \mu \cdot p_{h0} \cdot \left[z - z_0 \cdot \left(1 - e^{-z/z_0}\right)\right] \tag{2-55}$$

The above mentioned symmetrical pressures p_{hf} and p_{wf} **during storage** are fixed loads (which means that it is placed at its predetermined location) and must be applied on the vertical silo wall for all Action Assessments Classes.

7.4 Pressures on vertical walls of slender silos during filling and emptying the contents

During the filling and discharging process, the above mentioned stresses (i.e. p_{hf} and p_{wf}) are changing. For concentric filling, the wall pressures p_{hf} and p_{wf} gradually develop as the process progresses. For concentric emptying the barrel content, the normal pressure p_{hf} and the frictional traction p_{wf} must be multiplied with respectively C_h and C_w (EN 1991-4-1, 2006). The discharge factor on normal pressures (C_h) is larger than the discharge value on wall friction (C_w) (Rotter, 2001a). When a slender silo is discharged at its bottom (e.g. by a conical hopper), the values of C_h and C_w must be taken equal to the discharge factor for all solids $C_0 = 1.15$ and 1.10, respectively (AAC 2 and AAC 3).

$$p_{he} = C_h \cdot p_{hf} \tag{2-56}$$

$$p_{we} = C_w \cdot p_{wf} \tag{2-57}$$

The above mentioned stress patterns are also fully symmetrical and must be applied on the vertical silo wall for all Action Assessments Classes to take into account **the filling and discharging process**.

However, during this process, the pressures may change significantly and the stresses are redistributed over the shell surface (Nielsen, 2008). In some regions the stresses increase, while in other regions lower pressures can be found. In addition, the redistribution of stresses, and consequently the location of large stresses, vary with time (Nielsen & Andersen, 1981; Hartlen et al., 1984). This pressure redistribution largely depends on the shape of the flowing material, such as mass flow, pipe flow, and mixed flow (See Fig. 2-11). Other influencing factors of the pressure redistribution are the flexibility of the wall, the eccentricity of inlet and outlet, and accidental eccentric discharge (Nielsen, 2008; Sadowski, 2011). As the eccentricity of inlet/outlet increases, the non-symmetrical component of the loading will also increase. Possible causes of accidental eccentric discharge are blockages, feeder malfunctions, different packing densities, etc.

The consequence of this asymmetrical distribution of normal stresses is that the distribution of vertical stresses will also change, because of the long wave bending response of the shell (Rotter, 2001b). In certain areas of the silo wall, the compressive stresses will strongly increase, resulting in premature failure in these points. In other words, local asymmetrical low pressures are usually more damaging than very high symmetrical pressures (Rotter, 1996a; 1999). In what follows, two methods are discussed to realise such non-symmetrical distribution of stresses acting on the silo wall: (1) the use of free patch loads and (2) a simplified theory derived for a parallel-sided circular flow channel against the silo wall.

Method 1 for modelling asymmetrical pressures: patch loads

When asymmetrical pressures (increase or reduction) are present, a free patch load is an approximate way to amplify the asymmetrical pressures by placing a pressure normal to a small area of the silo wall where it will have the most damaging effect (the friction component is ignored). This technique can be applied in design (EN 1991-4, 2006) or in a finite element model. The patch load typically is defined as a multiple of the Janssen filling pressure at the same depth. As a consequence, a patch load in the vicinity of the top surface of the contents and the bottom of the silo (where the Janssen pressures are relatively small) will hardly influence the structural behaviour.

According to (EN 1991-4, 2006), a patch load should be applied to the cylindrical barrel when the filling and/or the discharge is eccentric (See Fig. 2-25 for thin-walled circular silos with $R/t > 400$). The free patch load should be placed on the silo wall in any vertical position below the equivalent surface pile to determine the worst position (AAC 3). For AAC 2, it is allowed as an alternative to take the depth z_p of the centre equal to the minimum of the Janssen reference depth z_0 (Eq. (2-53)) and the half of the height of the cylindrical barrel from the transition to the equivalent surface h_c. The patch loads extends over a small height s (Eq. (2-64)) and its magnitude p_p varies as a sine along the circumference p_{ps} (Eqs. (2-58) and (2-59)). The patch load amplitude is obtained by multiplication of the Janssen filling pressure p_h with a factor C_{pf} or C_{pe} (Eqs. (2-60) and (2-62)) that depends on the relevant eccentricity (surface pile during filling e_f and/or outlet e_o) (Eqs. (2-61) and (2-63)).

$$p_p = C_p \cdot p_h(z_p) \tag{2-58}$$

$$p_{ps}(\theta) = p_p \cdot cos(\theta) \tag{2-59}$$

$$C_{pf} = max\left(0.0; 0.2 \cdot C_{0p} \cdot \left[1 + 2E_f^2\right] \cdot \left[1 - e^{-1.5 \cdot (h_c/d_c - 1)}\right]\right) \tag{2-60}$$

$$E_f = \frac{2 \cdot e_f}{d_c} \tag{2-61}$$

$$C_{pe} = 0.42 \cdot C_{0p} \cdot [1 + 2E_e^2] \cdot \left[1 - e^{-1.5 \cdot (h_c/d_c - 1)}\right] \tag{2-62}$$

$$E_e = \frac{2 \cdot max(e_f; e_o)}{d_c} \tag{2-63}$$

$$s = 0.4 \cdot R \tag{2-64}$$

Where:

p_p the characteristic value of the amplitude of the filling/discharge patch pressure acting on the silo wall [MPa];

p_{ps} the characteristic value of the local filling/discharge patch pressure acting on

the silo wall [MPa];

θ the circumferential coordinate [°];

C_{op} the patch load solid reference factor (See last colum in Table 2-2) [-];

d_c the internal diameter of the circular cross-section [m];

h_c the height of the cylindrical barrel from the transition to the equivalent surface [m];

e_f the maximum eccentricity of the surface pile during filing [m];

e_o the outlet eccentricity [m];

s the height of patch load [m].

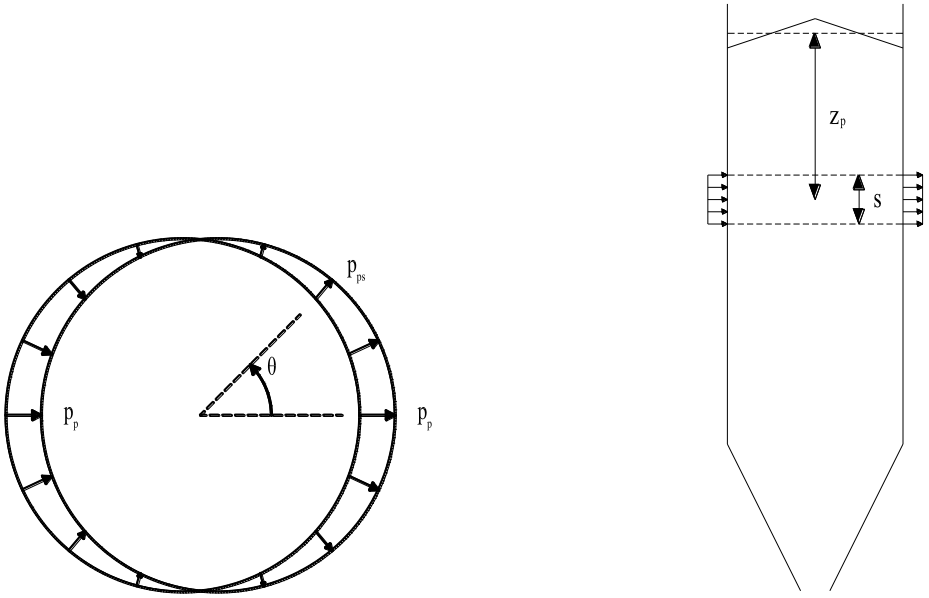

(a) Plan view. (b) Vertical cross-section.

Fig. 2-25 Asymmetrical local patch load for thin-walled circular silos (EN 1991-4, 2006).

For silos in AAC 1, this filling/discharge patch load may be ignored. For silos in AAC 2, this filling/discharge patch load may be substituted to a uniform increase of the symmetrical load. For silos in AAC 2 and AAC 3, the fixed symmetrical load and the free patch load must be applied simultaneously.

(Gillie & Rotter, 2002) demonstrated that a rectangular shaped patch load has the potential to increase the compressive stresses in the silo wall significantly. They conducted a parametric study to investigate the different variables of such a patch load. Both the pressure distribution within the patch load (e.g. uniform or bell-shaped) and the circumferential width will strongly influence the stress pattern in the silo wall. When the vertical width of the patch load is varied, almost all stresses are proportional to the vertical width, except for the compressive

meridional stress. In conclusion, the severity of a patch load depends on the location and the circumferential width of the patch load (Gillie & Rotter, 2002). The designer has to find the most critical combination of these two parameters.

Method 2 for modelling asymmetrical pressures

Additionally, for silos in AAC 2 and AAC 3 with large outlet eccentricities, a separate load case must be considered for discharging the bulk solids (EN 1991-4, 2006), including both normal pressures and frictional traction. A simplified method is developed to calculate the distribution of pressures resulting from a parallel-sided circular flow channel against the silo wall (See Fig. 2-26) (Rotter, 1986; Rotter et al., 1995; Chen et al.; 1995; Chen, 1996). The circumference of the silo wall is divided into four zones with different normal pressures: (1) the static Janssen pressures are applied outside the flow channel; (2) a large decrease of pressure within the flow channel; (3) and (4) increased pressures at the edges. For the complete calculation of the flow channel plan geometry, the static pressures, the channel edge pressures, and the flow channel pressures, the reader is referred to (EN 1991-4, 2006).

The structural behaviour of slender step-walled silos under the above mentioned load case due to eccentric discharge loading was investigated by (Sadowski, 2010; 2011). A major finding of these studies was that asymmetrical pressures are very severe for cylindrical steel silos: the failure loads corresponding with the asymmetrical pressure distribution (eccentric discharge) were far below those values of the symmetric pressure (concentric discharge). When the silo wall has a constant wall thickness over the entire silo height, the most critical location can be found at the base of the silo wall at the edge of the flow channel. In this location, the largest compressive stresses can be found. However, for a step-walled silo, the critical location shifts to midheight at the centre of the flow channel. There are two reasons why the critical location shifts. On the one hand, high compressive stresses develop close to midheight at the centre of the flow channel. On the other hand, the silo thickness is smaller at midheight compared to the base of the silo wall. Near the edges of the flow channel, axial tensile stresses will develop. This stress distribution was first identified by Rotter (Rotter, 1986).

7.5 Meridional axial compression in coexistence with internal pressures

Large horizontal pressures support the silo wall, making the structure stronger. In other words, a higher resistance against buckling can be obtained due to the finite stiffness of the stored granular solids (Wozniak, 1979; Nielsen, 2008).

In Fig. 2-27, the elastic reduction factor α (which is a measure of the reduction in buckling strength) is plotted against the internal pressure p due to bulk solids (uniform distribution). In the absence of internal pressure ($p = 0$), the elastic reduction factor is equal to the unpressurized value α_0. When the internal pressure p is present, the elastic reduction factor is equal to the pressurized value α_p. The latter is equal to the minimum of α_{pe} (elastic

pressurized value) and α_{pp} (plastic pressurized value). At first instance, the buckling strength increases because the internal pressures temper the disadvantageous effect of geometrical imperfections by reducing the zones of compressive stresses (i.e. elastic strengthening effect) (Calladine, 1983; Rotter and Teng, 1989). For higher internal pressures, the buckling strength decreases again (i.e. plastic weakening effect) due to a change in buckling mode and is known as the elephant's foot buckling (i.e. local plastic collapse) (Rotter, 1990; 2006). This mode is characterised by a membrane state inside the von Mises envelope, due to the locally increased bending stresses induced by geometric imperfections (Rotter, 1996b) and boundary conditions (Rotter, 1990; Rotter & Seide, 1987).

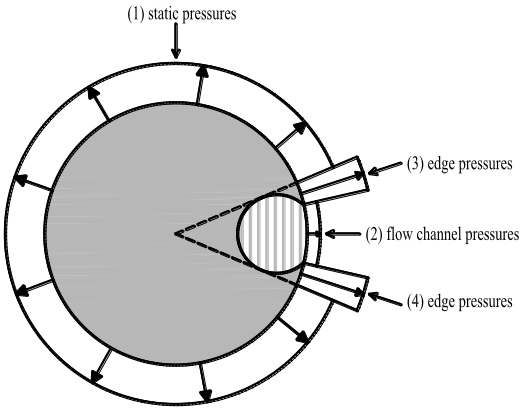

Fig. 2-26 Asymmetrical wall pressures during eccentric discharge.

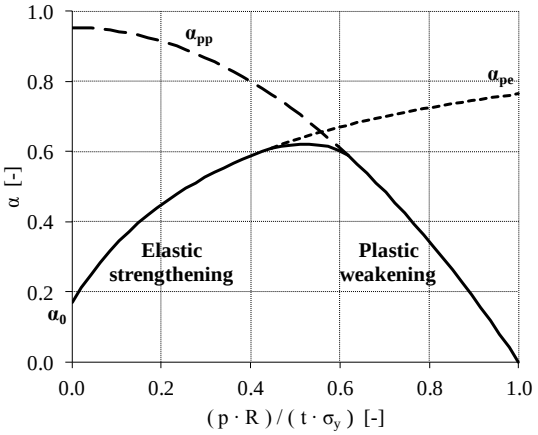

Fig. 2-27 Effect of internal pressure on the buckling strength.

As a result, when combining axial compression and internal pressures, two important questions arise: (1) which loading condition creates the critical compressive stress, and (2) which magnitude of the horizontal pressure can be assumed in combination with this critical stress (Gillie & Rotter, 2002). In other words, for the design of a silo, a load combination should be found which causes large vertical stresses (e.g. during discharge) combined with small horizontal pressures (e.g. during filling) which are guaranteed to be present (EN 1991-4, 2006). For the design process, the loading assessments (i.e. small horizontal stresses and large vertical stresses) and the corresponding characteristic values of the solid properties from Table 2-3 should be taken into account (EN 1991-4, 2006). In this way, the beneficial effect of internal pressures can be implemented in a safe manner, without overestimating the buckling strength, resulting in lighter structures.

From the above, it is clear that cylindrical steel silos are subjected to many different loading conditions, caused simply and solely by the contents of the silo. The bulk solids introduce two stress components into the silo wall. On the one hand, the bulk material applies a frictional drag on the silo wall. The frictional traction is either symmetrical or asymmetrical in circumferential direction and accumulates into a significant axial compression. In this work, the frictional traction on the silo surface will be replaced by a uniform line load on the upper

edge of the cylindrical barrel. Because the silo is supported on discrete supports, regions with increased compressive stresses (e.g. just above the supports) and regions with small compressive stresses (e.g. between the supports) will arise, making the structure prone to elastic shell buckling and/or plastic yielding. On the other hand, the bulk material exerts a normal internal pressure against the silo wall, which generally has a beneficial effect on the buckling strength. This component will be ignored in this investigation. In this way, a conservative treatment is obtained for the assessment of the elasto-plastic buckling load. Obviously, this assumed loading condition is not the only possible loading type which is severe for locally supported steel silos, and further research is necessary for other types of loading.

PART III.

8 Detailed information about support arrangements

To make it possible to empty the silo contents (by gravity), and for practical considerations (e.g. sufficient space under the hopper), the cylindrical barrel is placed in an elevated position. This can be realised either (1) by a continuous skirt, (2) by a beam grid (See Fig. 2-28 (a)), or (3) by a discretely supporting arrangement (See Fig. 2-28 (b)). A beam grid includes beams, columns, and wind braces and can support one or more silos simultaneously. The third alternative involves a limited number of narrow supporting columns around the silo circumference, whether or not by using local brackets. These columns transfer the mainly vertically oriented load from the silo structure to the foundation. For the stability of the structure, wind braces are needed between the columns. Such diagonal X-bracings can be either high-tensile strength rods or structural shape steel bracings.

(a) Indirectly via a beam grid.

(b) Directly via supporting columns.

Fig. 2-28 Supporting structure.

The supporting columns can be divided by the way of supporting and the shape of the cross-section. The first possibility is that the columns extend up to the (reinforced) lower edge of the cylindrical barrel. Such columns can be constructed as circular (hollow) profiles (See Fig. 2-29 (a)), rectangular shaped (hollow) sections, or I-shaped profiles (See Fig. 2-29 (b)). The columns can also extend over a certain height along the cylindrical barrel, and are called engaged columns. Rectangular shaped (hollow) sections (See Fig. 2-29 (c)) or U-shaped sections (See Fig. 2-29 (d)) are commonly used profiles.

(a) Circular. (b) I-profile. (c) Rectangular. (d) U-profile.

Fig. 2-29 Supporting structure.

Details connection supporting column base

In most cases, the column base is connected by welding to a thick steel base plate, which in turn is connected with the concrete foundation (e.g. a slab) or with a steel beam by means of anchor bolts (e.g. a cast-in-place bolt). This connection type is depicted in Fig. 2-30 and corresponds with a hinged support end.

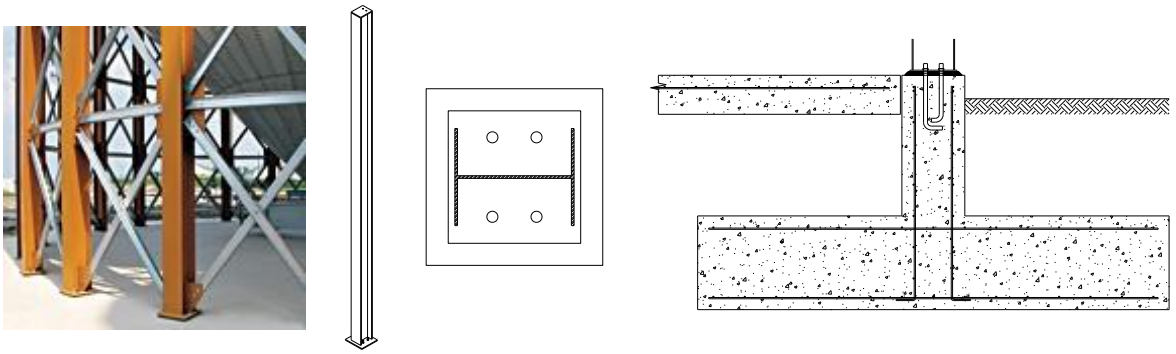

(a) 3D detail. (b) Plan detail. (c) Section detail.

Fig. 2-30 Connection column base - type 1.

In certain cases, the bottom side can be regarded as a clamped end due to the presence of stiffeners at the column base (See Fig. 2-31). Due the increased complexity of fabrication of such a node, the cost of a clamped lower edge will increase and therefore this type is less commonly used in silo construction.

(a) Example 1. (b) Example 2.

Fig. 2-31 Connection column base - type 2.

Details connection supporting column top

Now, a number of types will be discussed of the connection between the supporting column on the one hand and the elevated structure (i.e. the cylindrical barrel and the conical hopper) on the other hand.

For the first connection type (See Fig. 2-32), the supporting columns are concentrically placed relative to the cylindrical barrel and extend up to the bottom of the cylindrical barrel. At the top of each column, a steel plate and a steel support clip are provided for the attachment of a compression splice in circumferential direction. At first instance, the latter component is provided for the attachment (e.g. by bolting) of the top of the conical hopper and the lower edge of the cylindrical barrel wall. Secondly, this part acts as ring girder or ring beam, which is normally provided in larger discretely supported silos. Such a stiffener has bending stiffness and bending strength in the horizontal plane as well as normal to that plane and is provided to distribute the local supporting forces into the shell structure. Various cross-section geometries are possible for such a transition ring.

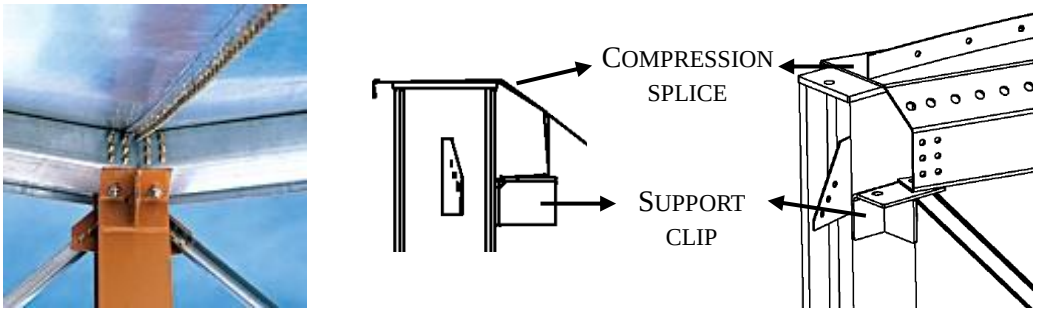

(a) Picture. (b) Section detail. (c) 3D detail.

Fig. 2-32 Connection column top - type 1a.

In Fig. 2-33, a very similar type is displayed, but now, an additional vertical compression splice is added between the supporting clip and the hopper wall.

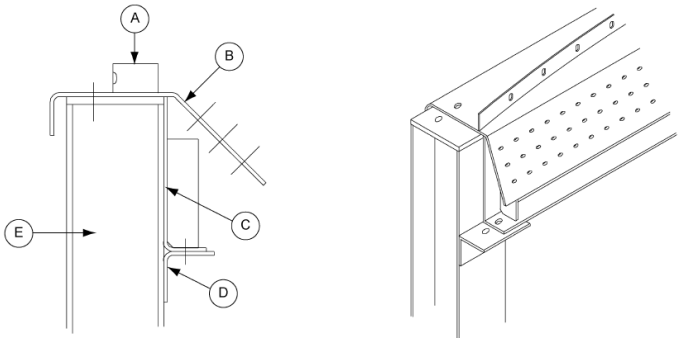

(A) Sealer strip

(B) Horizontal compression splice

(C) Vertical compression splice

(D) Supporting clip

(E) Supporting column

Fig. 2-33 Connection column top - type 1b.

Another variant is presented in Fig. 2-34. The vertical compression splice now is replaced by two vertical compression splice plates on both sides of the supporting column. Additionally, horizontal compression channels are provided between the supporting columns which act as ring girder.

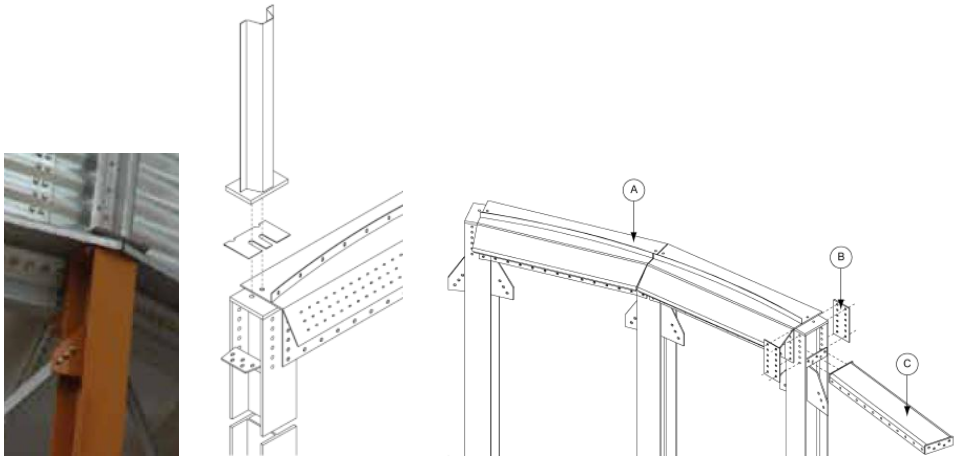

(A) Horizontal compression splice

(B) Vertical compression plate

(C) Horizontal compression channel

(a) Picture. (b) 3D detail. (c) 3D detail.

Fig. 2-34 Connection column top - type 1c.

A second possibility is that the concentrically placed supporting columns extend up to the transition ring at the lower edge of the cylindrical barrel. At the top of the columns, a steel end plate is provided (See Fig. 2-35 (a)) or a coupling part is mounted to increase the supporting surface (See Fig. 2-35 (b)). In both figures, longitudinal stiffeners are placed above the local supports to gradually transfer the supporting load into the shell wall.

A similar stiffening configuration will be investigated in this work: a transition ring at the lower edge of the cylindrical barrel, a partial-height U-shaped longitudinal stiffener above the local supports, and an upper ring above the terminations of the stringer stiffeners.

(a) Case 1. (b) Case 2.

Fig. 2-35 Connection column top - type 2.

The third alternative is to extend the concentrically placed columns up to the lower edge of a skirt. Where the plate will rest on the supporting columns, a steel support block (Fig. 2-36 (a) and (b)) or thick steel plate (Fig. 2-36 (c)) is provided, whether or not in combination with a circumferential stiffener. Above this point, a non-prismatic stiffener with decreasing cross-section may be attached to the skirt, to gradually introduce the supporting force into the shell structure.

(a) Case 1. (b) Case 2. (c) Case 3.

Fig. 2-36 Connection column top - type 3a.

In Fig. 2-37, another variant is depicted with a silo with a skirt with a relatively limited height. Ring stiffeners are placed at the upper and lower edge of the skirt, and one or more longitudinal stiffeners are attached to the external side of the silo wall above the supporting column.

(a) Case 1. (b) Case 2.

Fig. 2-37 Connection column top - type 3b.

A fourth alternative is the engagement of eccentrically positioned supporting columns, either directly attached to the cylindrical barrel or indirectly by means of a bracket (See Fig. 2-38). These connection types are used for smaller silo structures (Rotter, 2001a). The direct attachment will be investigated in detail in this work: the indirect attachment was extensively studied by means of numerical analyses by Doerich (Doerich, 2007).

(a) Case 1. (b) Case 2.

Fig. 2-38 Connection column top - type 4.

In this work, two different stiffening configurations will be numerically investigated. In the case of the partial-height U-shaped longitudinal stiffeners above the supporting columns (i.e. a variant of type 2 - see also Fig. 2-4 (c)), the supporting columns will be excluded from the numerical model and will be replaced by clamped supporting surfaces. In contrast, when cylindrical barrels are investigated with engaged rectangular shaped columns, obviously, the columns themselves will be included in the numerical model with a clamped lower edge (i.e. a variant of type 4 - see also Fig. 2-3 (c)).

In both cases, the horizontal and axial deformations are restricted in respectively the supporting surface and the supporting edge (See Section 9 in Chapter 3). As a consequence of the restricted vertical deformations along the whole supporting surface/edge, the rotation about the circumferential axis is also restricted. Due to the restriction of the circumferential rotation, these supporting conditions correspond with a too advantageous situation with respect to the majority of cases in practice. The influence of the type of support will be discussed further in Section 4 of Chapter 5.

Wind bracings

As can be seen on the above figures (e.g. Fig. 2-29 and Fig. 2-30), diagonal bracings are almost always added to stiffen the supporting columns (and optionally beams) to resist the wind loads on the structure. Frequently used types of bracings are cross bracings, K-bracings, and knee bracings (See Fig. 2-39).

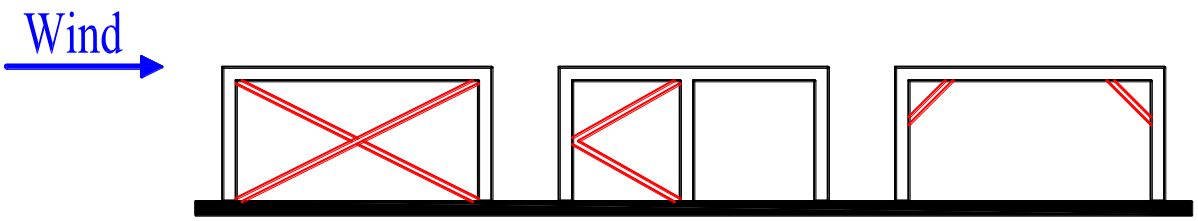

Fig. 2-39 Types of wind bracings: cross bracings (left), K-bracing (middle), and knee bracing (right).

When cables are used (for example cross bracing), it is necessary to use two cables to stabilise the structure against wind forces from both directions. One cable will work effectively in tension, while the other would just buckle. When rigid bracing members are used, a single brace can stabilise the structure.

9 Stiffening configuration

The cylindrical barrel can be either unstiffened or stiffened to ensure that the structure has the required buckling strength.

Unstiffened silo

The most obvious and simple solution is to sufficiently increase the thickness of the cylindrical barrel over its entire height. However, this corresponds with a rather uneconomical solution because the largest stresses only occur in clearly defined zones in both directions of the shell surface. In meridional direction, the applied forces exerted by the bulk solids and consequently the induced internal forces/stresses are much larger at lower levels. In circumferential direction, the largest stresses occur in the silo wall just above the local supports. In other words, for this solution, much material is added to the structure where it is not immediately necessary, for example at higher levels and between the local supports.

A more economical alternative is to progressively decrease the wall thickness from the bottom to the top of the barrel. It is perfectly possible to give each individual strake another wall thickness or to give only the bottom strake an increased wall thickness (Chen et al., 2011; Rathé and Greiner, 1996). Although this solution is undoubtedly a better alternative, too much material is added for example in the region between the local supports, because the stress level in the silo wall between the supports is much smaller than stress concentrations in the silo wall above the local supports.

Hence, the idea to keep the silo wall thickness to a strict minimum, and to increase the buckling strength (and stiffness) maximally by adding material very locally in the form of stiffeners.

Stiffened silo wall

Stiffeners are attached to a shell wall to give the wall additional strength and stiffness and are usually placed on the outside surface to avoid interference with the bulk solids. As a result of the presence of stiffeners, the unstiffened cylindrical barrel is transferred into an anisotropic structure. Depending on the direction of the axis, two types of stiffening members can be distinguished:

- **Longitudinal or stringer stiffeners** follow the meridian of the shell. They are provided to increase the stability, to assist with the introduction of local loads (e.g. above supports), or to carry axial loads. They are not intended to provide a primary load carrying capacity for bending due to transverse loads.
- **Ring stiffeners** follow the circumference of the shell at a fixed point on the meridian. It is assumed that a ring stiffener has no stiffness in the meridional plane of the structure. It is provided to increase the stability (e.g. against wind) or to introduce local loads acting in the plane of the ring.

Generally speaking, longitudinal stiffeners are much more useful than ring stiffeners, because the loads are mainly applied in the vertical direction.

In Fig. 2-40 (a), three examples are depicted of a cylindrical barrel stiffened with vertical stringer stiffeners. These partial-height or full-height stiffeners can be (uniformly) distributed over the entire circumference (example 1), or can be included just above the local supports (example 2 and 3). Furthermore, longitudinal stiffeners carry a large part of the vertical (compressive) load in the silo wall (depending on the relative stiffnesses of the stiffeners and the silo wall), and are restrained against buckling by their attachment to the silo wall. Due to the outstanding characteristics of the combined performance of the stiffener and the silo wall, this alternative is a highly economic alternative for locally supported steel silos (Rotter, 2011).

Ring stiffeners are used to provide circumferential uniformity in the axial membrane stresses (e.g. in (Topkaya and Rotter, 2013)) and to stiffen the cylindrical barrel against out-of-plane deformations (i.e. the maintenance of the circular shape at the ring**)**. As a result of the modified situation of stresses and deformations in the vicinity of the ring stiffener, the buckling strength will increase. The circumferential stiffeners can be distributed over the entire barrel height with fixed intervals (See Fig. 2-40 (b)**)** or can be placed only at a limited number of heights. Normally, the rings are attached to the shell wall at the junctions between the shell segments, at the base (i.e. a lower ring or a transition ring), or just above the terminations of the partial-height longitudinal stiffeners (i.e. an upper ring or an intermediate ring stiffener).

In practice, an orthogonally stiffened cylindrical barrel is little or not applied because of technical considerations (a lot of intersections between the longitudinal stringer stiffeners and the circumferential ring stiffeners). A better alternative is a corrugated steel silo wall: a vertically corrugated shell wall with external ring stiffeners or a horizontally corrugated shell wall with external vertical stiffeners. In such silos, the horizontally corrugated wall absorbs the horizontal tensile forces (caused by the wall pressures) and the vertical stiffeners absorb the vertical compressive forces (caused by wall friction) (Wójcik et al., 2001). These vertical stiffeners must have a sufficiently large buckling strength to avoid failure.

(a) Vertical. (b) Horizontal.

Fig. 2-40 Attachment of stiffeners.

A number of possible shapes of the vertical stiffener cross-section are depicted in Fig. 2-41: one or more rectangular plate(s), a U-shaped profile, an I-section, a reversed T-section, or a L-section. In (Vanlaere, 2006), the use of two rectangular partial-height plates at both edges of each local supporting column was extensively investigated. Since this type of stiffener tends to prematurely fail by buckling itself, one of the conclusions of this work was that there are other cross-sections shapes which are more suitable to use as meridional stiffener. From the results of (Vanlaere, 2006), the idea grew to connect the two rectangular plates with each other so that a U-shaped profile is obtained. Such a closed U-shaped profile has a much higher moment of inertia and consequently a larger resistance to buckling compared to the previously

studied alternative. This stiffener type will be thoroughly investigated in this work.

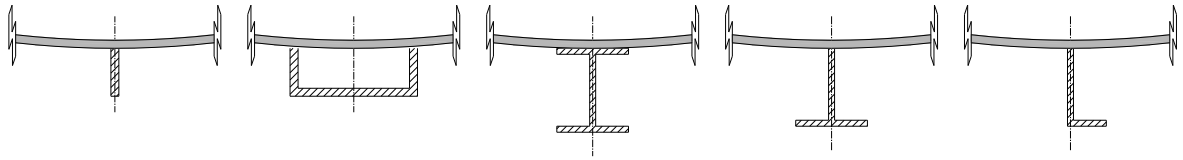

Fig. 2-41 Stiffeners cross-sections.

10 Key points of the state-of-the-art

From this chapter, it is clear that the design engineer has to make different assumptions/simplifications (e.g. the principle of "equivalent" geometric imperfections) and must take into account many parameters to design a silo structure, both on the side of the assessment of the loading conditions as on the prediction of the failure load.

On the one hand, an appropriate choice has to be made for the loading condition(s). A bulk solid will induce a frictional traction and a normal pressure to the silo wall. The magnitude of these stresses depends on the considered height (below the equivalent top surface of the bulk solids) and circumferential angle (when the pressure distribution is asymmetrical) and varies from time to time (e.g. during the different process stages: filling/storage/emptying of the contents). Furthermore, the pressures depend on many parameters, such as the bulk solid properties, the geometry and other parameters of the barrel and hopper (e.g. the eccentricity of the inlet and outlet), etc. Since the loadings are mainly vertically oriented and since a thin-walled cylindrical barrel is susceptible to axial compression, a simplified load model will be used in this work: a uniform compression load on the upper edge of the cylindrical barrel with the neglect of the (advantageous) internal pressures on the shell surface.

For shell structures subjected to axial compression, the decisive design state is the buckling limit state (and to a lesser extent the plastic limit state for very thick-walled silos). The real elasto-plastic buckling strength is affected by many parameters. Firstly, silo structures exhibit a strong non-linear behaviour before, during, and after failure. Both material non-linearity (plasticity) as well as geometrical non-linearity (pre-buckling deformations) play an important role. Secondly, the buckling strength is further reduced by the presence of unavoidable deviations relative to the perfect silo geometry and other types of (non-)geometric, material, and non-measurable imperfections in practice (e.g. variations in nominal thickness and material properties, residual stresses (near welds), etc). It is very difficult to make an appropriate choice for the set of parameters that define the (equivalent) imperfection: a shape, a location, an amplitude (related to the fabrication tolerance quality class), and an orientation. Finally, decisions must be made concerning the design approach, the buckling criteria, etc.

CHAPTER 3

Materials and methods

Nowadays, to better understand the failure behaviour of shell structures, the focus is on finite element research rather than on experimental research. This evolution is caused by powerful computers and reliable and user-friendly finite element software. In fact, both methods are complementary and have in common that they lead to a better knowledge, such as predicting the failure load. However, the procedure to reach this goal is fundamentally different, as is described below. Furthermore, the advantages and drawbacks of both methods are discussed.

For the first method, the development of a reliable numerical model is the most important work and is the key link to success. Once this model is developed, parametric studies can be performed in a relatively smooth manner by varying one or several parameters (e.g. dimensions, material, etc.), allowing the investigation of their influence to the failure behaviour. Currently, powerful computers can calculate such analyses relatively fast. In contrast, the processing and the interpretation of the results is a far more time-consuming task due to the large amount of results and the complexity of the structure (many factors influence each other and the failure behaviour). From the above, it can be wrongly inferred that this method only has advantages. Nothing is less true. A numerical model always is a simplification of the real situation, and not all aspects of the problem could be taken into account (e.g. the variation of thickness of the silo wall, the evenness of the local support, etc.). It is the task of the researcher to distinguish the significant aspects (such as geometrical imperfections) from the others which play minor roles (such as residual stresses). Another important question that must be asked is whether the results are reliable. To answer this question, experimental research is essential to verify the numerical model before the results can be considered as reliable. Furthermore, such experiments can reveal new insights and aspects that are useful to take into account in future numerical research. However, the execution of such experiments is time and material demanding, and is therefore much more expensive than numerical analyses. The fabrication of a scale model and the related actions (e.g. the measurement of the silo imperfections) take several days. Consequently, only a limited number of experiments can be performed and representative silo geometries should be carefully chosen in advance. An additional disadvantage of the experimental research is that only scale models can be tested in a lab environment because the test setup must be able to collapse the silo. Such a scale model is not entirely comparable to a real silo, both in terms of the fabrication process and the final condition. For example, a small deviation from the

perfect circular shape will instantly play a much larger role in a scale model compared to a full size silo. It is therefore important to keep in mind that, despite the differences between a scale and a full size silo, a scale model will be used for the verification of the numerical model.

In (Singer et al., 1998), eight primary reasons are listed why experiments still are of great importance for shell buckling, despite the existence of powerful computers and reliable finite element software. Below, the most important reasons are briefly mentioned which are relevant for this work.

Better understanding of (post-)buckling behaviour and the primary factors affecting it

To permit reliable modelling and to avoid non-realistic failure behaviour, it is important to completely understand the occurring physical phenomena and their cause by performing experimental tests. Secondly, by varying parameters one by one, the primary parameters can be distinguished from the secondary parameters by studying their influence to the behaviour before, during, and after failure.

To find new phenomena

Experiments can reveal new and unexpected failure behaviour and buckling patterns.

To obtain better inputs for computations

Experiments can lead to more realistic input and, consequently, more accurate output of a numerical model for the elasto-plastic failure load estimate. The behaviour is largely influenced by the correct input of boundary conditions, material properties, imperfections, residual stresses, and load applications. Improved inputs can be obtained from additional non-destructive tests, such as tensile tests and imperfection scans.

To obtain correlation factors between analysis and test

Correlation factors take into account the difference between test results and numerical predictions, which is caused by inaccuracies of inputs and by variations in failure behaviour of both the scale models tested and the numerical models.

In conclusion, numerical and experimental studies are both necessary to investigate the failure behaviour of silos. A limited number of experimental tests are conducted to verify the numerical model and to make sure that the numerical results can be considered as reliable. Afterwards, different extensive parametric studies are performed to investigate the influence of all relevant parameters to the failure behaviour.

Part I. Experiments

The Laboratory for Research on Structural Models (LMO) of Ghent University already has many years of experience in the field of experimental research to shell structures. In the past, unstiffened cylindrical steel silos with a constant and a stepped wall thickness were tested in the laboratory. In collaboration with the Technical University of Graz (which took the numerical research on their behalf), enhancements for the design procedure were proposed (Rathé and Greiner, 1996). In subsequent research, locally supported silos with ring and longitudinal stiffeners were extensively and successfully tested in the framework of the doctoral thesis of Vanlaere (Vanlaere, 2006). Similar to this work, Vanlaere used these tests to validate his numerical model. Because of the successful execution of experiments in the past, the existing test setup and procedures of fabrication were used as starting point. As will be discussed hereunder, several modifications were urged and implemented during the execution of the test series.

1 Geometries

The overall dimensions of the cylindrical silo originates from previous research (Rathé and Greiner, 1996; Vanlaere, 2006). To maintain agreement with this research, and not to modify the existing test setup, it was decided to give the silo radius and height the same values as in the existing test setup. The silo radius R is equal to 350mm, and the silo height h is 700mm. Based on the commercial available plate thicknesses and the range of radius-to-thickness ratios to use in the numerical investigation ($100 \leq R/t \leq 1000$), three silo thicknesses were initially selected: 0.8mm ($R/t = 437.5$), 1.0mm ($R/t = 350.0$), and 1.5mm ($R/t = 233.3$). Because plate thicknesses less than 0.8mm are not available, no experiments can be performed on relatively thin-walled silos ($R/t > 437.5$). After the execution of a parametric study in Abaqus, which is discussed further, the latter plate thickness was removed from the initial selection because the expected failure load F_u exceeded the maximum allowable load of the test setup (i.e. 248kN). The silo dimensions are summarized in Table 3-1. In all cases, the cylindrical silo is locally supported with four supports, equally spaced along the silo perimeter. The dimensions of the local supports depend on the dimensions of the stiffening configuration, and will be discussed later.

Table 3-1 Geometrical parameters of the cylinder.

PARAMETER	VALUE(S)	DIMENSION
R	350	mm
t	0.8; 1.0	mm
h	700	mm

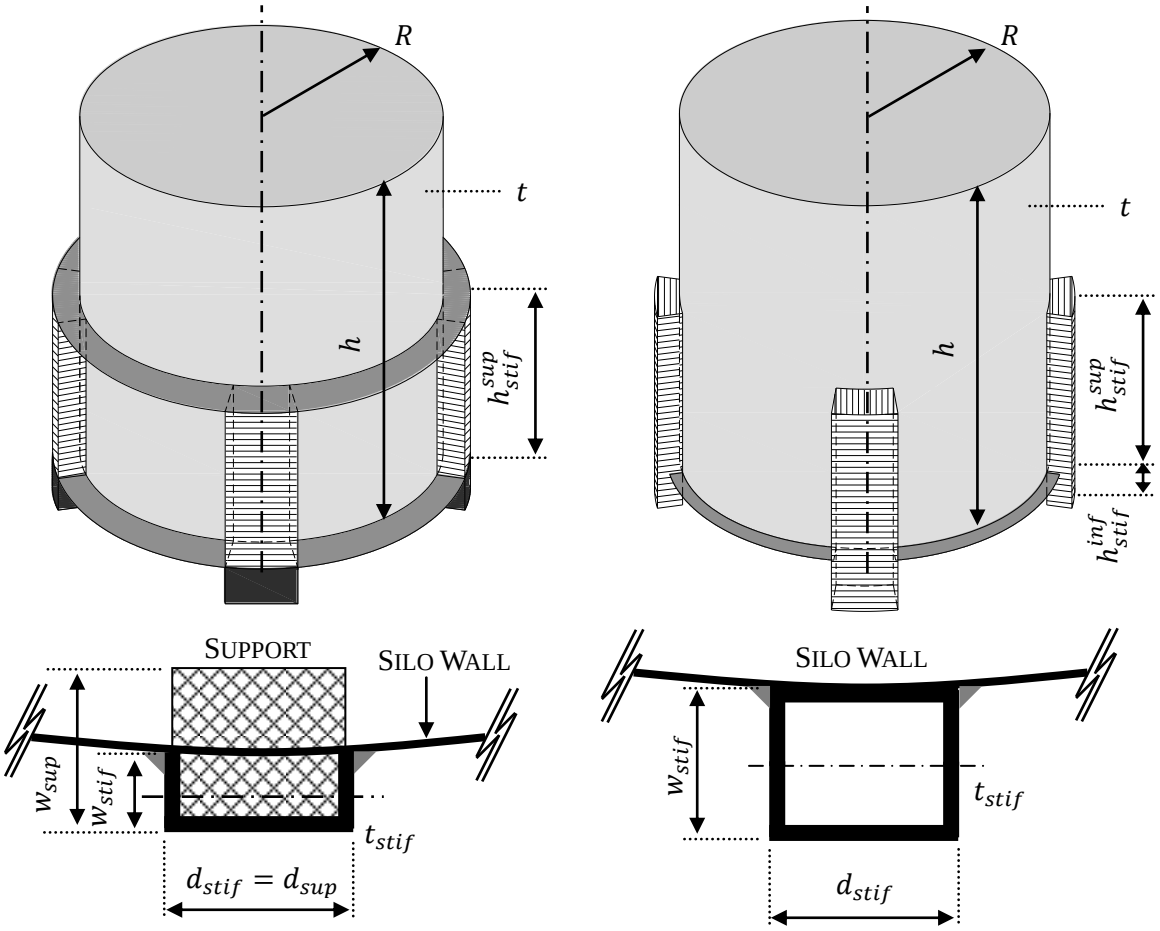

(a) U-shaped stiffeners. (b) Engaged column.

Fig. 3-1 Geometrical parameters of the locally supported barrels.

As already described in Chapter 2, two main types of arrangements will be investigated for locally supported cylindrical steel silos (See Fig. 3-1). The stiffening configuration consists either of U-shaped partial-height longitudinal stiffeners (and ring stiffeners) or of engaged columns, which is an engagement of the supporting column. From a section catalogue, a preliminary selection of cross-sections was made from a wide range of available cold-formed steel members. The final dimensions of the stiffeners/engaged columns were chosen based on exploratory parametric study in Abaqus. This numerical study has two purposes: (1) to predict the order of magnitude of the failure load, and (2) to estimate the influence of the variable parameters on the failure load. The first purpose is important to make sure that the expected

failure load can be applied by the hydraulic jack ($F_{max} = 400$kN) and can be absorbed by all parts of the test setup (maximum allowable load: the seven wire strand $F_k = 248$kN; the load cells which measure the supporting reaction forces: $F_k = 100$kN; the load cells which measure the total load $F_k = 500$kN and 200kN). The second purpose is important to decide which geometrical parameters will be varied during the test program, and which parameters will be kept constant. To simplify the numerical model, a number of assumptions were made, such as an ideal elasto-plastic material behaviour ($E = 210$GPa; $\nu = 0.3$; $\sigma_y = 235$MPa) and a perfect circular shape of the shell wall.

The results of the parametric study are presented in Fig. 3-2. In this figure, the advantageous influence can be found of an increasing plate thickness t, an increasing stiffener/column height h_{stif}^{sup}, and a larger cross-section of the stiffener/column on the failure load F_u.

In this way, the test program consists of eight different tests. The selected combinations are indicated in Fig. 3-2.

On the basis of the results of the numerical study, we had to decide which parameters should be varied and which should be kept constant.

- Silo wall thickness t: 0.8mm and 1.0mm;
- Cross-sections of the U-shaped stiffener (U.S.) and the engaged columns (E.C.) (d_{stif}xw_{stif}xt_{stif}): U.S.40x20x2mm; U.S.60x30x2mm; E.C.40x40x2mm; E.C.60x60x2mm;
- Stiffener/column height h_{stif}^{sup}: 300mm.

The dimensions of the U-shaped stiffeners and the rectangular supporting columns are presented in respectively Table 3-2 and Table 3-3, using the symbols presented in Fig. 3-1. The supported proportion μ_{sup} of the entire circumference is equal to 7.3% (d_{stif} = 40mm) and 10.9% (d_{stif} = 60mm).

Table 3-2 Geometrical parameters of the U-shaped longitudinal stiffeners.

PARAMETER	VALUE(S)	DIMENSION
$d_{stif}\ x\ w_{stif}\ x\ t_{stif}$	40 x 20 x 2 60 x 30 x 2	mm
h_{stif}^{sup}	300	mm

Table 3-3 Geometrical parameters of the square engaged columns.

PARAMETER	VALUE(S)	DIMENSION
$d_{stif}\ x\ w_{stif}\ x\ t_{stif}$	40 x 40 x 2 60 x 60 x 2	mm
h_{stif}^{sup}	300	mm
h_{stif}^{inf}	100	mm

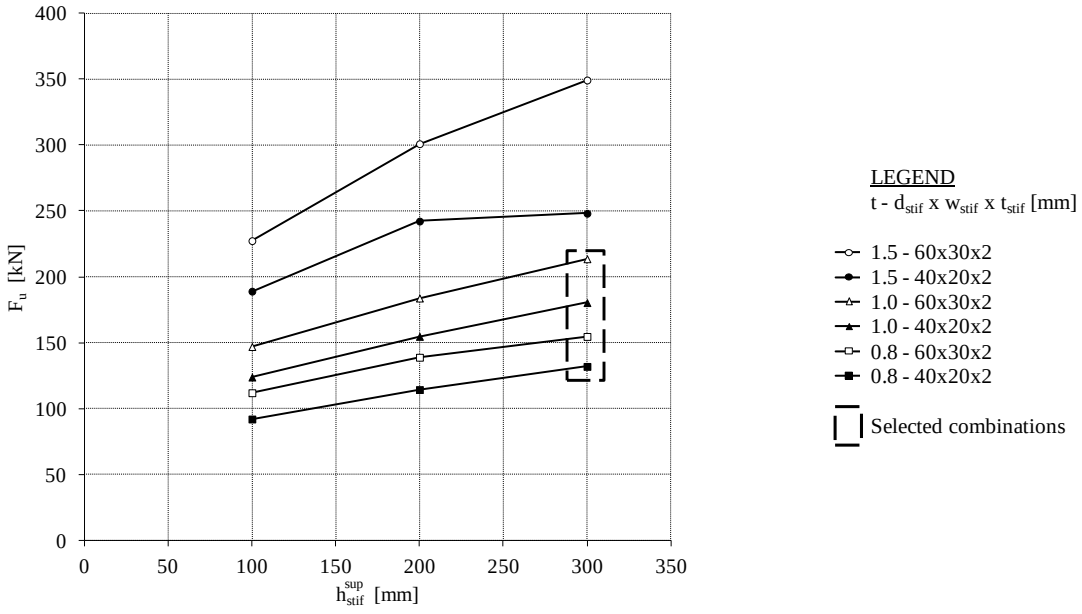

(a) U-shaped stiffeners.

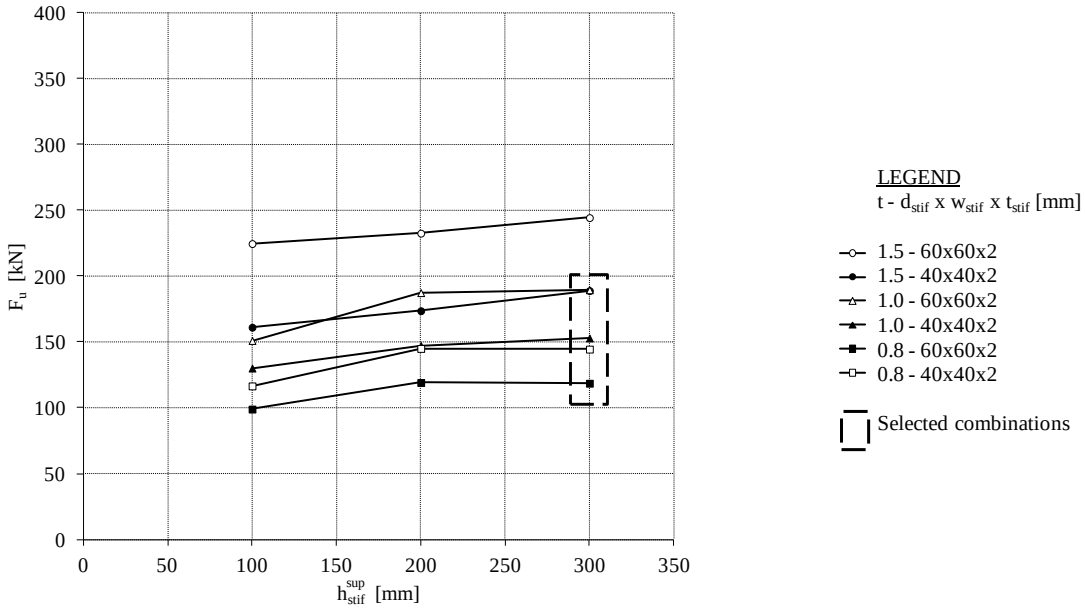

(b) Engaged columns.

Fig. 3-2 Results of the exploratory study.

For the U-shaped stiffeners, two ring stiffeners are added: an upper ring and a lower ring. In the case of engaged columns, only a lower ring is added. The widths in radial direction of the upper and the lower ring are respectively equal to and two times the radial width of the longitudinal stiffener/engaged column. The thickness of the ring stiffeners is always equal to the thickness of the silo wall.

Table 3-4 Geometrical parameters of the ring stiffeners

PARAMETER	VALUE(S)
w_{ur}	w_{stif}
t_{ur}	t
w_{lr}	$2 \cdot w_{stif}$
t_{lr}	t

Table 3-5 gives an overview of the eight selected geometries and the GMNA failure load of the exploratory parametric study.

Table 3-5 Selected geometries with their perfect elasto-plastic buckling load.

LABEL	t [mm]	$d_{stif}\ x\ w_{stif}\ x\ t_{stif}$ [mm]	F_u^{GMNA} [kN]
EU1	0.8	40 x 20 x 2	131.9
EU2	0.8	60 x 30 x 2	154.6
EU3	1.0	40 x 20 x 2	180.3
EU4	1.0	60 x 30 x 2	213.6
EK1	0.8	40 x 40 x 2	118.6
EK2	0.8	60 x 60 x 2	144.6
EK3	1.0	40 x 40 x 2	153.0
EK4	1.0	60 x 60 x 2	189.6

2 Test setup

The purpose of the test setup is to conduct a destructive test on the scale model to determine the maximum strength of the silo structure at the moment of failure. In other words, the test setup should be strong enough to resist the maximum expected failure load. As will become apparent later in this section, different components of the existing test setup (Vanlaere, 2006) had to be replaced, because they were not able to resist the expected loads.

The test setup will be discussed by means of Fig. 3-3 (for the U-shaped longitudinal stiffeners) and Fig. 3-4 (for the engaged columns) by considering the different components from bottom to top.

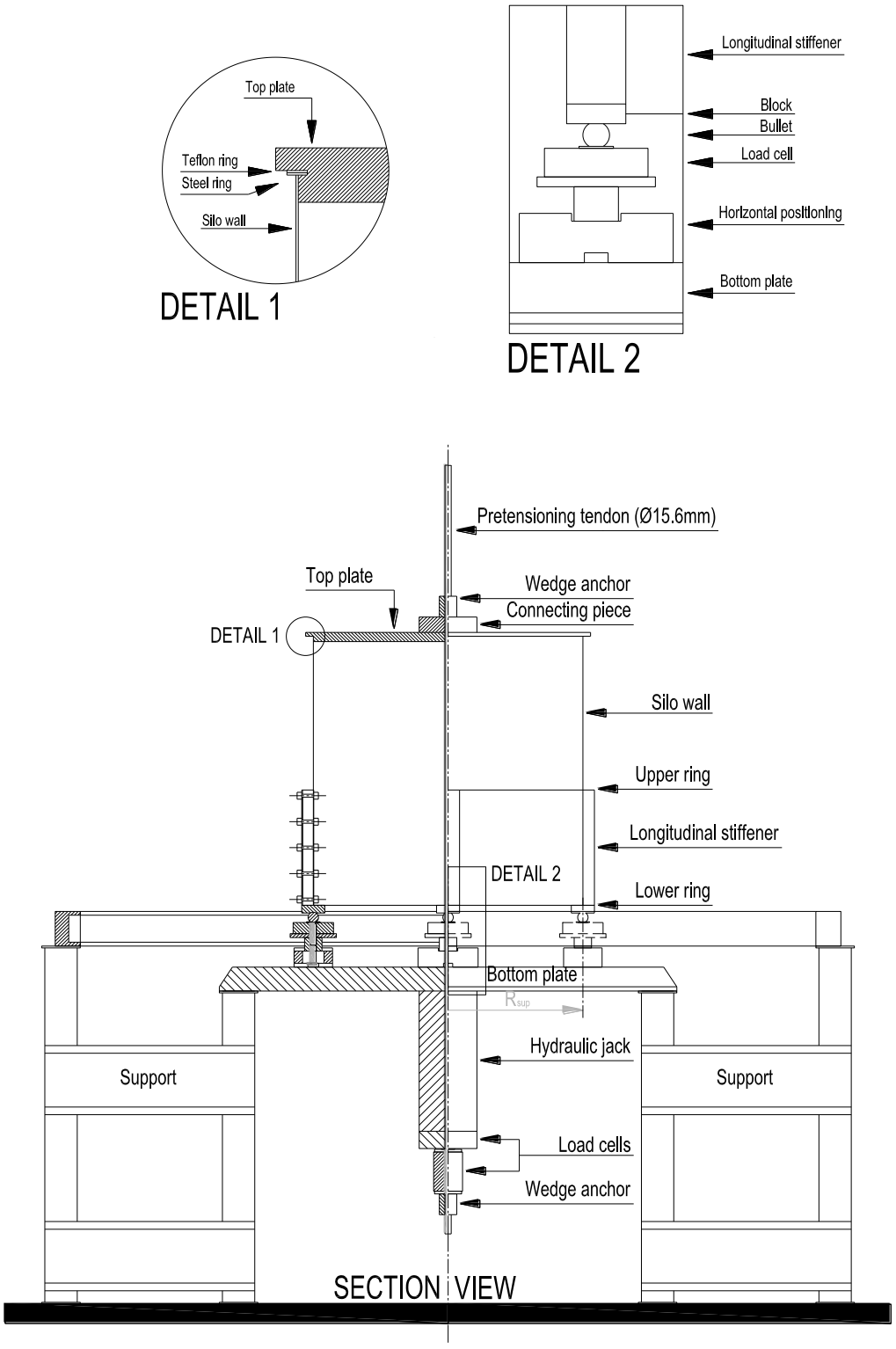

Fig. 3-3 Test setup for the U-shaped stiffeners.

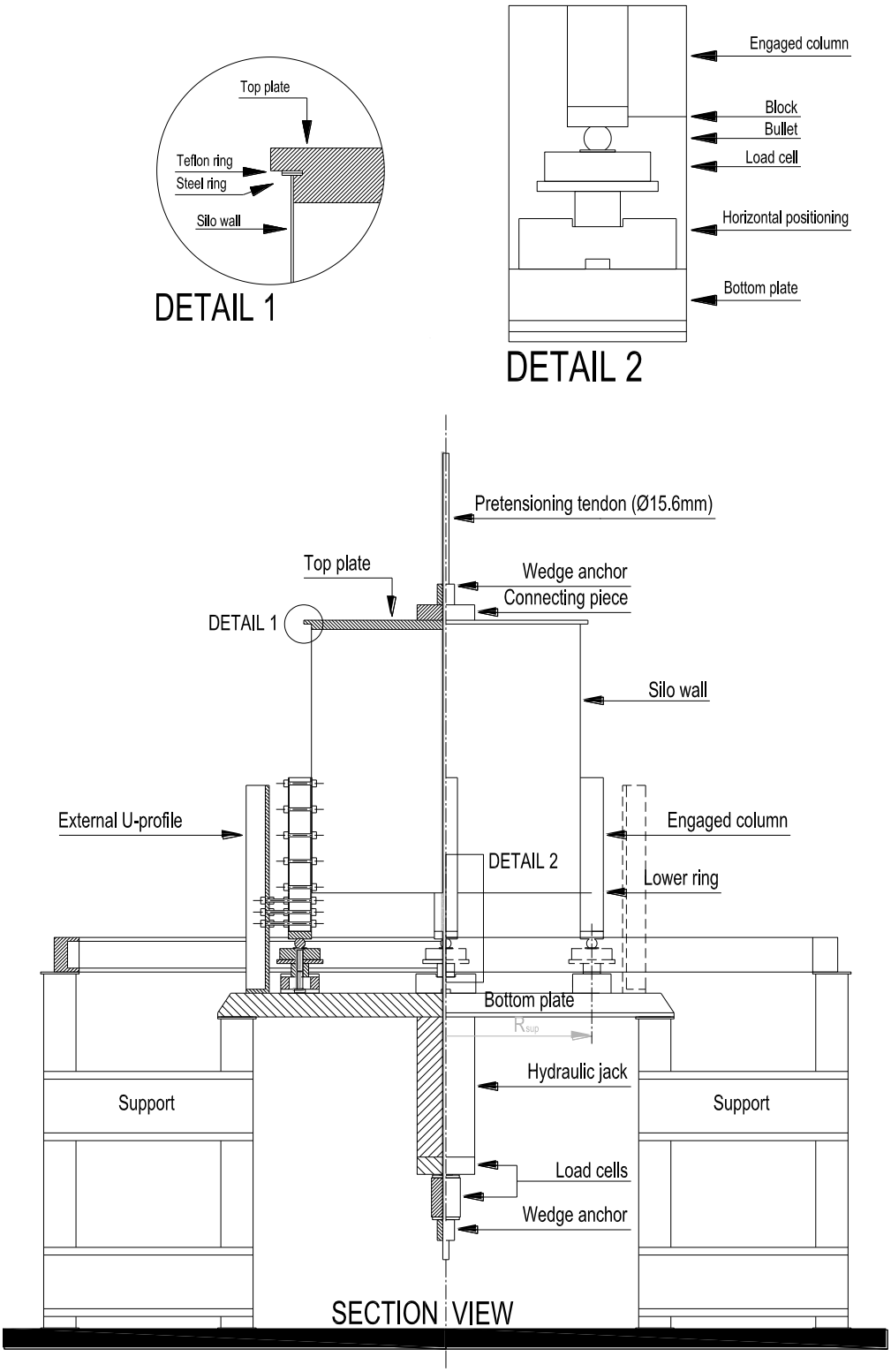

Fig. 3-4 Test setup for the engaged columns.

Four U-shaped profiles support the bottom plate and establish the connection with the ground. This bottom plate is a 62mm thick steel plate and can be considered as rigid base for the rest of the arrangement. On this bottom plate, four local supports of the silo are placed on a circle with radius R_{sup} and with a fixed angle in circumferential direction of 90 degrees. The centre of this circle coincides with the axis of the cylinder, while its circumference must coincide with the centre of gravity of the supporting points. The size of the radius R_{sup}, which is given in Table 3-6, depends on the type and the size of the longitudinal profiles, as presented in Fig. 3-3 and Fig. 3-4.

Table 3-6 Radius of the centroid of the support as a function of the profile.

B / H / T [MM] (PROFILE)	RADIUS R_{sup} [MM]
40/20/2 (U-section)	350
60/30/2 (U-section)	350
40/40/2 (SHS)	370
60/60/2 (SHS)	380

Each support consists of different parts (from below to above): (1) a fixed and a movable plate for the correct positioning of the support in circumferential and radial direction. The movable plate also serves as a flat surface for the loading cell; (2) the loading cell. The load cells measure the individual support reactions to know the distribution of the total load. This distribution is affected by the presence of imperfections in the shell wall and the not fully correct positioning of all parts.; (3) a steel bullet; (4) a cubic block as support of the profile/engaged column (See Fig. 3-5 and Detail 2 in Fig. 3-3 and Fig. 3-4).

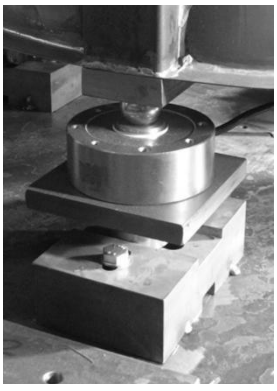

(a) U-shaped profile.

(b) Engaged column.

Fig. 3-5 Detail of the support of the silo.

A circular top plate is mounted at the top of the cylindrical barrel. This plate is pulled down by a tendon and exerts an axial force to the top edge of the silo. To uniformly distribute the total load over the entire circumference of the cylindrical barrel, two rings are placed between

the upper edge of the silo and the top plate (See Detail 1 in Fig. 3-3 and Fig. 3-4). The upper ring consists of teflon and needs to smoothen small irregularities between the contact surfaces. The lower steel ring protects the teflon ring, so that the latter could not be perforated by the large pressure and the sharp upper edge of the silo.

The axial force is applied by means of a hydraulic jack and a tie rod. The upper end of the tendon is anchored at the centre of the top plate (See Fig. 3-6 (a)). The tendon passes through the central hole of the top plate, the interior of the cylindrical barrel, the central hole in the bottom plate, the central hole in the hydraulic jack, and the central hole(s) in the load cell(s) (See Fig. 3-6 (b)). Its lower end is anchored at the centre of the lower load cell. The movable head of the jack pushes the load cell(s) and the anchorage downwards and brings the tie rod under tension. As a result, the top plate will pull down, and it will, in turn, compress the silo wall. The load cell(s) at the lower end of the tie rod measure the total reaction force exerted by the hydraulic jack.

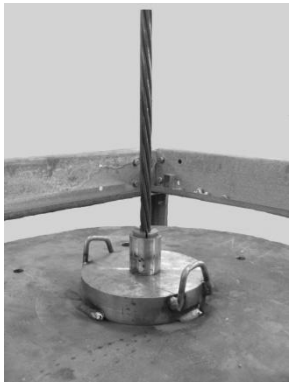

(a) Upper end of the tie rod.

(b) Lower end of the tie rod.

Fig. 3-6 Application of the axial force.

The test itself is fairly simple: the force exerted by the jack onto the model is increased slowly until instability occurs, preferably in the silo wall. At any particular time of the test, the sum of the support reactions must always be equal to the total reaction force plus the dead weight of the jack, tie rod, top plate, and cylindrical scale model.

3 Fabrication

In this section, the complete procedure for the fabrication of a scale model is discussed step by step. At first instance, all individual components must be manufactured before they could be assembled to a stiffened cylindrical silo by welding, soldering, and bolting.

3.1 Original method

The cylindrical silo wall and the ring stiffeners are both made out of rectangular steel plates, which initially have a length of 3000mm and a width of 1500mm. To ensure that all

components have the correct shape and size, and to optimally use the material, a plan was drawn of each steel plate. An example of such a plan is depicted in Fig. 3-7. As can be seen in this figure, the lower ring consists of two half-rings to minimise material wastage.

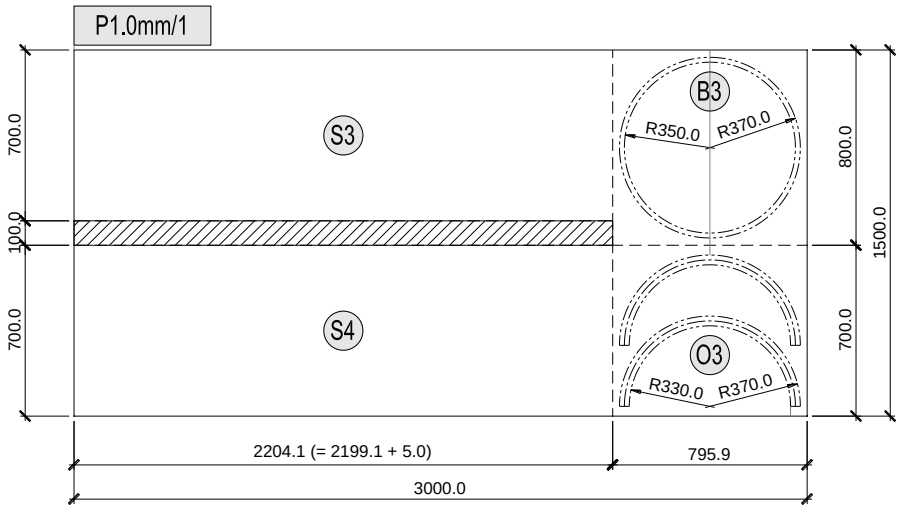

Fig. 3-7 Plan of a steel plate.

The first step in the fabrication step is the cutting of the steel plates to the desired size and shape. Two different types of cutting operations are used for this purpose. The flat plate of the steel silo has a rectangular shape with a length of 2204.1mm and a width of 700mm. Since this component has straight edges, a sheet shearing machine is used for this operation (See Fig. 3-8).

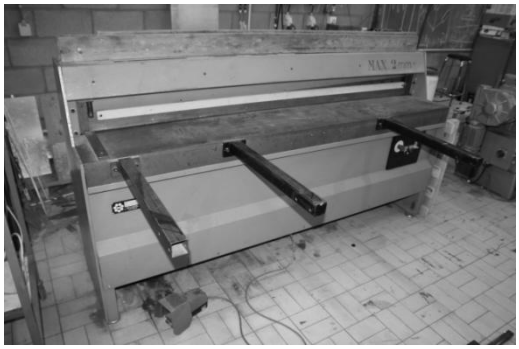

(a) Sheet shearing machine.

(b) Flat steel plate.

Fig. 3-8 Plate cutting operation.

In contrast, the ring stiffeners have a circular shape and curved edges. That is why it was decided to cut the rings with a laser cutting machine (Fig. 3-9). As a result, the ring stiffeners have the exact size and shape, and the soldering process is facilitated by the perfectly fitting connection between the rings and the silo wall.

(a) Laser cutting machine.

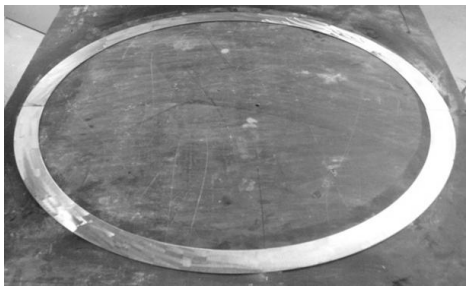

(b) Ring stiffener.

Fig. 3-9 Laser cutting.

Subsequently, the flat steel plate is rolled into a cylindrical shape with a bending machine (See Fig. 3-10).

(a) Bending machine.

(b) Rolling operation.

(c) Final result.

Fig. 3-10 Rolling process.

In the next step, the neighbouring longitudinal free edges of the curved cylinder are welded. Because the thickness of the parent material is very small, Tungsten Inert Gas (T.I.G.) welding is applied. This special welding technique is adopted to limit the residual stresses and weld deformations. The free edges are molten locally into each other along the seam, without the use of additional material. This results in a fine smooth weld as depicted in Fig. 3-11.

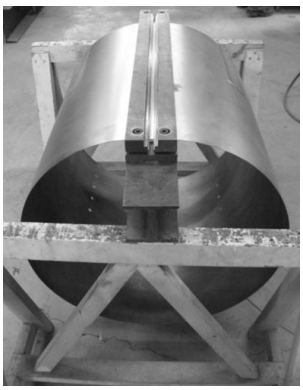

(a) Setup.

(b) Welding operation.

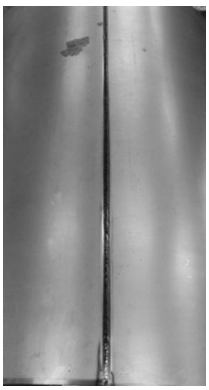

(c) Welding seam.

Fig. 3-11 Welding process.

Next, the other components are soldered to the cylinder wall with a silver-tin alloy, which

contains 97% tin and 3% silver. This soft solder has been chosen for the low melting temperature (approximately 230°C). In this way, large input of heat (compared to welding) is avoided and consequently also the displacements related to the cooling process. First, the longitudinal stiffeners/engaged columns are soldered, then the upper ring, and finally the lower ring (See Fig. 3-12).

(a) Longitudinal stiffener. (b) Upper ring. (c) Lower ring.

Fig. 3-12 Soldering process.

The result after completing the previous steps is shown in Fig. 3-13. The scale model now is ready to be tested.

3.2 Modifications

3.2.1 Attachment of the longitudinal stiffeners to the silo wall

During the first experiment, the silo structure failed at a relatively low load level, much lower than expected. This premature failure was caused by the loosening of the connection between the silo wall and the longitudinal stiffeners, which is depicted in Fig. 3-14. Nevertheless, all instructions, such as the preparation of the surface, were followed. In other words, the first experiment has demonstrated that the solder joint was no longer capable to transfer the load between both components by shear. However, a similar connection was used and approved in previous research (Vanlaere, 2006). In that study, the longitudinal stiffeners above the supports consisted of two rectangular unconnected plates, which only can absorb and transfer a small load. The soldered joint satisfied in all cases. In contrast, the longitudinal stiffeners now are U-shaped profiles, and can absorb larger forces. Consequently, the soldered connection should also be able to transfer a larger force by shear. However, this test has shown that the applied connection has its limitations and that the maximum strength is achieved at a too small load level.

Fig. 3-13 Assembled scale model.

Fig. 3-14 Failure of the silo structure.

A new solution had to be found to prevent this premature failure. The S-Sn97Ag3 solder is already a quite strong connection (tensile strength = 100MPa), and even stronger solders are not available. Switching over from soldering to welding was also not appropriate, since the heat input and the associated deformations should be minimised. Initial deformations are indeed very detrimental for the failure behaviour of such a silo. Hence, the choice was made to maintain the existing connection, and to realise an additional bolted connection, as illustrated in Fig. 3-3, Fig. 3-4, and Fig. 3-15. The bolts are provided over the entire height of the stiffener. In addition, a plate is provided on the internal side of the silo wall for the attachment.

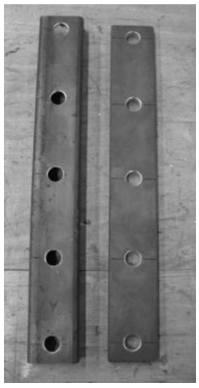

(a) Position of the holes.

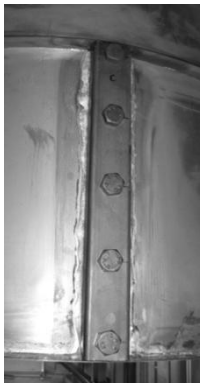

(b) External side.

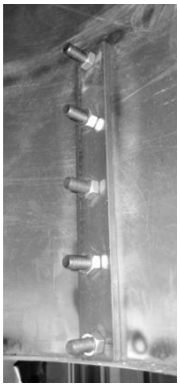

(c) Internal side.

Fig. 3-15 Modified attachment of the stiffeners/columns with the silo wall.

3.2.2 Attachment of the lower ring to the silo wall

In het beginning of the test series, the deviations from the perfect circular shape were found to be rather large at the bottom of the silo. To reduce these disadvantageous deformations, a circular wooden mould was built to use during the soldering of the lower ring. The outer

dimension of this mould is equal to the inner diameter of the silo wall, so that they perfectly fit together. By that measure, the circular shape of the lower edge of the silo was very well approximated.

4 Measurement of the imperfections

Geometric imperfections play a major role in the failure behaviour of thin-walled shell structures. Hence, the importance of the measurement of the geometric imperfections in the silo wall is clear. For each experiment, the imperfections are measured twice: once on the unstiffened silo wall (i.e. just after the welding of the longitudinal edge) and a second time on the stiffened silo wall (i.e. after the soldering of all stiffeners). On the basis of the first measurement, the influence of the rolling process on the circular shape can be viewed. The influence of the soldering process can be viewed when the first and the second measurement are compared with each other. Furthermore, the second measurement will be used for the validation analyses in Abaqus. In what follows, the functioning of the measurement device will first be explained. Afterwards, the procedure of the measurement will be explained.

In Fig. 3-16, the measurement device is presented. To be able to scan the entire silo surface, this setup consists of two major components which can move independently of each other: a horizontal circular plate and a vertical arm with laser sensor. During the measurement, the horizontal plate (and the silo) will constantly rotate about its vertical axis, while its position (i.e. the circumferential angle) is accurately determined all the time. The laser sensor on the vertical arm can move in vertical direction (up and down), and its position (i.e. the height) is also accurately determined all the time. The third and last measurement signal originates from the laser sensor. This sensor will constantly measure the distance between the sensor and the silo wall. This distance is measured perpendicularly to the silo wall, and is a measure for the amplitude of the geometric imperfection in the measured point. To conclude, the imperfection can be measured in each point due to the rotation of the horizontal plate (and the silo) and the vertical movement of the sensor.

(a) Unused condition.

(b) During the measurement.

Fig. 3-16 Device for the measurement of the geometric imperfections.

At the beginning of the measurement, the (un)stiffened cylinder is placed upside down on the horizontal plate. The upper edge of the cylinder and the outer circumference of the plate perfectly fit in each other. For the first measurement (i.e. the unstiffened silo), the top plate of the experimental setup can be fitted on the upper side of the inverted silo. In this way, the circular shape of the upper edge, and possibly the lower edge, of the silo wall is maintained during the measurement of the imperfections. To obtain a good view of the present imperfections, the cylinder wall is measured on different heights over the entire circumference. The step size in height Δh is 15mm (< gauge length l_{gx} in axial direction: 66.9mm if $t = 0.8$mm and 74.8mm if $t = 1.0$mm). Approximately 1250 to 1500 points are measured at each measuring round, corresponding with a step size in circumferential angle $\Delta\theta$ of 0.24-0.29° (<< gauge angle θ_{gx} in circumferential direction: 11.0° if $t = 0.8$mm and 12.3° if $t = 1.0$mm).

The measured imperfections will be used for the determination of the quality tolerance class (out-of-roundness and dimple parameter) and for the validation analysis in Abaqus. The method for the processing of the measurements and the above mentioned results are discussed in Section 2 of Chapter 4.

5 Tensile tests

An important aspect which is necessary for the validation analyses in Abaqus is the real material behaviour of the steel which is used for the experiments. To quantify the material properties, tensile tests were conducted on test specimens from the steel plates. The method to be applied is fully standardized and is described in (ISO 6892-1, 2009). This normative document deals with the shape and the dimensions of the test pieces, the conditions and the

procedures of testing, etc. In this section, the main issues will be considered.

The shape and dimensions of the standardized test pieces depend on the product type (here: steel plates) and their thickness (here: 0.8 or 1.0mm). The shape and the dimensions of the selected test piece are displayed in Fig. 3-17. The test piece includes a central zone with parallel edges, the region with transition radius between the parallel length and the gripped ends, and the end zones for the grips of the testing machine. The dimensions are given in Table 3-7.

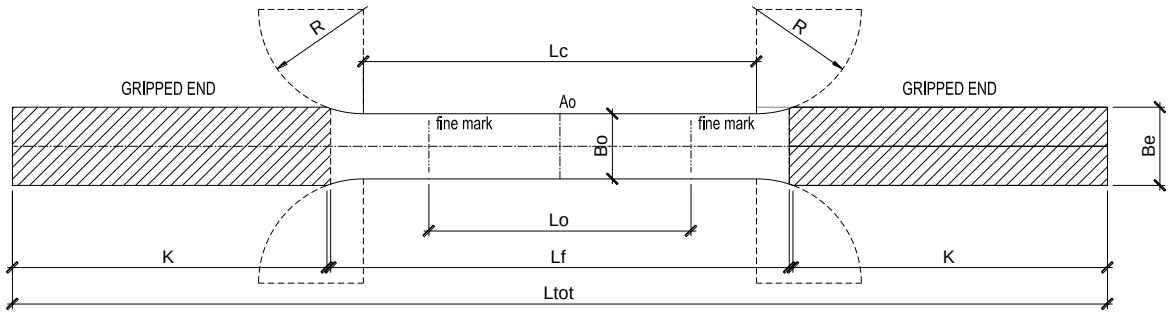

Fig. 3-17 Shape and dimensions of the test piece.

Six test pieces were obtained by machining from each steel plate: three in the longitudinal direction and three in the width direction. In this way, it can be investigated if the direction of the test piece influences the material behaviour. Furthermore, the level of scatter between the different test pieces of the same steel plate can be determined on the material properties.

Table 3-7 Dimensions of the test piece.

PARAMETER	VALUE	DIMENSION
L_o	50.0	mm
L_c	75.0	mm
L_f	87.5	mm
R	20.0	mm
K	60.0	mm
B_o	12.5	mm
B_e	15.0	mm

The tolerance for the nominal width B_o amounts ± 0.05mm. This means that the test piece may not have a width B_o smaller than 12.45mm or larger than 12.55mm. The maximum deviation between the measurements of the width B_o along the entire parallel length L_o is equal to 0.06mm.

The dimensions of the test piece (i.e. its width B_o and thickness t_o) should be measured at sufficient cross-sections (minimum of three is recommended) perpendicular to the longitudinal axis in the central region of the parallel length. The cross-sectional area is the product of the width B_o and the plate thickness t_o. Next, the original cross-sectional area S_o is obtained by taking the average of the calculated cross-sectional areas.

To determine the relevant material parameters, the test pieces should be subjected to a tensile test. This test involves straining the test pieces by tensiles forces to fracture. The testing apparatus that is used for such a test is depicted in Fig. 3-18.

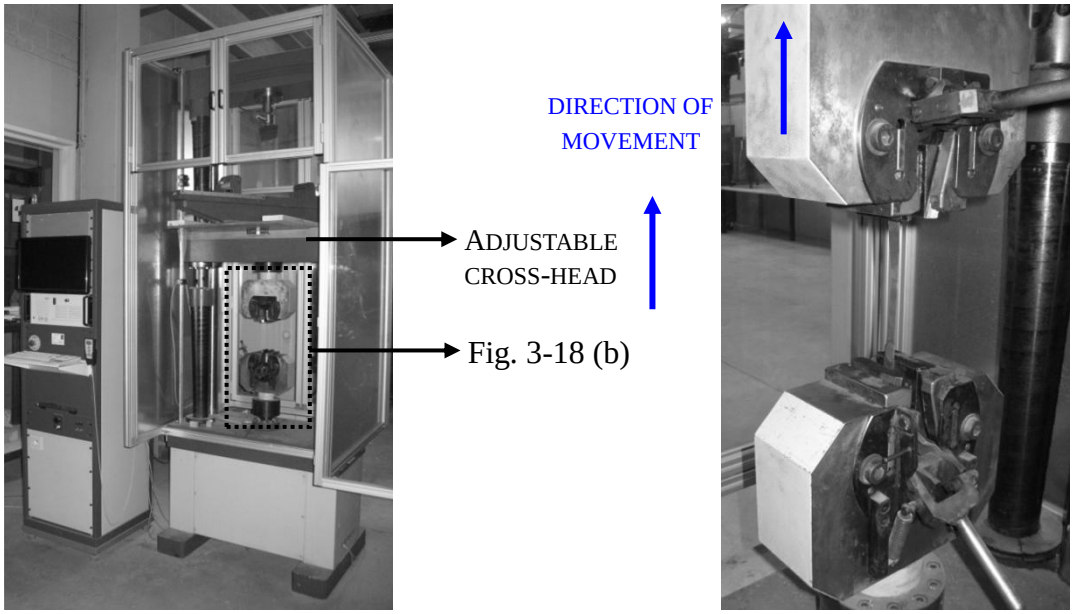

(a) Testing machine. (b) Test specimen gripped with serrated wedges.

Fig. 3-18 Testing apparatus.

At the beginning of the tensile test (after the loading train is assembled), the system is reset to zero. After the test piece is gripped at both ends, a preliminary force is applied to obtain a straight test piece and to ensure the alignment of the test piece and the grip arrangements. It is important that the load is applied as axially as possible. The velocity of applying the axial force is determined by strain rate control (See Table 3-8). The strain rate depends on the percentage elongation and can be controlled in two ways. In the beginning of the tensile test, the control of the strain rate is based on the information of an extensometer (E.). In the second part of the test, the control of the estimated strain rate over the parallel length is achieved by controlling the transversal crosshead separation rate (T.C.).

Table 3-8 Strain rates - Extensometer (E.) or Transversal Crosshead (T.C.).

PERCENTAGE ELONGATION [%]	STRAIN RATE $[s^{-1}]$
0.0	0.00007 (E.)
0.8	0.00050 (T.C.)
2.5	0.00100 (T.C.)
3.0	0.00300 (T.C.)
3.5	0.00670 (T.C.)

Although standard test equipment allows the use of the crosshead displacement to calculate the elongation of a tensile test specimen, much greater accuracy is achieved by direct measurement using an extensometer (See Fig. 3-19 (a)). This device is mounted directly onto the test specimen to accurately measure the elongation between two measuring points spaced by 50mm (See Fig. 3-19 (b)). Such a measurement allows to accurately determine the Young's modulus E and the yield point. During yielding, the extensometer is removed from the test piece and the crosshead displacement is used to calculate the elongation of the test piece.

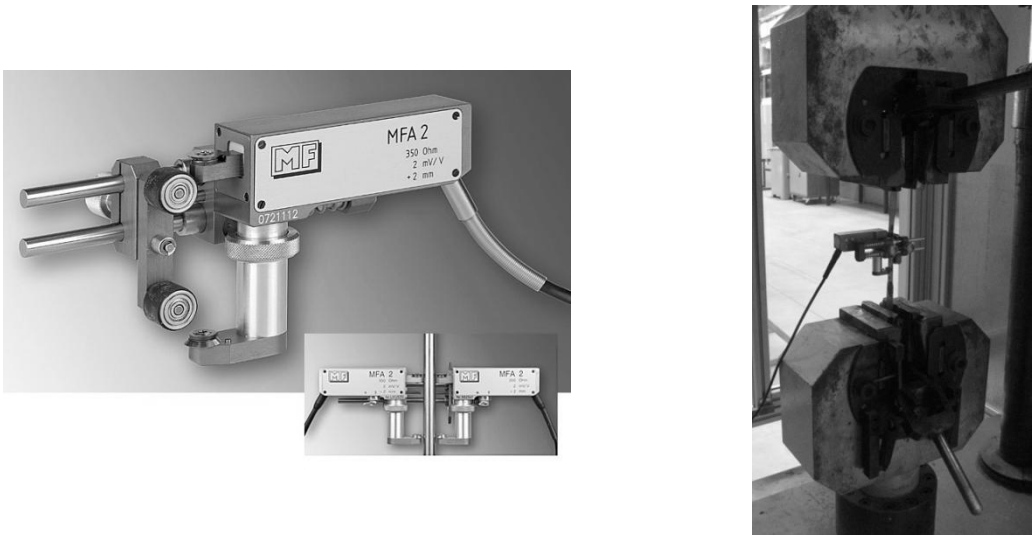

(a) The device. (b) At the start of the test.

Fig. 3-19 Extensometer.

For the validation of the numerical model, the material of the U-shaped stringer stiffeners and the engaged columns has not been tested to determine its real stress-strain behaviour, because it was adopted that other factors are influencing the failure behaviour much more and are thus more important to take into account.

Part II. Numerical model

Generally, the application of Finite Element Methods (FEM) has many advantages, especially compared to the past where algebraic theories and simplified models were used for the design of as well as for the research to shell structures and silos. In contrast, numerical models are able to accurately predict the failure load of geometries and sizes, which cannot be investigated in the field or in a lab. Furthermore, they provide detailed information about the stress and displacement fields (e.g. stress concentrations above local supports) and, consequently, knowledge about the behaviour before, during, and after failure. In Chapter 4, the numerical model will be validated against experimental results before it is extensively used for parametric studies in Chapter 5 and a design rule study in Chapter 6.

For the numerical part, Vanlaere had developed a numerical model for locally supported cylindrical steel silos with two rectangular longitudinal stiffeners above the supporting columns (Vanlaere, 2006). This model has been used as starting point for this investigation. During the six years research, the numerical model is gradually automated (in Python), optimised, and expanded with many new features, such as the supporting conditions, the conical hopper and roof, etc. In the following, the last version of the numerical model will be thoroughly discussed from every angle.

6 The finite element program Abaqus

The full numerical investigation was conducted with the commercial finite element program Abaqus (Abaqus, 2009). This widely used F.E.M. package is a powerful tool and has already proven its value for a great variety of applications in automotive industry, aerospace industry, and many other branches. Below, a description is given of the main aspects of the three-phase numerical research: (1) pre-processing; (2) processing; and (3) post-processing.

Pre-processing

During the pre-processing stage, the complete model is implemented (i.e. the geometry, the material, the boundary conditions, etc.) and the analysis and output parameters are defined. Abaqus has the advantage that two methods can be used for the input of the model. A first possibility is to use the graphical environment Abaqus/CAE, but this method is time-consuming when the number of variable parameters and models is large, as is here the case. To avoid a lot of manual work and to reduce the risk of errors during the parametric studies, the other method will be used: input files. The latter can be generated very fast with the use of the programming language Python and contain all necessary information concerning the numerical model (i.e. geometry, material, elements, etc.). Abaqus has an entire library with

commands and rules that has to be used in the code of an input file. At first instance, the development of the Python code to generate the input files will require more time, but has some significant advantages. The user knows everything about the input data, making it easier to make changes to the numerical model and to detect and solve warnings/errors. In addition, this method is very efficient and reliable: the input files are generated very fast and the risk of errors is strongly reduced if the code has been sufficiently tested in advance. Another advantage of this method is the ease of generation of input files for parametric studies with multiple variables.

Processing

At the beginning of each analysis, the input file is read and the model is generated. All analyses were conducted with 4 processors and with Abaqus Standard 6.9-2. These settings are always applied during the entire investigation in order not to influence the numerical results.

For most types of analyses (i.e. GMNA, GNA, MNA, GNIA, and GMNIA) (EN 1993-1-6, 2007), the modified Riks algorithm has been used. This algorithm is able to solve unstable, geometrically non-linear static problems (including buckling or collapse behaviour), where the load and/or displacement may decrease as the solution evolves (Abaqus, 2009). When a linear bifurcation analysis (i.e. LBA) was performed, the subspace iteration eigensolver was used to obtain the eigenvalue buckling estimates. For a more detailed description about these algorithms we refer to the manual (Riks, 1981; Crisfield, 1982; Abaqus, 2009).

Post-processing

The processing of the results is partly done automatically by Python scripts (e.g. the determination of the failure load), party manually in the Abaqus/Viewer environment (e.g. investigating stresses and deformations).

7 Geometry

A typical elevated silo consists of a conical roof, a cylindrical barrel, a conical hopper, a transition ring stiffener, a skirt, a supporting structure, and possibly additional longitudinal and ring stiffeners (See Fig. 3-20 (a)). However, in the numerical model, not all parts will be modelled and some simplifications will be introduced. For example, the conical roof and hopper are omitted in the model (See Fig. 3-20 (b) and (c)) and are replaced by boundary conditions (See Section 9).

The geometrical parameters of the cylindrical barrel, the supports and the stiffeners are now discussed. The range for the different parameters in the numerical investigation (Chapter 5) is also outlined here.

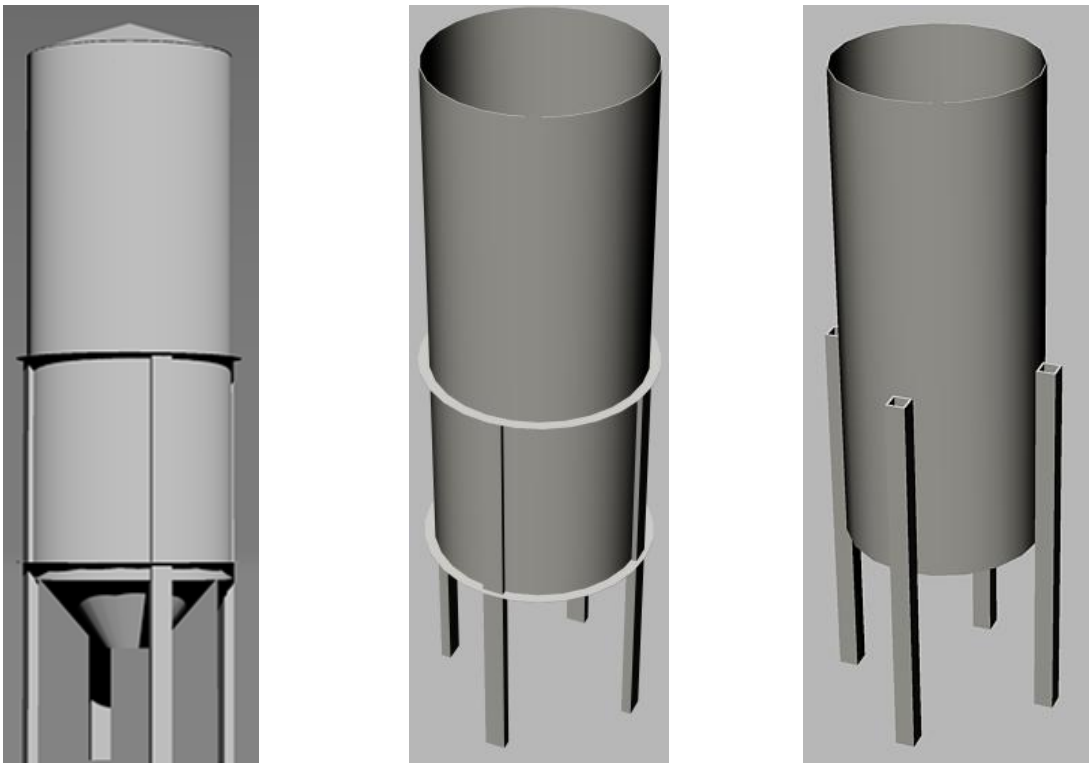

(a) Typical elevated silo.

(b) Simplified model - large silo with longitudinal and ring stiffeners.

(c) Simplified model - light silo with engaged columns.

Fig. 3-20 3D perspective of elevated silos.

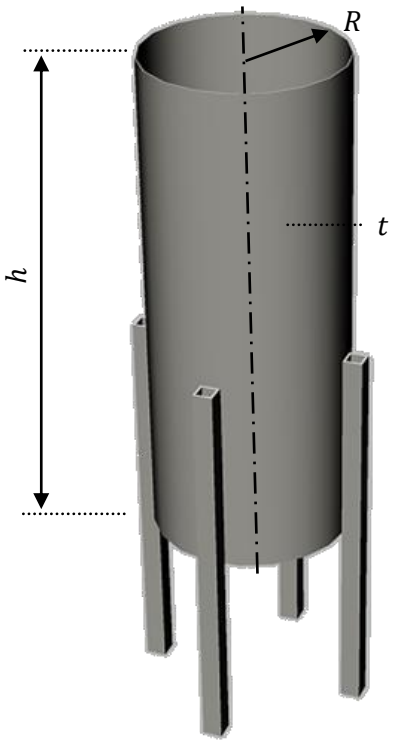

Fig. 3-21 Geometrical parameters of the cylindrical barrel.

The cylindrical barrel

The cylindrical barrel has three geometrical parameters: a radius R, a thickness t, and a height h (See Fig. 3-21).

The cylinder radius R is the only geometrical parameter which has an absolute value. For all numerical analyses (except for the verification analyses), the silo radius R is equal to 1.0m. All other geometrical parameters of the silo will be expressed as dimensionless quantities, and are relative to the cylinder radius R. By this choice, the failure load F_u is proportional to the square of the radius R (See Eq. (3-1)) or the ratio of the failure load F_u to the square of the radius R is a constant value. Consequently, the failure load for another radius $F_{u,R\,[m]}$ can always be calculated based on the failure load $F_{u,1[m]}$. This relationship is expressed in

Eq. (3-2).

$$F_u \sim 2\pi R \cdot t \cdot \sigma = 2\pi R \cdot \frac{R}{R/t} \cdot \sigma = 2\pi \cdot \frac{R^2}{R/t} \cdot \sigma = m \cdot R^2 \tag{3-1}$$

$$F_{u,R[m]} = F_{u,1[m]} \cdot \frac{(R\ [m])^2}{(1\ [m])^2} \tag{3-2}$$

When the reader still has doubts about this relationship (as a result of the way all dimensions are expressed relative to the radius R), the reader is referred to Section 3.1 of Chapter 5.

The radius-to-thickness ratio R/t determines the thickness of the cylindrical barrel section. A small value of this ratio corresponds with a thicker silo wall, a large value with a thin silo wall. Depending on the source consulted, other limits can be found for this parameter. The Eurocode and the ECCS limit the radius-to-thickness ratio to the range 20 to 5000 (EN 1993-1-6, 2007; ECCS, 2008). Outside this range, the buckling design rules of this standard should not be applied. However, this range is large and very general. In practice, most steel silos have a typical radius-to-thickness ratio between 300 and 3000 (Brown and Nielsen, 1998) or between 100/500 and 2000 (Rotter, 2004). In this investigation, the range of R/t is varied between 100 and 1000. This interval contains both thick-walled silos ($R/t \leq 200$), silos with intermediate thickness ($200 < R/t < 500$), and thin-walled silos ($R/t \geq 500$).

Depending on the silo height h, cylindrical silos can be divided into three categories: (1) short silos; (2) medium high silos; and (3) long silos (Rotter, 2004). In short silos, the boundary conditions at the upper edge of the cylindrical barrel influence the failure behaviour. For example, the (pre-)buckling displacements are restrained in the cylindrical barrel in the vicinity of the upper edge. In contrast, the failure behaviour of medium high silos is relatively independent of the silo height. The last category, i.e. the long silos, is not considered here. Such silos will fail by Euler buckling as a column, without distortion of the cross-section. This failure phenomenon is out of scope of this investigation. In this study, the range of the dimensionless silo height h/R is varied between 2.0 (i.e. a short silo) and 10.0 (i.e. a medium high silo).

Table 3-9 gives an overview of the geometrical parameters of the cylindrical barrel.

Table 3-9 Geometrical parameters of the cylinder.

PARAMETER	VALUE(S)	DIMENSION
R	1.0	m
R/t	100 - 1000	-
h/R	2.0 - 10.0	-

Supporting arrangement type 1

Local supports

The supporting columns are distributed over the whole circumference with equally spaced intervals, regardless of the number of supports. Four or six discrete supports are commonly used, but three or more than six are also found (EN 1993-4-1, 2007). In this study, the number of supporting columns is by default equal to four. However, sometimes six supports are considered, and in exceptional cases even more than six. The dimensions of the supports depends on the dimensions of the longitudinal stiffeners (type 1) or the engaged columns (type 2), and will be discussed below.

Table 3-10 Geometrical parameters of the local supports.

PARAMETER	VALUE(S)		DIMENSION
	Type 1	Type 2	
n_{sup}	4; 6 (8; 10; 12; 14)	4; 6 (8; 10; 12; 14)	-
d_{sup}/R	d_{stif}/R	d_{stif}/R	-
w_{sup}/R	$2 \cdot w_{stif}/R$	w_{stif}/R	-

Theoretically, the supported proportion of the circumference can vary from zero (i.e. $\mu_{sup} = 0$) to a condition where the entire circumference is supported (i.e. $\mu_{sup} = 1$). For "locally" supported silos, the supported proportion of the circumference μ_{sup} is close to zero.

Longitudinal stiffeners

The supporting columns are positioned concentrically underneath the silo wall. Above each supporting column, a longitudinal stiffener is placed on the exterior of the silo wall (Fig. 3-22 (a)), which has a U-shaped cross-section (See Fig. 3-22 (b)).

The circumferential width of the supporting column d_{sup} is equal to the circumferential width of the stiffener d_{stif}, while the radial width of the supporting column w_{sup} is equal to two times the radial width of the stiffener w_{stif}. In this way, the stringer stiffeners are completely supported by the concentric columns (See Fig. 3-22 (b)).

The width in circumferential direction is an important parameter and determines the degree of support along the circumference μ_{sup}. The ratio of the circumferential width to the silo radius d_{stif}/R is varied between 0.05 ($\mu_{sup} = 0.032$) and 0.30 ($\mu_{sup} = 0.191$). The ratio of the radial width to the circumferential width w_{stif}/d_{stif} determines the shape of the stiffener and is varied between 25% and 75%. This range corresponds with a large set of different U-

shapes, as illustrated in Fig. 3-23. From this figure, it could be wrongly deduced that the circumferential width d_{stif} remains constant, but as mentioned before, the width d_{stif} will also vary.

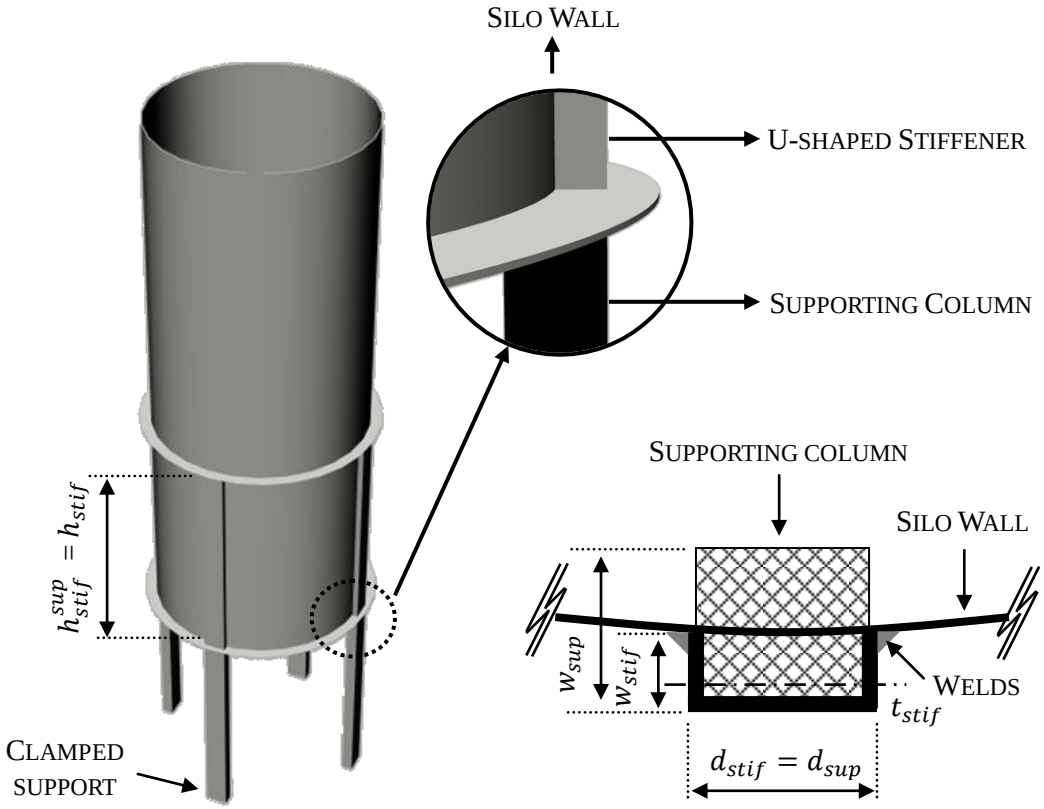

(a) 3D perspective. (b) Cross-section of the U-shaped stiffener.

Fig. 3-22 Supporting arrangement type 1.

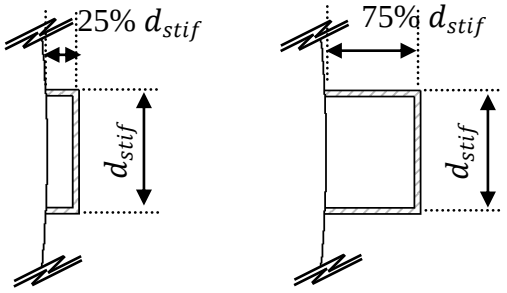

Fig. 3-23 Graphical representation of the outer limits of the ratio of the radial width to the circumferential width w_{stif}/d_{stif} (d_{stif} is also varied).

The range of the stiffener's thickness is determined by two restrictive conditions. Firstly, because of the necessity to weld the longitudinal stiffeners to the silo wall, a minimum thickness (i.e. 1x the silo thickness) and a maximum thickness (i.e. five times the silo thickness) is imposed (Eq. (3-3)) in Table 3-11). The second condition that should be met is that the stiffener should not be too thick or too thin compared to its circumferential width d_{stif} (Eq. (3-4)) in Table 3-11). The latter is based on local compression induced by local buckling

considerations (EN 1993-1-1, 2005). Class 4 cross-sections are those cross-sections in which local buckling will occur before the attainment of yield stress in one or more parts of the cross-section (EN 1993-1-1, 2005). Such "too thin" cross-sections are not considered here. The last restriction is presented in Fig. 3-24.

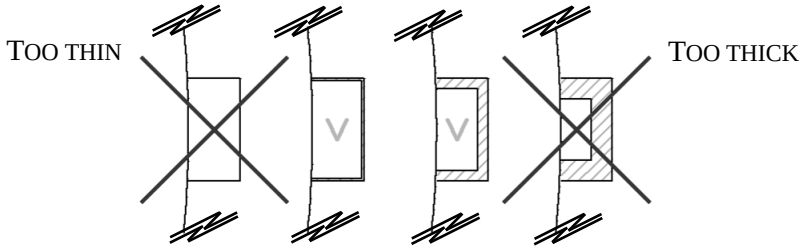

Fig. 3-24 Graphical representation of the outer limits of the ratio of the circumferential width of the stiffener to the stiffener's thickness d_{stif}/t_{stif} (Eq. (3-4)).

h_{stif}^{sup} or h_{stif} represents the height over which the stiffener is attached to the silo wall (See Fig. 3-22 (a)). This "attached" height h_{stif} is varied between 0.5 and 2.5 times the cylinder radius R.

Table 3-11 gives an overview of all geometrical parameters of the longitudinal stiffeners, including the imposed restrictions.

Table 3-11 Geometrical parameters of the U-shaped longitudinal stiffeners.

PARAMETER	VALUE(S)		DIMENSION
d_{stif}/R	0.05 - 0.30		-
w_{stif}/d_{stif}	25 - 75		%
t_{stif}/t	$1.0 \leq t_{stif}/t \leq 5.0$	(3-3)	-
	$10 \leq d_{stif}/t_{stif} \leq 40$	(3-4)	
h_{stif}^{sup} / R	0.5 - 2.5		-

Supporting arrangement type 2 - Engaged columns

The engaged columns are eccentrically positioned on the exterior side of the silo wall (See Fig. 3-25 (a)), have a square or a rectangular cross-section (See Fig. 3-25 (b)), and are the extension of the supporting columns.

The width in circumferential direction determines the degree of support along the circumference μ_{sup}. The ratio of the circumferential width to the silo radius d_{stif}/R is varied between 0.05 ($\mu_{sup} = 0.032$) and 0.30 ($\mu_{sup} = 0.191$). The ratio of the radial width to the circumferential width w_{stif}/d_{stif} determines the shape of the column and is

varied between 25% and 400%. This range corresponds with a large set of different shapes of the cross-section, as illustrated in Fig. 3-26. From this figure, it could be wrongly deduced that the circumferential width d_{stif} remains constant, but as mentioned before, the width d_{stif} will also vary.

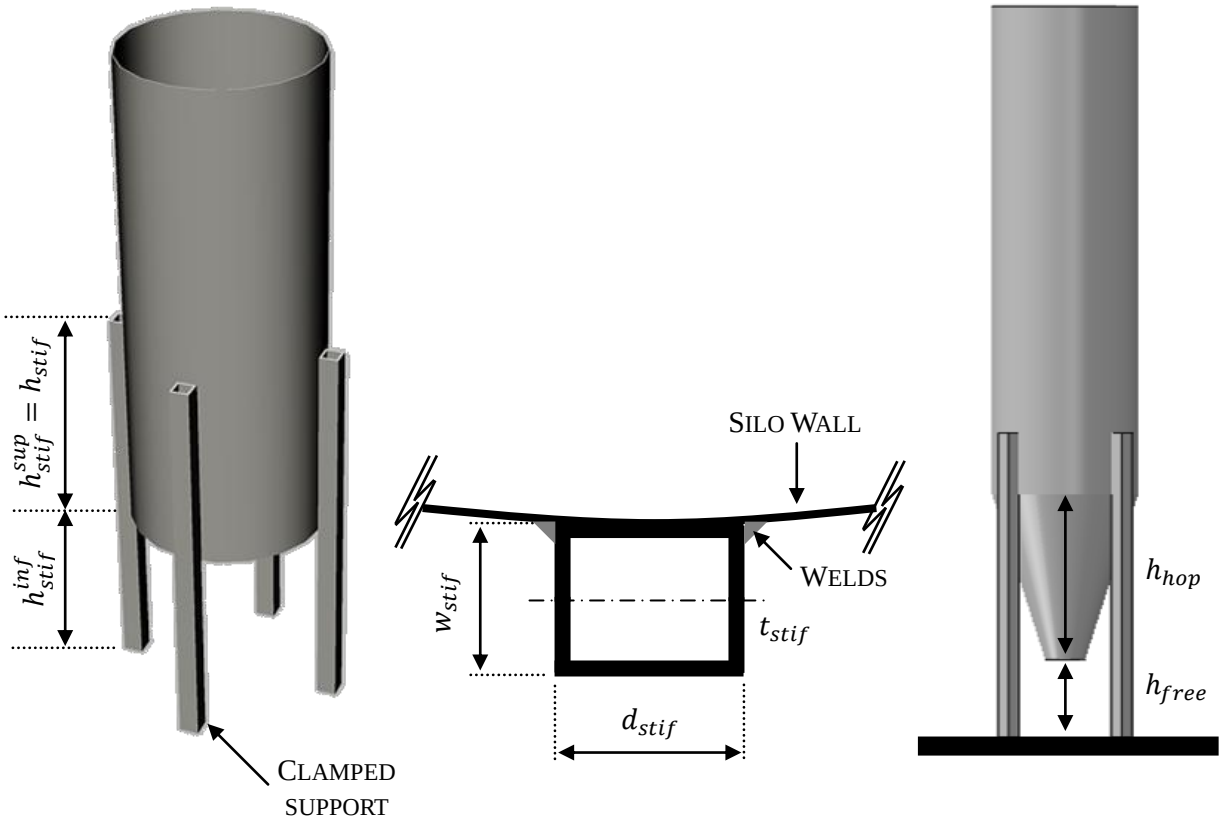

(a) 3D perspective.

(b) Cross-section of the engaged column.

(c) Graphical representation of a 75 degree hopper and clearance.

Fig. 3-25 Supporting arrangement type 2.

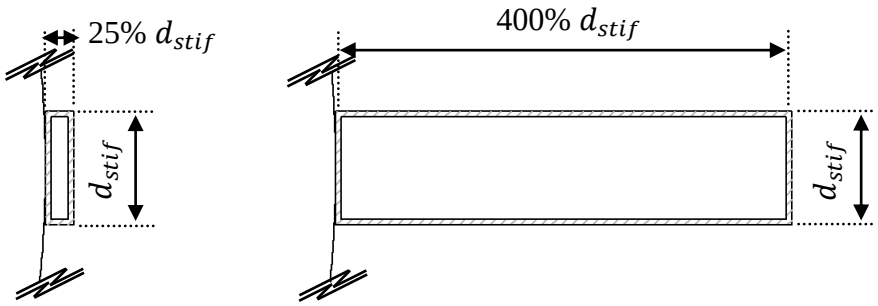

Fig. 3-26 Graphical representation of the outer limits of the ratio of the radial width to the circumferential width w_{stif}/d_{stif} (d_{stif} also varied).

For the column thickness, the same conditions are valid as discussed in the previous section (i.e. the U-shaped longitudinal stiffener). The limits for this interval are illustrated in Fig. 3-27.

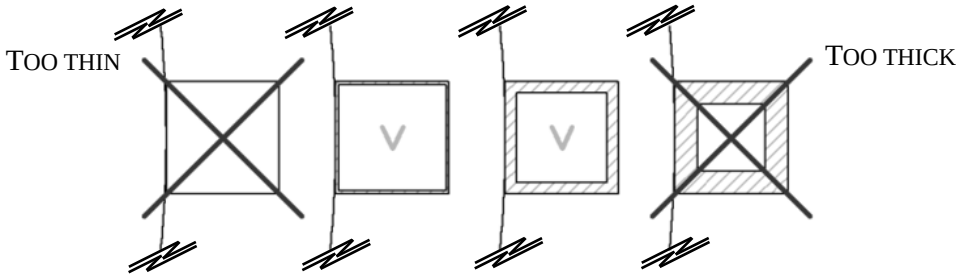

Fig. 3-27 Graphical representation of the outer limits of the ratio of the circumferential width of the column to the column thickness d_{stif}/t_{stif} (Eq. (3-9)(3-4)).

The total column height is divided into an "unattached" height h_{stif}^{inf} and an "attached" height h_{stif}^{sup} (See Fig. 3-25 (a)). The "unattached" height h_{stif}^{inf}, which is the height between the bottom of the cylindrical barrel and the clamped lower edge of the engaged column, is varied between 1.0 and 4.0 times the cylinder radius R. latter value corresponds with a 75° angle hopper and sufficient clearance under the hopper (See Fig. 3-25 (c)), to easily empty the contents of the silo. Furthermore, it is important to mention that a value of h_{stif}^{inf} equal to 4.0 was adopted as default value, while smaller values (i.e. 1.0 and 2.0) where considered only to investigate the influence of this height to the failure behaviour and load.

$$h_{hop} = \frac{R - r_0}{tg(\beta_{hop})} = \frac{R - 0.271 \cdot R}{tg(15°)} = 2.721 \cdot R \tag{3-5}$$

$$h_{free} = 1.6 \cdot R \tag{3-6}$$

$$h_{stif}^{inf} = h_{hop} + h_{free} = 4.321 \cdot R \approx 4.0 \cdot R \tag{3-7}$$

The "attached" height h_{stif}^{sup} represents the height over which the engaged column is attached to the silo wall. This height is varied between 0.5 and 2.0 times the cylinder radius R.

All geometrical parameters of the engaged columns, including the imposed restrictions, are given in Table 3-12.

Table 3-12 Geometrical parameters of the rectangular engaged columns.

PARAMETER	VALUE(S)		DIMENSION
d_{stif}/R	0.05 - 0.30		-
w_{stif}/d_{stif}	25 - 400		%
t_{stif}/t	$1.0 \leq t_{stif}/t \leq 5.0$	(3-8)	-
	$10 \leq d_{stif}/t_{stif} \leq 40$	(3-9)	
h_{stif}^{sup} / R	0.5 - 2.0		-
h_{stif}^{inf} / R	1.0 - 4.0		-

Ring stiffeners (upper and lower ring)

The ring stiffeners both have a width in radial direction w_r and a thickness t_r (See Fig. 3-28). The range of these parameters is given in Table 3-13.

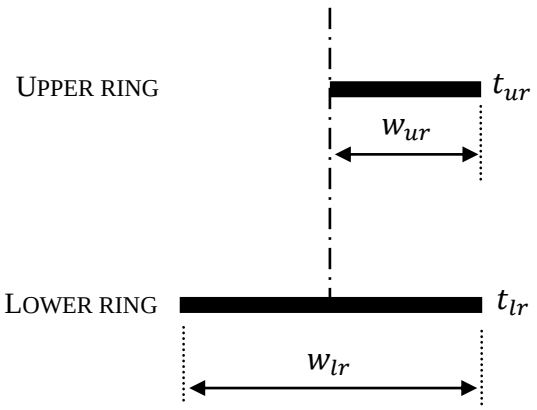

Fig. 3-28 Cross-section of the ring stiffeners.

Table 3-13 Geometrical parameters of the ring stiffeners.

PARAMETER	VALUE(S)		DIMENSION
w_{ur}/R	0.02 - 0.12		-
t_{ur}/t	$1.0 \leq t_{ur}/t \leq 5.0$	(3-10)	-
	$10 \leq w_{ur}/t_{ur} \leq 40$	(3-11)	
w_{lr}/R	0.02 - 0.24		-
t_{lr}/t	$1.0 \leq t_{lr}/t \leq 5.0$	(3-12)	-
	$10 \leq w_{lr}/t_{lr} \leq 40$	(3-13)	

Roof and hopper

In general, the conical roof and hopper are not included in the numerical model, except in the part where their influence is investigated and compared with the substitute boundary conditions (See Section 10 of Chapter 5). The symbols of the dimensions of the conical roof and hopper are depicted in Fig. 3-29 and their ranges are given in Table 3-14. In this work, the hopper and the roof are always concentrically positioned with respect to the cylindrical barrel.

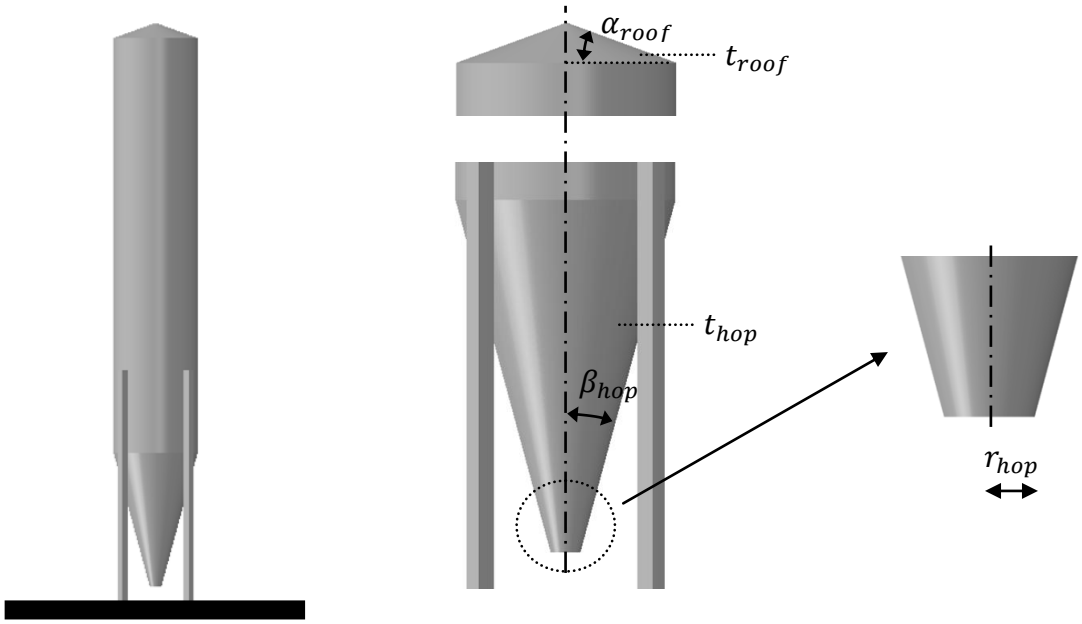

Fig. 3-29 Dimensions of the roof and the hopper.

Table 3-14 Geometrical parameters of the roof and the hopper.

PARAMETER	VALUE(S)		DIMENSION
α_{roof}	0; 10; 20		°
r_{roof}/R	0.000		-
t_{roof}/t	$1.0 \leq t_{roof}/t \leq 5.0$	(3-14)	-
β_{hop} (r_{hop}/R)	15 (0.271); 30 (0.147); 45 (0.100); 60 (0.100)		° (-)
t_{hop}/t	$1.0 \leq t_{hop}/t \leq 5.0$	(3-15)	-

8 Mesh

It is evident that the mesh is an important factor for finite element simulations. The search for a good mesh includes two issues: (1) the choice of a suitable element type and (2) the determination of an optimal mesh density. These choices determine the quality of the mesh, and consequently the accuracy of the results, the efficiency of the calculation, and the calculation cost (i.e. the computer resources and licenses). In the next sections, both topics will be addressed more fully.

Choice of the element type

For the choice of an appropriate element type, an element will be chosen in the family of the shell elements, because locally supported cylinders clearly belong to the family of shell structures. However, Abaqus provides a wide range of shell elements, such as 3D conventional shell elements, continuum or 3D solid shell elements, axisymmetric shell elements, etc. Since the thickness of the silo wall and the other parts are significantly smaller than the other dimensions, conventional shell elements will be used to model the relatively thin-walled structure. In addition, these elements can be used to model curved surfaces. The implementation of such conventional shell elements in a numerical model consists of two steps. Firstly, the geometry is specified at a reference surface. This reference surface will coincide with the shell's midsurface. Afterwards, a thickness is associated with each element.

The 3D conventional shell elements can be classified into three main categories:

- General-purpose conventional shell elements. Depending on the thickness of the shell elements, the thick or the thin shell theory is applied. In other words, these elements can be used for both thick and thin shell problems. Transverse shear deformation is allowed.
- Thick conventional shell elements. Such elements can be used when the shell thickness is more than about $1/15$ of a characteristic length on the shell surface. Furthermore, thick elements are needed when transverse shear deformation is important and when second-order interpolation is desired (Abaqus, 2009).
- Thin conventional shell elements. Thin elements can be used when the shell thickness is less than about $1/15$ of a characteristic length on the shell surface. Thin elements are suitable when transverse shear deformation is negligible and when the Kirchhoff constraint must be satisfied accurately (i.e. the shell normal remains orthogonal to the shell reference surface). For the thin shell elements considered here (See Table 3-15), the Kirchhoff constraint is satisfied numerically and the elements converge to the thin shell theory as the thickness decreases (Abaqus, 2009).

In Table 3-15, an overview is given of the classification of the conventional shell elements used in this investigation. The naming convention of the shell elements (See Table 3-15) is as follows. The first character defines the element type. The letter "S" corresponds with a shell element. The second character gives the number of nodes. The optional character "R", if present, indicates that reduced integration is applied. Such element has a reduced number of integration or gauss points for the numerical integration to evaluate the element stiffness. Compared to the full integration element, an element with reduced integration has one gauss point less in each direction. Only in these gauss points, the stresses are calculated and are extrapolated by shape functions to the other points. Reduced integration usually provides more accurate results (on the condition that the elements are not distorted or loaded in in-plane bending) and significantly reduces the calculation time (especially for 3D problems) (Abaqus, 2009). The optional character "5", if present, indicates that each node only possesses five (instead of six) degrees of freedom (DOFs): three displacement components and two in-surface rotation components. This feature is only available for thin shell elements, and can reduce the calculation time (Abaqus, 2009).

Table 3-15 Classification of the conventional shell elements.

NUMBER OF NODES	GENERAL PURPOSE	THICK	THIN
4	S4 / S4R		S4R5
8		S8R	S8R5
9			S9R5

In the doctoral thesis of Vanlaere, an investigation has been done to find the most suitable element type for locally supported steel silos with rectangular shaped longitudinal stiffeners. This investigation demonstrated that the S4R5 and the S8R5 element type were the most appropriate element types when the results and the calculation cost were used as criteria. Eventually, the S8R5 element was chosen because this element has a slightly smaller stiffness, and consequently the numerical model is slightly more conservative (Vanlaere, 2006).

In Section 2.1 of Chapter 5, an extensive parametric study has been performed to determine the influence of the element type (See Table 3-15) on the results (i.e. the failure behaviour and load) and calculation time, for different geometries and different types of shell analyses (EN 1993-1-6, 2007). In this work, the S8R5 thin shell element will be used for all components and analyses.

Mesh density

As already mentioned above, the mesh refinement is an important issue because of its relationship to accuracy and cost. Coarse meshes can yield inaccurate results, by which it is important to sufficiently refine the mesh to ensure that the results are adequate. In general, as

the mesh density increases (i.e. smaller element size), results are expected to become more accurate, and the numerical solution tends toward a unique value. When the change in solution is negligible, the mesh has been converged. However, coupled with the mesh refinement, an additional calculation cost (i.e. computer resources) and software licenses are involved. The designer has to judge at what level of refinement the results are acceptable. In other words, the main question is "What cost are you willing to pay for the accuracy you are receiving?".

The required mesh density depends on different factors, such as the desired degree of accuracy, the element types and shapes, the accurate representation of the (curved) surface, the type of loadings, the boundary conditions, the stress gradients, etc. Consequently, in practice, a mesh convergence study is necessary to determine the point of required mesh density by comparing the results of numerical models with a varying mesh density (See Section 2.2 in Chapter 5).

For locally supported cylindrical steel silos, whether or not stiffened, the region of failure (i.e. exhaustive yielding and/or instability), large stress gradients, and stress concentrations usually is in the same region. Indeed, these phenomena mostly occur just above the local supports or in the vicinity (next to or above) of the longitudinal stiffeners/engaged columns, and occur very locally. This situation is certainly interesting and lends itself to divide the shell surface into regions with different mesh refinement, as presented in Fig. 3-30. The shell surface where yielding/buckling occurs gets the finest mesh (i.e. the region outlined in black striped line). In the other regions (i.e. near the top of the cylindrical barrel and between the supports), failure is rare because the (axial) stresses are smaller and more uniformly distributed. Here, the numerical model gets a coarser mesh. In this way, the accuracy of the numerical model is maintained, while the calculation cost reduces.

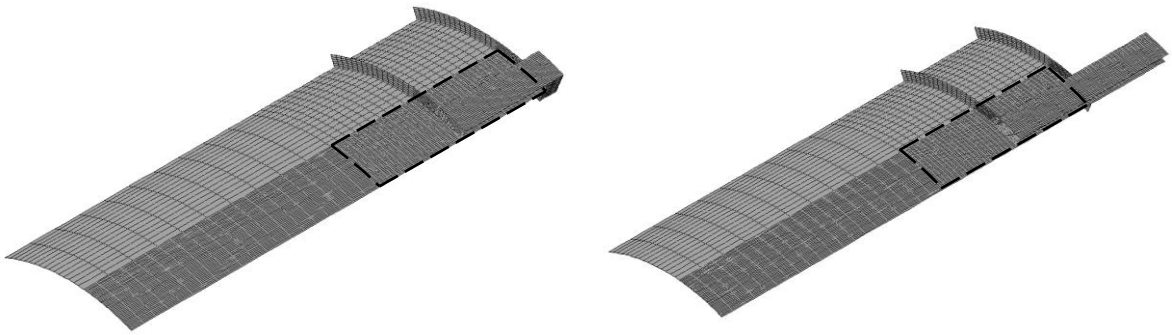

(a) Large silo stiffened with U-shaped longitudinal and ring stiffeners.

(b) Light silo with engaged columns.

Fig. 3-30 The geometry with a variable mesh refinement.

Next, the determination of the default mesh is discussed, which consist of two steps: (1) the determination of the size of the regions and (2) the determination of the element size in all regions. This reference mesh is based on the results of Vanlaere (Vanlaere, 2006).

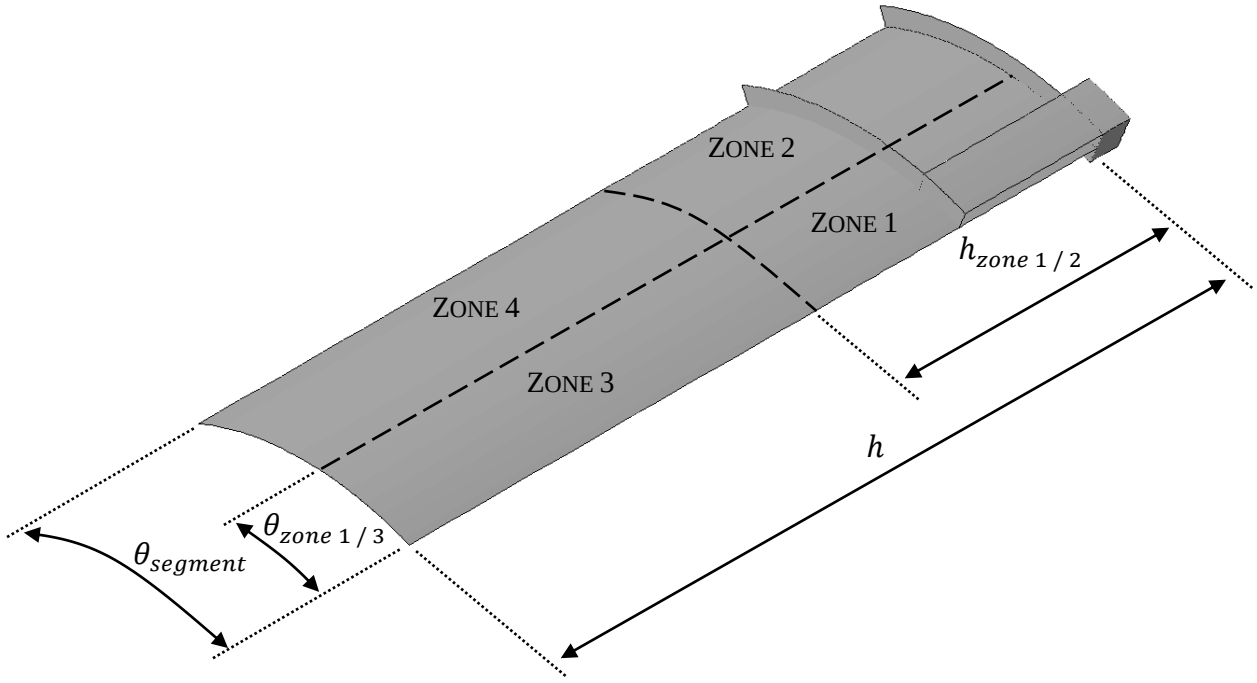

Fig. 3-31 Subdivision of the geometry into zones with a variable mesh refinement.

First, the parameters v_{axial} and v_{circ} are calculated. These values present the ratio of the distance (angle) of the first zone to the total distance (angle) of the cylinder segment, in respectively the axial and circumferential direction.

$$v_{axial} = \frac{h_{zone\ 1\ /\ 2}}{h} = \frac{max\left(2.0 \cdot h_{stif}^{sup}\ ;\ 1.2 \cdot h_{weld\ depression}\right)}{h} \tag{3-16}$$

$$v_{circ} = \frac{\theta_{zone\ 1\ /\ 3}}{\theta_{segment}} = \frac{max\left(d_{stif}\ ;\ d_{sup}\right)}{d_{segment}} \tag{3-17}$$

Next, the number of elements in each zone and in both directions can be determined by means of the formulas deduced by Vanlaere (Vanlaere, 2006). For example, with Eq. (3-18), the number of elements $n_{axial\ 1\ /\ 2}$ in axial direction of region 1 and 2 is obtained.

$$n_{axial\ 1\ /\ 2} = max\left(25\ ;\ round\left(\frac{62}{0.75 \cdot e^{[1-0.5\cdot(0.75-v_{axial})]\ \cdot\ log(v_{axial})}}\right)\right) \tag{3-18}$$

$$n_{axial\ 3\ /\ 4} = ceil\left(\frac{1}{3} \cdot n_{axial\ 1\ /\ 2} \cdot \frac{1 - v_{axial}}{v_{axial}}\right) \tag{3-19}$$

$$d_{segment} = \frac{2\pi R}{2 \cdot n_{sup}} \tag{3-20}$$

$$n_{circ\ 1\ /\ 3} = max\left(20\ ;\ round\left(\frac{67}{0.75 \cdot e^{[1-0.5\cdot(0.75-v_{circ})]} \cdot log(v_{circ})}\right)\right) \tag{3-21}$$

$$n_{circ\ 2\ /\ 4} = max\left(10\ ; ceil\left(\frac{1}{5} \cdot n_{circ\ 1\ /\ 3} \cdot \frac{0.75}{v_{circ}}\right)\right) \tag{3-22}$$

With the formulas Eqs. (3-23) to (3-26), the size of the elements can be determined in each region and in both directions.

$$s_{axial\ 1\ /\ 2} = \frac{v_{axial} \cdot h}{n_{axial\ 1\ /\ 2}} \tag{3-23}$$

$$s_{axial\ 3\ /\ 4} = \frac{(1 - v_{axial}) \cdot h}{n_{axial\ 3\ /\ 4}} \tag{3-24}$$

$$s_{circ\ 1\ /\ 3} = \frac{v_{circ} \cdot d_{segment}}{n_{axial\ 1\ /\ 3}} \tag{3-25}$$

$$s_{circ\ 2\ /\ 4} = \frac{(1 - v_{circ}) \cdot d_{segment}}{n_{axial\ 2\ /\ 4}} \tag{3-26}$$

The results of the mesh convergence study are presented in Section 1.2 of Chapter 5. The influence of the mesh refinement on the results (i.e. the failure behaviour and load) and the calculation time has been investigated for different geometries and different types of shell analyses (EN 1993-1-6, 2007).

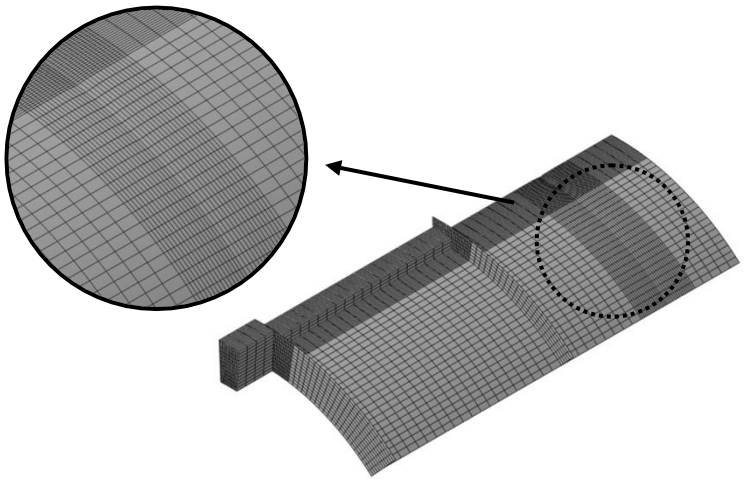

(a) The Abaqus model.

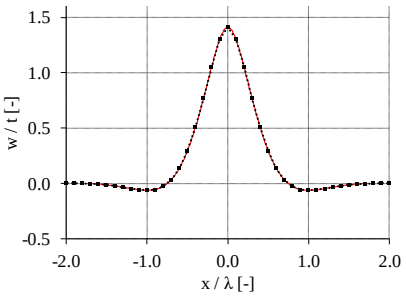

(b) The desired WD cross-section (red) and the effective cross-section in Abaqus (black), with indication of the element surfaces and the corner nodes.

Fig. 3-32 Refined mesh in the vicinity of the axisymmetric WD.

In the vicinity of a weld depression, an additional mesh refinement has been applied to model the shape with sufficiently accuracy (See Fig. 3-32).

9 Boundary conditions

In a numerical model, boundary conditions are defined (1) to model the connection of the structure with its environment (i.e. the conical roof and hopper + the substructure or the foundation) or (2) to apply symmetry.

Symmetry boundary conditions

Given the symmetrical nature of the cylinder (i.e. the geometry, the assumed loading and imperfections), it is appropriate to make use of symmetry to reduce the size of the numerical model as much as possible. In this way, a substantial reduction of the calculation cost can be obtained, without sacrificing accuracy.

Instead of a 360 degree model, only a segment of the structure is modelled with a circumferential angle $\theta_{segment}$. This angle depends on the number of supports n_{sup} and can be calculated by (3-27). For a structure with four equidistant local supports (i.e. the default number), the cylinder segment has a circumferential angle of 45 degrees.

$$\theta_{segment} = \frac{360°}{2 \cdot n_{sup}} \tag{3-27}$$

The cylinder segment starts from the vertical plane perpendicular to the silo wall halfway a local support and continues until the vertical plane midway between two supports (See Fig. 3-33 (a)). At the free edges created by the symmetry transformation (See Fig. 3-33 (b)), symmetry boundary conditions have to be applied to take into account the influence of the not modelled part of the structure.

At each node of the free edges, a local cylindrical coordinate system (R, T, Z) is defined of which the origin is located in the node. The R-axis corresponds to the radial direction, the T-axis is the direction of the horizontal tangent to the silo wall, and the Z-axis corresponds to the vertical axis. The applied boundary conditions are given by Eq. (3-28) and partially restrain the deformations in the node. The displacement in the direction of the T-axis, and the rotations about the R-axis and Z-axis are fully prevented.

$$U_T = \varphi_R = \varphi_Z = 0 \tag{3-28}$$

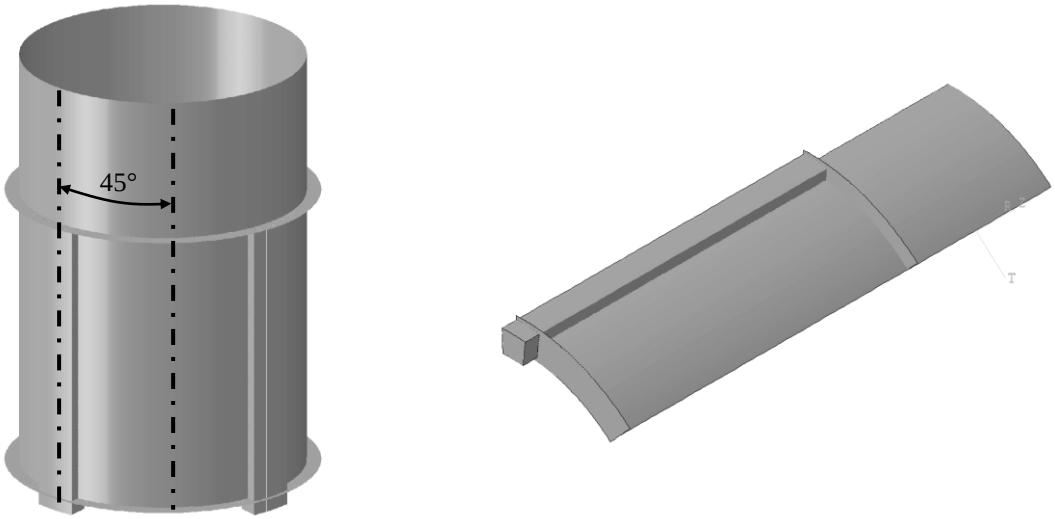

(a) 360 degree model. (b) 45 degree model.

Fig. 3-33 Symmetry boundary conditions.

For different cases, the results of one eighth of the shell were verified with results of a complete shell. An excellent agreement was found for both models, from which it can be concluded that the symmetry boundary conditions may be used without influencing the results. All figures in this work (except the validation analyses in Chapter 4), depicting a complete shell model, were obtained by mirroring the cylindrical segment in circumferential direction.

Boundary conditions at the top and lower edge of the cylindrical barrel

By default, the conical roof and the conical hopper are omitted from the numerical model. These components ensure that the circular shape is maintained at respectively the upper and the lower edge of the cylindrical barrel. This effect of the non-modelled parts will be applied by boundary conditions. Only if a lower or transition ring is present in the numerical model, these boundary conditions will not be applied to the lower edge, because the lower ring takes over the function of maintaining the circular shape. Similar to previous section, a local cylindrical coordination system is defined in each node of these edges. The following boundary conditions are applied.

$$U_R = U_T = \varphi_Z = 0 \tag{3-29}$$

The displacements in the direction of the R-axis and T-axis (i.e. the horizontal displacements) and the rotation about the Z-axis are fully prevented.

Supporting boundary conditions

Three different types of supports are considered: a fully clamped support (default), a hinged support, and a partially clamped support. These types are now discussed one by one.

- Fully clamped support (default type)

  In this case, the supports are completely rigid in all directions, and, consequently, the rotation about the circumferential axis is fully restrained. For both configurations, this type can be implemented by restraining all translational degrees of freedom at all nodes of the lower edge of the supporting column (Eq. (3-30)) (See top of Fig. 3-34 (a) and (b)). For silos with U-shaped stiffeners, another possibility is to replace the supporting column by a steel brick shaped volume consisting of solid elements (C3D20R) (See bottom of Fig. 3-34 (a)). The silo wall, the longitudinal stiffener, and the lower ring are rigidly attached to the upper side of the support. The nodes of the lower side of the support are restrained in all directions (Eq. (3-30)).

$$U_X = U_Y = U_Z = 0 \tag{3-30}$$

With supporting column:

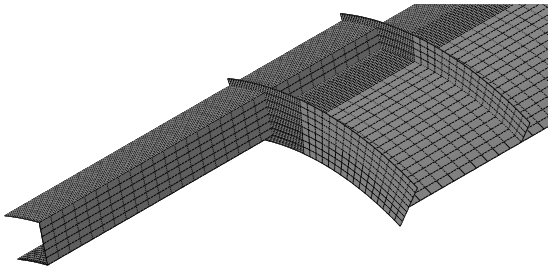

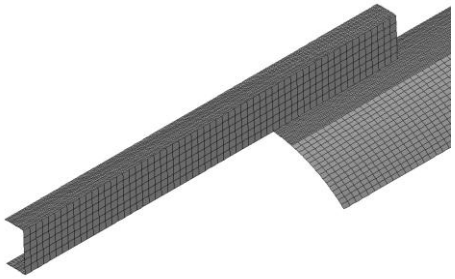

Without supporting column:

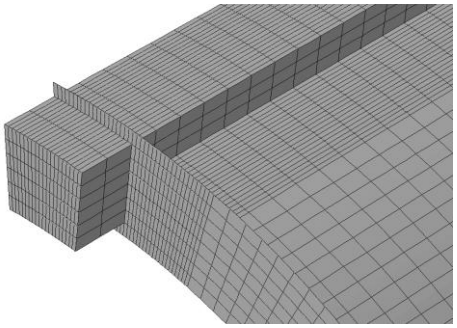

(a) Large silo stiffened with U-shaped longitudinal and ring stiffeners.

(b) Light silo with engaged columns.

Fig. 3-34 Fully clamped support.

- Hinged support

  In contrast to the fully clamped support, the circumferential rotation φ_T now is fully allowed. In Abaqus, this is implemented by the use of a rigid body.

Indeed, a rigid plate is modelled and attached to the lower edge of the supporting column (See Fig. 3-35 (a) and (b)). The reference point of the rigid body coincides with the centroid of the cross-section of the supporting column and is in Fig. 3-35 indicated by a blue cross. Only in this reference point, boundary conditions are coupled to model the influence of the support (Eq. (3-31)).

$$U_X = U_Y = U_Z = 0 \tag{3-31}$$

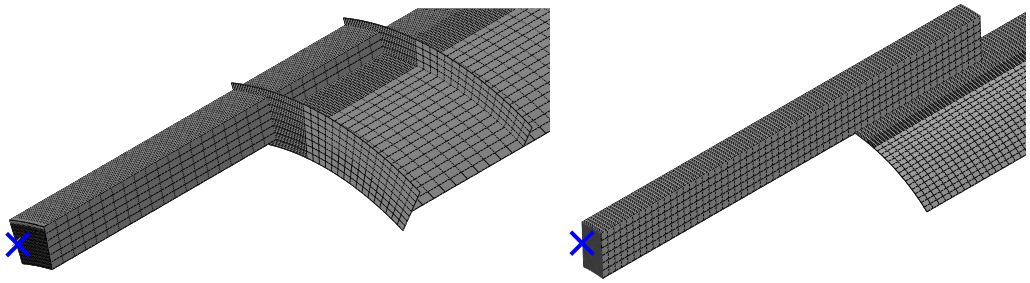

(a) Large silo stiffened with U-shaped longitudinal and ring stiffeners.

(b) Light silo with engaged columns.

Fig. 3-35 Hinged or partially clamped support.

- Partially clamped support

  As the name suggests, the circumferential rotation φ_T is now partially restrained. The way of modelling is very similar to the hinged support, namely a rigid plate (See Fig. 3-35) and boundary conditions coupled to the reference point (Eq. (3-32)).

  $$U_X = U_Y = U_Z = 0 \tag{3-32}$$

  In addition, a rotational spring with linear behaviour is added between the reference node and the ground. This spring partially prevents the rotation about the circumferential axis at the reference node. The linear behaviour is specified by a constant rotational spring stiffness C [kNm/rad].

  The influence of the supporting boundary conditions on the failure behaviour is discussed in Section 4 of Chapter 5.

10 Loading conditions

As fully described in Section 7 in Chapter 1, in this study, the cylindrical barrel will be subjected to vertical / axial compression and will be applied as a uniform line load q at the upper edge of the cylindrical barrel, as presented in Fig. 3-36. As a result, the axial stresses in the vicinity of the upper edge will be relatively uniform. In contrast, stress concentrations will arise in the silo wall just above / next to the longitudinal stiffeners, the engaged columns, and

the local supports.

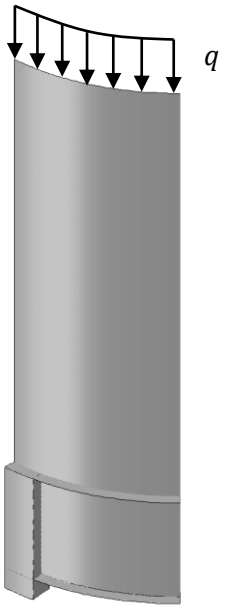

Fig. 3-36 The loading in the numerical model.

11 Material properties

The material behaviour depends on the type of shell analysis (See Section 4.5 in Chapter 2) (EN 1993-1-6, 2007). The first material behaviour is a purely linear elastic behaviour and will be applied for a LA, LBA, GNA, and GNIA analysis. In a stress-strain diagram, this behaviour is described by a straight line with slope equal to the Young's modulus E. A more realistic material behaviour, i.e. an ideal elasto-plastic behaviour, will used for a MNA, GMNA, and GMNIA analysis. The stress-strain relationship now is characterised by two stages. The initial elastic response is linear and is given by a line with slope equal to the Young's modulus E until the yield stress σ_y is reached. At this point, the plastic stage is reached, which is represented by a horizontal line in the stress-strain diagram. The default values of the material properties are given in Table 3-16.

Table 3-16 Default values of the material properties of the steel.

PARAMETER	VALUE	DIMENSION
E	210 000	MPa
ν	0.3	-
σ_y	235	MPa

For the verification analyses (Chapter 4), the real material behaviour of the used steel plates is taken into account. This behaviour is determined by means of tensile tests on test specimens. The tensile test (i.e. the test setup and the procedure) is discussed in Section 5 of Chapter 3,

the results are presented in Chapter 4.

12 Analysis parameters

The modified Riks algorithm has been used for GMNA, GNA, MNA, GNIA, and GMNIA analyses (Riks, 1972; 1979; 1981; Crisfield, 1982). This algorithm is especially useful for the prediction of unstable, geometrically non-linear collapse of a structure. Furthermore, this method is able to follow both rising and descending non-linear equilibrium paths. In the descending curves, the stiffness is negative and the structure must release energy to remain in equilibrium (Abaqus, 2009).

In this method, the current load magnitude F_{total} is defined by Eq. (3-33), in which F_o is the dead load (in this study: $F_o = 0kN$), F_{ref} is the reference load (in this study: $F_{ref} = 1kN$) distributed over the entire circumference of the upper edge of the cylindrical barrel), and LPF is the load proportionality factor.

$$F_{total} = F_o + LPF \cdot \left(F_{ref} - F_o\right) \tag{3-33}$$

As can be seen, the current load F_{total} is always proportional to the reference load F_{ref}. The relationship between these two loads is determined by one factor, namely the load proportionality factor LPF. This factor is an additional unknown, which is simultaneously solved with the displacements. Therefore, to be able to measure the progress of the solution, an extra quantity is defined in Abaqus, namely the arc-length l (Abaqus, 2009).

In Abaqus, the increments of LPF (and thus indirectly also the loading increments) are computed automatically. As Abaqus user, you can only partially control this automatic process by a number of input parameters, such as the initial increment in arc length $\Delta l_{initial}$, the total arc length scale factor l_{period} (by default 1), the minimum arc length l_{min}, and the maximum arc length l_{max}. The first two input parameters determine the initial load increment $\Delta\text{LPF}_{initial}$ (See Eq. (3-34)), while the minimum and the maximum allowed arc length influence the subsequent increments of the LPF.

$$\Delta LPF_{initial} = \frac{\Delta l_{initial}}{l_{period}} \tag{3-34}$$

In particular, the choice of the maximum arc length l_{max} is crucial to control the simulation. On the one hand, if this value is chosen rather small, the accuracy of the results will be satisfactory, but the number of increments increases, as a result of which the calculation cost increases. On the other hand, if a large value is adopted for the maximum arc length, the solution could become too coarse. In other words, as Abaqus user, you have to attempt to find a balance between accuracy and reasonable calculation cost. In this study, it was chosen to

keep the maximum number of increments equal to 300. Only for MNA analyses, this maximum number was not applied, due to the asymptotic nature of the progress of the load in time.

In the beginning of the research, a procedure was developed to make a good estimate of the maximum arc length l_{max} based on the expected failure load F_u^{exp}. This load was determined by an exploring simulation before the final simulation. This exploratory simulation was performed with a very large maximum arc length l_{max}, so that the failure load is already achieved within a minimum number of increments. In this way, this important parameter could be determined with a minimal effort of computing time. During the research, the relationship between the expected failure load F_u^{exp} and the maximum arc length l_{max} has gradually improved. And, furthermore, the estimation of l_{max} took into account the accuracy of the estimation of previous similar simulations of the queue.

13 Output parameters

Lastly, the output parameters should be given in Abaqus. The eigenvalues (LBA) or the load proportionality factor LPF at each increment (for the other shell analyses) are recorded anyway. The other output variables are written to the output database with a frequency of five increments. In this way, the size of the result files is significantly reduced.

Table 3-17 Default field output.

PARAMETER	LOCATION	FREQUENCY
Eigenvalue / LPF		1
Deformations	All nodes	5
Stresses	Midplane	5
Reaction forces	Support	5

14 Key points of the experimental and the numerical model

In the first part of the chapter, the determination of the geometry of the test series of scale models was presented. Next, the fabrication procedure and the experimental setup have been fully discussed. The topic of the second part of the chapter was the discussion of the numerical model with its parameters (e.g. mesh, geometry, etc.) and assumptions (e.g. the material behaviour). In this way, the reader can start the following chapters with sufficient knowledge about the experimental and numerical methods.

CHAPTER 4

Experimental results and validation of the numerical model

In the second part of Chapter 3, a full description is given of the numerical model. However, before simulations can be performed with this model, either in parametric studies (Chapter 5), or for the development of a design rule (Chapter 6), the finite element model must be verified. This verification implies that the results of the numerical model are compared with the experimental results, to determine whether sufficient agreement exists. If this is the case, the results of the numerical model can be labelled as reliable to predict the elasto-plastic failure load of axially compressed locally supported cylindrical steel silos.

The experimental test setup and the determination of the test programme (i.e. the dimensions, the fabrication method, etc. of the scale models) have been discussed in the first part of Chapter 3. In contrast, Chapter 4 focuses on the experimental results. Firstly, the results of all experiments (i.e. the failure load, the post-buckling deformed shape, etc.) are presented and interpreted. Secondly, an explanation is given on the processing of the measurements of the imperfections of the (un)stiffened scale models. This processing involves e.g. the determination of the quality tolerance class and the conversion to useful input data for the Abaqus model. After this description, the results of the imperfection measurements are presented. The next part is devoted to the processing of the results of the tensile tests and the results themselves are given. Then, the validation of the numerical model, which is the main purpose of this chapter, is presented and discussed. The chapter ends with some conclusions.

1 Experimental results

Table 4-1 gives an overview of all experiments with the dimensions of either the U-shaped longitudinal stiffeners (i.e. numerical model 1) or the engaged columns (i.e. numerical model 2). The last but one column gives the GMNA failure load F_u^{GMNA} predicted by Abaqus assuming a perfect structure (without small deviations relative to the perfect cylindrical shell wall), an ideal elasto-plastic material behaviour, and a completely clamped support (See Section 9 in Chapter 3). It is important to emphasize that these GMNA failure loads are obtained from the preliminary parametric study presented in Chapter 3 and not from the verification analyses given in this chapter. In the verification step at the end of this chapter, to estimate the experimental failure load F_u^{exp}, the factors just listed will be taken into account more accurately by the measurement of the initial imperfections in the shell wall, tensile tests

on the material used, etc. This experimental failure load F_u^{exp} is listed in the last column of Table 4-1.

Table 4-1 Selected geometries with the perfect GMNA load (obtained from the preliminary parametric study discussed in Chapter 3) and the experimental buckling load.

LABEL	$t\,[mm]$	$d_{stif}\ x\ w_{stif}\ x\ t_{stif}\ [mm]$	F_u^{GMNA} [KN]	F_u^{exp} [KN]
EU1	0.8	40 x 20 x 2	131.9	137.5
EU2	0.8	60 x 30 x 2	154.6	151.3
EU3	1.0	40 x 20 x 2	180.3	171.5
EU4	1.0	60 x 30 x 2	213.6	/
EK1	0.8	40 x 40 x 2	118.6	73.9
EK2	0.8	60 x 60 x 2	144.6	70.8
EK3	1.0	40 x 40 x 2	153.0	94.1
EK4	1.0	60 x 60 x 2	189.6	89.7

For all experiments (except EU1), an experimental failure load is obtained which is smaller than the initial and less accurate GMNA failure load (See Fig. 4-1). With the U-shaped stiffeners, the difference between these loads is each time minimal. In contrast, the difference is significant in the case of the engaged columns.

Before proceeding to the discussion of the experimental results, Fig. 4-2 is discussed. In this figure, a horizontal cross-section is depicted of the scale model with the indication of the numbering of the supports and the position of the meridional weld. This numbering will be applied consistently throughout this chapter.

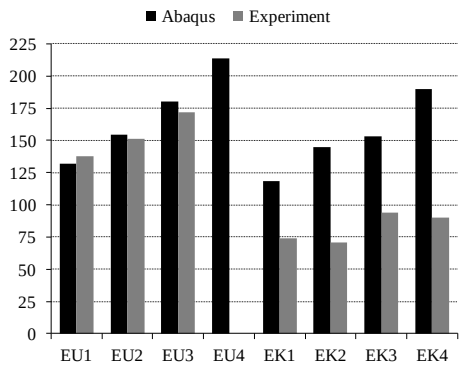

Fig. 4-1 Graphical comparison of the perfect GMNA load (obtained from the preliminary parametric study discussed in Chapter 3) with the experimental buckling load.

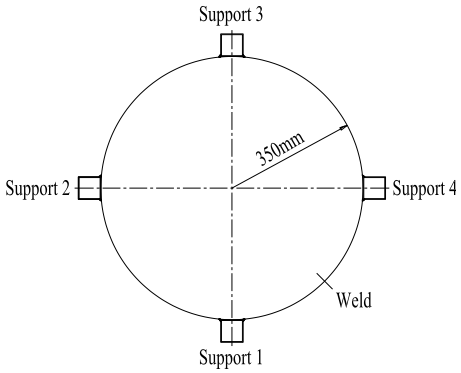

Fig. 4-2 Cross-section of the circular scale model.

All predetermined experiments were performed successfully, except for experiment EU4 (the

experimental failure load is missing in Table 4-1 and Fig. 4-1). This experiment failed two times in a row due to premature collapse of the structure and was not performed a third time. The first time, the scale model prematurely collapsed due to perforation of the PVC ring, which was placed between the upper edge of the silo and the top plate (See Fig. 4-3 (a)). This perforation was caused due to a combination of frequent use, the sharpness of the top edge of the barrel, and a relatively high compressive load (experiment EU4 has the largest failure load). After this experiment, the PVC ring was replaced by a teflon ring, combined with an underlying steel ring below, which protects the teflon ring against perforation. The second time, the steel supporting blocks perforated the lower ring (again experiment EU4 has the largest failure load), as a result of which the circumferential rotation of the supporting blocks was completely free, which is very disadvantageous for the failure behaviour (See Fig. 4-3 (b)).

(a) Perforation of the PVC ring. (b) Perforation of the lower ring.

Fig. 4-3 Premature failure of scale model EU4.

Now, all other experimental results are presented and discussed in the order of appearance in Table 4-1.

Experiment EU1

In Fig. 4-4, a few detailed photos are depicted of the post-buckling deformed shape of the silo wall. Above the top of U-shaped stiffener at support 1, an inclined buckle is formed. Two compressive buckles are visible in the unstiffened silo wall above the stiffeners at supports 2 and 3. In the vicinity of the stiffener at support 4, no large deformations can be observed.

(a) Support 1. (b) Region between support 2 (left) and support 1 (right). (c) Support 2. (d) Support 3.

Fig. 4-4 Post-buckling deformations (EU1).

Fig. 4-5 shows the progress of the measured load for each support as a function of time. For all supports, the measured load systematically increases until the first critical moment at $t_{u1} = 1071.815$s. At that moment, F_{sup}^{2} and F_{sup}^{4} start to decrease (slowly in the beginning, then more rapidly), while F_{sup}^{1} and F_{sup}^{3} start to increase more rapidly, because the second support fails. In other words, the buckle above stiffener 2 develops first (See Fig. 4-4 (c)). A few seconds later ($t_{u2} = 1073.598$s), F_{sup}^{3} starts to decrease due to failure of the third support. The secondary buckle above stiffener 3 is visible in Fig. 4-4 (d). At that same time, the not yet failed fourth support begins to absorb more load (i.e. an increase of F_{sup}^{4}). A fraction of a second later ($t_{u3} = 1073.604$s), the increasing supporting forces F_{sup}^{1} and F_{sup}^{4} also start to decrease, because an inclined buckle develops above stiffener 1 (See Fig. 4-4 (a)). In other words, thanks to this measurement we are not only able to determine the distribution of the applied load over the different supports, but also to deduce the sequence of failure of the supports.

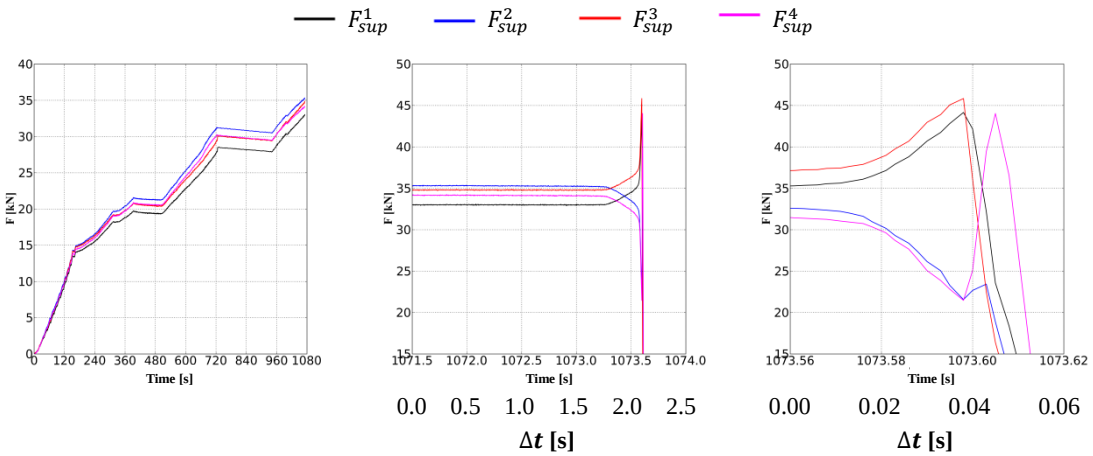

(a) During the entire experiment until failure. (b) At the moment of failure ($t_{u1} = 1071.815$s). (c) At the moment of failure ($t_{u2} = 1073.598$s).

Fig. 4-5 Magnitude of the supporting forces (EU1).

Table 4-2 gives an overview of all loads measured at the moment of failure of the second support. The average failure load of the structure is 137.9kN; the failure load of support 2 is 35.3kN.

Table 4-2 Failure load - total force and supporting forces (EU1).

TOTAL			SUPPORT		
$F_u^{load\ cell\ 1}$	138.4	kN	$F_{u,sup1}$	33.1	kN
$F_u^{load\ cell\ 2}$	137.7	kN	$\boldsymbol{F_{u,sup2}}$	**35.3**	**kN**
$F_u^{sum\ supports}$	137.5	kN	$F_{u,sup3}$	34.8	kN
$\boldsymbol{F_u^{average}}$	**137.9**	**kN**	$F_{u,sup4}$	34.2	kN

Fig. 4-6 shows the load-displacement diagram of all supports with the supporting force plotted on the vertical axis, the radial deformation of the top of the stiffener on the horizontal axis. Negative deformations correspond with the inward deformations. As can be seen, most stiffeners have the tendency to deform in inward direction when a compressive load is applied on the upper edge of the cylindrical barrel.

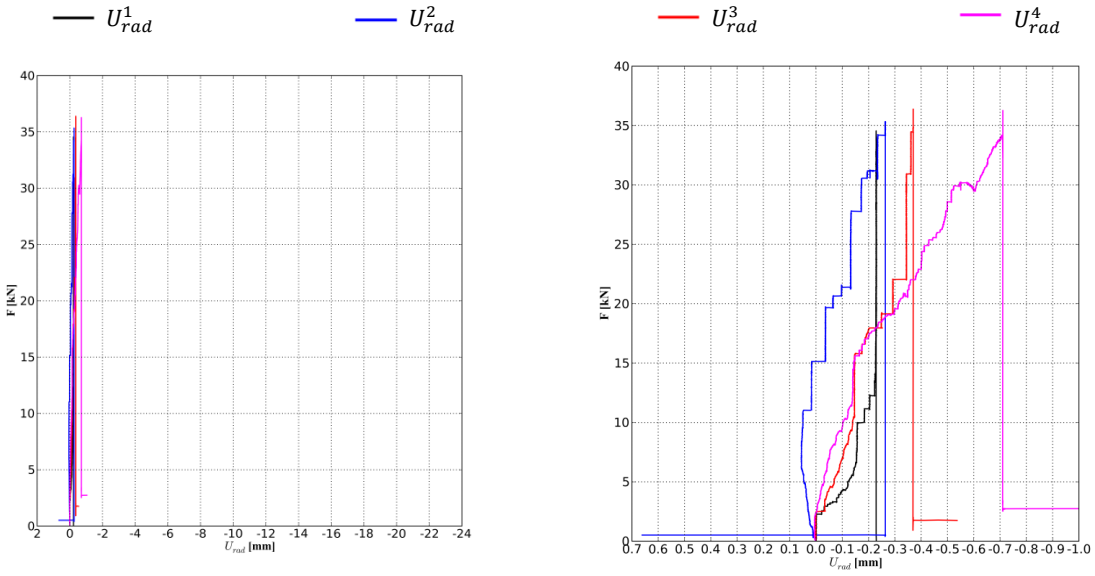

Fig. 4-6 Load-displacement diagram: the radial displacement of the top of the U-shaped stiffener versus the supporting force (EU1).

Experiment EU2

The upper side of the column collapsed in the immediate vicinity of the upper edge of the cylindrical barrel above the stiffeners at supports 1 and 2 (See Fig. 4-7 (a) and (b)). No large deformations are found above support 3. In the unstiffened silo wall above the top of U-shaped stiffener at support 4, a compressive buckle developed after failure (See Fig. 4-7 (c)).

(a) Support 1. (b) Support 2 (c) Support 4.

Fig. 4-7 Post-buckling deformations (EU2).

Fig. 4-8 shows the progress of the measured load for each support as a function of time. For all supports, the measured load systematically increases until the first critical moment at $t_{u1} = 709.376$s. At that moment, F_{sup}^{2} and F_{sup}^{4} start to decrease (slowly in the beginning, then more rapidly), while F_{sup}^{1} and F_{sup}^{3} start to increase more rapidly, because the fourth support fails. This abrupt moment is caused by the development of a primary buckle above stiffener 4 (See Fig. 4-7 (c)). A fraction of a second later ($t_{u2} = 709.604$s), the increasing forces F_{sup}^{1} and F_{sup}^{3} also start to decrease, because secondary deformations are developing in the unstiffened silo wall at the top of the barrel above stiffeners 1 and 2 (See Fig. 4-7 (a) and (b)).

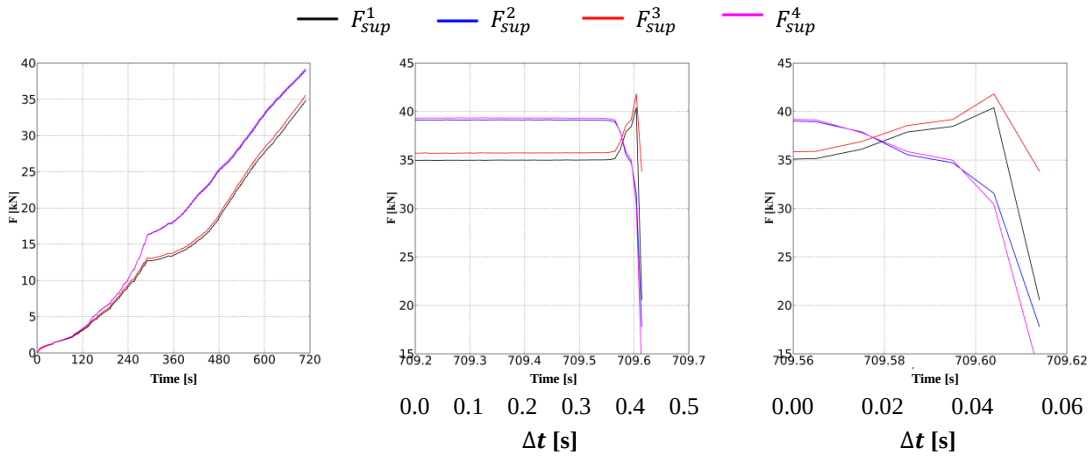

(a) During the entire experiment until failure.

(b) At the moment of failure ($t_{u1} = 709.376$s).

(c) At the moment of failure ($t_{u2} = 709.604$s).

Fig. 4-8 Magnitude of the supporting forces (EU2).

Table 4-3 gives an overview of all loads measured at the moment of failure of the fourth support. The average failure load of the structure is 151.3kN; the failure load of support 4 is 39.3kN.

Table 4-3 Failure load - total force and supporting forces (EU2).

TOTAL			SUPPORT		
$F_u^{load\ cell\ 1}$	154.7	kN	$F_{u,sup1}$	35.0	kN
$F_u^{load\ cell\ 2}$	150.0	kN	$F_{u,sup2}$	39.1	kN
$F_u^{sum\ supports}$	149.2	kN	$F_{u,sup3}$	35.7	kN
$\boldsymbol{F_u^{average}}$	**151.3**	**kN**	$\boldsymbol{F_{u,sup4}}$	**39.3**	**kN**

Fig. 4-9 shows a plot of the load-displacement diagram of all supports with the supporting force on the vertical axis and the radial deformation of the top of the stiffener on the horizontal axis. As can be seen, all stiffeners have the tendency to deform in inward direction (negative values) when a compressive load is applied on the upper edge of the cylindrical barrel. Before failure, the inward deformations of the different stiffeners are more or less similar and have the same order of magnitude. From the moment of failure, the largest inward deformations are observed for stiffener 4 (i.e. the first collapsed support).

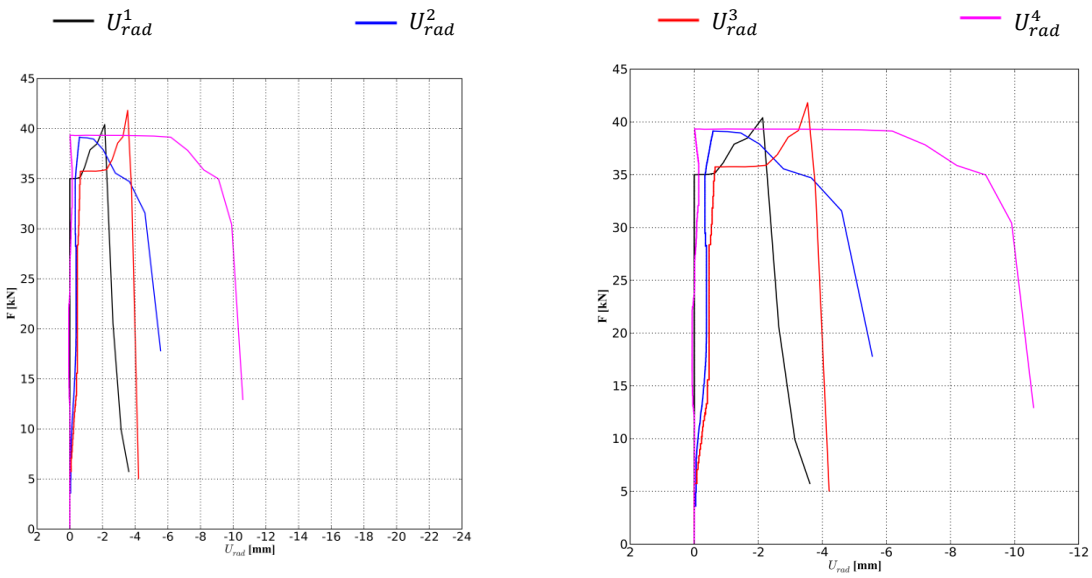

Fig. 4-9 Load-displacement diagram: the radial displacement of the top of the U-shaped stiffener versus the supporting force (EU2).

Experiment EU3

During the experiment, two buckles have been developed in the unstiffened silo wall, namely above U-shaped stiffeners at supports 2 and 3 (the right figures in Fig. 4-10). For those stiffeners, the inward inclination is always clearly visible on the left figures. In the vicinity of stiffeners at supports 1 and 4, no remarkable deformations are visible after failure.

(a) Support 2. (b) Support 3

Fig. 4-10 Post-buckling deformations (EU3).

Fig. 4-11 shows the progress of the measured load for each support as a function of time. For all supports, the measured load systematically increases until the first critical moment at $t_{u1} = 550.399$s. At that moment, F_{sup}^{1} and F_{sup}^{3} start to decrease (slowly in the beginning, then more rapidly), while F_{sup}^{2} and F_{sup}^{4} start to increase more rapidly. This abrupt moment is caused by the development of a primary buckle above stiffener 3 (See Fig. 4-10 (b)). A few seconds later ($t_{u2} = 552.184$s), the increasing forces F_{sup}^{2} and F_{sup}^{4} also start to decrease due to the formation of a second buckle above stiffener 2 (See Fig. 4-10 (a)).

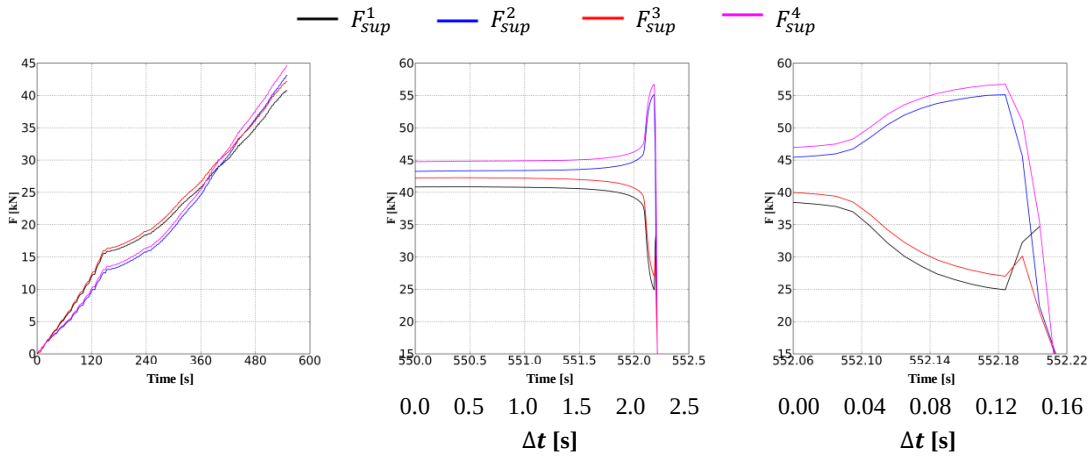

(a) During the entire experiment until failure.

(b) At the moment of failure ($t_{u1} = 550.399$s).

(c) At the moment of failure ($t_{u2} = 552.184$s).

Fig. 4-11 Magnitude of the supporting forces (EU3).

Table 4-4 gives an overview of all loads measured at the moment of failure of the third support. The average failure load of the structure is 171.5kN; the failure load of support 3 is 42.3kN.

Table 4-4 Failure load - total force and supporting forces (EU3).

TOTAL			SUPPORT		
$F_u^{load\ cell\ 1}$	171.8	kN	$F_{u,sup1}$	40.9	kN
$F_u^{load\ cell\ 2}$	-	kN	$F_{u,sup2}$	43.3	kN
$F_u^{sum\ supports}$	171.3	kN	$\boldsymbol{F_{u,sup3}}$	**42.3**	**kN**
$\boldsymbol{F_u^{average}}$	**171.5**	**kN**	$F_{u,sup4}$	44.8	kN

The radial deformations of the top of the U-shaped stiffeners are not measured for this experiment.

Experiment EK1

At the moment of failure, the silo wall after columns 1 and 4 has collapsed (See Fig. 4-12 (a) - (c)). In Fig. 4-12 (d), the inclination of those columns is displayed. In the vicinity of columns 2 and 3, no remarkable deformations are visible after failure.

(a) Support 1.

(b) Region between support 1 (left) and support 4 (right).

(c) Support 4.

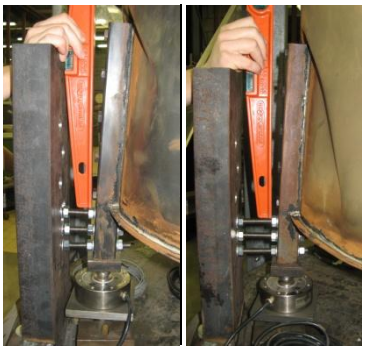

(d) Inclination column 1 (left) and column 4 (right).

Fig. 4-12 Post-buckling deformations (EK1).

Fig. 4-13 shows the progress of the measured load for each supporting column as a function of time. For all columns, the measured load systematically increases until the first critical moment at $t_{u1} = 246.509$s. At that moment, F_{sup}^2 and F_{sup}^4 start to decrease slowly, while

F_{sup}^{1} and F_{sup}^{3} increase further. This critical moment is caused by the development of large deformations in the vicinity of column 4 (See Fig. 4-12 (c)). These inward deformations of the silo wall are caused by the abrupt inward tilt of that column. A second later ($t_{u2} = 247.471$s), the increasing forces F_{sup}^{1} and F_{sup}^{3} also start to decrease due to the same phenomenon but at column 1 (See Fig. 4-12 (a)).

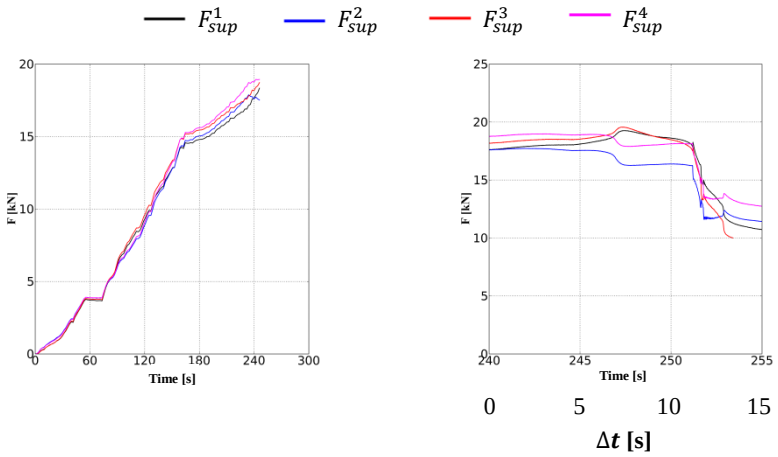

(a) During the entire experiment until failure.

(b) At the moment of failure ($t_{u1} = 246.509$s; $t_{u2} = 247.471$s).

Fig. 4-13 Magnitude of the supporting forces (EK1).

Table 4-5 gives an overview of all loads measured at the moment of failure of the fourth column. The average failure load of the structure is 73.9kN; the failure load of column 4 is 18.8kN.

Table 4-5 Failure load - total force and supporting forces (EK1).

TOTAL			SUPPORT		
$F_u^{load\ cell\ 1}$	75.7	kN	$F_{u,sup1}$	18.5	kN
$F_u^{load\ cell\ 2}$	72.5	kN	$F_{u,sup2}$	17.4	kN
$F_u^{sum\ supports}$	73.6	kN	$F_{u,sup3}$	18.9	kN
$\boldsymbol{F_u^{average}}$	**73.9**	**kN**	$\boldsymbol{F_{u,sup4}}$	**18.8**	**kN**

Fig. 4-14 shows a plot of the load-displacement diagram of all supports with the supporting force on the vertical axis and the radial deformation of the top of the engaged column on the horizontal axis. As can be seen, all columns have the tendency to deform in inward direction (negative values) when a compressive load is applied on the upper edge of the cylindrical barrel. Before failure, the inward deformations of the different columns are more or less similar and have the same order of magnitude. Further, the large inward post-failure deformations are visible of column 4 (i.e. the first collapsed support at t_{u1}) and column 1 (i.e.

the second collapsed support at t_{u2}).

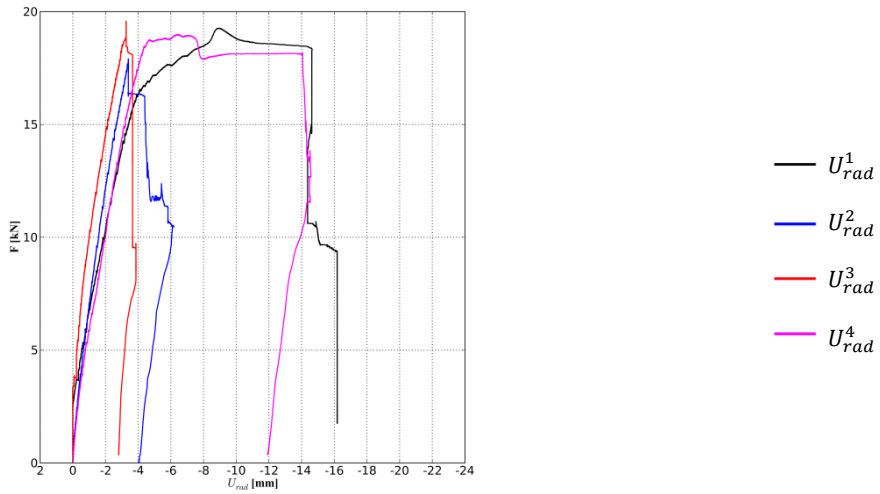

Fig. 4-14 Load-displacement diagram: the radial displacement of the top of the engaged column versus the supporting force (EK1).

Experiment EK2

At the moment of failure, the silo wall after columns 1 and 4 has collapsed (See Fig. 4-15 (a) - (c)). In Fig. 4-15 (d), the inclination of those columns is displayed. In the vicinity of columns 2 and 3, no remarkable deformations are visible after failure.

(a) Support 1.

(b) Region between support 1 (left) and support 4 (right).

(c) Support 4.

(d) Inclination column 1 (left) and column 4 (right).

Fig. 4-15 Post-buckling deformations (EK2).

Fig. 4-16 shows the progress of the measured load for each supporting column as a function of time. For all columns, the measured load systematically increases until the first critical moment at $t_{u1} = 259.031$s. At that moment, F_{sup}^{1} and F_{sup}^{3} start to decrease slowly, while F_{sup}^{2} and F_{sup}^{4} increase further. This critical moment is caused by the development of large deformations in the vicinity of column 1 (See Fig. 4-15 (a)). These inward deformations of the silo wall are caused by the abrupt inward tilt of that column. A few seconds later ($t_{u2} = 266.372$s), the increasing forces F_{sup}^{2} and F_{sup}^{4} also start to decrease due to the same phenomenon but at column 4 (See Fig. 4-15 (c)).

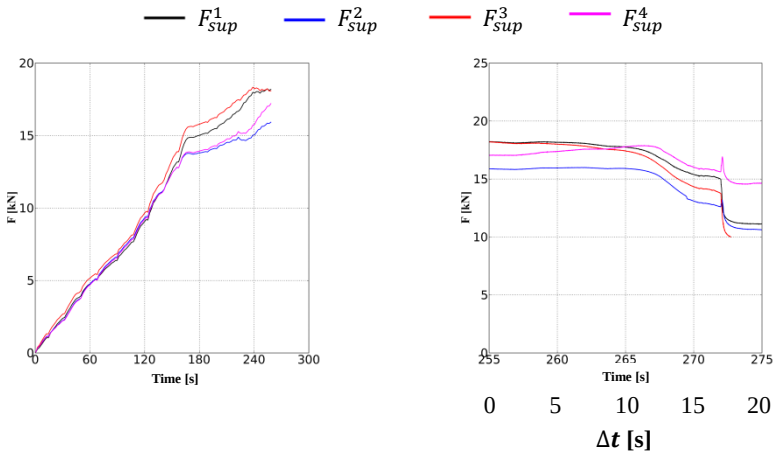

(a) During the entire experiment until failure.

(b) At the moment of failure ($t_{u1} = 259.031$s; $t_{u2} = 266.372$s).

Fig. 4-16 Magnitude of the supporting forces (EK2).

Table 4-6 gives an overview of all loads measured at the moment of failure of the first column. The average failure load of the structure is 70.8kN; the failure load of column 1 is 18.2kN.

Table 4-6 Failure load - total force and supporting forces (EK2).

TOTAL			SUPPORT		
$F_u^{load\ cell\ 1}$	72.6	kN	$\mathbf{F_{u,sup1}}$	**18.2**	**kN**
$F_u^{load\ cell\ 2}$	70.2	kN	$F_{u,sup2}$	16.0	kN
$F_u^{sum\ supports}$	69.6	kN	$F_{u,sup3}$	18.1	kN
$\boldsymbol{F_u^{average}}$	**70.8**	**kN**	$F_{u,sup4}$	17.3	kN

Fig. 4-17 shows a plot of the load-displacement diagram of all supports with the supporting force on the vertical axis and the radial deformation of the top of the engaged column on the horizontal axis. As can be seen, all columns have the tendency to deform in inward direction (negative values) when a compressive load is applied on the upper edge of the cylindrical

barrel. Before failure, the inward deformations of the different columns are more or less similar and have the same order of magnitude. Further the large inward post-failure deformations are visible of column 1 (i.e. the first collapsed support at t_{u1}) and column 4 (i.e. the second collapsed support at t_{u2}).

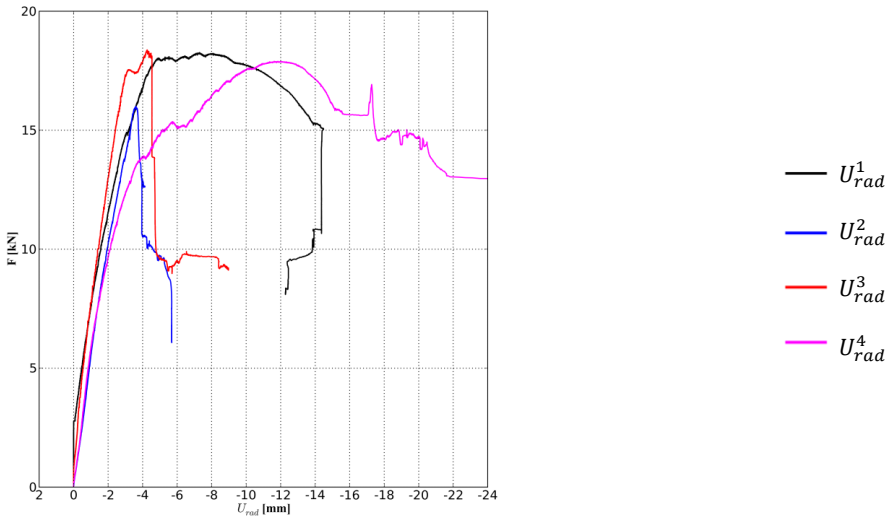

Fig. 4-17 Load-displacement diagram: the radial displacement of the top of the engaged column versus the supporting force (EK2).

Experiment EK3

At the moment of failure, the silo wall after columns 3 and 4 has collapsed (See Fig. 4-18 (a) - (c)). In Fig. 4-18 (d), the inclination of those columns is displayed. In the vicinity of columns 1 and 2, no remarkable deformations are visible after failure.

Fig. 4-19 shows the progress of the measured load for each supporting column as a function of time. For all columns, the measured load systematically increases until the first critical moment at $t_{u1} = 307.355$s. At that moment, F_{sup}^1 and F_{sup}^3 start to decrease very slowly, while F_{sup}^2 and F_{sup}^4 increase further. This critical moment is caused by the development of large deformations in the vicinity of column 3 (See Fig. 4-18 (a)). These inward deformations of the silo wall are caused by the abrupt inward tilt of that column. A few seconds later ($t_{u2} = 311.102$s), the increasing forces F_{sup}^2 and F_{sup}^4 also start to decrease due to the same phenomenon but at column 4 (See Fig. 4-18 (c)).

(a) Support 3.

(b) Region between support 4 (left) and support 3 (right).

(c) Support 4.

(d) Inclination column 3 (left) and column 4 (right).

Fig. 4-18 Post-buckling deformations (EK3).

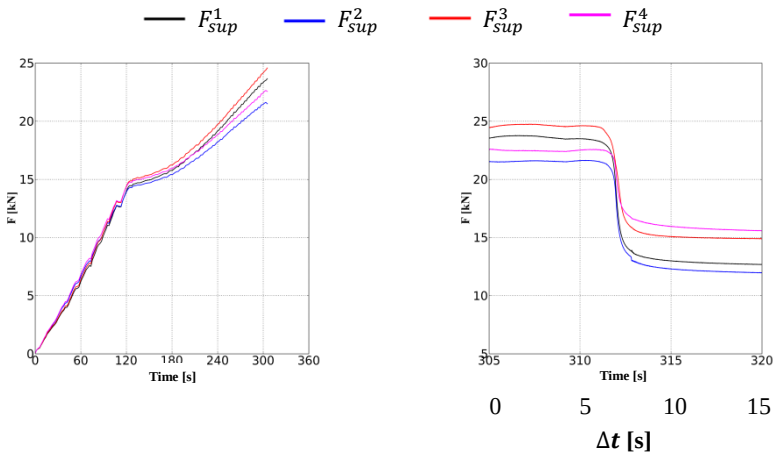

(a) During the entire experiment until failure.

(b) At the moment of failure ($t_{u1} = 307.355$s; $t_{u2} = 311.102$s).

Fig. 4-19 Magnitude of the supporting forces (EK3).

Table 4-7 gives an overview of all loads measured at the moment of failure of the third column. The average failure load of the structure is 94.1kN; the failure load of column 3 is 24.7kN.

Table 4-7 Failure load - total force and supporting forces (EK3).

TOTAL			SUPPORT		
$F_u^{load\ cell\ 1}$	96.9	kN	$F_{u,sup1}$	23.8	kN
$F_u^{load\ cell\ 2}$	92.7	kN	$F_{u,sup2}$	21.6	kN
$F_u^{sum\ supports}$	92.6	kN	$\boldsymbol{F_{u,sup3}}$	**24.7**	**kN**
$\boldsymbol{F_u^{average}}$	**94.1**	**kN**	$F_{u,sup4}$	22.5	kN

Fig. 4-20 shows a plot of the load-displacement diagram of all supports with the supporting force on the vertical axis and the radial deformation of the top of the engaged column on the horizontal axis. As can be seen, all columns have the tendency to deform in inward direction (negative values) when a compressive load is applied on the upper edge of the cylindrical barrel. Before failure, the inward deformations of the different columns are more or less similar and have the same order of magnitude. Further the large inward post-failure deformations are visible of column 3 (i.e. the first collapsed support at t_{u1}) and column 4 (i.e. the second collapsed support at t_{u2}).

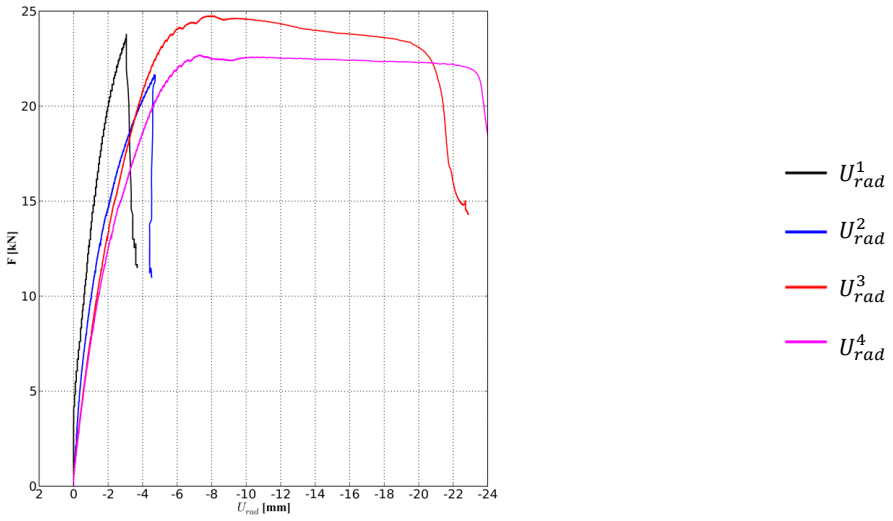

Fig. 4-20 Load-displacement diagram: the radial displacement of the top of the engaged column versus the supporting force (EK3).

Experiment EK4

At the moment of failure, the silo wall after columns 1 and 4 has collapsed (See Fig. 4-21 (a) - (c)). In Fig. 4-21 (d), the inclination of those columns is displayed. In the vicinity of columns 2 and 3, no remarkable deformations are visible after failure.

(a) Support 1.

(b) Region between support 1 (left) and support 4 (right).

(c) Support 4.

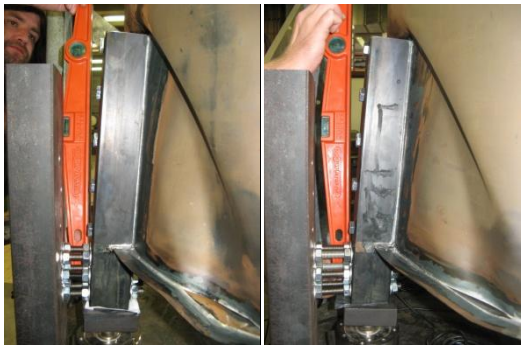

(d) Inclination column 1 (left) and column 4 (right).

Fig. 4-21 Post-buckling deformations (EK4).

Fig. 4-22 shows the progress of the measured load for each supporting column as a function of time. For all columns, the measured load systematically increases until the first critical moment at $t_{u1} = 513.283$s. At that moment, F_{sup}^{1} and F_{sup}^{3} start to decrease very slowly, while F_{sup}^{2} and F_{sup}^{4} increase further. This critical moment is caused by the development of large deformations in the vicinity of column 1 (See Fig. 4-21 (a)). These inward deformations of the silo wall are caused by the abrupt inward tilt of that column. A few seconds later ($t_{u2} = 520.028$s), the increasing forces F_{sup}^{2} and F_{sup}^{4} also start to decrease due to the same phenomenon but at column 4 (See Fig. 4-21 (c)).

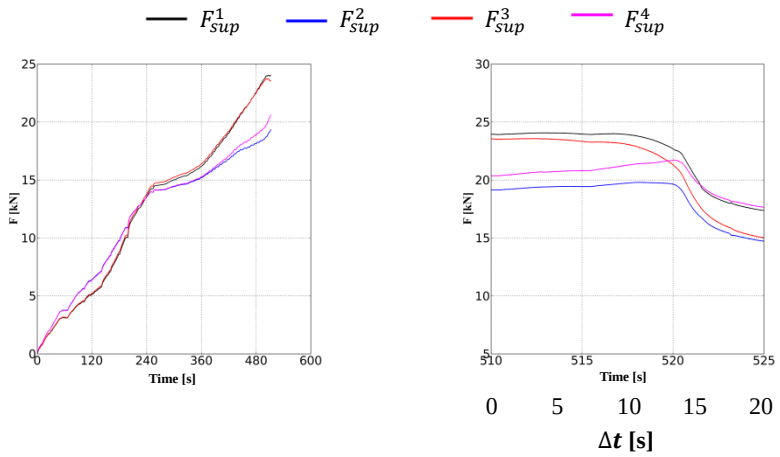

(a) During the entire experiment until failure.

(b) At the moment of failure ($t_{u1} = 513.283$s; $t_{u2} = 520.028$s).

Fig. 4-22 Magnitude of the supporting forces (EK4).

Table 4-8 gives an overview of all loads measured at the moment of failure of the first column. The average failure load of the structure is 89.7kN; the failure load of column 1 is 24.1kN.

Table 4-8 Failure load - total force and supporting forces (EK4).

TOTAL			SUPPORT		
$F_u^{load\ cell\ 1}$	92.3	kN	$\boldsymbol{F_{u,sup1}}$	**24.1**	**kN**
$F_u^{load\ cell\ 2}$	89.1	kN	$F_{u,sup2}$	19.4	kN
$F_u^{sum\ supports}$	87.7	kN	$F_{u,sup3}$	23.5	kN
$\boldsymbol{F_u^{average}}$	**89.7**	**kN**	$F_{u,sup4}$	20.7	kN

Fig. 4-23 shows a plot of the load-displacement diagram of all supports with the supporting force on the vertical axis and the radial deformation of the top of the engaged column on the horizontal axis. As can be seen, all columns have the tendency to deform in inward direction (negative values) when a compressive load is applied on the upper edge of the cylindrical barrel. Before failure, the inward deformations of the different columns are more or less similar and have the same order of magnitude. Further the large inward post-failure deformations are visible of column 1 (i.e. the first collapsed support at t_{u1}) and column 4 (i.e. the second collapsed support at t_{u2}).

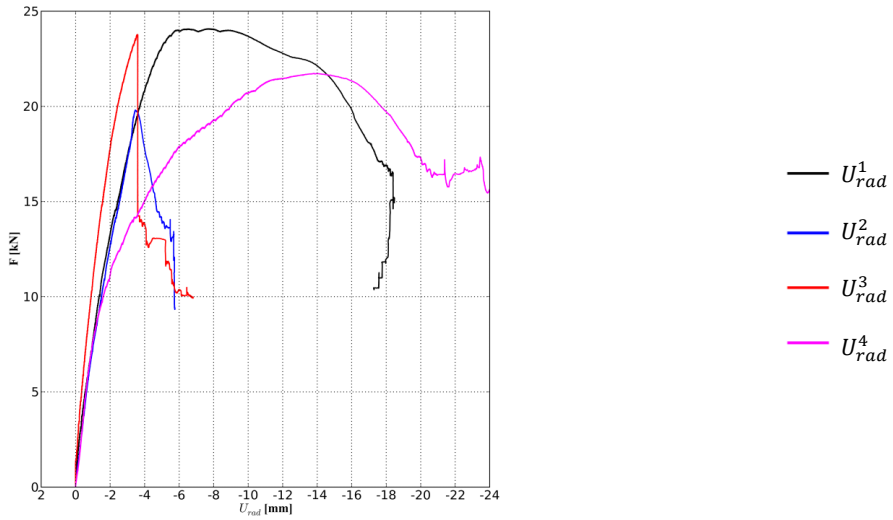

Fig. 4-23 Load-displacement diagram: the radial displacement of the top of the engaged column versus the supporting force (EK4).

Conclusion

From the experimental results, it is found that failure always occurs relatively fast and is characterized by failure of one support (primary buckle), shortly followed by one or two other supports (secondary buckles). Then, the total load starts to decrease very fast, as a result of which the other supports do not get a chance to fail.

2 Measurement of the imperfections

In Section 4 of Chapter 3, the setup and the procedure of the measurement of the imperfections is explained. In this section, first, the procedures for the processing of the large number of data points are discussed. Afterwards, the results (i.e. the contourplots and the quality tolerance class) are presented and discussed.

2.1 Preliminary processing steps

The data from the measurements of the initial imperfections is subjected to some preliminary processing steps by using a Python script to make it usable for the final processing, such as the determination of the out-of-roundness and the dimple parameter, the quality tolerance class, and for the input in Abaqus (to include initial deviations normal to the perfect shell wall in the numerical model) according to (EN 1993-1-6, 2007).

At first instance, the measured data is filtered to remove unusual data points, such as values outside the expected range, strange abrupt jumps, etc. In addition, the data points are deleted at the location of the stiffeners, because in these points, the distance is measured between the sensor and the stiffener (instead of the silo wall). Lastly, the data points are removed from the "non-measuring" rounds. These are the rounds at which a new height was set, and such a

round can be recognized by an abrupt jump of the height (i.e. $\Delta h = 15\text{mm}$) during the measurement. In other words, only the data of the "measuring" rounds (with a constant height) are used further.

After the filtering process, the remaining measured data points are converted. The measured height h_{meas} has to be converted because the measurement of the (un)stiffened silo occurs upside down. Because of this, the value of the height increases from the top to the bottom of the silo. For the corrected value of the height h_{corr}, the value of the height is zero at the bottom, and increases from the bottom to the top of the silo. For this conversion, formula (4-1) has been used, which can be derived from Fig. 4-24.

$$h_{corr} = h_{silo} - (h_{ave} - h_{ave}^{0}) - h_{start} \tag{4-1}$$

Where:

h_{corr} the corrected height of the current measuring round [m];

h_{silo} the silo height = 0.700m;

h_{ave} the average height of the current measuring round [m];

h_{ave}^{0} the average height of the first measuring round [m];

h_{start} the distance between the first measuring round and the top edge = 0.015m.

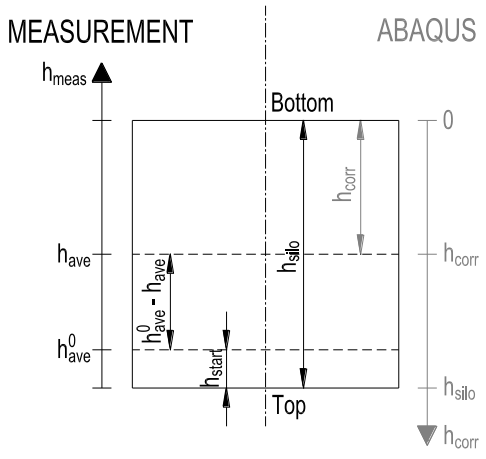

Fig. 4-24 Principle of the conversion of the height h.

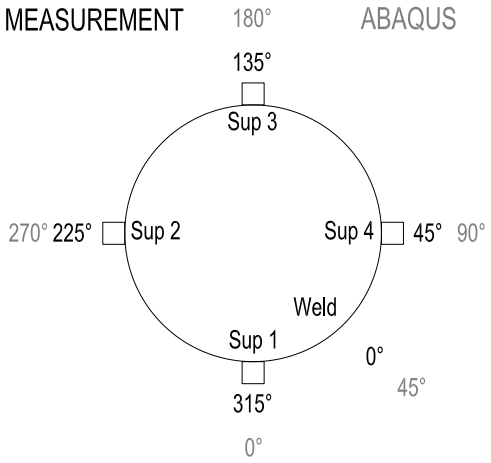

Fig. 4-25 Principle of the conversion of the circumferential angle θ.

For simplicity, the zero point of the circumferential angle is placed at the centre of the axial weld during the measurement. The weld is located in the middle between two supports (1 and 4) (See Fig. 4-25) so that the deformations in the direct vicinity of the weld have a minimal influence on the failure behaviour. However, in the numerical model, the zero point of the circumferential angle coincides with the middle of the first support (this was the author's choice during the programming of the complete numerical model in Python). Eq. (4-2), Eq.

(4-3), and Fig. 4-25 show the relationship between the measured angle θ_{meas} and the corrected angle θ_{corr}.

$$\theta_{meas} < 315° : \qquad \theta_{corr} = \theta_{meas} + 45° \tag{4-2}$$

$$\theta_{meas} \geq 315° : \qquad \theta_{corr} = \theta_{meas} - 315° \tag{4-3}$$

Where:

θ_{corr} the corrected angle [°];

θ_{meas} the measured angle [°].

At last, the distance measured between the sensor and the silo wall δ_{meas} is converted into the initial deviation of the silo wall δ_{corr}. It is assumed that the average measured distance of a complete round δ_{ave} coincides with the perfect silo wall. Negative values of the corrected initial deviations are inward, positive values outward.

$$\delta_{corr} = \delta_{meas} - \delta_{ave} \tag{4-4}$$

Where:

δ_{corr} the corrected initial deviation [m];

δ_{meas} the distance measured between the sensor and the silo wall [m];

δ_{ave} the average distance measured between the sensor and the silo wall of the current round [m].

After the above operations, the data is ready to be analysed further. The resulting dataset is rather extensive and includes about 60000 to 70000 measured points scattered all over the entire shell surface. This corresponds to approximately 47 measured heights (i.e. $\Delta h =$ 15mm) and about 1250-1500 measured deviations (relative to the perfect shell wall) in circumferential direction. On the basis of this dataset, the out-of-roundness parameter U_R and the dimple parameter U_{0x} are determined (in respectively Paragraphs 2.2 and 2.3), the initial deviations in the nodes of the mesh in Abaqus are deducted (in Paragraph 2.4) and the contourplots of the imperfections of the shell wall are generated.

2.2 Determination of the out-of-roundness parameter

The out-of-roundness parameter U_R is an estimate of the deviation of the real shape of the scale model relative to the perfect circular shape and is defined by Eq. (4-5). Over the entire shell surface, a sufficient number of internal diameters must be measured to be able to determine the maximum and the minimum diameter (See Fig. 4-26 (a)) (EN 1993-1-6, 2007).

$$U_R = \frac{\emptyset_{max} - \emptyset_{min}}{\emptyset_{nom}} \leq U_{R,max} \tag{4-5}$$

Where:

U_R the out-of-roundness parameter [-];

$U_{R,max}$ the out-of-roundness tolerance parameter [-];

$\emptyset_{max}$ the maximal measured internal diameter [m];

$\emptyset_{min}$ the minimal measured internal diameter [m];

$\emptyset_{nom}$ the nominal internal diameter [m].

The measurement of the diameters is automated by a Python script. In this way, the diameters can be determined fast and accurately in many points of the shell surface. All measured heights are passed through in increments of one degree. The diameter $\emptyset$ is obtained by the sum of the nominal diameter $\emptyset_{nom}$, the corrected initial deviation δ_θ at an angle θ, and the corrected initial deviation $\delta_{\theta+180°}$ at an angle $\theta + 180°$ (See Fig. 4-26 (b)).

$$\emptyset = \emptyset_{nom} + \delta_\theta + \delta_{\theta+180°} \tag{4-6}$$

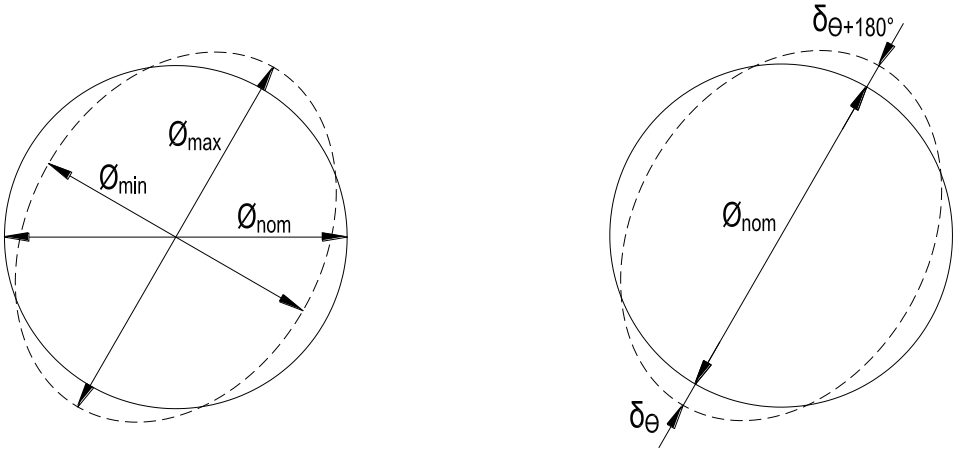

(a) The required diameters. (b) Along the circumferential circle.

Fig. 4-26 Measurement of the diameters for the determination of the out-of-roundness parameter U_R.

The tolerance values of the out-of-roundness parameter $U_{R,max}$ for the different fabrication tolerance classes are given in Table 4-9 (EN 1993-1-6, 2007).

Table 4-9 Recommended values of the out-of-roundness tolerance parameter $U_{R,max}$ (EN 1993-1-6, 2007).

QUALITY TOLERANCE CLASS	DESCRIPTION OF THE QUALITY	RANGE OF THE DIAMETER		
		$d[m] \leq 0.50m$	$0.50m < d[m] < 1.25m$	$1.25m \leq d[m]$
Class A	Excellent	0.014	0.007 + 0.0093·(1.25-d)	0.007
Class B	High	0.020	0.010 + 0.0133·(1.25-d)	0.010
Class C	Normal	0.030	0.015 + 0.0200·(1.25-d)	0.015

2.3 Determination of the dimple parameter

The dimple parameter U_{0x} is an estimate of the magnitude of local dimples and is defined by Eq. (4-7). In every position of the shell surface, a dimple measurement gauge with length l_{gx} should be placed in both meridional and circumferential direction to measure the depth of the dimple Δw_{0x}. The way the measurement should be performed is depicted in Fig. 4-27. The meridional gauge should be straight, while the circumferential gauge should have a curvature equal to the intended radius of curvature R of the middle surface of the silo wall. In regions of meridional compressive stresses, the length of the gauge l_{gx} can be calculated by using Eq. (4-8) (EN 1993-1-6, 2007).

$$U_{0x} = \frac{\Delta w_{0x}}{l_{gx}} \leq U_{0,max} \tag{4-7}$$

$$l_{gx} = 4 \cdot \sqrt{R \cdot t} \tag{4-8}$$

Where:

U_{0x} the dimple parameter [-];

$U_{0,max}$ the dimple tolerance parameter [-];

Δw_{0x} the maximal measured depth of the initial dimple [m];

l_{gx} the length of the gauge [m];

R the silo radius [m];

t the silo thickness [m].

The measurement of the depth of the dimples is automated by a Python script. In this way, the dimple measurement gauge can be placed fast and accurately in many points of the shell

surface. The complete shell surface is passed through in increments of 1mm in meridional direction and increments of one degree in circumferential direction.

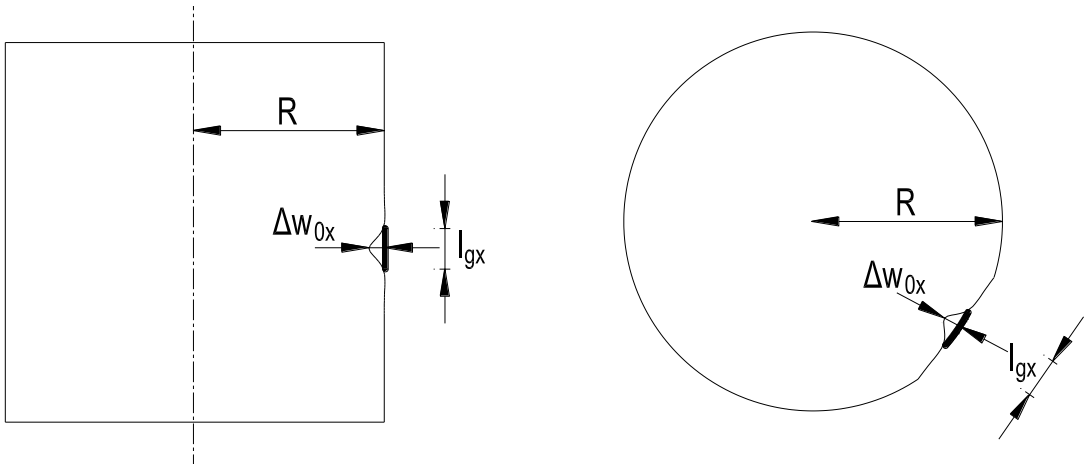

(a) Along the meridional. (b) Along the circumferential circle.

Fig. 4-27 Measurement of the initial deviations Δw_{0x} for the determination of the dimple parameter U_0.

The tolerance values of the dimple parameter $U_{0,max}$ for the different fabrication tolerance classes are given in Table 4-10 (EN 1993-1-6, 2007).

Table 4-10 Recommended values of the dimple tolerance parameter $U_{0,max}$ (EN 1993-1-6, 2007).

QUALITY TOLERANCE CLASS	DESCRIPTION OF THE QUALITY	$U_{0,max}$ [-]
Class A	Excellent	0.006
Class B	High	0.010
Class C	Normal	0.016

2.4 Determination of the imperfection amplitude in each node in Abaqus

For the verification analyses, the measurement data of the initial deviations of the stiffened silo wall are taken into account. However, the positions of the measured points are scattered over the entire shell surface, and do not coincide with the nodes of the mesh in Abaqus. For all nodes of the shell surface, the magnitude of the initial deviation has to be computed by linear interpolation by using the measured initial deviations in the immediate vicinity. To control the influence of this necessary conversion, it was always checked whether the contourplot of the imperfections before and after the conversion are in agreement with each other. For one experiment, these contourplots are presented in Fig. 4-28. For that illustrative example and for all other cases, a good agreement is always found between the measured imperfections (scattered) and the imperfections used in Abaqus (nodes of the mesh).

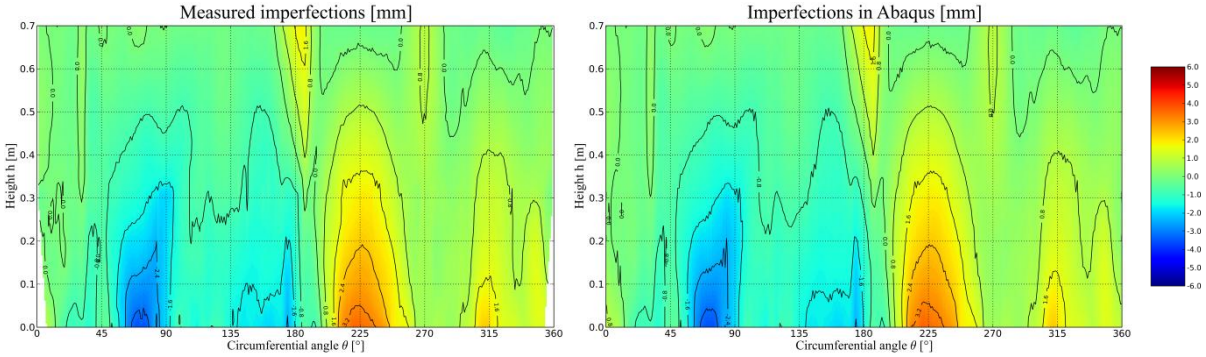

(a) Measured points. (b) Nodes in Abaqus.

Fig. 4-28 Contourplot of the geometric imperfections (example: EU1).

2.5 The results of the measurement of the imperfections

In Table 4-11, the tolerance parameters $U_{\mathrm{R},max}$ and $U_{0,max}$ are presented for the dimensions of the scale model (i.e. $\emptyset_{nom} = 700\text{mm}$; $t_1 = 0.8\text{mm}$ and $t_2 = 1.0\text{mm}$). In the fourth column, the value $(\Delta\emptyset)_{max}$ is calculated as a function of the quality tolerance class. This value represents the tolerated difference between the maximum measured internal diameter $\emptyset_{max}$ and the minimum measured internal diameter $\emptyset_{min}$ for a specific quality class. In the fifth and sixth column, the tolerated measured depths of the initial dimple $(\Delta w_{0x})_{max}$ are calculated for respectively a silo with thickness 0.8mm (t_1) and 1.0mm (t_2).

Table 4-11 Recommended values of the dimple tolerance parameters for the scale model of the silo.

QUALITY TOLERANCE CLASS	DESCRIPTION OF THE QUALITY	$U_{\mathrm{R},max}$ [-]	$(\Delta\emptyset)_{max}$ [mm]	$U_{0,max}$ [-]	$(\Delta w_{0x})_{max}$ [mm]	
					$t = t_1$	$t = t_2$
				$l_{gx} =$	66.9mm	74.8mm
				$\theta_{gx} =$	11.0°	12.3°
Class A	Excellent	0.012	8.5	0.006	0.402	0.449
Class B	High	0.017	12.1	0.010	0.669	0.748
Class C	Normal	0.026	18.2	0.016	1.071	1.197

In Appendix B, the contourplots of the measured imperfections of the shell wall are included for all scale models and for both measurement rounds. In these figures, the height h [mm] (relative to the lower edge of the silo) is plotted on the vertical axis, the circumferential angle θ [°] on the horizontal axis. The center of the local supports are located at circumferential angles of respectively 0°, 90°, 180°, and 270°. The longitudinal weld is located in the middle between the first and the second support and has a circumferential angle of 45°. The measured

deviations Δw_0 are expressed in mm. The red colour corresponds to an outward (radial) deformation, the blue colour to an inward (radial) deformation. In addition, the locations are displayed in blue of the maximum and minimal measured internal diameter (necessary for the calculation of the out-of-roundness parameter) and the meridional and circumferential gauge corresponding with the maximum measured amplitude of initial dimple (necessary for the calculation of the dimple parameter).

Table 4-12 and Table 4-13 give an overview of the most important results of the determination of the quality tolerance class of the first measurement round of the complete unstiffened silo wall and the second measurement round of the complete stiffened silo wall, respectively.

For most measurements, the out-of-roundness parameter U_R is below the most severe threshold value of the out-of-roundness parameter (i.e. $U_{R,max} = 0.012$ - See Table 4-11), as a result of which the quality tolerance class A is easily met in most cases. In other words, the difference between the maximum measured internal diameter $\emptyset_{max}$ and the minimum measured internal diameter $\emptyset_{min}$ is usually smaller than 8.5mm.

In contrast, the criterion for the dimple parameter appears to be much more difficult to achieve: the dimple parameter U_0 does not meet the least severe threshold value of the dimple parameter (i.e. $U_{0,max} = 0.016$), and cannot even be classified as a quality tolerance class C silo. This can be attributed to the very small values of the maximum allowable depth of the initial dimple $(\Delta w_{0x})_{max}$ (See Table 4-11) in combination with the small size of the silo. In most cases, these tolerated values are exceeded by the depths measured over a distance of 66.9 or 74.8mm (i.e. the gauge length) in a greater or lesser degree: the measured depths range between 0.9 and 3.1mm, while the maximum allowable depth is equal to 1.07mm (if t = 0.8mm) or 1.20mm (if t = 1.0mm). In silos with real dimensions, this criterion should be easier to meet.

Table 4-12 Quality tolerance class for the first measurement (i.e. the complete unstiffened silo).

LABEL	$\emptyset_{min}$ [mm]	$\emptyset_{max}$ [mm]	U_R [-]	CLASS	Δw_{0x} [mm]	U_{0x} [-]	CLASS
EU1	698.78	701.42	0.003766	A	1.00	0.015	C
EU2	697.48	704.34	0.009790	A	2.52	0.038	/
EU3	698.50	701.64	0.004484	A	1.61	0.022	/
EU4	-	-	-	-	-	-	-
EK1	698.58	702.72	0.005911	A	1.21	0.018	/
EK2	698.53	702.41	0.005548	A	2.03	0.030	/
EK3	696.15	701.44	0.007564	A	3.09	0.041	/
EK4	696.72	701.61	0.006992	A	2.30	0.031	/

Table 4-13 Quality tolerance class for the second measurement (i.e. the complete stiffened silo).

LABEL	$\emptyset_{min}$ [mm]	$\emptyset_{max}$ [mm]	U_R [-]	CLASS	Δw_{0x} [mm]	U_{0x} [-]	CLASS
EU1	697.77	703.32	0.007929	A	0.88	0.013	C
EU2	695.70	702.97	0.010388	A	2.09	0.031	/
EU3	695.84	706.08	0.014637	B	0.91	0.012	C
EU4	-	-	-	-	-	-	-
EK1	688.61	706.48	0.025527	C	1.98	0.030	/
EK2	697.20	704.12	0.009881	A	1.36	0.020	/
EK3	696.63	701.69	0.007223	A	1.39	0.019	/
EK4	696.61	703.47	0.009798	A	1.46	0.020	/

In Appendix B, for each measurement, the calculated out-of-roundness and dimple parameters are plotted on two separate horizontal colorbars with scale divisions of the recommended values of respectively the out-of-roundness and the dimple tolerance parameters (EN 1993-1-6, 2007).

3 Tensile tests

3.1 Introduction

Tensile tests were conducted to quantify the material properties of the flat steel plates, which were used for the cylindrical barrel and the ring stiffener(s). Each tensile test results in two sets of stress-strain data points. For the one set, the elongation (and thus the strain) of the test specimen is calculated on the basis of the direct measurement using an extensometer, in the other case the crosshead displacement is used. Below, these data sets are discussed more thoroughly.

Fig. 4-29 Example of a test specimen after fracture.

For the first set of stress-strain data points, an extensometer has been used to measure the elongation of the test specimens accurately. An extensometer provides an accurate measurement of the elongation of the test specimen between two measuring points, resulting consequently in an accurate determination of the strain. The extensometer has only been used during the first part of the tensile test. In other words, only the stress-strain data point of the elastic part (before yielding) and the beginning of the plastic part of the material behaviour are measured with the extensometer (See Fig. 4-30). From this measurement, two important things are derived. Firstly, the Young's modulus E is assessed as the slope between two data points ((1) and (2) in Fig. 4-30) of the first straight part of the curve. Secondly, the elastic limit or the yield point can be determined. This point corresponds with the shift from elastic to plastic behaviour.

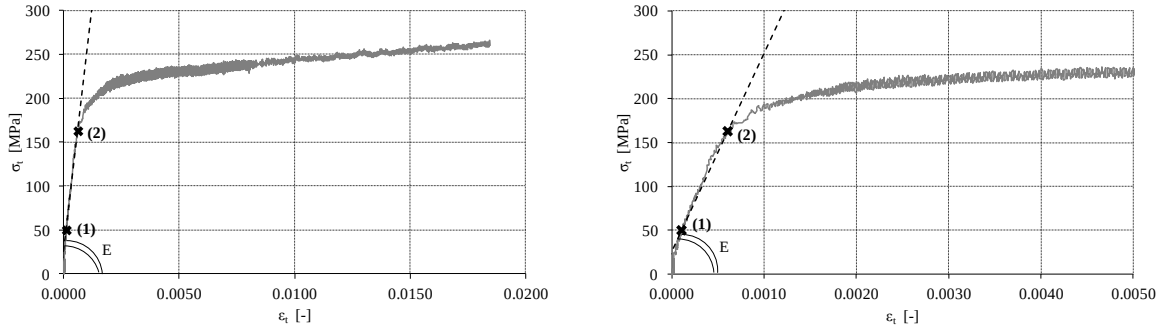

(a) Full diagram. (b) Diagram in detail.

Fig. 4-30 The first stress-strain diagram measured with an extensometer.

An example of the second stress-strain diagram is presented in Fig. 4-31. Now, the strain is calculated using the crosshead displacement for the entire period of the tensile test. This diagram is used for the accurate determination of the post-yield behaviour (strain hardening) up to the moment of failure (when the maximum strength is reached).

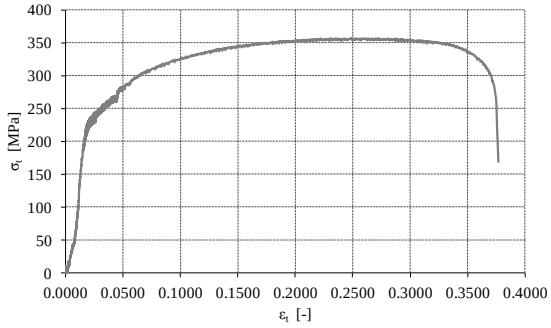

Fig. 4-31 The second stress-strain diagram.

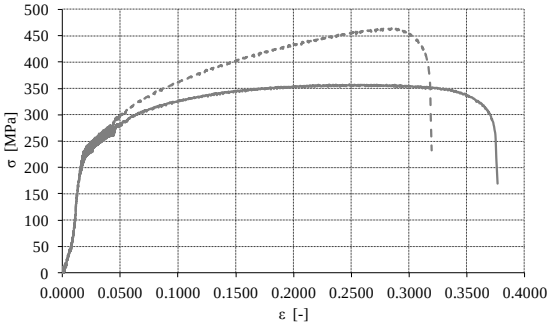

Fig. 4-32 The nominal stress-strain relationship (solid line) versus the true stress-strain relationship (dashed line).

3.2 Engineering versus true stresses and strains

The stresses and strains of the above mentioned test data are nominal stresses and strains. The nominal or engineering stress σ_e is defined as the force per unit undeformed area (Eq. (4-9)), and the conjugated nominal or engineering strain ε_e is the length change per unit undeformed length (Eq. (4-10)). As can be seen, in both equations, the value in denominator represents the undeformed state of the material.

$$\sigma_e = \frac{F}{A_0} \tag{4-9}$$

$$\varepsilon_e = \frac{\Delta L}{L_0} = \frac{L - L_0}{L_0} \tag{4-10}$$

Where:

σ_e the engineering stress [MPa];

F the tensile force [N];

A_0 the undeformed cross-section of the test piece [mm²];

ε_e the engineering strain [-];

ΔL the length change of the test piece [mm];

L the deformed length of the test piece [mm];

L_0 the undeformed length of the test piece [mm].

However, the mathematical model in Abaqus that describes metal plasticity does not require the engineering stress σ_e and engineering strain ε_e. Instead, the stress-strain relationship is expressed by true stresses σ_t and true strains ε_t (Abaqus, 2009). For these values, the tensile force F and the change in length ΔL are no longer expressed relative to the undeformed state (respectively A_0 and L_0) but to the deformed state (respectively A and L), taking into account the change in area during the finite deformations. In this way, the compressive and the tensile behaviour are independent of the structure's geometry or the nature of the applied loads (Abaqus, 2009). The relationships between the true stress/strain and the nominal stress/strain are given below. The result of this conversion is shown in Fig. 4-32.

$$\sigma_t = \frac{F}{A} = (1 + \varepsilon_e) \cdot \sigma_e \tag{4-11}$$

$$\varepsilon_t = \int_{L_0}^{L} \frac{dL}{L} = ln\left(\frac{L}{L_0}\right) = ln(1 + \varepsilon_e) \tag{4-12}$$

Where:

σ_t the true stress [MPa];

σ_e the engineering stress [MPa];

F the tensile force [N];

A the deformed cross-section of the test piece [mm²];

ε_t the true strain [-];

ε_e the engineering strain [-];

dL the small change in length of the test piece [mm];

L the deformed length of the test piece [mm];

L_0 the undeformed length of the test piece [mm].

Abaqus approximates the stress-strain material behaviour by extrapolation between the given data points. The elastic behaviour is defined by the Young's modulus E and the coefficient of Poisson ν. The plastic behaviour is defined by the yield stresses σ_t and the corresponding true plastic strain values ε_t^{pl} of the material. This value is obtained by subtracting the true elastic strain ε_t^{el} from the total strain ε_t (See Eq. (4-13)).

$$\varepsilon_t^{pl} = \varepsilon_t - \varepsilon_t^{el} = \varepsilon_t - \frac{\sigma_t}{E} \tag{4-13}$$

Where:

ε_t the true strain [-];

ε_t^{pl} the true plastic strain [-];

ε_t^{el} the true elastic strain [-];

σ_t the true stress [MPa];

E the Young's modulus [MPa].

3.3 The results of the tensile tests

For each steel plate, six tensile pieces were machined and tested: three in the longitudinal direction and three in the width direction. In this way, it can be checked if there is a large spread in the material behaviour and if the results depend on the direction.

For all test pieces of steel plate 0.8mm-4, the results are shown in Fig. 4-33 (strains derived from the extensometer measurement) and Fig. 4-34 (strains derived from the crosshead displacement). From these figures, it can be concluded that the tensile tests on the different test pieces give rather similar results, independently of the direction, and that the spread in the stress-strain relationship is relatively limited.

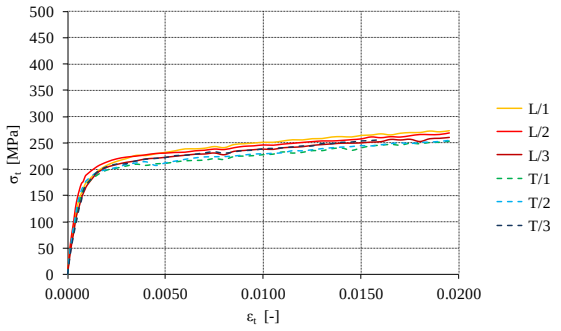

Fig. 4-33 The first part of the stress-strain diagram (0.8mm-4).

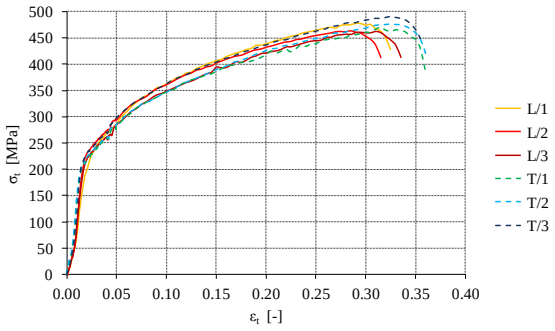

Fig. 4-34 The second part of the stress-strain diagram (0.8mm-4).

In Fig. 4-35, the averaged stress-strain curves are shown for all steel plates. It is found that yielding already starts at stress levels of approximately 180MPa for the 0.8mm thick plates and 160MPa for 1mm thick plates, which is smaller than the value of 235MPa, which was initially adopted for the perfect GMNA failure load. Another finding is that in the plastic region, the stresses of the 1.0mm steel plates are systematically smaller than the stresses of the 0.8mm steel plates. In Fig. 4-36, an example is given of the conversion of the continuous curve of the measured stress-strain data to a limited number of points. Between the input data, Abaqus applies linear interpolation for the determination of intermediate values.

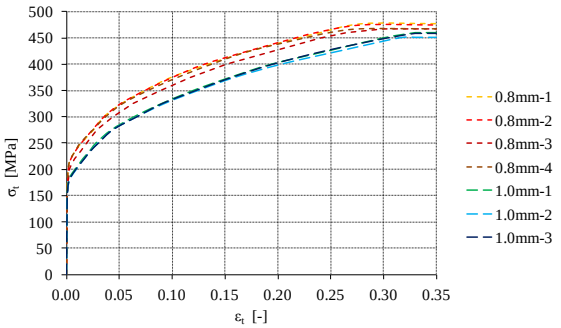

Fig. 4-35 The stress-strain diagram for the different steel plates.

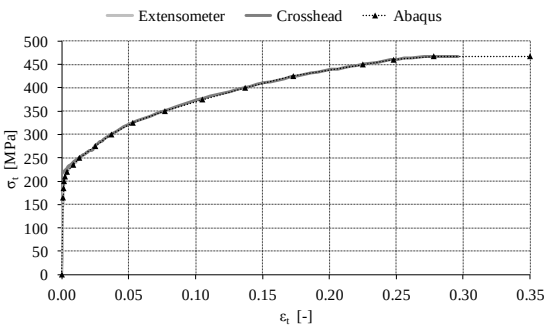

Fig. 4-36 The measured stress-strain diagram versus the stress-strain diagram in Abaqus (0.8mm-4).

In Table 4-14, the Young moduli are given for all steel plates. The values of E vary between approximately 190000MPa and 223000MPa.

Table 4-14 The modulus of elasticity and standard deviation for the steel plate.

PLATE	YOUNG'S MODULUS E [MPA]	STANDARD DEVIATION OF E [MPA]
0.8mm/1	222 765	11 474
0.8mm/2	218 231	13 876
0.8mm/3	198 621	5 544
0.8mm/4	211 101	12 747
1.0mm/1	227 116	11 483
1.0mm/2	205 568	16 918
1.0mm/3	204 954	16 077

4 Validation of the numerical model

Before the numerical model can be used with sufficient reliability for the prediction of the elasto-plastic failure load of a locally supported barrel, the numerical model must be validated, which is the purpose of this section. The validation of the numerical model will be done by comparing the experimental results (presented in Section 1 of this chapter) with the results obtained from Abaqus.

For all experiments, the comparison consists of three parts: comparison of (1) the failure load, (2) the post-buckling deformed shape, and (3) the radial deformation of the top of the stiffener/column as a function of the corresponding supporting force (by means of load-displacement diagrams). For the first step, the factor k, which is defined as the ratio of the experimental failure load $F_u^{experiment}$ to the Abaqus failure load F_u^{Abaqus} (See Eq. (2-39)), must lie in the range $0.8 < k < 1.2$ (See Eq. (2-40)) (EN 1993-1-6, 2007).

The numerical model takes into account the measurement of the imperfections of the shell wall (Section 2) and the results of the tensile test (Section 3). Because the measured imperfections are not symmetrical in circumferential direction, symmetry cannot be applied, and a 360 degree model has to be used. Furthermore, to obtain accurate results and to have a good agreement between the measured imperfections and the imperfections in Abaqus (only applied in the element nodes), a mesh size of 5mm has been chosen in all directions (i.e. axial/circumferential/radial) (See Fig. 4-37 (a) and (b)). In Fig. 4-37 (c), the meridional weld halfway between column 1 and column 4 can be clearly observed. The other settings, such as the supporting boundary conditions, will be discussed separately for the model with the U-shaped longitudinal stiffeners and the model with the engaged columns, since both models differ slightly from each other.

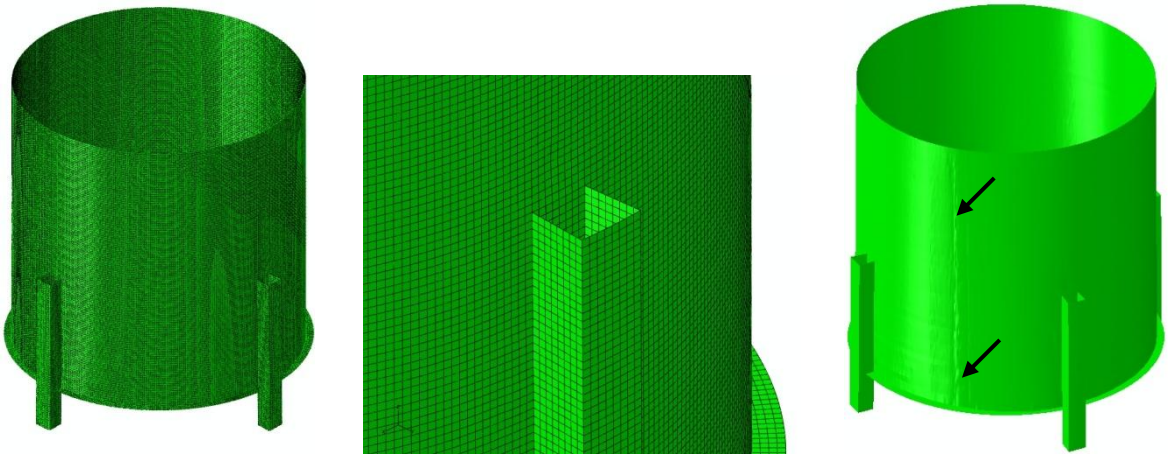

(a) Mesh of the complete model. (b) Detail of the mesh density. (c) Initial imperfections in the vicinity of the meridional weld.

Fig. 4-37 Impressions of the numerical model (EK1).

4.1 Model 1 - U-shaped longitudinal stiffeners

Specific settings numerical model with U-shaped longitudinal stiffeners

The support steel block under the supported part of the scale model is replaced in Abaqus by a rigid plate with a reference node at its centre (See Fig. 4-38). In this node, the boundary conditions of Eqs. (4-14) or (4-15) are imposed, which corresponds with a rigid and a pinned support, respectively.

$$U_R = U_T = U_Z = \varphi_R = \varphi_T = \varphi_Z = 0 \tag{4-14}$$

$$U_R = U_T = U_Z = 0 \tag{4-15}$$

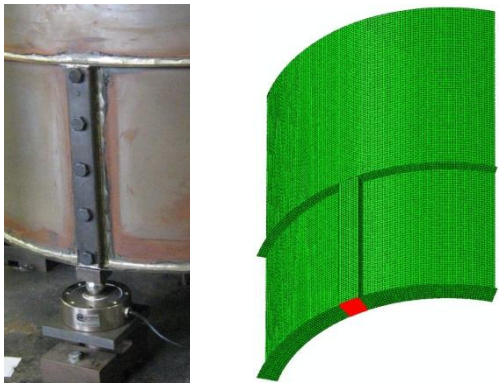

Fig. 4-38 Local supports: Experiment (left) and Abaqus (right).

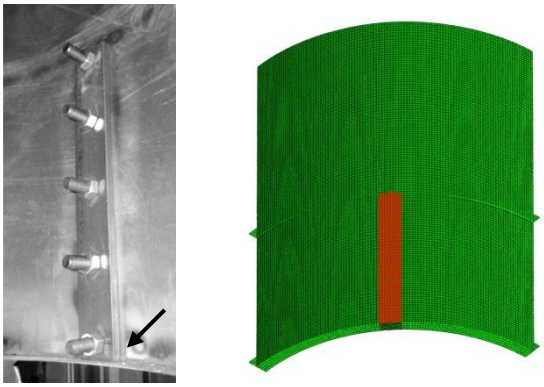

Fig. 4-39 Bolted steel plate on the internal side of the silo wall: Experiment (left) and Abaqus (right).

Behind the longitudinal stiffener and on the internal side of the silo wall, an additional 5mm thick steel plate is provided for the attachment of the stiffener to the silo wall by bolting. This steel plate is also included in Abaqus as a shell surface with the same nodes as the silo wall (See Fig. 4-39). For both support types, two alternatives are considered: the radial deformations at the nodes of the steel plate are completely restricted (abbreviated as "U_{rad} restricted") or are completely free (abbreviated as "U_{rad} free"). As will be seen later, the circumstances in experimental setup (abbreviated as "Exp.") are somewhere in between due to the presence of a bolted connection with the silo wall and because the lower edge of the steel plate rests on the lower ring (left figure in Fig. 4-39).

Experiment EU1

The experimental failure load is equal to 137.5kN, while the GMNIA failure load ranges between 118.1kN (U_{rad} free) and 144.9kN (U_{rad} restricted) for the pinned supports and between 116.3kN (U_{rad} free) and 144.9kN (U_{rad} restricted) for the clamped supports. Clearly, the failure load of the pinned and the clamped supported numerical model is relatively small. Since the experimental failure load is fairly close to the upper limit of the GMNIA failure load, it can be deduced that, for this experiment, the radial deformations of the shell wall, against which the steel plates were bolted, were indeed largely prevented (See Fig. 4-40).

Table 4-15 Failure load - experiments versus Abaqus (EU1).

		F_u [kN]	k [-]
EXPERIMENT		137.5	
ABAQUS -	U_{rad} FREE (PIN.)	118.1	1.16
	U_{rad} RESTRICTED (PIN.)	144.9	0.95
	U_{rad} FREE (CLA.)	116.3	1.18
	U_{rad} RESTRICTED (CLA.)	144.9	0.95

Fig. 4-40 Internal side of the deformed shell wall at support 2 (EU1).

For all supports, the post-buckling deformed shape of the silo wall is depicted in Fig. 4-41, and both for experimental scale model (upper row) as for the Abaqus model with clamped supports (lower row). During the experiment, a primary buckle has been developed above stiffener 2, a secondary buckle above stiffener 3, and finally an inclined buckle above stiffener 1. In contrast, in Abaqus, the deformations (and failure) arise more or less simultaneously for all supports: inward primary buckles are visible above all longitudinal stiffeners, and secondary inclined buckles are developing after failure on the left and the right side of the top of the longitudinal stiffeners (4 times enlarged for better visibility). Clearly, the post-buckling deformed shape in Abaqus of the silo wall near columns 2 and 3 are in very good agreement with their corresponding experimental deformations patterns.

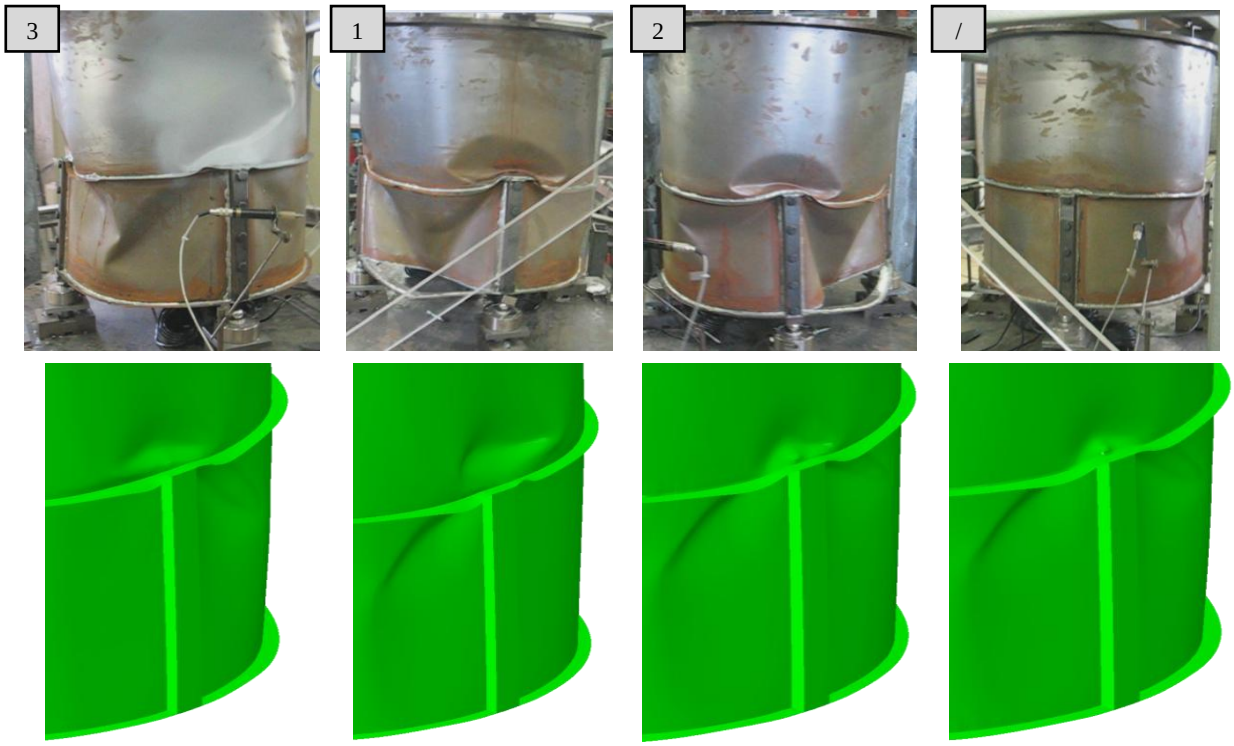

(a) Support 1. (b) Support 2. (c) Support 3. (d) Support 4.

Fig. 4-41 Post-buckling deformations: experiment (upper row) and numerical model U_{rad} free (Cla.) (lower row, deformation scale factor x4) (EU1).

In Fig. 4-42, for each support, the total supporting load is plotted against the radial deformation U_{rad} of the top of the longitudinal stiffener. The curves "U_{rad} restricted" are not shown since the here considered radial deformation is completely restricted and the corresponding load-displacement diagram is a vertical line. The experimental measurement of the radial deformation of the top of the second longitudinal stiffener probably is incorrect, making a comparison with the numerical result difficult. The curves of support 3 and 4 show a relatively good agreement in the first part between the experimental measurement and the numerical result. At higher loads, the curve U_{rad} free bends earlier to failure than the experimental curve. By comparing the load-displacement curves between the pinned and the clamped supports, the pinned supports have larger stiffnesses than the clamped supports.

At the moment of maximum total load, the experimental failure load of the supports ranges between 33.1 and 35.3kN (See Table 4-2), while the numerical values are systematically smaller for U_{rad} free (pinned supports: 25.3-32.0kN; clamped supports: 29.1-31.6kN) and larger for U_{rad} restricted (pinned supports: 31.6-38.3kN; clamped supports: 36.1-38.5kN). Clearly, the difference in load at the supports at the moment of failure between the pinned and the clamped supports can be ignored.

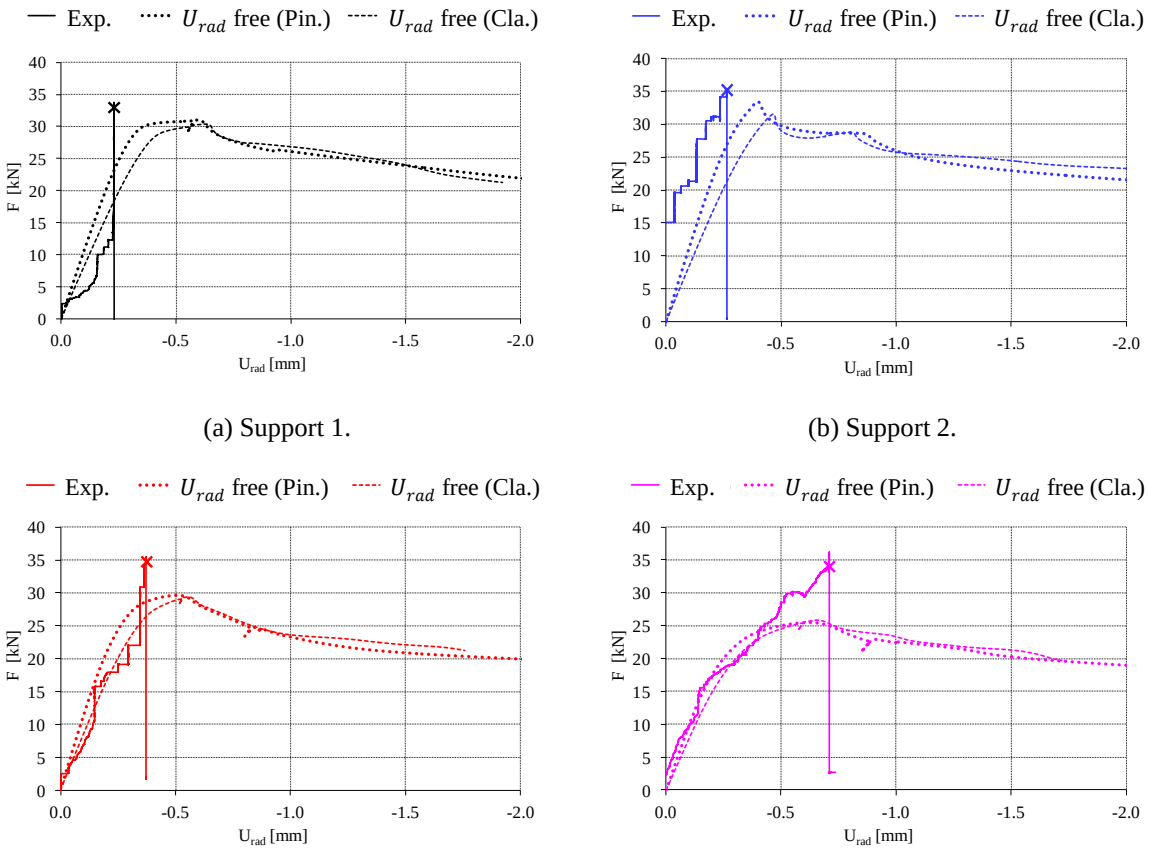

(a) Support 1.

(b) Support 2.

(c) Support 3.

(d) Support 4.

Fig. 4-42 Load-displacement diagrams: the radial displacement of the top of the longitudinal stiffener versus the supporting force (EU1).

In Fig. 4-44, contourplots are depicted of the axial stresses at the moment of failure in the shell wall in the vicinity of all stiffeners. Above all U-shaped stiffeners, relatively large compressive stresses are found over a certain zone in circumferential angle (larger than 200MPa, which corresponds to the point of initial yielding). In other words, the failure of this scale model is strongly influenced by material non-linearity or yielding.

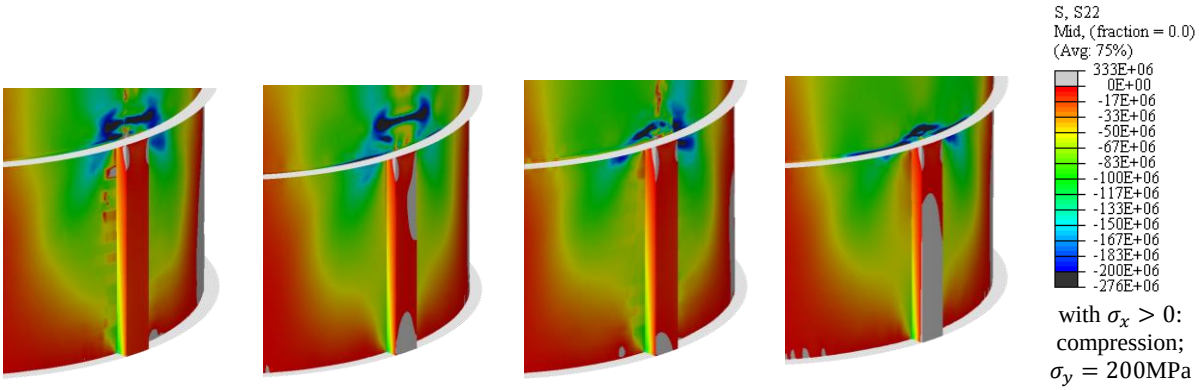

(a) Support 1. (b) Support 2. (c) Support 3. (d) Support 4.

Fig. 4-43 Contourplots of the axial stresses at the moment of failure (numerical model U_{rad} free) (EU1).

Experiment EU2

The experimental failure load is equal to 151.3kN, while the GMNIA failure load ranges between 117.1kN (U_{rad} free) and 143.6kN (U_{rad} restricted) for the pinned supports and between 119.7kN (U_{rad} free) and 143.5kN (U_{rad} restricted) for the clamped supports. In other words, the experimental value is 5.4% above the numerical upper limit. Consequently, the larger failure load cannot only be explained by the restriction of the radial deformations of the shell wall against which the steel plates were bolted. This deviation can be caused by small inaccuracies during the experiment, such as the positioning of the scale model in the test setup, the non-uniformity of the applied load, etc. Furthermore, the failure load of the pinned and the clamped supported numerical model is relatively small.

Table 4-16 Failure load - experiments versus Abaqus (EU2).

		F_u [kN]	k [-]
EXPERIMENT		151.3	
ABAQUS	U_{rad} FREE (PIN.)	117.1	1.29
	U_{rad} RESTRICTED (PIN.)	143.6	1.05
	U_{rad} FREE (CLA.)	119.7	1.26
	U_{rad} RESTRICTED (CLA.)	143.5	1.05

For all supports, the post-buckling deformed shape of the silo wall is depicted in Fig. 4-44, and both for experimental scale model (upper row) as for the Abaqus model with clamped supports (lower row). During the experiment, a primary buckle has been developed above stiffener 4, while the more irregular deformation pattern in the silo wall below the upper edge (above support 1 and 2) has been developed after failure. In contrast, in Abaqus, the deformations (and failure) arise more or less simultaneously for all supports: inward primary buckles are visible above all longitudinal stiffeners, and secondary inclined buckles are developing after failure on the left and the right side of the top of the longitudinal stiffeners (4 times enlarged for better visibility).

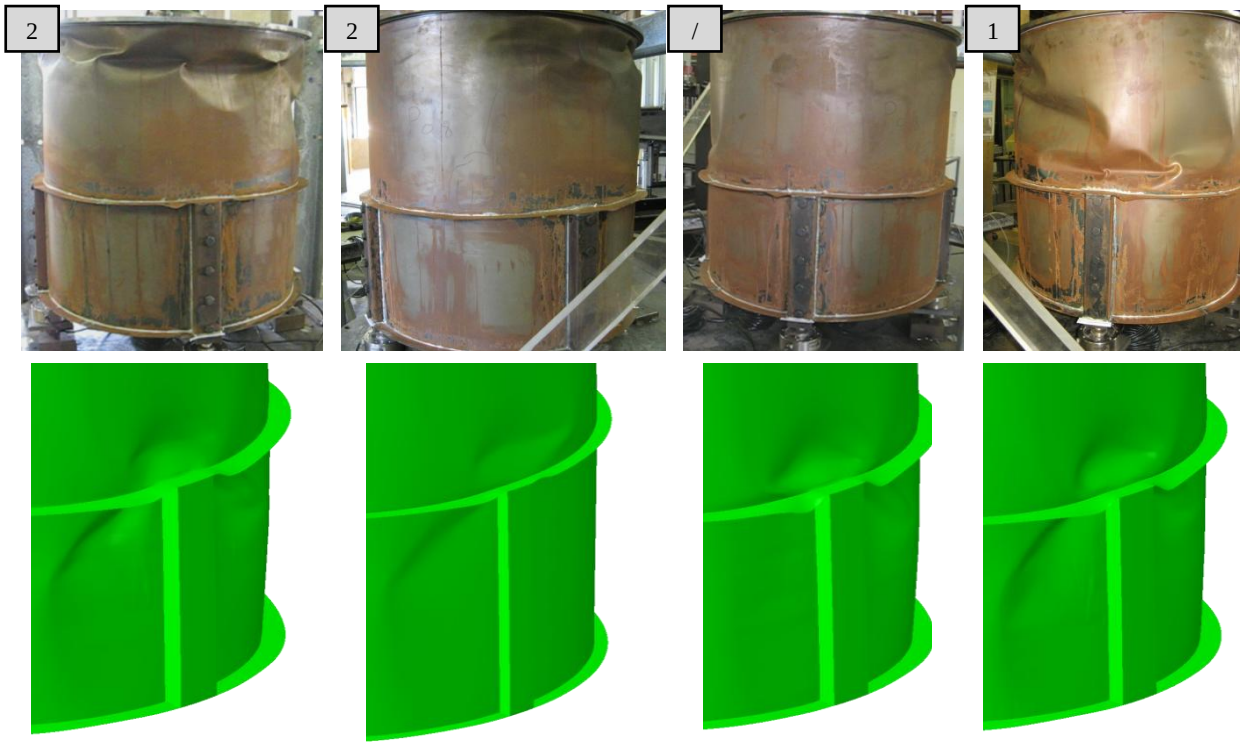

(a) Support 1. (b) Support 2. (c) Support 3. (d) Support 4.

Fig. 4-44 Post-buckling deformations: experiment (upper row) and numerical model U_{rad} free (Cla.) (lower row, deformation scale factor x4) (EU2).

In Fig. 4-45, for each support, the total supporting load is plotted against the radial deformation U_{rad} of the top of the longitudinal stiffener. The curves "U_{rad} restricted" are not shown since the here considered radial deformation is completely restricted and the corresponding load-displacement diagram is a vertical line. All curves show a relatively good agreement in the first part between the experimental measurement and the numerical result. At higher loads, the curve U_{rad} free bends earlier to failure than the experimental curve. Furthermore, the load-displacement curves of the pinned and the clamped supports are approximately equal to each other before and at the moment of failure.

At the moment of maximum total load, the experimental failure load of the supports ranges between 35.0 and 39.3kN (See Table 4-3), while the numerical values are systematically smaller for U_{rad} free (pinned supports: 28.3-30.0kN; clamped supports: 28.8-30.1kN) and slightly smaller for U_{rad} restricted (pinned supports: 35.4-36.2kN; clamped supports: 35.4-36.2kN). Clearly, the difference in load at the supports at the moment of failure between the pinned and the clamped supports can be ignored.

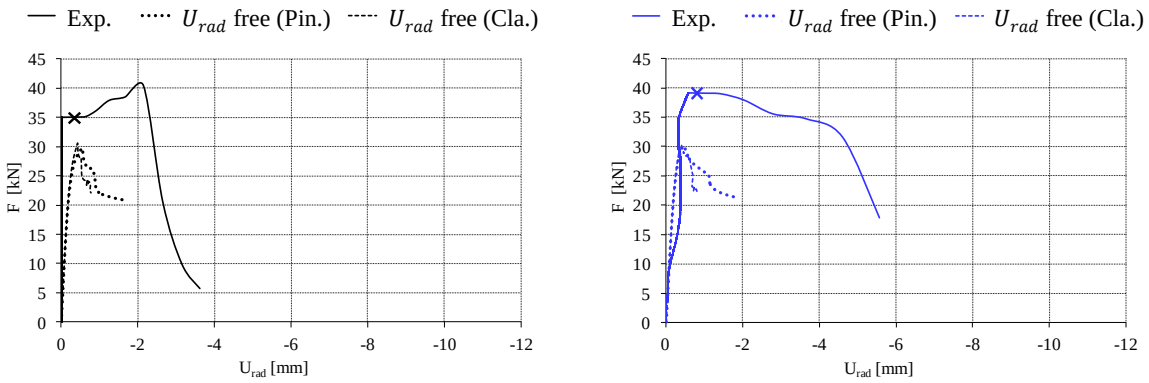

(a) Support 1.

(b) Support 2.

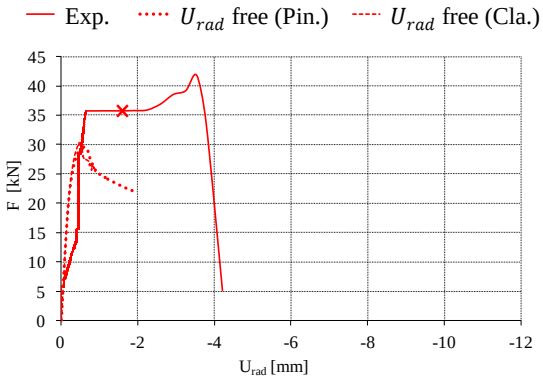

(c) Support 3.

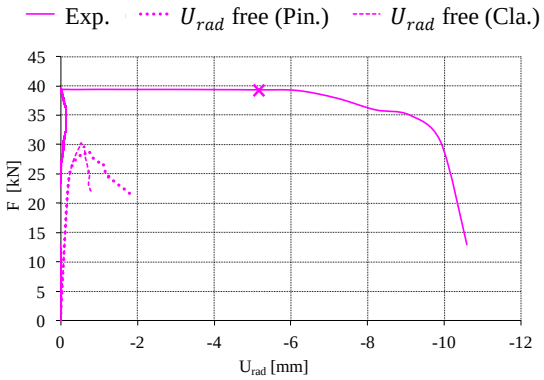

(d) Support 4.

Fig. 4-45 Load-displacement diagrams: the radial displacement of the top of the longitudinal stiffener versus the supporting force (EU2).

Experiment EU3

The experimental failure load is equal to 171.5kN, while the GMNIA failure load ranges between 148.2kN (U_{rad} free) and 182.6kN (U_{rad} restricted) for the pinned supports and between 147.2kN (U_{rad} free) and 182.6kN (U_{rad} restricted) for the clamped supports. Clearly, the failure load of the pinned and the clamped supported numerical model is relatively small. Since the experimental failure load is fairly close to the upper limit of the GMNIA failure load, it can be deduced that, for this experiment, the radial deformations of the shell wall, against which the steel plates were bolted, were indeed largely prevented.

Table 4-17 Failure load - experiments versus Abaqus (EU3).

		F_u [kN]	k [-]
EXPERIMENT		171.5	
ABAQUS	U_{rad} FREE (PIN.)	148.2	1.16
	U_{rad} RESTRICTED (PIN.)	182.6	0.94
	U_{rad} FREE (CLA.)	147.2	1.17
	U_{rad} RESTRICTED (CLA.)	182.6	0.94

For all supports, the post-buckling deformed shape of the silo wall is depicted in Fig. 4-46, and both for experimental scale model (upper row) as for the Abaqus model with clamped supports (lower row). During the experiment, a primary buckle has been developed above stiffener 3 and a secondary buckle above stiffener 2. In contrast, in Abaqus, the deformations (and failure) arise more or less simultaneously for all supports: inward primary buckles are visible above all longitudinal stiffeners (4 times enlarged for better visibility). After failure, secondary inclined buckles are developing on the left and the right side of the top of the longitudinal stiffeners (here only above stiffener 3).

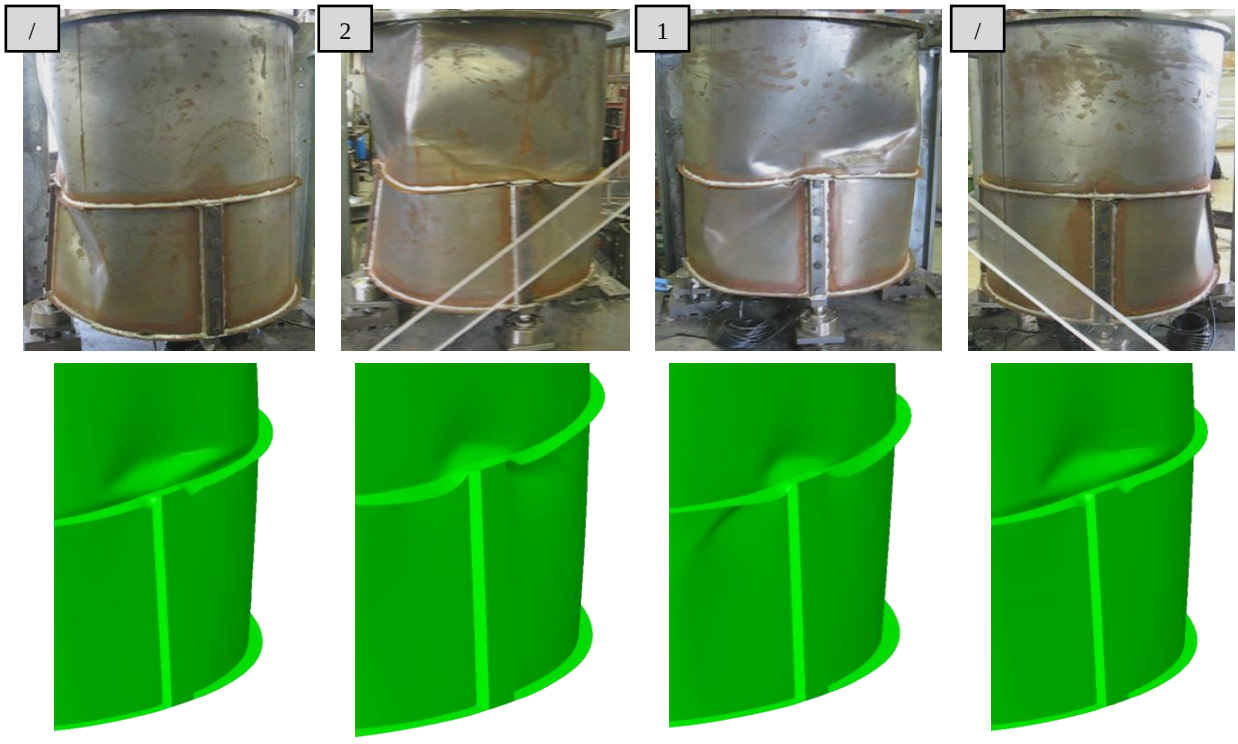

(a) Support 1. (b) Support 2. (c) Support 3. (d) Support 4.

Fig. 4-46 Post-buckling deformations: experiment (upper row) and numerical model U_{rad} free (Cla.) (lower row, deformation scale factor x4) (EU3).

The radial deformation U_{rad} of the top of the longitudinal stiffeners was unfortunately not measured during this first experiment (in the beginning of the test series). Consequently, only the curves corresponding with the numerical model U_{rad} free are depicted in Fig. 4-47 and comparison with the experimental curve is not possible. From this figure, it can be derived that, before and at the moment of failure, the load-displacement curves of the pinned supports are slightly higher than the clamped supports.

At the moment of maximum total load, the experimental failure load of the supports ranges between 40.9 and 44.8kN (See Table 4-4), while the numerical values are systematically smaller for U_{rad} free (pinned supports: 33.6-39.3kN; clamped supports: 34.0-41.1kN) and larger for U_{rad} restricted (pinned supports: 41.3-48.7kN; clamped supports: 41.3-48.8kN). Clearly, the difference in load at the supports at the moment of failure between the pinned and the clamped supports can be ignored.

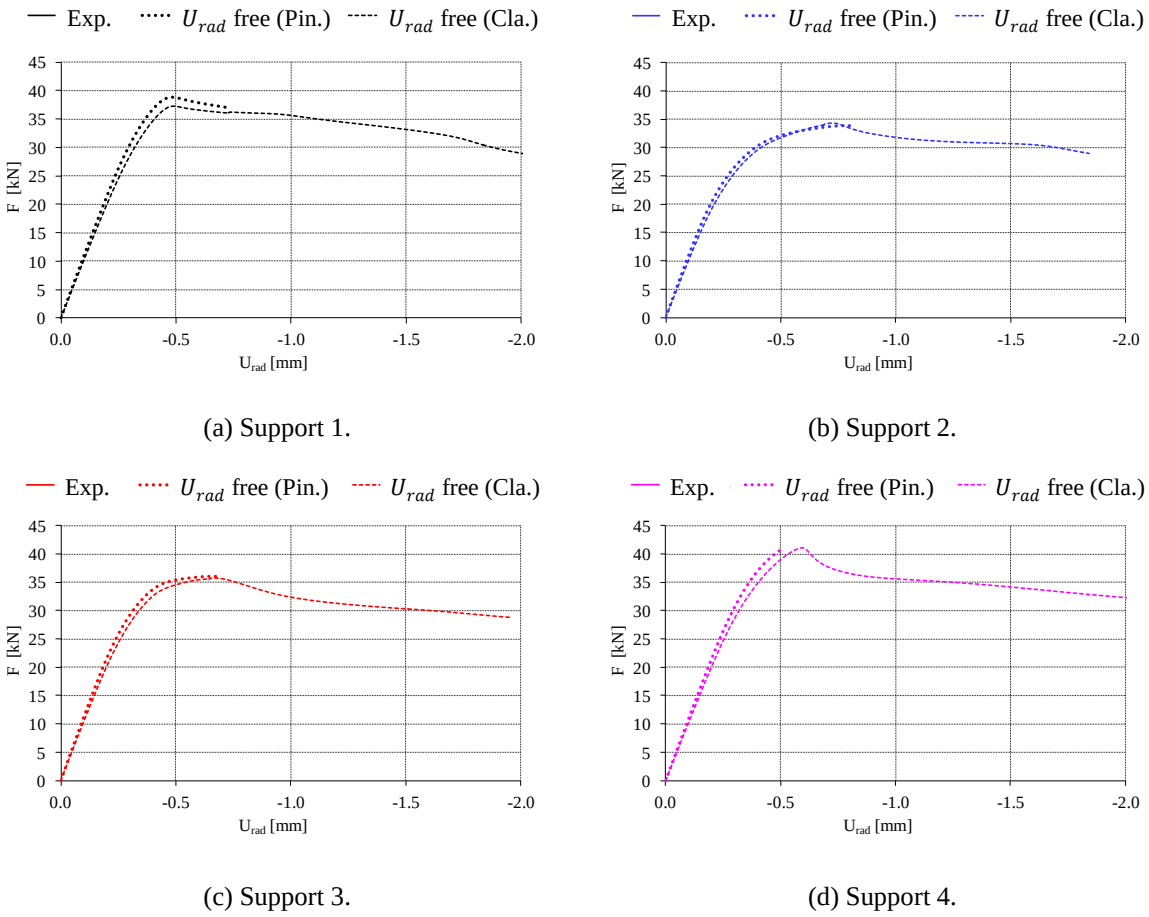

(a) Support 1.

(b) Support 2.

(c) Support 3.

(d) Support 4.

Fig. 4-47 Load-displacement diagrams: the radial displacement of the top of the longitudinal stiffener versus the supporting force (EU3).

Conclusions

For the first configuration (i.e. the locally supported barrel with U-shaped longitudinal stiffeners and two ring stiffeners), Table 4-18 gives an overview of the experimental and the

GMNIA failure loads F_u and the factor k. For all experiments, it can be concluded that the experimental setup best corresponds with the second model where the radial displacement U_{rad} is completely restricted in the nodes of the shell wall at the internal attached 5mm thick steel plates. Between the model with pinned and clamped supports, the difference in failure load is relatively small. However, when the load-displacement diagrams are compared, the stiffness of the pinned supports generally is larger than with the clamped supports.

Table 4-18 Overview failure load model 1- experiments versus Abaqus.

	EXPERIMENT	ABAQUS							
		U_{rad} FREE (PIN.)		U_{rad} RESTRICTED (PIN.)		U_{rad} FREE (CLA.)		U_{rad} RESTRICTED (CLA.)	
	F_u [kN]	F_u [kN]	k_{free} [-]	F_u [kN]	k_{res} [-]	F_u [kN]	k_{free} [-]	F_u [kN]	k_{res} [-]
EU1	137.5	118.1	1.16	144.9	0.95	116.3	1.18	144.9	0.95
EU2	151.3	117.1	1.29	143.6	1.05	119.7	1.26	143.5	1.05
EU3	171.5	148.2	1.16	182.6	0.94	147.2	1.17	182.6	0.94

Overall, it can be concluded that the first numerical model is able to predict the elasto-plastic failure load with a relatively good accuracy (i.e. $0.8 < k_{res} < 1.2$). The agreement is not perfect, but the magnitude of the predicted failure load is reliable, and similar post-buckling patterns and load-displacement diagrams are obtained for the experiments on the one hand and for Abaqus on the other.

4.2 Model 2 - Engaged columns

Specific settings numerical model with engaged columns

The support steel block under the bottom of the engaged column is replaced in Abaqus by a rigid plate with a reference node at its centre (See Fig. 4-48) and the below boundary conditions.

$$U_R = U_T = U_Z = 0 \tag{4-16}$$

As can be seen, all translational degrees of freedom are restricted in the reference node. For the rotation φ_T about the circumferential axis, three different situations can be distinguished: (1) the circumferential rotation φ_T is completely free (i.e. a pinned support, abbreviated as "Pin."), (2) the circumferential rotation φ_T is completely restricted (i.e. a clamped support, abbreviated as "Cla."), and (3) the circumferential rotation φ_T is partially restricted (i.e. a partially clamped support, abbreviated as "P.C.") by the use of a rotational spring (with stiffness C) in the reference node. As will be demonstrated later, the columns in the

experimental setup (abbreviated as "Exp.") are best corresponding with the partially clamped columns. On the left figure of Fig. 4-48, the bolted connection between the bottom of the engaged column and an external profile can be observed.

Two alternatives have been taken into consideration for such partially clamped columns: (1) the rotation stiffness C is equal for all columns to obtain the best possible agreement between the experimental and the numerical failure load (i.e. P.C. 1) and (2) the rotation stiffness C is different for all columns to obtain the best possible agreement between the experimental and the numerical load-displacement curve (i.e. P.C. 2).

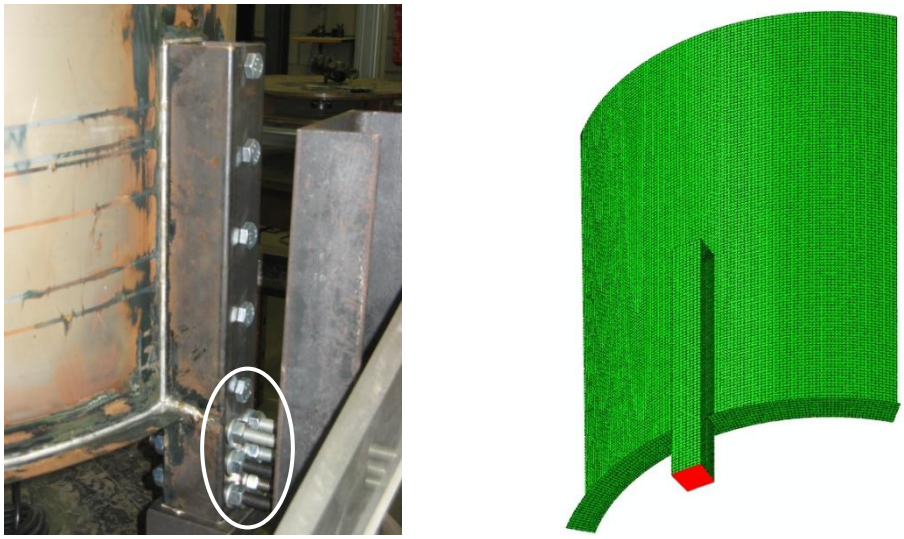

Fig. 4-48 Local supports: Experiment (left) and Abaqus (right).

Behind the engaged column and on the internal side of the silo wall, an additional 5mm thick steel plate is provided for the attachment of the column to the silo wall by bolting. This steel plate is not included in Abaqus, because from the numerical simulations, it appeared that it had a negligible influence on the results.

Experiment EK1

The experimental failure load is equal to 73.9kN, while the GMNIA failure load ranges between 49.6kN (pinned columns) and 92.9kN (clamped columns). In other words, the columns in the test setup can be classified as "partially" clamped columns. Indeed, with a constant rotation stiffness C of 19.5kNm/rad (See Table 4-20) in the reference node of each support (P.C. 1) or with a variable rotation stiffness C which ranges from 15.0 to 35.0kNm/rad (See Table 4-20) in the reference node of each support (P.C. 2), the GMNIA failure load is approximately equal to the experimental failure load.

Table 4-19 Failure load - experiments versus Abaqus (EK1).

		F_u [kN]	k [-]
EXPERIMENT		73.9	
ABAQUS	PINNED	49.6	1.49
	P.C. 1	73.9	1.00
	P.C. 2	73.4	1.01
	CLAMPED	92.9	0.80

Table 4-20 Rotation stiffnesses for partially clamped columns (P.C.) (EK1).

NUMBER SUPPORT	C $[kNm/rad]$	
	P.C. 1	P.C. 2
1	19.5	16.0
2	19.5	19.5
3	19.5	35.0
4	19.5	15.0

For all supporting columns, the post-buckling deformed shape of the silo wall is depicted in Fig. 4-49, and both for experimental scale model (upper row) as for the Abaqus model (lower row). During the experiment, column 4 failed first, column 1 a short period later, while columns 2 and 3 did not fail. This can be clearly seen in the deformation patterns after collapse: only engaged column 1 and 4 and the behind silo wall are fully deformed inwardly. In contrast, in Abaqus, the deformations (and failure) arise more or less simultaneously for all supporting columns: the inward directed columns deform the shell wall inwardly, creating a reverse bell-shaped pattern in the silo wall behind the supporting columns (4 times enlarged for better visibility).

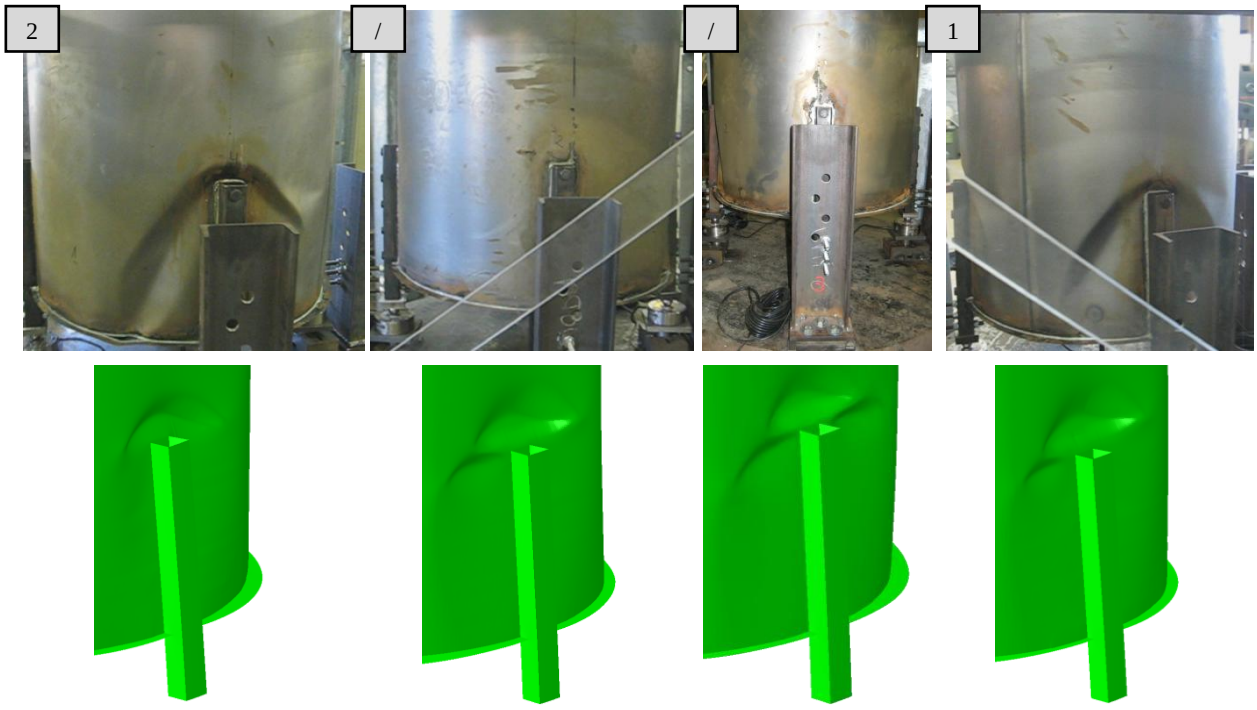

(a) Support 1. (b) Support 2. (c) Support 3. (d) Support 4.

Fig. 4-49 Post-buckling deformations: experiment (upper row) and numerical model P.C. 2 (lower row, deformation scale factor x4) (EK1).

In Fig. 4-50, for each support, the total supporting load is plotted against the radial deformation U_{rad} of the top of the engaged column. The solid curve represents the experimental measurement (Exp.) and is each time situated between the lower curve of a pinned column (Pin.) and the upper curve of a clamped support (Cla.). In fact, the last two curves are the outer limits between which the partially clamped columns (P.C.) are situated. In other words, the columns in the experimental test setup can be classified as partially clamped columns (P.C.).

The partially restriction of the circumferential rotation φ_T of the bottom of the supporting column is modelled in Abaqus by means of a rotational spring (with stiffness C) in the reference node. Two situations are considered for the partially restriction. Firstly, the rotation stiffness C is constant for all columns (i.e. P.C. 1) to obtain the same total failure load in experimental setup and in Abaqus. However, a relatively large deviation is sometimes obtained between the experimental and the calculated load-displacement curve, especially for larger loads (for example for column 3). Therefore, a second alternative has been considered (i.e. P.C. 2) where the rotation stiffness C is varied for all columns. The constant value of C of P.C. 1 has been used as starting point of P.C. 2 and the best value of C has been determined by iteration for each column, for which the best agreement is found between the experimental and the numerical load-displacement diagrams. In this way, a relatively good agreement is achieved between both curves for all columns, while the error on the total failure load slightly increases.

At the moment of maximum total load, the experimental failure load of the supports ranges between 17.4 and 18.9kN (See Table 4-5), while the numerical values of the models P.C. 1 and P.C. 2 are varying between 18.0-18.9kN and 17.7-20.8kN, respectively.

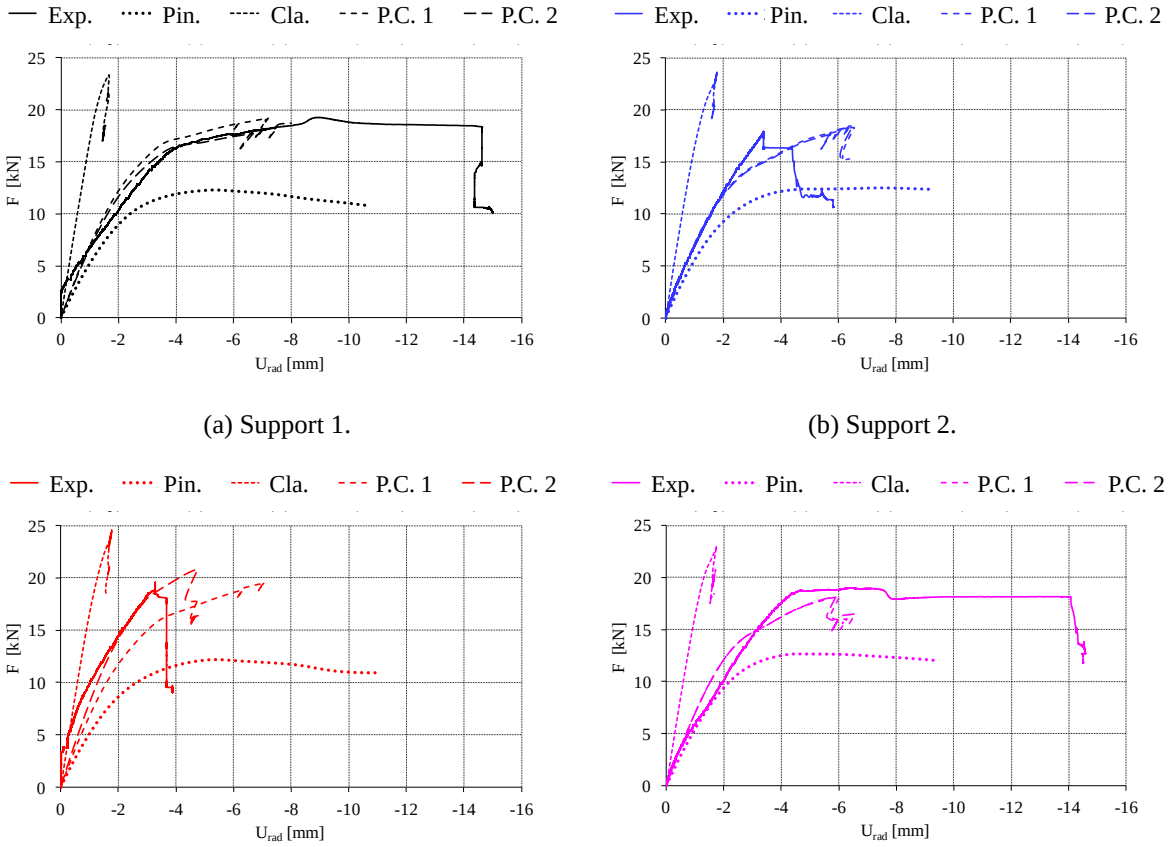

(a) Support 1.

(b) Support 2.

(c) Support 3.

(d) Support 4.

Fig. 4-50 Load-displacement diagrams: the radial displacement of the top of the engaged column versus the supporting force (EK1).

The axial stresses at the moment of failure are depicted in Fig. 4-51. On these contourplots, it can be seen that relatively large compressive stresses occur in the shell wall just above the top of each engaged columns. These high stress concentrations are developing over a certain zone in circumferential angle (larger than 200MPa, which corresponds to the point of initial yielding). In other words, the failure of this scale model is influenced by material non-linearity or yielding.

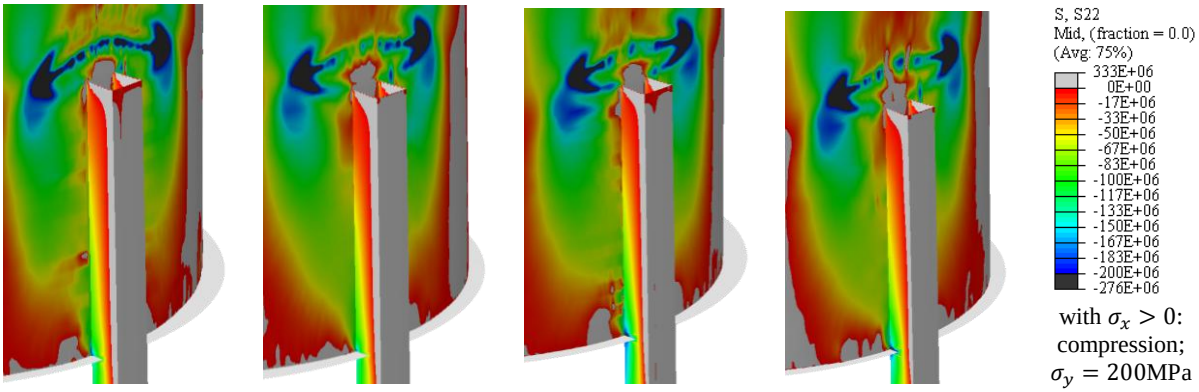

(a) Support 1. (b) Support 2. (c) Support 3. (d) Support 4.

Fig. 4-51 Contourplots of the axial stresses at the moment of failure (numerical model P.C. 2) (EK1).

Experiment EK2

The experimental failure load is equal to 70.8kN, while the GMNIA failure load ranges between 47.9kN (pinned columns) and 92.1kN (clamped columns). In other words, the columns in the test setup can be classified as "partially" clamped columns. Indeed, with a constant rotation stiffness C of 50.0kNm/rad (See Table 4-22) in the reference node of each support (P.C. 1) or with a variable rotation stiffness C which ranges from 15.0 to 40.0kNm/rad (See Table 4-22) in the reference node of each support (P.C. 2), the GMNIA failure load is approximately equal to the experimental failure load.

Table 4-21 Failure load - experiments versus Abaqus (EK2).

		F_u [kN]	k [-]
EXPERIMENT		70.8	
ABAQUS	PINNED	47.9	1.48
	P.C. 1	71.3	0.99
	P.C. 2	66.1	1.07
	CLAMPED	92.1	0.77

Table 4-22 Rotation stiffnesses for partially clamped columns (P.C.) (EK2).

NUMBER SUPPORT	C $[kNm/rad]$	
	P.C. 1	P.C. 2
1	50.0	30.0
2	50.0	30.0
3	50.0	40.0
4	50.0	15.0

For all supporting columns, the post-buckling deformed shape of the silo wall is depicted in Fig. 4-52, and both for experimental scale model (upper row) as for the Abaqus model (lower row). During the experiment, column 1 failed first, column 4 a short period later, while columns 2 and 3 did not fail. This can be clearly seen in the deformation patterns after collapse: only engaged column 1 and 4 and the behind silo wall are fully deformed inwardly. In contrast, in Abaqus, the deformations (and failure) arise more or less simultaneously for all

supporting columns: the inward directed columns deform the shell wall inwardly, creating a reverse bell-shaped pattern in the silo wall behind the supporting columns (2 times enlarged for better visibility).

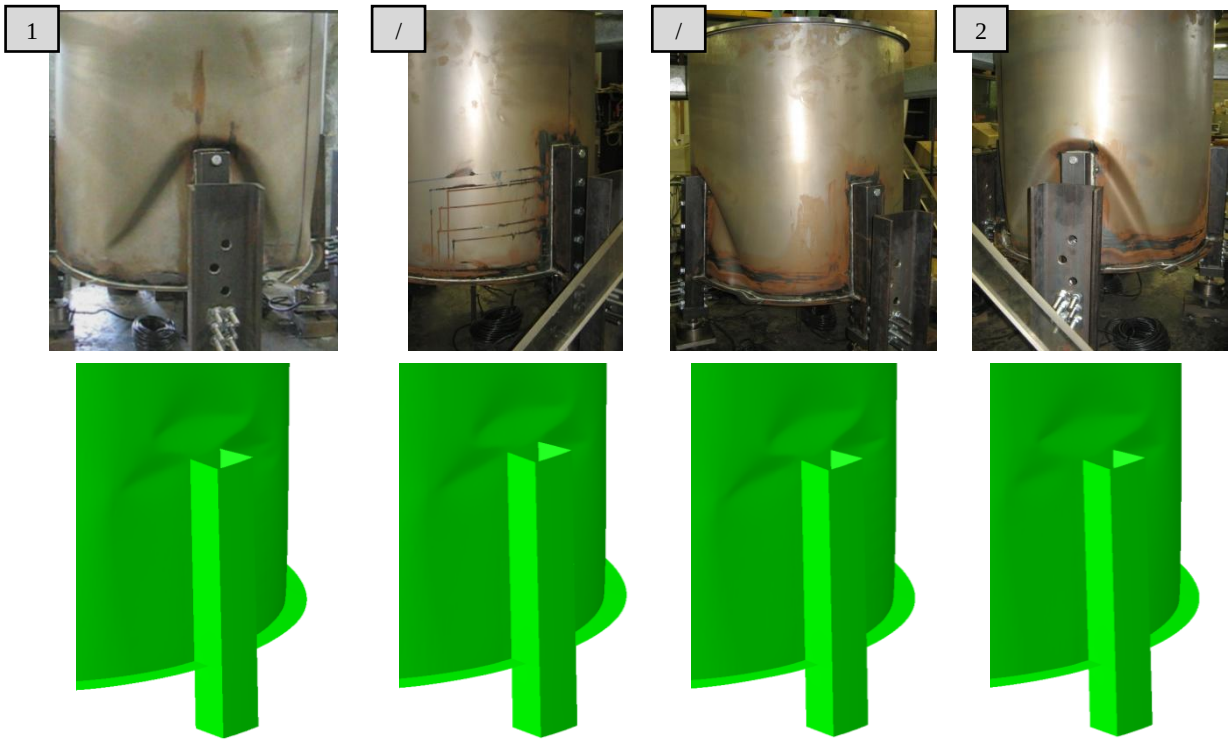

(a) Support 1. (b) Support 2. (c) Support 3. (d) Support 4.

Fig. 4-52 Post-buckling deformations: experiment (upper row) and numerical model P.C. 2 (lower row, deformation scale factor x2) (EK2).

In Fig. 4-53, for each support, the total supporting load is plotted against the radial deformation U_{rad} of the top of the engaged column. The solid curve represents the experimental measurement (Exp.) and is each time situated between the lower curve of a pinned column (Pin.) and the upper curve of a clamped support (Cla.). In fact, the last two curves are the outer limits between which the partially clamped columns (P.C.) are situated. In other words, the columns in the experimental test setup can be classified as partially clamped columns (P.C.).

The partially restriction of the circumferential rotation φ_T of the bottom of the supporting column is modelled in Abaqus by means of a rotational spring (with stiffness C) in the reference node. Two situations are considered for the partially restriction. Firstly, the rotation stiffness C is constant for all columns (i.e. P.C. 1) to obtain the same total failure load in experimental setup and in Abaqus. However, a relatively large deviation is sometimes obtained between the experimental and the calculated load-displacement curve, especially for larger loads (for example for column 4). Therefore, a second alternative has been considered (i.e. P.C. 2) where the rotation stiffness C is varied for all columns. The constant value of C of

P.C. 1 has been used as starting point of P.C. 2 and the best value of C has been determined by iteration for each column, for which the best agreement is found between the experimental and the numerical load-displacement diagrams. In this way, a relatively good agreement is achieved between both curves for all columns, while the error on the total failure load slightly increases.

At the moment of maximum total load, the experimental failure load of the supports ranges between 16.0 and 18.2kN (See Table 4-6), while the numerical values of the models P.C. 1 and P.C. 2 are varying between 17.0-17.9kN and 14.8-17.3kN, respectively.

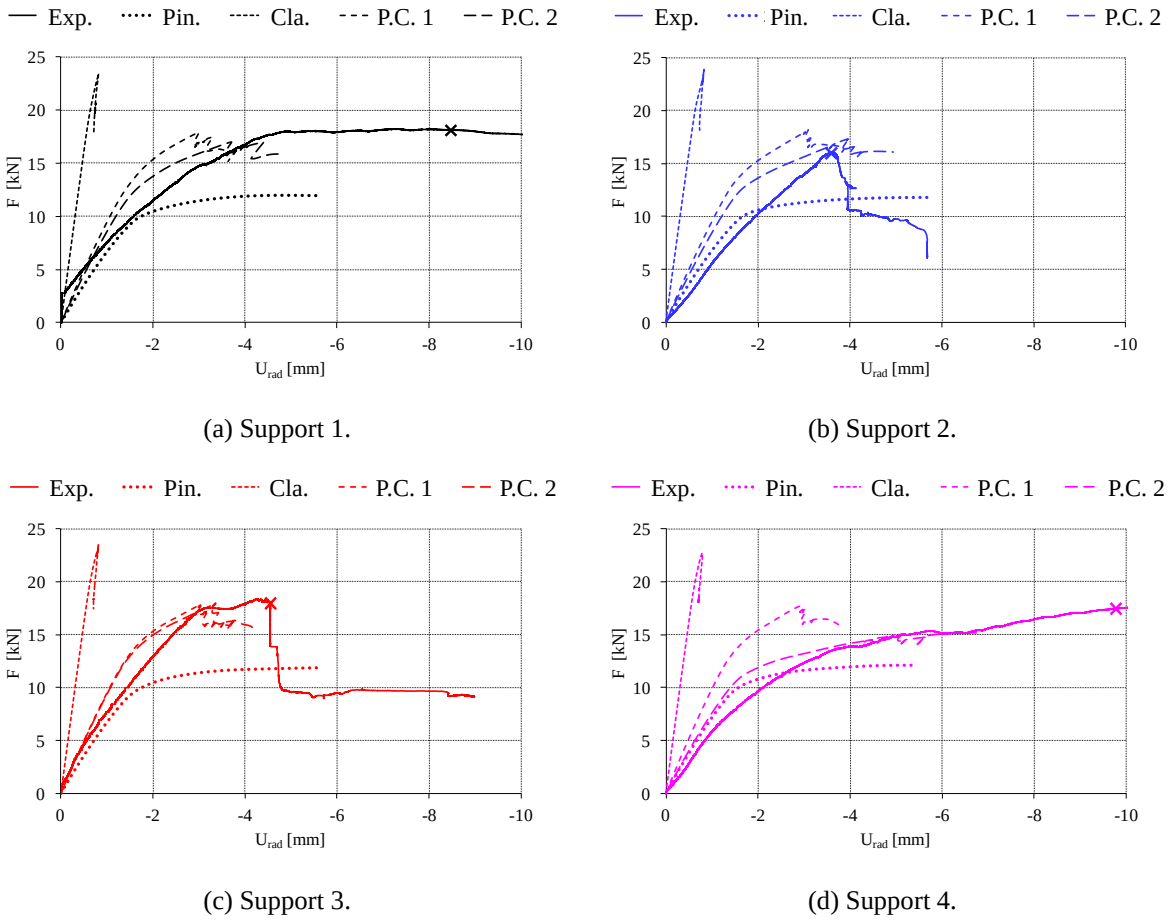

(a) Support 1.

(b) Support 2.

(c) Support 3.

(d) Support 4.

Fig. 4-53 Load-displacement diagrams: the radial displacement of the top of the engaged column versus the supporting force (EK2).

Experiment EK3

The experimental failure load is equal to 94.1kN, while the GMNIA failure load ranges between 60.1kN (pinned columns) and 114.9kN (clamped columns). In other words, the columns in the test setup can be classified as "partially" clamped columns. Indeed, with a constant rotation stiffness C of 22.0kNm/rad (See Table 4-24) in the reference node of each support (P.C. 1) or with a variable rotation stiffness C which ranges from 19.0 to 50.0kNm/rad (See Table 4-24) in the reference node of each support (P.C. 2), the GMNIA failure load is approximately equal to the experimental failure load.

Table 4-23 Failure load - experiments versus Abaqus (EK3).

		F_u [kN]	k [-]
EXPERIMENT		94.1	
ABAQUS	PINNED	60.1	1.57
	P.C. 1	94.3	1.00
	P.C. 2	94.5	1.00
	CLAMPED	114.9	0.82

Table 4-24 Rotation stiffnesses for partially clamped columns (P.C.) (EK3).

NUMBER SUPPORT	C $[kNm/rad]$	
	P.C. 1	P.C. 2
1	22.0	50.0
2	22.0	20.0
3	22.0	25.0
4	22.0	19.0

For all supporting columns, the post-buckling deformed shape of the silo wall is depicted in Fig. 4-54, and both for experimental scale model (upper row) as for the Abaqus model, and whether or not with mesh visible (middle and lower row). During the experiment, column 3 failed first, column 4 a short period later, while columns 1 and 2 did not fail. This can be clearly seen in the deformation patterns after collapse: only engaged column 3 and 4 and the behind silo wall are fully deformed inwardly. In contrast, in Abaqus, the deformations (and failure) arise more or less simultaneously for all supporting columns: the inward directed columns deform the shell wall inwardly, creating a reverse bell-shaped pattern in the silo wall behind the supporting columns (2 times enlarged for better visibility). Clearly, the post-buckling deformed shape in Abaqus of the silo wall near columns 3 and 4 are in very good agreement with their corresponding experimental deformations patterns.

In Fig. 4-55, for each support, the total supporting load is plotted against the radial deformation U_{rad} of the top of the engaged column. The solid curve represents the experimental measurement (Exp.) and is each time situated between the lower curve of a pinned column (Pin.) and the upper curve of a clamped support (Cla.). In fact, the last two curves are the outer limits between which the partially clamped columns (P.C.) are situated. In other words, the columns in the experimental test setup can be classified as partially clamped columns (P.C.).

The partially restriction of the circumferential rotation φ_T of the bottom of the supporting column is modelled in Abaqus by means of a rotational spring (with stiffness C) in the reference node. Two situations are considered for the partially restriction. Firstly, the rotation stiffness C is constant for all columns (i.e. P.C. 1) to obtain the same total failure load in experimental setup and in Abaqus. However, a relatively large deviation is sometimes obtained between the experimental and the calculated load-displacement curve, especially for larger loads (for example for column 1). Therefore, a second alternative has been considered (i.e. P.C. 2) where the rotation stiffness C is varied for all columns. The constant value of C of P.C. 1 has been used as starting point of P.C. 2 and the best value of C has been determined by iteration for each column, for which the best agreement is found between the experimental and the numerical load-displacement diagrams. In this way, a relatively good agreement is achieved between both curves for all columns, while the error on the total failure load slightly increases.

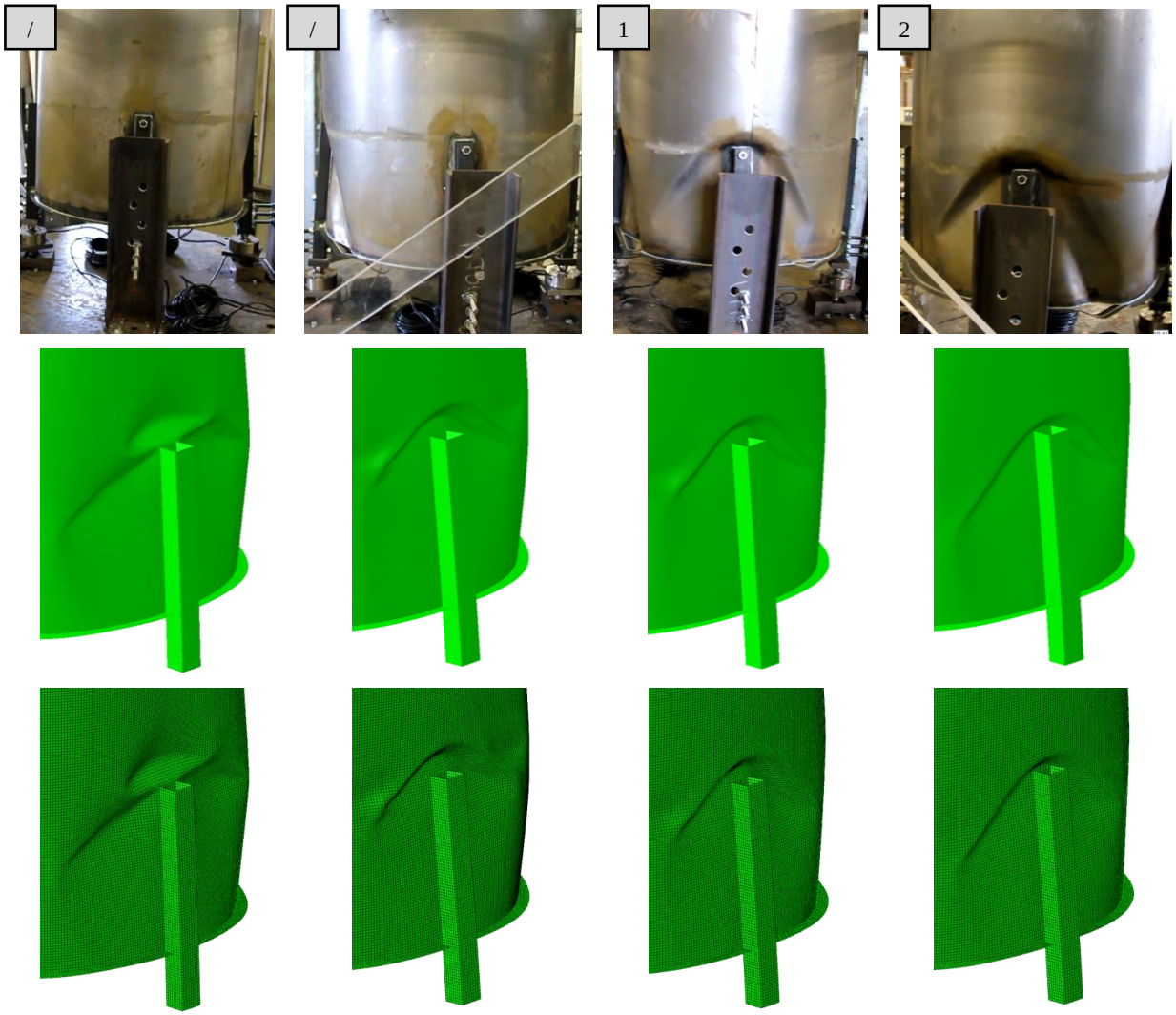

(a) Support 1. (b) Support 2. (c) Support 3. (d) Support 4.

Fig. 4-54 Post-buckling deformations: experiment (upper row) and numerical model P.C. 2 (middle and lower row, deformation scale factor x2) (EK3).

At the moment of maximum total load, the experimental failure load of the supports ranges between 21.6 and 24.7kN (See Table 4-7), while the numerical values of the models P.C. 1 and P.C. 2 are varying between 22.1-24.0kN and 22.2-24.6kN, respectively.

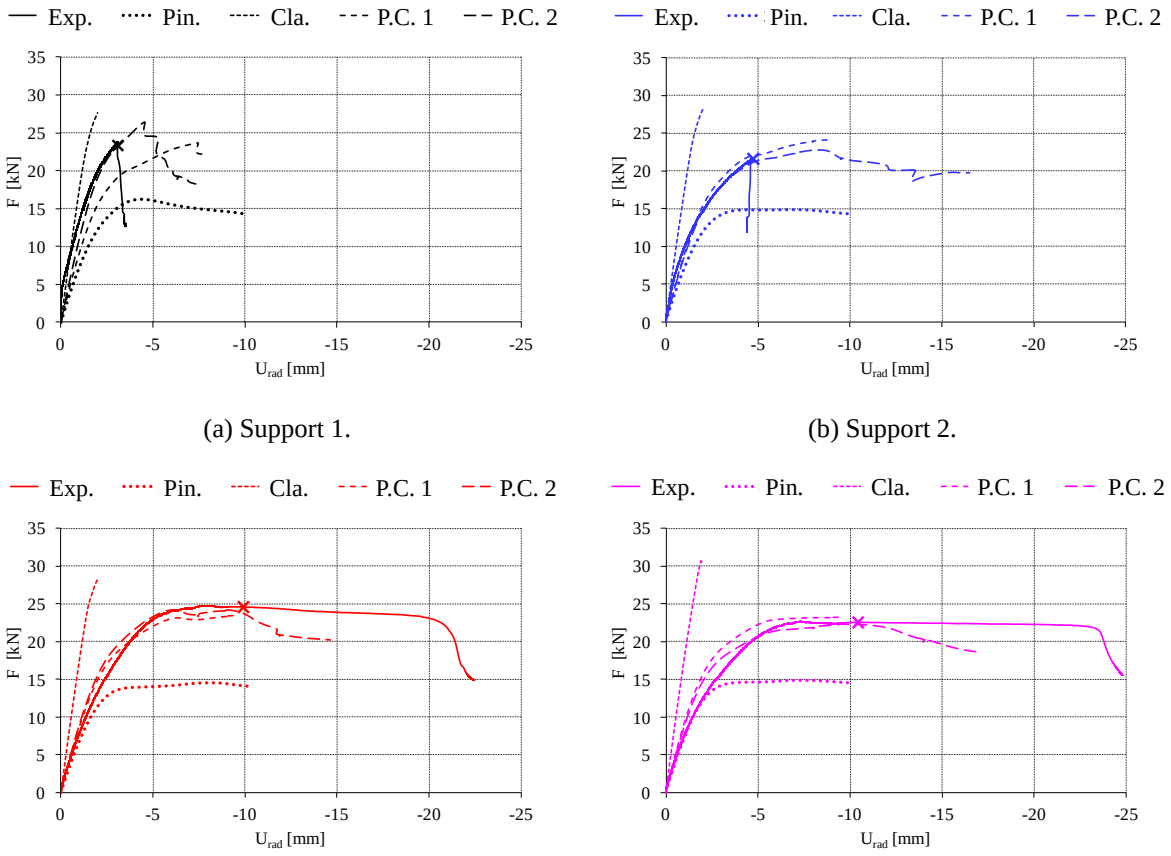

(a) Support 1.

(b) Support 2.

(c) Support 3.

(d) Support 4.

Fig. 4-55 Load-displacement diagrams: the radial displacement of the top of the engaged column versus the supporting force (EK3).

Experiment EK4

The experimental failure load is equal to 89.8kN, while the GMNIA failure load ranges between 66.9kN (pinned columns) and 130.3kN (clamped columns). In other words, the columns in the test setup can be classified as "partially" clamped columns. Indeed, with a constant rotation stiffness C of 19.0kNm/rad (See Table 4-26) in the reference node of each support (P.C. 1) or with a variable rotation stiffness C which ranges from 15.0 to 23.0kNm/rad (See Table 4-26) in the reference node of each support (P.C. 2), the GMNIA failure load is approximately equal to the experimental failure load.

For all supporting columns, the post-buckling deformed shape of the silo wall is depicted in Fig. 4-56, and both for experimental scale model (upper row) as for the Abaqus model (lower row). During the experiment, column 1 failed first, column 4 a short period later, while columns 2 and 3 did not fail. This can be clearly seen in the deformation patterns after

collapse: only engaged column 1 and 4 and the behind silo wall are fully deformed inwardly. In contrast, in Abaqus, the deformations (and failure) arise more or less simultaneously for all supporting columns: the inward directed columns deform the shell wall inwardly, creating a reverse bell-shaped pattern in the silo wall behind the supporting columns (2 times enlarged for better visibility). Clearly, the initiated post-buckling deformed shape in Abaqus of the silo wall near columns 1 and 4 are in very good agreement with their corresponding experimental deformations patterns.

Table 4-25 Failure load - experiments versus Abaqus (EK4).

		F_u [kN]	k [-]
EXPERIMENT		89.8	
ABAQUS	PINNED	66.9	1.34
	P.C. 1	90.6	0.99
	P.C. 2	89.4	1.00
	CLAMPED	130.3	0.69

Table 4-26 Rotation stiffnesses for partially clamped columns (P.C.) (EK4).

NUMBER SUPPORT	C $[kNm/rad]$	
	P.C. 1	P.C. 2
1	19.0	23.0
2	19.0	15.0
3	19.0	21.0
4	19.0	17.0

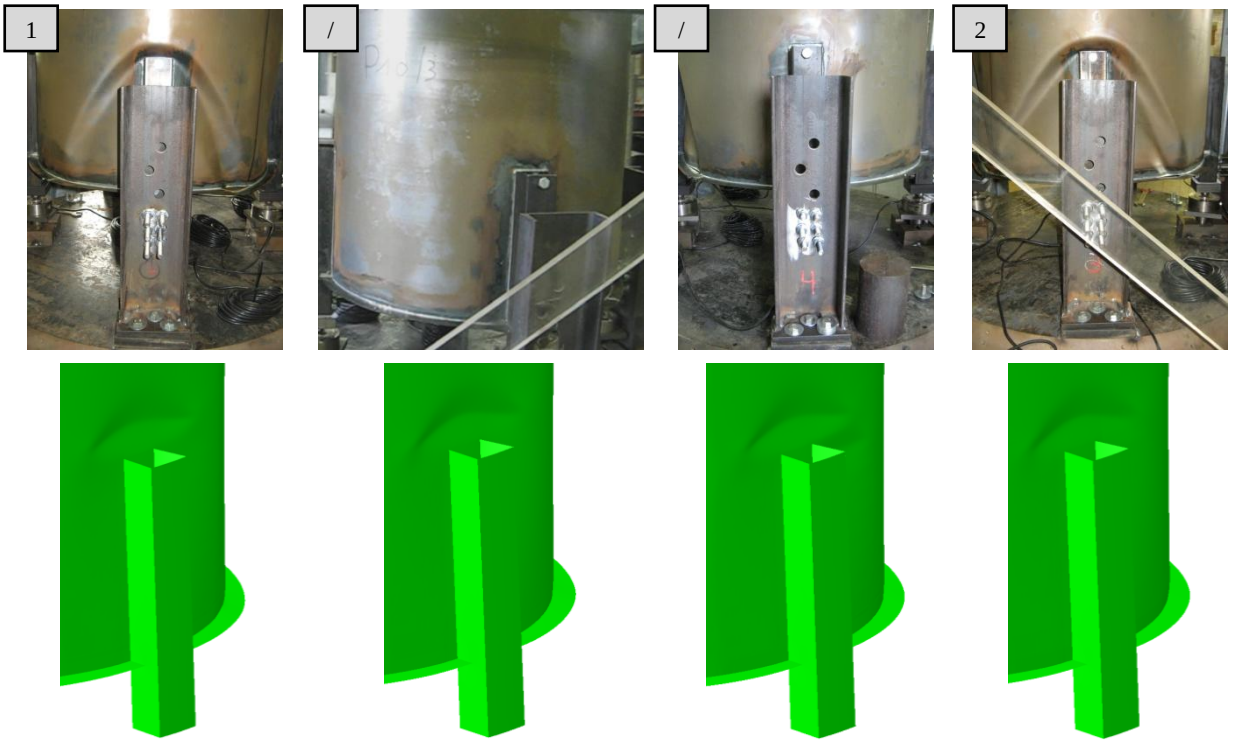

(a) Support 1. (b) Support 2. (c) Support 3. (d) Support 4.

Fig. 4-56 Post-buckling deformations: experiment (upper row) and numerical model P.C. 2 (lower row, deformation scale factor x2) (EK4).

In Fig. 4-57, for each support, the total supporting load is plotted against the radial deformation U_{rad} of the top of the engaged column. The solid curve represents the experimental measurement (Exp.) and is each time situated between the lower curve of a pinned column (Pin.) and the upper curve of a clamped support (Cla.). In fact, the last two curves are the outer limits between which the partially clamped columns (P.C.) are situated. In other words, the columns in the experimental test setup can be classified as partially clamped columns (P.C.).

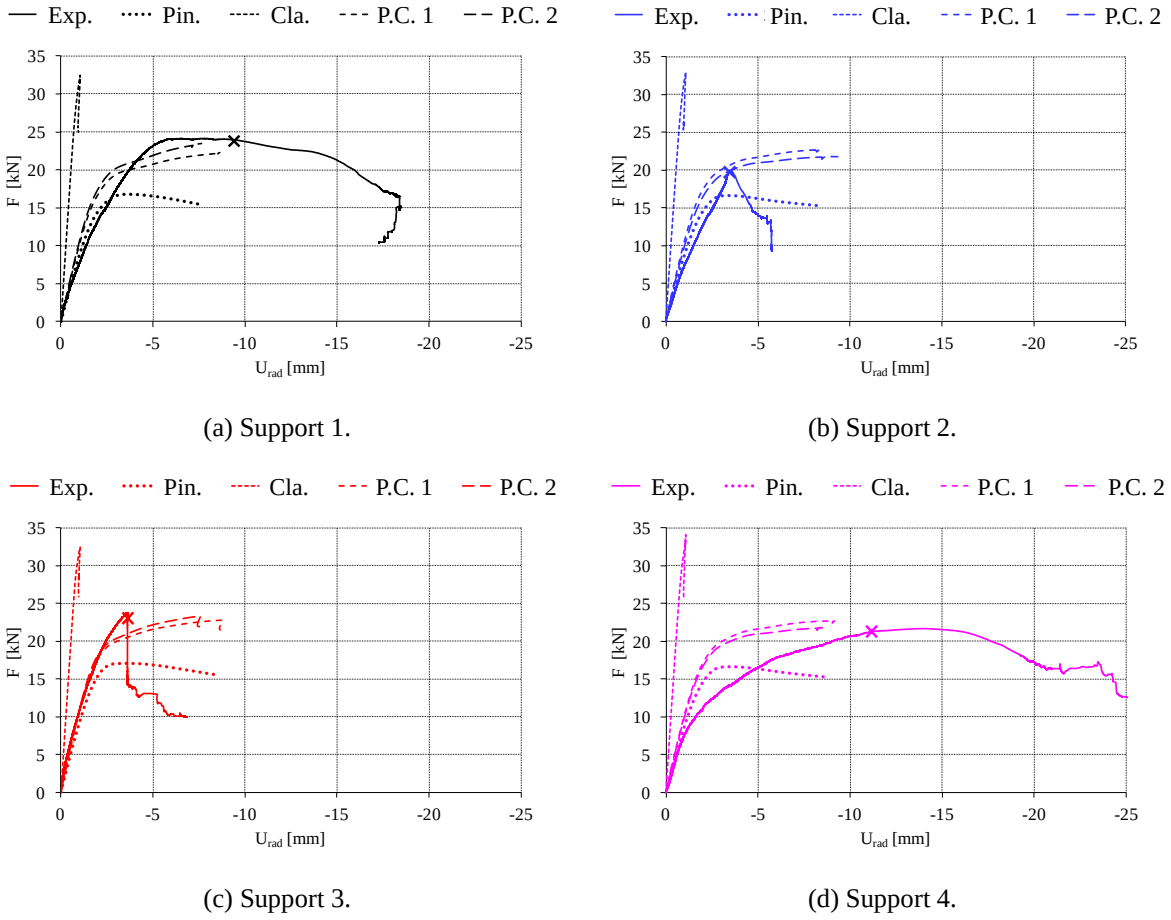

(a) Support 1.

(b) Support 2.

(c) Support 3.

(d) Support 4.

Fig. 4-57 Load-displacement diagrams: the radial displacement of the top of the engaged column versus the supporting force (EK4).

The partially restriction of the circumferential rotation φ_T of the bottom of the supporting column is modelled in Abaqus by means of a rotational spring (with stiffness C) in the reference node. Two situations are considered for the partially restriction. Firstly, the rotation stiffness C is constant for all columns (i.e. P.C. 1) to obtain the same total failure load in experimental setup and in Abaqus. However, a relatively large deviation is sometimes obtained between the experimental and the calculated load-displacement curve, especially for larger loads (for example for column 4). Therefore, a second alternative has been considered (i.e. P.C. 2) where the rotation stiffness C is varied for all columns. The constant value of C of P.C. 1 has been used as starting point of P.C. 2 and the best value of C has been determined by

iteration for each column, for which the best agreement is found between the experimental and the numerical load-displacement diagrams. In this way, a relatively good agreement is achieved between both curves for all columns, while the error on the total failure load slightly increases.

At the moment of maximum total load, the experimental failure load of the supports ranges between 19.4 and 24.1kN (See Table 4-8), while the numerical values of the models P.C. 1 and P.C. 2 are varying between 22.2-22.8kN and 20.9-23.4kN, respectively.

Conclusions

Table 4-27 gives an overview of the experimental and the GMNIA failure loads F_u and the factor k. As can be deduced from this table and also from the previously plotted results (post-buckling deformations and load-displacement diagrams), a good agreement has been found between the experimental results on the one hand and the numerical model of the cylindrical barrel with engaged columns (i.e. the second configuration) on the other hand. By using partially clamped columns, which partially restrict the circumferential rotation at the bottom of the column, the experimental results can be accurately numerically calculated.

Table 4-27 Overview failure load model 2- experiments versus Abaqus.

	EXPERIMENT	ABAQUS PINNED		ABAQUS PARTIALLY CLAMPED 1		ABAQUS PARTIALLY CLAMPED 1		ABAQUS CLAMPED	
	F_u [kN]	F_u [kN]	k_{Pin} [-]	F_u [kN]	$k_{P.C.}$ [-]	F_u [kN]	$k_{P.C.}$ [-]	F_u [kN]	k_{Cla} [-]
EK1	73.9	49.6	1.49	73.9	**1.00**	73.4	**1.01**	92.9	0.80
EK2	70.8	47.9	1.48	71.3	**0.99**	66.1	**1.07**	92.1	0.77
EK3	94.1	60.1	1.57	94.3	**1.00**	94.5	**1.00**	114.9	0.82
EK4	89.8	66.9	1.34	90.6	**0.99**	89.4	**1.00**	130.3	0.69

In Table 4-28, the rotation stiffnesses C are given for all experiments and for both partially clamped alternatives. These values have been iteratively determined until the best correspondence was found between the experimental and the numerical failure load of the structure (P.C. 1) or the experimental and the numerical load-displacement diagram of the column (P.C. 2). In general, most columns have a rotation stiffness C between 15 and 30kNm/rad.

Table 4-28 Overview rotation stiffnesses C [kNm/rad] for partially clamped columns model 2.

	EK1		EK2		EK3		EK4	
NUMBER SUPPORT	$C_{P.C.1}$	$C_{P.C.2}$	$C_{P.C.1}$	$C_{P.C.2}$	$C_{P.C.1}$	$C_{P.C.2}$	$C_{P.C.1}$	$C_{P.C.2}$
1	19.5	16.0	50.0	30.0	22.0	50.0	19.0	23.0
2	19.5	19.5	50.0	30.0	22.0	20.0	19.0	15.0
3	19.5	35.0	50.0	40.0	22.0	25.0	19.0	21.0
4	19.5	15.0	50.0	15.0	22.0	19.0	19.0	17.0

Overall, it can be concluded that the second numerical model is able to predict the elasto-plastic failure load with a very good accuracy (i.e. $0.8 < k_{P.C.} < 1.2$) and the validation of the numerical model can be regarded as successful.

5 Relationship between the influence of imperfections on the failure load and the quality tolerance class

In this section, it is checked if there is a relationship between the influence of geometrical imperfections (using the second measurement of the complete stiffened silo wall) on the one hand and the fabrication quality class on the other hand. In other words, are the out-of-roundness parameter U_r and the dimple parameter U_{0x} representative for the estimate of the (disadvantageous) influence of the measured imperfections?

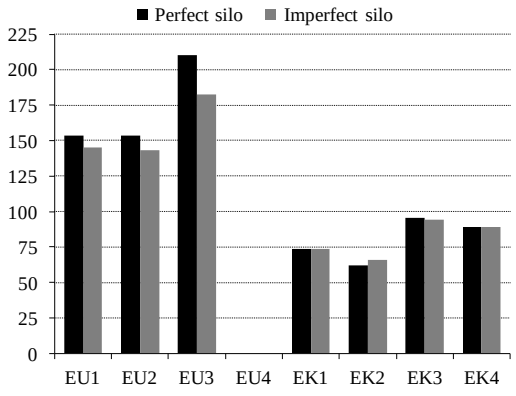

Fig. 4-58 Graphical comparison of the perfect GMNA load with the imperfect GMNIA load (the numerical model was used which gave the best agreement with the experimental results).

Using the validated numerical model (i.e. the model which shows the best agreement with the experimental results), the GMNA failure load (perfect silo wall) and the GMNIA failure load (imperfect silo wall) of each experiment are determined and plotted in Fig. 4-58. For the three models with U-shaped longitudinal stiffeners (i.e. EU1 - EU3), the imperfections always have a disadvantageous influence on the failure load, ranging from -5.5% to -13.1%. In contrast, the influence of the imperfections on the failure load is negligible in the case of the engaged columns (i.e. EK1 - EK4), ranging from -0.8% (disadvantageous) to +6.7% (advantageous). From this comparison, it can be concluded that the failure behaviour is more influenced by material non-linearity (see contourplots of the axial compressive stresses in Fig. 4-43 and Fig. 4-51) and geometric non-linearity (e.g. the

restriction of the circumferential rotation of the bottom of the engaged columns), rather than by geometrical imperfections.

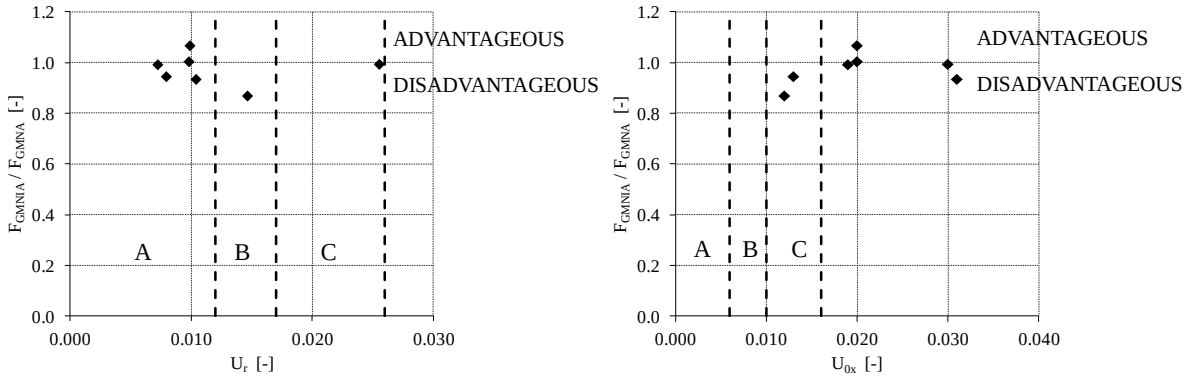

(a) ... the out-of-roundness parameter U_r. (b) ... the dimple parameter U_{0x}.

Fig. 4-59 Relationship between the ratio of the perfect and the imperfect failure load F_{GMNIA}/F_{GMNA} and ...

For all experiments, the dimensionless ratio F_{GMNIA}/F_{GMNA} is plotted against the out-of-roundness parameter U_r (Fig. 4-59 (a)) and the dimple parameter U_{0x} (Fig. 4-59 (b)) determined in Section 2. Clearly, there is no direct relationship between F_{GMNIA}/F_{GMNA} and the quality parameters according to (EN 1993-1-6, 2007).

6 Conclusions of the experimental results and validation

In this chapter, the experimental results were first discussed. In total, seven scale models were subjected to an increasing meridional compression on the upper edge of the barrel until failure occurred. The results obtained from these experiments were then used in the second part of the chapter to try to validate the numerical model. This validation has been done by performing geometrically and materially non-linear shell analyses with imperfections (GMNIA), taking into account the real material behaviour (tensile tests) and the real imperfections of the silo wall (measurement of the initial deviations perpendicular to the silo wall). In comparison with the default numerical model, the complete circumference was modelled (the imperfections were non-symmetrical in circumferential direction) and a relatively fine mesh size was adopted (partly to model the imperfections in the element nodes accurately). Furthermore, the influence of the connection of the bolted steel plate and the real supporting boundary conditions were considered to improve the agreement between the experimental and the numerical results.

For both configurations (i.e. the U-shaped longitudinal stiffeners and the engaged columns), a relatively good agreement has been found between the experimental and the numerical results. The agreement of the failure loads (and thus the quality of the numerical model) improved as the calculation was performed with increased accuracy (to reduce the error caused by

modelling simplifications).

To conclude, it can be summarized that the numerical model is able to predict the elasto-plastic failure load of axially compressed locally supported cylindrical steel silos with sufficient accuracy, and the validated finite element model can be used for further numerical research. In what follows, parametric studies will be performed to investigate the influence of many (geometrical) parameters on the failure load/-behaviour (Chapter 5) and a design rule study will be done to compare the results with the current design rule and to develop new interaction parameters (Chapter 6).

CHAPTER 5

Numerical research: parametric study

The numerical investigation of this work explores the failure behaviour of locally supported cylindrical steel silos by means of several parametric studies. In each parametric study, most parameters are kept constant, while a limited number of parameters are varied at the same time. In this way, the influence of the variable parameters can be mapped more easily.

This chapter discusses successively the influence to the failure behaviour of the mesh (i.e. element types and mesh density), the cylindrical barrel, the supporting columns, the U-shaped longitudinal stiffeners, the non-prismatic stiffeners, the ring stiffeners, the engaged columns, imperfections, the conical roof, and the conical hopper.

1 Definition of some frequently used terms

To inform the reader of the applied sign conventions, frequently used terms, nomenclature of the paths, etc., this section is especially dedicated to these issues. In this way, constant repetition of certain terms is avoided.

Dimensionless failure load and dimensionless stress

Frequently, the failure load will be expressed as a dimensionless load by dividing the value of the failure load F_u by a "reference" load F_{ref}. Generally, the failure load F_u is equal to the first maximum value of a GMNA or a GMNIA calculation. The reference load F_{ref} is calculated using Eq. (5-1) and is equal to the product of the cross-section of the silo wall A_{shell} and a reference stress σ_{ref}. This stress is equal to the minimum of the yield stress σ_y (standard value: 235MPa) and the critical buckling stress σ_{cr} (Eq. (2-1)).

$$F_{ref} = A_{shell} \cdot \sigma_{ref} = (2\pi R \cdot t) \cdot \sigma_{ref} \tag{5-1}$$

Where:

F_{ref} the reference load [kN];

R the radius of the cylinder [m];

t the thickness of the shell wall [mm];

σ_{ref} the reference stress [MPa].

When the axial stress distribution is plotted along paths, the absolute value of the axial stress σ_x or circumferential stress σ_θ is made dimensionless by dividing it by the same reference stress σ_{ref} as mentioned above.

Table 5-1 gives an overview of the reference stress σ_{ref} as a function of the radius-to-thickness ratio R/t and a Young's modulus E of 210GPa. By using the above definition of the stress, the yield stress σ_y will be used for thick-walled silos, while the critical buckling stress σ_{cr} will be applied for thin-walled silos.

Table 5-1 Reference stress as a function of the radius-to-thickness ratio R/t with $E = 210$GPa.

R/t	σ_y	σ_{cr}	$\min(\sigma_y; \sigma_{cr})$
[-]	[MPa]	[MPa]	[MPa]
100	235.0	1270.5	235.0
200	235.0	635.3	235.0
250	235.0	508.2	235.0
333.3	235.0	381.2	235.0
500	235.0	254.1	235.0
666.6	235.0	190.6	190.6
1000	235.0	127.1	127.1

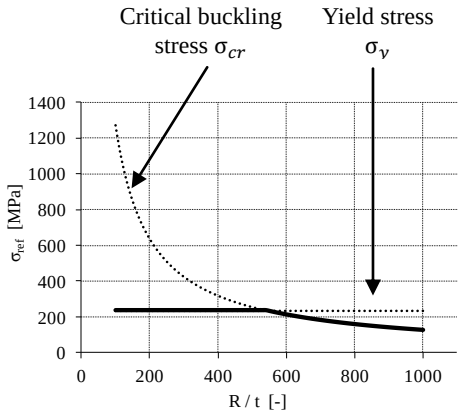

Fig. 5-1 Reference stress as a function of the radius-to-thickness ratio R/t with E = 210GPa.

Cross-section of stiffeners and cylindrical barrel

The value A_{stif} quantifies the amount of cross-sectional material of the U-shaped stiffeners or the engaged columns and can be determined using respectively Eq. (5-2) and Eq. (5-3). Frequently, this value is made dimensionless by dividing it by the cross-section of the shell surface A_{shell} (Eq. (5-4)).

$$A_{stif} = n_{sup} \cdot \left(d_{stif} + 2 \cdot w_{stif}\right) \tag{5-2}$$

$$A_{stif} = n_{sup} \cdot \left(2 \cdot d_{stif} + 2 \cdot w_{stif}\right) \tag{5-3}$$

$$A_{shell} = 2\pi R \cdot t \tag{5-4}$$

Nomenclature of the paths

In Fig. 5-2, the trajectory, the direction, and the naming of some example paths is displayed on the structure.

The circumferential paths in the silo wall are defined at a certain height h_{path} starting from the meridional in the centre of a local support ($\theta = 0°$) to the meridional midway between two supports ($\theta = 45°$) (See Fig. 5-2 (a)). For example, path PC/S-h1.10 is a circumferential path in the silo wall at a height h_{path} equal to 1.10 times the attached height of the stiffener h_{stif}^{sup}.

Table 5-2 Explanation of the nomenclature of the paths.

FIRST LETTER	SECOND LETTER = DIRECTION	/	THIRD LETTER = COMPONENT	/	H1.10 = LOCATION
P = Path	A = Axial		S = Silo wall		h + height relative to h_{stif}^{sup}
	C = Circumferential		U = prismatic U-shaped stiffener (See Fig. 5-47 (a))		
			Ur = non-prismatic U-shaped stiffener in radial direction (See Fig. 5-47 (b))		
			VU = non-prismatic U-shaped stiffener in circumferential direction (See Fig. 5-47 (c))		
			VR = rectangular shaped stiffener inclined in circumferential direction (See Fig. 5-47 (d))		
			U+VR = prismatic U-shaped stiffener + rectangular shaped stiffener inclined in circumferential direction (See Fig. 5-47 (e))		

For the different types of longitudinal stiffeners (U, Ur, VU, VR, and U+VR: abbreviations are given in Fig. 5-47), the paths together with their direction are displayed in Fig. 5-2 (b). For example, path PC/U-h0.50 is a circumferential path in U-shaped stiffener at a height h_{path} equal to 0.50 times the attached height of the stiffener h_{stif}^{sup}.

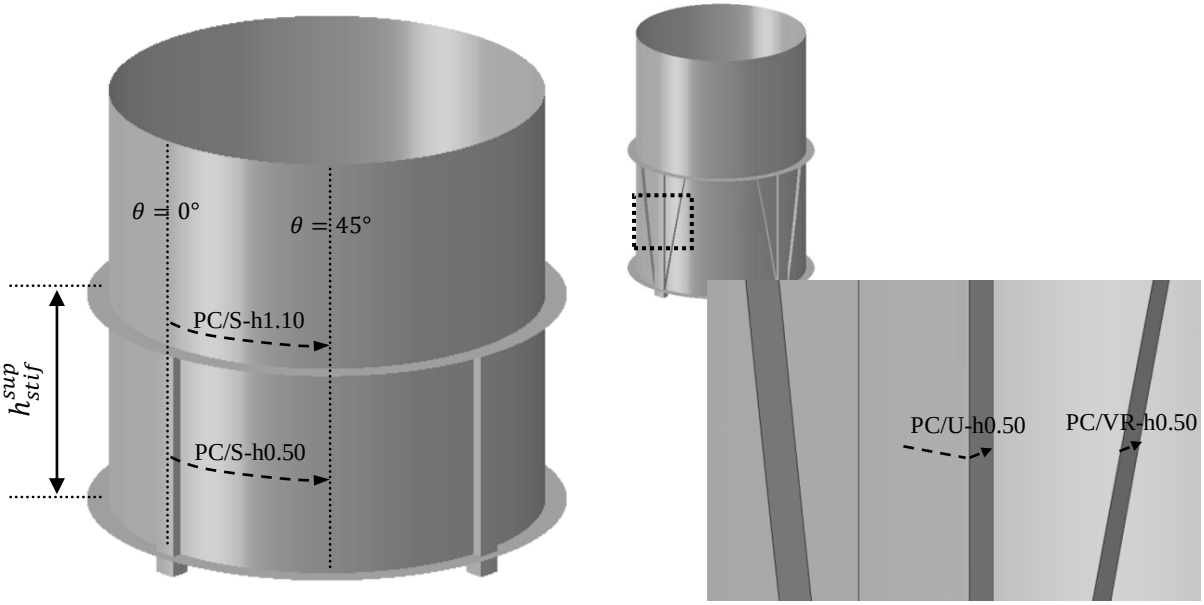

(a) Circumferential path in the silo wall.

(b) Paths in the longitudinal stiffeners.

Fig. 5-2 Graphical representation of the trajectory and the direction of the paths.

2 Mesh study

In Section 8 of Chapter 3, the mesh has been discussed in detail and a choice has been made for the mesh related parameters based on previous work of Vanlaere (2006). The mesh related parameters include the element type(s) and the mesh density in the different regions of the numerical model. In the default or reference model, S8R5 shell elements are used for all parts (except for the rigid supports) and the shell surface is divided into four regions with a variable mesh density (See Fig. 3-30). The determination of the size of these regions and the number of elements in each region and direction is calculated by Eqs. (3-23) to (3-26).

In this mesh study, the above mentioned mesh related parameters of the reference model have been questioned. This will be done in two stages: first the suitability of the S8R5 shell element is investigated (Section 2.1); afterwards a convergence study is performed to verify the mesh density (Section 2.2). For both substudies, the results (i.e. the failure behaviour and load) and the calculation cost will be compared between the "standard" model and the numerical model with variable element type or mesh. The variable geometrical parameters are given in Table 5-3 and Table 5-4. Respectively, 28 and 112 geometries were investigated for the first and second sub study. In this way, more general conclusions can be drawn.

Table 5-3 Geometrical parameters of the longitudinal stiffeners / the engaged columns (mesh study) (part 1).

COMPONENT	PARAMETER	VALUE(S)	DIMENSION
SILO	R/t	100; 200; 250; 333.3; 500; 666.6; 1000	-
	h/R	$h_{stif}^{sup}/R = 1.0$: 2.0 [b]; 10.0 [a, b] $h_{stif}^{sup}/R = 2.0$: 3.0 [b]; 10.0 [a, b]	-
STIFFENERS	n_{sup}	4	-
	Type(s)	U-shaped longitudinal stiffeners (U.S.) Engaged columns (E.C.)	
	d_{stif}/R	See Table 5-3	-
	w_{stif}/d_{stif}	U.S.: 25 E.C.: 100	%
	h_{stif}^{sup}/R	1.0; 2.0	-
	h_{stif}^{inf}/R	U.S.: / E.C.: 4.0	-
	t_{stif}/t	max. [c]	-

[a]: Mesh study 1 - Suitability of the S8R5 element

[b]: Mesh study 2 - Mesh convergence study

[c]: Minimum (min.), average (ave.), or maximum (max.) thickness - restrictions

Table 5-4 Circumferential width of the longitudinal stiffeners / the engaged columns (mesh study) (part 2).

R/t	d_{stif}/R					
	0.05	0.10	0.15	0.20	0.25	0.30
100	-	-	X [b]	-	-	X [a, b]
200	-	-	X [b]	-	-	X [a, b]
250	-	-	X [b]	-	-	X [a, b]
333.3	-	-	X [b]	-	-	X [a, b]
500	-	X [b]	-	X [a, b]	-	-
666.6	-	X [b]	-	X [a, b]	-	-
1000	-	X [b]	X [a, b]	-	-	-

[a]: Mesh study 1 - Suitability of the S8R5 element

[b]: Mesh study 2 - Mesh convergence study

2.1 Mesh study 1 - Suitability of the S8R5 element

The suitability of the choice for the S8R5 element type, which is the default element type in previous research (Vanlaere, 2006), is investigated for 28 geometries distributed over the entire range of silos considered in this work (See Table 5-3 and Table 5-4). The suitability will be verified by comparing the failure load from the "standard" model (with S8R5 elements) with the failure load obtained from models with other conventional shell elements in Abaqus (See Section 8 of Chapter 3). In total, numerical simulations were performed with seven combinations of shell elements. Two general-purpose shell elements (i.e. S4 and S4R), one thick shell element (i.e. S8R), and two thin shell elements (i.e. S4R5 and S8R5) will be considered. In addition, two extra combinations were taken into account consisting of a combination of a general or a thin shell element for the shell wall surface (i.e. S4R or S8R5) and a thick shell element for the stiffeners (i.e. S8R). An overview is given in Table 5-5. Furthermore, the influence of the type of shell elements will be investigated for five different types of shell analyses (EN 1993 1-6, 2007): LBA, GNA, MNA, GMNA, and GMNIA with an inwardly oriented weld depression (WD) type A and quality class C as imperfection shape. In total, 980 numerical simulations were performed.

Table 5-5 Combinations of shell elements.

COMBINATION	TYPE SHELL ELEMENTS	ELEMENT TYPE		
		SHELL SURFACE	LONGITUDINAL & RING STIFFENERS	ENGAGED COLUMN
1	General	S4	S4	S4
2	General	S4R	S4R	S4R
3	Thick	S8R	S8R	S8R
4	Thin	S4R5	S4R5	S4R5
5 = Reference	Thin	S8R5	S8R5	S8R5
6	General - thick	S4R	S8R	S8R
7	Thin - thick	S8R5	S8R	S8R

In the graphs below, a dimensionless failure load $\left(F_u - F_{u,ref}\right)/F_{u,ref}$ is plotted on the vertical axis, where F_u and $F_{u,ref}$ represent the failure load of respectively the model considered and the standard or reference model consisting of S8R5 elements. In other words, the reference model is conservative for positive values of the dimensionless ratio ($F_{u,ref} < F_u$), and is on the unsafe side for negative values of the dimensionless ratio ($F_{u,ref} > F_u$). On the horizontal axis, the combination of shell elements is mentioned.

In Fig. 5-3, the results are depicted for four geometries. It can be found that the deviations of the failure load relative to the failure load of the standard model are relatively limited (-2% up to $+2\%$). When considering all combinations, the deviation generally ranges between -5% up to $+5\%$ with a few peaks up to 10%. The average standard deviation is equal to $+1.28\%$. In other words, in general, the results of the S8R5 elements are slightly conservative compared to other element types. In addition to the excellent results in terms of the failure load, it is found that the standard model also performs relatively well in terms of computational time.

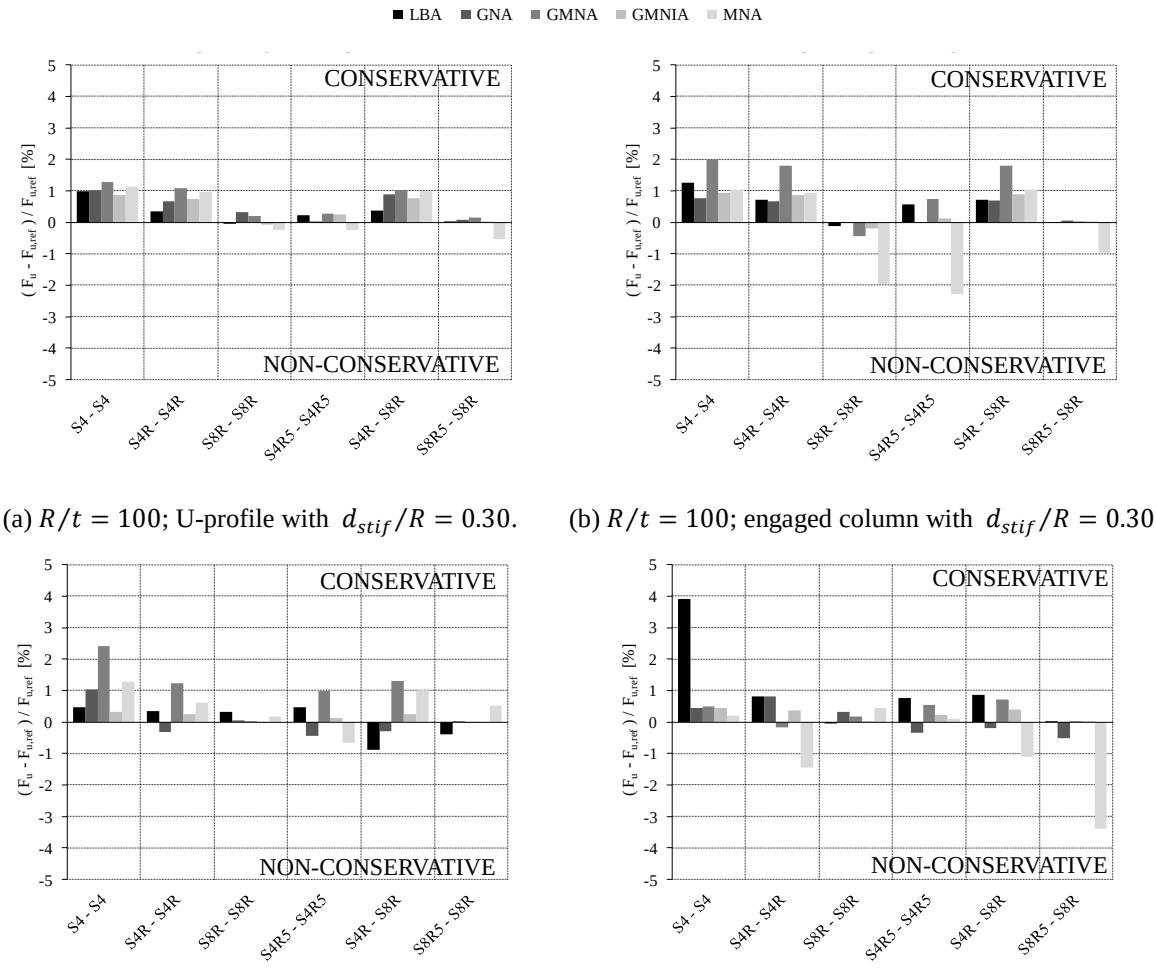

(a) $R/t = 100$; U-profile with $d_{stif}/R = 0.30$.

(b) $R/t = 100$; engaged column with $d_{stif}/R = 0.30$.

(c) $R/t = 500$; U-profile with $d_{stif}/R = 0.20$.

(d) $R/t = 500$; engaged column with $d_{stif}/R = 0.20$.

Fig. 5-3 Influence of the element type on the failure load for different types of shell analyses ($h_{stif}^{sup}/R = 2.0$).

To conclude, it seems that the S8R5 elements are appropriate for the numerical research to locally supported cylindrical steel silos.

2.2 Mesh study 2 - Mesh convergence study

A frequently used approach for mesh convergence studies is to search a mesh which provides almost the same results as a more refined mesh. A possible criterion is that the model is converged as the failure load is changed less than 1% as a result of a doubling of the mesh size. This criterion will be used here.

For 112 geometries distributed over the entire range of silos considered (See Table 5-3 and Table 5-4), 1008 GMNA calculations were performed with a numerical model consisting of S8R5 elements with nine different mesh densities. The variable mesh density d_{mesh} is equal to 15%, 25%, 50%, 75%, 100%, 125%, 150%, 175%, and 200% of the mesh density of the reference model d_{ref} (See Section 8 in Chapter 3). The ratio d_{mesh}/d_{ref} is shown on the horizontal axis in Fig. 5-4. On the left vertical axis, the dimensionless GMNA failure load

F_u/F_{ref} is shown, on the right vertical axis the average computational time per increment relative to the reference model is depicted. For all cases, the (dimensionless) failure load exhibits an asymptotic progress with increasing mesh density. More important is that the mesh density of the reference model (i.e. $d_{mesh}/d_{ref} = 100\%$) is always situated in the approximately horizontal plateau and that a doubling of the mesh size leads to minor changes in failure load (less than 1%). Moreover, the average calculation time per increment is still relatively small compared to those of finer meshes. Very similar results are found for geometries which are not included in this work. In other words, this study confirms that the mesh density adopted by (Vanlaere, 2006) is sufficiently refined and that, both in terms of failure load and computational time, there is no reason to adjust the reference mesh density.

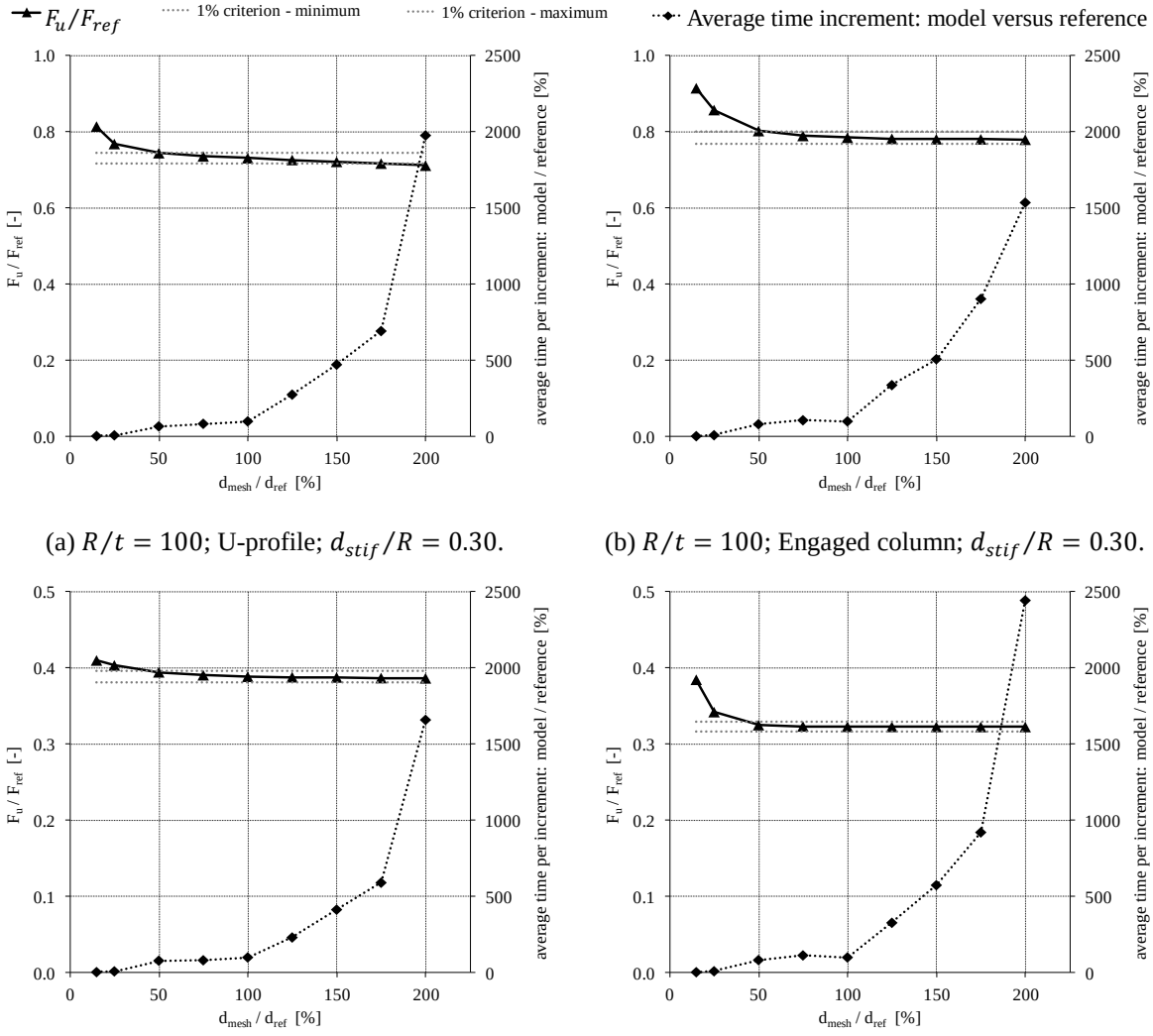

(a) $R/t = 100$; U-profile; $d_{stif}/R = 0.30$.

(b) $R/t = 100$; Engaged column; $d_{stif}/R = 0.30$.

(c) $R/t = 500$; U-profile; $d_{stif}/R = 0.10$.

(d) $R/t = 500$; Engaged column; $d_{stif}/R = 0.10$.

Fig. 5-4 Influence of the mesh density on the dimensionless GMNA failure load F_u/F_{ref} and the computational time ($h_{stif}^{sup}/R = 1.0$; $h/R = 10.0$).

Subsequent to the above study, it was also examined whether an increase of the area of the finest mesh (i.e. zone 1 in Fig. 3-31) has an influence on the results. This study demonstrated that an increase of the region of finest mesh in radial or axial direction not affects or hardly affects the failure load. In other words, the subdivision of the numerical model in regions with finer and coarser meshes can be used in further numerical research without problems.

3 Silo geometry

The cylindrical barrel has three geometrical parameters, namely the silo radius R, the silo thickness t (constant over the entire height), and the silo height h. In this order, their influence will be investigated on the failure behaviour one by one.

3.1 Silo radius

The cylinder radius R is the only parameter which gets an absolute value, while all other geometrical parameters will be expressed as dimensionless parameters relative to the cylinder radius. To convert the failure load of the default cylinder radius (i.e. 1.0m) to another cylinder radius, Eq. (3-2) can be used. To be sure the above reasoning and method is valid, numerical simulations were performed with a silo radius equal to 1.0m and 3.0m for a wide range of stiffening configurations and different shell calculations. It is expected that the failure load corresponding with a 3m radius silo is exactly 9 times (i.e. $(3m/1m)^2$) larger than the failure load of a 1m radius silo.

In Fig. 5-5, the GMNA failure load F_u is plotted against the ratio of the cross-section of the stiffener/column to the cross-section of the cylindrical barrel A_{stif}/A_{shell} for thick-walled and thin-walled silos (i.e. $R/t = 200$ and 1000) and both for U-shaped stiffeners and engaged columns. For all cases, similar curves are found for both cylinder radii, and if $F_u^{R=3m}$ is divided by $F_u^{R=1m}$, a value of 9 is always obtained. In other words, an increase in cross-section of the stiffener/column has relatively speaking the same influence on the failure behaviour and load in a 1m radius silo as in a 3m silo radius, on the condition that all other geometrical parameters are expressed as dimensionless parameters relative to the cylinder radius R and are kept constant. Similar results are found for other calculation types (LBA, GNA, and MNA).

Conclusions

To conclude, Eq. (3-2) is valid for the conversion of the failure load between silos with different radii. Last, and most important, is that the results, trends, and findings conducted in this work derived from 1m radius silos are also applicable for cylindrical silos with other radii, for perfect as well as for imperfect silos.

When the silo radius R changes with a factor s and the radius-to-thickness ratio R/t remains constant, then the initial (equivalent) imperfection shape introduced in the silo wall is scaled with the same factor s. Using Eqs. (2-46) to (2-48), it can be calculated that the ratio of the imperfection amplitude and the silo wall thickness δ_{max}/t increases with the same factor s. Furthermore, the size of the imperfection in circumferential and meridional direction will also scale with the same factor s, for weld depressions (Eqs. (2-44) and (2-45)) as well as for imperfection shapes where a preceding numerical analysis is required (e.g. a linear bifurcation mode of the perfect shell).

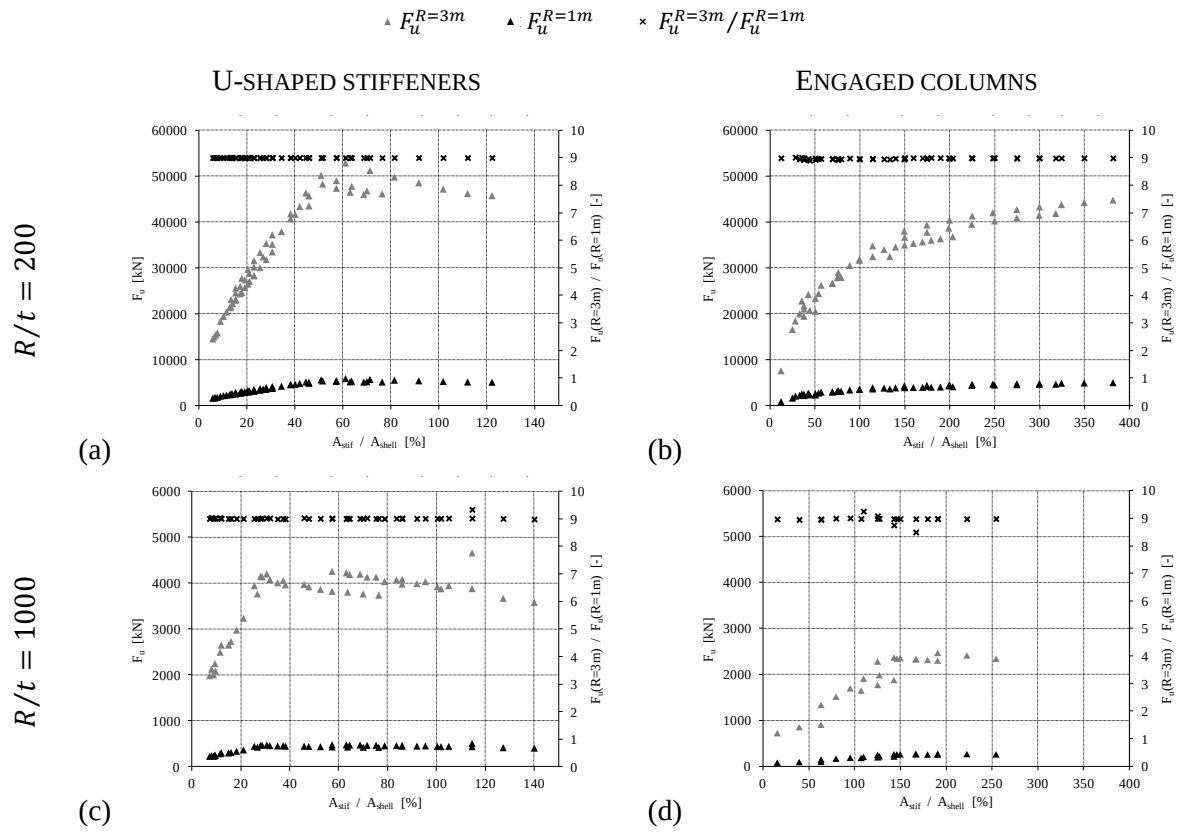

Fig. 5-5 Influence of the cylinder radius R for U-shaped stiffeners/engaged columns with a variable cross-section A_{stif} on the GMNA failure load F_u.

3.2 Radius-to-thickness ratio

The thickness t or radius-to-thickness ratio R/t is by far the most important geometrical parameter of the cylindrical barrel. In this work, the value of R/t is varied in the range from 100 to 1000 (See Section 7 of Chapter 3). By increasing the radius-to-thickness ratio R/t, the failure behaviour will shift from plastic yielding to elastic buckling. Of course, the transition between these two types of failure is not suddenly, but extends over a transition range of R/t values where both plasticity and elastic buckling influence the failure behaviour and consequently the failure load. In addition, it is important to mention that it is assumed that the thickness remains constant over the entire surface of the cylindrical barrel.

For 4 U-shaped longitudinal stiffeners (Fig. 5-6 (a)) and for 4 engaged columns (Fig. 5-6 (b)), the GMNA failure load F_u is plotted against the radius-to-thickness ratio R/t. From this figure, it is immediately clear that the failure load F_u strongly increases as the radius-to-thickness ratio R/t decreases. At larger values of R/t (> 500), the increase in failure load is rather moderate, while at smaller values of R/t (< 500), the increase in failure load is rapidly growing and is relatively large. When the silo thickness t is increased by a factor X, then the failure load F_u will be increased by a value greater than X. For example, the ratio of the thicknesses between the most thick-walled silo (i.e. $R/t = 100$) and the most thin-walled silo (i.e. $R/t = 1000$) is equal to ten, while the failure load will increase by a factor greater than ten (in this case: up to 28 Fig. 5-6 (a) and 44 in Fig. 5-6 (b)). When two relatively thin silos are compared with each other (e.g. $R/t = 800$ and $R/t = 1000$ with $X = 1.25$), the increase of the failure load is substantially smaller than the other example: up to 1.32 in Fig. 5-6 (a) and 1.31 in Fig. 5-6 (b)). In other words, there is a large difference in gain between the thin-walled silos (which fail by pure elastic buckling) and the thick-walled silos silos (which fail by (elasto-)plastic collapse).

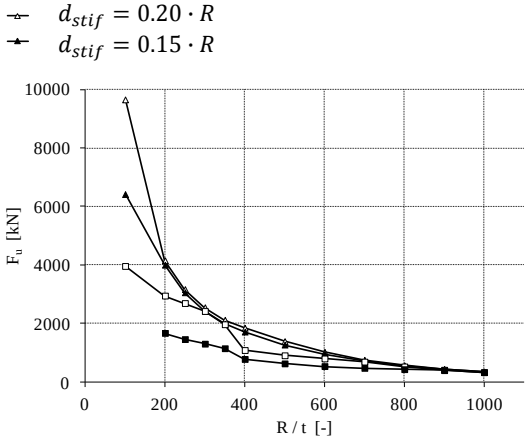

(a) For U-shaped stiffeners ($w_{stif} = 30\% \cdot d_{stif}$).

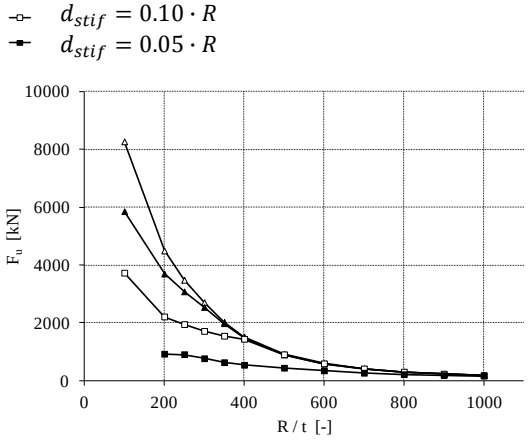

(b) For engaged columns ($w_{stif} = 100\% \cdot d_{stif}$).

Fig. 5-6 Influence of the radius-to-thickness ratio R/t on the GMNA failure load F_u ($h_{stif}^{sup}/R = h_{stif}^{inf}/R = 1.0$; t_{stif}/t = max.).

It is also noteworthy that the influence of the stiffener/column cross-section is much larger for thick-walled silos than for thin-walled silos. Indeed, the spread on the failure load in Fig. 5-6 increases when the value R/t decreases (thin → thick). For thin-walled silos, elastic buckling will occur at relatively small stress levels and most stiffeners/columns do not have any problem to absorb the rather limited reaction forces and to gradually transfer these forces into the silo wall. In most cases, buckling will occur in the unstiffened silo wall above the stiffener/column, and the critical stress mainly depends on the thickness and deformations in the silo wall at that point, rather than on the dimensions of the stiffener/column. This is the reason why the cross-section of the stiffener/column has a smaller influence on the failure load. In contrast, for thick-walled silos, a large region of yield stresses will develop in the

unstiffened silo wall and in that case, it is important that the stiffener/column can absorb a sufficiently large force to maximise the ultimate strength in the silo wall (depending on the yield stress). Hence, the reason that the cross-section of the stiffener/column plays a much greater role in thick-walled silos.

Next, for a U-shaped stiffener and for an engaged column (with $d_{stif}/\mathrm{R} = 0.20$), the failure behaviour will be investigated by comparing the GMNA failure load with the MNA load (only plastic yielding) and the GNA load (pure elastic buckling) (See Fig. 5-7). The ratio of the GMNA to the MNA load is equal to the dimensionless (plastic) resistance χ and expresses the degree of plasticity. The degree of elasticity is determined by means of the ratio of the GMNA to the GNA load and is called the dimensionless elastic resistance Λ. In a modified capacity curve, this ratio is equal to the ratio of the relative generalised stiffness $\chi \cdot \lambda^2$ and the elastic imperfection reduction factor α. The fourth and last curve in Fig. 5-7 represents the relative slenderness λ.

Fig. 5-7 will be clarified by splitting up both graphs into zones with different failure behaviour. In the case of thin-walled silos (i.e. $R/t \geq 500$ or $\lambda \geq 1$), the GMNA failure load is equal to the GNA failure load, or, in other words, plasticity is not involved in the analysis and the degree of elasticity Λ is equal to the unity. In this zone, failure of the silo will occur by elastic buckling only. By increasing the thickness of the silo wall ($R/t < 500$), the degree of elasticity Λ decreases, while the degree of plasticity χ increases. For the U-shaped longitudinal stiffener, the latter evolves to the unity. In other words, if $R/t = 100$, the failure phenomenon is pure plastic yielding, and in the intermediate region ($100 < R/t < 500$), failure will occur by an interaction of elastic buckling and plastic yielding (i.e. plastic buckling). In contrast, for the considered engaged column, the value χ is always smaller than the unity, which implies that, for this specific column geometry, the silo with intermediate and thick silo wall thickness (i.e. $R/t < 500$ or $\lambda < 1$) will fail by elasto-plastic collapse. Full plastic yielding, without the interaction of stability, does not occur for this specific column geometry, but can certainly occur with thick-walled silos in combination with other engaged columns.

This illustrative example has made it clear that the boundaries between the different failure phenomena depend on the stiffening configuration. In other words, it is difficult to say exactly at which value of the ratio R/t the failure phenomenon will change. Furthermore, the failure phenomenon is influenced by other geometrical parameters (e.g. the height of the stiffener/column) and of course also by the yield stress σ_y. To conclude, the only way to be able to determine precisely what the type of failure occurs, is not only to perform a GMNA calculation, but also to execute additional calculations, such as MNA and GNA calculations.

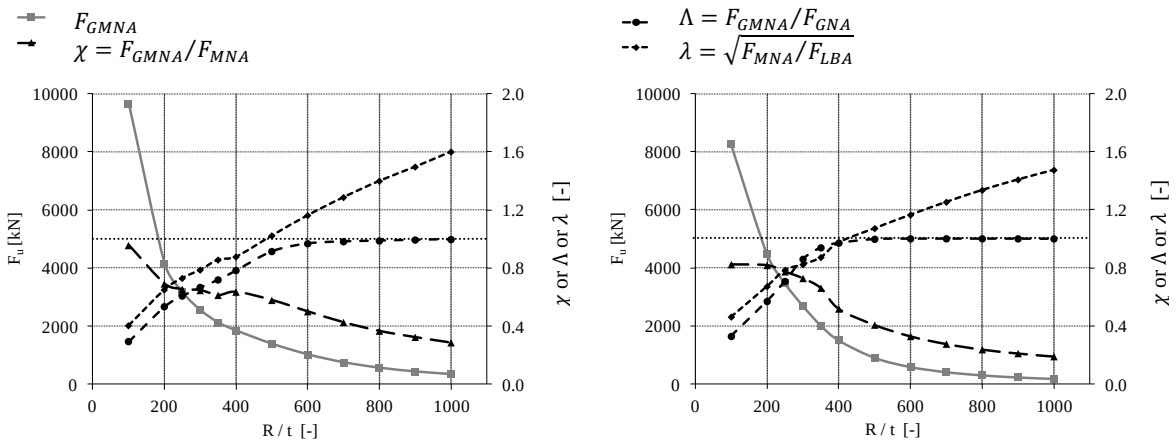

(a) For a U-shaped stiffener with $d_{stif}/\mathrm{R} = 0.20$; $w_{stif} = 30\% \cdot d_{stif}$.

(b) For an engaged column with $d_{stif}/\mathrm{R} = 0.20$; $w_{stif} = 100\% \cdot d_{stif}$.

Fig. 5-7 Influence of the radius-to-thickness ratio R/t on the GMNA failure load F_u, the dimensionless strength χ, the dimensionless elastic strength Λ, and the relative slenderness λ ($h_{stif}^{sup}/R = h_{stif}^{inf}/R = 1.0$; t_{stif}/t = max.).

When thickening the silo wall, both the stress field and the deformations of the structure are influenced, influencing the failure behaviour and consequently the maximum load. This will be illustrated in Fig. 5-8 and Fig. 5-9 for one column geometry. Similar findings can be found for other column geometries or for silos stiffened with U-shaped longitudinal stiffeners.

At the moment of failure (i.e. the first maximum load), the axial stresses in the whole structure (Fig. 5-8 (a)) and the maximum axial stress in the silo wall (Fig. 5-8 (b)) both increase with an increased silo thickness t. For the most thick-walled silo ($R/t = 200$), the axial stresses reach 1.15 times the yield stress σ_y in the silo wall in a rather extensive area above the termination of the columns. In contrast, as the silo thickness t decreases (increase of R/t), the axial stresses remain far below the yield stress in the whole structure. For the most thin-walled silo ($R/t = 1000$), the maximum axial stress is equal to 23% of the maximum yield stress (i.e. $1.15 \cdot \sigma_y$) and is 49% of the elastic critical buckling stress σ_{cr}.

The post-buckling deformed shape of the silo is also completely different between the thick and the thin silo wall (Fig. 5-9 (a)). The yielding region above the column will deform plastically for the thick-walled silos (elasto-plastic collapse), while two buckles are formed besides the top of the column when the silo is thin-walled (pure elastic buckling). Furthermore, the radial displacement U_R of the top of the column at the moment of failure also increases because of the increased failure load (See Fig. 5-9 (b)).

Conclusions

From the above, it is clearly demonstrated that the radius-to-thickness ratio R/t has the most significant impact on the failure behaviour and the corresponding failure load.

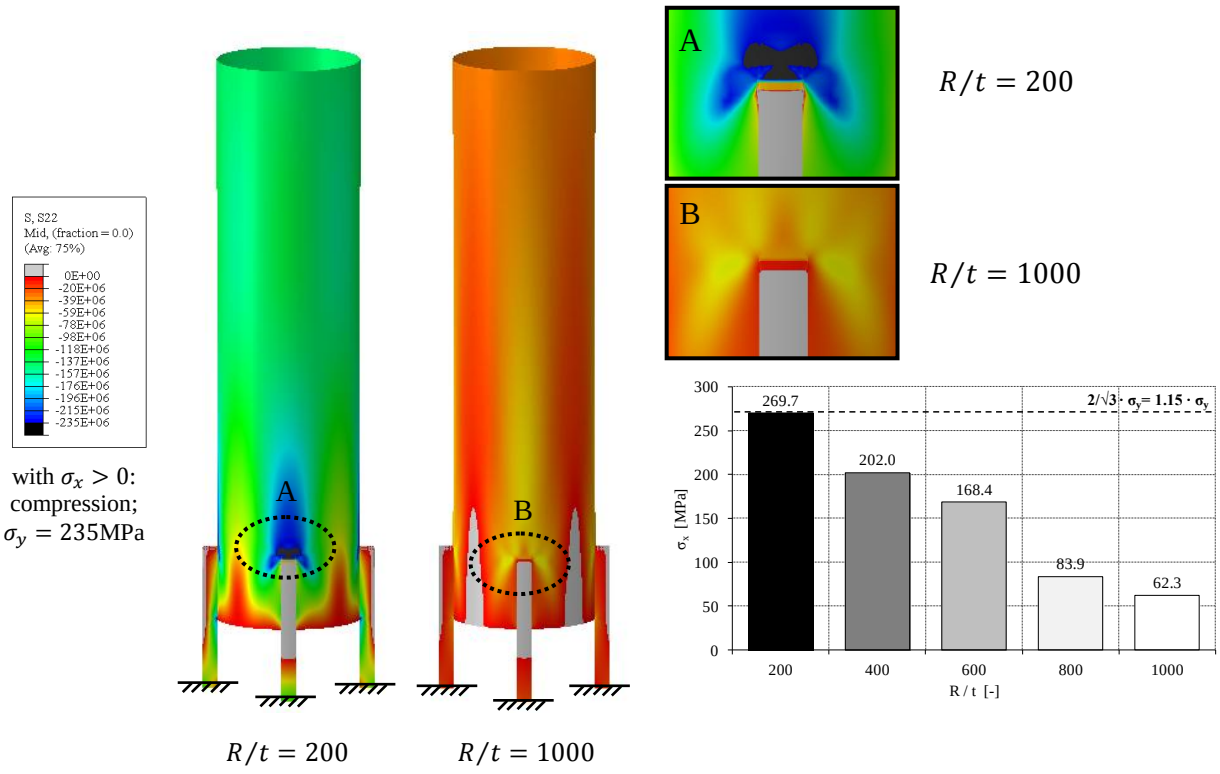

(a) Contourplots of the axial stresses σ_x [Pa].

(b) Maximum axial stress σ_x in the silo wall.

Fig. 5-8 Influence of the radius-to-thickness ratio R/t on the stress pattern at the moment of failure (engaged column with $d_{stif}/\mathrm{R} = 0.20$; $w_{stif} = 100\% \cdot d_{stif}$; $h_{stif}^{sup}/R = h_{stif}^{inf}/R = 1.0$; t_{stif}/t = max.).

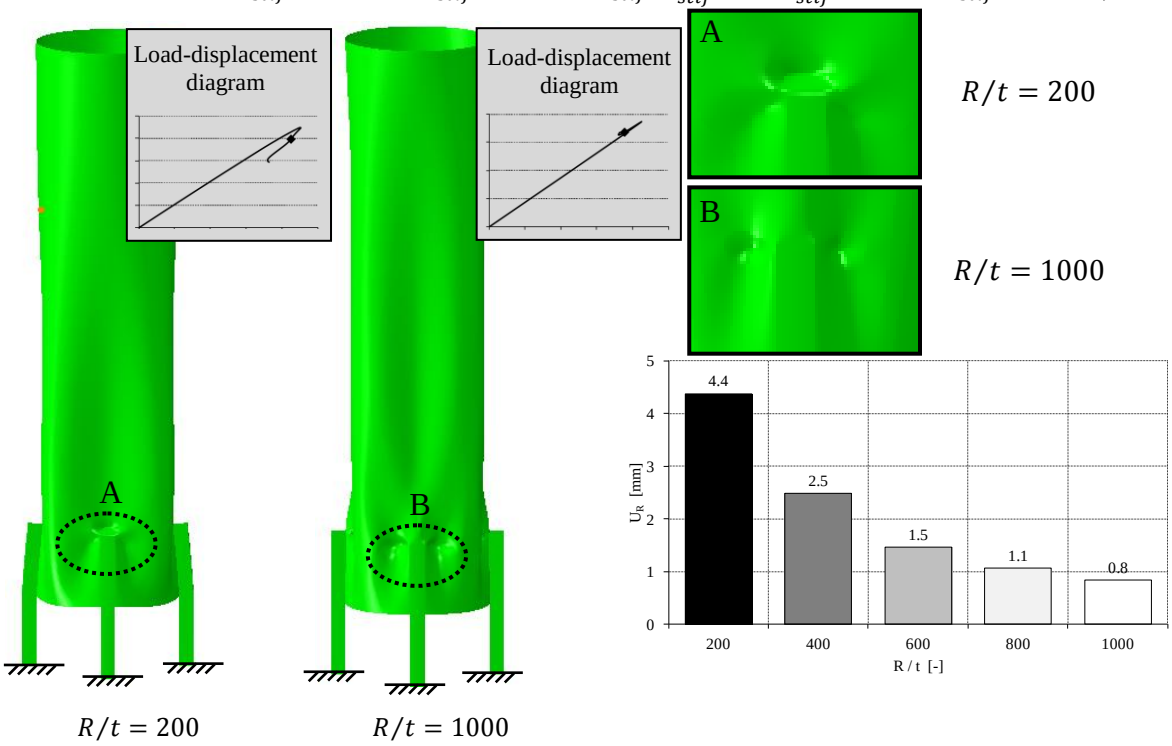

(a) Contourplot of the post-buckling deformations (deformation scale factor: 15x).

(b) Inward radial deformation U_R of the top of the column at the moment of maximum load.

Fig. 5-9 Influence of the radius-to-thickness ratio R/t on the deformations at and after failure (engaged column with $d_{stif}/\mathrm{R} = 0.20$; $w_{stif} = 100\% \cdot d_{stif}$; $h_{stif}^{sup}/R = h_{stif}^{inf}/R = 1.0$; t_{stif}/t = max.).

3.3 Silo height

The silo height influences the failure behaviour due to two reasons. Firstly, boundary conditions are coupled to the upper edge of the cylindrical barrel imposing that the circular shape is maintained due to the presence of the (non-modelled) roof (See Section 9 in Chapter 3). Secondly, the uniform line load is applied at the upper edge (See Section 10 in Chapter 3). As a result of the presence of the boundary conditions and the loading at the upper edge, the stress field (more uniform) and deformations (partially restricted) are influenced in the vicinity of the upper edge. For short cylinders, with a small distance between the top of the barrel and the location of failure, the failure behaviour will be strongly affected. In contrast, if the upper edge is far removed from the zone where yielding and/or elastic buckling occurs, a change in height does not affect the failure behaviour and the failure load anymore.

In this study, the effect of the silo height is being investigated for approximately 290 different geometries, which equates to 2160 GMNA calculations. In this way, the effect of the silo height can be studied for a whole range of different geometries.

To know the exact influence of the height, the dimensionless GMNA failure load F_u/F_{ref} is plotted against the ratio of the cylinder height to the cylinder radius h/R in Fig. 5-10 for a number of U-shaped stringer stiffeners and engaged columns and for different radius-to-thickness ratios (i.e. $R/t = 200; 500$). In this way, the influence can be observed for both stiffening configurations and for different failure phenomena.

For the U-shaped stiffeners, a similar trend is observed for all cases, independently of the radius-to-thickness ratio R/t of the silo and the geometry of the stringer stiffeners. With increasing silo height h, the failure load first decreases (short silos, here: $h/R \leq (h/R)_t = 3.0$) and then remains constant (intermediately high and high silo, here: $h/R > (h/R)_t = 3.0$). In other words, if the height is chosen large enough, the failure load and behaviour are independent of the silo height (i.e. the horizontal plateau in Fig. 5-10 (a) and (b)).

For silos supported by engaged columns, different trends have been observed when the silo height h is changed, depending on the radius-to-thickness ratio R/t and the geometry of the column. When the silo height h increases for thick-walled silos (See Fig. 5-10 (c) with $R/t = 200$), the failure load first decreases (short silo, here: $h/R \leq 2.0$), then increases (intermediately high silos, here: $2.0 < h/R \leq 6.0$), and finally remains constant (high silos, here: $h/R > 6.0$). For thin-walled silos (See Fig. 5-10 (d) with $R/t = 500$), the influence of the silo height depends on the cross-section of the geometry (here: d_{stif}/R has been varied). When the silo height h increases for columns with a small cross-section (small value of d_{stif}/R), the failure load first increases (short and intermediately high silos, here: $h/R \leq 6.0$) and then remains constant (high silos, here: $h/R > 6.0$). For columns with a larger cross-section (large value of d_{stif}/R), the failure load first increases (short and intermediately high

silos, here: $h/R \leq 4.0$), then suddenly decreases (intermediately high silos, here: $4.0 < h/R \leq 6.0$), and finally remains constant (high silos, here: $h/R > 6.0$).

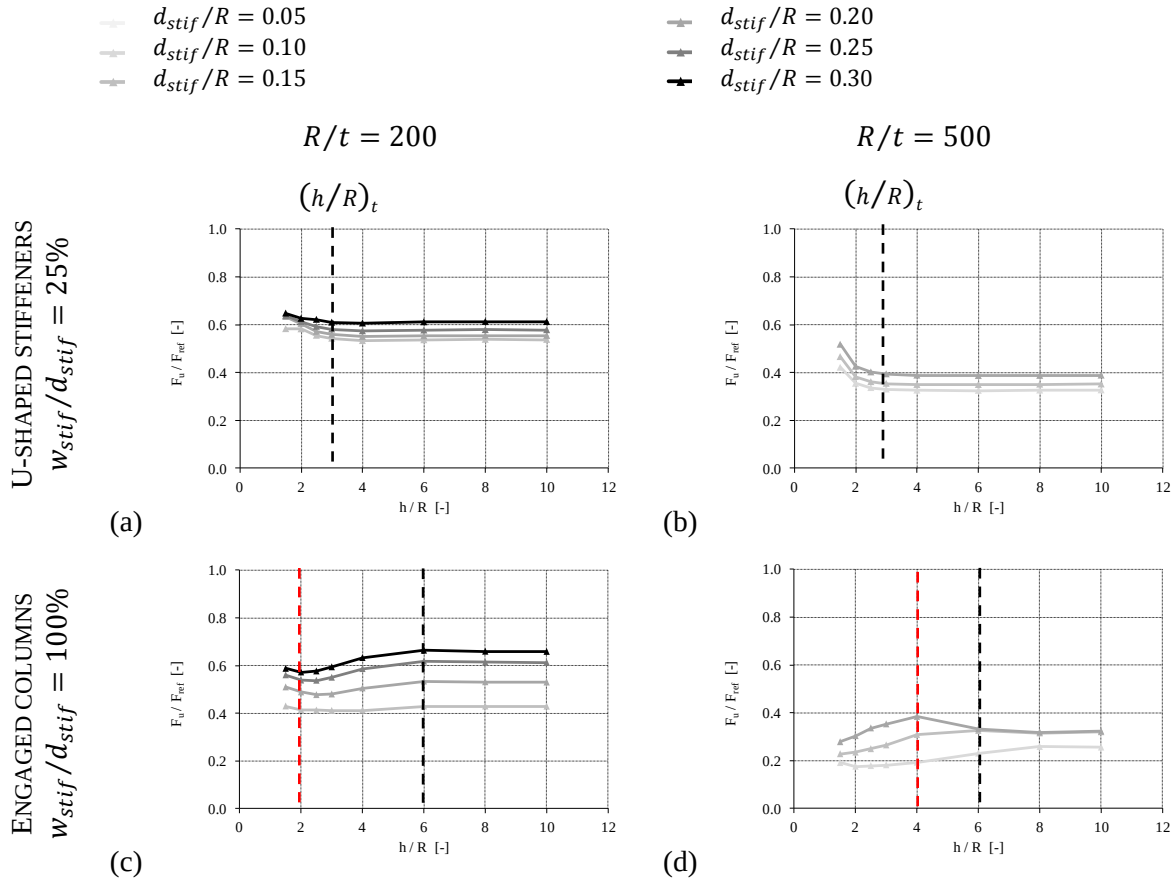

Fig. 5-10 Influence of the cylinder height to cylinder radius h/R to the dimensionless GMNA failure load F_u/F_{ref} for U-shaped stiffeners/engaged columns ($h_{stif}^{sup}/R = 1.0$; $h_{stif}^{inf}/R = 4.0$; t_{stif}/t = max.).

The above-mentioned trends (failure load F_u versus silo height h) and the limits of h/R between short, intermediately high, and high silos are not only valid for a radius-to-thickness ratio R/t equal to 200 and 500 and attached height h_{stif}^{sup}/R equal to 1.0; it is important to mention that similar trends were also found for other radius-to-thickness ratios (i.e. $R/t = 100; 250; 333; 666; 1000$) and for other attached heights (i.e. $h_{stif}^{sup}/R = 0.5; 1.5; 2.0$).

Indeed, for silos which fail by plastic yielding and elasto-plastic buckling ($100 \leq R/t < 500$), similar trends/limits can be observed as for $R/t = 200$. For silos which fail by pure elastic buckling ($R/t \geq 500$), the trends derived for $R/t = 500$ can be applied.

The limits of h/R between short, intermediately high, and high silos are not constant and also depend on other factors. For example, in Fig. 5-10 (d), the influence of the silo height depends on the cross-section of the column (d_{stif}/R). For U-shaped stiffeners, the transition height $(h/R)_t$ between a short silo and an intermediately high silo will increase when the attached stiffener height h_{stif}^{sup} increases. From this study, it has found that the transition height h_t is

approximately equal to the stiffener height h_{stif}^{sup} plus two times the cylinder radius R.

$$h_t = h_{stif}^{sup} + 2R \tag{5-5}$$

In what follows, the influence of the stiffener height h to the failure behaviour will be discussed by means of contourplots of the failure pattern and graphs of the axial stresses/deformations in circumferential direction at the height of failure.

U-shaped stiffeners with $R/t = 200$

In Fig. 5-11 (a), contourplots of the axial stress field at the moment of maximum load are depicted for three different silo heights. In all cases, elasto-plastic failure will occur in the silo wall just above terminations of the U-shaped stiffeners. On the basis of these contourplots, the minimal differences in axial stresses at the moment of maximum load cannot be detected by eye. Therefore, additional plots are generated of the dimensionless displacements U_R/t (the radial displacement component divided by the silo wall thickness) and the dimensionless stress σ_x/σ_y (the axial stress at the moment of failure divided by the yield stress) along path PC/S-h1.15 at the moment of maximum load (respectively plotted in Fig. 5-11 (b) and (c)).

From Fig. 5-11 (b), it can be seen that both the inwardly oriented (when $\theta < 22.5°$) and the outwardly oriented (when $\theta > 22.5°$) displacements increase as the silo height h increases. This can be attributed to the larger distance between the location being examined, and the upper edge of the cylindrical barrel where all horizontal displacements are completely restricted. The larger inwardly oriented deformations at $\theta = 0°$ (i.e. the location of yielding) cause a **flattening effect** of the silo wall, as a result of which the **effective yield stress** σ_y^{eff} slightly **decreases** (See $\theta = 0°$ in Fig. 5-11 (c)).

In Fig. 5-11 (c), for the shorter silos (here: $h/R \leq 3.0$), the axial stresses decrease over the entire circumference when the silo height h increases (partly due to the lower effective yield stress), resulting in a smaller failure load F_u. For intermediately high silos (here: $3.0 < h/R < 8.0$), the axial stresses in the second part of the curve ($\theta > \pm 22.5°$) start to increase again as the silo height h increases. Now, the decrease of axial stresses in the first part of the curve is about as large as the increase in the second part, resulting in a constant failure load F_u. For high silos (here: $h/R \geq 8.0$), the axial stress distribution remains more or less constant and the failure load F_u is independent of the silo height.

The relationship between the deformations before failure (i.e. flattening of the silo wall) and the reduction of the effective yield stress σ_y^{eff} will be discussed in detail in Section 3.4.

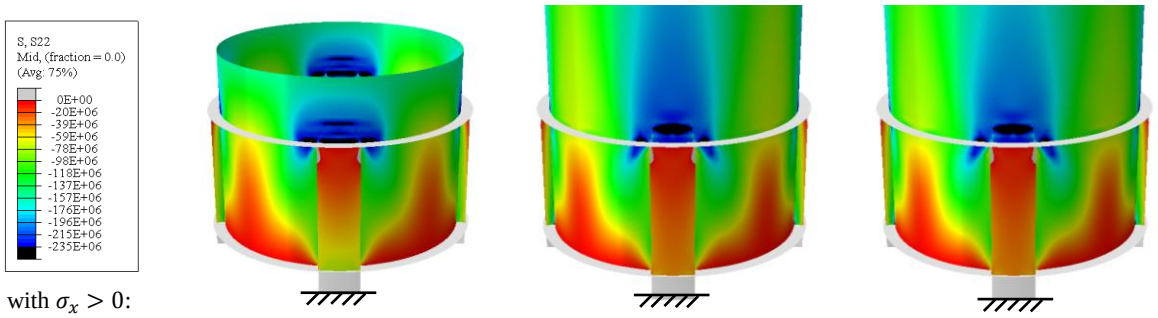

(a) Contourplots of axial stress σ_x at the moment of failure [Pa].

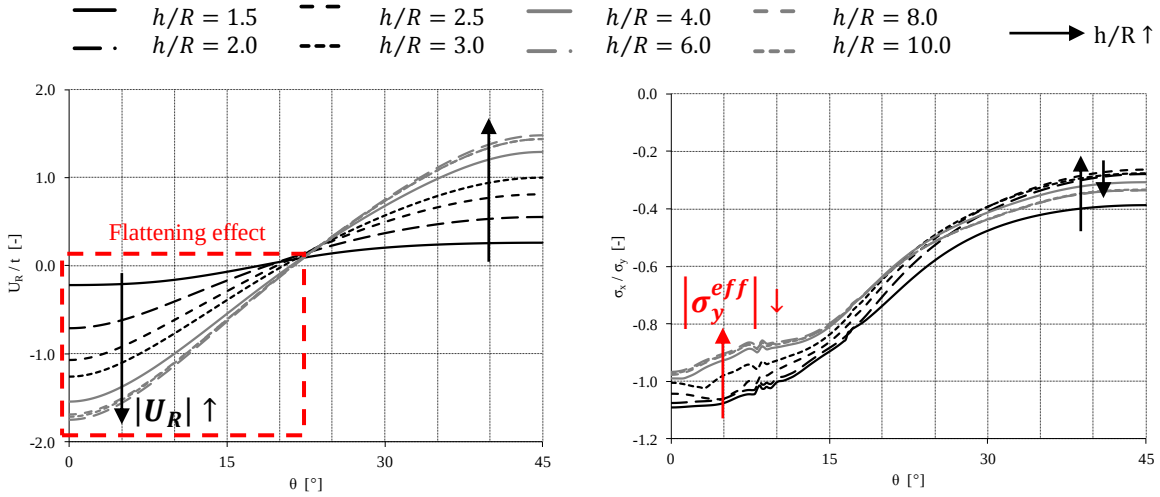

(b) Plot of the ratio of the radial displacement at the moment of failure to the silo wall thickness U_R/t [-] against the circumferential angle θ [°] for a circumferential path PC/S-h1.15 ($h_{path}/h_{stif}^{sup} = 1.15$).

(c) Plot of the ratio of the axial stress at the moment of failure to the yield stress σ_x/σ_y [-] against the circumferential angle θ [°] for a circumferential path PC/S-h1.15 ($h_{path}/h_{stif}^{sup} = 1.15$).

Fig. 5-11 Influence of the ratio of the height to the radius of the silo h/R on the failure behaviour (U-shaped longitudinal stiffener with $d_{stif}/\mathrm{R} = 0.30$; $w_{stif}/d_{stif} = 25\%$; $h_{stif}^{sup}/R = 1.0$; t_{stif}/t = max.).

U-shaped stiffeners with $R/t = 500$

For three different silo heights, the post-buckling deformations are depicted in Fig. 5-12 (a). For all cases, the location of elastic buckling is situated in the silo wall just above terminations of the U-shaped stiffeners.

In Fig. 5-12 (b), the dimensionless radial displacements U_R/t (i.e. the radial displacement at the moment of failure divided by the silo wall thickness) are given along path PC/S-h1.15. Again, the deformations (both inwardly and outwardly oriented) increase as the silo height h increases because of the larger distance between the location being examined, and the upper edge of the cylindrical barrel where all horizontal displacements are completely restricted. The larger inwardly oriented deformations cause a **flattening effect** of the silo wall, resulting in a **decrease of the critical buckling stress** σ_{cr} (See $\theta = 0°$ in Fig. 5-12 (c)).

In Fig. 5-12 (c), the dimensionless stress σ_x/σ_y (the axial stress at the moment of failure divided by the yield stress) is plotted along path PC/S-h1.15. At first instance, it can be noted that this value is always smaller than the unity, which means that failure is purely elastic (without yielding). For shorter silos (here: $h/R \leq 3.0$), the axial stresses decrease over the entire circumference when the silo height h increases (partly due to the lower critical buckling stress), resulting in a smaller failure load F_u. For intermediately high silos (here: $3.0 < h/R < 8.0$), the axial stresses in the second part of the curve ($\theta > \pm 22.5°$) start to increase again as the silo height h increases. Now, the decrease of axial stresses in the first part of the curve is about as large as the increase in the second part, resulting in a constant failure load F_u. For high silos (here: $h/R \geq 8.0$), the axial stress distribution remains more or less constant and the failure load F_u is independent of the silo height.

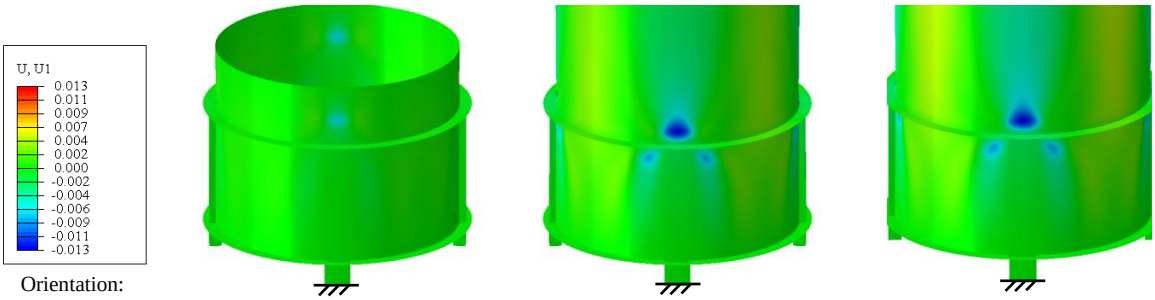

(a) Contourplots of post-buckling radial deformations U_R [m].

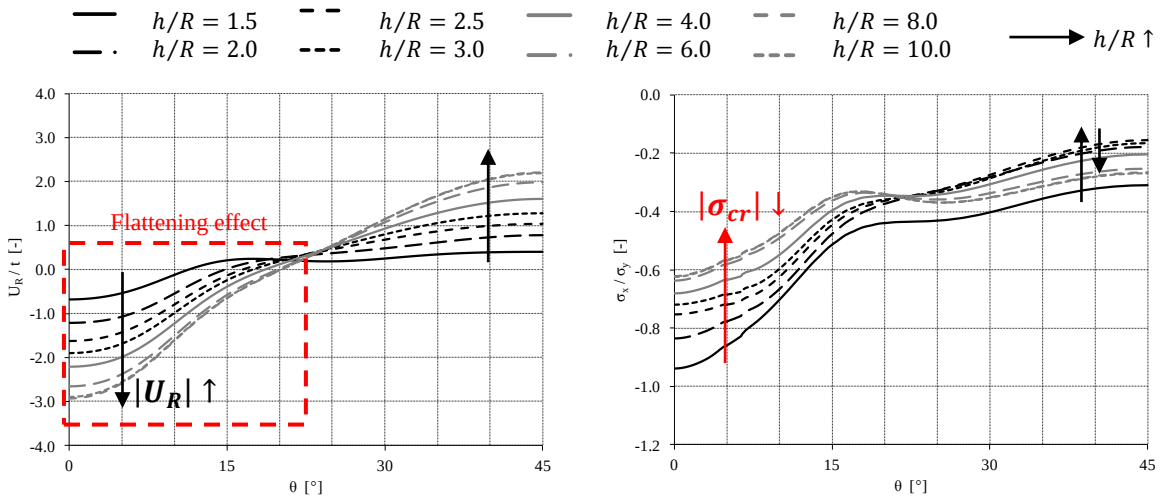

(b) Plot of the ratio of the radial displacement at the moment of failure to the silo wall thickness U_R/t [-] against the circumferential angle θ [°] for a circumferential path PC/S-h1.15 ($h_{path}/h_{stif}^{sup} = 1.15$).

(c) Plot of the ratio of the axial stress at the moment of failure to the yield stress σ_x/σ_y [-] against the circumferential angle θ [°] for a circumferential path PC/S-h1.15 ($h_{path}/h_{stif}^{sup} = 1.15$).

Fig. 5-12 Influence of the ratio of the height to the radius of the silo h/R on the failure behaviour (U-shaped longitudinal stiffener with $d_{stif}/\mathrm{R} = 0.20$; $w_{stif}/d_{stif} = 25\%$; $h_{stif}^{sup}/R = 1.0$; t_{stif}/t = max.).

The relationship between the pre-buckling deformations (i.e. flattening of the silo wall) and the reduction of the critical buckling stress σ_{cr} will be discussed in detail in Section 3.4.

Engaged columns with $R/t = 200$

In Fig. 5-13 (a), contourplots are shown for the axial stresses at the moment of maximum load. Similar to the U-shaped longitudinal stiffeners, elasto-plastic failure will occur in the silo wall just above the top of the engaged columns.

The dimensionless radial displacements U_R/t (i.e. the radial displacement divided at the moment of maximum load by the silo wall thickness) along path PC/S-h1.15 are plotted in Fig. 5-13 (b). On the basis of this figure, it can be derived that both the inwardly oriented and outwardly oriented deformations increase as the silo height h increases because of the larger distance between the location being examined, and the upper edge of the cylindrical barrel where all horizontal displacements are completely restricted. These larger inwardly oriented deformations cause a **flattening effect** of the silo wall, resulting in a **small decrease of the effective yield stress** σ_y^{eff} (See $\theta = 0°$ in Fig. 5-13 (c)).

Fig. 5-13 (c) represents the axial stress distribution σ_x/σ_y at the moment of maximum load along path PC/S-h1.15. The below findings describe the behaviour of the stress field with an increase of the silo height h. For short and intermediately high silos (here: $h/R \leq 6.0$), the axial stress will decrease in the first part of the curve ($\theta < \pm 15°$), partly due to the flattening effect, and will increase in the second part of the curve ($\theta > \pm 15°$). The decrease of axial stresses in the first part is smaller than the increase in the second part, resulting in a larger failure load F_u. For high silos (here: $h/R > 6.0$), the axial stress distribution is hardly affected by the silo height and the failure load F_u remains constant.

The relationship between the deformations before failure (i.e. flattening of the silo wall) and the reduction of the effective yield stress σ_y^{eff} will be discussed in detail in Section 3.4.

Engaged columns with $R/t = 500$

For thin-walled silos in combination with engaged columns, the location of elastic buckling shifts from the silo wall just above the top of the engaged column for shorter silos ($h/R < 4.0$) to two buckles in the silo wall on both sides of the engaged columns ($h/R > 4.0$) (See Fig. 5-14 (a)). This other failure pattern also immediately explains why the failure load F_u abruptly decreases at a height h/R of 4.0 (See Fig. 5-10 (d)).

In Fig. 5-14 (b), the dimensionless axial stress distribution σ_x/σ_y at the moment of failure is plotted along a circumferential path PC/S-h1.15. By means of this figure, the influence of an increasing height h will be discussed on the stress distribution. If $h/R < 4.0$, the axial stresses are better distributed in circumferential direction in the first part ($\theta < \pm 25°$) and are

decreasing in the second part ($\theta > \pm 30°$), resulting in an increase of the failure load F_u. If $h/R > 4$, the axial stresses start to decrease again, especially at the critical location. This can be explained by the difference of the location of buckling.

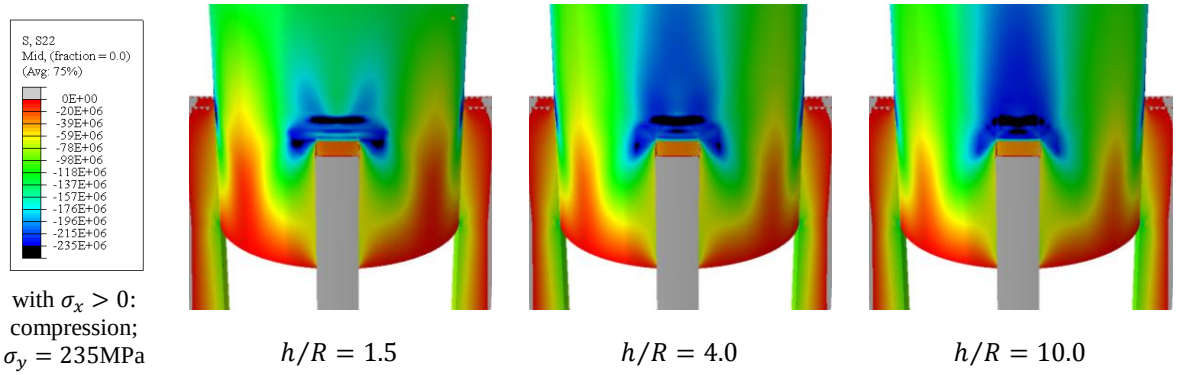

(a) Contourplots of axial stress σ_x at the moment of failure [Pa].

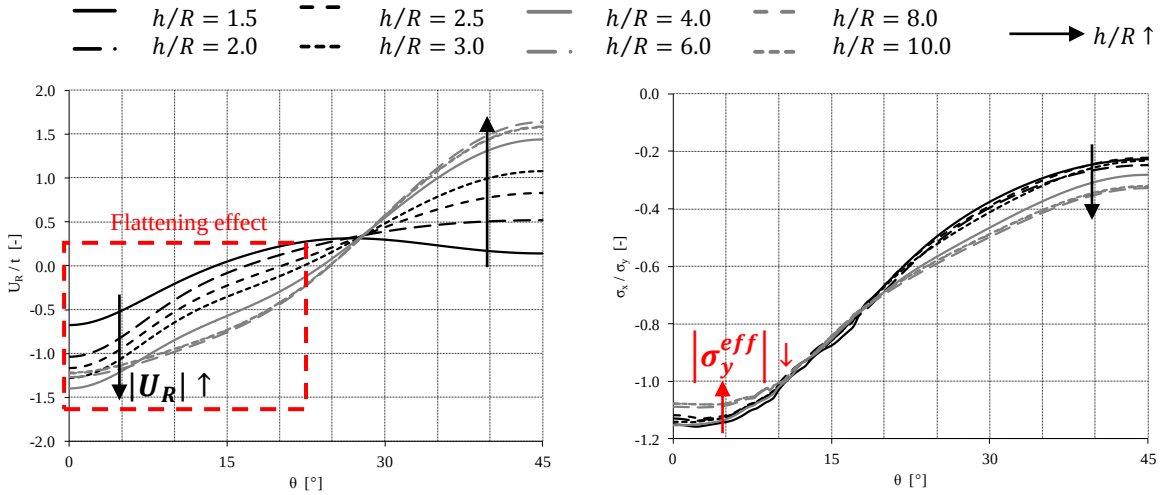

(b) Plot of the ratio of the radial displacement at the moment of failure to the silo wall thickness U_R/t [-] against the circumferential angle θ [°] for a circumferential path PC/S-h1.15 ($h_{path}/h_{stif}^{sup} = 1.15$).

(c) Plot of the ratio of the axial stress at the moment of failure to the yield stress σ_x/σ_y [-] against the circumferential angle θ [°] for a circumferential path PC/S-h1.15 ($h_{path}/h_{stif}^{sup} = 1.15$).

Fig. 5-13 Influence of the ratio of the height to the radius of the silo h/R on the failure behaviour (engaged column with $d_{stif}/\mathrm{R} = 0.30$; $w_{stif}/d_{stif} = 100\%$; $h_{stif}^{sup}/R = h_{stif}^{inf}/R = 1.0$; t_{stif}/t = max.).

Therefore, a second plot has been made of the axial stresses, but now at a height of $0.95 \cdot h_{stif}^{sup}$ (i.e. path PC/S-h0.95 in path Fig. 5-14 (c)). This circumferential path coincides with the axial height where the two buckles are formed. By increasing the silo height h, the axial stresses increase in the middle zone of the path PC/S-h0.95 ($7° < \theta < 30°$) when $h/R < 4$, but remain below the critical value of the buckling stress. When $h/R > 4$, the critical buckling stress is reached sooner at $\theta = \pm 12°$ and $0.95 \cdot h_{stif}^{sup}$ (see Fig. 5-14 (c)) than at $\theta = 0°$ and $1.15 \cdot h_{stif}^{sup}$ (see Fig. 5-14 (b)), resulting in premature failure and a decreasing

failure load F_u when the silo height increases. For high silos (here: $h/R \geq 8.0$), the axial stress distribution is hardly affected by the silo height (both in Fig. 5-14 (b) and (c)), resulting in a constant failure load F_u.

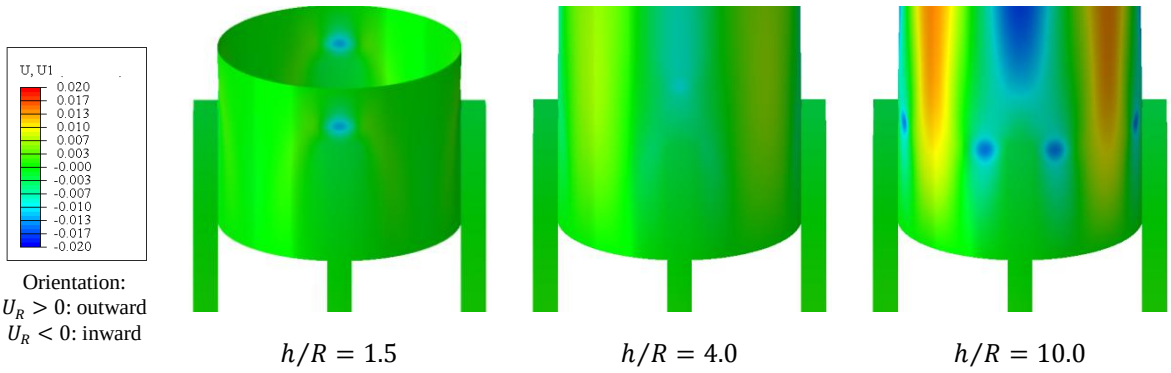

(a) Contourplots of post-buckling radial deformations U_R [m].

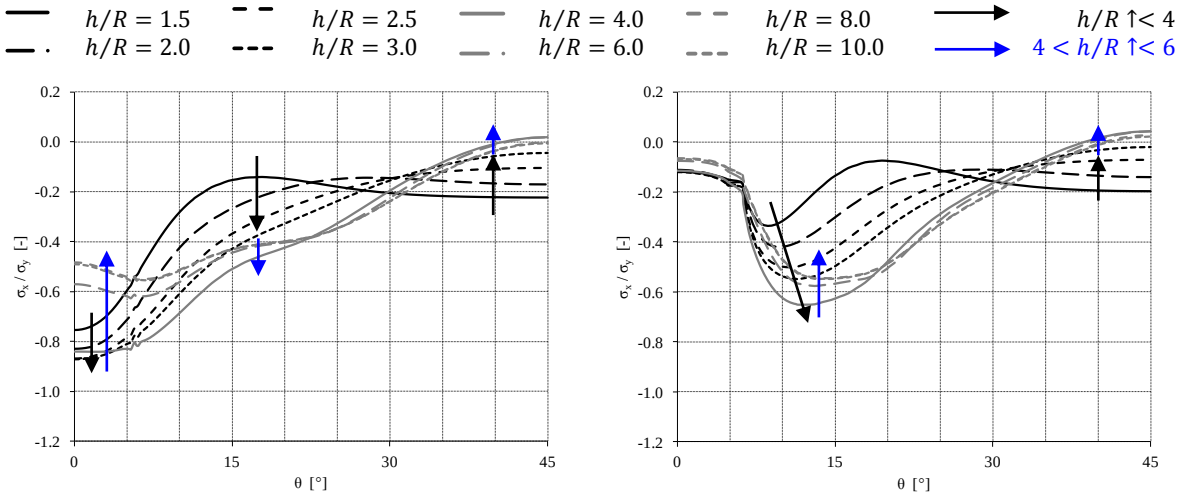

(b) Plot of the ratio of the axial stress at the moment of failure to the yield stress σ_x/σ_y [-] against the circumferential angle θ [°] for a circumferential path PC/S-h1.15 ($h_{path}/h_{stif}^{sup} = 1.15$).

(c) Plot of the ratio of the axial stress at the moment of failure to the yield stress σ_x/σ_y [-] against the circumferential angle θ [°] for a circumferential path PC/S-h0.95 ($h_{path}/h_{stif}^{sup} = 0.95$).

Fig. 5-14 Influence of the ratio of the height to the radius of the silo h/R on the failure behaviour (engaged column with $d_{stif}/\mathrm{R} = 0.20$; $w_{stif}/d_{stif} = 100\%$; $h_{stif}^{sup}/R = h_{stif}^{inf}/R = 1.0$; t_{stif}/t = max.).

Conclusions

From the above, it can be concluded that the silo height h influences both the deformations and the stress field in the silo wall in its direct vicinity, but also at greater distances from the upper edge (thus also in the region where failure occurs). As a consequence, the effective yield stress σ_y^{eff} (for thick-walled silos), the critical buckling stress σ_{cr} (for thin-walled silos) (See Section 3.4), and the failure load are influenced by the silo height h for silos with short and intermediate height (i.e. $h/R < \pm 8.0$). In contrast, for high silos ($h/R \geq \pm 8.0$), the failure load is independent of the silo height h. Therefore, for most subsequent studies, a

value of h/R equal to 10 will be adopted to exclude the influence of the silo height on the failure behaviour.

3.4 Deformations before failure

In Fig. 5-15, a circle segment of the silo wall is depicted in both undeformed state (black) and deformed state (gray). During an increase of the compressive load on the upper edge of the cylindrical barrel, the silo wall and the stiffener/engaged column tend to deform in inward direction in the regions above the local supporting columns (blue arrows). In contrast, the regions between two supports have the tendency to deform in outward direction (red arrows). From the previous part, it appeared that these (pre-failure) deformations are increasing when the height of the silo h increases.

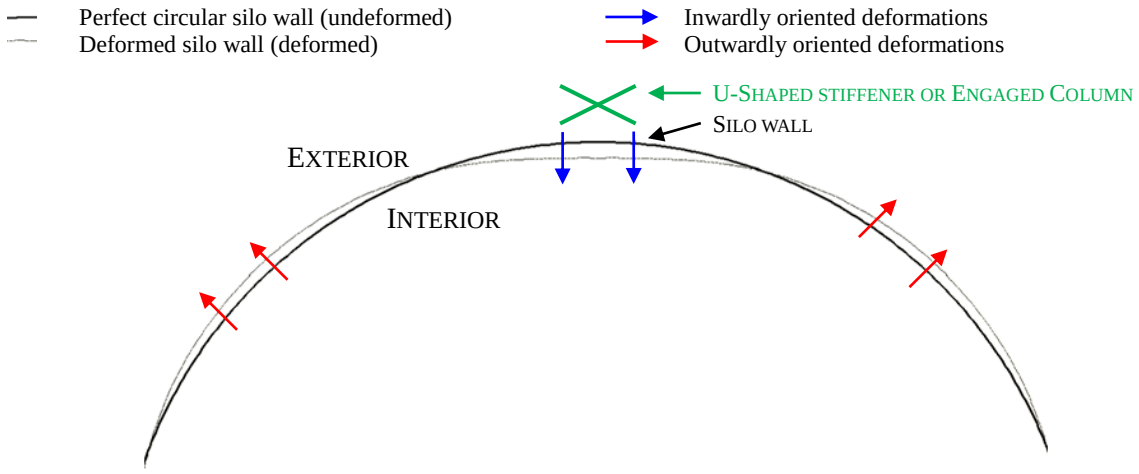

Fig. 5-15 Deformations before failure.

Generally, the critical location of failure, regardless of the failure phenomenon (yielding and/or buckling), coincides with the inwardly oriented "flattened" silo wall, in the direct vicinity of the top of the stiffener/column. Depending on the failure phenomenon, the relationship between the increasing pre-failure deformations and the decreasing critical failure stress can be explained differently.

First, these inward deformations will cause smaller compressive or small tensile stresses σ_θ in circumferential direction, resulting in a decrease of effective yield stress σ_y^{eff} in axial direction according to the von Mises yield criterion (for thick-walled silos). In Fig. 5-16, the decrease of the effective yield stress σ_y^{eff} is indicated with a red arrow.

Second, the flattened silo wall locally has a larger effective radius of curvature r (i.e. a smaller curvature $1/r$). As a consequence, the critical buckling stress σ_{cr}, which can be calculated using Eq. (2-1), will decrease (for thin-walled silos). Although this critical buckling stress was defined for perfect isotropic cylindrical shells subjected to a uniform axial

compression and with classical boundary conditions (Timoshenko, 1910), a similar reasoning can be used for locally supported cylindrical shells.

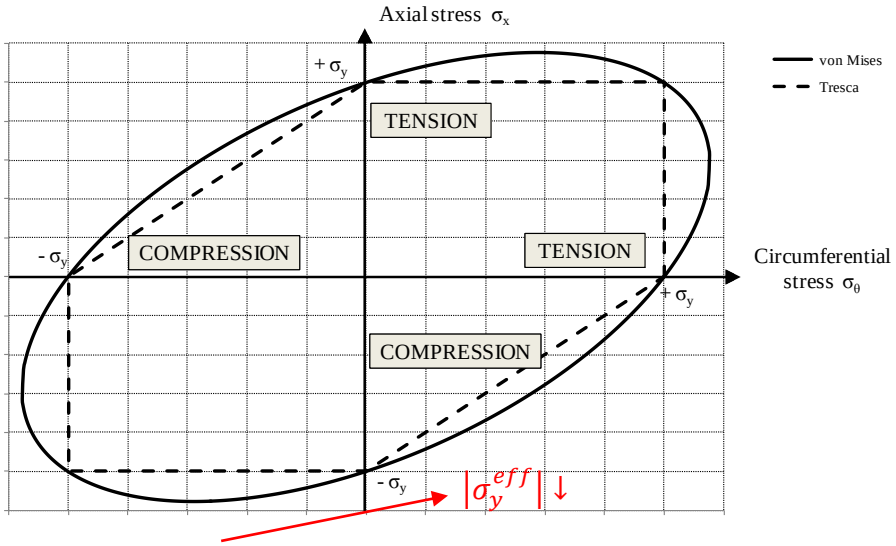

Fig. 5-16 Yielding surface of von Mises (ellipse) and Tresca (hexagon).

In addition to the silo height, there are also other factors that influence the deformations before failure, such as the moment of inertia of the stiffener/engaged column, the eccentricity and the height of the stiffener/supporting column, the definition of the support (clamped or pinned), and the presence of ring stiffeners (e.g. an upper ring, a transition ring or a lower ring). These parameters will be covered in Section 4 - Supporting arrangements, Section 5 - U-shaped stiffeners, and Section 8 - Engaged columns.

Conclusions

Since the effective yield stress σ_y^{eff} (for thick-walled silos) and the critical buckling stress σ_{cr} (for thin-walled silos) both depend on the (inward) deformations before failure (yielding and/or buckling), these deformations should be reduced as much as possible in the critical zone. As will be seen later, measures that hamper these deformations (e.g. the presence of an intermediate ring stiffener at the top of the U-shaped stiffener) are advantageous for the failure behaviour of such a structure, both for thick and for thin silo walls.

The influence of the U-shaped longitudinal stiffeners and the engaged columns on the inward deformations before failure (and consequently the effective yielding stress and the critical buckling stress) will discussed more in detail in Section 5.1 and Section 8.4, respectively.

3.5 Definition of the geometrical parameters of the silo for the design rule

This section concludes with an enumeration of the geometrical parameters which will be used for the deduction of the design rule (See Chapter 6).

Table 5-6 Geometrical parameters of the cylindrical barrel (design rule).

PARAMETER	VALUE(S)	DIMENSION
R	1.0	m
R/t	100; 200; 250; 333.3; 500; 666.6; 1000	-
h/R	High silo: 10 Intermediately high silo $h_{stif}^{sup}/R = 0.5;\ 1.0$: 2.0 $h_{stif}^{sup}/R = 1.5;\ 2.0$: 3.0	-

4 Supporting arrangement

It goes without saying that the discrete way of supporting is an important feature that should be taken into account when the failure behaviour of "locally" supported steel silos is thoroughly investigated. In this investigation, two main support-stiffener configurations are considered.

4.1 Types of supporting arrangements

Type 1 - U-shaped longitudinal stiffener

For this type, the supporting arrangement is closely related to the stiffener configuration (See Fig. 3-22), and as will be discussed below, the dimensions of the supporting columns are coupled to the dimensions of the stiffeners.

Above each supporting column, a longitudinal U-shaped stiffener is placed (Eq. (5-6)). Furthermore, it is adopted that the longitudinal stiffener is fully supported by the underlying supporting column (See Fig. 3-22 (b)). It is also adopted that the circumferential width of the support d_{sup} is equal to the circumferential width of the stiffener d_{stif} (Eq. (5-7)). Because the centrically positioned column (relative to the silo wall) has the same radial width on the inside and the outside of the silo wall surface (See Fig. 5-17 (a)), the radial width of the support w_{sup} is equal to twice the radial width of the stiffener w_{stif} (Eq. (5-8)).

$$n_{sup} = n_{stif} \tag{5-6}$$

$$d_{sup} = d_{stif} \tag{5-7}$$

$$w_{sup} = 2 \cdot w_{stif} \tag{5-8}$$

The influence of the number and the dimensions of U-shaped longitudinal or stringer stiffeners will be discussed in detail in Section 5 - U-shaped stiffeners. Since the dimensions of the stringer stiffeners and the underlying supports are coupled to each other, it is thus

important to know that as the dimensions of the stringer stiffener are changed, the same changes are imposed on the underlying column according to Eqs. (5-6) to (5-8).

Type 2 - Engaged columns

Now, the supporting columns have a rectangular cross-section, are eccentrically positioned relative to the silo wall, and are engaged to the shell surface along a specific distance (See Fig. 3-25 and Fig. 5-17 (b)). The influence of the number and the dimensions of engaged columns will be discussed in detail in Section 8 - Engaged columns.

For a complete description of the geometry of the supporting and the stiffening configuration, the reader is referred to Section 7 of Chapter 3.

4.2 Pinned versus clamped support boundary conditions

In this section, we will deal with the influence of the support boundary conditions of the (ec)centric supporting columns on the failure load. Two extreme conditions can be distinguished: (1) the circumferential rotation φ_T is completely free at the lower edge of the column = a pinned support (left in Fig. 5-17 (a) and (b)) and (2) the circumferential rotation is completely restricted at the lower edge of the column (i.e. $\varphi_T = 0$) = a clamped support (right in Fig. 5-17 (a) and (b)). In practice, a local support usually behaves somewhere in between (See Section 8 in Chapter 2).

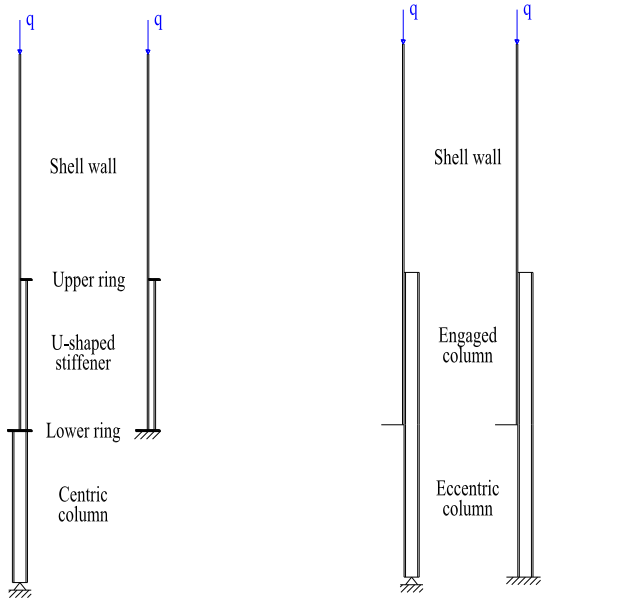

(a) U-shaped stiffeners with centric supporting columns.

(b) Engaged columns with eccentric supporting columns.

Fig. 5-17 Vertical cross-section of the structure through the centre of a local support.

For both supporting conditions, the dimensionless GMNA failure load F_u/F_{ref} is plotted in Fig. 5-18 for a cylindrical barrel with a variable thickness R/t and for one U-shaped stiffener ($d_{stif}/R = 0.20$; $w_{stif}/d_{stif} = 25\%$; $t_{stif}/t =$ max.; $h_{stif}^{inf}/R = 4.0$) and for one engaged column ($d_{stif}/R = 0.20$; $w_{stif}/d_{stif} = 100\%$; $t_{stif}/t =$ max.; $h_{stif}^{inf}/R = 4.0$) with a variable attached height h_{stif}^{sup}/R. The stiffness EI and the unattached column height h_{stif}^{inf}/R are kept constant in Fig. 5-18, which does not mean that these parameters do not influence the

behaviour, on the contrary.

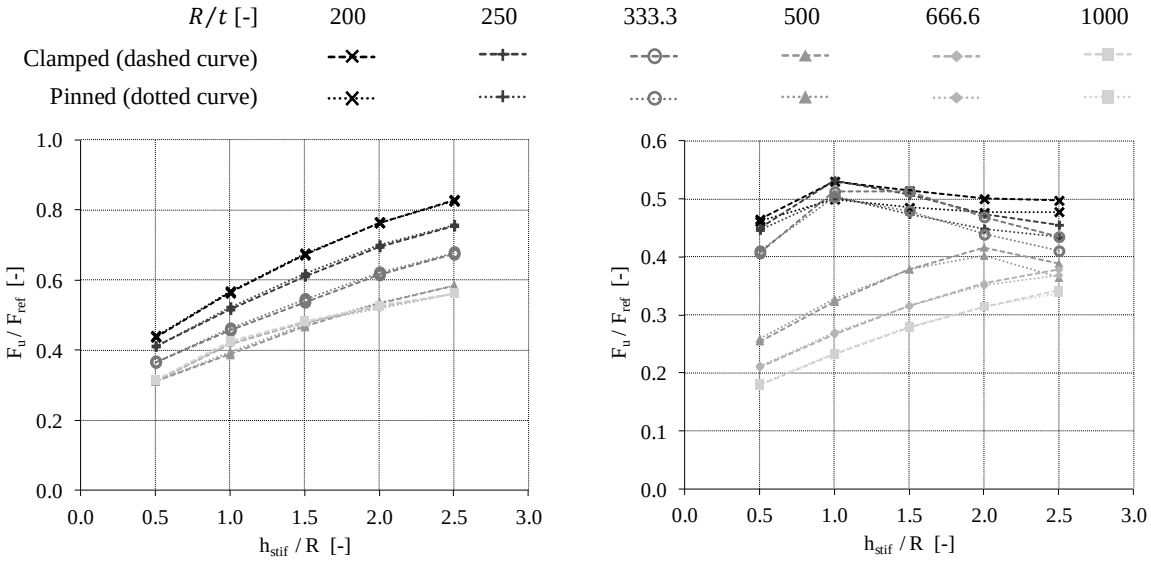

(a) U-shaped stiffeners ($w_{stif}/d_{stif} = 25\%$). (b) Engaged columns ($w_{stif}/d_{stif} = 100\%$).

Fig. 5-18 Dimensionless GMNA failure load F_u/F_{ref} for a silo with a variable radius-to-thickness ratio R/t and for one U-shaped stiffener/engaged column geometry ($d_{stif}/R = 0.20$; $t_{stif}/t =$ max.; $h_{stif}^{inf}/R = 4.0$) with a variable attached height to cylinder radius ratio h_{stif}^{sup}/R.

For both configurations and for all cases (R/t), the curve corresponding with the pinned support almost coincides with the curve corresponding with the clamped support. The ratio of the failure load of a silo with pinned supports F_u^{pinned} to the the failure load of silo with clamped supports $F_u^{encastred}$ is approximately equal to 100% for the U-shaped stiffeners and ranges between 93% and 100% for the engaged columns. In other words, it (almost) does not matter for the failure load (for these specific cases) whether or not the circumferential rotation φ_T is prevented at the lower edge of the supporting columns. Why the support type hardly influences the failure behaviour is explained below.

First of all, it is important to emphasize that the moment of failure (and thus failure load) is influenced, among other things, by the disadvantageous inwardly oriented deformations in the critical region of the silo wall in the vicinity of the top of the U-shaped stiffener/engaged column. The reason why these deformations before failure are disadvantageous is that they influence the effective yield stress σ_y^{eff} (for thick-walled silos) as well as the critical buckling stress σ_{cr} (for thin-walled silos) (as discussed in Section 3.4).

In addition to the release (pinned supports) or the restriction (clamped supports) of the circumferential rotation at the bottom of the columns (by means of boundary conditions), several other elements hamper the disadvantageous inward deformations at the top of the U-shaped stiffeners and the engaged columns: the presence of a lower ring stiffener or a

transition ring, the attachment of the U-shaped stiffener/engaged column to the silo wall, and the presence of an upper ring stiffener. Furthermore, the stiffness EI and the eccentricity (relative to the silo wall) of the stiffener/column cross-section influence the behaviour.

Nevertheless, there are a number of differences between the two configurations why the ratio $F_u^{pinned}/F_u^{encastred}$ for the engaged columns is slightly smaller than for the U-shaped stiffeners. In the case of U-shaped stiffeners, the eccentricity (relative to the silo wall) of the support column cross-section is zero and the eccentricity (relative to the silo wall) of the longitudinal stiffener is relatively small. In contrast, engaged columns display a larger eccentricity (relative to the silo wall) of the column cross-section (positioned on the external side of the shell wall) and no upper ring is present at the top of engaged columns. Consequently, to prevent large inwardly oriented disadvantageous displacements at the top of the column/stiffener (See Sections 5.1 and 8.4), the minimum stiffness EI will be larger for an eccentric engaged column than for a centric positioned column/U-shaped stiffeners under the same conditions (e.g. the same height h_{stif}^{inf}).

For all numerical calculations in this work and for both configurations, the support will always be considered as **a fully clamped support**, which restricts all horizontal deformations as well as the circumferential rotation. For U-shaped stiffeners, the concentric supporting column is not included in the model and is replaced by a brick shaped volume. The top of this volume is rigidly attached to the nodes of the supported lower edge of the supported part of the shell wall, longitudinal stiffener, and lower ring. The translational degrees of freedom are completely restricted at the bottom of the volume. In contrast, the engaged supporting columns are of course included in the model.

Conclusions

In Section 8 of Chapter 2, an overview was given of frequently used supporting configurations for cylindrical barrels. The connection of the supporting columns with the foundation (bottom) and the barrel transition (top) can be fabricated in different ways, and also the shape of the cross-section can be varied. In this study, only rectangular shaped columns were considered which are concentrically or eccentrically positioned, for the U-shaped stiffeners and the engaged columns, respectively. For these configurations, the influence of the extreme conditions for the connection column-foundation to the failure behaviour was investigated here.

This study has revealed that, for all considered geometries (not all results are presented in Fig. 5-18), the difference in failure load between a pinned and a clamped locally supported silo is larger for eccentric engaged columns than for U-shaped stiffeners with centric positioned columns, but always remains relatively small. In what follows, clamped supports will be used.

5 U-shaped stiffeners

In previous research, the use of two rectangular partial-height plates at both edges of each local supporting column was extensively investigated by Vanlaere (Vanlaere, 2006). The latter study has demonstrated that such a stiffener frequently tends to fail prematurely by buckling of its own. As a result of this finding, one of the conclusions was that there are other cross-sections shapes which are more suitable to use as meridional stiffener.

From the results of (Vanlaere, 2006), the idea grew to connect the two rectangular plates with each other so that a U-shaped profile is obtained. Such a closed U-shaped profile has a larger cross-section, has a much higher moment of inertia and consequently has a larger resistance to buckling compared to the previously studied alternatives. The influence of the geometry of this type of longitudinal stiffener will be thoroughly investigated in this section. The study consists of five main parts: (1) a comparison between unstiffened and stiffened cylindrical barrels (Section 5.1), (2) an exploratory study where the influence of all geometrical parameters is investigated one by one (Section 5.2), (3) an investigation of the influence of the degree of support (Section 5.3), (4) an optimisation study where the optimal stiffener is determined (shape and height) (Section 5.4), and (5) the determination of the scope of the geometrical parameters for the final study (Section 5.5).

5.1 Comparison between unstiffened and stiffened locally supported silos

This first study tries to reveal what is the best choice to increase the failure load of a locally supported silo as much a possible while adding a minimum amount of material. In this study, three different possible solutions are examined and compared with each other. In all cases, the supporting columns terminate at the lower edge of the cylindrical barrel.

The difference between the three alternatives is the place where additional material is added to the silo geometry. For the first alternative, the thickness of the silo wall is increased over the entire circumference and height (Fig. 5-19 (a)), while for the second alternative, the thickness of the silo wall is only increased over a limited height at the bottom of the silo (Fig. 5-19 (b)). In contrast, for the third alternative, material is added very locally with stiffening members ((Fig. 5-19 (c)) where a U-shaped longitudinal stiffener is provided above each supporting column. In this manner, the support reaction force is transferred more gradually into the silo wall, spreading the load better in circumferential direction, reducing the peak stresses near the supports. In addition, two ring stiffeners are included, more specifically a base ring at the lower edge of the cylindrical barrel, and an intermediate ring at the terminations of the U-shaped stringer stiffeners. These stiffeners prevent (large) out-of-roundness displacements and to a lesser extent, the axial stresses are spread more in circumferential direction. It is expected that those alternatives - in the order in which they are presented above - are increasingly economical due to an improvement of the location where the additional material is added.

Indeed, the material is more and more concentrated to the region where it is really needed, namely the silo wall just above the local supports.

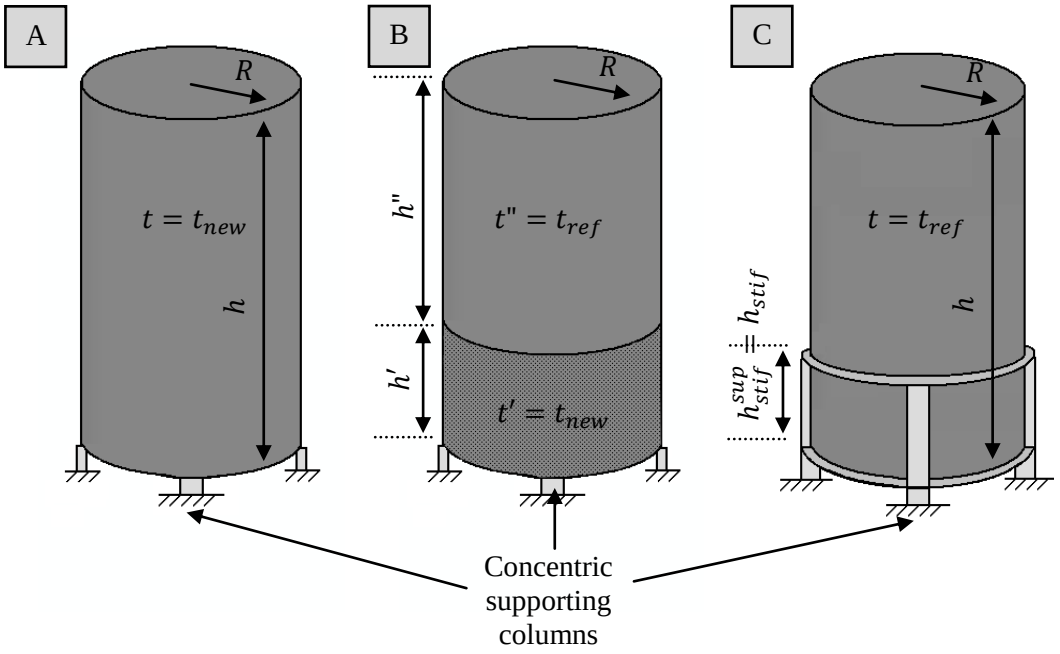

(a) Unstiffened shell wall with an increased thickness over the entire height h.

(b) Unstiffened shell wall with only an increased thickness in the lower region (h').

(c) Shell wall with U-shaped longitudinal stiffeners.

Fig. 5-19 Alternatives for a locally supported cylindrical silo.

In Fig. 5-20, the dimensionless GMNA failure load F_u/F_{ref} is plotted against the dimensionless material parameter V_{extra}/V_{ref} for the three above mentioned solutions, and for thick-walled silos (i.e. $R/t = 200$) as well as for thin-walled silos (i.e. $R/t = 1000$). In this way, conclusions can be drawn for different failure behaviours, respectively for (elasto-)plastic collapse and for pure elastic buckling.

The dimensionless material parameter is equal to the additional steel volume V_{extra} compared to the volume of steel of the unstiffened "reference" cylindrical barrel (Eq. (5-9) for alternative (A), Eq. (5-10) for alternative (B), and Eq. (5-11) for alternative (C)), divided by the reference material parameter V_{ref}. The latter is equal to the volume of steel of the unstiffened "reference" cylindrical barrel (Eq. (5-12)).

Alternative (A):
$$V_{extra} = A_{extra} \cdot \mathrm{h} = (2\pi \mathrm{R} \cdot \mathrm{t_{extra}}) \cdot \mathrm{h}$$
$$V_{extra} = \left[2\pi R \cdot \left(t_{new} - t_{ref}\right)\right] \cdot h \quad (5\text{-}9)$$

Alternative (B):
$$V_{extra} = A_{extra} \cdot \mathrm{h'} = (2\pi \mathrm{R} \cdot \mathrm{t_{extra}}) \cdot \mathrm{h'}$$
$$V_{extra} = \left[2\pi R \cdot \left(t_{new} - t_{ref}\right)\right] \cdot h' \quad (5\text{-}10)$$

Alternative (C):
$$V_{extra} = n_{stif} \cdot A_{stif} \cdot h_{stif} \quad (5\text{-}11)$$

"Reference" silo: $V_{ref} = V_{shell} = A_{shell} \cdot h = \left(2\pi R \cdot t_{ref}\right) \cdot h$ (5-12)

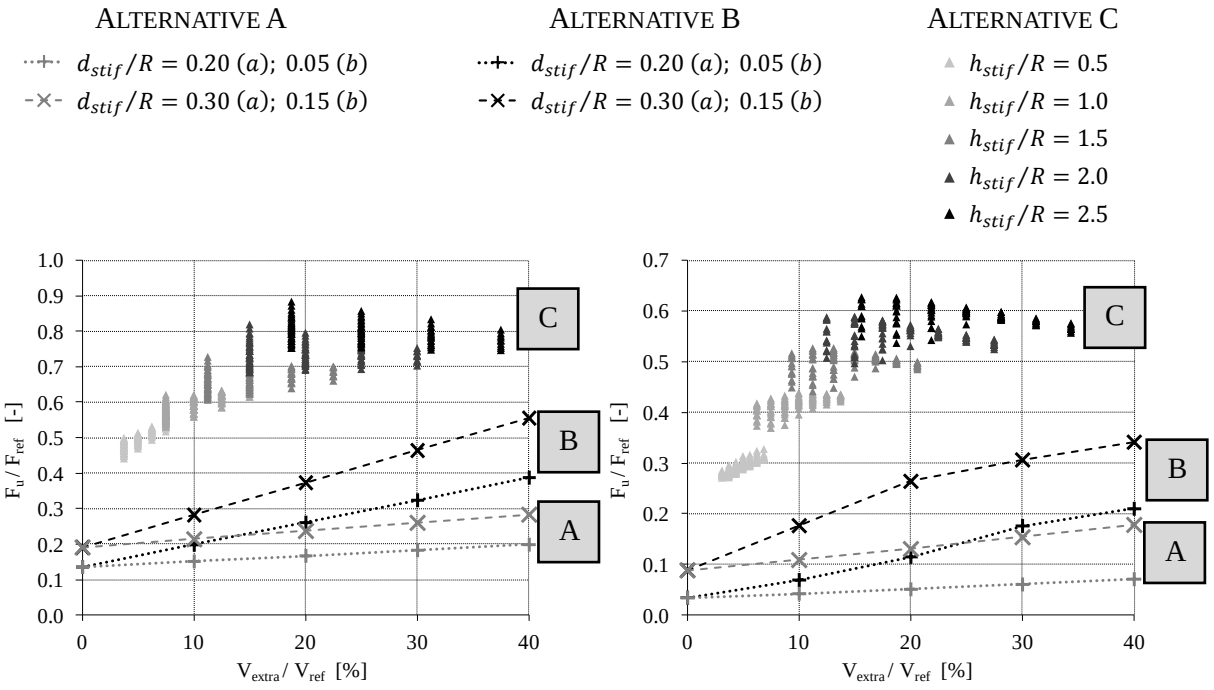

(a) Thick-walled silos ($R/t = 200$). (b) Thin-walled silos ($R/t = 1000$).

Fig. 5-20 Unstiffened silo wall versus stiffened silo wall.

Fig. 5-20 shows immediately that alternative (A), which corresponds with an increased silo wall thickness over the entire silo height, is the worst-case scenario, because material is added in the zone with elevated stresses (i.e. just above the local supports) as well as in the regions with a lower/uniformly distributed axial stresses. In other words, a lot of material is added in regions where it is not really necessary, such as the silo wall between the supports and the silo wall at the top of the cylindrical barrel.

A first improvement (i.e. alternative (B)) is to increase the silo thickness only in the bottom zone of the cylindrical barrel. When the height h' decreases (in Fig. 5-20: $h' = 2.0 \cdot R$), the slope of the curves increases, especially compared to alternative (A). This means that a larger failure load is obtained with the same quantity of material. From a certain height h', the slope of the curves will decrease again. For all calculated heights h', alternative (B) can never match the failure load of a stiffened silo (C). Indeed, alternative (C) is always better than alternative (B) for an arbitrary value of V_{extra}/V_{ref}. This finding can be explained on the basis of the material which is less necessary at certain locations, for example in the region between the supports. The other reasons are discussed more extensively below.

Both for thick-walled and for thin-walled silos, the stiffened silo wall or alternative (C) is the most economical and effective solution to increase the failure load with a minimal increase in

steel. Indeed, the failure load of alternative (C) is for an arbitrary value of V_{extra}/V_{ref} always higher than the failure loads of possibilities (A) and (B). In what follows, several reasons are listed why this stiffening configuration is such an economical solution for locally supported silos subjected to axial compression, rather than increasing the silo wall thickness (in the lower region) of the cylindrical barrel.

- Combining a U-shaped stiffener with a relatively thin silo wall guarantees an excellent performance of both parts. Firstly, the stiffener **absorbs a significant part of the vertical load**, thereby relieving the load in the silo wall just above the supports. The ratio of the load which is carried by the stiffener to the total load depends on the relative stiffnesses of the stiffener and the silo wall. Afterwards, the longitudinal stiffener **gradually transfers** the absorbed load **into the silo wall** by shear stresses, resulting in a better distribution of the axial stresses over the entire circumference. Secondly, the stiffener is **restrained against buckling** by its attachment to the silo wall. However, it is important to note that when the cross-section of the stiffener is relatively small, premature failure of the silo structure will occur due to plastic yielding of the stiffener itself. In the optimisation study (Section 5.4), these cases are not considered.
- When U-shaped stiffeners are used, the eccentricity of the concentric columns is zero (the centre of the supporting columns coincides with the midplane of the silo wall). Furthermore, the radial width of the longitudinal stiffeners is limited (in this study: $w_{stif}^{max} = 75\% \cdot d_{stif}$), so that its centroid is located relatively close to the silo wall, restricting the introduction of moments into the silo wall. Due to the **limited eccentricity** of both the supporting columns and the longitudinal stiffeners, the introduction of bending moments into the silo wall is relatively small. This is beneficial to the strength of the silo structure, because such a silo structure is less efficient at carrying bending moments, especially compared to axial forces.
- Another important parameter that is strongly related to the failure load is **the degree to which the circumferential rotation of the top of the stiffener is allowed**. In the case of U-shaped stiffeners, this rotation is completely prevented at the bottom of the U-shaped stiffener due to the choice of the type of support. Indeed, the rigid supports hamper any horizontal displacements and, more important here, the rotation of the bottom of the U-shaped stiffener.
  However, a higher longitudinal stiffener tends to move easier in inward direction than a shorter stiffener, since the distance between the rigid lower edge and its top increases. This detrimental effect can be clearly seen in Fig. 5-20. When comparing the scatter of points between a short stiffener (i.e. $h_{stif}/R = 0.5$) and a long stiffener (i.e. $h_{stif}/R = 2.5$), respectively an increasing and decreasing trend in the failure load can be observed for the same stiffener cross-sections.
- The fourth, and last, reason is the advantageous effect of **the upper ring stiffener**. This "intermediate" ring stiffener is situated just above the U-shaped stiffeners (i.e. the

transition height between the stiffened and the unstiffened silo wall) and encompasses the entire circumference. At this height, the out-of-roundness displacements are largely prevented, which benefits the failure behaviour (i.e. yielding and/or buckling) in the unstiffened silo wall above the terminations of the U-shaped stringer stiffeners.

In fact, the above mentioned reasons amount to the same thing: reducing the eccentricity of the supporting columns (and the longitudinal stiffeners), the hampering of the circumferential rotation of the supports, the addition of an upper ring stiffener, these measures all reduce the inwardly oriented pre-failure deformations in the critical zone (i.e. the unstiffened silo wall above the terminations of the U-shaped stiffeners). Such reduced inwardly oriented deformations are disadvantageous for the effective yield stress σ_y^{eff} (for thick-walled silos) as well as the critical buckling stress σ_{cr} (for thin-walled silos) in this area, as is discussed in Section 3.4.

Conclusions

In this paragraph, the reasons for the advantageous failure behaviour of a locally supported cylindrical steel silo, combined with a U-shaped stiffener and ring stiffeners, were described in detail. Clearly, it is an excellent alternative to use such U-shaped stringer stiffeners above the local supports to maximally strengthen a silo structure subjected to axial compression.

5.2 Exploratory parametric study

In this part, the influence of all geometrical parameters on the failure behaviour/load will be discussed in detail, both for thick-walled silos (i.e. $R/t = 200$) as for thin-walled silos (i.e. $R/t = 1000$).

The default values were used for the geometry of the cylindrical barrel and the ring stiffeners. The width in circumferential direction d_{stif}, the radial width w_{stif}, the thickness t_{stif}, and the height h_{stif} of the U-shaped stiffener were varied within the ranges given in Table 5-7. All parts have a standard elasto-plastic material behaviour with a yield stress σ_y equal to 235MPa.

Table 5-7 Geometrical parameters of the U-shaped longitudinal stiffeners (exploratory study).

PARAMETER	VALUE(S)	DIMENSION
n_{sup}	4	-
d_{stif}/R	$R/t = 200$: 0.05; 0.10; 0.15; 0.20; 0.25; 0.30 $R/t = 1000$: 0.05; 0.10; 0.15; 0.20	-
w_{stif}/d_{stif}	10; 20; 30; 40; 50; 60; 70	%
h_{stif}^{sup}/R	0.5; 1.0; 1.5; 2.0	-
t_{stif}/t	min.; ave.; max. *	-

*: Minimum(min.), average (ave.), or maximum (max.) thickness - restrictions

To be able to investigate the influence of the geometry of the U-shaped longitudinal stiffeners, 103 ($R/t = 200$) and 47 ($R/t = 1000$) different cross-sections were calculated (both the shape and dimensions were varied) for 4 different stiffener's heights h_{stif}. This corresponds with about 600 GMNA calculations. In what follows, the influence of all geometrical parameters on the failure behaviour/-load is investigated one by one.

5.2.1 Cross-section of the U-shaped stiffener

In this section, the influence of the total quantity of material in the cross-section of the U-shaped stiffener on the failure load and failure behaviour is investigated.

Thick-walled silos

As already mentioned before, 103 different cross-sections were calculated (both the shape and dimensions were varied) for 4 different stiffener's heights h_{stif} ($h_{stif}/R = 0.5; 1.0; 1.5; 2.0$). These results are given in Fig. 5-21. In this figure, the dimensionless GMNA failure load F_u/F_{ref} of the silo structure is plotted against the ratio of the stiffener's cross-section to the cross-section of the silo wall A_{stif}/A_{shell} (expressed in percentage) for different stiffener's heights h_{stif}. Since the radius-of-thickness ratio R/t is constant (200), the values of F_{ref} and A_{shell} remain constant too.

Clearly, the cross-section of a stringer stiffener has a significant impact on the maximum load of such a silo. In each case, the graph consists of a scattered cloud of points in which two branches with different slope can be distinguished. The first branch corresponds with stiffeners with a small cross-section and is a rapidly increasing branch until a certain transition point is reached where the slope changes abruptly. For stiffeners with a larger cross-section, the curve is a slowly rising branch (Fig. 5-21 (a) and (b): $h_{stif}/R = 0.5; 1.0$), a horizontal branch (Fig. 5-21 (c): $h_{stif}/R = 1.5$), or a decreasing branch (Fig. 5-21 (d):

$h_{stif}/R = 2.0$). Clearly, the slope of the second branch depends on the stiffener height h_{stif}. In other words, it appears that the influence of the stiffener's cross-section A_{stif} is related to the stiffener's height h_{stif}. This finding will be explained in detail in Section 5.2.5. In what follows, the other findings will be clarified by studying the silo behaviour and failure patterns.

In the first branch (i.e. the rapidly rising curve in Fig. 5-21, when $A_{stif}/A_{shell} < \left(A_{stif}/A_{shell}\right)_{transition}$), the failure load increases consistently when adding material to the stiffener's cross-section. This can be attributed to the location where yielding occurs. Indeed, it turns out that the silo wall and the longitudinal stiffeners just above the discrete supports fail by plastic yielding, while the axial stresses in the silo wall above the stiffeners are far below the yield stress (See failure pattern P.1 in Fig. 5-22 (a)). In other words, the material in the stiffened region is completely exhausted, while the material of the cylindrical barrel (in the unstiffened zone) is not yet fully utilized. In conclusion, a small increase of the stiffener's cross-section means a rapid increase of the failure load because more material can yield in the stiffened zone above the local supports.

The location of the transition between the two branches depends on the stiffener's height h_{stif} (See Fig. 5-21). When the stiffener's height h_{stif} increases, the dimensionless stiffener's cross-section $\left(A_{stif}/A_{shell}\right)_{transition}$ and the corresponding failure load are both increasing, because a higher longitudinal stiffener can spread the load better in circumferential direction by shear than a shorter stiffener. As a result of this better distribution of stresses/forces, failure will occur at higher load levels. To ensure that a higher stiffener could absorb this increasing force, the stiffener's cross-section must therefore be increased too.

Another finding is that the failure load of the approximately horizontal branch in Fig. 5-21 (i.e. the second branch after the transition point) increases when the stiffener's height h_{stif} increases, because a larger stiffener height improves the stress distribution in circumferential direction. The positive influence of the attached stiffener height h_{stif} to the failure behaviour is discussed in detail in Section 5.2.5.

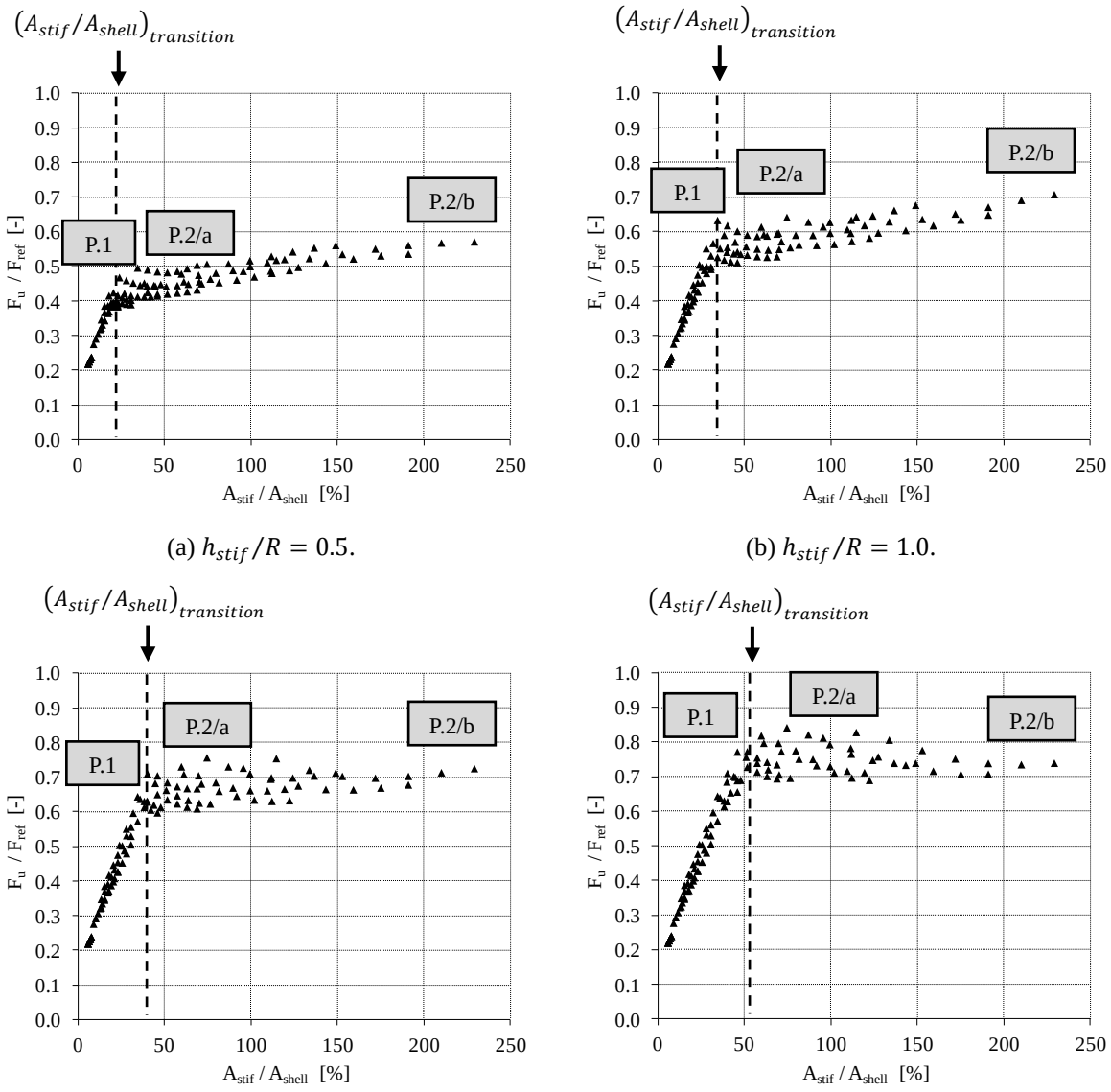

(a) $h_{stif}/R = 0.5$.

(b) $h_{stif}/R = 1.0$.

(c) $h_{stif}/R = 1.5$.

(d) $h_{stif}/R = 2.0$.

Fig. 5-21 Dimensionless GMNA failure load F_u/F_{ref} as a function of the ratio of the cross-section of the longitudinal stiffeners to the cross-section of the silo wall A_{stif}/A_{shell} for different stiffener heights ($R/t = 200$).

For U-shaped longitudinal stiffeners with a large cross-section (i.e. $A_{stif}/A_{shell} > (A_{stif}/A_{shell})_{transition}$ in Fig. 5-21), the failure pattern will be of type P.2/a (See Fig. 5-22 (b)) or type P.2/b (See Fig. 5-22 (c)). In both cases, failure will occur in the silo wall just above the top of the longitudinal stiffener, because the longitudinal stiffener is now able to absorb a sufficiently large reaction force, and introduce the load gradually into the silo wall by shear. As a result, the failure load of the stiffened silo structure increases. The only difference between these patterns is that yielding in the silo wall just above the local supports is still present for type P.2/a and not for type P.2/b.

From the above mentioned turning or transition point, which corresponds with the beginning of the second curve in Fig. 5-21, the maximum load continues to increase less rapidly due two reasons. By comparing Fig. 5-22 (b) with Fig. 5-22 (c), it can be seen that (1) the yielding region above the top of the U-shaped stiffener is extended in circumferential direction and (2) the axial stresses are slightly better distributed in circumferential direction. Both can be attributed to, for example, an increase of the width of the support d_{sup} (and stiffener) in circumferential direction. In Section 5.2.2, the influence of the width in circumferential direction will further be discussed in detail.

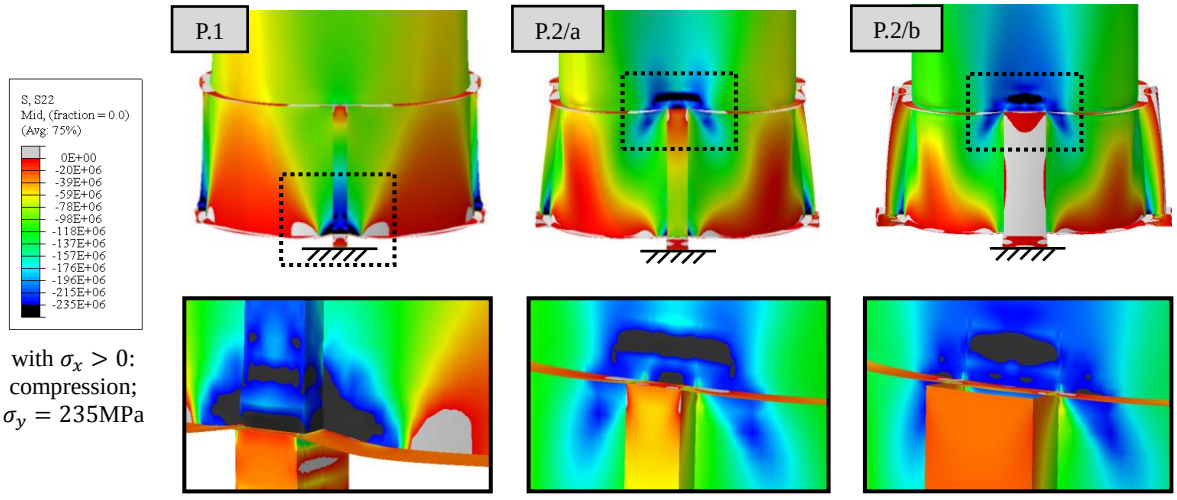

(a) Small cross-section. (b) Average cross-section. (c) Large cross-section.

Fig. 5-22 Contourplot of the axial stresses σ_x at the moment of maximum load [Pa] ($R/t = 200$; $h_{stif}/R = 1.0$).

In addition, a scatter can be observed in the results of Fig. 5-21, in particular in the second branch. This scatter is caused due to the wide range of different shapes of the stiffener's cross-section that are explored in the present study (with a constant quantity of cross-sectional material). This topic, and the determination of the optimal shape of the stiffener's cross-section, are covered in depth in Section 5.4.

Thin-walled silos

Similar to the previous part, the influence of the stiffener's cross-section A_{stif} is investigated for thin-walled silos (here: $R/t = 1000$). In total, 47 different cross-sections were calculated (both the shape and dimensions were varied) for 4 different stiffener's heights h_{stif} ($h_{stif}/R = 0.5; 1.0; 1.5; 2.0$). In Fig. 5-23, the dimensionless GMNA failure load F_u/F_{ref} of the silo structure is plotted against the ratio of the stiffener's cross-section to the cross-section of the silo wall A_{stif}/A_{shell} (expressed in percentage) for different stiffener's heights h_{stif}. Since the radius-of-thickness ratio R/t is constant (1000), the values of F_{ref} and A_{shell} remain constant too.

Again, it appears that the cross-section of the stringer stiffeners has a significant impact on the buckling load. Each graph generally consists of a scattered cloud of points in which two branches with different slope can be distinguished. The first branch corresponds with a rapidly increasing failure load for smaller cross-sections until a certain transition point is reached. In this point, the slope of the buckling load changes abruptly. The dimensionless stiffener's cross-section $\left(A_{stif}/A_{shell}\right)_{transition}$ and the corresponding failure load are both increasing as the stiffener's height h_{stif} increases. The same reasoning as for the thick-walled silos can be used to explain this shift of the transition point (See previous paragraph). The rapidly increasing branch is followed by an approximately constant (Fig. 5-23 (a) and (b): $h_{stif}/R = 0.5; 1.0$) or a slightly decreasing (Fig. 5-23 (c) and (d): $h_{stif}/R = 1.5; 2.0$) branch for larger cross-sections. Clearly, the slope of the second branch depends on the stiffener height h_{stif}. This finding will be explained when the influence of the height is discussed (i.e. in Section 5.2.5).

Another finding is that the failure load of the approximately horizontal branch in Fig. 5-23 (i.e. the second branch after the transition point) increases when the stiffener's height h_{stif} increases, because a larger stiffener height improves the stress distribution in circumferential direction. The positive influence of the attached stiffener height h_{stif} to the failure load and behaviour is discussed in detail in Section 5.2.5.

The abrupt transition of the slope suggests that the stiffener's cross-section strongly influences the buckling behaviour. Indeed, for smaller cross-sections (i.e. $A_{stif}/A_{shell} < \left(A_{stif}/A_{shell}\right)_{transition}$), premature failure will occur in the stiffened region (E.1 in Fig. 5-23), because the stiffener cannot fully absorb the supporting load. This premature type of failure of the stiffening configuration must be avoided. In contrast, for longitudinal stiffeners with a large cross-section (i.e. $A_{stif}/A_{shell} > \left(A_{stif}/A_{shell}\right)_{transition}$), failure will shift to the unstiffened silo wall just above the terminations of the U-shaped stiffener (E.2 in Fig. 5-23). Now, the suitable stiffener is able to gradually transfer the support load into the silo wall, spreading the load in circumferential direction and reaching a maximum failure load. All buckling modes will be discussed later more in detail.

The value $\left(A_{stif}/A_{shell}\right)_{transition}$ increases with the stiffener's height h_{stif}, because a higher stiffener must be able to absorb a higher load due to its better distribution of the stresses in the circumferential direction of the shell wall.

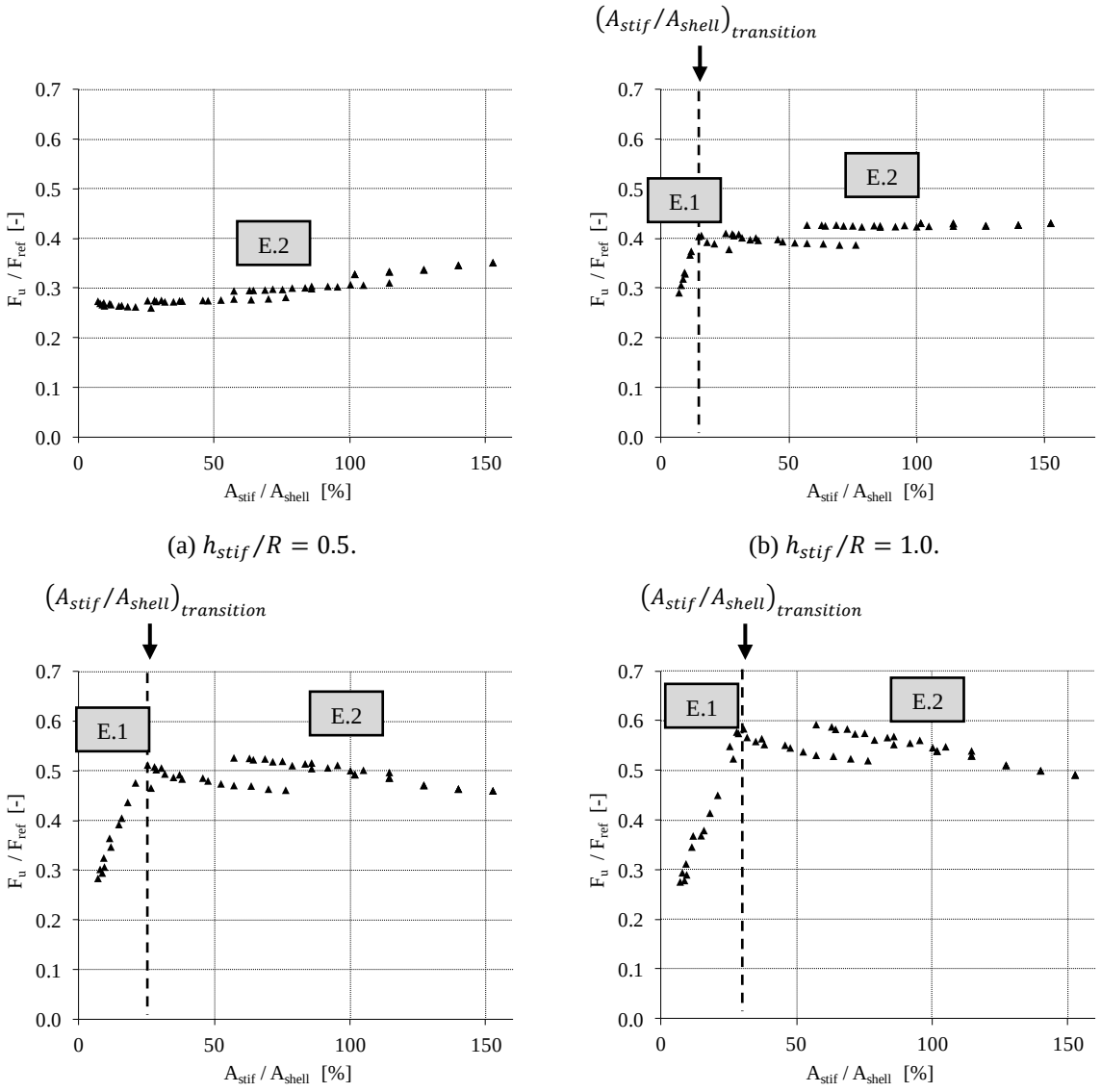

(a) $h_{stif}/R = 0.5$.

(b) $h_{stif}/R = 1.0$.

(c) $h_{stif}/R = 1.5$.

(d) $h_{stif}/R = 2.0$.

Fig. 5-23 Dimensionless GMNA failure load F_u/F_{ref} as a function of the ratio of the cross-section of the longitudinal stiffeners to the cross-section of the silo wall A_{stif}/A_{shell} for different stiffener heights ($R/t = 1000$).

In the previous paragraphs, some important findings were formulated concerning the influence of the stiffener's cross-section A_{stif} and its relation to the stiffener's height h_{stif}. In what follows, these findings will be clarified by studying the silo behaviour and buckling patterns.

Failure mode E.1/a If a U-shaped stiffener is placed above a discrete support, the stiffener will absorb a large part of the supporting load, depending on the relative stiffnesses of the stiffener and the silo wall, and transfer it gradually into the silo wall. However, if the longitudinal stiffeners have a relatively small cross-section, the maximal absorbable load for each stiffener (i.e. $A_{stif} \cdot \sigma_y$) is rather limited. In other words, the material of the stiffeners is already fully exhausted (i.e. yielding of the entire stiffener's cross-section, see Fig. 5-24) at a relatively small load level. At that point, the stiffeners are not able to absorb more load, and the maximum load of the structure is reached before the buckling load of the silo wall is reached.

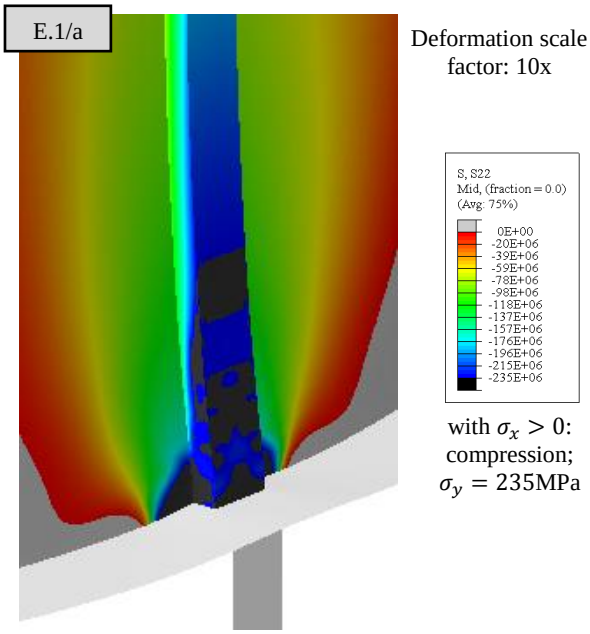

Fig. 5-24 Contourplot of the axial stresses σ_x at the moment of maximal load for stiffeners with a relatively small cross-section (E.1/a) [Pa].

After reaching the maximum load of the silo structure, the stress level in the thin-walled silo wall just adjacent to the U-shaped stiffeners will increase further. From a certain point, a critical stress level will be reached, causing two elastic buckles in that area. This post-buckling deformation shape can be observed in the plots of Fig. 5-25.

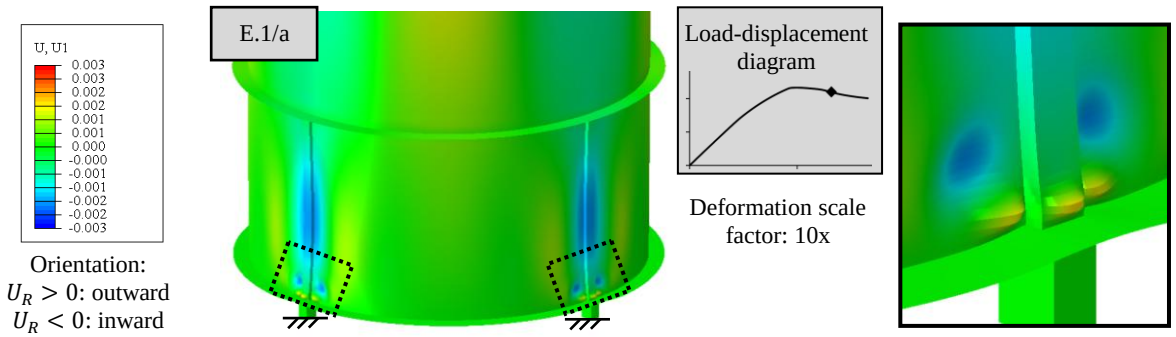

Fig. 5-25 Post-buckling radial deformations U_R for stiffeners with a relatively small cross-section (E.1/a) [m].

Failure mode E.1/b Similar to the previously discussed failure mode E.1/a, premature failure will also occur in the stiffened region due to yielding of the entire relatively small cross-section of the longitudinal stiffeners (Fig. 5-26 (a)). However, in the case of higher longitudinal stiffeners, the post-buckling deformations (See Fig. 5-26 (b)) are different from those of failure mode E.1/a. Indeed, at the moment of maximum load level, a plastic hinge is formed in the U-shaped stiffener, causing high rotations at that point, and the stiffener

collapses inwardly.

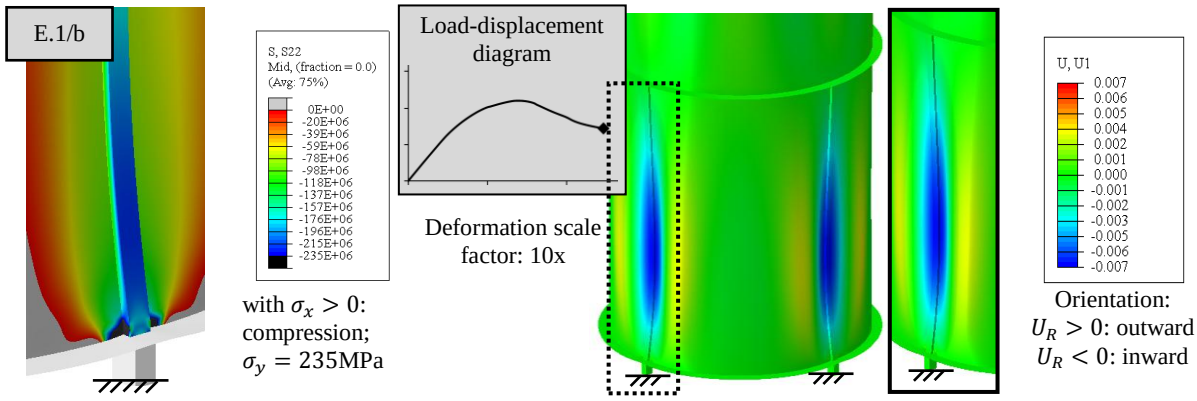

(a) Contourplot of the axial stresses σ_x at the moment of maximal load [Pa].

(b) Post-buckling radial deformations U_R [m].

Fig. 5-26 Failure mode E.1/b for high stiffeners with a relatively small cross-section.

Failure modes E.2/a and E.2/b As can been seen in Fig. 5-23, a maximum buckling load is reached for longitudinal stiffeners with an intermediate and a large cross-section (E.2). In these cases, the stiffener is able to absorb the supporting load without problems, and afterwards, to transfer this load gradually into the silo wall.

For a stiffener with a small width in circumferential direction d_{stif}, one buckle will be formed in the silo wall above the centre of the stiffener. This buckling pattern is called E.2/a and is shown in the left side of Fig. 5-27 (a). In contrast, when the distance between the flanges of the U-shaped stiffener increases (i.e. larger value of d_{stif}), two separate buckles are formed. This buckling mode is called E.2/b and is shown in the right side of Fig. 5-27 (a).

At the height corresponding with the centre of the buckle(s), a circumferential path PC/S-h1.15 ($h_{path}/h_{stif}^{sup} = 1.15$) has been created in the unstiffened silo wall along which the axial stresses at the moment of buckling. The buckling and post-buckling radial deformations are plotted in Fig. 5-27 (b). For the stiffener corresponding with E.2/a (small value of d_{stif}), the highest axial stresses are located in the area just above the terminations of the stringer stiffeners ($\theta < 10°$), while the axial stress level in the intermediate area between the stiffeners ($\theta > 10°$) is substantially lower. In the area of the elevated stress concentrations ($\theta < 10°$), failure will occur due to elastic buckling in the unstiffened silo wall (See left side of Fig. 5-27 (b)). For the stiffener corresponding with E.2/b (larger value of d_{stif}), the highest axial stresses can be found at a circumferential angle θ between 5 and 6°, which corresponds with the circumferential angle of the flange of the U-shaped longitudinal stiffener and the location of one of the two buckles (See right side of Fig. 5-27 (b)).

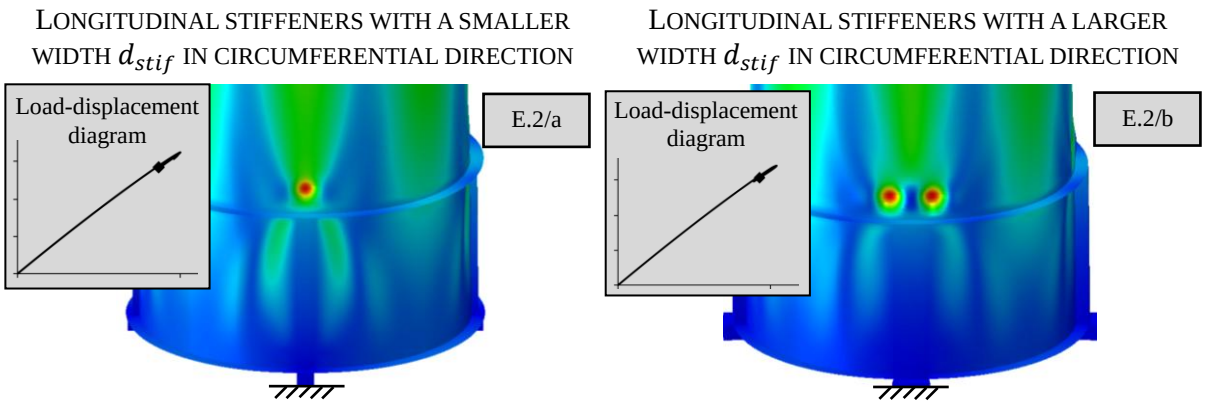

(a) Contourplot of the post-buckling deformations (left: E.2/a, right: E.2/b).

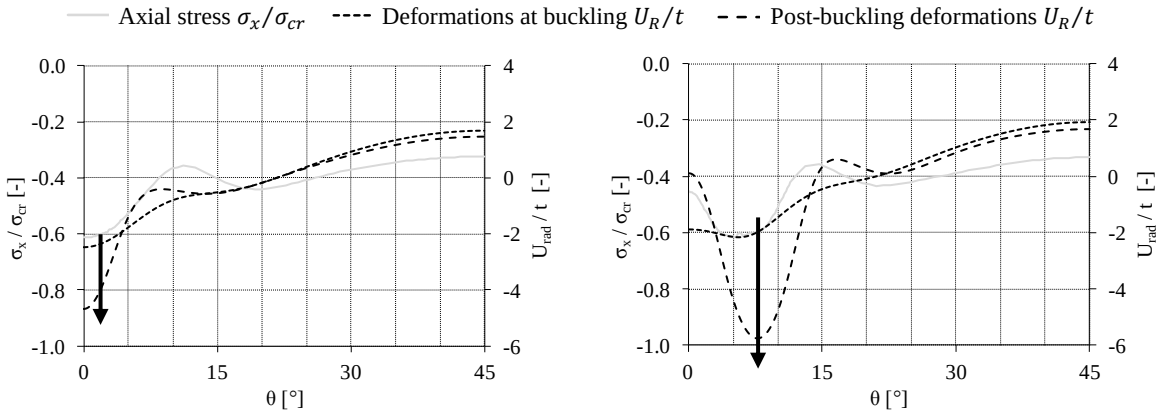

(b) Stresses and deformations in the silo wall along PC/S-h1.15 (left: E.2/a, right: E.2/b).

Fig. 5-27 Failure behaviour of longitudinal stiffener's with a relatively large cross-section.

Conclusions

The U-shaped longitudinal stiffeners which correspond with the rapidly increasing branch in Fig. 5-21 and Fig. 5-23 have a cross-section which is too small. Consequently, the stiffener can only absorb a limited supporting load, resulting in premature failure (plastic yielding or elasto-plastic buckling) in the stiffened region (i.e. the silo wall and the stiffener itself just above the local supports). This situation should be avoided at all times because the maximum load of the silo wall has not yet been reached (i.e. the approximately horizontal branch in Fig. 5-21 and Fig. 5-23). The U-shaped longitudinal stiffeners corresponding with the latter branch have a larger cross-section (i.e. $A_{stif}/A_{shell} > \left(A_{stif}/A_{shell}\right)_{transition}$). Only in that way, a sufficiently large supporting load can be absorbed and then introduced in the silo wall, by which the maximum absorbable load of the silo wall is reached. Furthermore, for these cases, failure (plastic yielding and/or elastic buckling) will occur in the unstiffened silo wall just above the terminations of the stringer stiffeners. The above findings are valid both for thick-walled and for thin-walled silos.

At first sight, it can be concluded that a longitudinal stiffener with an intermediate value of

the cross-section is optimal, thus with a value equal to $\left(A_{stif}/A_{shell}\right)_{transition}$, because a further increase of the stiffener's cross-section A_{stif} usually will lead to a limited increase or decrease (depending on the stiffener's height h_{stif}) of the failure load. This will also be apparent from the results of Section 5.4.1.

In Section 5.4, the optimal combination of shape and height of a U-shaped longitudinal stiffener will be determined and investigated more in detail. It will be demonstrated that when the failure load must be further increased, it is more interesting to increase the stiffener's height h_{stif} than increasing the value of A_{stif}/A_{shell} above $\left(A_{stif}/A_{shell}\right)_{transition}$ to minimise the use of material.

5.2.2 Width in circumferential direction of the U-shaped stiffener

Since the silos are discretely supported, the degree of support is a very important geometrical parameter. It was chosen to give the stringer stiffener the same width in circumferential direction as the supporting column (or $d_{stif} = d_{sup}$). In other words, the flanges of the U-shaped profile coincide with the edges of the supporting column. In this way, a maximum failure load is obtained for a constant degree of support along the circumference (i.e. a constant value of μ_{sup}).

Thick-walled silos

The results of the dimensionless GMNA failure load F_u/F_{ref} for a varying width d_{stif}/R are presented in Fig. 5-28 for stringer stiffeners with a variable height ($0.5 \leq h_{stif}/R \leq 2.0$). The bilineair curves suggest that again each branch corresponds with a different location of the plastic yielding zone, as already mentioned in Paragraph 5.2.1. Indeed, for silos with a small circumferential width d_{stif} (i.e. $d_{stif}/R < \left(d_{stif}/R\right)_{transition}$), the silo will fail by premature yielding of the stiffened zone just above the supports (failure mode P.1 displayed in Fig. 5-22 (a)). This corresponds with the rapidly increasing branch in Fig. 5-21.

However, from a particular width d_{stif} (i.e. black dashed line in Fig. 5-28, $d_{stif}/R \geq \left(d_{stif}/R\right)_{transition}$), the slope of the curve reduces significantly, and thus reducing the advantageous effect of the circumferential width d_{stif} on the dimensionless failure load F_u/F_{ref}. Moreover, the area of failure moves to the unstiffened silo wall above the terminations of the U-shaped longitudinal stiffeners (failure pattern P.2 displayed in Fig. 5-22 (b)). As will be shown below, the effect of the width d_{stif} in the second branch largely depends on the height of stiffener h_{stif}. Indeed, by comparing the slope of the second branch of an intermediately high stringer stiffener (Fig. 5-28 (b)) and a high stringer stiffener (Fig. 5-28 (d)), the circumferential width d_{stif} is more favourable for a shorter stiffener than for a

higher longitudinal stiffener.

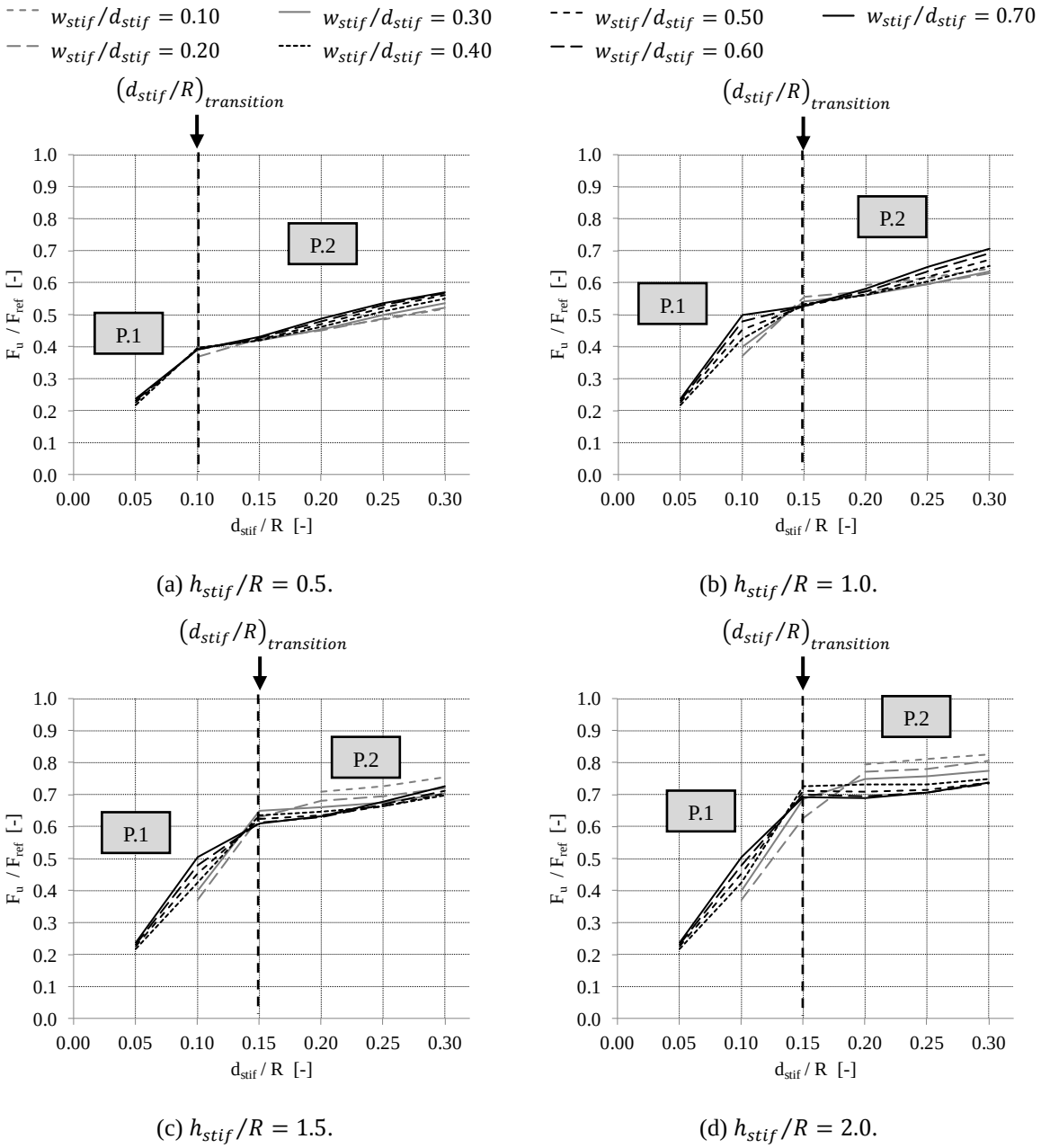

(a) $h_{stif}/R = 0.5$.

(b) $h_{stif}/R = 1.0$.

(c) $h_{stif}/R = 1.5$.

(d) $h_{stif}/R = 2.0$.

Fig. 5-28 Dimensionless GMNA failure load F_u/F_{ref} as a function of the ratio of the circumferential width of the longitudinal stiffener to the silo radius d_{stif}/R for different stiffener heights ($R/t = 200$; t_{stif}/t = max.).

The previous finding will be illustrated in Fig. 5-29. In this figure, the distribution of the dimensionless axial stress σ_x/σ_y at the moment of maximum load is plotted along a circumferential path in the silo wall just above the upper ring, which corresponds with the height in the unstiffened silo wall where yielding occurs (as in failure pattern P.2). However, for silos with a small circumferential width $d_{stif}/R = 0.05; 0.10 < (d_{stif}/R)_{transition}$, premature failure occurs by (elasto-)plastic yielding in the stiffened region above the local supports (i.e. failure pattern P.1), resulting in small axial stresses in the unstiffened silo wall

(much lower than the yield stress: $\sigma_x/\sigma_y \ll 1$). In contrast, for silos with a larger circumferential width ($d_{stif}/R \geq \left(d_{stif}/R\right)_{transition}$), plastic yielding will shift to the unstiffened silo wall as displayed in Fig. 5-22 (b) (i.e. failure pattern P.2).

When P.2 is the failure pattern, the width d_{stif} has a more advantageous effect on the failure load in the case of shorter longitudinal stiffener (See Fig. 5-28 (b)) than for a higher longitudinal stiffener (See Fig. 5-28 (d)). This can be addressed to the fact that, within the limited height of the stiffened zone, the axial stresses could not be maximally spread over the circumference of the silo wall. By increasing the circumferential width d_{stif}, the circumferential distance/angle over which the stresses must be distributed is reduced, increasing the stress level between the supports (See $\theta > 10°$ in Fig. 5-29 (a)). In other words, the stresses are spread more quickly over the circumferential for a constant small stiffener height. In contrast, for silos with higher longitudinal stiffener's (Fig. 5-28 (d)), this beneficial effect does not occur, because the stresses can perfectly be spread in circumferential direction within the height of the stiffened zone (See $\theta > 10°$ in Fig. 5-29 (b)). In this case, an additional width in circumferential direction is no longer necessary.

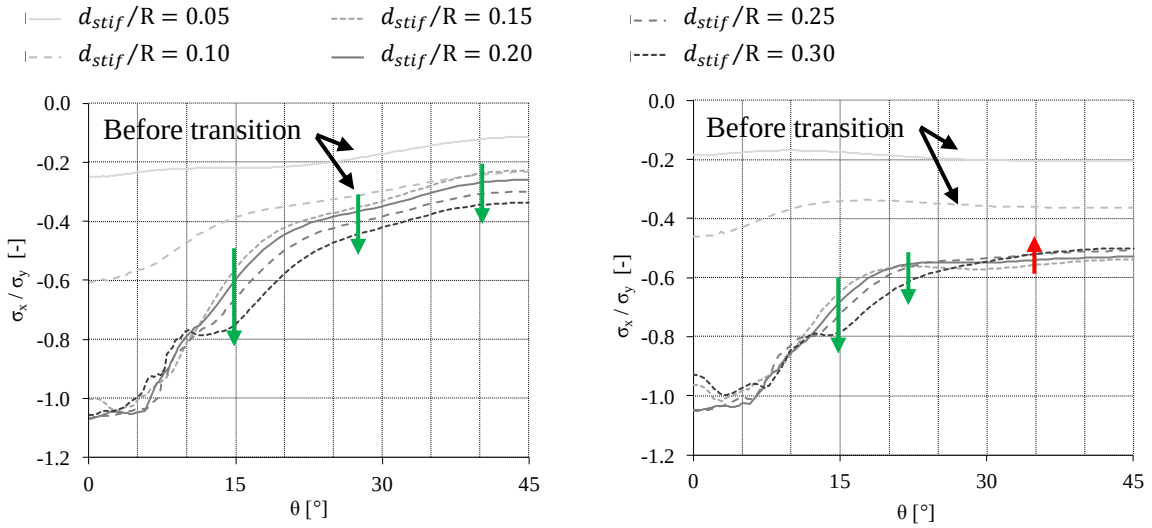

(a) Short stringer stiffener ($h_{stif}/R = 1.0$) (PC/S-h1.15).

(b) High stringer stiffener ($h_{stif}/R = 2.0$) (PC/S-h1.075).

Fig. 5-29 Axial stress distribution σ_x/σ_y at the moment of maximum load along a circumferential path just above the upper ring.

Independent of the stringer's height, a second but less pronounced effect of the width d_{stif} on the maximum load can be observed. By increasing the circumferential width d_{stif}, the plastic yielding zone is slighty extended in circumferential direction. However, this is negligible with respect to the first-mentioned finding.

Thin-walled silos

In Fig. 5-30, the dimensionless GMNA failure load F_u/F_{ref} is plotted against the width in circumferential direction d_{stif}/R for stringer stiffeners with a variable height ($0.5 \leq h_{stif}/R \leq 2.0$). In the left-hand side of all graphs, the failure load increases rapidly (i.e. $d_{stif}/R < \left(d_{stif}/R\right)_{transition}$). This corresponds with premature failure of the stiffened region above the local supports (i.e. failure mode E.1). For $d_{stif}/R \geq \left(d_{stif}/R\right)_{transition}$, the failure load remains approximately constant (slight increase or decrease) and failure shifts to the unstiffened silo wall above the terminations of the stringer stiffeners (i.e. failure mode E.2).

For higher stringer stiffeners ($h_{stif}/R \geq 1.5$), it can be observed in Fig. 5-30 that the failure load decreases again when d_{stif}/R increases above its transition value. This finding is not caused by the increasing circumferential width, but by the way the radial width w_{stif} is defined. Indeed, when d_{stif} increases and w_{stif}/d_{stif} remains constant, the radial width w_{stif} will increase with the same amount as d_{stif}. Since the latter has an unfavourable effect, as will be demonstrated in Section 5.2.3, the results in Fig. 5-30 (c) and (d) are misleading and the circumferential width d_{stif} certainly has a favourable effect, also for higher stringer stiffeners.

Conclusions

Both for thick-walled and for thin-walled silos, it can be concluded that the circumferential width d_{stif}/R must have a minimum value to avoid premature failure by (elasto-)plastic yielding in the stiffened silo wall and stiffeners just above the local supports (that are respectively failure pattern P.1 and E.1).

Above a certain minimum value of the circumferential width d_{stif}/R, the additional circumferential width influences the failure load to a lesser degree, depending on the stiffener's height h_{stif}. The higher the longitudinal stiffener is, the smaller the beneficial influence of the circumferential width d_{stif}/R on the failure load. The reason for this less pronounced effect for higher stiffeners is that the supporting forces (and axial stresses) are already better distributed in circumferential direction when the stiffener's height increases.

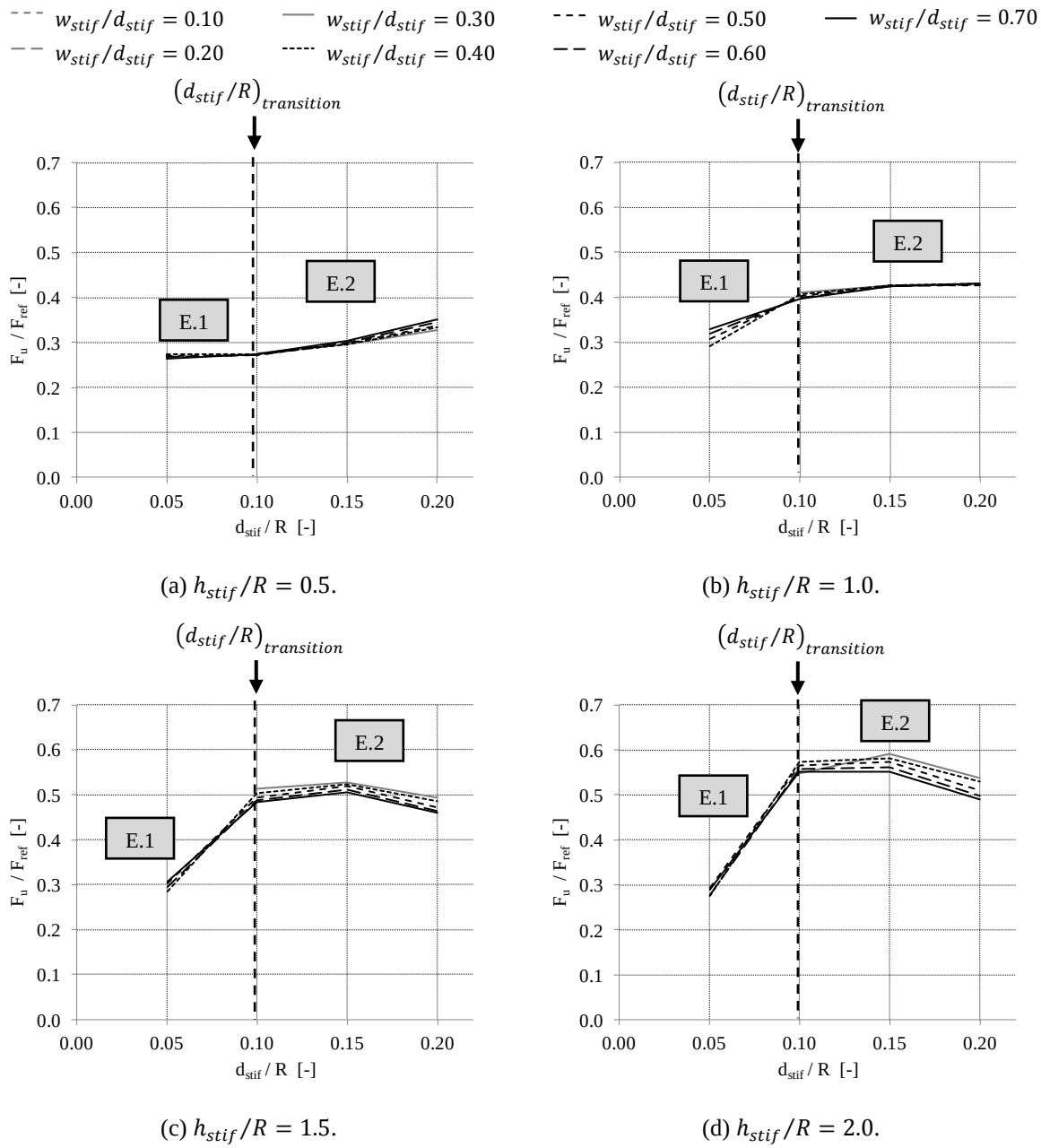

(a) $h_{stif}/R = 0.5$.

(b) $h_{stif}/R = 1.0$.

(c) $h_{stif}/R = 1.5$.

(d) $h_{stif}/R = 2.0$.

Fig. 5-30 Dimensionless GMNA failure load F_u/F_{ref} as a function of the ratio of the circumferential width of the longitudinal stiffener to the silo radius d_{stif}/R for different stiffener heights ($R/t = 1000$; $t_{stif}/t =$ min.).

5.2.3 Width in radial direction of the U-shaped stiffener

In Fig. 5-31, the dimensionless GMNA failure load F_u/F_{ref} is plotted against the ratio of the radial width (variable) and the circumferential width (constant) w_{stif}/d_{stif} for different heights of the longitudinal stiffeners ($0.5 \leq h_{stif}/R \leq 2.0$). As mentioned before, the width in radial direction w_{stif} of the U-shaped longitudinal stiffeners is varied between 10 and 70 percent of its width in circumferential direction d_{stif}.

The stiffener geometries where premature failure occurs in the stiffened region above the local supports (i.e. failure modes P.1 and E.1) are not considered, because in these cases, all dimensions of the stiffener's cross-section have an advantageous effect (thus also the radial width w_{stif}), since in that case, more material can yield before the silo fails by (elasto-)plastic yielding in the stiffened region. Thus, both for the thick-walled silo (i.e. $R/t = 200$ in Fig. 5-31 (a)) and for the thin-walled silo (i.e. $R/t = 1000$ in Fig. 5-31 (b)), a stiffener cross-section has been considered which coincides with the approximately horizontal branch in respectively Fig. 5-21 and Fig. 5-23. In other words, for both cases, failure (i.e. (elasto-) plastic yielding or elastic buckling) occurs in the unstiffened silo wall above the top of the stringer stiffeners (respectively P.2 for $R/t = 200$ and E.2 for $R/t = 1000$).

In Fig. 5-31 (a), the longitudinal stiffener has a dimensionless circumferential width d_{stif}/R of 0.20 and a maximum stiffener's thickness. In Fig. 5-31 (b), the longitudinal stiffener has a dimensionless circumferential width d_{stif}/R of 0.15 and a minimum stiffener's thickness. For the latter geometry, the cases where the radial width w_{stif} is equal to 10 and 20 percent of the circumferential width d_{stif} are not calculated because Eqs. (3-3) to (3-4) (See Table 3-11) are not met.

In general, the radial width w_{stif} has a minor influence on the failure load F_u, compared to the circumferential width d_{stif} (as discussed in previous section). Furthermore, one can observe that the influence of the radial width w_{stif} on the failure load depends on the stiffener's height h_{stif}. Indeed, a large radial width w_{stif} is slightly beneficial for shorter longitudinal stiffeners and becomes more and more unfavourably for higher longitudinal stiffeners.

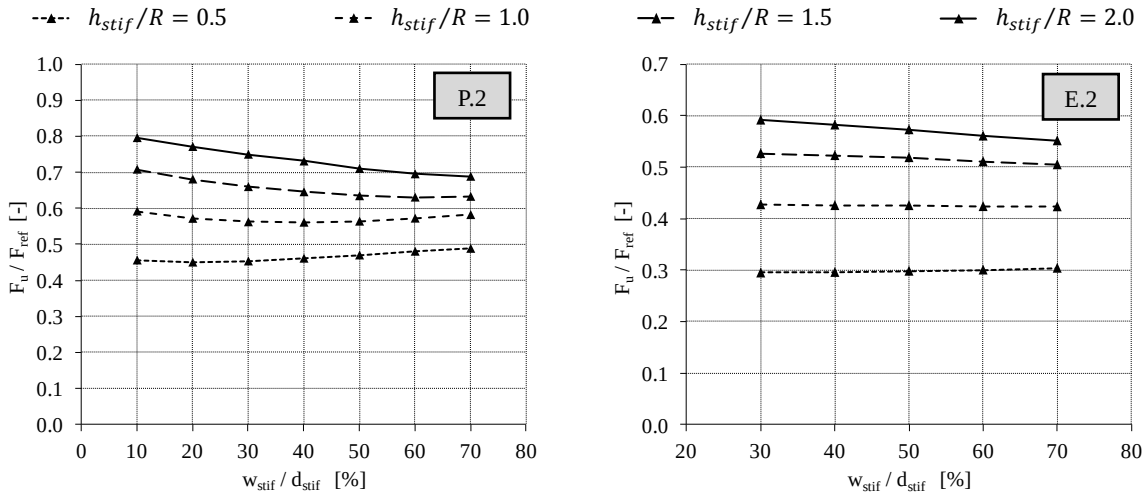

(a) Thick-walled silo ($R/t = 200$; $d_{stif}/R = 0.20$; t_{stif}/t = max.).

(b) Thin-walled silo ($R/t = 1000$; $d_{stif}/R = 0.15$; t_{stif}/t = min.).

Fig. 5-31 Dimensionless GMNA failure load F_u/F_{ref} as a function of the ratio of the radial width to the circumferential width of the longitudinal stiffener w_{stif}/d_{stif} for different stiffener heights (variable A_{stif}/A).

To explain the latter unfavourable effect for higher stringer stiffeners, a new parameter is introduced, namely the eccentricity e_{stif}, which corresponds to the centre of gravity of the support reaction forces relative to the shell wall.

$$e_{stif} = \frac{\left(F_{sup,silo} \cdot 0\right) + \sum\left(F_{sup,stiffener,i} \cdot e_i\right)}{F_{sup,silo} + F_{sup,stiffener}} \tag{5-13}$$

In this equation, the reaction forces $F_{sup,silo}$ and $F_{sup,stiffener}$ ($F_{sup,stiffener,i}$) are absorbed in respectively the supported silo wall and (a part of) the longitudinal U-shaped stiffener. The eccentricity e_{stif} is always measured from the silo wall and a positive value corresponds with a reaction force on the exterior of the silo wall.

Thick-walled silos

For stiffeners with a small radial width w_{stif}, the eccentricity e_{stif} of the reaction force is limited, since all material of the stiffener has been added in the vicinity of the silo wall. The reaction force will be largely absorbed by the web and less by the flanges of the stiffener. By increasing the radial width w_{stif}, the reaction force moves in outward direction and the eccentricity of the reaction force e_{stif} increases (See Fig. 5-32 (a)), resulting in the tendency of the longitudinal stiffener to deform more in inward direction.

In Fig. 5-32 (b), the radial deformations are plotted for a circumferential path in the silo wall just above the upper ring ($h_{path}/h_{stif}^{sup} = 1.075$). The inwardly oriented deformations above the terminations of the longitudinal stiffener ($0° \leq \theta \leq 22°$) are increasing as the width w_{stif} (and the eccentricity) increase. Clearly, the upper ring cannot prevent these inward deformations of the silo wall in its vicinity.

In Fig. 5-32 (c), the dimensionless compressive axial stress σ_x/σ_y at the moment of failure is plotted along a circumferential path in the silo wall just above the stiffeners ($h_{path}/h_{stif}^{sup} = 1.075$). From this figure, it appears that the effective yield stress σ_y^{eff} above the top of the stiffener ($\theta \leq 10°$) and the axial stresses σ_x in the region between the stiffeners ($10° \leq \theta \leq 45°$) are both decreasing when the radial width w_{stif} increases.

The decrease of the effective yield stress σ_y^{eff} can be attributed to the flattening effect of the silo wall above the stiffener (See Fig. 5-32 (b)). For a more detailed discussion of the relationship between the deformations before failure and the reduced effective yield stress, the reader is referred to Section 3.4.

The decrease of the axial stresses σ_x between the stiffeners is due to the less rapid (and thus less efficient) transfer of the supporting force between the stiffener on the hand and the silo

wall on the other hand, assuming that stiffener height h_{stif} remains constant. Indeed, an increased value of the eccentricity e_{stif} means that the reaction force is absorbed by more distant material of the stiffener with respect to the silo wall. The flanges will absorb more force, the web less.

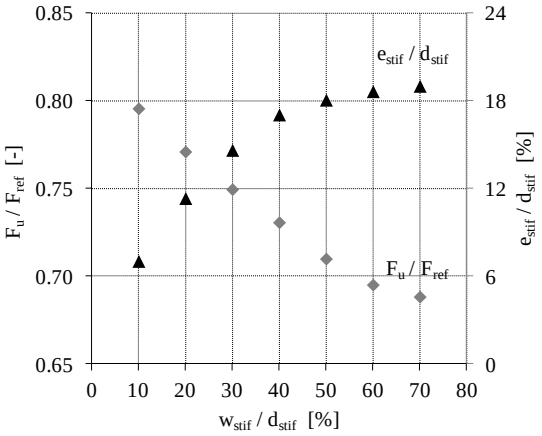

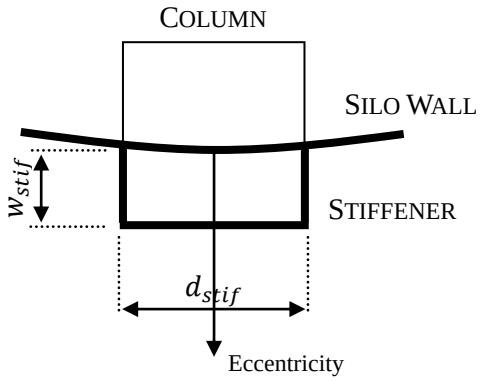

(a) The dimensionless GMNA failure load F_u/F_{ref} and the ratio of the eccentricity of the support to the circumferential direction e_{stif}/d_{stif} as a function of the ratio of the radial width to the circumferential width of the longitudinal stiffeners w_{stif}/d_{stif}.

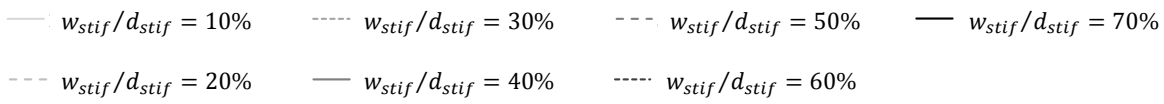

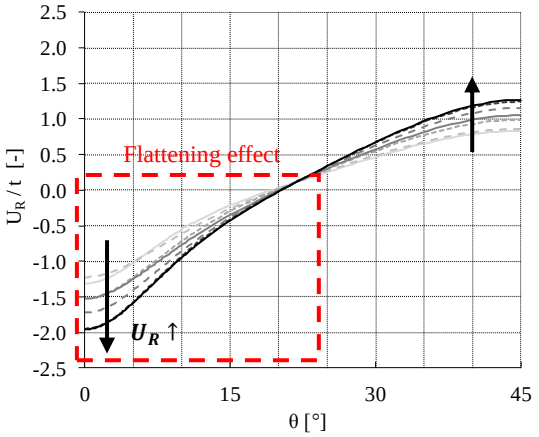

(b) Plot of the ratio of the radial deformation at the moment of failure to the silo wall thickness U_R/t [-] against the circumferential angle θ [°] for a circumferential path PC/S-h1.075 (h_{path}/h_{stif} = 1.075).

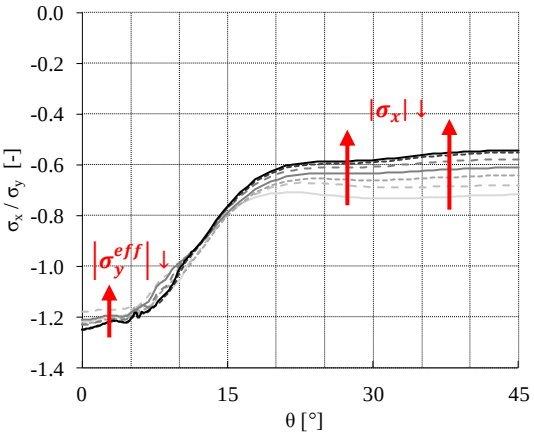

(c) Plot of the ratio of the axial stress at the moment of failure to the yield stress σ_x/σ_y [-] against the circumferential angle θ [°] for a circumferential path PC/S-h1.075 (h_{path}/h_{stif} = 1.075).

Fig. 5-32 Failure behaviour for a thick-walled silo (R/t = 200) and a U-shaped stiffener (d_{stif}/R = 0.20; t_{stif}/t = max.; h_{stif}/R = 2.0) with a variable radial width w_{stif}.

Thin-walled silos

For stiffeners with a small radial width w_{stif}, the eccentricity e_{stif} of the reaction force is rather limited, since all material is in the vicinity of the silo wall. By increasing the radial width w_{stif}, the eccentricity e_{stif} of the reaction force increases, as can be seen in Fig. 5-33 (a). This effect can be partially attributed to the larger distance between the web of the stiffener and the silo wall. In other words, the reaction forces shifts in outward direction, resulting in the tendency of the longitudinal stiffener to deform easier inwardly.

In Fig. 5-33 (b), the radial deformations are plotted for a circumferential in the unstiffened silo wall above the upper ring ($h_{path}/h_{stif}^{sup} = 1.075$). And, indeed, the inwardly oriented deformations just above termination of the stringer stiffeners ($\theta < 15°$) increase as the radial width w_{stif} increases (and consequently also the eccentricity e_{stif}). Clearly, the upper ring cannot fully prevent the inwardly oriented deformations of the stiffener and the unstiffened silo wall.

In Fig. 5-33 (c), the dimensionless compressive axial stress σ_x/σ_{cr} at the moment of failure is plotted along a circumferential path in the silo wall just above the stiffeners ($h_{path}/h_{stif}^{sup} = 1.075$). From this figure, it appears that the critical buckling stress σ_{cr} above the top of the stiffener ($\theta \leq 5°$) and the axial stresses σ_x in the region between the stiffeners ($5° \leq \theta \leq 45°$) are both decreasing when the radial width w_{stif} increases.

The decrease of the critical buckling stress σ_{cr} can be attributed to the flattening effect of the silo wall above the stiffener (See Fig. 5-33 (b)). For a more detailed discussion of the relationship between the deformations before failure and the reduced critical buckling stress, the reader is referred to Section 3.4.

The decrease of the axial stresses σ_x between the stiffeners is due to the less rapid (and thus less efficient) transfer of the supporting force between the stiffener on the one hand and the silo wall on the other hand, assuming that the stiffener height h_{stif} remains constant. Indeed, an increased value of the eccentricity e_{stif} means that the reaction force is absorbed by more distant material of the stiffener with respect to the silo wall. The flanges will absorb more force, the web less.

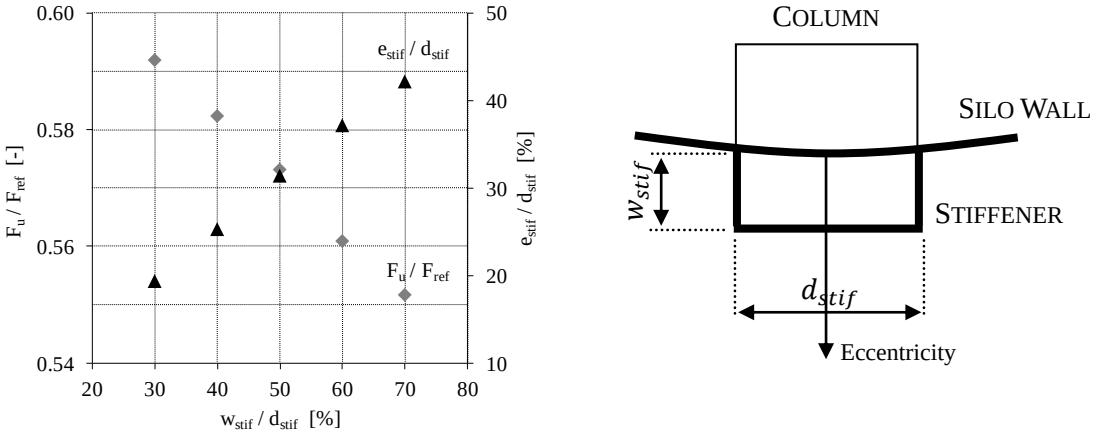

(a) The dimensionless GMNA failure load F_u/F_{ref} and the ratio of the eccentricity of the support to the circumferential direction e_{stif}/d_{stif} as a function of the ratio of the radial width to the circumferential width of the longitudinal stiffeners w_{stif}/d_{stif}.

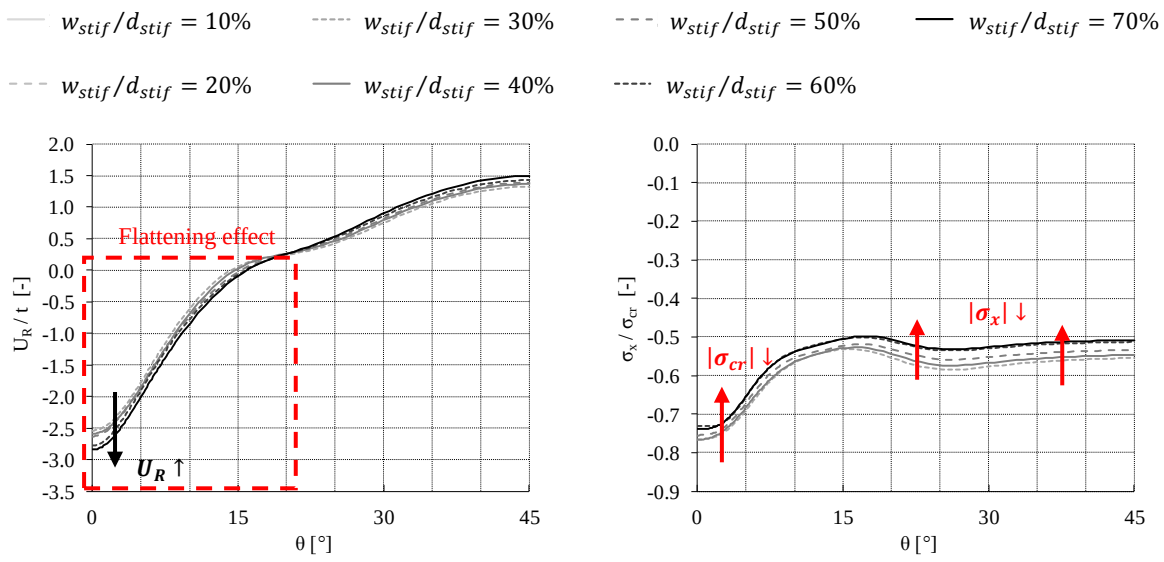

(b) Plot of the ratio of the radial deformation at the moment of failure to the silo wall thickness U_R/t [-] against the circumferential angle θ [°] for a circumferential path PC/S-h1.075 (h_{path}/h_{stif} = 1.075).

(c) Plot of the ratio of the axial stress at the moment of failure to the critical buckling stress σ_x/σ_{cr} [-] against the circumferential angle θ [°] for a circumferential path PC/S-h1.075 (h_{path}/h_{stif} = 1.075).

Fig. 5-33 Failure behaviour for a thin-walled silo (R/t = 1000) and a U-shaped stiffener (d_{stif}/R = 0.15; t_{stif}/t = min.; h_{stif}/R = 2.0) with a variable radial width w_{stif}.

Conclusions

In conclusion, it can be said that a small radial width w_{stif} is preferable (both for thick as for thin silos), because an increased radial width w_{stif} has two disadvantages.

First, a larger radial width w_{stif} will induce increased deformations in the silo wall before failure. At the critical location of failure in the silo wall above the top of the stiffener, the inward oriented deformations (i.e. the flattening effect) will lead to a reduction of the effective

yield stress (thick-walled silos) and the critical buckling stress (thin-walled silos) (See Section 3.4 for more information).

Second, the force is less efficiently transferred from the stiffener to the silo wall, because the reaction force is absorbed by more distant material of the stiffener with respect to the silo wall.

In addition, this choice (for a small radial width w_{stif}) is more important as the stiffener's height h_{stif} increases, since the first disadvantageous effect becomes increasingly important.

5.2.4 Wall thickness of the U-shaped stiffener

Thick and thin-walled silos

The relationship between the dimensionless failure load F_u/F_{ref} and the ratio of the stiffener's thickness to the silo thickness t_{stif}/t is displayed in Fig. 5-34 for two different cases and for different stiffener heights ($0.5 \leq h_{stif}/R \leq 2.0$). The minimum, average, and maximum value of t_{stif}/t are plotted within the interval defined by Eqs. (3-3) to (3-4). This interval depends on the silo thickness (i.e. R/t) and the circumferential and radial width of the stiffener (i.e. d_{stif}/R and w_{stif}/d_{stif}).

The graphs in Fig. 5-34 show that an increasing stiffener's wall thickness has a negligible influence on the failure load F_u, and, consequently also on the failure behaviour. This finding is only valid when the stiffening configuration, and in particular the longitudinal stiffeners, can largely absorb and transfer the load between the stiffener and the silo wall, without premature failure (failure modes P.2 and E.2). This corresponds with the approximately horizontal branch of Fig. 5-21 (if $R/t = 200$) and Fig. 5-23 (if $R/t = 1000$).

In contrast, when the longitudinal stiffeners are not able to absorb the supporting load and the longitudinal stiffeners prematurely fail before the silo wall in the direct vicinity of the top of the stringer stiffener fails (i.e. P.1 for $R/t = 200$ and E.1 for $R/t = 1000$), the stiffener's thickness has an appreciable influence on the failure load of the structure (cannot be derived from Fig. 5-34).

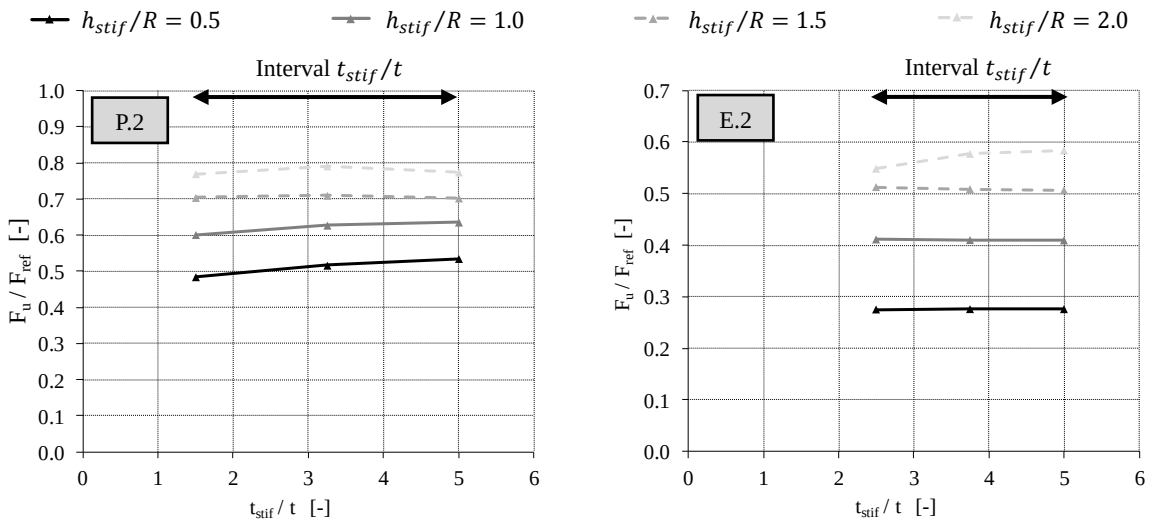

(a) $R/t = 200$; $d_{stif}/R = 0.30$. (b) $R/t = 1000$; $d_{stif}/R = 0.10$.

Fig. 5-34 Dimensionless GMNA failure load F_u/F_{ref} as a function of the ratio of the stiffener's thickness to the silo thickness t_{stif}/t for different stiffener heights ($w_{stif}/d_{stif} = 30\%$) (with $A_{stif}/A > (A_{stif}/A)_{transition}$).

Conclusions

The stiffener's wall thickness has a minor influence on the failure behaviour and failure load, on the condition that failure occurs in the unstiffened silo wall above the top of the partial-height longitudinal stiffeners. Similar results were found for other cross-sections.

5.2.5 Height of the U-shaped stiffener

The height of the stiffener determines the height of the stiffened cylindrical barrel, the position in axial direction of the upper ring, and the distance over which the longitudinal stiffener is attached to the silo structure along which the stiffener can transfer the supporting load into the silo wall by shear. As will be seen, this parameter strongly influences the failure load, both for thick-walled as for thin-walled silos.

Thick-walled silos

Fig. 5-35 shows the dimensionless GMNA failure load F_u/F_{ref} for different stiffener geometries (d_{stif}/R = variable; $w_{stif}/R = 0.06$; t_{stif}/t = max. according to Eqs. (3-3) to (3-4)). The height of the longitudinal stiffener h_{stif}/R is plotted on the horizontal axis.

The figure shows that the stiffener's height h_{stif} has no effect to the failure load if the stiffener has a relatively small cross-section A_{stif} ($A_{stif}/A_{shell} < (A_{stif}/A_{shell})_{transition}$) or a limited circumferential width d_{stif} (here: $d_{stif}/R < (d_{stif}/R)_{transition} = 0.15$), corresponding to the situation where the silo fails by (elasto-)plastic yielding in the stiffened area above the local supports (i.e. failure mode P.1). In this case, an additional stiffener height

is unnecessary.

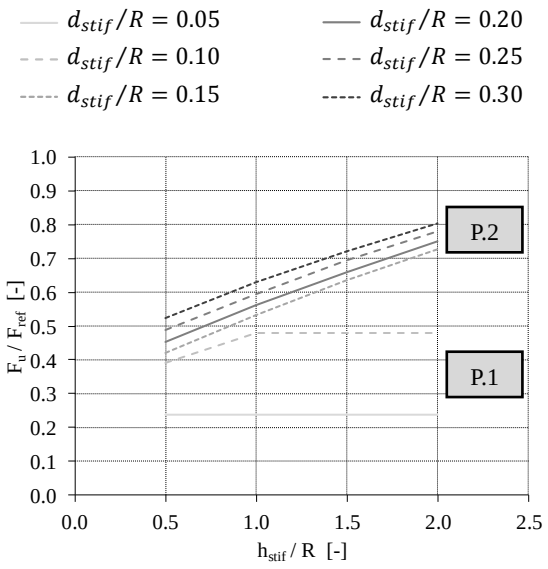

Fig. 5-35 Dimensionless GMNA failure load F_u/F_{ref} for a variable ratio of the stiffener's height to the cylinder radius h_{stif}/R ($R/t = 200$; $w_{stif}/R = 0.06$; t_{stif}/t = max.).

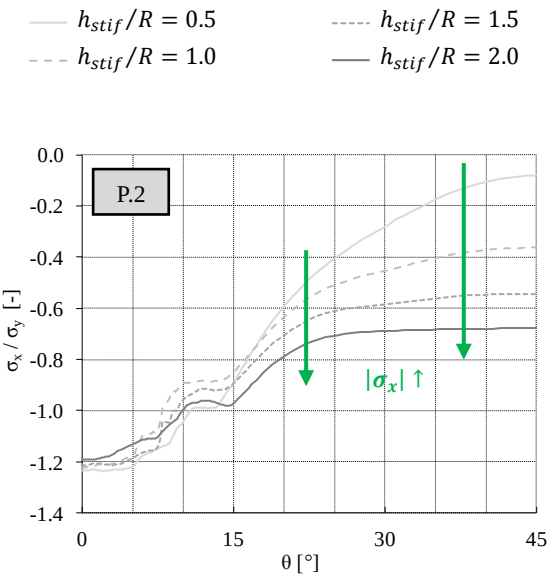

Fig. 5-36 Plot of the ratio of the axial stress at the moment of failure to the yield stress σ_x/σ_y [-] against the circumferential angle θ [°] for a circumferential path PC/S-h1.015 ($h_{path}/h_{stif}^{sup} = 1.015$) for a longitudinal stiffener with $d_{stif}/R = 0.30$; $w_{stif}/R = 0.06$; t_{stif}/t = max. ($R/t = 200$).

In contrast, for stiffeners with a larger cross-section A_{stif} ($A_{stif}/A_{shell} \geq (A_{stif}/A_{shell})_{transition}$) or a larger circumferential width d_{stif} (here: $d_{stif}/R \geq (d_{stif}/R)_{transition} = 0.15$), the silo fails by (elasto-)plastic yielding in the unstiffened silo wall above the terminations of the stiffener (i.e. failure mode P.2). For such stiffeners, the stiffener's height h_{stif} has a significant influence on the failure behaviour. Indeed, as the height of the stiffeners increases, the failure load increases substantially due to a more gradual transfer of the reaction force from the stiffener to the silo wall. This can be attributed to the larger distance over which the load can be transferred (by shear) between the stiffener on the one hand and the silo wall on the other hand.

This results in a better distribution of the axial compressive stresses over the entire circumference of the silo wall. The latter can be clearly distinguished in Fig. 5-36. In this figure, the axial stress distribution at the moment of maximum load is plotted along a circumferential path just above the upper ring. Clearly, the axial stresses σ_x are much distributed over the entire circumference as the stiffener's height h_{stif} increases ($\theta \geq 10°$).

Thin-walled silos

Fig. 5-37 shows the dimensionless GMNA failure load F_u/F_{ref} for different stiffener

geometries (d_{stif}/R = variable; $w_{stif}/R = 0.06$; t_{stif}/t = min. according to Eqs. (3-3) to (3-4)). The height of the longitudinal stiffener h_{stif}/R is plotted on the horizontal axis.

The figure shows that the stiffener's height h_{stif} has no effect to the failure load if the stiffener has a relatively small cross-section A_{stif} ($A_{stif}/A_{shell} < \left(A_{stif}/A_{shell}\right)_{transition}$) or a limited circumferential width d_{stif} (here: $d_{stif}/R < \left(d_{stif}/R\right)_{transition} = 0.10$), corresponding to the situation where the silo fails by (elasto-)plastic yielding in the stiffened area above the local supports (i.e. failure mode E.1). In this case, an additional stiffener height is unnecessary.

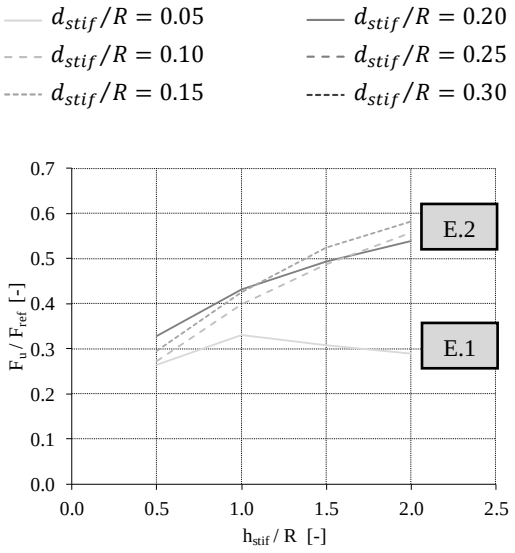

Fig. 5-37 Dimensionless GMNA failure load F_u/F_{ref} for a variable ratio of the stiffener's height to the cylinder radius h_{stif}/R ($R/t = 1000$; $w_{stif}/R = 0.06$; t_{stif}/t = min.).

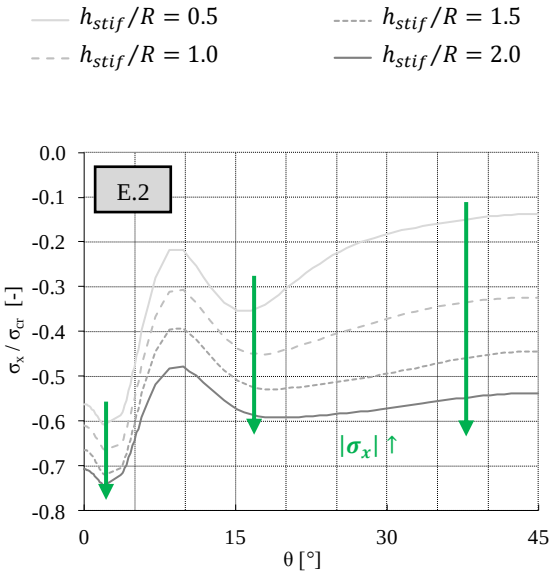

Fig. 5-38 Plot of the ratio of the axial stress at the moment of failure to the critical buckling stress σ_x/σ_{cr} [-] against the circumferential angle θ [°] for a circumferential path PC/S-h1.015 ($h_{path}/h_{stif}^{sup} = 1.015$) for a longitudinal stiffener with $d_{stif}/R = 0.10$; $w_{stif}/R = 0.06$; t_{stif}/t = min. ($R/t = 1000$).

In contrast, for stiffeners with a larger cross- section A_{stif} ($A_{stif}/A_{shell} \geq \left(A_{stif}/A_{shell}\right)_{transition}$) or a larger circumferential width d_{stif} (here: $d_{stif}/R \geq \left(d_{stif}/R\right)_{transition} = 0.10$), the silo fails by pure elastic buckling in the unstiffened silo wall above the terminations of the stiffener (i.e. failure mode E.2). For such stiffeners, the stiffener's height h_{stif} has a significant influence on the failure behaviour. Indeed, as the height of the stiffeners increases, the buckling load increases substantially due to a more gradual transfer of the reaction force from the stiffener to the silo wall. This can be attributed to the larger distance over which the load can be transferred (by shear) between the stiffener on the one hand and the silo wall on the other hand.

This results in a better distribution of the axial compressive stresses over the entire circumference of the silo wall. The latter can be clearly distinguished in Fig. 5-38. In this figure, the axial stress distribution at the moment of failure is plotted along a circumferential path just above the upper ring. Clearly, the axial stresses σ_x are much distributed over the entire circumference as the stiffener's height h_{stif} increases.

Conclusions

For stiffener's with a small cross-section (i.e. $A_{stif}/A_{shell} < \left(A_{stif}/A_{shell}\right)_{transition}$), an additional stiffener height h_{stif} is unnecessary, because premature failure will occur in the stiffened region just above the local supports due (elasto-)plastic yielding. On the contrary, for stiffener's with an intermediate and a large cross-section (i.e. $A_{stif}/A_{shell} \geq \left(A_{stif}/A_{shell}\right)_{transition}$), the stiffener's height h_{stif} is very advantageous (within the investigated range of heights: $0.5 \leq h_{stif}/R \leq 2.0$) and can lead to a significant increase of the failure load F_u, as can be clearly observed in Fig. 5-35 for thick-walled silos ($R/t = 200$) and Fig. 5-37 for thin-walled silos ($R/t = 1000$). The reason for this beneficial effect of the stiffener's height h_{stif} is that a higher longitudinal stiffener can distribute the axial stresses in circumferential direction (by shear) compared to a shorter longitudinal stiffener. It is important to mention that similar findings have been found for U-shaped stiffeners with other cross-sections.

5.3 Degree of support along the circumference

In this section, the influence of the degree of support along the circumference μ_{sup} on the failure load is investigated for thick-walled silos (i.e. $R/t = 200$) and for thin-walled silos (i.e. $R/t = 1000$). The variable supporting degree in circumferential direction is obtained by changing the circumferential width of the support/stiffener ($d_{sup} = d_{stif}$) and the number of local supports n_{sup}. The other geometrical parameters of the U-shaped stiffeners remain constant. All geometrical parameters of the longitudinal stiffeners are listed in Table 5-8. The cylindrical barrel and ring stiffeners have the default values for their geometry. All parts have a standard elasto-plastic material behaviour with a yield stress σ_y equal to 235MPa.

Table 5-8 Geometrical parameters of the U-shaped longitudinal stiffeners (variation of the degree of circumference).

PARAMETER	VALUE(S)	DIMENSION
n_{sup}	4; 6; 8; 10; 12; 14	-
d_{stif}/R	$R/t = 200$: 0.05; 0.10; 0.15; 0.20; 0.25; 0.30 $R/t = 1000$: 0.05; 0.10; 0.15; 0.20	-
w_{stif}/d_{stif}	30	%
h_{stif}^{sup}/R	1.0	-
t_{stif}/t	max.*	-

*: Minimum (min.), average (ave.), or maximum (max.) thickness - restrictions

In addition, unstiffened cylindrical barrels are calculated with four supports and a variable degree of support to compare the behaviour of unstiffened and stiffened cylindrical barrels.

Thick and thin-walled silos

In Fig. 5-39, the dimensionless GMNA failure load F_u/F_{ref} is plotted against the percentage of support along the circumference μ_{sup} for the above mentioned combinations. When comparing the silos stiffened with U-shaped stiffeners (i.e. the black curves) with the unstiffened cylindrical barrel (i.e. the gray curve), then it is found that fairly high loads are obtained at relatively small support rates due to the presence of the longitudinal stiffeners above the local supports. Without the presence of longitudinal stiffeners, the degree of support μ_{sup} must be 80% or more to resist similar loads. A second finding is that for the different values of the circumferential width d_{stif}, the curve consists of a rapidly increasing branch for a small number of supports and an approximately horizontal branch for a larger number of supports. The transition between these branches depends on the stiffener geometry (d_{stif}), and varies from 15 to 40%. Furthermore, the failure load F_u of the horizontal branch is respectively about 93% for the thick-walled silos and 81% for the thin-walled silos of the reference load F_{ref} with a constant stiffener height h_{stif} equal to the cylinder radius R. By increasing the stiffener's height h_{stif}, these curves will increase further.

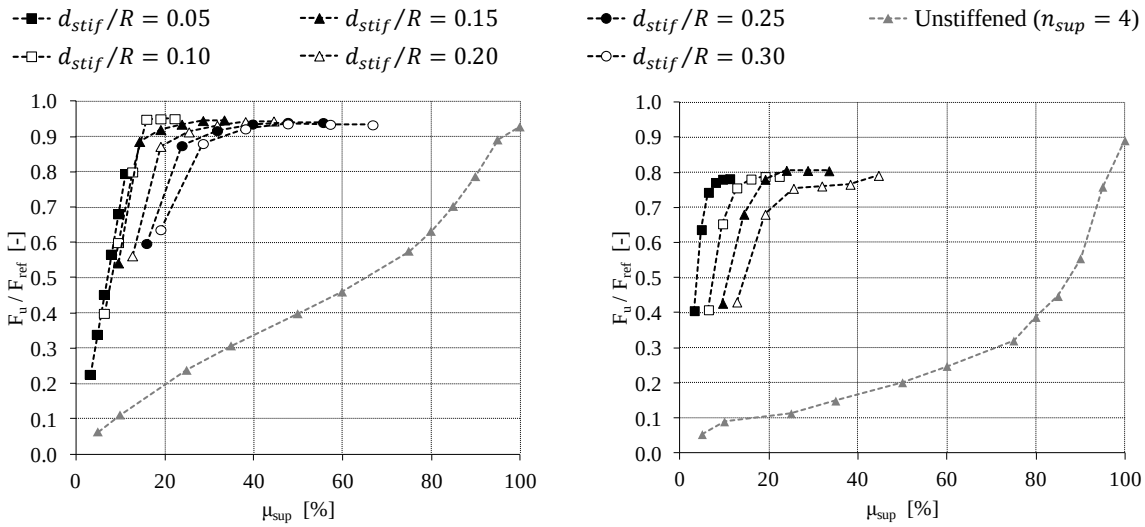

(a) Thick-walled silo ($R/t = 200$). (b) Thin-walled silo ($R/t = 1000$).

Fig. 5-39 Influence of the degree of circumferential support μ_{sup} on the dimensionless GMNA failure load for an unstiffened silo and a silo stiffened with U-shaped stiffeners ($w_{stif}/d_{stif} = 30\%$; t_{stif}/t = max.; $h_{stif}/R = 1.0$).

Conclusions

To conclude, the application of U-shaped partial-height longitudinal stiffeners above the discrete supports of cylindrical barrels (with a small value of μ_{sup}) is very advantageous to increase the failure load significantly, certainly compared to non-stiffened locally supported cylindrical barrels.

5.4 Optimisation parametric study

In this section, the "optimal U-shaped stiffener" will be determined, which is defined as a stiffener to which as little as possible material is added to obtain a certain failure load of the silo structure. This parametric study is separated in two substudies. At first instance, the influence of the height and the cross-section of the stiffener on the failure load is investigated and compared (Section 5.4.1). Afterwards, the stiffener's height and quantity of material of the stiffener's cross-section are kept constant, and the optimal dimensions of the U-shaped cross-section are determined (Section 5.4.2).

To determine the dimensions of the optimal U-shaped cross-section (See Fig. 5-40), the failure load has been computed for a large number of combinations of (d_{stif}, w_{stif}, and t_{stif}), while keeping the quantity of cross-sectional material A_{stif}/A_{shell} constant. In fact, A_{stif} is equal to the product of the (constant) number of local supports $n_{sup} = n_{stif}$ (= 4), the variable stiffener's developed length L_{stif} (represented in Fig. 5-40), and the variable stiffener's thickness t_{stif} (Eq. (5-14)). In other words, the stiffener's perimeter L_{stif} is inversely proportional to the stiffener's thickness t_{stif}, to keep the quantity of cross-sectional

material A_{stif} constant.

$$A_{stif} = n_{stif} \cdot L_{stif} \cdot t_{stif} \tag{5-14}$$

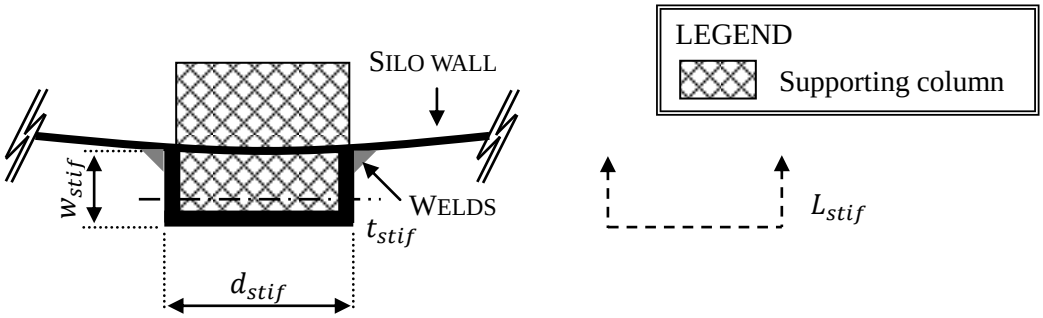

Fig. 5-40 U-shaped cross-section.

Only those thicknesses are considered for which Eqs. (3-3) to (3-4) are valid. Furthermore, the stiffener's perimeter L_{stif} is determined according to Eq. (5-15) and is changed by varying the circumferential width d_{stif} and the radial width w_{stif} within the corresponding intervals of Table 5-9.

$$L_{stif} = d_{stif} + 2 \cdot w_{stif} = d_{stif} \cdot \left(1 + 2 \cdot \frac{w_{stif}}{d_{stif}}\right) = d_{stif} \cdot (1 + 2p) \tag{5-15}$$

This optimisation study of the stiffener's cross-section has been done for different values of A_{stif}/A_{shell} (chosen on the basis of the exploratory study from Section 5.2: Fig. 5-21 for $R/t = 200$ and Fig. 5-23 for $R/t = 1000$) and for different stiffener's heights h_{stif}/R. The chosen values are given in Table 5-9.

Table 5-9 Geometrical parameters of the U-shaped longitudinal stiffeners (optimisation study).

PARAMETER	VALUE(S)	DIMENSION
n_{sup}	4	-
A_{stif}/A_{shell}	$R/t = 200$: 60; 80; 100; 120 $R/t = 1000$: 50; 60; 70; 80; 90; 100; 110	%
d_{stif}/R	$R/t = 200$: [0.15; 0.30] $R/t = 1000$: [0.05; 0.20]	-
w_{stif}/d_{stif}	[25; 75]	%
h_{stif}^{sup}/R	0.5; 1.0; 1.5; 2.0; 2.5	-
t_{stif}/t	variable	-

Before proceeding to the more detailed discussion of the optimal stiffener, it should be noted that in this study only stiffeners are taken into account which strengthen the structure in such a way that failure (yielding and/or buckling) occurs in the unstiffened silo wall above the terminations of the longitudinal stiffeners. On the basis of the results obtained from the previous extensive parametric study (Section 5.2), the longitudinal stiffeners which fail prematurely were omitted from this optimisation study.

5.4.1 Stiffener's height versus cross-section of the stiffener

In Fig. 5-41, the dimensionless GMNA failure load F_u/F_{ref} is displayed on a contourplot based on the results of the **optimal shape** of the stiffener's cross-section (which will be determined in Section 5.4.2) for each considered stiffener height h_{stif} and for each cross-section A_{stif}. The stiffener's height h_{stif}/R is plotted on the vertical axis, and the variable material parameter V_{extra}/V_{ref} (See Eq. (5-11) and Eq. (5-12)) on the horizontal axis. The latter parameter is proportional to the cross-section A_{stif} and the height h_{stif} of the longitudinal stiffeners.

As clearly shown in Fig. 5-41, a higher longitudinal stiffener is preferred over a stiffener with a large cross-section (despite the fact that only the optimal shapes were taken into account) to increase the failure load, both for thick-walled silos (Fig. 5-41 (a)) and for thin-walled silos (Fig. 5-41 (b)). In addition, for short stiffeners, the cross-section has a slightly beneficial influence on the failure load, while for higher stiffeners, it turns out that the cross-section is rather slightly unfavourable.

From these results, we can conclude that an increase of the stiffener's height is more effective to increase the failure load than an increase of the stiffener's cross-section. In the next paragraph, the optimal shape of the stiffener's cross-section will be determined.

5.4.2 Determination of the optimal cross-section

At first instance, the optimal shape of the stringer stiffeners are determined for the thick-walled silos (i.e. $R/t = 200$), and afterwards, for thin-walled silos (i.e. $R/t = 1000$). Finally, some conclusions are drawn.

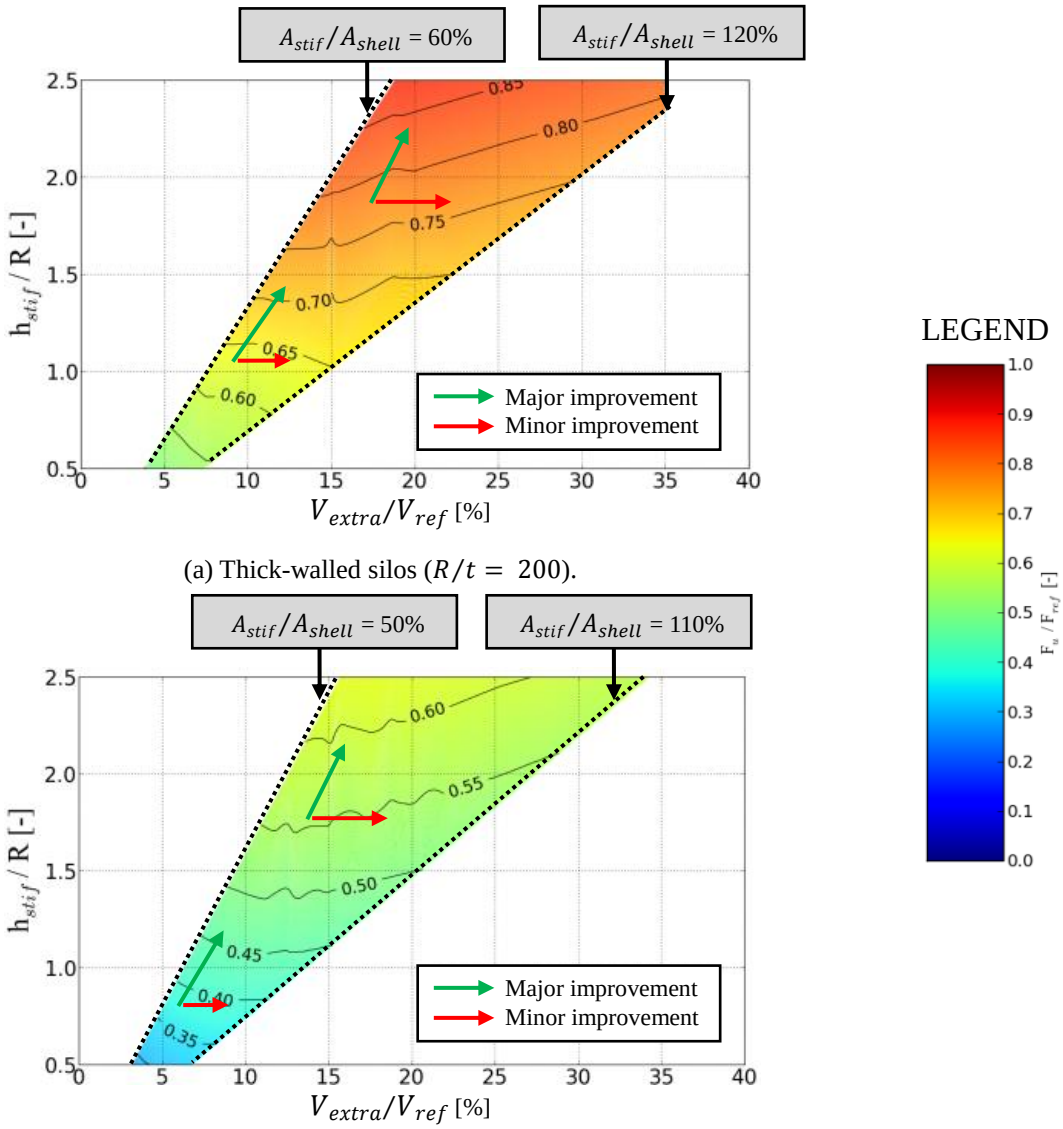

(a) Thick-walled silos ($R/t = 200$).

(b) Thin-walled silos ($R/t = 1000$).

Fig. 5-41 Dimensionless GMNA failure load F_u/F_{ref} for variable stiffener height (h_{stif}/R) on the vertical axis and variable dimensionless material parameter (V_{extra}/V_{ref}) on the horizontal axis.

Thick-walled silos

In the figure below, the dimensionless GMNA failure load F_u/F_{ref} is depicted for a thick-walled silo (i.e. $R/t = 200$) for very different U-shaped cross-sections with a constant cross-section A_{stif}/A_{shell} equal to 60 percent, respectively for an intermediately high stiffener ($h_{stif}/R = 1.0$) in Fig. 5-42 (a) and a high stiffener ($h_{stif}/R = 2.5$) in Fig. 5-42 (b).

Both graphs consist of parallel descending curves, indicating that the ratio of the radial width to the circumferential width w_{stif}/d_{stif} should be minimised (I). This finding is in clear agreement with the results and conclusions from Section 5.2.3. In short, a large radial width w_{stif} has two disadvantages. First, the pre-failure deformations become larger, which in turn reduce the effective yield stress σ_y^{eff} in the critical location (the silo wall just above the top of

the stiffener). Second, the transfer of force between the stiffener and the silo wall is less efficient. For the full description of the changing behaviour, the reader is referred to Section 5.2.3.

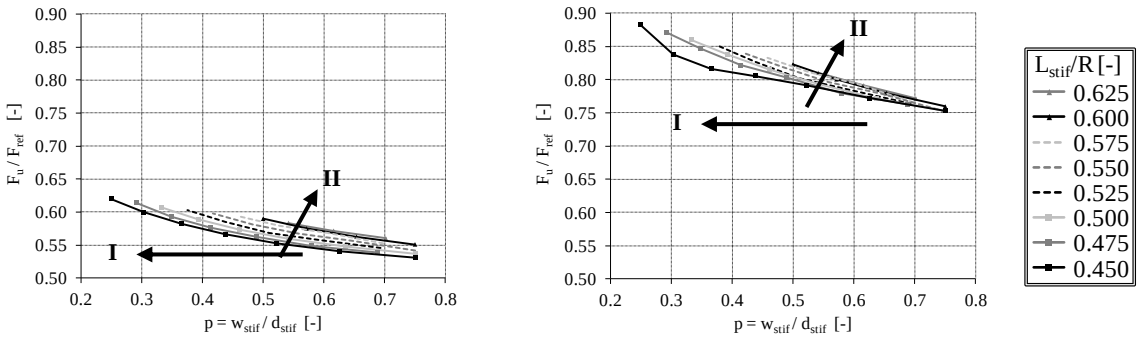

(a) Intermediately high stiffener ($h_{stif}/R = 1.0$). (b) High stiffener ($h_{stif}/R = 2.5$).

Fig. 5-42 Dimensionless GMNA failure load F_u/F_{ref} for cross-sections with variable dimensions (d_{stif}, w_{stif}, and t_{stif}) and a constant quantity of material $A_{stif}/A_{shell} = 60\%$ for $R/t = 200$.

Another interesting finding is the trend that the curves in Fig. 5-42 move upward as the total developed length of the stiffener L_{stif} increases and its thickness t_{stif} decreases (II). In other words, **a thin stiffener with a large developed length** is preferable to a thick stiffener with a small developed length, because a longitudinal stiffener with a larger total length generally has a larger width in circumferential direction d_{stif}, and consequently the silo is supported by wider supporting columns in circumferential direction ($d_{sup} = d_{stif}$). It goes without saying that an increase of the relatively limited supported proportion of the circumference μ_{sup} is beneficial for the failure behaviour of such a locally supported silo (See Sections 5.2.2 and 5.3).

Thin-walled silos

For thin-walled silos, similar findings and trends can be deduced for the optimal shape (See Fig. 5-43) as for thick-walled silos.

Again, the ratio of the radial width to the circumferential width w_{stif}/d_{stif} has to be chosen not too large (I), which is in good agreement with the results and conclusions from Section 5.2.3. In short, a large radial width w_{stif} has two disadvantages. First, the pre-buckling deformations become larger, which in turn reduce the critical buckling stress σ_{cr} in the critical location (the silo wall just above the top of the stiffener). Second, the transfer of force between the stiffener and the silo wall is less efficient. For the full description of the changing behaviour, the reader is referred to Section 5.2.3.

Another interesting finding is the trend that the curves in Fig. 5-43 move upward as the total developed length of the stiffener L_{stif} increases and its thickness t_{stif} decreases (II). In other

words, **a thin stiffener with a large developed length** is preferable to a thick stiffener with a small developed length.

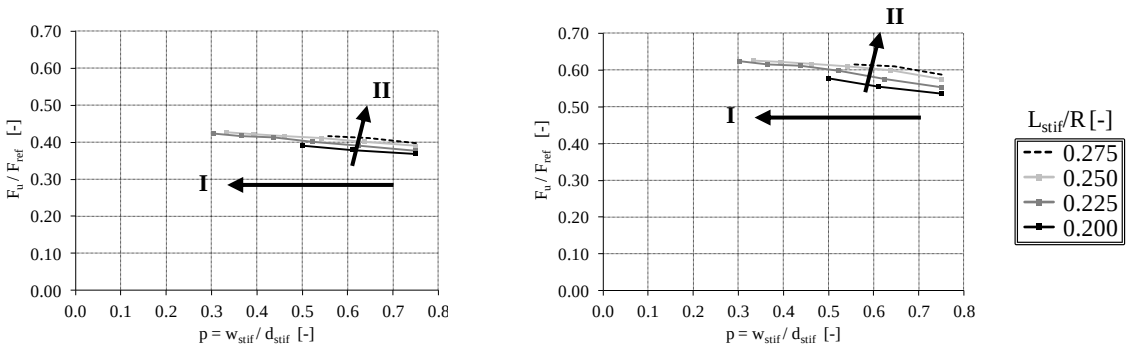

(a) Intermediately high stiffener ($h_{stif}/R = 1.0$). (b) High stiffener ($h_{stif}/R = 2.5$).

Fig. 5-43 Dimensionless GMNA failure load F_u/F_{ref} for cross-sections with variable dimensions (d_{stif}, w_{stif}, and t_{stif}) and a constant quantity of material $A_{stif}/A_{shell} = 60\%$ for $R/t = 1000$.

Conclusions

To conclude, the above mentioned results are graphically presented in Fig. 5-44. A thin U-shaped stiffener with a large width in circumferential direction d_{stif} (i.e. a wider support) (See Fig. 5-44 (a)) and a small radial width w_{stif} (i.e. a limited eccentricity) (See Fig. 5-44 (b)) is preferable to increase the failure load maximally. These findings are valid for both thick-walled silos (failure by (elasto-)plastic yielding) and thin-walled silos (failure by pure elastic buckling). Furthermore, similar results were found for other values of the stiffener's cross-section A_{stif}/A_{shell}.

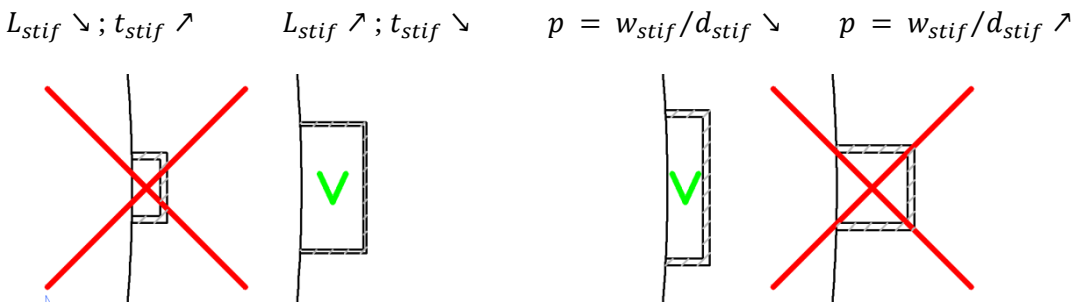

(a) Variable length L_{stif} and thickness t_{stif}. (b) Constant length L_{stif} and thickness t_{stif}.

Fig. 5-44 Graphical representation of the conclusions for the optimal U-shaped stiffener.

The optimisation study has explored a wide range of U-shaped partial-height longitudinal stiffeners by varying all the geometrical parameters (i.e. the height and all parameters of the cross-section) to determine the optimal configuration. This study demonstrates that the choice of the dimensions of the longitudinal stiffeners has an important influence on the failure load and the corresponding failure behaviour. The following conclusions can be drawn:

- Within the examined range of the stiffener heights ($0.5 \cdot R \leq h_{stif} \leq 2.5 \cdot R$), this study shows that the "attached" height has a significant advantageous influence on the failure behaviour. This finding is related to the better stress distribution of the axial stresses around the circumference of the silo wall.
- The best solution to achieve a high failure load is to provide a high U-shaped longitudinal stiffener with an intermediate cross-section.
- For all examined cases, it appears that a thin stiffener with a large developed length is preferred over a thick stiffener with a small developed length (for a constant quantity of material).
- For the investigated range of geometries, the optimal shape of the cross-section of a U-shaped longitudinal has a small ratio of the radial width to the circumferential width (i.e. small eccentricity) and a sufficiently large width in circumferential direction (i.e. large degree of support μ_{sup} in circumferential direction).

Finally, it is important to notice that the above findings and conclusions are based on the range of geometrical parameters of the stiffeners given in Table 5-9 and are not valid for U-shaped partial-height longitudinal stiffeners with a relatively small cross-section. Such stiffeners were excluded from this optimisation study because in these cases, premature failure occurs at relatively small load levels due to (elasto-)plastic yielding of the stiffened region just above the local supports. Consequently, these U-shaped stiffeners are not suitable to use as longitudinal stiffeners above the discrete supporting columns of cylindrical steel barrels.

5.5 Definition of the geometrical parameters of the U-shaped longitudinal stiffeners for the design rule

Based on the results of the foregoing studies (Paragraphs 5.2, 5.3 and 5.4), a range is defined for all geometrical parameters of the U-shaped longitudinal stiffeners. The chosen values are given in Table 5-10 and Table 5-11.

Only for the range of the circumferential width d_{stif}, an additional parametric study is performed to make an appropriate choice for the final study (with $0.05 \leq d_{stif}/R \leq 0.30$). In Fig. 5-45, the influence of the ratio of the circumferential width to the cylinder radius d_{stif}/R on the dimensionless GMNA failure load F_u/F_{ref} is plotted for two different radius-to-thickness ratios R/t. Based on the magnitude of the failure load and the failure pattern, the range of d_{stif}/R is chosen for each radius-to-thickness ratio R/t separately.

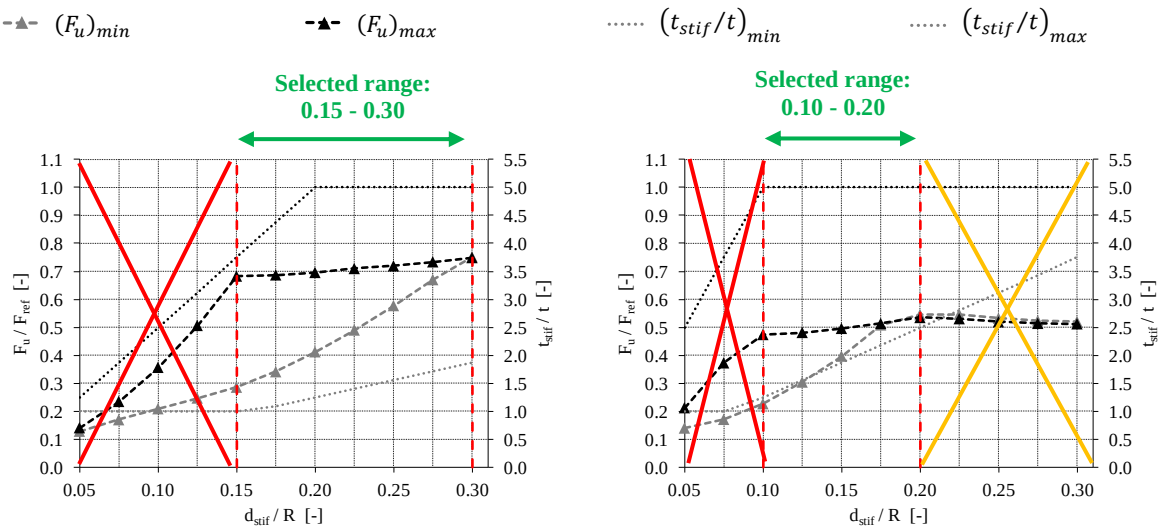

(a) $R/t = 250$. (b) $R/t = 500$.

Fig. 5-45 Dimensionless GMNA failure load F_u/F_{ref} as a function of the ratio of the circumferential width to the cylinder radius d_{stif}/R for the minimum and maximum ratio of t_{stif}/t ($n_{sup} = 4$; $w_{stif}/d_{stif} = 25\%$; $h_{stif}/R = 2.0$).

For small values of d_{stif}/R, premature failure will occur in the stiffened silo wall just above the local support, in the silo wall as well as in the longitudinal stiffener, which must be avoided at all times. This range is indicated in Fig. 5-45 with red crosses and is excluded from the final study. However, very large values of d_{stif}/R are also not selected for the range of the final study (indicated with orange crosses). Indeed, when an additional increase of d_{stif}/R does not lead to an additional increase of the failure load (e.g. in $d_{stif}/R > 0.20$ in Fig. 5-45 (b)), the values of d_{stif}/R are not chosen.

Table 5-10 Geometrical parameters of the U-shaped longitudinal stiffeners (design rule) (part 1).

PARAMETER	VALUE(S)	DIMENSION
n_{sup}	4; 6	-
d_{stif}/R	0.05; 0.10; 0.15; 0.20; 0.25; 0.30 = f (R/t) Combinations: See Table 5-11	-
w_{stif}/d_{stif}	25	%
h_{stif}^{sup}/R	0.5; 1.0; 1.5; 2.0	-
t_{stif}/t	min.; ave.; max. * = f (R/t; d_{stif}/R) Combinations: See Table 5-11	-

*: Minimum (min.), average (ave.), or maximum (max.) thickness - restrictions

Table 5-11 Geometrical parameters of the U-shaped longitudinal stiffeners (design rule) (part 2).

	d_{stif}/R																	
	0.05			0.10			0.15			0.20			0.25			0.30		
t_{stif}/t / R/t	min.	ave.	max.	min.	ave.	max.	min.	ave.	max.	min.	ave.	max.	min.	ave.	max.	min.	ave.	max.
100	-	-	-	-	-	-	-	-	X	X	-	X	X	-	X	X	X	X
200	-	-	-	-	-	-	-	-	X	X	X	X	X	X	X	X	-	X
250	-	-	-	-	-	-	-	X	X	X	X	X	X	X	X	X	-	X
333.3	-	-	-	-	X	X	X	X	X	X	X	X	X	-	X	X	-	X
500	-	-	-	X	X	X	X	X	X	X	-	X	-	-	-	-	-	-
666.6	-	-	-	X	-	X	X	-	X	X	-	-	-	-	-	-	-	-
1000	-	-	-	X	-	X	X	-		-	-	-	-	-	-	-	-	-

Remark: the average (ave.) thickness is calculated only if the difference between the minimum (min.) and the maximum (max.) thickness is sufficiently large.

6 Non-prismatic longitudinal stiffeners

6.1 Introduction

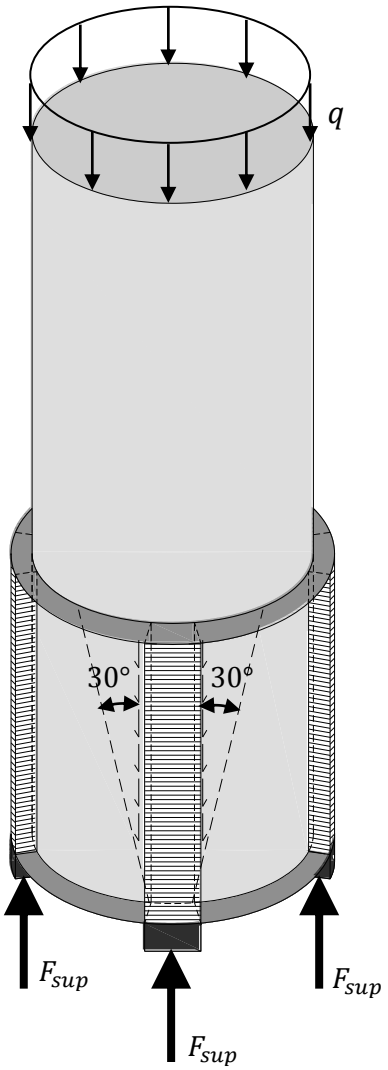

Fig. 5-46 Simplified representation of the load transfer of the shell wall to the longitudinal stiffeners.

In the previous section it was shown that the U-shaped longitudinal stiffeners provide a good solution as stiffening configuration to maximise the failure load for cylindrical steel silos with a limited number of narrow supports. However, in this part, we want to go one step further by optimising the shape of these profiles.

In Fig. 5-46, the way in which the stiffeners absorb and transfer forces is displayed in simplified form. Above each local support, the U-shaped stiffener absorbs a large part of the supporting load F_{sup} (depending on the relative stiffnesses of the stiffeners and the silo wall). Along its height, the stiffener gradually transfers the absorbed load into the silo wall by shear. In the same figure, an angle of 30° to the vertical is shown to indicate that the forces/stresses are gradually spread in circumferential direction. In other words, very high stresses can be found within a relatively small region (i.e. the support width) just above the local supports, both in the silo wall and the stiffener. In contrast, at the top of the U-shaped stiffeners, the stresses are much better distributed over a wider zone in circumferential direction. On the basis of this principle and the U-shaped stiffener as starting point, a number of alternative stiffener types will be investigated. All alternatives are illustrated in Fig. 5-47.

A first alternative is to reduce the cross-section of the U-shaped stiffener in upward direction (See Fig. 5-47 (b)). Since the force is gradually transferred from the stiffener to the silo wall, the internal force and stress level in the stiffener decrease in upward direction. It is expected that it is probably not necessary to keep the cross-section of the stiffener constant over its entire height. If this were true, then a quantity of material could be saved compared to the

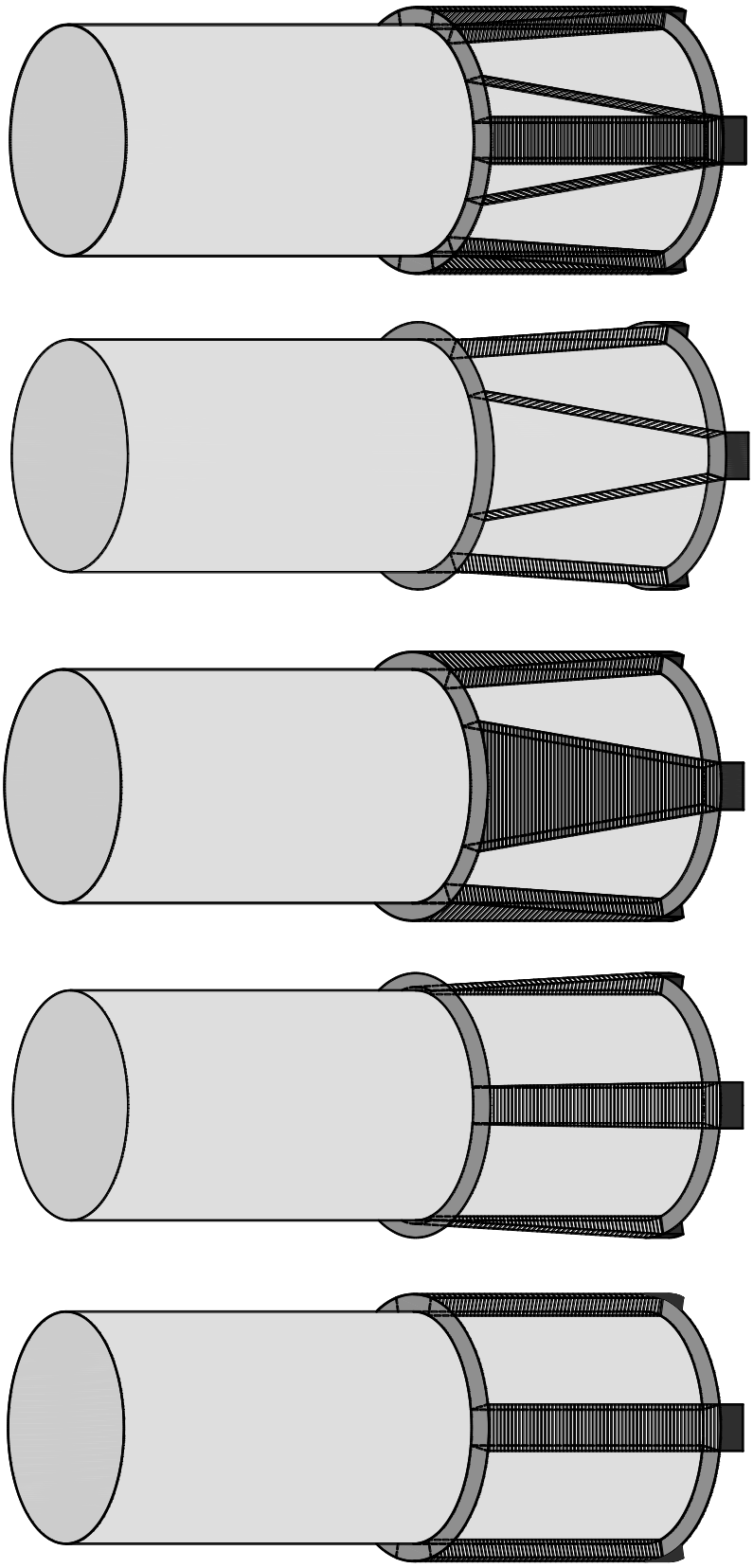

(a) Prismatic U-shaped stiffener (U).

(b) Non-prismatic U-shaped stiffener in radial direction (Ur).

(c) Non-prismatic U-shaped stiffener in circumferential direction (VU).

(d) Rectangular shaped stiffener inclined in circumferential direction (VR).

(e) Prismatic U-shaped stiffener + rectangular shaped stiffener inclined in circumferential direction (U + VR).

Fig. 5-47 Representation of the alternative stiffening shapes.

traditional U-shaped stiffener (See Fig. 5-47 (a)). From now on, this stiffener type is called "Ur".

For the other alternatives (depicted in Fig. 5-47 (c) - (e)), it is investigated whether or not it is advantageous to incline the flanges of the longitudinal stiffener under a certain angle to facilitate the distribution of forces/stresses in circumferential direction. Based on this idea, the (failure) behaviour of three types will be explored. Type "VU" is a U-shaped stiffener with angled flanges (See Fig. 5-47 (c)). Type "VR" is similar to type VU, but without web plate parallel to the silo wall (See Fig. 5-47 (d)). The last alternative is depicted in Fig. 5-47 (e)) and is called "U + VR". This stiffener consists of a traditional U-shaped longitudinal stiffener (i.e. type U) combined with two additional angled flanges (i.e. type VR).

6.2 Non-prismatic longitudinal stiffeners in radial direction

In this section, it is investigated whether it is possible to reduce the stiffener's cross-section in upward direction without reducing the failure load. This non-prismatic longitudinal stiffener is abbreviated as type Ur (See Fig. 5-47 (b)).

6.2.1 Exploratory study

Since this alternative has not been studied yet in the past, we started with a detailed investigation of only two geometries. One thick-walled silo (i.e. case 1 with $R/t = 200$) and one thin-walled silo (i.e. case 2 with $R/t = 1000$) was selected with different dimensions of the longitudinal stiffeners, as given in Table 5-12.

Table 5-12 Geometrical parameters of the longitudinal stiffeners (exploratory study Ur).

PARAMETER	VALUE(S)	DIMENSION
n_{sup}	4	-
d_{stif}/R	$R/t = 200$: 0.25 $R/t = 1000$: 0.10	-
w_{stif}/d_{stif}	50	%
h_{stif}^{sup}/R	1.0	-
t_{stif}/t	$R/t = 200$: max.* $R/t = 1000$: min.*	-

*: Minimum (min.), average (ave.), or maximum (max.) thickness - restrictions

In Fig. 5-48, the symbols of the geometrical parameters of a Ur stiffener are depicted. The same symbols are used as for a U stiffener, only for the radial width at the top of the Ur stiffener, a new symbol is created. From now on, this parameter will be denoted by w_{stif}^{sup}. The

range of ratios of the radial widths at the top and the bottom of the stiffener w_{stif}^{sup}/w_{stif} are given in Table 5-13. A value equal to 100% corresponds with a U stiffener, smaller values are Ur stiffeners.

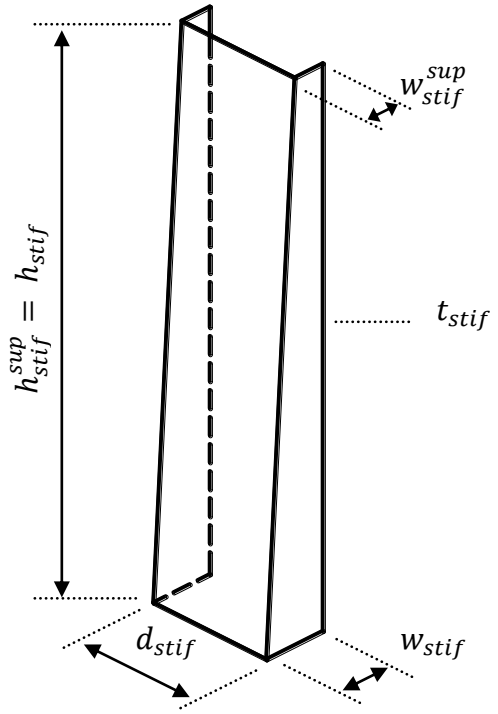

Fig. 5-48 Geometrical parameters of a non-prismatic longitudinal stiffener in radial direction.

Table 5-13 Determination of w_{stif}^{sup}/w_{stif} for the parametric study (exploratory study Ur).

Model	w_{stif}^{sup}/w_{stif} [%]
Ur-020	20
Ur-040	40
Ur-060	60
Ur-080	80
Ur-100 (= U)	100

In Fig. 5-49, the dimensionless GMNA failure load F_u/F_{ref} is plotted against the ratio of the radial widths at the top and the bottom of the stiffener w_{stif}^{sup}/w_{stif}. For both cases, the failure load does not decrease when the cross-section of the stiffener is reduced in upward direction. This result is positive, but further research is necessary to map the behaviour of a Ur stiffener.

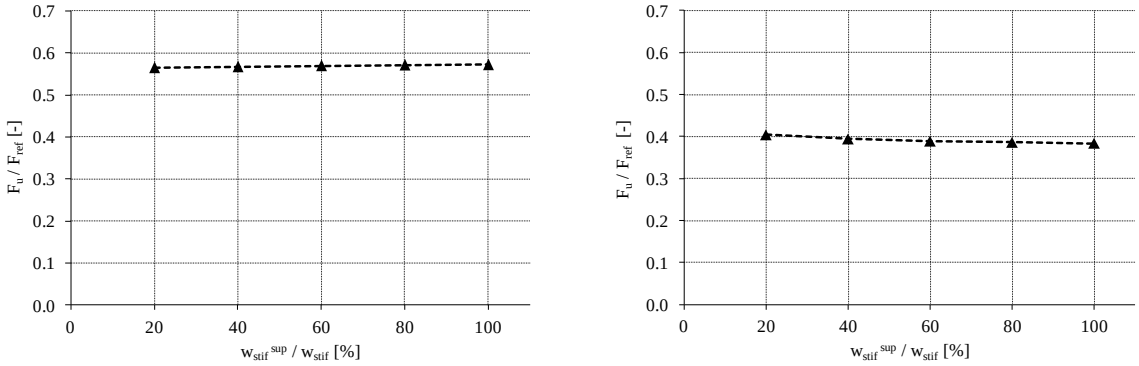

(a) Case 1 ($R/t = 200$). (b) Case 2 ($R/t = 1000$).

Fig. 5-49 Dimensionless GMNA failure load F_u/F_{ref} as a function of the ratio of the radial widths at the top and the bottom of the longitudinal stiffener w_{stif}^{sup}/w_{wtif} (exploratory study: alternative Ur).

Case 1 ($R/t = 200$)

The contourplots of the axial stresses at the moment of maximum load and the post-buckling deformations are depicted in Fig. 5-50 of the extreme geometries of the investigated area. On the left hand side, the contourplots of a U stiffener ($w_{stif}^{sup}/w_{stif} = 100\%$) are given. On the right hand side, a Ur stiffener is shown with $w_{stif}^{sup}/w_{stif} = 20\%$. On the basis of these contourplots, no differences can be observed in the failure behaviour (here: elasto-plastic buckling) between the two cases. Indeed, both failure patterns look identical with the same region of exhaustive yielding and the same post-buckling deformations above the top of the stiffener.

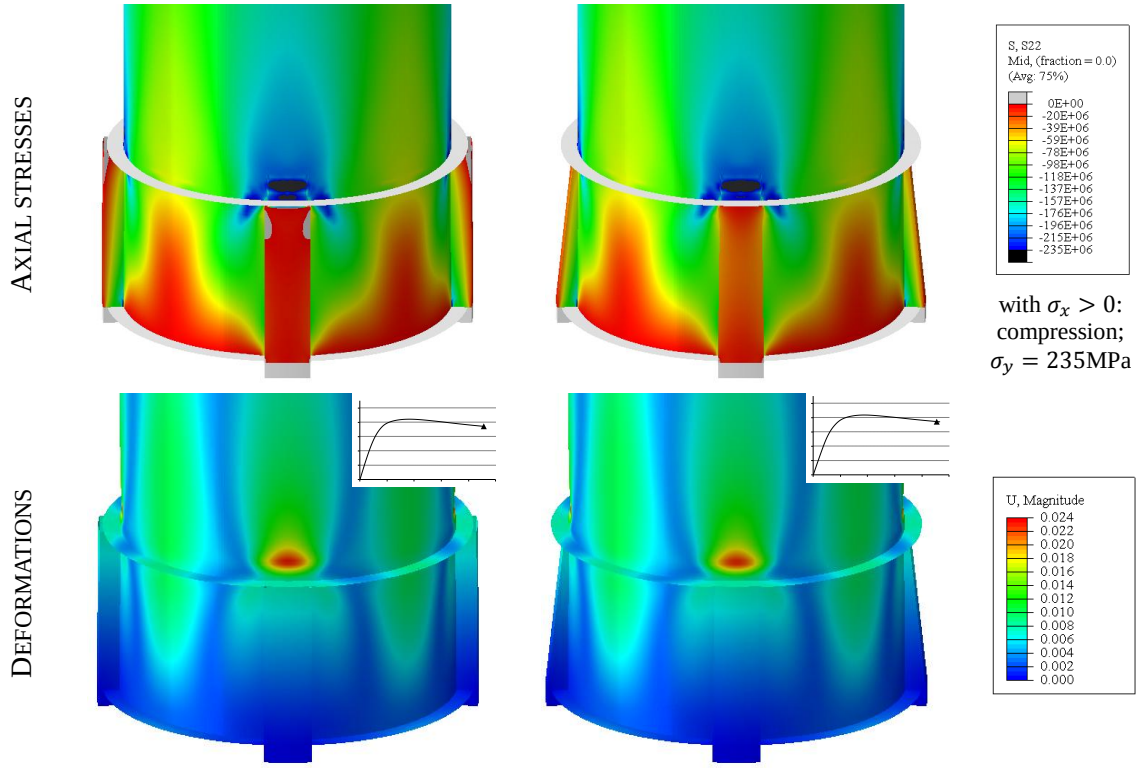

(a) U-profile ($w_{stif}^{sup}/w_{stif} = 100\%$). (b) Ur with $w_{stif}^{sup}/w_{stif} = 20\%$.

Fig. 5-50 Contourplots of the axial stresses σ_x at the moment of maximum load [Pa] and the post-buckling deformations U [m] for case 1 (type Ur; $R/t = 200$).

Since it is very difficult to observe minor differences in the failure behaviour by means of the contourplots in Fig. 5-50, additional paths have been created to investigate the influence of w_{stif}^{sup}/w_{stif} on the failure behaviour. In Fig. 5-51, the axial stresses at the moment of maximum load are depicted in the silo wall (left) and in the stiffener (right) and at two different heights within the stiffened region (20% and 80% of the height of the stiffener). It is found that the axial stresses in the silo wall are hardly affected by an upward reduction of the stiffener's cross-section (See Fig. 5-51 (a) and (b)), in contrast to the axial stresses in the stiffener itself (See Fig. 5-51 (c) and (d)). From these figures, two findings can be observed.

Firstly, the axial stresses in the stiffener increase as the value of w_{stif}^{sup}/w_{stif} decreases ((I) and (II)). Secondly, the axial stresses increases more at the top of the stiffener (II) compared to the bottom of the stiffener (I).

These increased stresses ((I) and (II)) are caused as a consequence that the same force at certain height has to be absorbed by less material at that height (thus a smaller stiffener's cross-section) due to a decrease of the value w_{stif}^{sup}/w_{stif}. Furthermore, the reduction varies linearly with the height, as a result of which the stress reduction depends also on the considered height. For example, the reduction of the stiffener's cross-section at a height of 20% of the stiffener's height is only $1/4$ of the reduction of the stiffener's cross-section at a height of 80% of the stiffener's height.

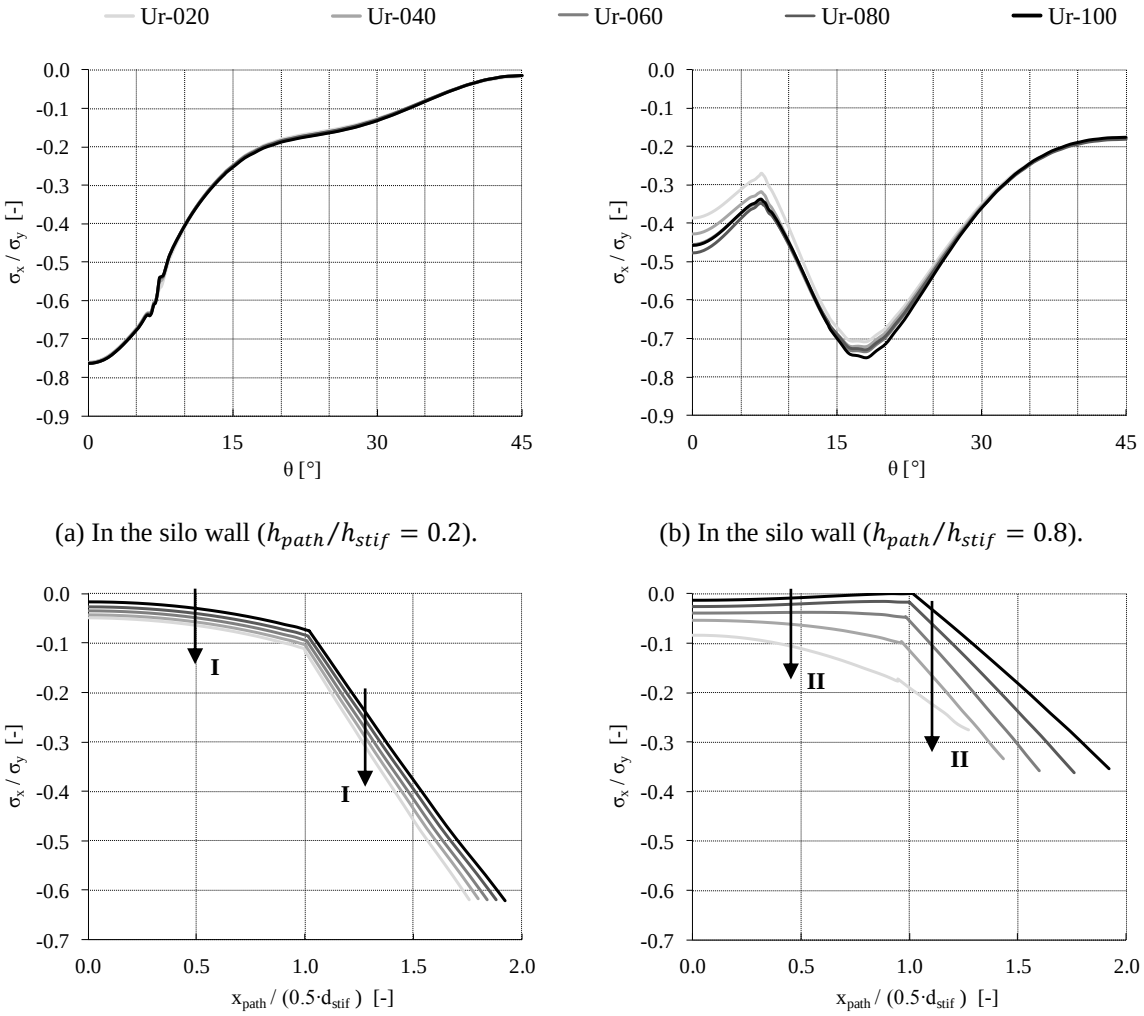

(a) In the silo wall ($h_{path}/h_{stif} = 0.2$).

(b) In the silo wall ($h_{path}/h_{stif} = 0.8$).

(c) In the stiffener ($h_{path}/h_{stif} = 0.2$).

(d) In the stiffener ($h_{path}/h_{stif} = 0.8$).

Fig. 5-51 Distribution of the axial stresses σ_x at the moment of maximum load divided by the yield stress σ_y for case 1 (type Ur; $R/t = 200$).

Case 2 ($R/t = 1000$)

In Fig. 5-52, the contourplots of the axial stresses at the moment of maximum load and the post-buckling deformations are depicted of the extreme geometries of the investigated area, namely $w_{stif}^{sup}/w_{stif} = 100\%$ (i.e. U stiffener) on the left hand side and $w_{stif}^{sup}/w_{stif} = 20\%$ (i.e. a Ur stiffener) on the right hand side. No differences can be observed on these contourplots, neither in the stress pattern at the moment of buckling nor in the post-buckling deformations. In other words, both geometries will fail in a very similar way as a result of elastic buckling in the unstiffened silo wall just above the top of the stiffener.

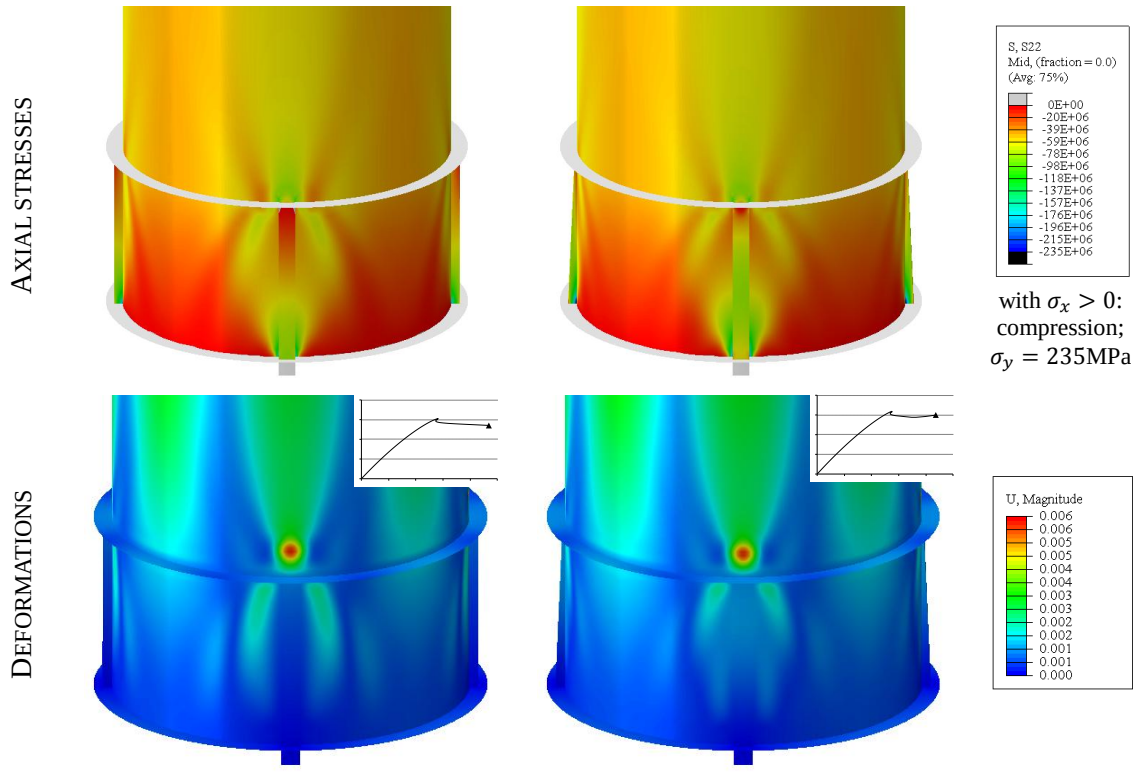

(a) U-profile ($w_{stif}^{sup}/w_{stif} = 100\%$). (b) Ur with $w_{stif}^{sup}/w_{stif} = 20\%$.

Fig. 5-52 Contourplots of the axial stresses σ_x at the moment of maximum load [Pa] and the post-buckling deformations U [m] for case 2 (type Ur; $R/t = 1000$).

Again, it is very difficult to observe minor differences in the failure behaviour by means of the contourplots in Fig. 5-52. Therefore, additional paths have been created to investigate the influence of w_{stif}^{sup}/w_{stif} on the failure behaviour (See Fig. 5-53). In this figure, the axial stresses (at the moment of maximum load) are depicted in the silo wall (left) and in the stiffener (right) and at two different heights within the stiffened region (20% and 80% of the height of the stiffener).

Very similar results are found as the thick-walled silos, except that the magnitude of the stresses (and failure load) is much smaller for the thin-walled silos due to elastic buckling. It is found that the axial stresses in the silo wall are hardly affected by an upward reduction of

the stiffener's cross-section (See Fig. 5-53 (a) and (b)) in contrast to the axial stresses in the stiffener itself (See Fig. 5-53 (c) and (d)). From these figures, two findings can be observed. Firstly, the axial stresses in the stiffener increase as the value of w_{stif}^{sup}/w_{stif} decreases ((I) and (II)). Secondly, the axial stresses increases more at the top of the stiffener (II) compared to the bottom of the stiffener (I).

These increased stresses ((I) and (II)) are caused as a consequence that the same force at certain height has to be absorbed by less material at that height (thus a smaller stiffener's cross-section) due to a decrease of the value w_{stif}^{sup}/w_{stif}. Furthermore, the reduction varies linearly with the height, as a result of which the stress reduction depends also on the considered height. For example, the reduction of the stiffener's cross-section at a height of 20% of the stiffener's height is only $1/4$ of the reduction of the stiffener's cross-section at a height of 80% of the stiffener's height.

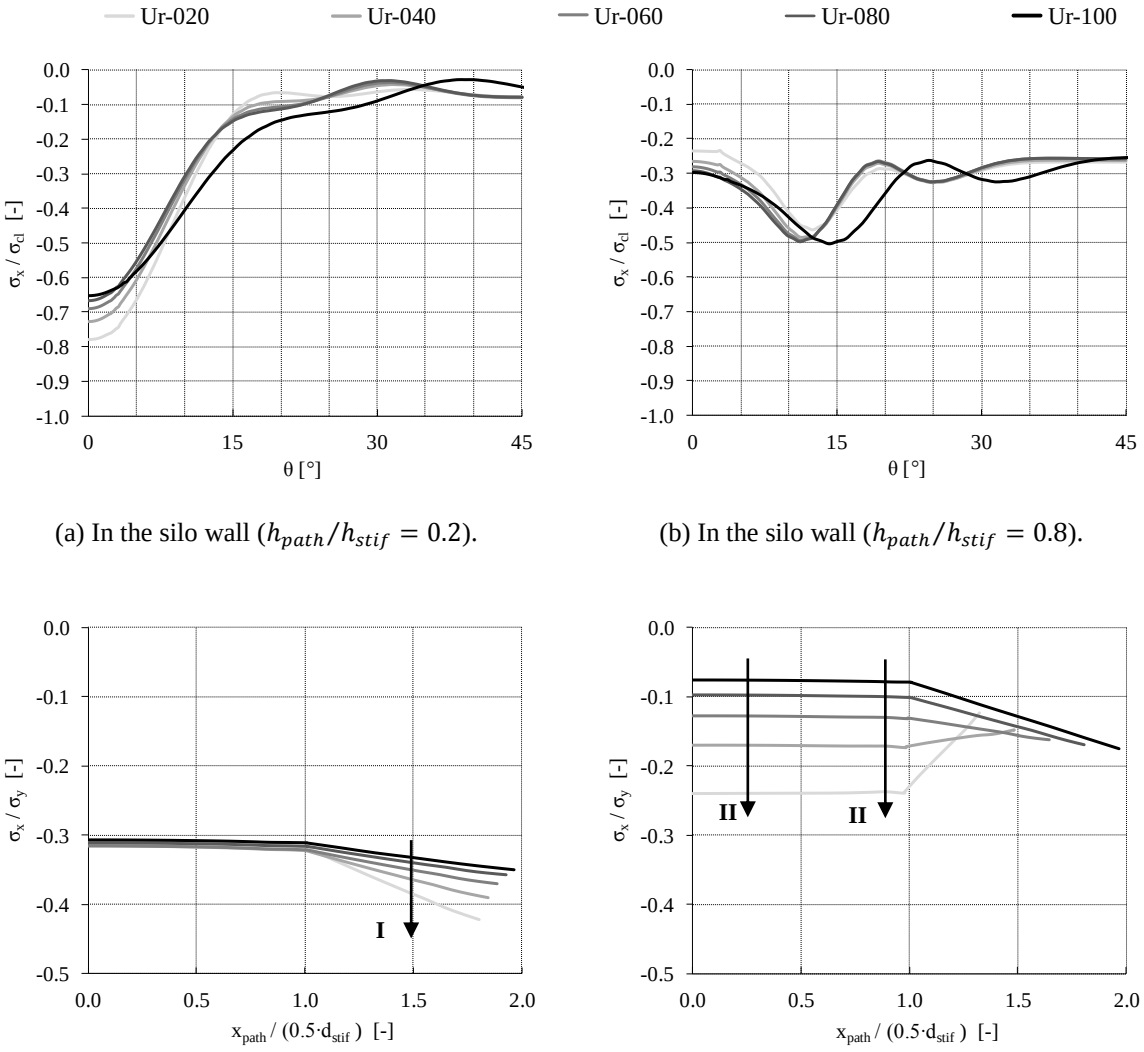

(a) In the silo wall ($h_{path}/h_{stif} = 0.2$).

(b) In the silo wall ($h_{path}/h_{stif} = 0.8$).

(c) In the stiffener ($h_{path}/h_{stif} = 0.2$).

(d) In the stiffener ($h_{path}/h_{stif} = 0.8$).

Fig. 5-53 Distribution of the axial stresses σ_x at the moment of maximum load divided by the critical buckling stress σ_{cl} or the yield stress σ_y for case 2 (type Ur; $R/t = 1000$).

Conclusions

For a traditional U profile, the axial stresses are decreasing in upward direction (i.e. smaller axial stresses at the top than at the bottom of the stiffener), since the force in the stiffener is gradually transferred into the silo wall by shear. In other words, the higher in the stiffener, the less the material is used.

Reducing the stiffener's cross-section in upward direction (i.e. a Ur profile, see Fig. 5-47 (b)) is a solution for an optimal use of the material, especially in the upper part of the longitudinal stiffener, because the force in the stiffener decreases in upward direction. A (larger) reduction of the stiffener's cross-section at a certain height will lead to a (larger) increase of the axial stresses at that height (and thus a better use of the material) because the same force has to be absorbed by less material. These same trends have been observed for both investigated cases when w_{stif}^{sup}/w_{stif} decreases.

For other geometries, it is expected that a reduction of the stiffener's cross-section will not cause problems due to premature failure of the stiffener, as long as the increased axial stresses remain below the effective yield stress σ_y^{eff} in each point of the longitudinal stiffener.

6.2.2 Extensive parametric study

In the exploratory study, the influence of w_{stif}^{sup}/w_{stif} was investigated for only two cases and compared with the traditional U profile. On the basis of these initial results, it was found that a Ur profile can be a well optimised alternative for a U profile. Such a Ur profile contains less material compared to a U profile and has approximately the same failure load.

In this extensive parametric study, it is checked whether this last finding can also be extended to other geometries. This has been done by performing GMNA calculations for all U-shaped longitudinal stiffeners defined in Section 5.5 (i.e. Table 5-10 and Table 5-11) with a variation of the ratio of the radial width at the top and the radial width at the bottom of the stiffener w_{stif}^{sup}/w_{stif} in the range given in Table 5-13. A Ur and U profile correspond to a value of the parameter w_{stif}^{sup}/w_{stif} of respectively smaller than and equal to 100%. In total, 220 different geometries were investigated in this study, which equates to 1100 GMNA calculations. In this way, the effect of the decreasing cross-section can be studied for a wide range of different geometries.

To know the exact influence of the reduction of the stiffener's cross-section in upward direction, the dimensionless GMNA failure load F_u/F_{ref} of a number of stiffener geometries is plotted against the parameter w_{stif}^{sup}/w_{stif} in Fig. 5-54 for silos with different radius-to-thickness ratios (i.e. $R/t = 200; 500; 1000$) and for different stiffener heights (i.e. $h_{stif}/R = 1.0; 2.0$). In this way, the influence can be observed for different failure phenomena and for

different stiffener shapes and heights.

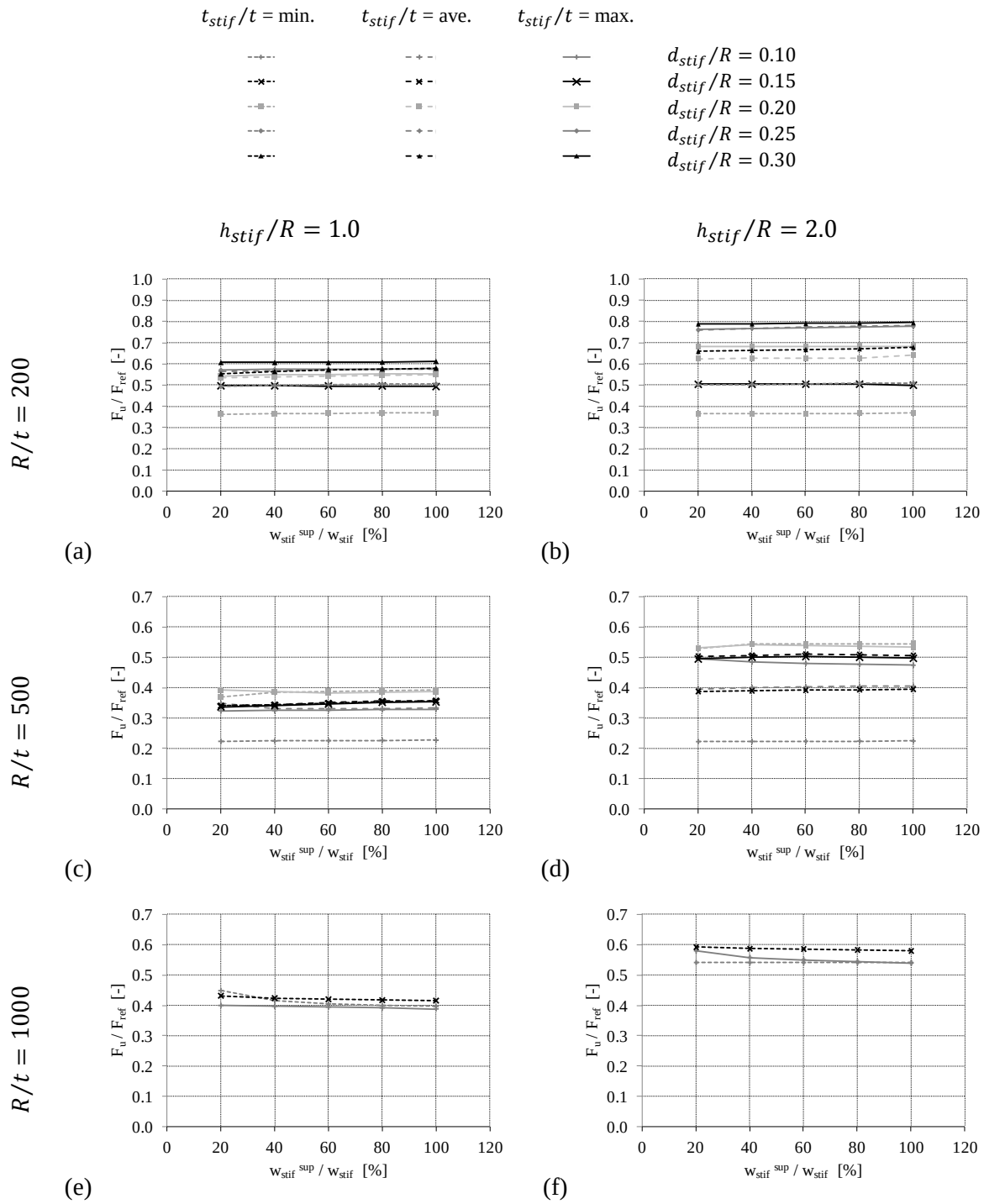

Fig. 5-54 Influence of the ratio of the radial widths at the top and the bottom of the longitudinal stiffener w_{stif}^{sup}/w_{wtif} to the dimensionless GMNA failure load F_u/F_{ref} for silos with different radius-to-thickness ratios R/t and for different stiffener heights h_{stif}^{sup}/R (extensive parametric study: alternative Ur).

All curves in Fig. 5-54 are approximately horizontal, which means that the failure load remains constant as the parameter w_{stif}^{sup}/w_{stif} decreases (i.e. a larger reduction of the

stiffener's cross-section in upward direction). Furthermore, similar results have been found for silos with other radius-to-thickness ratios (i.e. $R/t = 100; 250; 333.3; 666.6$) and stiffeners with other heights (i.e. $h_{stif}/R = 0.5; 1.5$) and shapes.

Conclusions

Of the many results that are obtained in this study, it can be concluded that the alternative Ur profile is a worthy alternative to the traditional U-profile. In other words, for the geometries studied here, it is perfectly possible to decrease the stiffener's cross-section in upward direction (here: $w_{stif}^{sup}/w_{stif} \geq 20\%$) without losing strength.

6.3 Non-prismatic longitudinal stiffeners in circumferential direction

In this section, it is investigated whether it is possible to increase the failure load by spreading the flanges of the partial-height longitudinal stiffeners. Three alternatives are investigated: the VU stiffener (See Fig. 5-47 (c)), the VR stiffener (See Fig. 5-47 (d)), and the U+VR stiffener (See Fig. 5-47 (e)).

6.3.1 Exploratory study

Since these alternatives have not been studied yet in the past, we started with a detailed investigation of only two geometries. One thick-walled silo (i.e. case 1 with $R/t = 200$) and one thin-walled silo (i.e. case 2 with $R/t = 1000$) was selected with different dimensions of the longitudinal stiffeners, as given in Table 5-14.

Table 5-14 Geometrical parameters of the longitudinal stiffeners (exploratory study VU, VR, U+VR).

PARAMETER	VALUE(S)	DIMENSION
n_{sup}	4	-
d_{stif}/R	$R/t = 200$: 0.25 $R/t = 1000$: 0.10	-
w_{stif}/d_{stif}	50	%
h_{stif}^{sup}/R	1.0	-
t_{stif}/t	$R/t = 200$: max.* $R/t = 1000$: min.*	-

*: Minimum (min.), average (ave.), or maximum (max.) thickness - restrictions

In Fig. 5-55, the symbols of the geometrical parameters of a VU or VR or U+VR stiffener are depicted. The same symbols are used as for a U stiffener: only for the circumferential width at the top of the stiffener, a new symbol is created. From now on, this parameter will be denoted

by d_{stif}^{sup}. The inclination of the flanges can be expressed on the basis of two different angles: (1) the angle in circumferential direction θ_{stif}^{sup} and (2) the angle relative to the vertical β_{stif} (See Fig. 5-55).

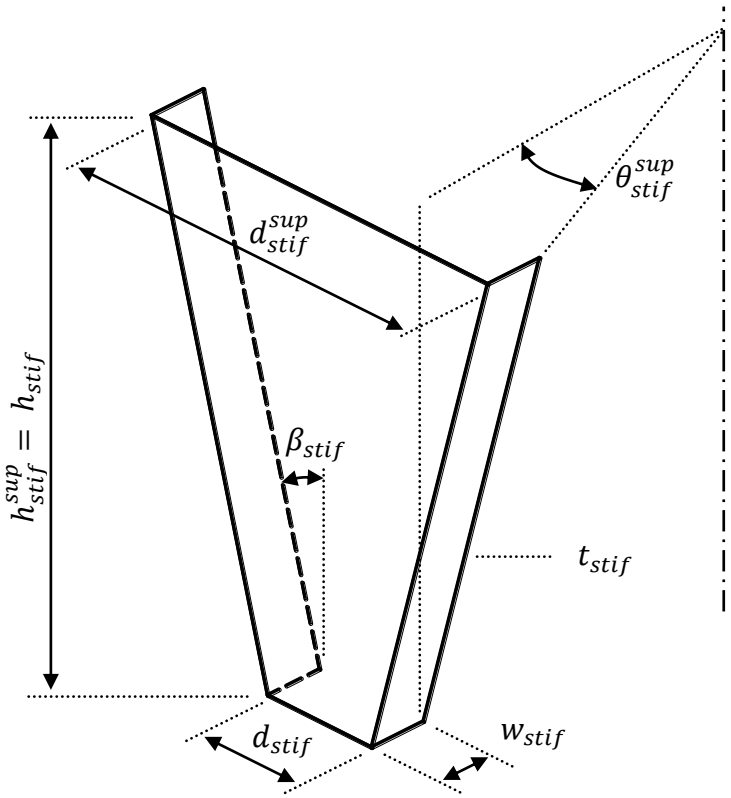

Fig. 5-55 Geometrical parameters of a non-prismatic longitudinal stiffener in circumferential direction.

The range of ratios of the difference between the circumferential width at the top d_{stif}^{sup} and the bottom d_{stif} of the stiffener to the cylinder radius R are given in Table 5-15. A value equal to 0.0 corresponds with a U stiffener, larger values are VU or VR or U+VR stiffeners. Additionally, the circumferential angle θ_{stif}^{sup} has been calculated for the whole range. This angle is varied between 0.0 and 14.3 degrees.

Table 5-15 Determination of the inclination for the parametric study (exploratory study VU, VR, U+VR).

MODEL	$\left(d_{stif}^{sup} - d_{stif}\right)/R$ [-]	θ_{stif}^{sup} [°]
V d-00	0.00	0.0
V d-05	0.05	1.4
V d-10	0.10	2.9
V d-15	0.15	4.3
V d-20	0.20	5.7
V d-25	0.25	7.2
V d-30	0.30	8.6
V d-35	0.35	10.0
V d-40	0.40	11.5
V d-45	0.45	12.9
V d-50	0.50	14.3

In Fig. 5-56, the dimensionless GMNA failure load F_u/F_{ref} is plotted against the circumferential angle θ_{stif}^{sup} for the three alternatives. For all alternatives and for both cases, there is an initial increase in failure load as the inclination of the flanges increases (i.e. increasing angle θ_{stif}^{sup}). At a certain point, the failure load increases less rapidly (Fig. 5-56 (a)) or decreases again (Fig. 5-56 (b)).

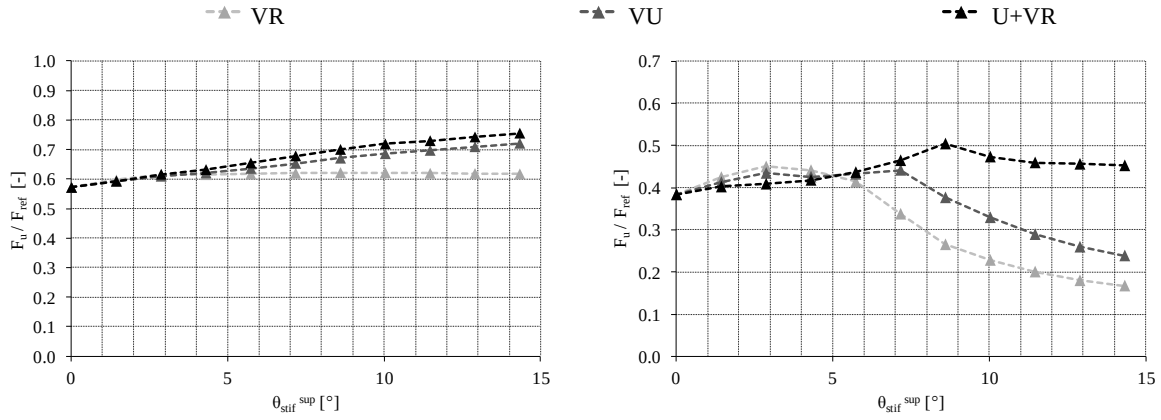

(a) Case 1 ($R/t = 200$). (b) Case 2 ($R/t = 1000$).

Fig. 5-56 Dimensionless GMNA failure load F_u/F_{ref} as a function of the circumferential angle θ_{stif}^{sup} (exploratory study: alternatives VU, VR, U+VR).

Based on these two graphs, we are tempted to say that the VR, VU, and U+VR stiffener in this order are better alternatives for the traditional U stiffener. In the next part, the failure

behaviour of all alternatives and for both cases will be investigated in detail by means of contourplots of axial stresses and post-buckling deformations, and graphs of the axial stress distributions along paths in the silo wall and the stiffener(s).

6.3.1.1 VU stiffener

Now, we will start to take a closer look at the VU stiffener with variable inclination of the flanges (See Fig. 5-47 (c)).

Silo wall - case 1 ($R/t = 200$)

In Fig. 5-57, the contourplots of the axial stresses at the moment of maximum load are shown for three different stiffener inclination angles θ_{stif}^{sup}. The web of the stiffener is made invisible so that the stresses in the shell wall behind the stiffener would be visible. Independently of the angle θ_{stif}^{sup}, the silo wall just above the local support yields completely. In Fig. 5-57 (a), a VU stiffener without inclination is depicted. In fact, this corresponds with a U stiffener. In this case, a small region above the upper ring yields with more or less the same width in circumferential direction as the U stiffener. By increasing the inclination θ_{stif}^{sup} of the flanges (See Fig. 5-57 (b) and (c)), two regions of yielding are developing in the silo wall, namely just above and just below the upper ring. The circumferential width of both regions increases with the angle of the flanges and have approximately the same circumferential width as the top of the VU stiffener. In other words, by increasing the slope of the flanges of the VU stiffener, the axial stresses are better distributed in circumferential direction since a wider circumferential part of the silo wall yields, resulting in an increasing failure load (See Fig. 5-56 (a)).

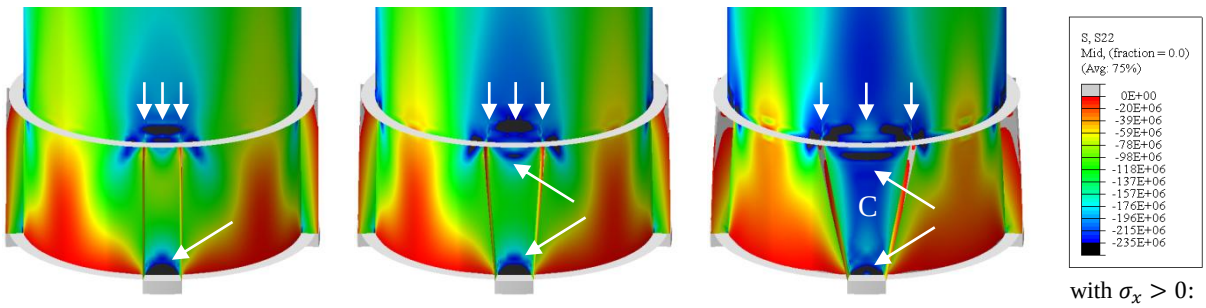

(a) $\theta_{stif}^{sup} = 0°$. (b) $\theta_{stif}^{sup} = 4.3°$. (c) $\theta_{stif}^{sup} = 11.5°$.

with $\sigma_x > 0$: compression; $\sigma_y = 235$MPa

Fig. 5-57 Contourplots of the axial stresses σ_x at the moment of maximum load [Pa] (type VU; $R/t = 200$) (remark: web of the VU stiffener is invisible).

The distribution of axial stresses in circumferential direction is plotted in Fig. 5-58 for two different heights in the silo wall: at 90% of the stiffener height (i.e. in the stiffened region just below the upper ring) and at 110% of the stiffener height (i.e. in the unstiffened region just above the upper ring). These heights correspond with the location of yielding depicted in Fig. 5-57. The vertical dashed red lines in the figures correspond with the circumferential angle of

the flange of the VU stiffener.

In Fig. 5-58 (a), three trends can be observed with an increasing slope of the VU stiffener: (I) both the circumferential width and the magnitude of the axial stresses increase between the flanges, (II) the stress peak just adjacent to the flange moves with the inclined flange of the VU stiffener and remains constant in magnitude, and (III) the axial stresses are better distributed between the VU stiffeners. The first trend will be called the **channeling effect** and is the effect that the axial stresses are, as it were, "concentrated" in the silo wall between the flanges (I) (while the axial stresses in the silo wall between two stiffeners are negligible). In Fig. 5-57 (c), this stress concentration is indicated with the letter C and the very narrow area between the flanges of the VU stiffener is coloured in blue. The second and third trend ((II) and (III)) are caused by the gradual transfer of force from the stiffener to the silo wall (by shear) and is named the **spreading effect**.

In Fig. 5-58 (b), the axial stresses in the central zone between the flanges of the VU stiffener are decreasing (IV), the region of large axial stresses moves with the top of the inclined flange of the VU stiffener and the total width of yielding in circumferential direction also increases (V), and the axial stresses between the VU stiffeners are increasing (VI).

For both heights, it can be concluded that the axial stresses are better distributed in circumferential direction as the inclination of the flanges of the VU stiffener increases.

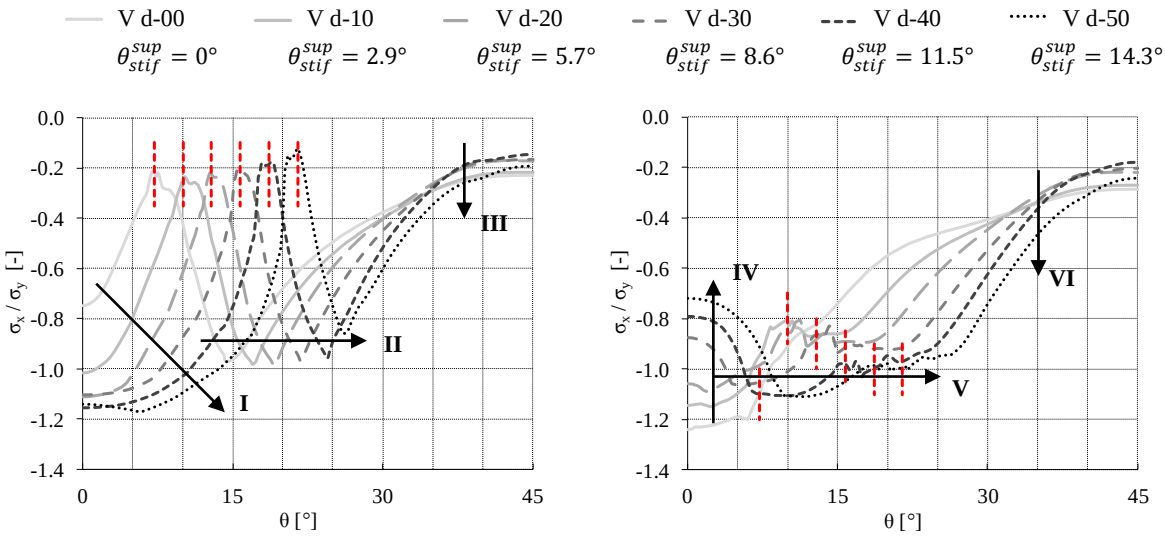

(a) $h_{path}/h_{stif} = 0.90$. (b) $h_{path}/h_{stif} = 1.10$.

Fig. 5-58 Distribution of the axial stresses at the moment of maximum load in the silo wall (type VU; $R/t = 200$).

Silo wall - case 2 ($R/t = 1000$)

In Fig. 5-59, the contourplots of the post-buckling deformations are shown for three different stiffener inclination angles θ_{stif}^{sup}. For the U stiffener ($\theta_{stif}^{sup} = 0°$), the silo fails by pure elastic buckling in the region just above the upper ring. From the moment of buckling, a buckle develops in the unstiffened silo wall above the top of the U stiffener (See Fig. 5-59 (a)). For VU stiffeners with a small inclination of the flanges ($\theta_{stif}^{sup} \leq 7.2°$), two separate buckles develop in the unstiffened silo wall just above the end of the flanges (See Fig. 5-59 (b)). In contrast, for VU stiffeners with a large inclination of the flanges ($\theta_{stif}^{sup} > 7.2°$), the location of buckling shifts to the stiffened silo wall between the flanges of the VU stiffener (See Fig. 5-59 (c)). Furthermore, it is found that the height of the buckle in the stiffened region between the flanges moves downwardly as the inclination of the flanges increases further.

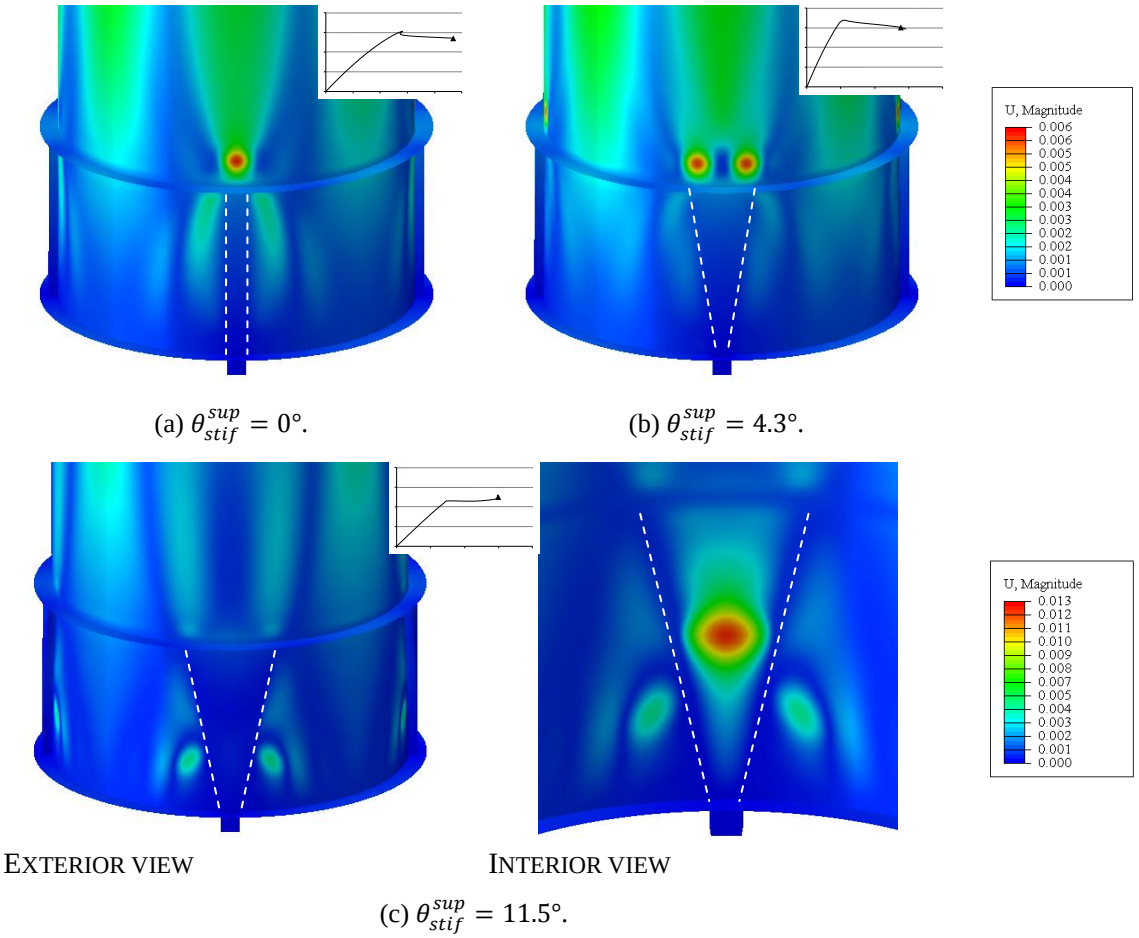

(a) $\theta_{stif}^{sup} = 0°$. (b) $\theta_{stif}^{sup} = 4.3°$.

(c) $\theta_{stif}^{sup} = 11.5°$.

Fig. 5-59 Contourplots of the post-buckling deformations U [m] (type VU; $R/t = 1000$).

The movement of the location of elastic buckling from the unstiffened region above the VU stiffener (Fig. 5-59 (b)) to the stiffened region between the flanges of the VU stiffener (Fig. 5-59 (c)) is caused by the **channeling effect**, which is increasingly important as the slope of flanges increases (and the **spreading effect** less important). This tendency can be noticed on the contourplots of the axial stresses at the moment of maximum load in Fig. 5-60. In this

figure, the web of the stiffener is made invisible so that the stresses in the shell wall behind the stiffener would be visible. For all cases, the largest axial stresses are found in the silo wall just above the local support and at the location of the buckle. For the U stiffener and VU stiffeners with a small inclination of the flanges ($\theta_{stif}^{sup} \leq 7.2°$), this latter area is located just above the stiffener, while for VU stiffeners with a large inclination of the flanges ($\theta_{stif}^{sup} > 7.2°$), the largest stresses occur in the stiffened silo wall between the flanges.

At first instance, the stresses are distributed better in circumferential direction as the slope of the flanges of the VU stiffener increases (compare Fig. 5-60 (a) and (b)), resulting in an increasing failure load ($\theta_{stif}^{sup} \leq 7.2°$ in Fig. 5-56 (b)). However, from a certain inclination ($\theta_{stif}^{sup} > 7.2°$), the failure load starts to decrease in Fig. 5-56 (b). This premature failure is caused by the **channeling effect**: the axial stresses are "concentrated" in the silo wall between the flanges. In Fig. 5-60 (c), this stress concentration is indicated with the letter C and the very narrow area between the flanges of the VU stiffener is coloured in yellow/green.

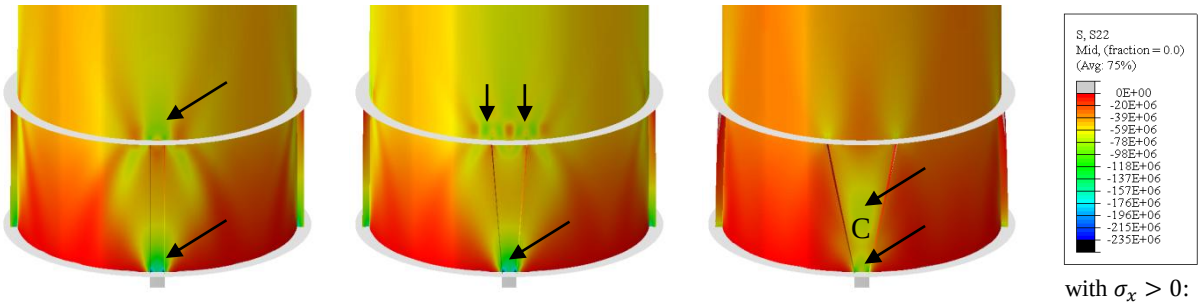

(a) $\theta_{stif}^{sup} = 0°$. (b) $\theta_{stif}^{sup} = 4.3°$. (c) $\theta_{stif}^{sup} = 11.5°$. with $\sigma_x > 0$: compression; $\sigma_y = 235$MPa

Fig. 5-60 Contourplots of the axial stresses σ_x at the moment of maximum load [Pa] (type VU; $R/t = 1000$) (remark: web of the VU stiffener is invisible).

The distribution of axial stresses in circumferential direction is plotted in Fig. 5-61 for two different heights in the silo wall: at 50% of the stiffener height (i.e. halfway the stiffened region just) and at 110% of the stiffener height (i.e. in the unstiffened region just above the upper ring). These heights correspond with the location of elastic buckling depicted in Fig. 5-59. The vertical dashed red lines in the figures correspond with the circumferential angle of the flange of the VU stiffener.

In Fig. 5-61 (a), two trends can be observed with an increasing slope of the VU stiffener. Firstly, the magnitude of the axial stresses increases between the flanges (I). This is called the **channeling effect** and will cause premature buckling of the structure when $\theta_{stif}^{sup} > 7.2°$. When $\theta_{stif}^{sup} > 8.6°$, the axial stresses in the channel between the flanges starts to decrease again at 50% of the stiffener height (purple arrow) because the region with the axial stresses (and the buckle) moves downwardly. Secondly, due to the **spreading effect**, the stress peak just adjacent to the flange moves with the inclined flange of the VU stiffener (IIa) and the

axial stresses increase between the VU stiffeners (IIIa) when $\theta_{stif}^{sup} \leq 7.2°$. When the inclination of the flanges is increased further ($\theta_{stif}^{sup} > 7.2°$), premature "channel" buckling occurs in the stiffened silo wall and the stress peak weakens (IIb) and the axial stresses between the VU stiffeners decrease (IIIb). In other words, by increasing the inclination of the flanges of the VU stiffener, the channeling effect becomes more important (and causes premature buckling): the spreading effect weakens.

In Fig. 5-61 (b), when the inclination of the flanges of the VU stiffener increases and $\theta_{stif}^{sup} \leq 7.2°$, the axial stresses in the central zone between the flanges of the VU stiffener are decreasing (IV), the region of large axial stresses moves with the top of the inclined flange of the VU stiffener (Va), and the axial stresses between the VU stiffeners are increasing (VIa). When the inclination of the flanges of the VU stiffener is increased further ($\theta_{stif}^{sup} > 7.2°$), premature "channel" buckling occurs in the stiffened region and the axial stresses are decreasing over the entire circumference (IV, Vb, and VIb), including the stress peak above the flange termination (Vb).

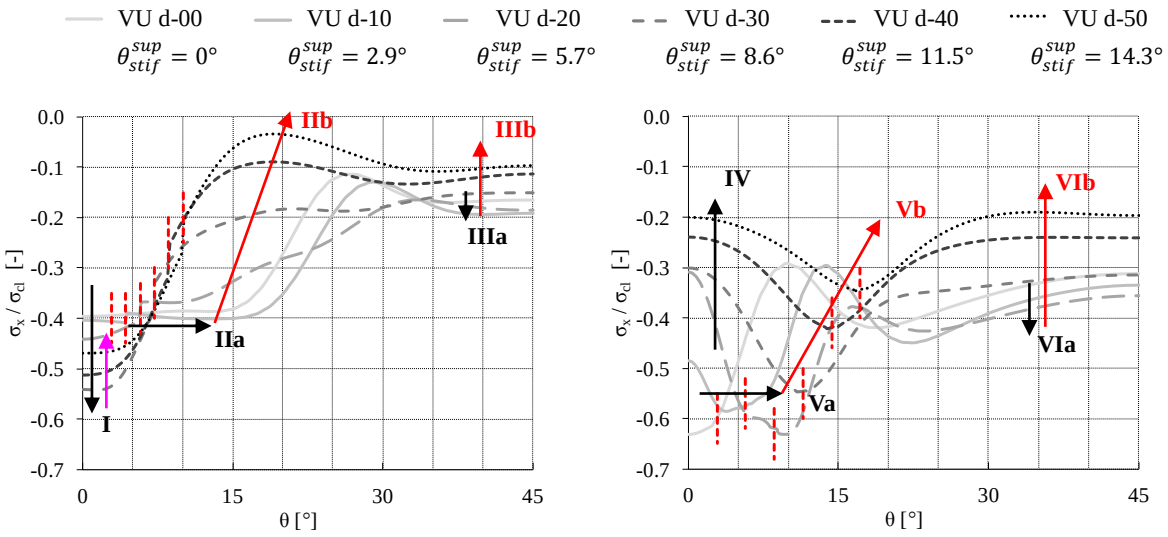

(a) $h_{path}/h_{stif} = 0.50$. (b) $h_{path}/h_{stif} = 1.10$.

Fig. 5-61 Distribution of the axial stresses at the moment of maximum load in the silo wall (type VU; $R/t = 1000$).

VU stiffener

The influence of the inclination of the flanges of the VU stiffener on the axial stresses in the stiffener is presented in Fig. 5-62. From this figure, it is found that the axial stresses at the moment of maximum load decrease as the angle θ_{stif}^{sup} increases for both cases ($R/t = 200; 1000$), in the web (I) as well as in the flanges (II) of the stiffener.

In other words, the flanges and web of the VU stiffener absorb an increasingly smaller

supporting force when the inclination increases. As a consequence, less force can be transferred by shear into the silo wall and the **spreading effect** weakens. In contrast, the silo wall directly above the support absorbs a larger part of the supporting force and the **channeling effect** becomes increasingly important, causing possibly premature "channel" failure.

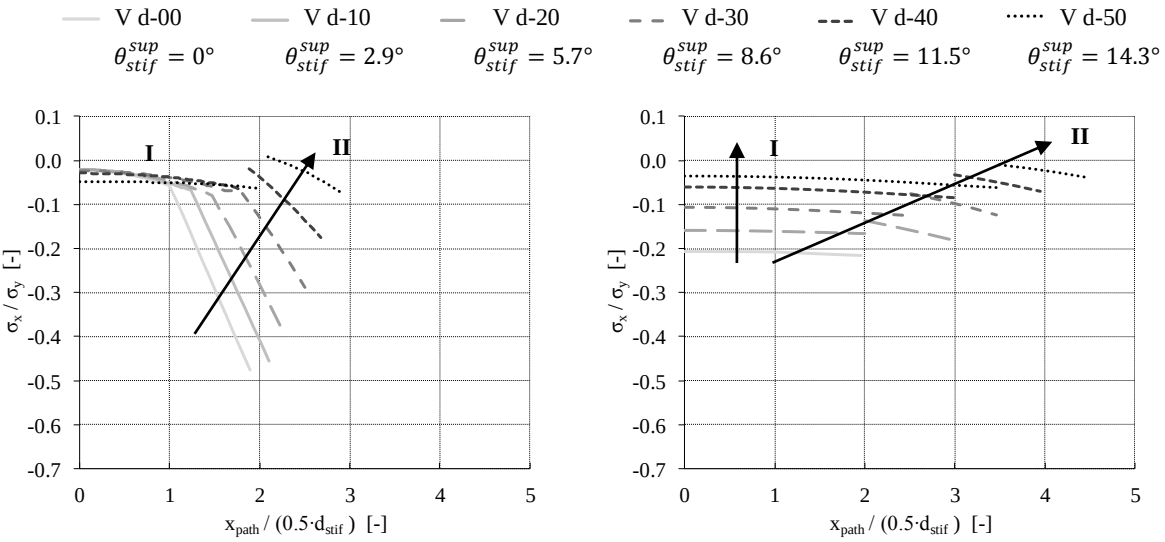

(a) $R/t = 200$. (b) $R/t = 1000$.

Fig. 5-62 Distribution of the axial stresses at the moment of maximum load in the stiffener (type VU; $h_{path}/h_{stif} = 0.50$).

Spreading and channeling effect

In this part, the spreading and channeling effect are discussed more in detail.

When the inclination of the flanges of a VU stiffener increases, one of the main findings of the previous part is that the channeling effect becomes more important, and the spreading effect less important. The channeling effect is clearly visible on the contourplots of the axial stresses at the moment of maximum load for a VU stiffener with large inclination. In Fig. 5-57 (c) ($R/t = 200$) and Fig. 5-60 (c) ($R/t = 1000$), the axial stresses are very large in the silo wall between the flanges of the VU stiffener (respectively blue and yellow colour + indicated with the letter C), while the axial stresses are relatively small in the silo wall on the other sides of the flanges (respectively green-red and red colour).

The spreading and channeling effect are both illustrated in Fig. 5-63 by means of arrows, representing the dispersion of the axial stresses in the silo wall in circumferential direction.

A U stiffener (Fig. 5-63 (a)) absorbs a large part of the supporting force at its bottom and gradually transfers this force into the silo wall by shear. This transfer by shear is shown with magenta arrows along the lines of intersection of the flanges of the U stiffener and the silo wall. The higher in the stiffened region, the better the axial stresses are distributed in

circumferential direction. This phenomenon is depicted with green arrows and is called the **spreading effect**. For a U stiffener, the channeling effect does not exist. The axial stresses in the area outside the spreading zone, which is denoted with red crosses, are relatively small.

In contrast, for a VU stiffener with a large inclination of its flanges (Fig. 5-63 (b)), a large part of the supporting force is directly introduced into the silo wall and is "concentrated" in the silo wall between the flanges. The dispersion of axial stresses between the flanges is depicted with blue arrows and is called the **channeling effect**. However, the lower half of this channel zone (indicated with a dark red ellipse) is susceptible to premature failure or "channel" failure, because the axial stresses are concentrated over a relatively narrow region between the flanges and the silo wall thickness is rather limited (compared to the stiffener). The remaining part of the supporting force is absorbed by the VU stiffener and is gradually transferred into the silo wall by shear. This part is depicted with green arrows and is called the **spreading effect**, but this effect weakens as the inclination of the flanges increases. In other words, the axial stresses in the area outside the channel zone, which is denoted with red crosses, are decreasing as the inclination of the flanges increases.

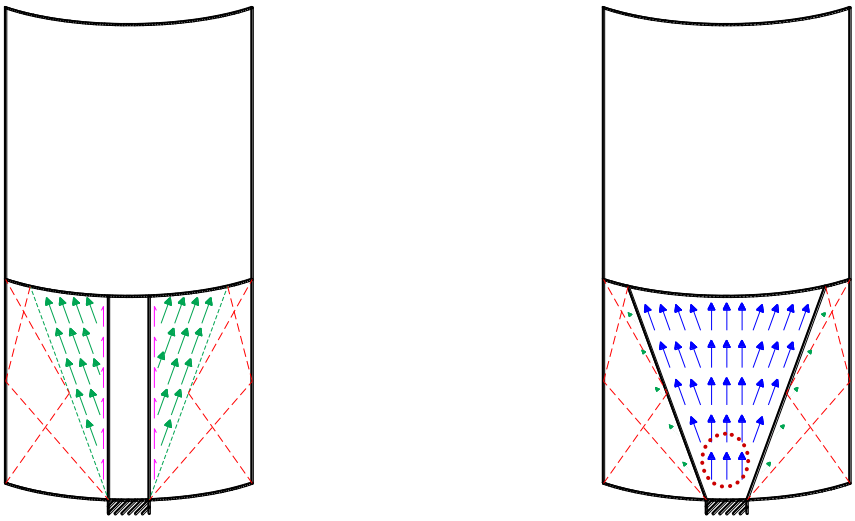

(a) U stiffener. (b) VU stiffener.

Fig. 5-63 Illustration of the spreading effect (green) and channeling effect (blue).

Conclusions

At the start of this study, it was assumed that by inclining the flanges of a VU stiffener, the spreading effect (of axial stresses in circumferential direction), which is typical of a traditional U stiffener, would be promoted. From the above results, it appears that the opposite of the intended purpose is true: the advantageous spreading effect weakens, while the channeling effect becomes more important. This latter effect is disadvantageous, because it can lead to premature "channel" failure in the narrow region between the flanges (as was the case for geometry 2).

Since the stress level in (the web of the) the VU stiffener is relatively small, the idea arose to eliminate the web of the stiffener and to investigate a VR stiffener with variable inclination. This stiffening configuration is depicted in Fig. 5-47 (d).

6.3.1.2 VR stiffener

In this section, the failure behaviour of a VR stiffener with variable inclination of the flanges will be investigated (See Fig. 5-47 (d)).

Silo wall - case 1 ($R/t = 200$)

In Fig. 5-64, the contourplots of the axial stresses at the moment of maximum load are shown for three different stiffener inclination angles θ_{stif}^{sup}. For a VR stiffener without inclination of the flanges, the silo wall just above the local support and the region above the top of the VR stiffener yield completely (See Fig. 5-64 (a)). The latter yielding region has more or less the same width in circumferential direction as the R stiffener. For VR stiffeners with a small inclination of the flanges ($\theta_{stif}^{sup} \leq 4.3°$), two regions of yielding are developing and are extending in circumferential direction, namely in the silo wall just above and just below the upper ring (See Fig. 5-64 (b)). The circumferential width of both regions increases with the angle of the flanges and have approximately the same circumferential width as the top of the VR stiffener. In other words, by increasing the slope of the flanges of the VR stiffener, the axial stresses are better distributed in circumferential direction since a wider circumferential part of the silo wall yields, resulting in an increasing failure load when $\theta_{stif}^{sup} \leq 4.3°$ (See Fig. 5-56 (a)). For VR stiffeners with a large inclination of the flanges ($\theta_{stif}^{sup} > 4.3°$), premature failure occurs by extensive yielding in the narrow area between the flanges (See Fig. 5-64 (c)). Again, it appears that the **channeling effect** is increasingly important as the slope of flanges increases (indicated with the letter C in Fig. 5-64 (c)), while the **spreading effect** becomes less important. Due to this premature failure, the failure load decreases when $\theta_{stif}^{sup} > 4.3°$ (See Fig. 5-56 (a)).

An attentive reader will wonder why the channeling effect in a thick-walled silo does not occur with a VU stiffener, in contrast to a VR stiffener here. A VR stiffener (without web) has a much smaller cross-section compared to a VU stiffener (with web), is already exhausted by plastic yielding at a smaller load level, and absorbs a smaller percentage of the total supporting force (depends on the relative stiffness of the stiffener and the silo). In other words, the silo wall just above the local support absorbs a larger part of the total supporting force in the case of a VR stiffener (I). In addition, when the inclination of the flanges of a VR (or VU) stiffener increases, the channeling effect becomes increasingly important, and the percentage of the total supporting force directly introduced in the silo wall increases even further (II). The combined effect of (I) and (II) causes channeling failure for a VR stiffener to

occur at smaller inclination angles than for a VU stiffener.

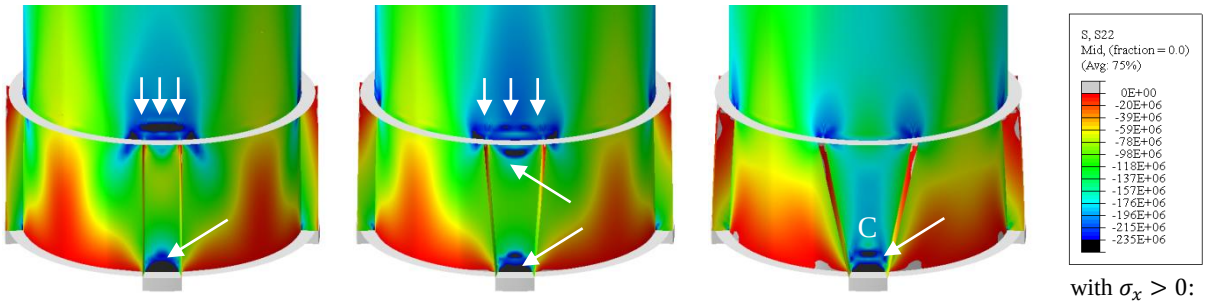

(a) $\theta_{stif}^{sup} = 0°$. (b) $\theta_{stif}^{sup} = 4.3°$. (c) $\theta_{stif}^{sup} = 11.5°$. with $\sigma_x > 0$: compression; $\sigma_y = 235$MPa

Fig. 5-64 Contourplots of the axial stresses σ_x at the moment of maximum load [Pa] (type VR; $R/t = 200$).

The distribution of axial stresses in circumferential direction is plotted in Fig. 5-65 for two different heights in the silo wall: at 90% of the stiffener height (i.e. in the stiffened region just below the upper ring) and at 110% of the stiffener height (i.e. in the unstiffened region just above the upper ring). These heights correspond with the location of yielding depicted in Fig. 5-64. The vertical dashed red lines in the figures correspond with the circumferential angle of the flange of the VR stiffener.

Firstly, the trends are observed when the slope of the flanges of the VR stiffener increases below $\theta_{stif}^{sup} \leq 4.3°$ (no channel failure). In Fig. 5-65 (a), the magnitude of the axial stresses increases between the flanges of the VR stiffener (Ia), the stress peak adjacent to the flange moves with the inclined flange of the VR stiffener (IIa), and the axial stresses between the VR stiffeners increase (III). (Ia) is the result of the channeling effect, (IIa) and (III) of the spreading effect. In Fig. 5-65 (b), the axial stresses in the central zone between the flanges of the VR stiffener are decreasing (IV), the region of large axial stresses moves with the top of the inclined flange of the VR stiffener (Va), and the axial stresses between the VR stiffeners are increasing (VI).

However, from a certain point ($\theta_{stif}^{sup} > 4.3°$), premature channel failure occurs in the narrow area between the flanges just above the local support. This results in a decrease of the axial stresses in a large part of the circumference: (Ib), (IIb), (IV), and (Vb).

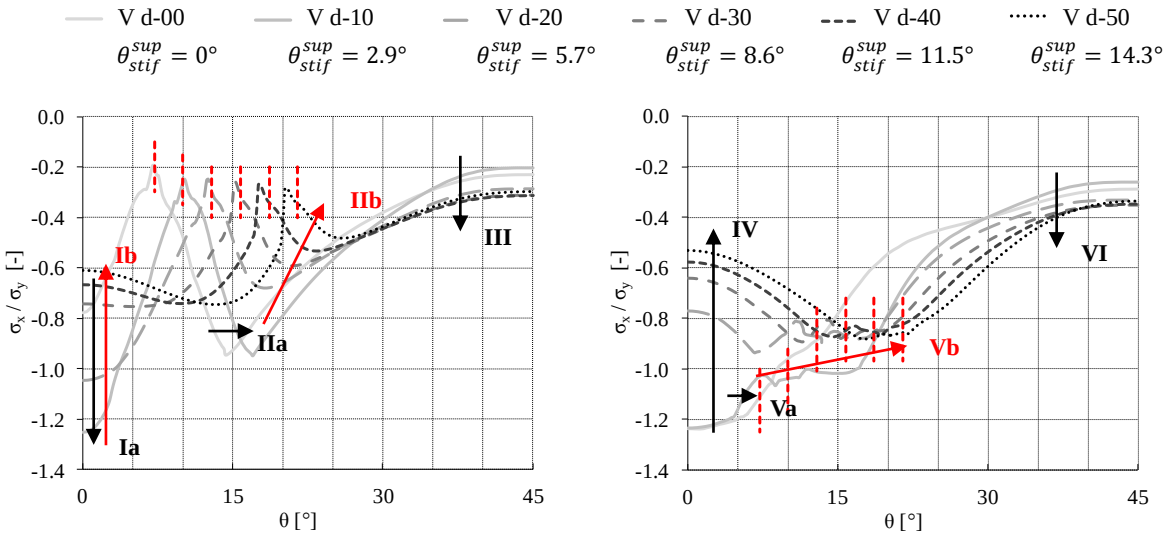

(a) $h_{path}/h_{stif} = 0.90$. (b) $h_{path}/h_{stif} = 1.10$.

Fig. 5-65 Distribution of the axial stresses at the moment of maximum load in the silo wall (type VR; $R/t = 200$).

Silo wall - case 2 ($R/t = 1000$)

In Fig. 5-66, the contourplots of the post-buckling deformations are shown for three different stiffener inclination angles θ_{stif}^{sup}. For the R stiffener ($\theta_{stif}^{sup} = 0°$), the silo fails by pure elastic buckling in the region just above the upper ring. From the moment of buckling, a buckle develops in the unstiffened silo wall above the top of the R stiffener (See Fig. 5-66 (a)). For VR stiffeners with a small inclination of the flanges ($\theta_{stif}^{sup} \leq 4.3°$), two separate buckles develop in the unstiffened silo wall just above the end of the flanges (See Fig. 5-66 (b)). In contrast, for VR stiffeners with a large inclination of the flanges ($\theta_{stif}^{sup} > 4.3°$), the location of buckling shifts to the stiffened silo wall between the flanges of the VR stiffener (See Fig. 5-66 (c)). Furthermore, it is found that the height of the buckle in the stiffened region between the flanges moves downwardly as the inclination of the flanges increases further.

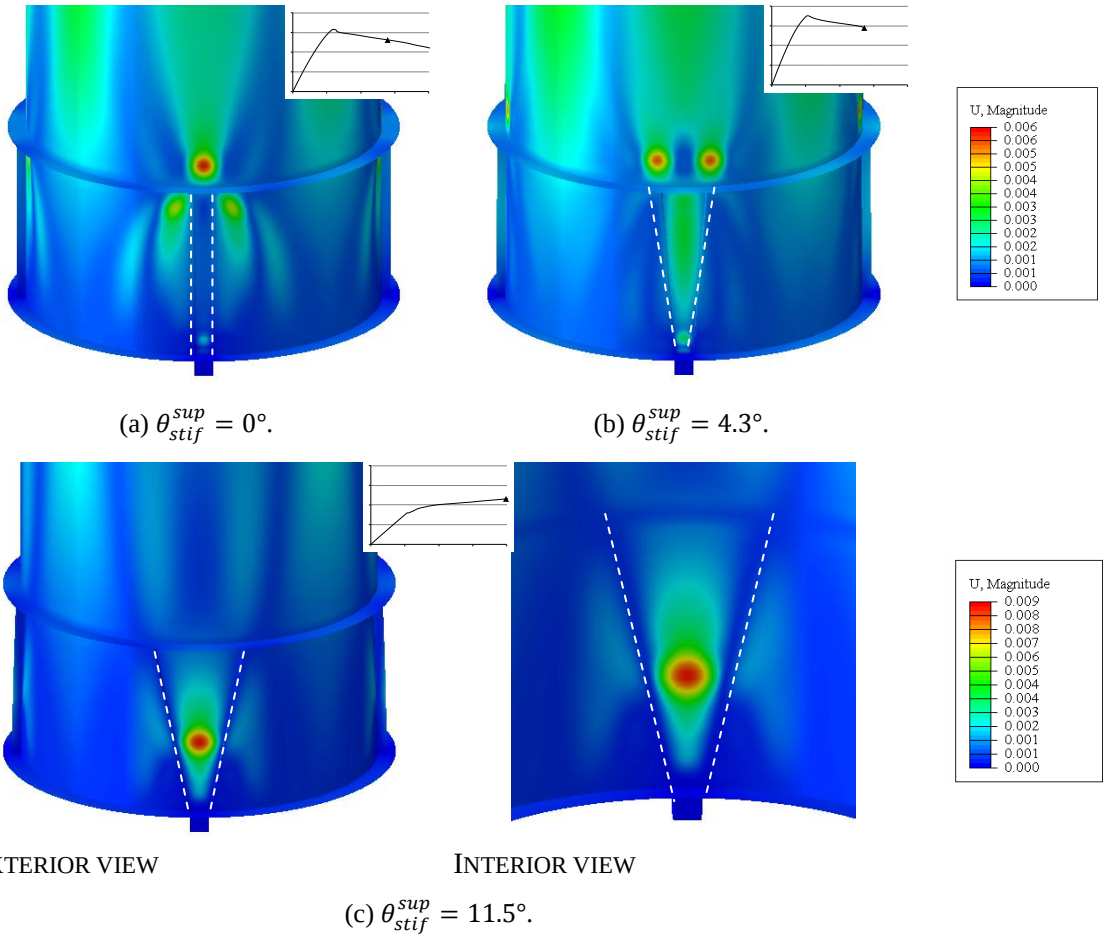

(a) $\theta_{stif}^{sup} = 0°$. (b) $\theta_{stif}^{sup} = 4.3°$.

(c) $\theta_{stif}^{sup} = 11.5°$.

Fig. 5-66 Contourplots of the post-buckling deformations U [m] (type VR; $R/t = 1000$).

The movement of the location of elastic buckling from the unstiffened region above the VR stiffener (Fig. 5-66 (b)) to the stiffened region between the flanges of the VR stiffener (Fig. 5-66 (c)), can be attributed to the **channeling effect**, which is increasingly important as the slope of flanges increases (and the **spreading effect** less important). This tendency can be noticed on the contourplots of the axial stresses at the moment of maximum load in Fig. 5-67. For all cases, the largest axial stresses are found in the silo wall just above the local support and at the location of the buckle. For the R stiffener and VR stiffeners with a small inclination of the flanges ($\theta_{stif}^{sup} \leq 4.3°$), this latter area is located just above the stiffener, while for VR stiffeners with a large inclination of the flanges ($\theta_{stif}^{sup} > 4.3°$), the largest stresses occur in the stiffened silo wall between the flanges.

At first instance, the stresses are distributed better in circumferential direction as the slope of the flanges of the VR stiffener increases (compare Fig. 5-67 (a) and (b)), resulting in an increasing failure load ($\theta_{stif}^{sup} \leq 4.3°$ in Fig. 5-56 (b)). However, from a certain inclination ($\theta_{stif}^{sup} > 4.3°$), the failure load starts to decrease in Fig. 5-56 (b). This premature failure is caused by the **channeling effect**: the axial stresses are "concentrated" in the silo wall between the flanges. In Fig. 5-67 (c), this stress concentration is indicated with the letter C and the

very narrow area between the flanges of the VR stiffener is coloured in yellow/green.

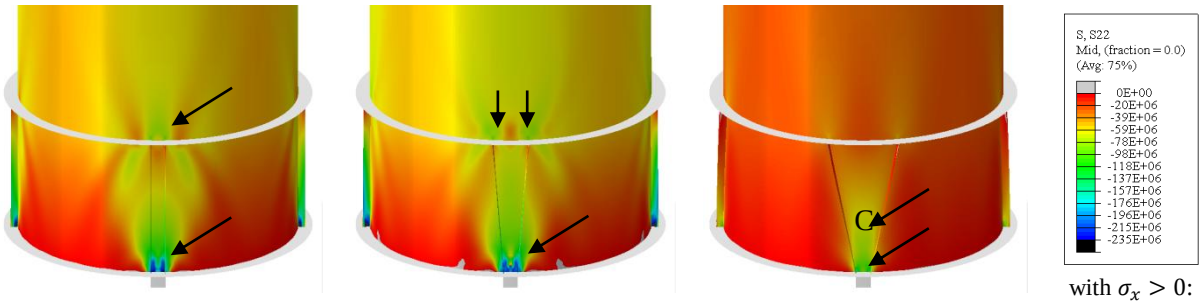

(a) $\theta_{stif}^{sup} = 0°$. (b) $\theta_{stif}^{sup} = 4.3°$. (c) $\theta_{stif}^{sup} = 11.5°$. with $\sigma_x > 0$: compression; $\sigma_y = 235$MPa

Fig. 5-67 Contourplots of the axial stresses σ_x at the moment of maximum load [Pa] (type VR; $R/t = 1000$).

The distribution of axial stresses in circumferential direction is plotted in Fig. 5-68 for two different heights in the silo wall: at 50% of the stiffener height (i.e. halfway the stiffened region just) and at 110% of the stiffener height (i.e. in the unstiffened region just above the upper ring). These heights correspond with the location of elastic buckling depicted in Fig. 5-66. The vertical dashed red lines in the figures correspond with the circumferential angle of the flange of the stiffener.

In Fig. 5-68 (a), two trends can be observed with an increasing slope of the VR stiffener. Firstly, the magnitude of the axial stresses increases between the flanges (I). This is called the **channeling effect** and will cause premature buckling of the structure when $\theta_{stif}^{sup} > 4.3°$. When $\theta_{stif}^{sup} > 5.7°$, the axial stresses in the channel between the flanges starts to decrease again at 50% of the stiffener height (purple arrow) because the region with the axial stresses (and the buckle) moves downwardly. Secondly, due to the **spreading effect**, the stress peak just adjacent to the flange moves with the inclined flange of the VR stiffener (IIa) and the axial stresses increase between the VR stiffeners (IIIa) when $\theta_{stif}^{sup} \leq 4.3°$. When the inclination of the flanges is increased further ($\theta_{stif}^{sup} > 4.3°$), premature "channel" buckling occurs in the stiffened silo wall and the stress peak weakens (IIb) and the axial stresses between the VR stiffeners decrease (IIIb). In other words, by increasing the inclination of the flanges of the VR stiffener, the channeling effect becomes more important (and causes premature buckling), and the spreading effect weakens.

In Fig. 5-68 (b), when the inclination of the flanges of the VR stiffener increases and $\theta_{stif}^{sup} \leq 4.3°$, the axial stresses in the central zone between the flanges of the VR stiffener are decreasing (IV), the region of large axial stresses moves with the top of the inclined flange of the VR stiffener (Va), and the axial stresses between the VR stiffeners are increasing (VIa). When the inclination of the flanges of the VR stiffener is increased further ($\theta_{stif}^{sup} > 4.3°$), premature "channel" buckling occurs in the stiffened region and the axial stresses are

decreasing over the entire circumference (IV, Vb, and VIb), inclusiding the stress peak above the termination flanges (Vb).

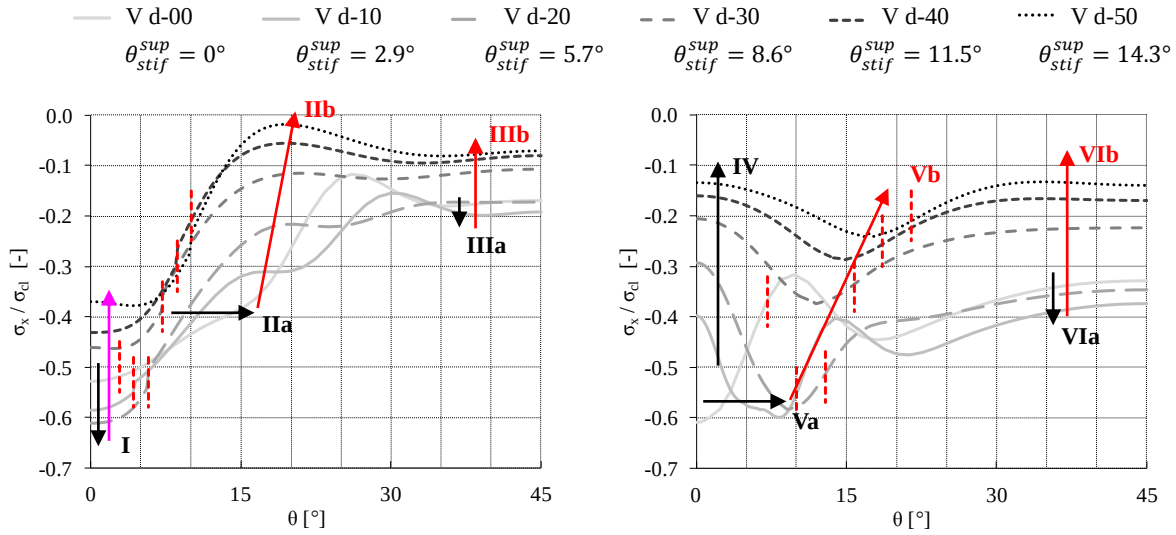

(a) $h_{path}/h_{stif} = 0.50$. (b) $h_{path}/h_{stif} = 1.10$.

Fig. 5-68 Distribution of the axial stresses at the moment of maximum load in the silo wall (type VR; $R/t = 1000$).

VR stiffener

The influence of the inclination of the flanges of the VR stiffener on the axial stresses in the stiffener is presented in Fig. 5-69. From this figure, it is found that the axial stresses at the moment of maximum load decrease as the angle θ_{stif}^{sup} increases for both cases ($R/t = 200; 1000$) over the entire radial width of the flange of the stiffener (I).

In other words, the flanges of the VR stiffener absorb an increasingly smaller supporting force when the inclination increases. As a consequence, less force is transferred by shear into the silo wall and the **spreading effect** weakens. In contrast, the silo wall directly above the support absorbs a larger part of the supporting force and the **channeling effect** becomes increasingly important, causing possibly premature "channel" failure.

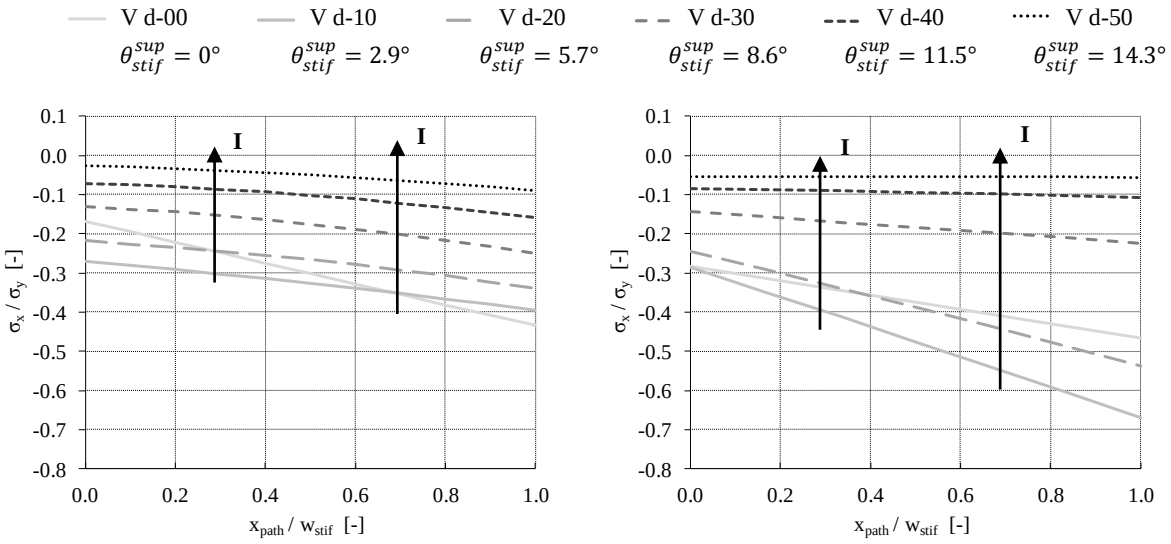

(a) $R/t = 200$. (b) $R/t = 1000$.

Fig. 5-69 Distribution of the axial stresses at the moment of maximum load in the stiffener (type VR; $h_{path}/h_{stif} = 0.50$).

Spreading and channeling effect

For the discussion of the spreading and channeling effect, the reader is referred to the corresponding part in Section 6.3.1.1, since the same explanation is valid for both effects for VR and VU stiffeners with variable inclination of the flanges.

Conclusions

At the start of this study, it was assumed that by inclining the flanges of a VU or a VR stiffener, the spreading effect (of axial stresses in circumferential direction), which is typical of a traditional U and R stiffener, would be promoted. However, from the above results, it appears that the opposite of the intended purpose is true: the advantageous spreading effect weakens, while the channeling effect becomes more important. This latter effect is disadvantageous, because it can lead to premature "channel" failure in the narrow region between the flanges.

To eliminate the possibility of premature "channel" failure in the narrow area between the flanges, the idea arose to maintain the traditional U stiffener and to add an additional VR stiffener with variable inclination above each support. This stiffening configuration is depicted in Fig. 5-47 (e).

6.3.1.3 U + VR stiffener

In this section, the failure behaviour of a U+VR stiffener with variable inclination of the flanges of the VR stiffener will be investigated (See Fig. 5-47 (e)).

Silo wall - case 1 ($R/t = 200$)

In Fig. 5-70, the contourplots of the axial stresses at the moment of maximum load are shown for three different stiffener inclination angles θ_{stif}^{sup}. The web of the U stiffener is made invisible so that the stresses in the shell wall behind the U stiffener would be visible. Independently of the angle θ_{stif}^{sup}, the silo wall just above the local support yields completely. In Fig. 5-70 (a), a U stiffener is depicted. In this case, a small region above the upper ring yields with more or less the same width in circumferential direction as the U stiffener. By increasing the inclination θ_{stif}^{sup} of the flanges of the VR stiffener (See Fig. 5-70 (b) and (c)), the region of plastic yielding in the silo wall just above the upper ring expands in circumferential direction. Its circumferential width increases with the angle of the flanges of the VR stiffener and has approximately the same circumferential width as the top of the VR stiffener. In other words, by increasing the slope of the flanges of the VR stiffener, the axial stresses are better distributed in circumferential direction since a wider circumferential part of the silo wall yields, resulting in an increasing failure load (See Fig. 5-56 (a)).

Furthermore, from the contourplots of the axial stresses shown in Fig. 5-70, it can be noticed that the channel effect in the narrow region behind the flanges of the VR stiffener does not occur, even not for large inclination angles θ_{stif}^{sup} of the VR stiffener.

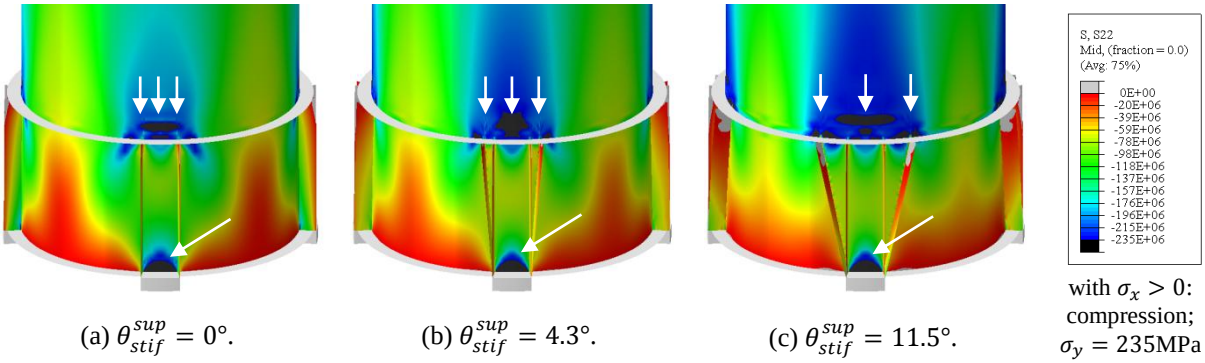

(a) $\theta_{stif}^{sup} = 0°$. (b) $\theta_{stif}^{sup} = 4.3°$. (c) $\theta_{stif}^{sup} = 11.5°$.

with $\sigma_x > 0$: compression; $\sigma_y = 235$MPa

Fig. 5-70 Contourplots of the axial stresses σ_x at the moment of maximum load [Pa] (type U+VR; $R/t = 200$) (remark: web of the U stiffener is invisible).

In Fig. 5-71, the distribution of axial stresses in the silo wall in circumferential direction is plotted at a height of 110% of the stiffener height (i.e. in the unstiffened region just above the upper ring). This height corresponds with the location of yielding depicted in Fig. 5-70. The vertical dashed red lines in the figure correspond with the circumferential angle of the flange of the VR stiffener.

When the inclination of the flanges of the VR stiffeners increases, the axial stresses in the central zone between the flanges of the U stiffener are decreasing but remain above the unity (I), the region of large axial stresses ($\sigma_x/\sigma_y > 1$) expands in circumferential direction from the top of the flange of the U stiffener to the top of the inclined flange of the VR stiffener,

resulting in an increased circumferential width of yielding (II), and the axial stresses between the VR stiffeners are also increasing (III).

For this geometry and this stiffening configuration (U+VR), it can be concluded that, as the inclination of the flanges of the VR stiffener increases, the axial stresses are much better distributed in circumferential direction over the stiffened region.

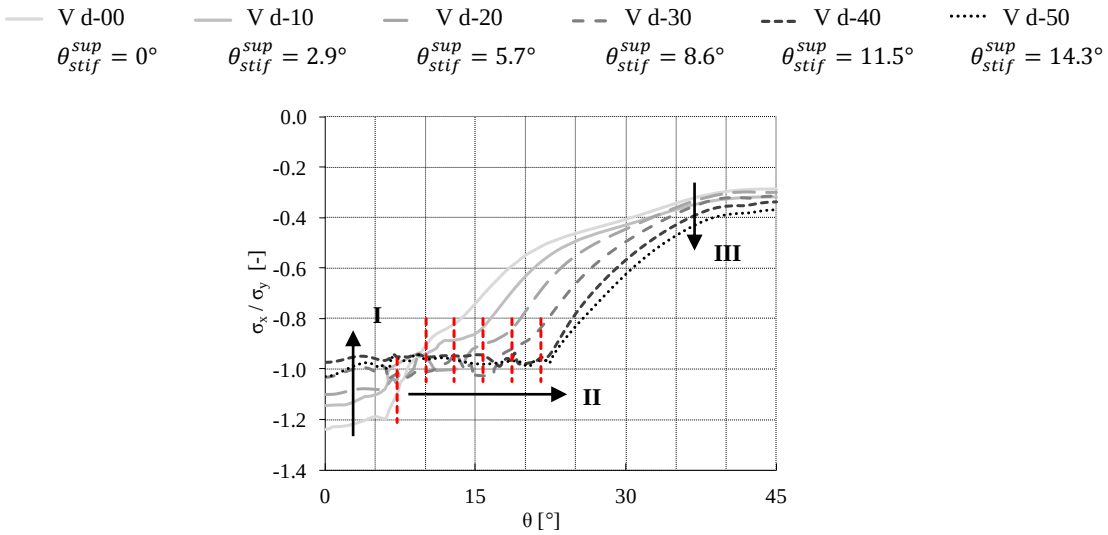

Fig. 5-71 Distribution of the axial stresses at the moment of maximum load in the silo wall (type U+VR; $R/t = 200$) ($h_{path}/h_{stif} = 1.10$).

Silo wall - case 2 ($R/t = 1000$)

In Fig. 5-72, the contourplots of the post-buckling deformations are shown for three different stiffener inclination angls θ_{stif}^{sup}. For the U stiffener ($\theta_{stif}^{sup} = 0°$), the silo fails by pure elastic buckling in the region just above the upper ring. From the moment of buckling, a buckle develops in the unstiffened silo wall above the top of the U stiffener (See Fig. 5-72 (a)). For U+VR stiffeners with a small inclination of the flanges ($\theta_{stif}^{sup} \leq 8.6°$), two separate buckles develop in the stiffened silo wall just next to the end of the flanges of the VR stiffener (See Fig. 5-72 (b)). For U+VR stiffeners with a large inclination of the flanges ($\theta_{stif}^{sup} > 8.6°$), the location of buckling shifts again to the unstiffened silo wall above the U stiffener (See Fig. 5-72 (c)).

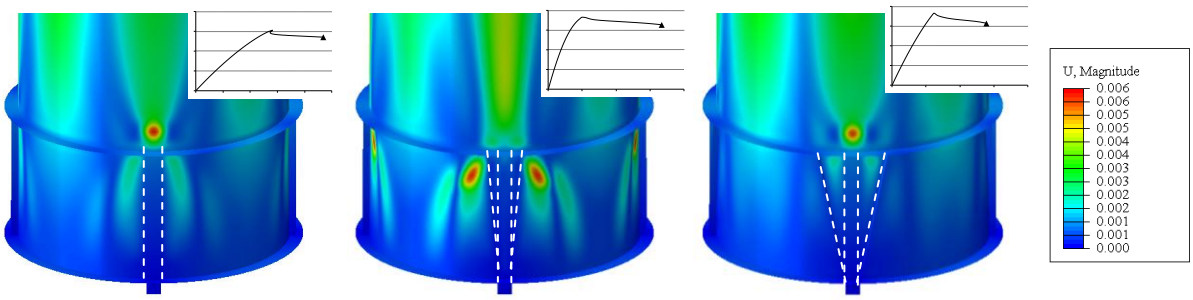

(a) $\theta_{stif}^{sup} = 0°$. (b) $\theta_{stif}^{sup} = 4.3°$. (c) $\theta_{stif}^{sup} = 11.5°$.

Fig. 5-72 Contourplots of the post-buckling deformations U [m] (type U+VR; $R/t = 1000$).

In Fig. 5-73, the contourplots of the axial stresses at the moment of maximum load are depicted. The web of the U stiffener is made invisible so that the stresses in the shell wall behind the U stiffener would be visible. For all cases, three different regions with large axial stresses are found in the silo wall. The first region is the silo wall just above the local support. The second region is located in the stiffened silo wall just below the upper ring. For the U stiffener ($\theta_{stif}^{sup} = 0°$) and for U+VR stiffeners with a small inclination of the flanges of the VR stiffener ($\theta_{stif}^{sup} \leq 8.6°$), high stress peaks occur just next to the flanges of respectively the U and the VR stiffener. For U+VR stiffeners with a large inclination of the flanges of the VR stiffener ($\theta_{stif}^{sup} > 8.6°$), high stress peaks occur in the silo wall between the flanges of the U stiffener and the flanges of the VR stiffener. The third region is the unstiffened silo wall just above the upper ring and has more or less the same circumferential width as the U+VR stiffener. Within this region, the highest stress peaks occur in the middle above the U stiffener and at the top of the flanges of the VR stiffener. Buckling will occur in one of the above mentioned zones, depending on where the critical buckling stress is reached first.

Furthermore, from the contourplots of the axial stresses shown in Fig. 5-73, it can be noticed that the channel effect in the narrow region behind the flanges of the VR stiffener does not occur, even not for large inclination angles θ_{stif}^{sup} of the VR stiffener.

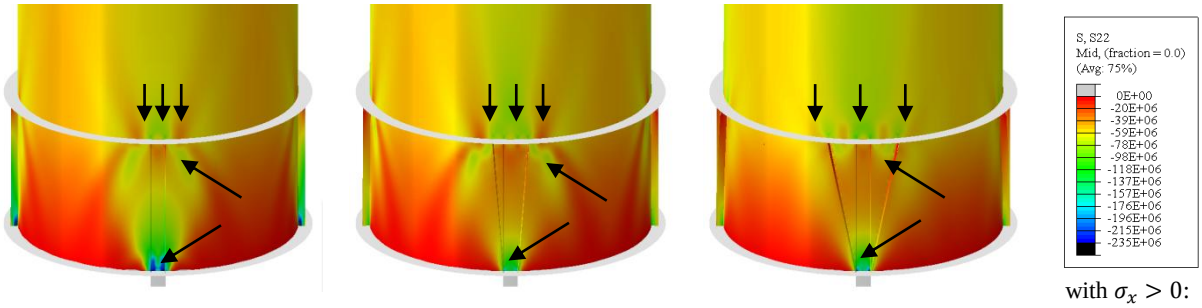

(a) $\theta_{stif}^{sup} = 0°$. (b) $\theta_{stif}^{sup} = 4.3°$. (c) $\theta_{stif}^{sup} = 11.5°$.

with $\sigma_x > 0$: compression; $\sigma_y = 235$MPa

Fig. 5-73 Contourplots of the axial stresses σ_x at the moment of maximum load [Pa] (type U+VR; $R/t = 1000$).

In Fig. 5-74, the distribution of axial stresses in the silo wall in circumferential direction is plotted at a height of 110% of the stiffener height (i.e. in the unstiffened region just above the upper ring). This height corresponds with the location of buckling depicted in Fig. 5-72. The vertical dashed red lines in the figure correspond with the circumferential angle of the flange of the VR stiffener.

When the inclination of the flanges of the VR stiffener increases and $\theta_{stif}^{sup} \leq 8.6°$, the axial stresses in the central zone above the U stiffener are decreasing (Ia), the circumferential width of the region of large axial stresses expands from the top of the flange of the U stiffener to the top of the inclined flange of the VR stiffener (IIa), and the axial stresses between the VR stiffeners are increasing (IIIa). When the inclination of the flanges of the VR stiffener is increased further ($\theta_{stif}^{sup} > 8.6°$), the stress peak above the inclined VR stiffener decreases (IIb) and the axial stresses between the VR stiffeners are decreasing (IIIb).

For this geometry and this stiffening configuration (U+VR), it can be concluded that, as the inclination of the flanges of the VR stiffener increases, the axial stresses are better distributed in circumferential direction over the stiffened region when $\theta_{stif}^{sup} \leq 8.6°$. From $\theta_{stif}^{sup} = 8.6°$, the distribution of the axial stresses in circumferential direction decreases again.

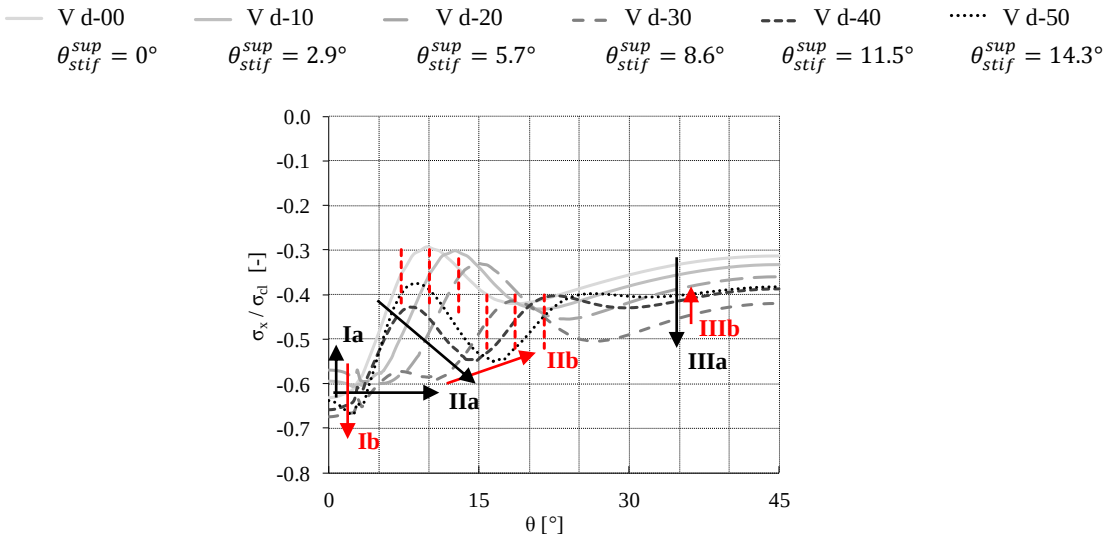

Fig. 5-74 Distribution of the axial stresses at the moment of maximum load in the silo wall (type U+VR; $R/t = 1000$) ($h_{path}/h_{stif} = 1.10$).

U + VR stiffener

The influence of the inclination of the flanges of the VR stiffener on the axial stresses at the moment of maximum load in both stiffeners is presented in Fig. 5-75. From this figure, it is found that the axial stresses in the U stiffener remain more or less unchanged as the slope of the VR stiffener increases, while the axial stresses in the VR stiffener clearly decrease (II).

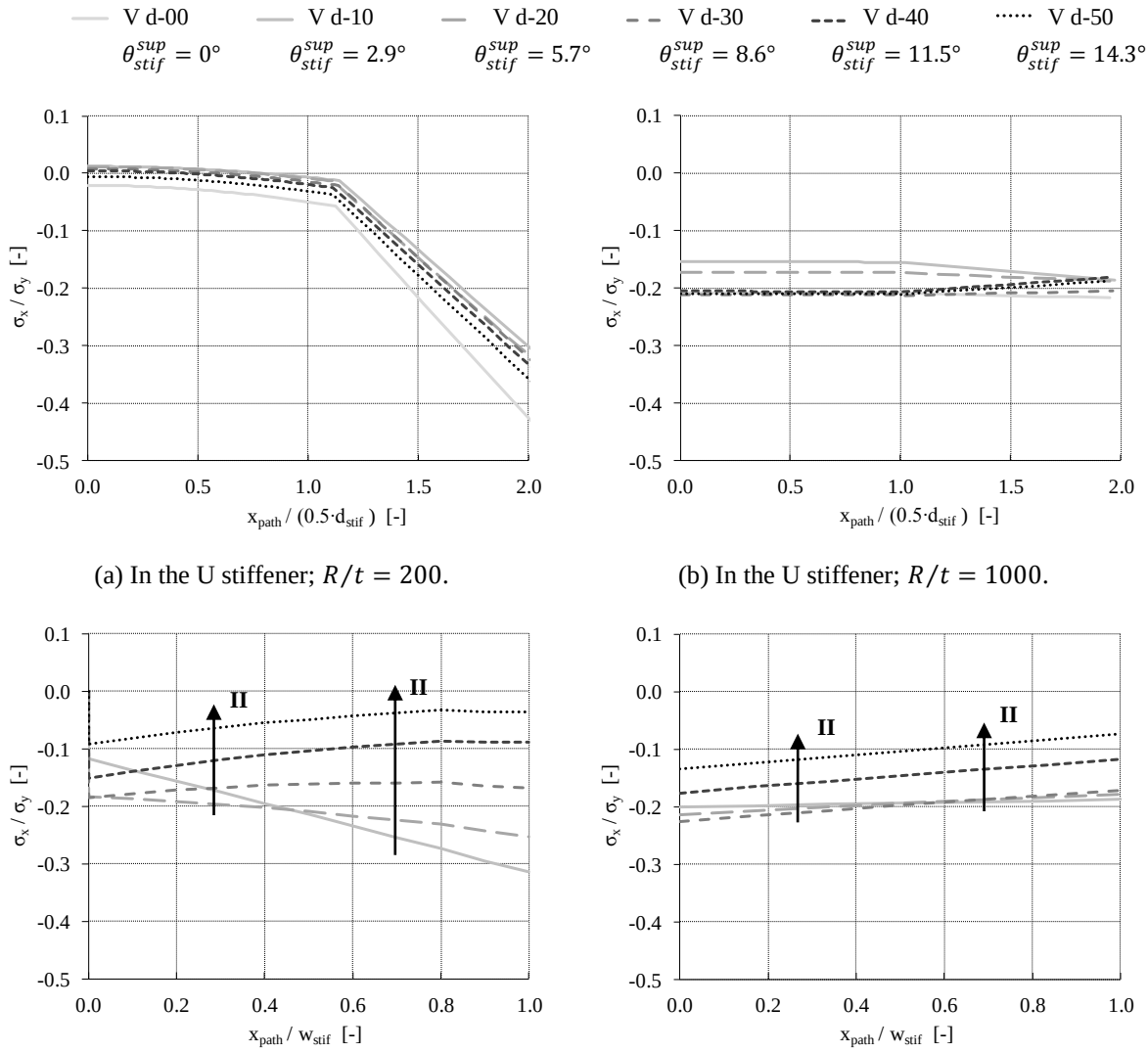

(a) In the U stiffener; $R/t = 200$.

(b) In the U stiffener; $R/t = 1000$.

(c) In the VR stiffener; $R/t = 200$.

(d) In the VR stiffener; $R/t = 1000$.

Fig. 5-75 Distribution of the axial stresses at the moment of maximum load in the stiffener (type U+VR; $h_{path}/h_{stif} = 0.50$).

Conclusions

For both cases, the U+VR stiffening configuration leads to the highest increase of the failure load compared to a traditional U profile (See Fig. 5-56).

Furthermore, the presence of a traditional U stiffener combined with a VR stiffener with inclined flanges **promotes the advantageous spreading effect** up to a certain slope of the VR stiffener. And, more important, the presence of a U stiffener above the support **excludes the disadvantageous channeling effect**, which was found for the VU and the VR stiffener, and which was the cause of premature failure in these cases.

For the above mentioned reasons, it was decided to choose the U+VR stiffening configuration for the extensive parametric study (Section 6.3.2).

For other geometries, it is expected that an increase of the inclination of the flanges of the VR stiffener leads to a better distribution of the axial stresses in circumferential direction. In certain cases, it is likely that the axial stresses are again less well spread in circumferential direction as an " optimal" inclination angle is exceeded.

6.3.2 Extensive parametric study

In the exploratory study, the failure behaviour of three stiffening arrangements (i.e. VU; VR; U+VR) was investigated and compared with each other for two geometries. On the basis of these initial results, it was found that a U+VR configuration is the best alternative to increase the failure load by improving the distribution of axial stresses in circumferential direction.

In this extensive parametric study, it is checked whether this last finding can also be extended to other geometries. This has be done by performing GMNA calculations for all U-shaped longitudinal stiffeners defined in Section 5.5 (i.e. Table 5-10 and Table 5-11) with a variation of the inclination of the flange of the VR stiffener within the whole range of possible inclinations. This range is defined by the parameter p_{stif}^{sup} which is depicted in Fig. 5-76. A value of 0% corresponds with the U stiffener (without inclination), a value of 100% corresponds with U+VR stiffener with maximum inclination $\theta_{stif,max}^{sup}$. This maximum slope can be calculated by using Eqs. (5-16) - (5-17) and is defined by the angle at which the inclined flanges of two adjacent stiffeners touch each other at their top.

$$\theta_{stif,max}^{sup} = 0.5 \cdot \left(\frac{360°}{n_{sup}} - \theta_{stif} \right) \tag{5-16}$$

$$\theta_{stif} = 360° \cdot d_{stif} / (2\pi R) \tag{5-17}$$

Where n_{sup} is the number of supports; d_{stif} is the circumferential width of the bottom of the U stiffener; R is the cylinder radius.

The calculated values of p_{stif}^{sup} are given in Table 5-16 and depend on the radius-to-thickness ratio R/t of the cylinder. Due to the large number of investigated geometries (220) and possible values of p_{stif}^{sup}, 28 cases were isolated for which the range (a) was applied, while for the subsequent geometries only the values of p_{stif}^{sup} of the range (b) were calculated. In total, 1240 GMNA calculations were performed to create a clear picture concerning the influence of the inclination of the U+VR stiffener and to determine the best possible inclination (or a zone) to maximise the failure load.

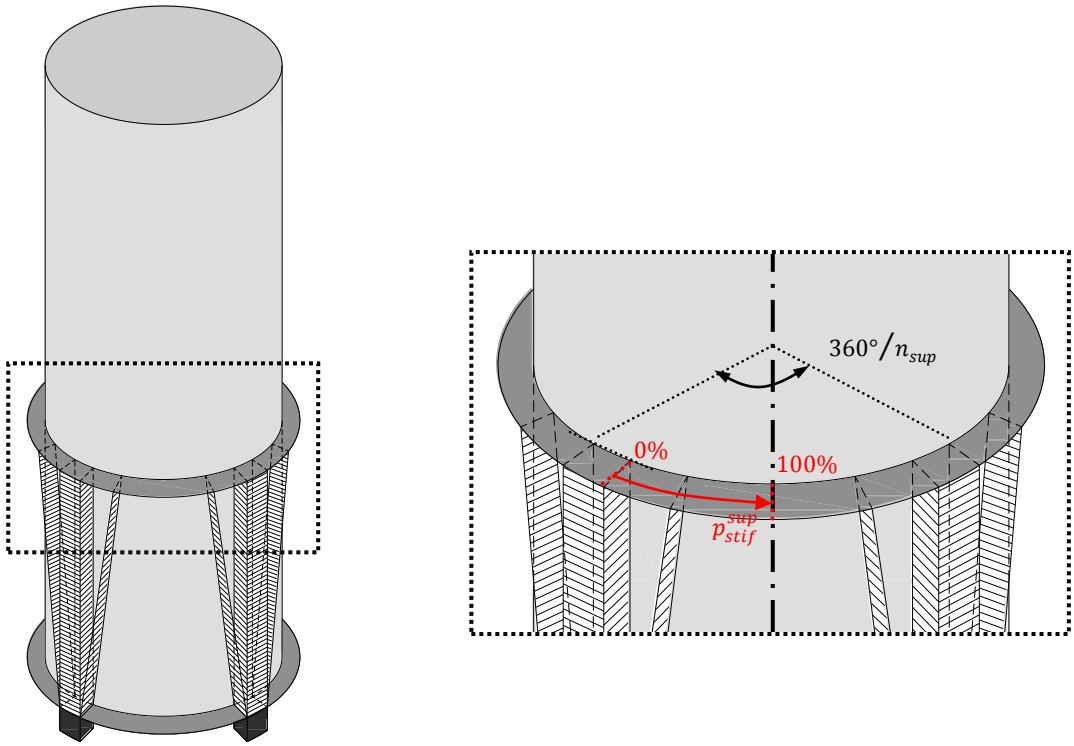

Fig. 5-76 Parameter p_{stif}^{sup}.

Table 5-16 Range of the parameter p_{stif}^{sup} [%].

R/t	VALUE(S) p_{stif}^{sup} [%]	
100; 200; 250; 333.3	(a)	5; 10; 20; 30; 40; 50; 60; 70; 80; 90
	(b)	5; 10; 20; 40; 60
500; 666.6; 1000	(a)	5; 10; 20; 30; 40; 50; 60
	(b)	5; 10; 20; 30; 40

Results

In the figures below, the dimensionless GMNA failure load F_u/F_{ref} is plotted against the angle θ_{stif}^{sup} for a number of stiffener shapes and heights (i.e. $h_{stif}/R = 1.0; 2.0$), each time for a different radius-to-thickness ratio R/t. The results for the thick-walled silos (i.e. $R/t = 100$) are presented in Fig. 5-77, for the silos with intermediate thickness (i.e. $R/t = 200; 250; 333.3$) in Fig. 5-78, and for thin-walled silos (i.e. $R/t = 500; 666.6; 1000$) in Fig. 5-79. In this way, more general conclusions can be drawn for different failure phenomena and for different stiffener shapes and heights.

In Fig. 5-77, the influence of an increasing inclination angle θ_{stif}^{sup} of the VR stiffener on the failure load is depicted for the thick-walled silos (i.e. $R/t = 100$). Most curves are rapidly increasing in the beginning for small values of θ_{stif}^{sup} and are approximately horizontal for

medium and high values of θ_{stif}^{sup}. On the basis of these results, the range between 5 and 15 degrees can be identified as the most preferred inclination angle. The failure load of a U+VR configuration within this range is approximately 10 to 20 percent higher than a traditional U stiffener. Similar results have been found for silos with stiffeners with other heights (i.e. $h_{stif}/R = 0.5; 1.5$).

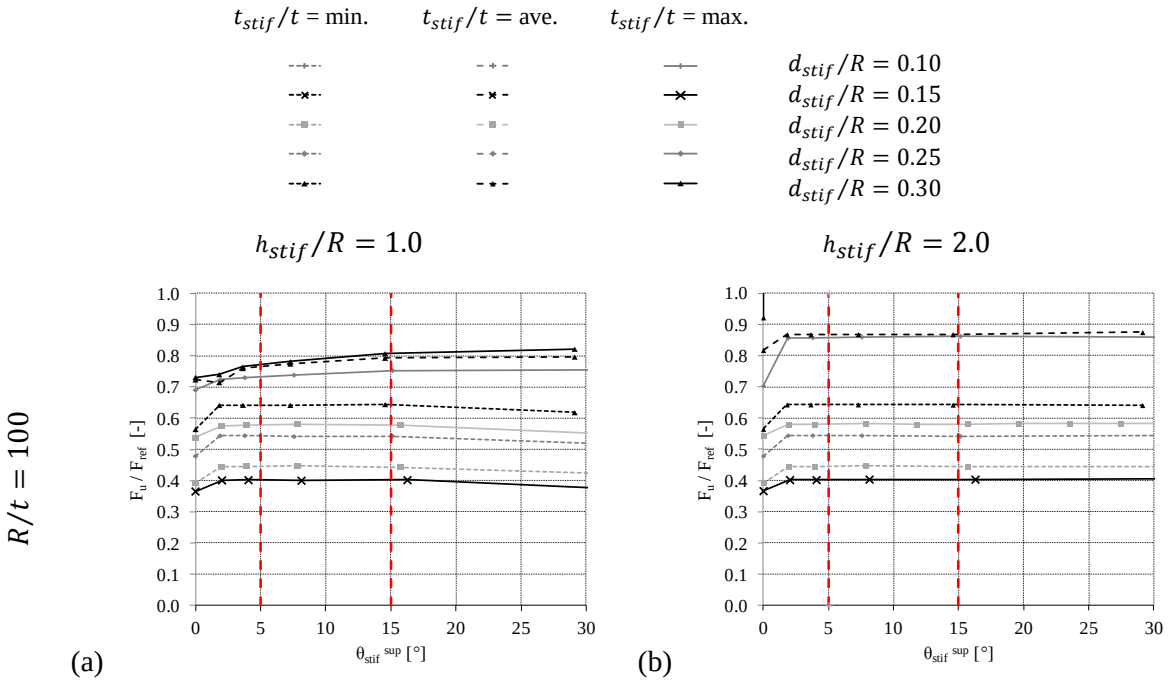

Fig. 5-77 Influence of the inclination angle θ_{stif}^{sup} of the VR stiffener to the dimensionless GMNA failure load F_u/F_{ref} for thick-walled silos ($R/t = 100$) and for different stiffener heights h_{stif}^{sup}/R (extensive parametric study: alternative U+VR).

When the inclination angle θ_{stif}^{sup} of the VR stiffener increases for silos with intermediate silo thickness (i.e. $R/t = 200; 250; 333.3$), the failure load increases rapidly for small values of the angle θ_{stif}^{sup}, then less rapidly for intermediately high values of the angle θ_{stif}^{sup}, and remains constant or decreases for high values of the angle θ_{stif}^{sup} (See Fig. 5-78). On the basis of these results, the range between 15 and 20 degrees can be identified as the most preferred inclination angle. The failure load of a U+VR configuration within this range is approximately 10 to 20 percent higher than a traditional U stiffener. Similar results have been found for silos with stiffeners with other heights (i.e. $h_{stif}/R = 0.5; 1.5$).

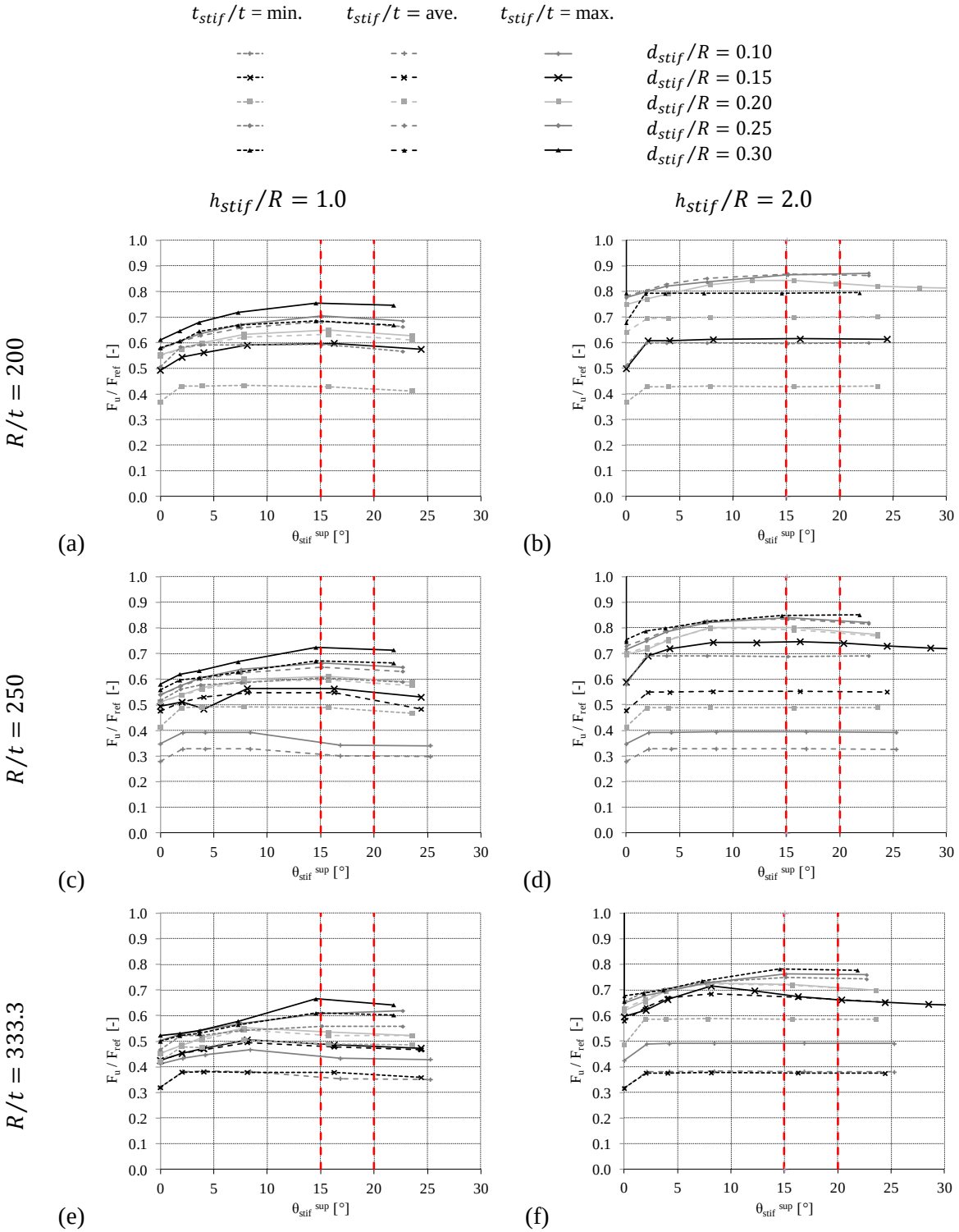

Fig. 5-78 Influence of the inclination angle θ_{stif}^{sup} of the VR stiffener to the dimensionless GMNA failure load F_u/F_{ref} for silos with intermediate thickness ($R/t = 200; 250; 333.3$) and for different stiffener heights h_{stif}^{sup}/R (extensive parametric study: alternative U+VR).

When the inclination angle θ_{stif}^{sup} of the VR stiffener increases for thin-walled silos (i.e. $R/t = 500;\ 666.6; 1000$), the buckling load rapidly increases for small values of the angle θ_{stif}^{sup} and decreases again for higher values of the angle θ_{stif}^{sup} (See Fig. 5-79). The optimal

range of the inclination angle, corresponding with the maximum buckling load, is between 6 and 10 degrees. The failure load of a U+VR configuration within this range is approximately 15 to 25 percent higher than a traditional U stiffener. Similar results have been found for silos with stiffeners with other heights (i.e. $h_{stif}/R = 0.5; 1.5$).

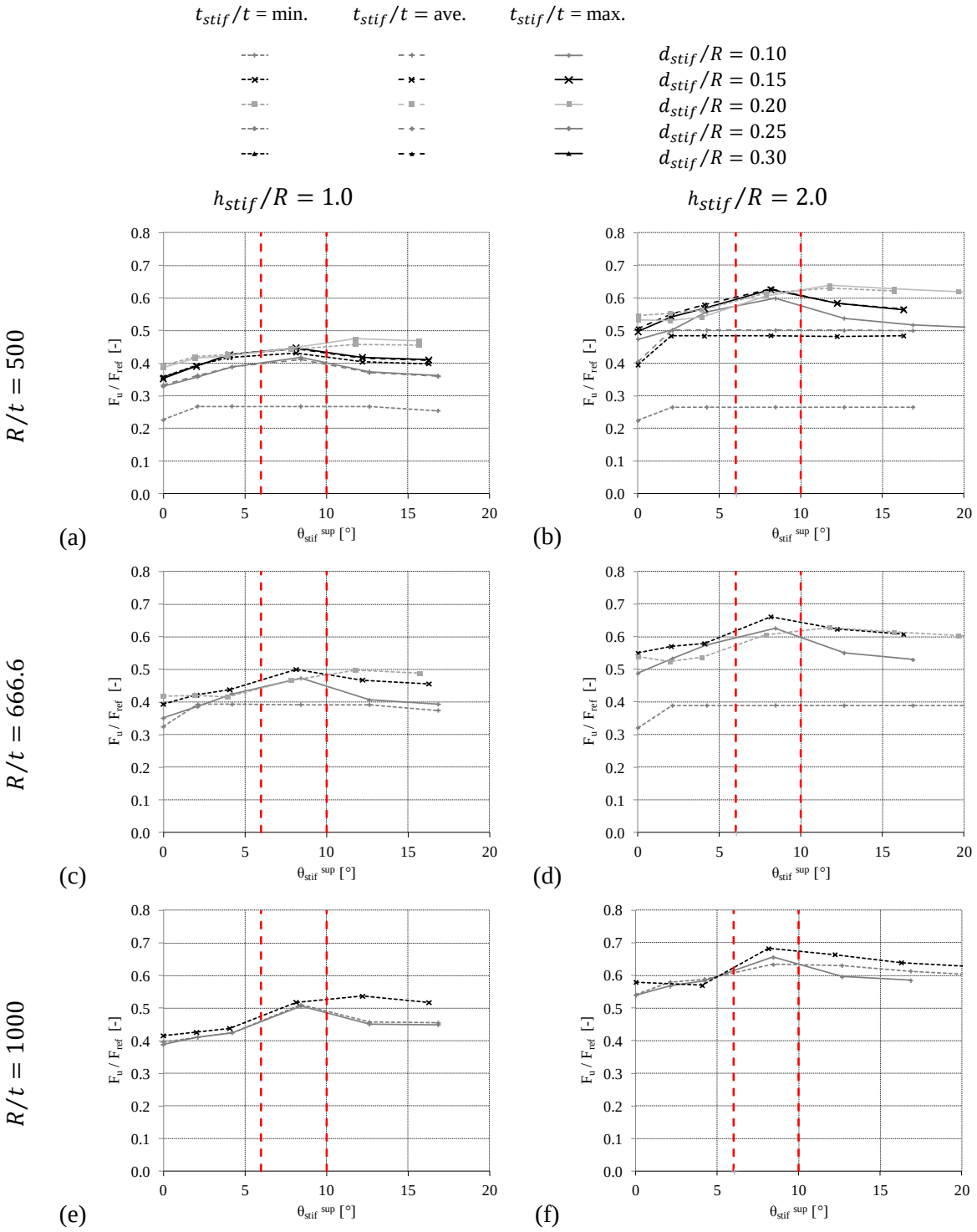

Fig. 5-79 Influence of the inclination angle θ_{stif}^{sup} of the VR stiffener to the dimensionless GMNA failure load F_u/F_{ref} for thin-walled silos ($R/t = 500; 666.6; 1000$) and for different stiffener heights h_{stif}^{sup}/R (extensive parametric study: alternative U+VR).

Comparison with the U-shaped stiffeners

From the above results, it is demonstrated that it is possible to increase the failure load of a traditional U-shaped stiffener further by adding two inclined flanges above each support (i.e. the U+VR configuration). Now, it is checked whether or not the increase of the failure load is also interesting in terms of material use.

Therefore, the dimensionless GMNA failure load F_u/F_{ref} is plotted against the dimensionless material parameter V_{extra}/V_{ref}, similar to Fig. 5-20 in Section 5.1, for the U+VR configurations of the current extensive study and the U-shaped stiffeners of the comparison study of Section 5.1. In this way, the failure load and the material use of both configurations types can be simultaneously compared with each other, though for both parametric studies not identical ranges were used for the geometrical parameters of the cross-section of the U-shaped stiffeners.

The dimensionless material parameter V_{extra}/V_{ref} is equal to the additional steel volume V_{extra} (Eq. (5-11) for the U-stiffeners and Eq. (5-18) to (5-20) for the U+VR configuration) compared to the volume of steel of the unstiffened "reference" cylindrical barrel (Eq. (5-12)).

$$\text{Alternative (U+VR):}\quad V_{extra} = \mathrm{V}_{\mathrm{extra}}^{\mathrm{U}} + \mathrm{V}_{\mathrm{extra}}^{\mathrm{VR}} \tag{5-18}$$

$$\text{Alternative (U):}\quad \mathrm{V}_{\mathrm{extra}}^{\mathrm{U}} = n_{stif} \cdot \left(d_{stif} + 2 \cdot w_{stif}\right) \cdot t_{stif} \cdot h_{stif} \tag{5-19}$$

$$\text{Alternative (U+VR):}\quad \mathrm{V}_{\mathrm{extra}}^{\mathrm{VR}} = n_{stif} \cdot 2 \cdot \mathrm{w}_{\mathrm{stif}} \cdot t_{stif} \cdot \sqrt{\left(\frac{d_{stif}^{sup} - d_{stif}}{2}\right)^2 + h_{stif}^2} \tag{5-20}$$

In Fig. 5-80, the results are presented for thick-walled silos (i.e. $R/t = 200$) as well as for thin-walled silos (i.e. $R/t = 1000$) and a constant stiffener height h_{stif} of $2.0 \cdot R$. From these plots, it is observed that with the same amount of material V_{extra}/V_{ref}, higher failure loads can be obtained for the U+VR configuration than for the U stiffeners (indicated in the figure by black arrows).

Conclusions

Of the many results that are obtained in this study, it can be concluded that the U+VR stiffening configuration is a worthy alternative to the traditional U-profile. In other words, for the geometries studied here, it is perfectly possible to increase the failure load further by inclining the flanges of the VR stiffener, enhancing the distribution of axial stresses over the entire circumference.

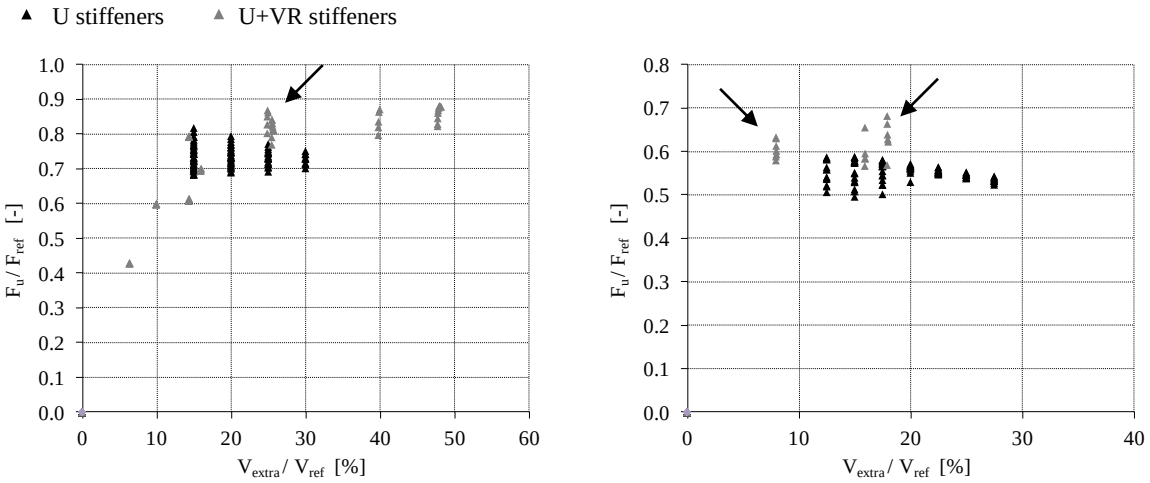

(a) Thick-walled silos ($R/t = 200$). (b) Thin-walled silos ($R/t = 1000$).

Fig. 5-80 U stiffeners versus U+VR stiffeners ($h_{stif}/R = 2.0$).

7 Ring stiffeners

In this part, the influence of the dimensions of both ring stiffeners (i.e. the lower and the upper ring) is investigated on the failure behaviour/load based on the results of GMNA calculations. The dimensions of the ring stiffeners were varied within the ranges given in Table 5-17. The default geometrical parameters were used for the cylindrical barrel (only its thickness was varied), the dimensions of the U-shaped partial-height stiffeners are given in Table 5-18. This corresponds with 28 different combinations of the geometry of the barrel-stiffener, which all collapse in the unstiffened silo wall just above the top of the stiffeners. All parts have a standard elasto-plastic material behaviour with a yield stress σ_y equal to 235MPa.

Table 5-17 Geometrical parameters of the ring stiffeners (exploratory study ring stiffeners).

PARAMETER	VALUE(S)	DIMENSION
w_{ur}/R	0.02; 0.04; 0.06; 0.08; 0.10; 0.12	-
t_{ur}/t	[min. *; max. *]	-
w_{lr}/R	0.08; 0.12; 0.16; 0.20; 0.24	-
t_{lr}/t	[min. *; max. *]	-

*: Minimum (min.) or maximum (max.) thickness - restrictions

Table 5-18 Geometrical parameters of the U-shaped stiffeners (exploratory study ring stiffeners).

PARAMETER	VALUE(S)	DIMENSION
n_{sup}	4	-
d_{stif}/R	$R/t = 100;\ 200; 250; 333.3$: 0.20; 0.30 $R/t = 500; 666.6;\ 1000$: 0.10; 0.15	-
w_{stif}/d_{stif}	25	%
h_{stif}^{sup}/R	1.0; 2.0	-
t_{stif}/t	max.*	-

*: Minimum (min.), average (ave.), or maximum (max.) thickness - restrictions

In the result section, the moment of inertia I_r of the ring stiffeners cross-section, which is defined as in Eq. (5-21), appears to be the key parameter of the ring stiffeners.

$$I_r = \frac{1}{12} \cdot w_r^3 \cdot t_r \tag{5-21}$$

Where:

w_r the radial width of the ring stiffener measured from the silo wall (thus the half of the actual width for the lower ring) [mm];

t_r the thickness of the ring stiffener [mm].

First, the upper ring is examined in Section 7.1, then the lower ring in Section 7.2. Finally, a choice has been made for the dimensions of both ring stiffeners for the design rule (See Section 7.3).

7.1 Upper ring

In Fig. 5-81, the results are depicted for 4 combinations of barrel-longitudinal U-shaped stiffener for a wide range of geometries of the upper ring (both the radial width w_{ur} and the thickness t_{ur} are varied) and also without upper ring (i.e. the red dashed horizontal line). The dimensionless GMNA failure load F_u/F_{ref} is plotted on the vertical axis, the moment of inertia I_r of the upper ring on the horizontal axis.

The red dashed curve represents a cylindrical barrel without upper ring ($I_r = 0$) and is the lower bound of the failure load. All curves (with upper ring) display a similar trend (also the cases which are not presented here). By increasing the moment of inertia I_r of the upper ring, the failure load of the structure increases rapidly in the beginning (for small values of I_r) and progressively increases to an upper bound (for larger values of I_r).

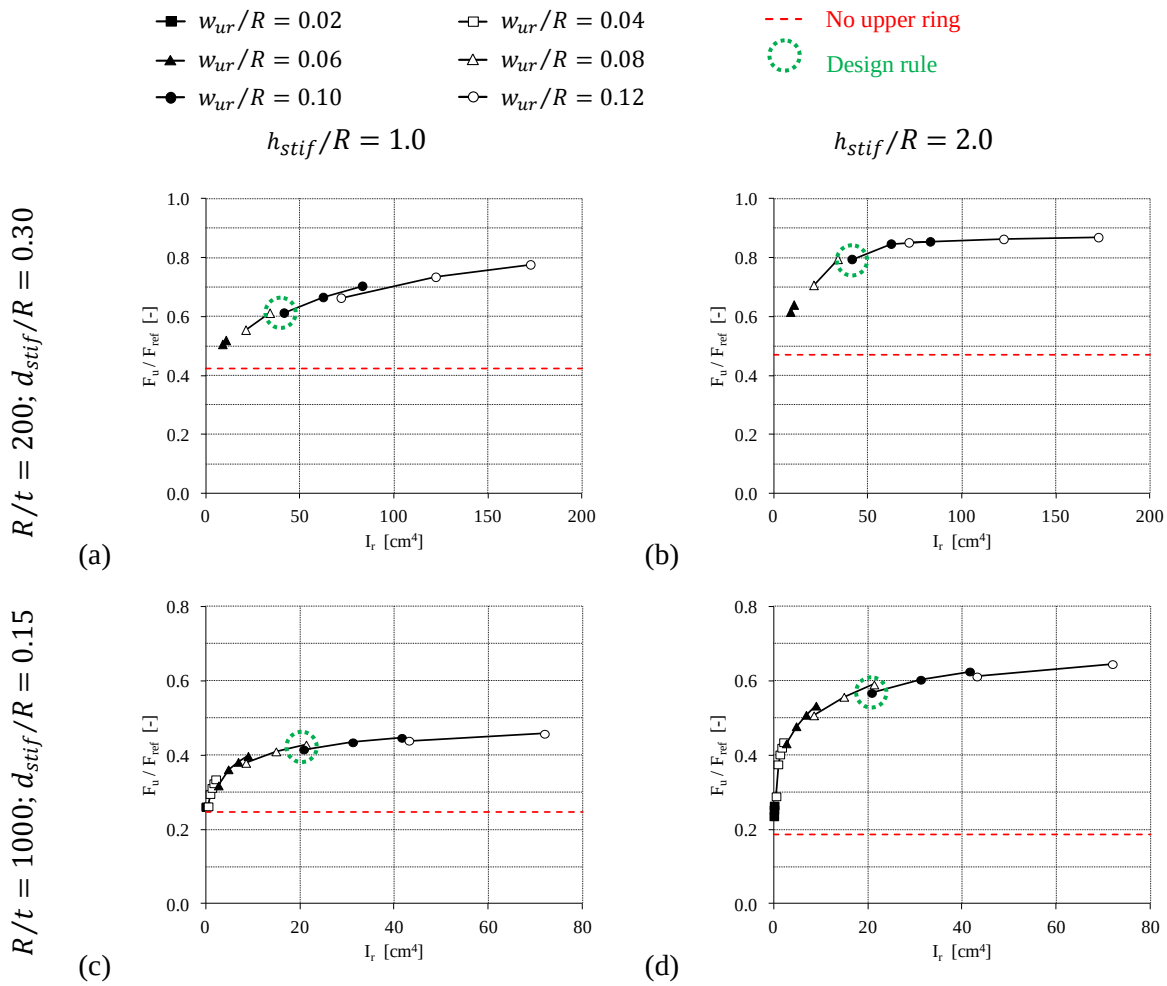

Fig. 5-81 Dimensionless GMNA failure load F_u/F_{ref} as a function of the moment of inertia I_r of the upper ring (both the radial width w_{ur} and the thickness t_{ur} are varied).

By increasing the dimensions of the upper ring (and consequently the moment of inertia I_r), the upper ring greatly influences the (radial) deformations and the (axial) stresses in its vicinity. This multiple role of an upper ring will be demonstrated for two structures on the basis of the radial deformations along a circumferential path PC/S-h1.0 ($h_{path}/h_{stif} = 1.0$; height corresponds with the upper ring) and the axial stresses along circumferential path PC/S-h1.075 ($h_{path}/h_{stif} = 1.075$; height just above the upper ring), both at the moment of maximum load. The red curve represents the results without upper ring ($I_r = 0$). The colour of the other curves depends on the moment of inertia I_r of the upper ring and varies between white ($I_r = I_{r,min} \approx 0$) and black ($I_r = I_{r,max}$).

Thick-walled silo

In Fig. 5-82, the results are depicted for the structure of Fig. 5-81 (b), corresponding with a thick-walled silo (i.e. $R/t = 200$) combined with a high longitudinal stiffener ($d_{stif}/R = 0.30$; $h_{stif}/R = 2.0$).

The dimensionless radial deformation U_R/t of the silo wall at the connection with the upper ring, at the moment of maximum load, is depicted in Fig. 5-82 (a). Clearly, the inwardly oriented deformations above the stiffeners ($\theta < 22.5°$) are decreasing (Ia) as well as the outwardly oriented deformations between two stiffeners ($\theta > 22.5°$) are decreasing (Ib) when the moment of inertia I_r of the upper ring increases. Not only the deformations before failure (shown here), but also the deformations during and after failure are partially restricted due the presence of an upper ring. Moreover, the restriction of the deformations is not limited to the silo wall at the connection of the upper ring, but is also felt at larger distances from the upper ring.

Fig. 5-82 (b) plots the dimensionless axial stress σ_x/σ_y at the moment of maximum load in the silo wall just above the connection with the upper ring (which corresponds with the height of yielding). Because an upper ring with a larger moment of inertia I_r reduces the inward deformations of the silo wall above the stiffener more (Ia), the effective yield stress σ_y^{eff} increases (IIa) above the stiffener (i.e. the first part of the path) (See Section 3.4 for more information). Furthermore, the axial stress σ_x between two stiffeners (i.e. the second part of the path) also increases (IIb), partly due to the above mentioned increase of the effective yield stress σ_y^{eff} (IIa), but also due to the presence of an upper ring. In other words, the upper ring promotes the distribution of the axial stresses in circumferential direction. As a result of the increased axial stress distribution over the entire circumference (IIa and IIb), the failure load F_u also increases when the moment of inertia I_r of the upper ring increases.

In Fig. 5-82 (c), the reader can recognize the same asymptotic trend for the radial deformation U_r (at $\theta = 0°$; $h = h_{stif}$) and axial stresses σ_x (at $\theta = 0°/45°$; $h = 1.075 \cdot h_{stif}$) as the failure load F_u in Fig. 5-81 (b) as a function of the moment of inertia I_r of the upper ring. In other words, the moment of inertia I_r appears to be an important and representative parameter, not only for the failure load, but also for the deformations and the stresses in the vicinity of the upper ring.

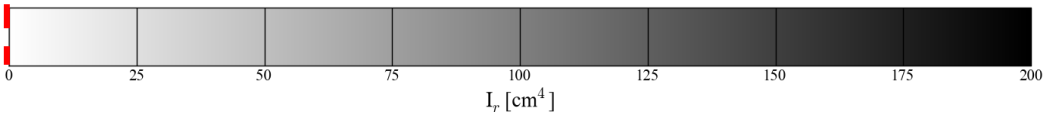

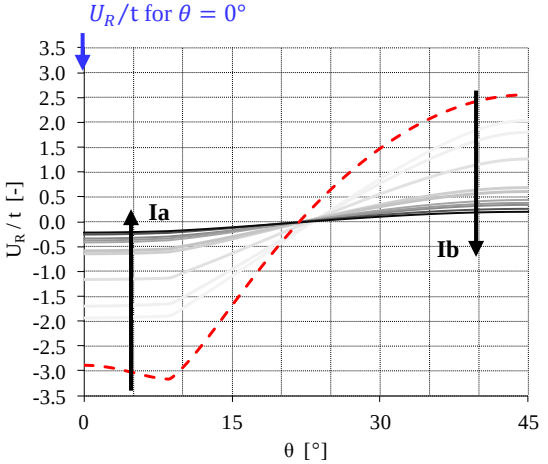

(a) Plot of the ratio of the radial displacement at the moment of failure to the silo wall thickness U_R/t [-] against the circumferential angle θ [°] for a circumferential path PC/S-h1.0 ($h_{path}/h_{stif} = 1.0$).

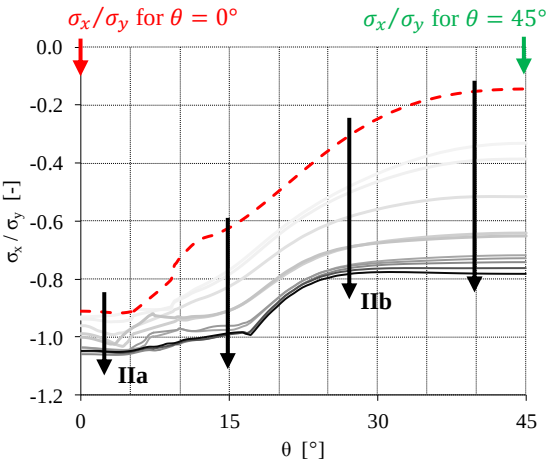

(b) Plot of the ratio of the axial stress at the moment of failure to the yield stress σ_x/σ_y [-] against the circumferential angle θ [°] for a circumferential path PC/S-h1.075 ($h_{path}/h_{stif} = 1.075$).

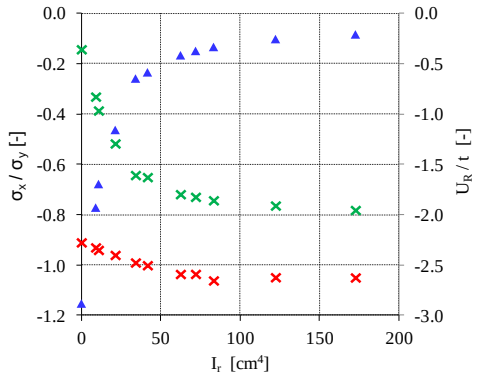

(c) U_R/t [-] for θ = 0° (See Fig. 5-82 (a)) and σ_x/σ_y [-] for θ = 0°; 45° (See Fig. 5-82 (b)) as a function of the moment of inertia of the ring stiffener.

Fig. 5-82 Deformations and stress behaviour as a function of the moment of inertia I_r of the upper ring (both the radial width w_{ur} and the thickness t_{ur} are varied) for the geometry plotted in Fig. 5-81 (b) (i.e. $R/t = 200$; $d_{stif}/R = 0.30$; $h_{stif}/R = 2.0$).

Thin-walled silo

In Fig. 5-83, the results are depicted for the structure of Fig. 5-81 (d), corresponding with a thin-walled silo (i.e. $R/t = 1000$) combined with a high longitudinal stiffener ($d_{stif}/R = 0.15$; $h_{stif}/R = 2.0$). As will be shown, very similar results are obtained as for the previous thick-walled silo.

Fig. 5-83 (a) shows the dimensionless radial deformations U_R/t of the silo wall at the connection with the upper ring, at the moment of maximum load. Again, when the moment of inertia I_r of the upper ring increases, both the inward ($\theta < 22.5°$) and the outward ($\theta > 22.5°$) deformations are decreasing (i.e. respectively (Ia) and (Ib)). Not only the pre-buckling

deformations (shown here), but also the deformations during and after buckling (i.e. the formation of buckle(s)) are partially restricted due the presence of an upper ring. Moreover, the restriction of the deformations is not limited to the silo wall at the connection of the upper ring, but is also felt at larger distances from the upper ring.

The dimensionless axial stress σ_x/σ_{cr} at the moment of maximum load in the silo wall just above the connection with the upper ring (which corresponds with the height of yielding) is given in Fig. 5-83 (b). Because an upper ring with a larger moment of inertia I_r reduces the inward deformations of the silo wall above the stiffener more (Ia), the critical buckling stress σ_{cr} increases (IIa) above the stiffener (i.e. the first part of the path) (See Section 3.4 for more information). Furthermore, the axial stress σ_x between two stiffeners (i.e. the second part of the path) also increases (IIb), partly due to the previous mentioned increase of critical buckling stress σ_{cr} (IIa), but also due to the presence of an upper ring. In other words, the upper ring promotes the distribution of the axial stresses in circumferential direction. As a result of the increased axial stress distribution over the entire circumference (IIa and IIb), the failure load F_u also increases when the moment of inertia I_r of the upper ring increases.

In Fig. 5-83 (c), the reader can recognize the same asymptotic trend for the radial deformation U_r (at $\theta = 0°;\ h = h_{stif}$) and axial stresses σ_x (at $\theta = 0°/45°;\ h = 1.075 \cdot h_{stif}$) as the failure load F_u in Fig. 5-83 (d) as a function of the moment of inertia I_r of the upper ring. In other words, the moment of inertia I_r appears to be an important and representative parameter, not only for the buckling load, but also for the deformations and the stresses in the vicinity of the upper ring.

Conclusions

The presence of an upper ring at the top of a U-shaped longitudinal stiffener can significantly increase the failure load, on the condition that failure (due to plastic yielding and/or elastic buckling) occurs in the unstiffened silo wall just above the stiffener (and not prematurely in the stiffened region above the local supports).

An asymptotic relationship has been found between the failure load and the moment of inertia I_r of the upper ring. Not only the failure load, but also the deformations (mainly radial) and the axial stresses in the vicinity of the upper ring can be related to the moment of inertia I_r. From these results, it can be concluded that the moment of inertia I_r is an important and representative parameter for the upper ring.

For the calculation of the moment of inertia I_r of the upper ring, the radial width w_{ur} is raised to the third power and the thickness t_{ur} not (See Eq. (5-21)). As a consequence, when two ring stiffeners should be chosen with the same amount of material in the cross-section, a thin and wide upper ring is preferable to a thick and narrow upper ring.

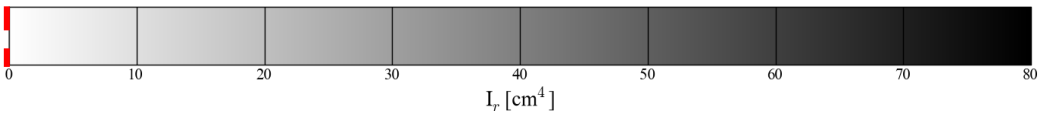

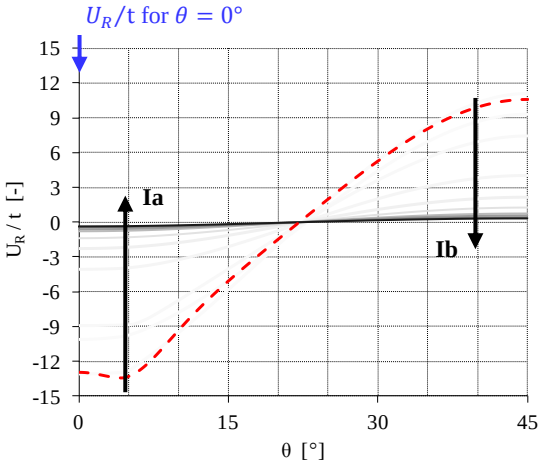

(a) Plot of the ratio of the radial displacement at the moment of failure to the silo wall thickness U_R/t [-] against the circumferential angle θ [°] for a circumferential path PC/S-h1.0 ($h_{path}/h_{stif} = 1.0$).

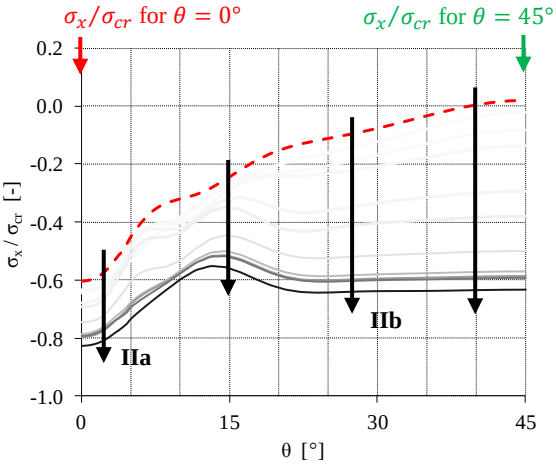

(b) Plot of the ratio of the axial stress at the moment of failure to the critical buckling stress σ_x/σ_{cr} [-] against the circumferential angle θ [°] for a circumferential path PC/S-h1.075 ($h_{path}/h_{stif} = 1.075$).

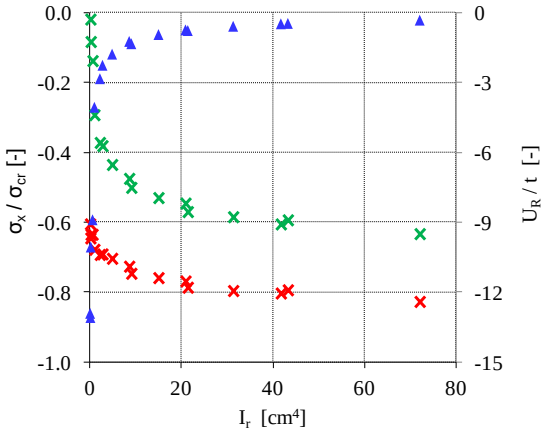

(c) U_R/t [-] for θ = 0° (See Fig. 5-83 (a)) and σ_x/σ_{cr} [-] for θ = 0°; 45° (See Fig. 5-83 (b)) as a function of the moment of inertia of the ring stiffener.

Fig. 5-83 Deformations and stress behaviour as a function of the moment of inertia I_r of the upper ring (both the radial width w_{ur} and the thickness t_{ur} are varied) for the geometry plotted in Fig. 5-81 (d) (i.e. $R/t = 1000$; $d_{stif}/R = 0.15$; $h_{stif}/R = 2.0$).

7.2 Lower ring

In Fig. 5-84, the results are depicted for 4 combinations of barrel-longitudinal U-shaped stiffeners for a wide range of geometries of the lower ring (both the radial width w_{lr} and the thickness t_{lr} are varied) and also without lower ring (i.e. the red dashed horizontal line). The dimensionless GMNA failure load F_u/F_{ref} is plotted on the vertical axis; the moment of inertia I_r of the lower ring on the horizontal axis.

The red dashed curve represents a cylindrical barrel without lower ring ($I_r = 0$) and is the

lower bound of the failure load. For most cases (with lower ring), a horizontal curve is obtained, which indicates that the failure load is independent of the dimensions of the lower ring stiffener (within the range of this study). For a number of cases (e.g. in Fig. 5-84 (b)), a similar trend is obtained as for the upper ring. By increasing the moment of inertia I_r of the lower ring, the failure load of the structure increases rapidly in the beginning (for small values of I_r) and progressively increases to an upper bound (for larger values of I_r).

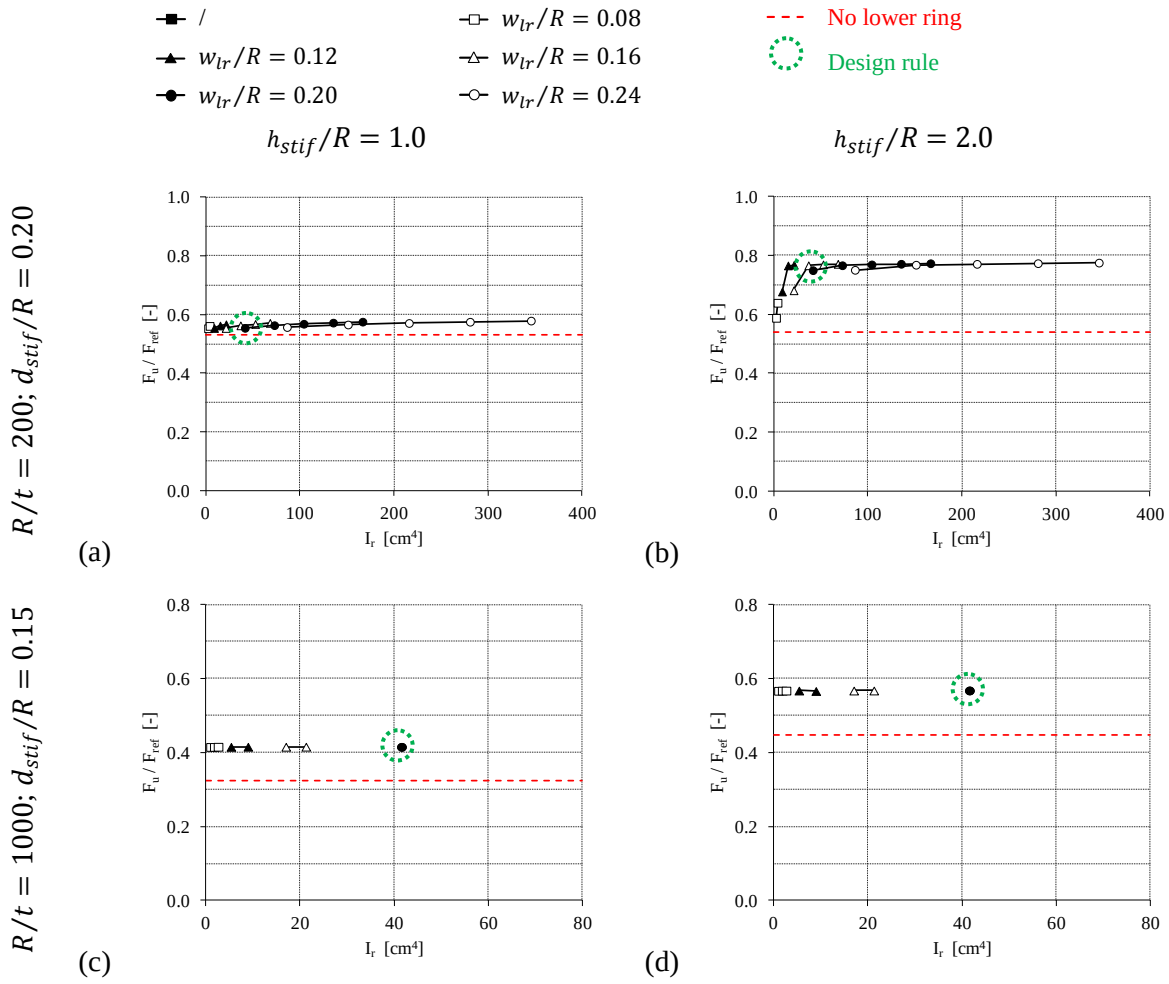

Fig. 5-84 Dimensionless GMNA failure load F_u/F_{ref} as a function of the moment of inertia I_r of the lower ring (both the radial width w_{lr} and the thickness t_{lr} are varied).

Thick-walled silo

In Fig. 5-85, the results are depicted for the structure of Fig. 5-84 (b), corresponding with a thick-walled silo (i.e. $R/t = 200$) combined with a high longitudinal stiffener ($d_{stif}/R = 0.20$; $h_{stif}/R = 2.0$).

Fig. 5-85 (a) shows the dimensionless radial deformation U_R/t of the silo wall, at the moment of maximum load, along a circumferential path PC/S-h0.0 ($h_{path}/h_{stif} = 0.0$), which corresponds with the lower edge of the cylindrical barrel and the connection with the lower ring. The red curve represents the results without lower ring ($I_r = 0$). The colour of the other

curves depends on the moment of inertia I_r of the lower ring and varies between white ($I_r = I_{r,min} \approx 0$) and black ($I_r = I_{r,max}$). For all cases, the deformations are approximately zero at the supports (Ia) ($\theta < 5.7°$). Between the supports (i.e. $\theta > 5.7°$), the radial deformations with any ring stiffener ($U_R^{max} = \pm 0.12 \cdot t$) are much smaller than the deformations without ring stiffener ($U_R^{max} = \pm 1.9 \cdot t$). Furthermore, when the moment of inertia I_r of the lower ring increases, the outwardly oriented deformations just next to the support and the inwardly oriented deformations in the middle of two supports are both decreasing (Ib and Ic).

Similar to the previous graph, the dimensionless axial stress σ_x/σ_y at the moment of maximum load in the silo wall just above the lower edge of the cylindrical barrel and the lower ring (i.e. PC/S-h0.0 with $h_{path}/h_{stif} = 0.05$) is plotted in Fig. 5-85 (b).

Without lower ring ($I_r = 0$) or with lower ring stiffeners with a small value of I_r, high axial stress concentrations ($\sigma_x = \sigma_y^{eff}$) are developing in the silo wall just above the support ($\theta < 5.7°$) (IIa), resulting in premature failure of the structure. For lower ring stiffeners with an intermediate or high value of I_r, the axial stresses remain below the effective yield stress ($\sigma_x < \sigma_y^{eff}$) (IIa). In other words, whether or not the occurrence of premature failure of the silo wall just above the local supports ($\sigma_x <$ or $> \sigma_y^{eff}$) hangs on a tread, and the presence of a lower ring with a small moment of inertia I_r can cause a large difference in failure behaviour. Furthermore, when the moment of inertia I_r of the lower ring increases, the axial stresses σ_x next to the support ($5.7° < \theta < 20°$) are increasing (IIb), while axial stresses σ_x in the middle of two supports ($\theta > 20°$) are not influenced (IIc).

In Fig. 5-85 (c), the reader can recognize an asymptotic trend for the radial deformation U_r (at $\theta = 45°$; $h = 0$) and axial stress σ_x (at $\theta = 10°$; $h = 0.05$) as a function of the moment of inertia I_r of the lower ring. Again, the moment of inertia I_r can be used as a representative parameter, not only for the failure load, but also for the deformations and the stresses in the vicinity of the lower ring.

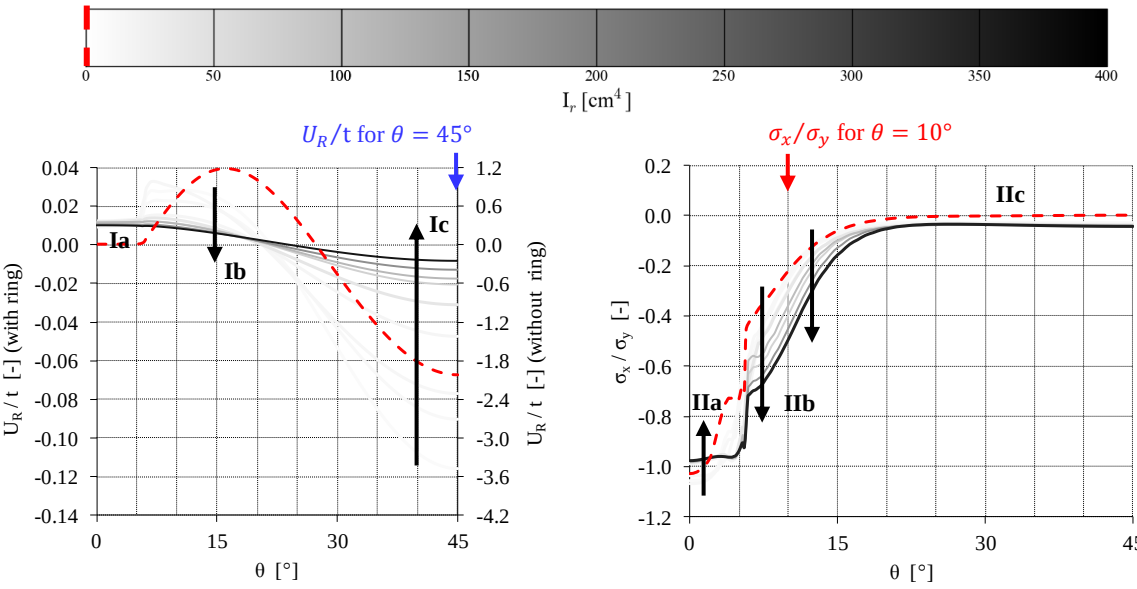

(a) Plot of the ratio of the radial displacement at the moment of failure to the silo wall thickness U_R/t [-] against the circumferential angle θ [°] for a circumferential path PC/S-h0.0 ($h_{path}/h_{stif} = 0.0$).

(b) Plot of the ratio of the axial stress at the moment of failure to the yield stress σ_x/σ_y [-] against the circumferential angle θ [°] for a circumferential path PC/S-h0.05 ($h_{path}/h_{stif} = 0.05$).

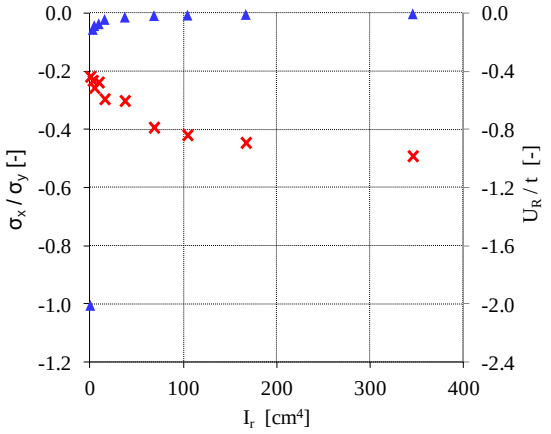

(c) U_R/t [-] for θ = 45° (See Fig. 5-85 (a)) and σ_x/σ_y [-] for θ = 10° (See Fig. 5-85 (b)) as a function of the moment of inertia of the ring stiffener.

Fig. 5-85 Deformations and stress behaviour as a function of the moment of inertia I_r of the lower ring (both the radial width w_{lr} and the thickness t_{lr} are varied) for the geometry plotted in Fig. 5-84 (b) (i.e. $R/t = 200$; $d_{stif}/R = 0.20$; $h_{stif}/R = 2.0$).

Failure behaviour for silos without ring stiffener

From Fig. 5-84, it can be seen that the failure load corresponding with a cylindrical barrel without lower ring (i.e. the red dashed curve) is systematically lower than the failure load obtained with an arbitrary lower ring. Without the presence of a lower ring, the lower edge of the cylindrical barrel can deform freely, resulting in premature failure of the barrel at its lower edge. This buckling mode is illustrated in Fig. 5-86 for a thick-walled and a thin-walled silo.

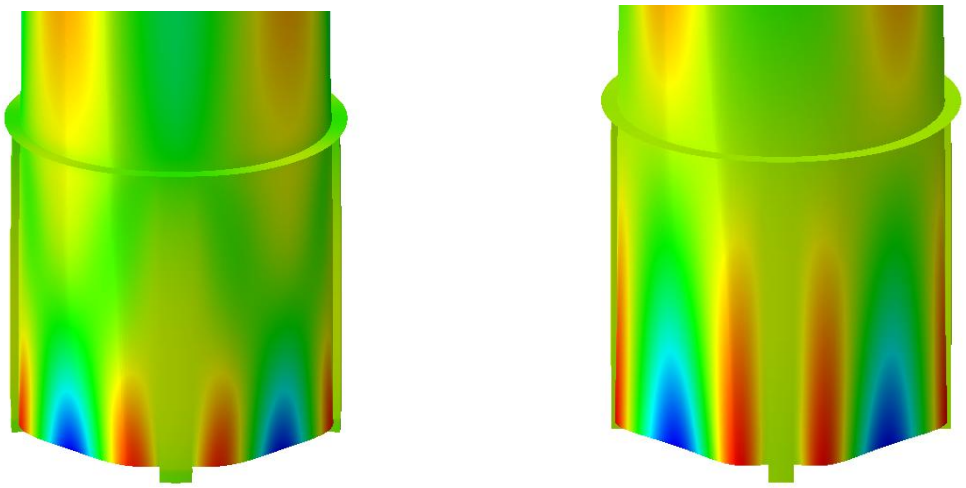

(a) $R/t = 200$; $d_{stif}/R = 0.20$. (b) $R/t = 1000$; $d_{stif}/R = 0.15$.

Fig. 5-86 Contourplots of the post-buckling deformations for silos without ring stiffener ($h_{stif}/R = 2.0$).

However, it is important to mention that the calculations without lower ring are rather intended to illustrate the failure behaviour and to compare it with the situation with ring stiffener. In practice, the situation where the lower edge of the barrel can deform freely will never occur due the presence of a hopper below the barrel.

Conclusions

A lower ring generally has, in contrast to an upper ring stiffener, a smaller impact on the failure behaviour and load of the structure.

The lower ring stiffener restricts the radial deformations at the lower edge of the cylindrical barrel, and introduces a (small) part of the supporting load directly in the silo wall just next to the local support.

In some cases, a silo with a lower ring with a very small moment of inertia I_r prematurely fails in the stiffened silo wall just above the local supports due to high stress concentrations ($\sigma_x = \sigma_y^{eff}$) .

An asymptotic relationship has been found between the failure load and the moment of inertia I_r of the lower ring. Not only the failure load, but also the deformations (mainly radial) and the axial stresses in the vicinity of the lower ring can be related to the moment of inertia I_r. From these results, it can be concluded that the moment of inertia I_r is a representative parameter for the lower ring.

For the calculation of the moment of inertia I_r of the lower ring, the (half of the total) radial width w_{lr} is raised to the third power and the thickness t_{lr} not (See Eq. (5-21)). As a consequence, when two lower ring stiffeners should be chosen with the same amount of

material in the cross-section, a thin and wide lower ring is preferable to a thick and narrow lower ring.

7.3 Definition of the geometrical parameters of the ring stiffeners for the design rule

Based on the results of the exploratory study, a choice had to be made for the dimensions of the ring stiffeners. When this decision was made, the following elements were taken into account.

- For simplicity, it is preferred to make the dimensions of the ring stiffeners (dimensionless relative to the cylinder radius R**) independent of other geometrical parameters**, such as the radius-to-thickness ratio R/t, the supporting and stiffening configuration, etc.;
- For both the upper ring and the lower ring, it holds that a **thin and wide ring stiffener** is in preference to a thick and narrow ring stiffener;
- For practical considerations (welding), it is preferable to choose a **thin ring stiffener** of which the ratio of the thicknesses of the ring and the barrel t_r/t is not too large.

The chosen geometrical parameters for the upper and lower ring are given in Table 5-19.

Table 5-19 Geometrical parameters of the ring stiffeners (design rule).

PARAMETER	VALUE(S)	DIMENSION
w_{ur}/R	0.10	-
t_{ur}/t	min. *	-
w_{lr}/R	0.20	-
t_{lr}/t	min. *	-

*: Minimum (min.), average (ave.), or maximum (max.) thickness - restrictions

8 Engaged columns

A simple alternative for lighter silos is to extend the supporting columns over a certain distance along the external side of the shell wall. In this section, the influence of the geometry of the engaged rectangular shaped columns will be thoroughly investigated. The study consists of five main parts: (1) an exploratory study where the influence of all geometrical parameters is investigated one by one (Section 8.1), (2) an investigation of the influence of the degree of support (Section 8.2), (3) an optimisation study where the optimal column is determined (shape and height) (Section 8.3), (4) a discussion of a few important aspects concerning the failure behaviour (Section 8.4), and (5) the determination of the scope of the geometrical parameters for the final study (Section 8.5).

8.1 Exploratory parametric study

In this part, the influence of all geometrical parameters on the failure behaviour/load will be discussed in detail, both for thick-walled silos (i.e. $R/t = 200$) as for thin-walled silos (i.e. $R/t = 1000$).

The default values were used for the geometry of the cylindrical barrel. The width in circumferential direction d_{stif}, the radial width w_{stif}, the thickness t_{stif}, and the heights h_{stif}^{sup} and h_{stif}^{inf} of the engaged columns were varied within the ranges given in Table 5-20. All parts have a standard elasto-plastic material behaviour with a yield stress σ_y equal to 235MPa.

Table 5-20 Geometrical parameters of the engaged columns (exploratory study).

PARAMETER	VALUE(S)	DIMENSION
n_{sup}	4	-
d_{stif}/R	$R/t = 200$: 0.05; 0.10; 0.15; 0.20; 0.25; 0.30 $R/t = 1000$: 0.05; 0.10; 0.15; 0.20	-
w_{stif}/d_{stif}	50; 75; 100	%
h_{stif}^{sup}/R	0.5; 1.0; 1.5; 2.0	-
h_{stif}^{inf}/R	1.0; 2.0; 4.0	-
t_{stif}/t	min.; ave.; max. *	-

*: Minimum (min.), average (ave.), or maximum (max.) thickness - restrictions

To be able to investigate the influence of the geometry of the engaged columns, 52 ($R/t = 200$) and 14 ($R/t = 1000$) different cross-sections were calculated (both the shape and dimensions were varied) for 16 different combinations of the column heights (i.e. h_{stif}^{sup} and

h_{stif}^{inf}). This corresponds with 1056 GMNA calculations.

In what follows, the influence of all geometrical parameters on the failure behaviour/-load is investigated one by one, except for the influence of w_{stif}. Due to the limited variation of the shape of the column cross-section (mainly columns with a square cross-section were considered here, i.e. with $w_{stif}/d_{stif} = 100\%$), it is difficult to derive relationships between the radial width w_{stif} and the failure load. In contrast, in the optimisation study of Section 8.3, the focus is on determining the optimal shape of the cross-section and thus the optimal ratio of the value w_{stif}/d_{stif}.

8.1.1 Cross-section of the engaged column

In this section, the influence of the total quantity of material in the cross-section of the engaged column on the failure load and failure behaviour is investigated.

Thick-walled silos

As already mentioned before, 52 different cross-sections were calculated (both the shape and dimensions were varied) for 16 different combinations of the heights of the column (i.e. h_{stif}^{sup} and h_{stif}^{inf}). These results are given in Fig. 5-87. In this figure, the dimensionless GMNA failure load F_u/F_{ref} of the silo structure is plotted against the ratio of the cross-section of the column to the cross-section of the silo wall A_{stif}/A_{shell} (expressed in percentage) for different attached heights h_{stif}^{sup} and free heights h_{stif}^{inf}. Since the radius-of-thickness ratio R/t is constant (200), the values of F_{ref} and A_{shell} remain constant too.

Clearly, the cross-section of an engaged column has a significant impact on the maximum load of such a silo. In each case, the graph consists of a scattered cloud of points with variable slope. For small values of the cross-section A_{stif}, the failure load strongly increases. For intermediately high and high values of A_{stif}, the rapidly rising curve gradually merges into an approximately horizontal branch (Fig. 5-87 (a)) or a slowly rising branch (Fig. 5-87 (b) - (d)).

Clearly, the slope, but also the failure load, of the last part of the curve depends on the attached column height h_{stif}^{sup}. The slope increases as the height h_{stif}^{sup} increases, while the failure load increases up to the critical height (here: $h_{stif,crit}^{sup} = 1.0$) and remains more or less unchanged above the critical height. In other words, it appears that the influence of the cross-section of the column A_{stif} is related to the attached column height h_{stif}^{sup}. The influence of the attached height will be explained in detail in Section 8.1.5.

The unattached or free column height h_{stif}^{inf} is disadvantageous for the failure load. Indeed, the

failure loads for the columns with a large free height (i.e. $h_{stif}^{inf} = 4.0$) are systematically smaller than the loads for the columns with a small free height (i.e. $h_{stif}^{inf} = 1.0$) in Fig. 5-87, especially for cross-sections with intermediately high and high values of A_{stif}. The influence of the unattached height will be explained further in Section 8.1.5.

In addition, a marked scatter can be observed in the results of Fig. 5-87, in particular in the second branch. This scatter is caused due to the range of different shapes of the column cross-section that is explored in the present study (with a constant quantity of cross-sectional material). This topic, and the determination of the optimal shape of the column cross-section, are covered in depth in Section 8.3.

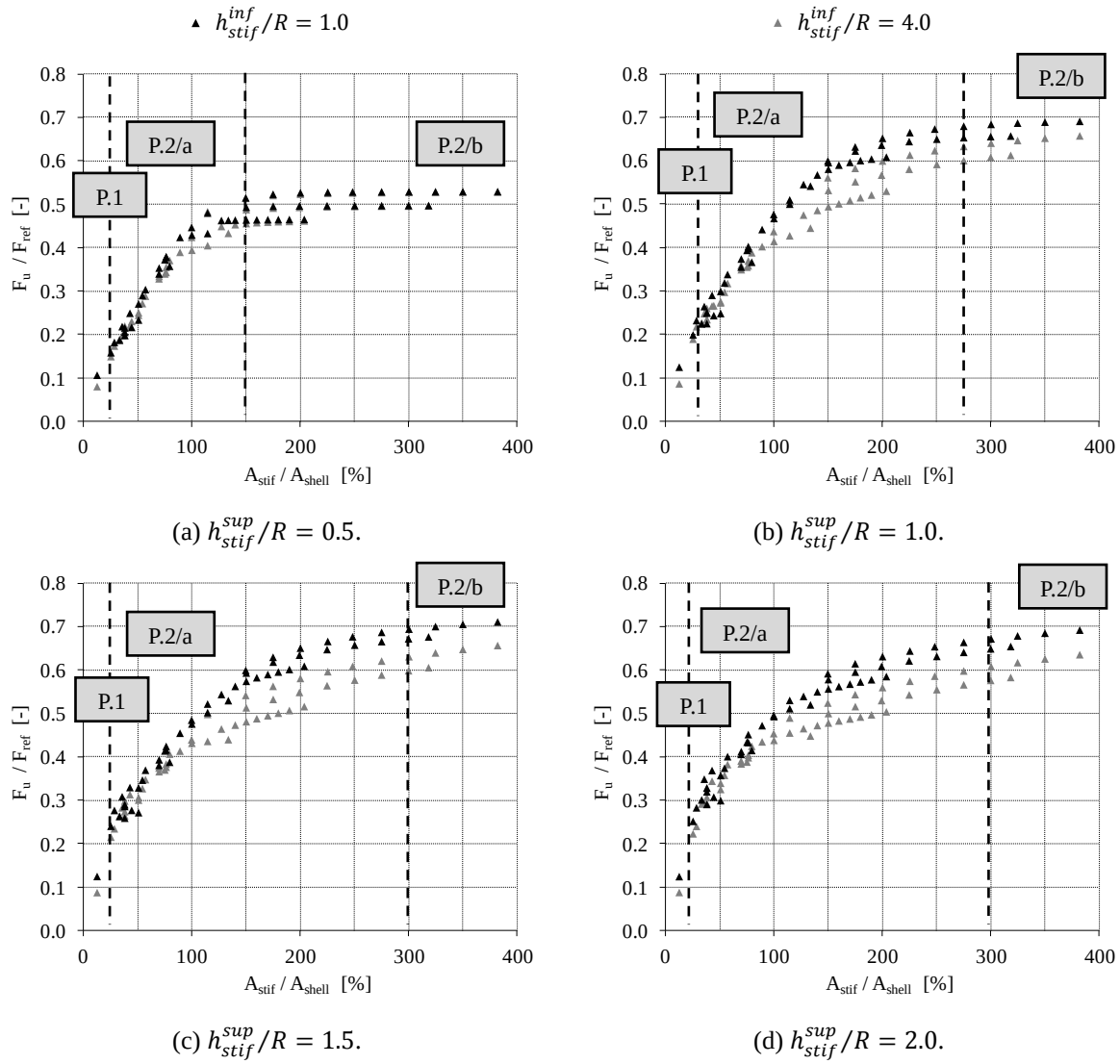

(a) $h_{stif}^{sup}/R = 0.5$.

(b) $h_{stif}^{sup}/R = 1.0$.

(c) $h_{stif}^{sup}/R = 1.5$.

(d) $h_{stif}^{sup}/R = 2.0$.

Fig. 5-87 Dimensionless GMNA failure load F_u/F_{ref} as a function of the ratio of the cross-section of the engaged columns to the cross-section of the silo wall A_{stif}/A_{shell} for different column heights ($R/t = 200$).

In Fig. 5-87, P.1, P.2/a, and P.2/b are the different failure patterns that were found for the thick-walled silos (which fail by elasto-plastic buckling). These patterns largely depend on the cross-section A_{stif} of the engaged column and will be discussed now one by one.

In the first case, it is only the column which starts to yield, while the axial stresses in the silo wall have not yet reached the yield stress (i.e. failure pattern P.1). This occurs with columns with a very small cross-section A_{stif}, which corresponds with the first part of the rising branches in Fig. 5-87. In Fig. 5-88 (a) and Fig. 5-88 (b), the axial stresses are plotted, respectively in the silo wall and in the engaged column, each time at the moment of failure (maximum load). As can be seen, the interior (compressed) flange of the columns starts to yield, while the axial stresses in the silo wall are much lower than the yield stress. In other words, the material of the silo wall is only partially used and the F_{GMNA} load is much smaller than the F_{MNA} load. The (enlarged) post-buckling deformations of the silo and a columns are depicted in Fig. 5-88 (c) and Fig. 5-88 (d). At failure, the whole cross-section of the column is yielding, and the columns collapse by the formation of plastic hinges, while the deformations in the silo wall are relatively small. Because of this premature failure of the columns, the maximum possible strength of the silo wall is clearly not fully utilized.

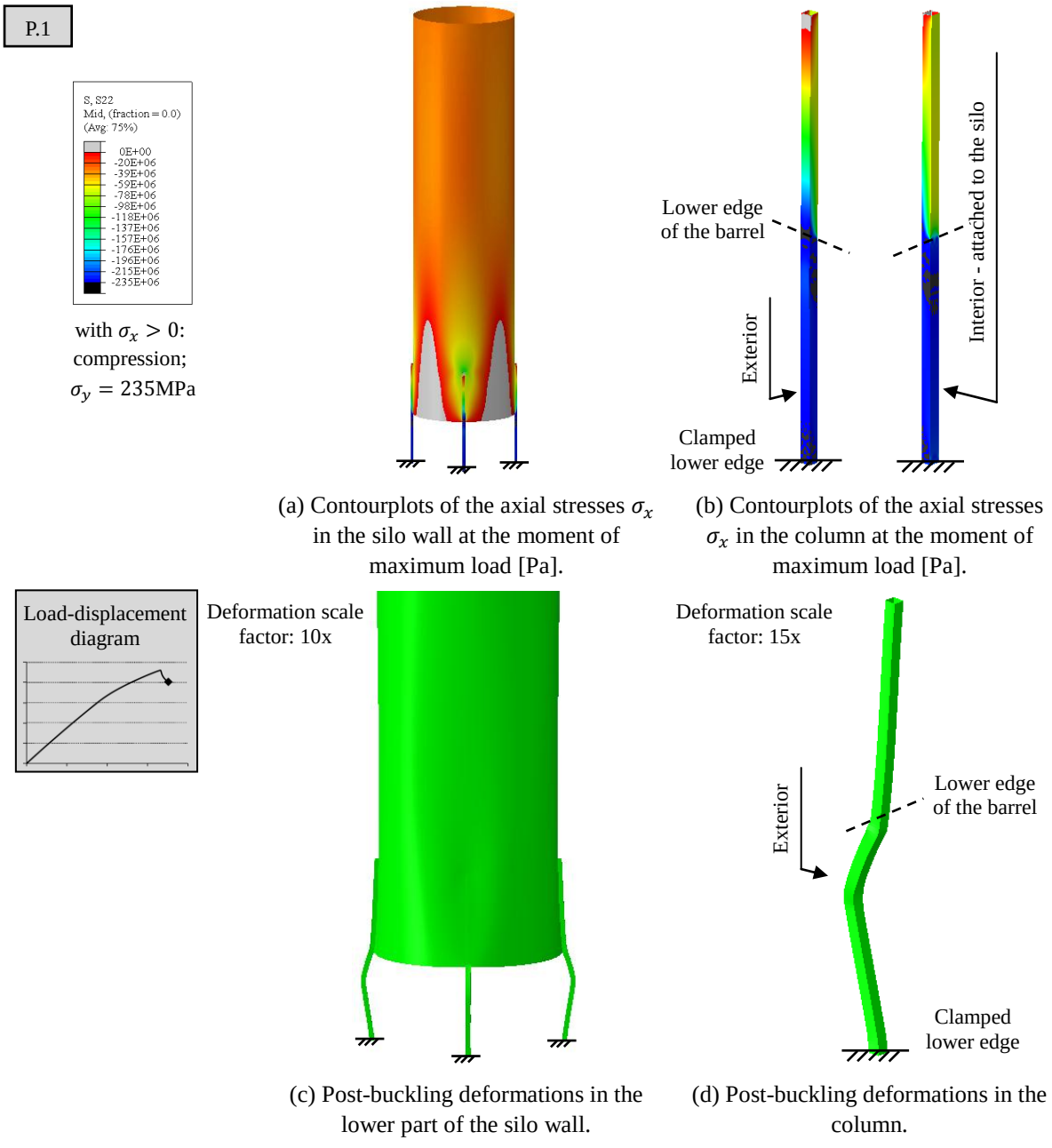

(a) Contourplots of the axial stresses σ_x in the silo wall at the moment of maximum load [Pa].

(b) Contourplots of the axial stresses σ_x in the column at the moment of maximum load [Pa].

(c) Post-buckling deformations in the lower part of the silo wall.

(d) Post-buckling deformations in the column.

Fig. 5-88 Failure behaviour for a column with a small cross-section (type P.1) ($R/t = 200$; $h_{stif}^{sup}/R = 1.0$).

The second part of the rising branches in Fig. 5-87 corresponds with engaged columns with an average cross-section A_{stif}. For failure pattern P.2/a, yielding occurs in both the interior flange of the column as well as in a limited region of the silo wall above the terminations of the column (Fig. 5-89 (a) and Fig. 5-89 (b)). Due to premature failure by plastic buckling (see Fig. 5-89 (c)), the maximum possible strength of the silo wall is not reached. Furthermore, inwardly oriented deformations can be observed in the silo wall above the top of the column, because such an average column may not fully prevent the tendency to undergo an inwardly oriented displacement (Fig. 5-89 (d)).

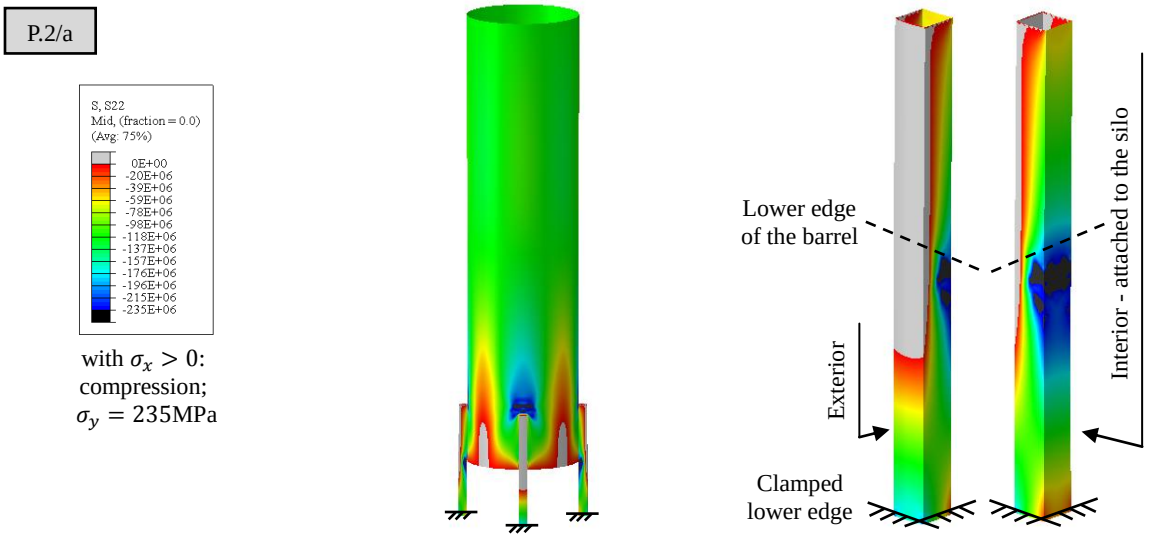

(a) Contourplots of the axial stresses σ_x in the silo wall at the moment of maximum load [Pa].

(b) Contourplots of the axial stresses σ_x in the column at the moment of maximum load [Pa].

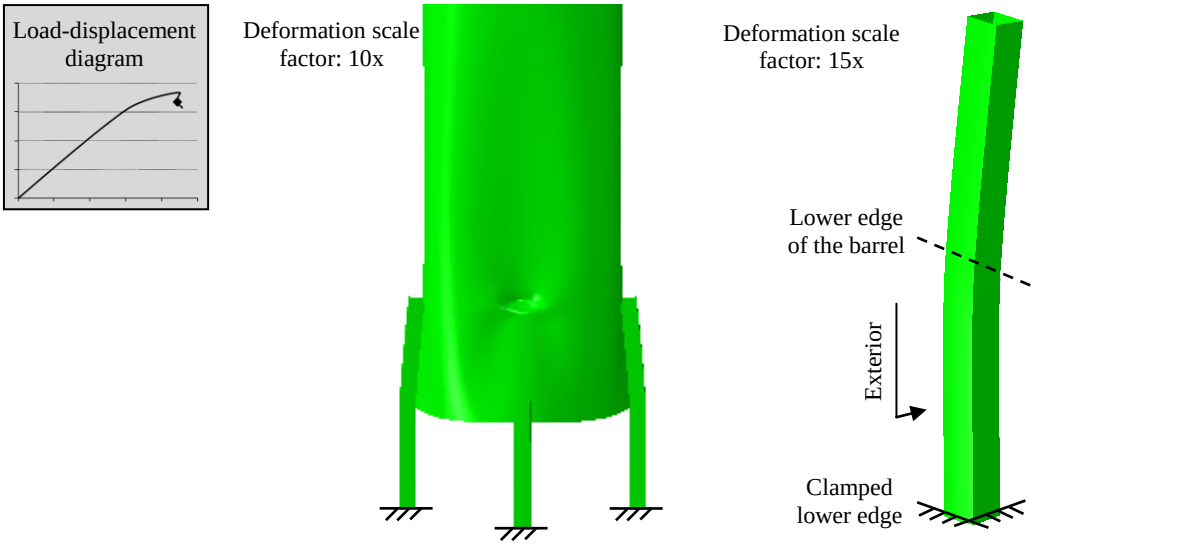

(c) Post-buckling deformations in the lower part of the silo wall.

(d) Post-buckling deformations in the column.

Fig. 5-89 Failure behaviour for a column with an average cross-section (type P.2/a) ($R/t = 200$; $h_{stif}^{sup}/R = 1.0$).

In the latter case, which corresponds with the approximately horizontal branches in Fig. 5-87, an engaged column is added with a large cross-section A_{stif}. In this case, the axial stresses do not reach the yield stress in the column (Fig. 5-90 (b)), while a yielding zone is developed in the silo wall above the termination of the column (Fig. 5-90 (a)) (i.e. failure pattern P.2/b). However, this zone could not extend to the area in the silo wall between the columns, due to premature failure by plastic buckling (see Fig. 5-90 (c)). Indeed, the strength of the silo wall F_{GMNA} does not reach the maximum possible strength of the silo wall (i.e. the plastic limit load or F_{MNA}). However, the reaching of the horizontal branch (see Fig. 5-87) indicates that nevertheless the material of the silo wall is maximally used for the corresponding silo wall

thickness t and yield stress σ_y.

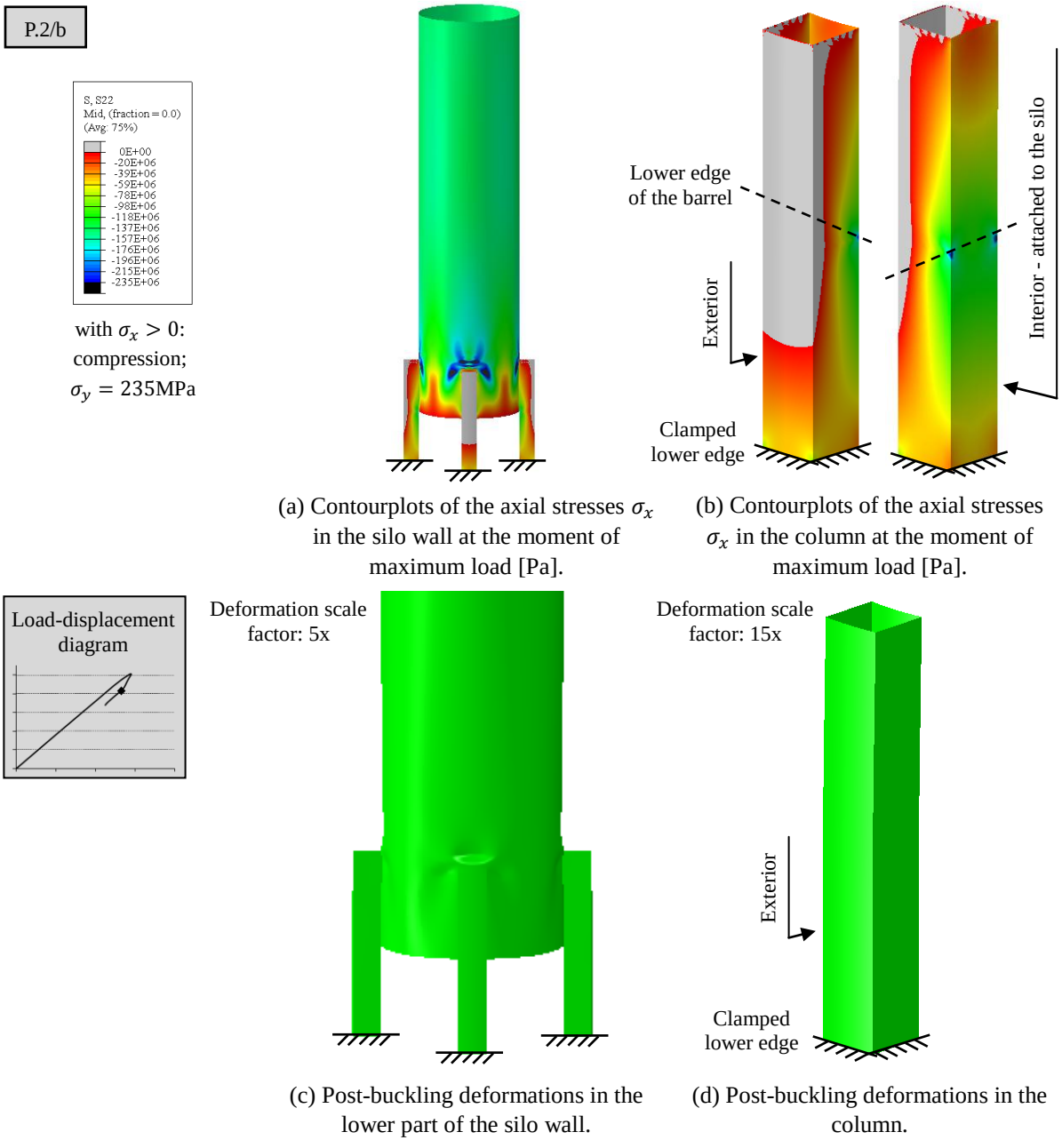

(a) Contourplots of the axial stresses σ_x in the silo wall at the moment of maximum load [Pa].

(b) Contourplots of the axial stresses σ_x in the column at the moment of maximum load [Pa].

(c) Post-buckling deformations in the lower part of the silo wall.

(d) Post-buckling deformations in the column.

Fig. 5-90 Failure behaviour for a column with a large cross-section (type P.2/b) ($R/t = 200$; $h_{stif}^{sup}/R = 1.0$).

To conclude, for silos with a relatively thick silo wall, the cross-section of the column A_{stif} determines whether or not the material of the silo wall is maximally used. The cross-section of the engaged columns should be sufficiently large so that a yielding zone could develop in the silo wall above the column, causing failure by plastic yielding (and elastic buckling). Only in this way, the material of the silo wall is maximally utilized.

Thin-walled silos

Similar to the previous part, the influence of the cross-section of the column A_{stif} is investigated for thin-walled silos (here: $R/t = 1000$). In total, 14 different cross-sections were calculated (both the shape and dimensions were varied) for 16 different combinations of the heights of the column (i.e. h_{stif}^{sup} and h_{stif}^{inf}). In Fig. 5-91, the dimensionless GMNA failure load F_u/F_{ref} of the silo structure is plotted against the ratio of the column cross-section to the cross-section of the silo wall A_{stif}/A_{shell} (expressed in percentage) for different attached column heights h_{stif}^{sup}. Since the radius-of-thickness ratio R/t is constant (1000), the values of F_{ref} and A_{shell} remain constant too.

Again, the cross-section of an engaged column has a significant impact on the maximum load of such a silo. All columns plotted in Fig. 5-91 are classified into two categories (E.1 and E.2), depending on the failure behaviour of the silo structure. Failure pattern E.1 corresponds with slender engaged columns with a small value of the cross-section A_{stif}, which fail prematurely (the approximately horizontal branch is not reached) by elastic buckling. Failure pattern E.2 corresponds with engaged columns with a large value of the cross-section A_{stif}. In this case, a further increase of the column cross-section does not lead to an increase of the buckling load F_u anymore. In what follows, these failure patterns will be discussed more in detail.

The influence of the attached column height h_{stif}^{sup} and the unattached column height h_{stif}^{inf} will be explained in detail in Section 8.1.5.

Furthermore, a marked scatter can be observed in the results of Fig. 5-91, in particular in the approximately horizontal maximum. This scatter is caused due to the range of different shapes of the column cross-section that are explored in the present study (with a constant quantity of cross-sectional material). This topic, and the determination of the optimal shape of the column cross-section, are covered in depth in Section 8.3.

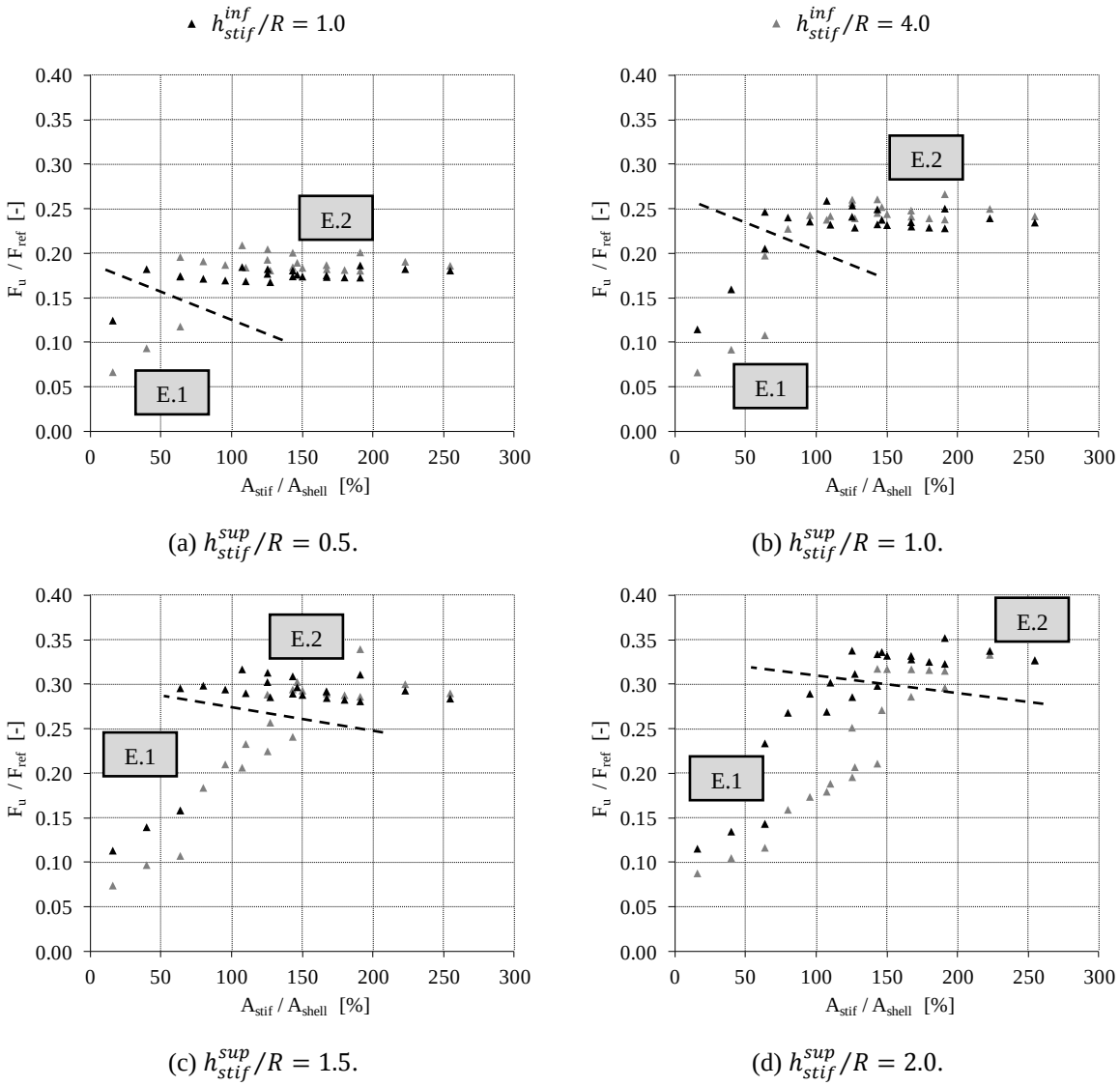

(a) $h_{stif}^{sup}/R = 0.5$. (b) $h_{stif}^{sup}/R = 1.0$.

(c) $h_{stif}^{sup}/R = 1.5$. (d) $h_{stif}^{sup}/R = 2.0$.

Fig. 5-91 Dimensionless GMNA failure load F_u/F_{ref} as a function of the ratio of the cross-section of the engaged columns to the cross-section of the silo wall A_{stif}/A_{shell} for different column heights ($R/t = 1000$).

In Fig. 5-92, the deformations at the moment of and after buckling are depicted in the case of a slender column (i.e. buckling pattern E.1). The deformed shape before and at the moment of buckling are elongated zones in the silo wall (see Fig. 5-92 (a)), which are inwardly oriented at the backside of the columns and above the columns, and in contrast, outwardly oriented between the columns. These elongated zones with relatively large deformations are caused by the slender engaged columns which can easily deform inwardly. This can be explained by the relatively small moment of inertia I_{stif}, allowing circumferential rotation, and consequently deformations in radial direction. In Fig. 5-92 (b) and (c), the post-buckling deformations are shown of the whole structure and the engaged column, respectively. From these figures, it can be determined that, from the moment of failure, a buckle develops in the silo wall just above the top of the inwardly oriented engaged column.

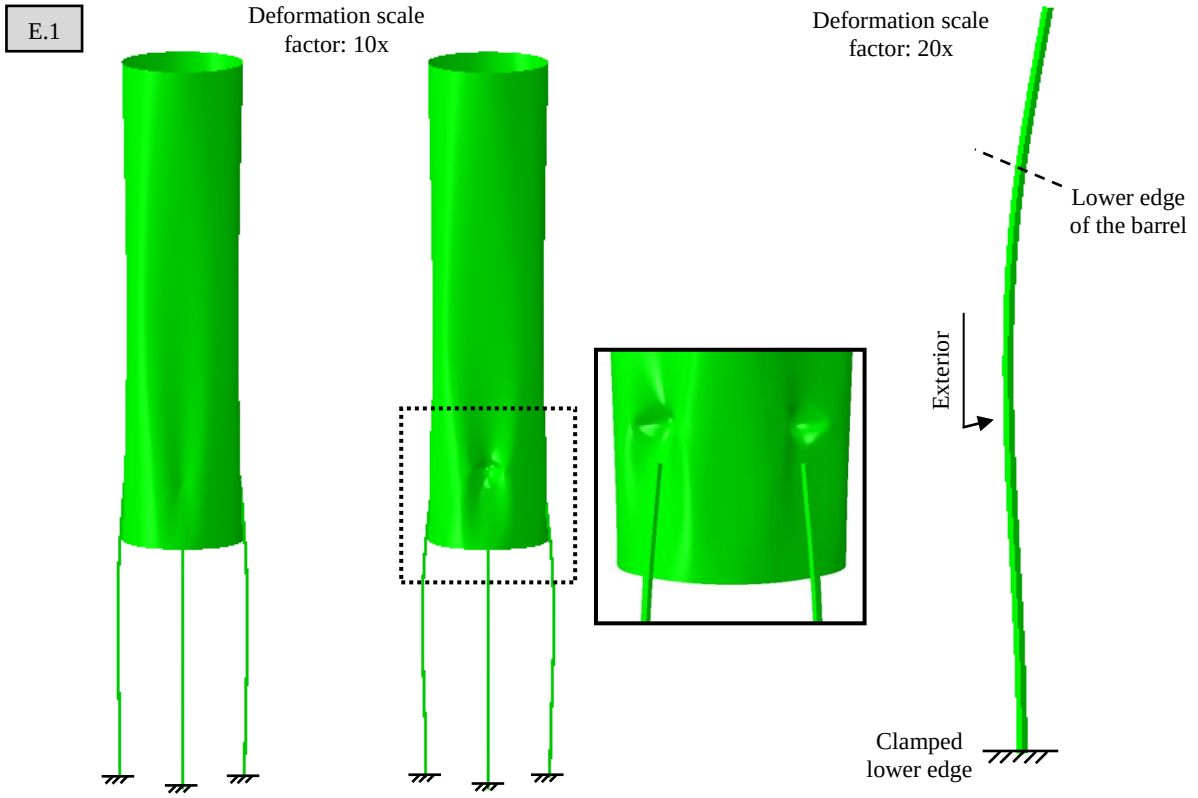

(a) Pre-buckling deformations in the silo wall.

(b) Post-buckling deformations in (the lower part of) the silo wall.

(c) Post-buckling deformation of the column.

Fig. 5-92 Contourplots of the (post-)buckling deformations for a slender engaged column with a small cross-section (type E.1) ($R/t = 1000$; $h_{stif}^{sup}/R = 1.0$; $h_{stif}^{inf}/R = 4.0$).

For the standard engaged columns (i.e. buckling pattern E.2), the post-buckling deformed shape is shown in Fig. 5-93. Clearly, the deformed shape is rather different than in the case of the slender columns: two local buckles appear in the silo wall on both sides of the engaged column, a short distance under the top of the column. Furthermore, the deformations in the column after buckling are negligible to those in the silo wall (and consequently also before and at the moment of buckling). In other words, by increasing the cross-section A_{stif}, the moment of inertia of the column I_{stif} increases, and the resistance to the circumferential rotation increases, reducing the radial deformations in the column - before, during, and after buckling.

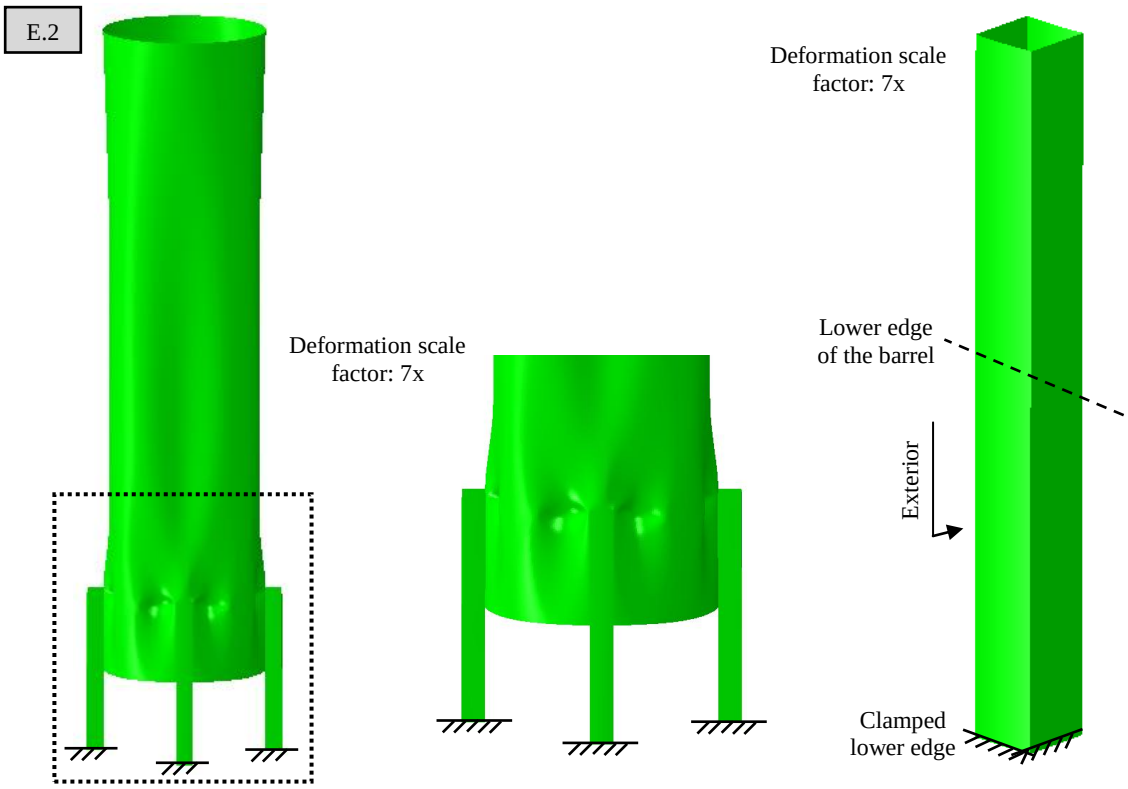

(a) The silo wall. (b) The lower part of the silo wall. (c) The column.

Fig. 5-93 Contourplots of the post-buckling deformations for a standard engaged column with a large cross-section (type E.2) ($R/t = 1000$; $h_{stif}^{sup}/R = 1.0$).

From the above results, it appears that the moment of inertia of the cross-section of the column I_{stif} plays an important role in the failure behaviour of the structure. Therefore, the results of Fig. 5-91 are plotted again in Fig. 5-94, but now with the moment of inertia I_{stif} on the horizontal axis. Frome these figures, the transition from a slender column with a small value of I_{stif} (E.1) to a standard column with a large value of I_{stif} (E.2) can be better observed. The transition is indicated by a black ($h_{stif}^{inf}/R = 1.0$) or a gray ($h_{stif}^{inf}/R = 4.0$) vertical line in the graphs. The moment of inertia corresponding with the transition between a slender and a standard column increases as the attached column height h_{stif}^{sup} increases and is systematically larger for the columns with a large free height (i.e. $h_{stif}^{inf} = 4.0$) than for the columns with a small free height (i.e. $h_{stif}^{inf} = 1.0$). In other words, a higher engaged column needs a cross-section with a larger moment of inertia I_{stif} than a shorter engaged column to increase the resistance to the circumferential rotation, and to reduce the radial deformations in the column - before, during, and after buckling. In Section 8.1.5, the influence of the attached and unattached column heights (i.e. h_{stif}^{sup} and h_{stif}^{inf}) will be discussed further.

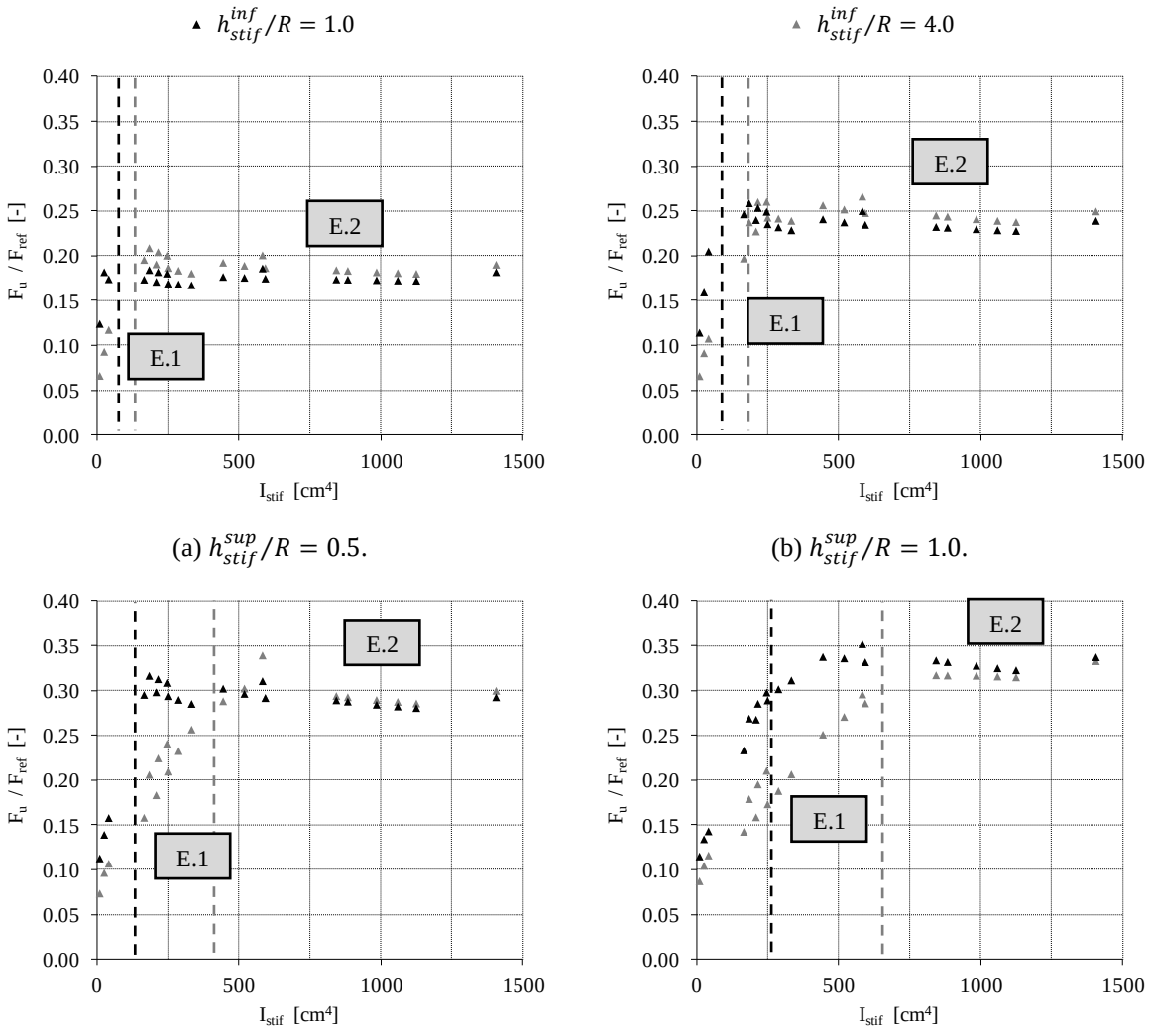

(a) $h_{stif}^{sup}/R = 0.5$.

(b) $h_{stif}^{sup}/R = 1.0$.

(c) $h_{stif}^{sup}/R = 1.5$.

(d) $h_{stif}^{sup}/R = 2.0$.

Fig. 5-94 Dimensionless GMNA failure load F_u/F_{ref} as a function of the moment of inertia of the cross-section of the engaged columns I_{stif} for different column heights ($R/t = 1000$).

To conclude, for silos with a relatively thin silo wall, failure of the silo always occurs by elastic buckling. The post-buckling deformations of the silo wall above/next to the columns are inwardly oriented. To hinder these deformations, the engaged columns must have a sufficiently large moment of inertia I_{stif}. In fact, these deformations influence the curvature of the silo wall, and consequently the critical buckling stress σ_{cr}.

Conclusions

The engaged columns which correspond with the rapidly increasing branches in Fig. 5-87, Fig. 5-91, and Fig. 5-94 have a too small cross-section and/or moment of inertia. This results in premature failure of the structure because the engaged column only can absorb a limited supporting load (P.1) or the engaged column is not able to resist the detrimental inwardly oriented pre-buckling deformations (E.1). This situation should be avoided at all times because the maximum load of the silo wall has not yet been reached (i.e. the approximately

horizontal branch in Fig. 5-87, Fig. 5-91, and Fig. 5-94). The engaged columns corresponding with the latter branch have an average/a larger cross-section and/or moment of inertia. Only in that way, a sufficiently large supporting load can be absorbed and then gradually introduced in the silo wall, by which the maximum absorbable load of the silo wall is reached. Furthermore, for these cases, failure (plastic yielding and/or elastic buckling) occurs in the unstiffened silo wall just above the terminations or next the top of the engaged columns. The above findings are valid both for thick-walled and for thin-walled silos.

It can be concluded that an engaged column with an intermediate value of the cross-section is the optimal, because a further increase of the column cross-section A_{stif} usually leads to a limited increase or decrease (depending on the column height h_{stif}) of the failure load. This will also be apparent from the results of Section 8.3.1.

8.1.2 Width in circumferential direction of the engaged column

Thick and thin-walled silos

Since the silos are discretely supported, the degree of support μ_{sup} and the circumferential width of the column d_{stif} are very important geometrical parameters.

The results of the dimensionless GMNA failure load F_u/F_{ref} for a varying width d_{stif}/R are presented in Fig. 5-95 for engaged columns with a variable attached height ($0.5 \leq h_{stif}^{sup}/R \leq 2.0$). The bilineair curves suggest that again each branch corresponds with a different location of failure, as already mentioned in Paragraph 8.1.1.

Initally, an increase of the circumferential width d_{stif} leads to a significant increase of the failure load F_u. From a certain point, an increase of the circumferential width d_{stif} does no longer lead to an increase of the failure load F_u. This can be explained by the above mentioned failure patterns. Indeed, for the silos supported by engaged columns with a small circumferential width d_{stif} ($d_{stif}/R = 0.05$), the silo fails by premature plastic yielding and/or elastic buckling of the column itself (i.e. P.1 for $R/t = 200$ and E.1 for $R/t = 1000$). When the circumferential width d_{stif} is increased further, failure shifts to the silo wall in the vicinity of the top of the engaged column, corresponding with P.2 ($R/t = 200$) and E.2 ($R/t = 1000$).

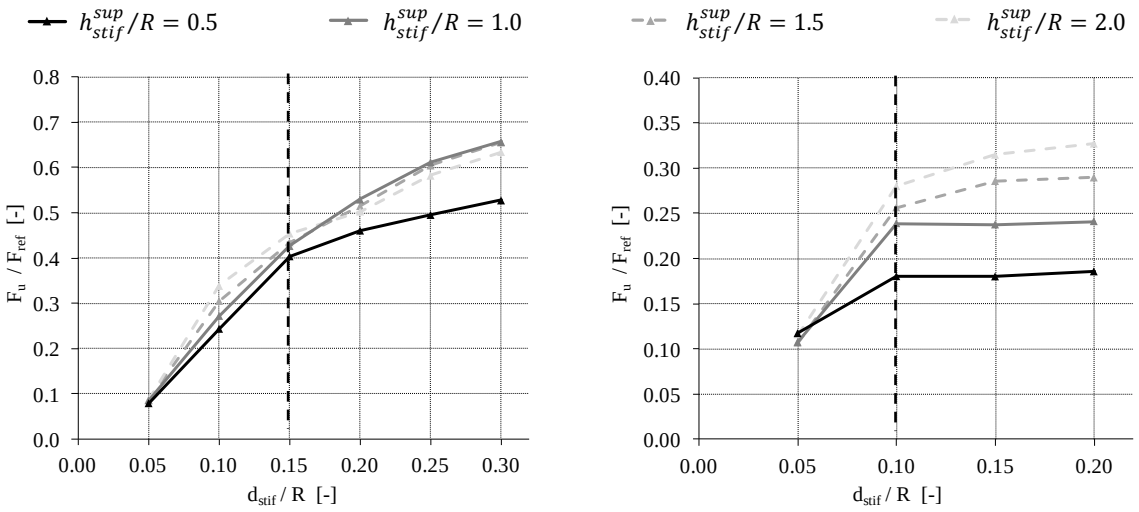

(a) $R/t = 200$. (b) $R/t = 1000$.

Fig. 5-95 Dimensionless GMNA failure load F_u/F_{ref} as a function of the ratio of the circumferential width of the engaged column to the silo radius d_{stif}/R for different attached heights h_{stif}^{sup} ($w_{stif}/d_{stif} = 100\%$; t_{stif}/t = max.; $h_{stif}^{inf}/R = 4.0$).

Conclusions

Both for thick-walled and for thin-walled silos, it can be concluded that the circumferential width d_{stif}/R must have a minimum value to avoid premature failure by (elasto-)plastic yielding (that are respectively failure pattern P.1 and E.1).

Above a certain minimum value of the circumferential width d_{stif}/R, the additional circumferential width influences the failure load to a lesser degree, depending on the height of the column h_{stif}^{sup}.

8.1.3 Width in radial direction of the engaged column

To keep the number of calculations within reasonable bounds, mainly engaged columns with a square cross-section (i.e. $d_{stif} = w_{stif}$) were investigated in the preliminary study. In this way, it is difficult to investigate the influence of the radial width to the failure behaviour. In the optimisation study of Section 8.3, the optimal shape of the engaged column (i.e. the optimal ratio of w_{stif}/d_{stif}) will be investigated in detail.

8.1.4 Wall thickness of the engaged column

Thick and thin-walled silos

The relationship between the dimensionless GMNA failure load F_u/F_{ref} and the ratio of the column thickness to the silo thickness t_{stif}/t is displayed in Fig. 5-96 for two different cases

and for different attached column heights ($0.5 \leq h_{stif}^{sup}/R \leq 2.0$). The minimum, average, and maximum value of t_{stif}/t are plotted within the interval defined by Eqs. (3-8) to (3-9). This interval depends on the silo thickness (i.e. R/t) and the circumferential and radial width of the column (i.e. d_{stif}/R and w_{stif}/d_{stif}).

The graphs in Fig. 5-96 show that an increasing column wall thickness has a negligible influence on the failure load F_u, and, consequently also on the failure behaviour. This finding is only valid when the engaged supporting columns are able to absorb and transfer the load between the foundation and the silo wall, without premature failure (failure modes P.2 and E.2). This corresponds with the approximately horizontal branch of Fig. 5-87 (if $R/t = 200$), Fig. 5-91, and Fig. 5-94 (if $R/t = 1000$).

In contrast, when the engaged columns cannot absorb the supporting load and the engaged columns prematurely fail before the silo wall in the direct vicinity of the top of the engaged column fails (i.e. P.1 for $R/t = 200$ and E.1 for $R/t = 1000$), the column thickness has an appreciable influence on the failure load of the structure (cannot be derived from Fig. 5-96).

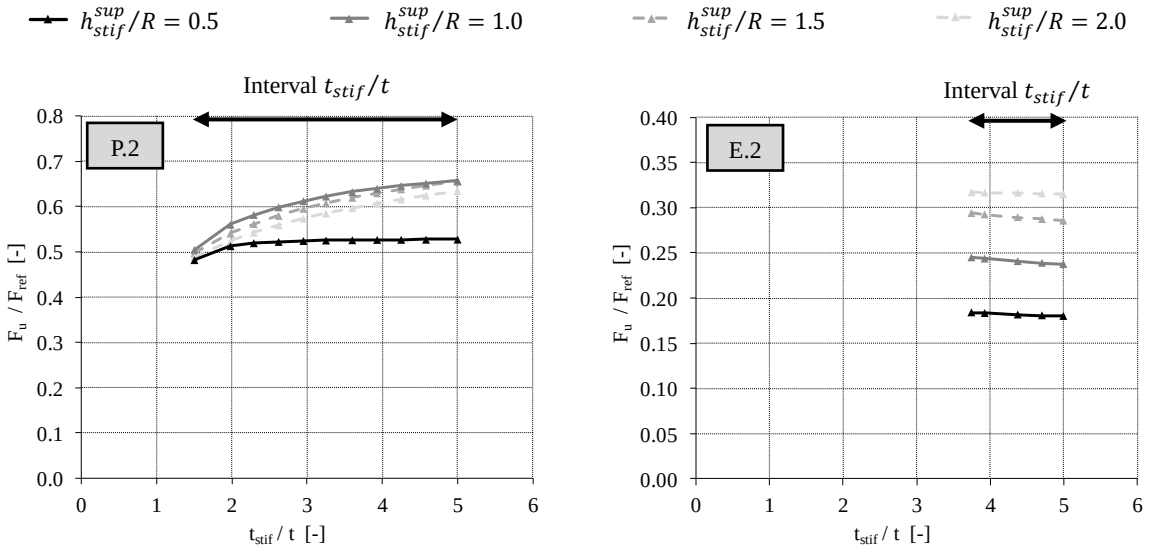

(a) $R/t = 200$; $d_{stif}/R = 0.30$. (b) $R/t = 1000$; $d_{stif}/R = 0.15$.

Fig. 5-96 Dimensionless GMNA failure load F_u/F_{ref} as a function of the ratio of the thickness of the engaged column to the silo thickness t_{stif}/t for different attached heights h_{stif}^{sup} ($w_{stif}/d_{stif} = 100\%$; $h_{stif}^{inf}/R = 4.0$).

Conclusions

The column wall thickness has a minor influence on the failure behaviour and failure load, on the condition that failure occurs in the silo wall in the vicinity of the top of the engaged supporting column. Similar results were found for other cross-sections.

8.1.5 Height of the engaged column

The total height of an engaged column is divided into two components: (1) the distance between the clamped lower edge and the lower edge of the cylindrical barrel (i.e. the "unattached" or free height h_{stif}^{inf}) and (2) the distance of the engagement of the supporting column along the silo wall (i.e. the "attached" height h_{stif}^{sup}). As will be seen, the column height strongly influences the failure load, for thick-walled as well as for thin-walled silos.

Thick-walled silos

Attached column height

Fig. 5-97 represents the dimensionless GMNA failure load F_u/F_{ref} for different column geometries: for several attached heights of the column h_{stif}^{sup}, the cross-section of the column A_{stif} is varied ($h_{stif}^{inf} = 1.0$). As seen in previous section, an increased cross-section of the column leads to a higher failure load. The increase is not infinite and is limited by the silo wall. This corresponds with the approximately horizontal branch in Fig. 5-97. In general, the horizontal branch is located higher with an increase of the height of the column h_{stif}^{sup}. However, this is not always the case.

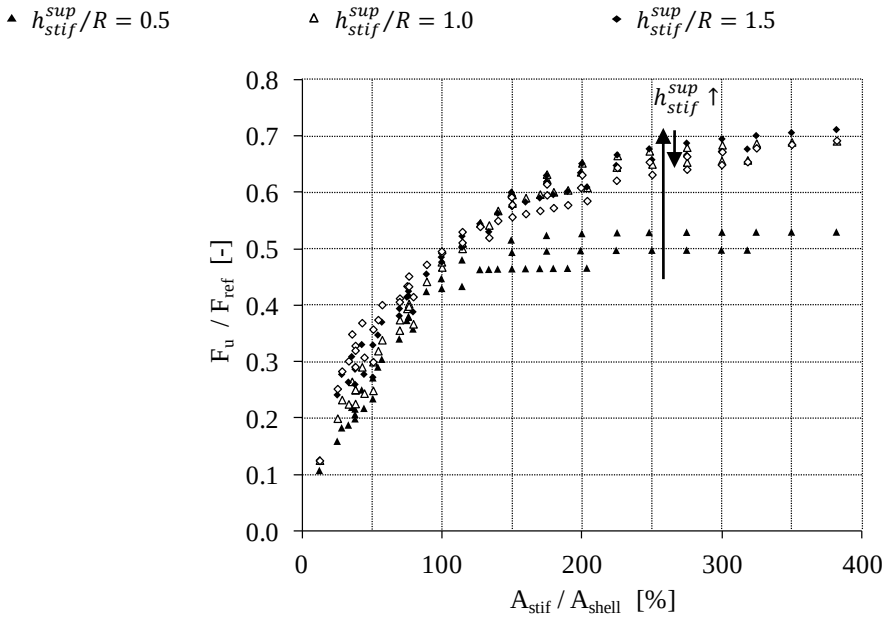

Fig. 5-97 Dimensionless GMNA failure load F_u/F_{ref} as a function of the ratio of the cross-section of the engaged columns to the cross-section of the silo wall A_{stif}/A_{shell} for different attached heights h_{stif}^{sup} ($w_{stif}/d_{stif} = 100\%$; $h_{stif}^{inf}/R = 1.0$).

In Fig. 5-98, the failure load is plotted against the attached column height h_{stif}^{sup} for one specific cross-section located in the horizontal branch of Fig. 5-97 ($d_{stif}/R = w_{stif}/R = 0.20$; t_{stif}/t = max.) and for different unattached column heights h_{stif}^{inf}. At the beginning, the maximum failure load increases significantly with increasing height h_{stif}^{sup}. From a certain turning point, the additional height h_{stif}^{sup} has a disadvantageous influence on the maximum failure load, assuming that the cross-section of the column remains constant. In what follows, the height h_{stif}^{sup} which corresponds with the maximum failure will further be denoted as the critical height $h_{stif,crit}^{sup}$.

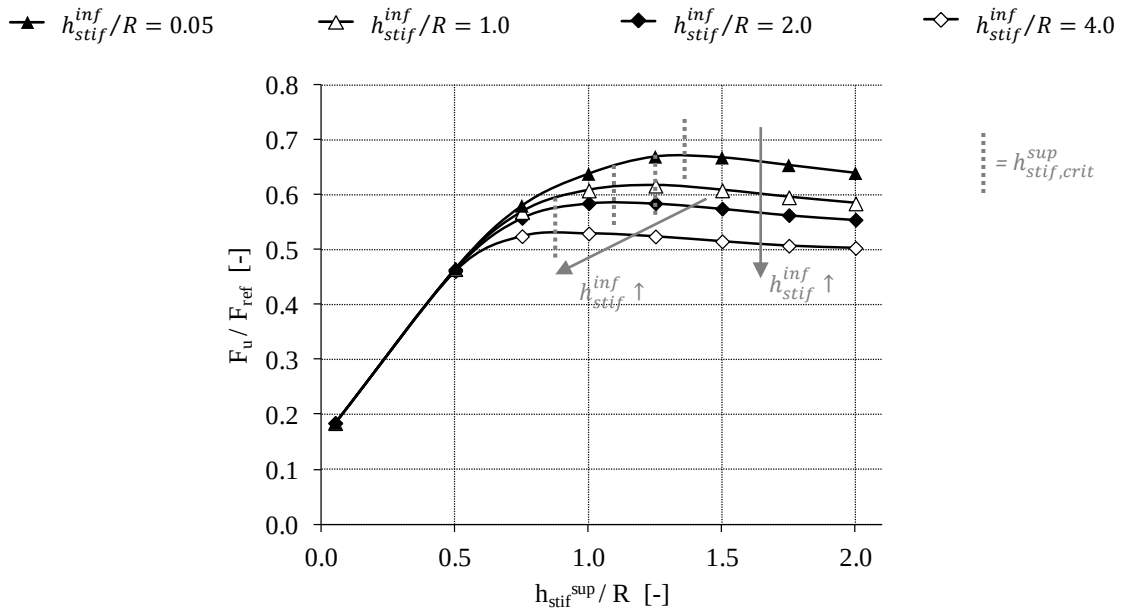

Fig. 5-98 Dimensionless GMNA failure load F_u/F_{ref} as a function of the attached column height h_{stif}^{sup} ($d_{stif}/R = 0.20$; $w_{stif}/d_{stif} = 100\%$; t_{stif}/t = max.).

Now, the above mentioned interesting finding will be explained on the basis of the stresses in the silo wall. With increasing column height h_{stif}^{sup}, there are two opposing effects influencing the failure load. First of all, the column height h_{stif}^{sup} represents the height of the engaged column over which the column is attached to the silo wall. As this distance increases, the supporting load is transferred more gradually from the column to the silo by shear stresses. As a result, the stresses are spread better in circumferential direction, reducing the stresses in the silo wall above the terminations of the column. In Fig. 5-99 (a), the distribution of the axial stresses is shown for a circumferential path located above the column (PC/S-h1.015 with $h_{path}/h_{stif}^{sup} = 1.015$). Clearly, the axial stresses σ_x between the supports ($\theta > 25°$) are higher as the height of the column h_{stif}^{sup} increases. This better distribution of the axial stresses in circumferential direction results in a higher failure load. On the other side, the higher the engaged column, the more the column tends to deform inwardly (assuming that the cross-

section of the column remains constant). This results in a flattened silo wall in the vicinity of the top of the column, which is clearly visible in Fig. 5-99 (b). In this figure, increased negative or inwardly oriented radial deformations can be observed in the silo wall above the column ($\theta < 20°$). In this critical region where yielding occurs, these deformations are disadvantageous because they reduce the effective yield stress σ_y^{eff} (See $\theta < 9°$ in Fig. 5-99 (a)). In Section 3.4, more information is given on the flattening effect (i.e. the influence of the deformations before failure on the effective yield stress). The reduction of the effective yield stress increases as the column height h_{stif}^{sup} increases. In other words, the second effect tends to reduce the failure load when the height of the column h_{stif}^{sup} increases.

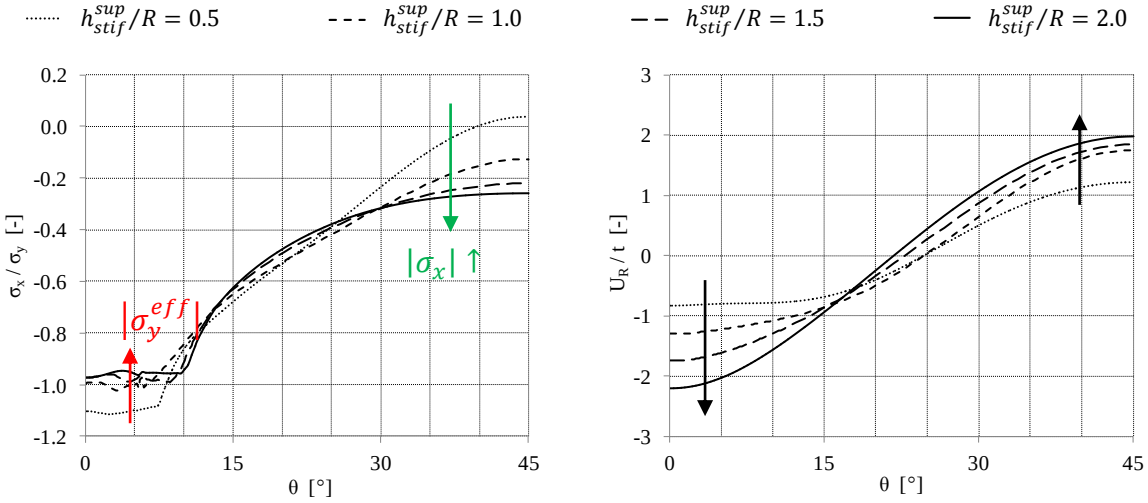

(a) Plot of the ratio of the axial stress at the moment of failure to the yield stress σ_x/σ_y [-] against the circumferential angle θ [°].

(b) Plot of the ratio of the radial displacement at the moment of failure to the silo thickness U_R/t [-] against the circumferential angle θ [°].

Fig. 5-99 Stress distribution and radial displacements in the silo wall at the moment of maximum load along circumferential path PC/S-h1.015 ($h_{path}/h_{stif}^{sup} = 1.015$) for a variable attached column height h_{stif}^{sup} ($d_{stif}/R = 0.20$; $w_{stif}/d_{stif} = 100\%$; t_{stif}/t = max.; $h_{stif}^{inf}/R = 1.0$).

In summary, it can be said that the additional column height h_{stif}^{sup} initially has a positive impact on the failure load through a better distribution of the stresses in circumferential direction. However, above a certain critical height $h_{stif,crit}^{sup}$, the disadvantageous influence of the decreasing effective yield stress gets the upper hand and the failure load decreases. Consequently, the column height h_{stif}^{sup} can best be chosen before this point. This conclusion is confirmed by the results of the other analysis, performed on engaged columns with other dimensions.

Unattached column height

The dimensions of the hopper, the accessibility of the bottom of the silo, etc. determine the lower part of the column height h_{stif}^{inf}, which is the distance between the bottom of the engaged column and the lower edge of the cylindrical barrel. Its influence will be discussed in this section.

For one cross-section located in the horizontal branch of Fig. 5-97 ($d_{stif}/R = w_{stif}/R = 0.20$; t_{stif}/t = max.), the influence of the unattached height of the column h_{stif}^{inf} on the dimensionless GMNA failure load F_u/F_{ref} can be observed in Fig. 5-98. By increasing the attached column height h_{stif}^{sup}, the failure load first increases significantly and then decreases slowly. The larger the value of the unattached column height h_{stif}^{inf}, (1) the smaller the value of the attached column height $h_{stif,crit}^{sup}$ corresponding with the transition between increasing and decreasing load and (2) the smaller the failure load corresponding with the second part of the curve (i.e. $h_{stif}^{sup} > h_{stif,crit}^{sup}$).

The disadvantageous impact of the larger free column height h_{stif}^{inf} can also be assigned to the flattening effect of the silo wall above the termination of the engaged column (See Section 3.4). As a consequence of the reduction of the effective yield stress σ_y^{eff} in the critical region, yielding occurs earlier (i.e. with a lower load).

Summarized, the unattached or free column height h_{stif}^{inf} has a negative influence on the failure load.

Thin-walled silos

In Fig. 5-100, the column height h_{stif}^{sup} is plotted against the dimensionless GMNA failure load F_u/F_{ref} for engaged columns with variable dimensions of the cross-section A_{stif} ($h_{stif}^{inf} = 1.0$). Clearly, for standard columns (i.e. the horizontal branch), the column height h_{stif}^{sup} has a positive effect on the failure load. However, this finding appears to be incorrect for slender columns (i.e. the rising branch), as will be demonstrated in the following paragraphs. The behaviour of the slender and the standard columns are therefore discussed separately.

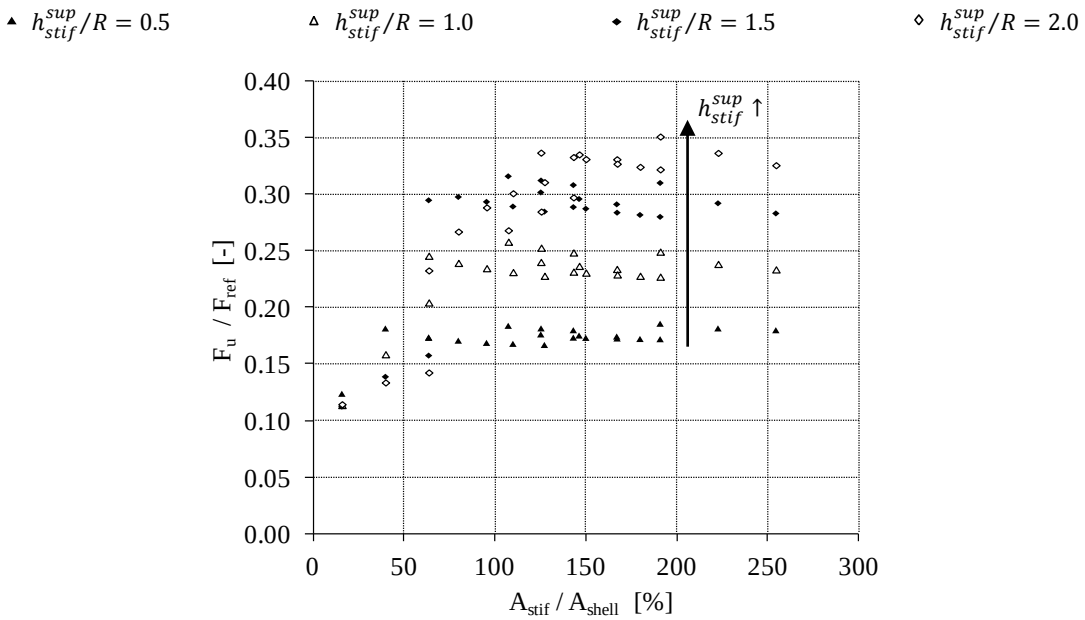

Fig. 5-100 Dimensionless GMNA failure load F_u/F_{ref} as a function of the ratio of the cross-section of the engaged columns to the cross-section of the silo wall A_{stif}/A_{shell} for different attached heights h_{stif}^{sup} ($w_{stif}/d_{stif} = 100\%$; $h_{stif}^{inf}/R = 1.0$).

Firstly, the slender columns will be discussed. For a (very) slender column (see Fig. 5-101 (a) and (b)), an additional column height h_{stif}^{sup} initially has a positive influence, and from a certain point, clearly has a negative influence on the failure load. The height h_{stif}^{sup} which corresponds with the maximum failure will further be denoted as the critical height $h_{stif,crit}^{sup}$. The value of the critical height $h_{stif,crit}^{sup}$ depends on the unattached column height h_{stif}^{inf}. The larger the unattached column height h_{stif}^{inf} is, the smaller the value of $h_{stif,crit}^{sup}$ can increase before the maximum failure load can be achieved (in the case of a slender column!).

This turning point can be explained by the radial deformations and the axial stresses in the silo wall above the column (i.e. the region where elastic buckling occurs). From the critical height $h_{stif,crit}^{sup}$, the deformations (at the top) of the slender column are not sufficiently prevented by the too low moment of inertia I_{stif}. These increased inwardly oriented deformations of the column are disadvantageous because they flatten the silo wall and influence the curvature of the silo wall, which in turn reduces the critical buckling stress σ_{cr} (See Section 3.4).

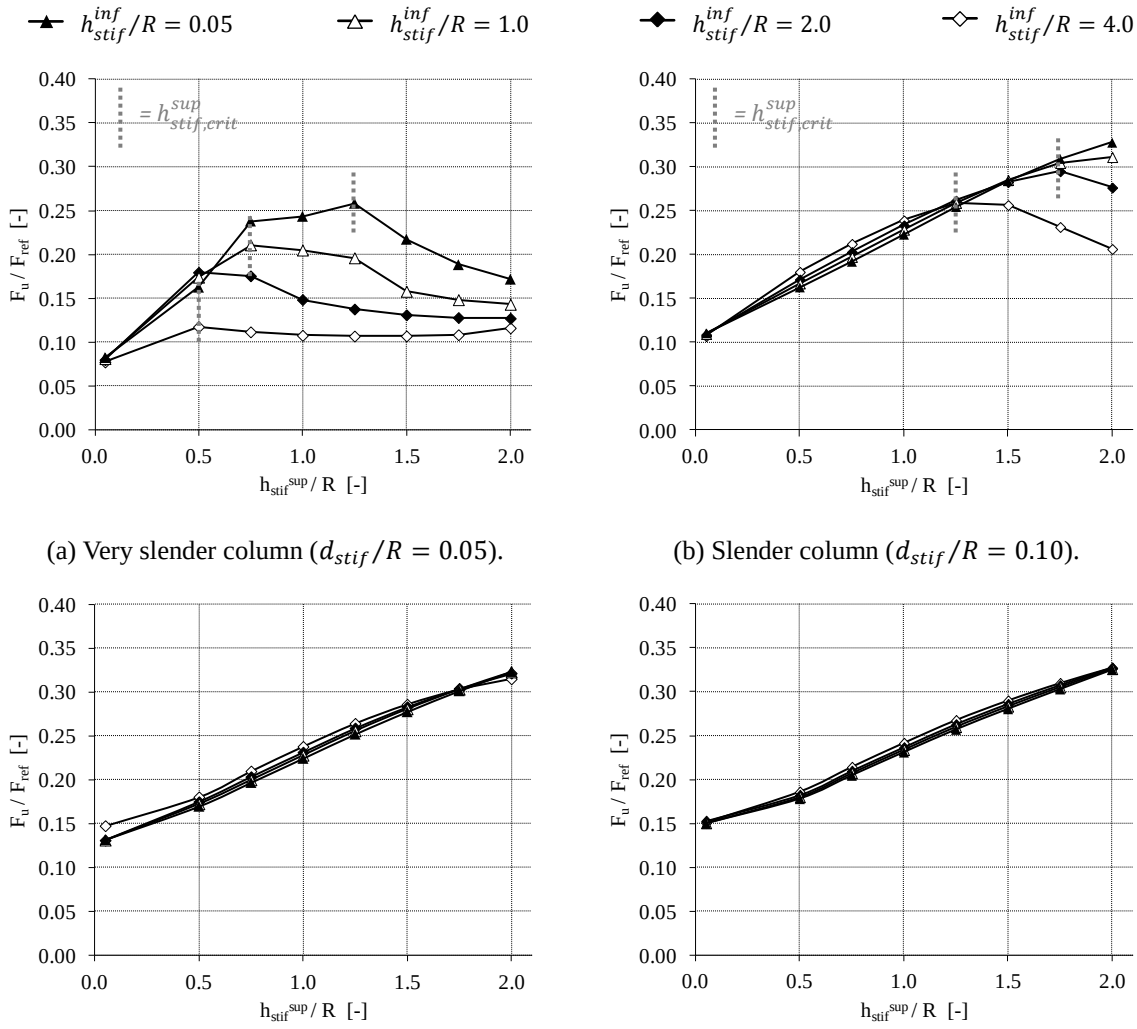

(a) Very slender column ($d_{stif}/R = 0.05$).

(b) Slender column ($d_{stif}/R = 0.10$).

(c) Standard column ($d_{stif}/R = 0.15$).

(d) Standard column ($d_{stif}/R = 0.20$).

Fig. 5-101 Dimensionless GMNA failure load F_u/F_{ref} as a function of the attached column height h_{stif}^{sup} ($w_{stif}/d_{stif} = 100\%$; t_{stif}/t = max.).

In contrast, for the standard columns (see Fig. 5-101 (c) and (d)), the failure load is positively influenced by an increasing attached column height h_{stif}^{sup} and is independent of the unattached column height h_{stif}^{inf}. In this case, the deformations of the column are negligible compared to those in the silo wall, due to a large moment of inertia I_{stif}. By increasing the column height h_{stif}^{sup}, the location of the buckles (besides the top of the column) moves upward (Fig. 5-102 (a)). Furthermore, due to a better distribution of the axial stresses in circumferential direction (Fig. 5-102 (b)), which is an advantage of the larger attached distance between the column and the silo wall, the same axial stresses at the buckle are obtained with a larger failure load.

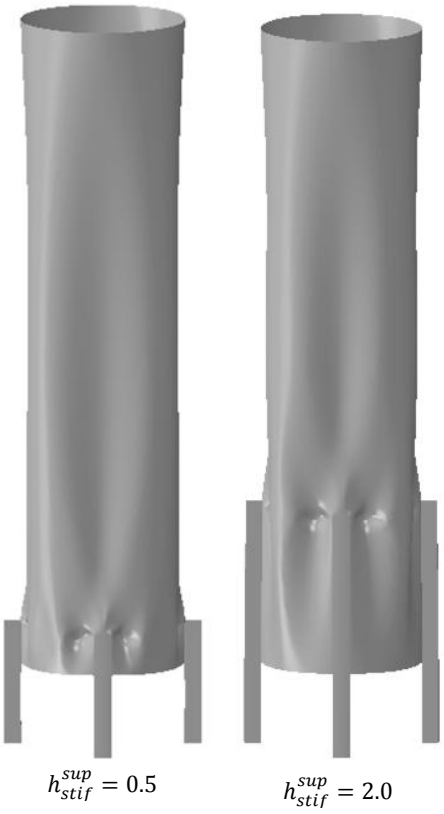

(a) Post-buckling deformations.

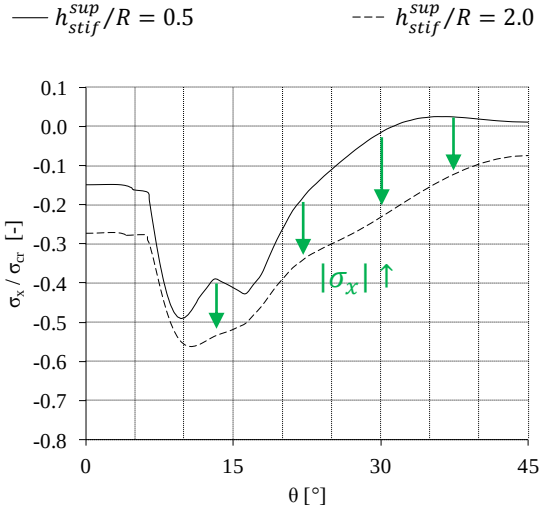

(b) Plot of the ratio of the axial stress at the moment of failure to the yield stress σ_x/σ_y [-] along circumferential path PC/S-h1.015 ($h_{path}/h_{stif}^{sup} = 1.015$).

Fig. 5-102 Buckling behaviour of a standard column with a variable attached column height h_{stif}^{sup} ($d_{stif}/R = 0.20$; $w_{stif}/d_{stif} = 100\%$; t_{stif}/t = max.; $h_{stif}^{inf}/R = 1.0$).

To conclude, for standard engaged columns, the attached column height h_{stif}^{sup} is advantageous for the failure load. Furthermore, the failure load is independent of the unattached column height h_{stif}^{inf}.

Conclusions

The height h_{stif}^{sup} over which the column is attached to the silo wall initially has a positive effect on the failure load F_u (due to a better stress distribution in circumferential direction) up to a certain critical value $h_{stif,crit}^{sup}$ after which the additional height h_{stif}^{sup} has a disadvantageous effect. In contrast, the unattached column height h_{stif}^{inf} always has a disadvantageous influence on the failure load F_u. Both decreases of the failure load are caused by a reduction of the effective yield stress σ_y^{eff} (thick-walled silos) or the critical buckling stress σ_{cr} (thin-walled silos) due to the flattening effect (See Section 3.4).

These findings were found for thick-walled ($R/t = 200$) as well as for thin-walled silos

($R/t = 1000$) and within the following ranges of heights: $0.5 \leq h_{stif}^{sup}/R \leq 2.0$ and $h_{stif}^{inf}/R \leq 4.0$. It is important to mention that similar findings were obtained for engaged columns with other cross-sections.

Only for the standard columns in combination with the thin-walled silos, no critical value $h_{stif,crit}^{sup}$ has been found within the investigated range of heights (i.e. $0.5 \leq h_{stif}^{sup}/R \leq 2.0$) and the failure load is independent of the unattached column height h_{stif}^{inf} ($h_{stif}^{inf}/R \leq 4.0$).

8.2 Degree of support along the circumference

In this section, the influence of the degree of support along the circumference μ_{sup} on the failure load is investigated for thick-walled silos (i.e. $R/t = 200$) and for thin-walled silos (i.e. $R/t = 1000$). The variable supporting degree in circumferential direction is obtained by changing the circumferential width of the engaged (supporting) column ($d_{sup} = d_{stif}$) and the number of supporting columns n_{sup}. The other geometrical parameters of the engaged columns remain constant. All geometrical parameters of the columns are listed in Table 5-21. The cylindrical barrel has the default values for its geometry. All parts have a standard elasto-plastic material behaviour with a yield stress σ_y equal to 235MPa.

Table 5-21 Geometrical parameters of the engaged columns (variation of the degree of circumference).

PARAMETER	VALUE(S)	DIMENSION
n_{sup}	4; 6; 8; 10; 12; 14	-
d_{stif}/R	$R/t = 200$: 0.05; 0.10; 0.15; 0.20; 0.25; 0.30 $R/t = 1000$: 0.05; 0.10; 0.15; 0.20	-
w_{stif}/d_{stif}	100	%
h_{stif}^{sup}/R	1.0	-
h_{stif}^{inf}/R	1.0	-
t_{stif}/t	max.*	-

*: Minimum (min.), average (ave.), or maximum (max.) thickness - restrictions

In addition, unstiffened cylindrical barrels are calculated with four supports and a variable degree of support to compare the behaviour of a cylindrical barrel with and without the engagement of the supporting columns.

Thick and thin-walled silos

In Fig. 5-103, the dimensionless GMNA failure load F_u/F_{ref} is plotted against the percentage of support along the circumference μ_{sup} for the above mentioned combinations. When comparing the cylindrical barrels with (i.e. the black curves) and without (i.e. the gray curve) the engagement of the supporting columns, then it is found that fairly high loads are obtained at relatively small support rates due to the engagement of a small number of supporting columns. Without the engagement of the supporting columns, the degree of support μ_{sup} must be 90% or more to resist similar loads. A second finding is that for the different values of the circumferential width d_{stif}, the curve consists of a rapidly increasing branch for a small number of supports and an approximately horizontal branch for a larger number of supports. The transition between these branches depends on the column geometry (d_{stif}), and varies from 15 to 40%. Furthermore, the failure load F_u of the horizontal branch is respectively about 95% for the thick-walled silos and 64% for the thin-walled silos of the reference load F_{ref} with a constant attached column height h_{stif}^{sup} equal to the cylinder radius R.

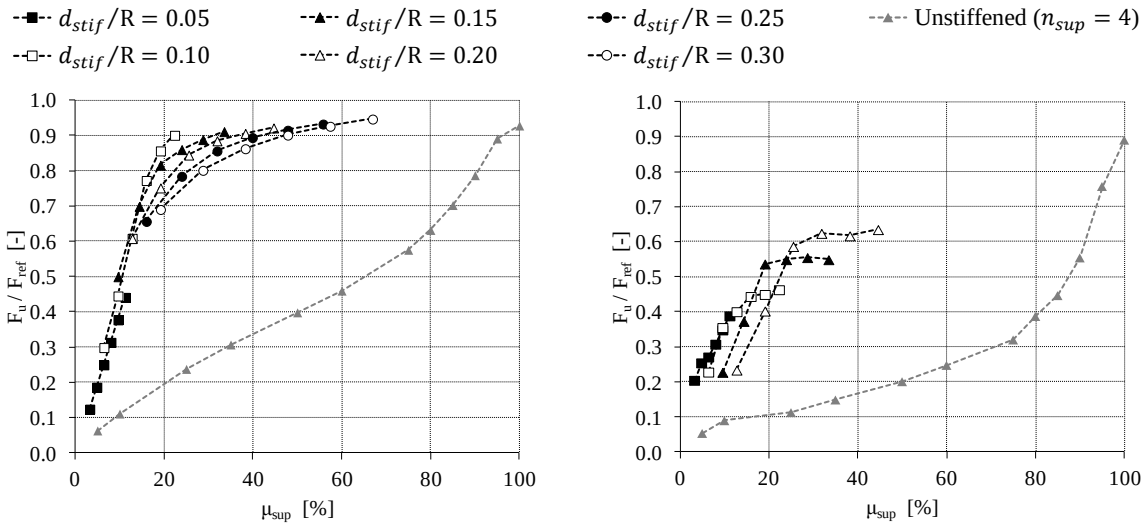

(a) Thick-walled silo ($R/t = 200$). (b) Thin-walled silo ($R/t = 1000$).

Fig. 5-103 Influence of the degree of circumferential support μ_{sup} on the dimensionless GMNA failure load F_u/F_{ref} for an unstiffened silo and a silo with engaged columns ($w_{stif}/d_{stif} = 100\%$; t_{stif}/t = max.; $h_{stif}^{sup}/R = h_{stif}^{inf}/R = 1.0$).

Conclusions

To conclude, the engagement of a limited number of supporting columns for discretely supported cylindrical barrels (with a small value of μ_{sup}) is advantageous to increase the failure load significantly, certainly compared to non-stiffened locally supported cylindrical barrels without the engagement of the supporting columns.

8.3 Optimisation parametric study

In this section, the "optimal engaged column" will be determined, which is defined as a supporting column to which as little as possible material is added to obtain a certain failure load of the silo structure. This parametric study is separated in two substudies. At first instance, the influence of the attached column height and the cross-section of the column on the failure load is investigated and compared (Section 8.3.1). Afterwards, the attached column height and quantity of material of the column cross-section are kept constant, and the optimal dimensions of the column cross-section are determined (Section 8.3.2). Finally, some conclusions are drawn.

To determine the dimensions of the optimal column cross-section (See Fig. 5-104), the failure load has been computed for a large number of combinations of (d_{stif}, w_{stif}, and t_{stif}), while keeping the quantity of cross-sectional material A_{stif}/A_{shell} constant. In fact, A_{stif} is equal to the product of the (constant) number of local engaged columns n_{sup} (= 4), the variable developed length of the column L_{stif} (represented in Fig. 5-104), and the variable column thickness t_{stif} (Eq. (5-22)). In other words, the column perimeter L_{stif} is inversely proportional to the column thickness t_{stif}, to keep the quantity of cross-sectional material A_{stif} constant.

$$A_{stif} = n_{stif} \cdot L_{stif} \cdot t_{stif} \tag{5-22}$$

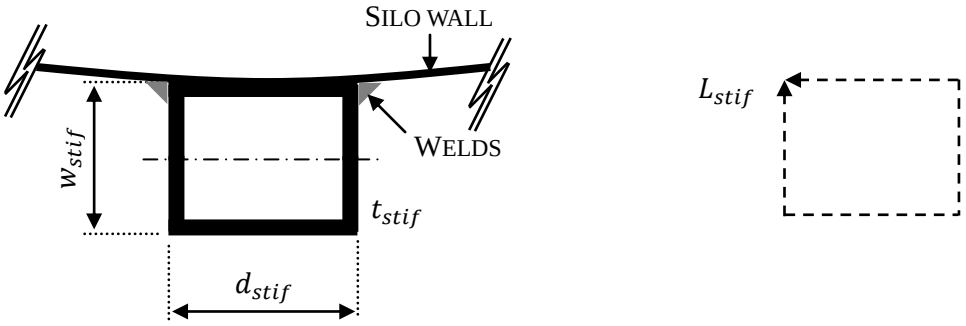

Fig. 5-104 Cross-section of the column.

Only those thicknesses are considered for which Eqs. (3-8) to (3-9) are valid. Furthermore, the column perimeter L_{stif} is determined according to Eq. (5-23) and is changed by varying the circumferential width d_{stif} and the radial width w_{stif} within the corresponding intervals of Table 5-22.

$$L_{stif} = 2 \cdot \left(d_{stif} + w_{stif}\right) = 2 \cdot d_{stif} \cdot \left(1 + \frac{w_{stif}}{d_{stif}}\right) = 2 \cdot d_{stif} \cdot (1 + p) \tag{5-23}$$

This optimisation study of the column cross-section has been done for different values of A_{stif}/A_{shell} (chosen on the basis of the exploratory study from Section 8.1: Fig. 5-87 for $R/t = 200$ and Fig. 5-91 for $R/t = 1000$) and for different column heights h_{stif}^{sup}/R. The chosen values are given in Table 5-22.

Table 5-22 Geometrical parameters of the engaged columns (optimisation study).

PARAMETER	VALUE(S)	DIMENSION
n_{sup}	4	-
A_{stif}/A_{shell}	$R/t = 200$: 100; 150; 200; 250; 300 $R/t = 1000$: 50; 75; 100; 125; 150	%
d_{stif}/R	$R/t = 200$: [0.10; 0.30] $R/t = 1000$: [0.05; 0.20]	-
w_{stif}/d_{stif}	[25; 400]	%
h_{stif}^{sup}/R	0.5; 1.0; 1.5; 2.0	-
h_{stif}^{inf}/R	4.0	-
t_{stif}/t	variable	-

Before proceeding to the more detailed discussion of the optimal engaged column, it should be noted that in this study only columns are taken into account which strengthen the structure in such a way that failure (yielding and/or buckling) occurs in the silo wall near and above the engaged columns. On the basis of the results obtained from the previous extensive parametric study (Section 8.1), the engaged columns which fail prematurely were omitted from this optimisation study.

8.3.1 Attached column height versus cross-section of the column

In Fig. 5-105, the dimensionless GMNA failure load F_u/F_{ref} is displayed on a contourplot based on the results of the **optimal shape** of the cross-section of the column (which will be determined in Section 8.3.2) for each considered attached column height h_{stif}^{sup} and for each cross-section A_{stif}. The column height h_{stif}^{sup}/R is plotted on the vertical, and the variable material parameter V_{extra}/V_{ref} (See Eq. (5-12)) on the horizontal axis. The latter parameter is proportional to the cross-section A_{stif} and the height h_{stif}^{sup} of the engaged columns.

From this figure, it turns that the column height h_{stif}^{sup} is advantageous when $h_{stif}^{sup} \leq 1.0$. Below this threshold, an increase of material in the column (height and/or cross-section) substantially increases the failure load. In contrast, above this threshold, a relatively large amount of material should be added to (the cross-section of) the column to obtain a small

increase in the failure load. In other words, above a certain critical height $h_{stif,crit}^{sup}$ (in this study: $h_{stif,crit}^{sup}/R = 1.0$), adding extra material to the column does not outweigh any gain in failure load, both for thick-walled silo (Fig. 5-105 (a)) and for thin-walled silos (Fig. 5-105 (b)). This does not mean that an extension of the column above the critical height $h_{stif,crit}^{sup}$ is not beneficial anymore for the failure load, especially for columns with a large cross-section. However, in terms of economical use of material, this solution is less interesting due to the minor increase of the failure load.

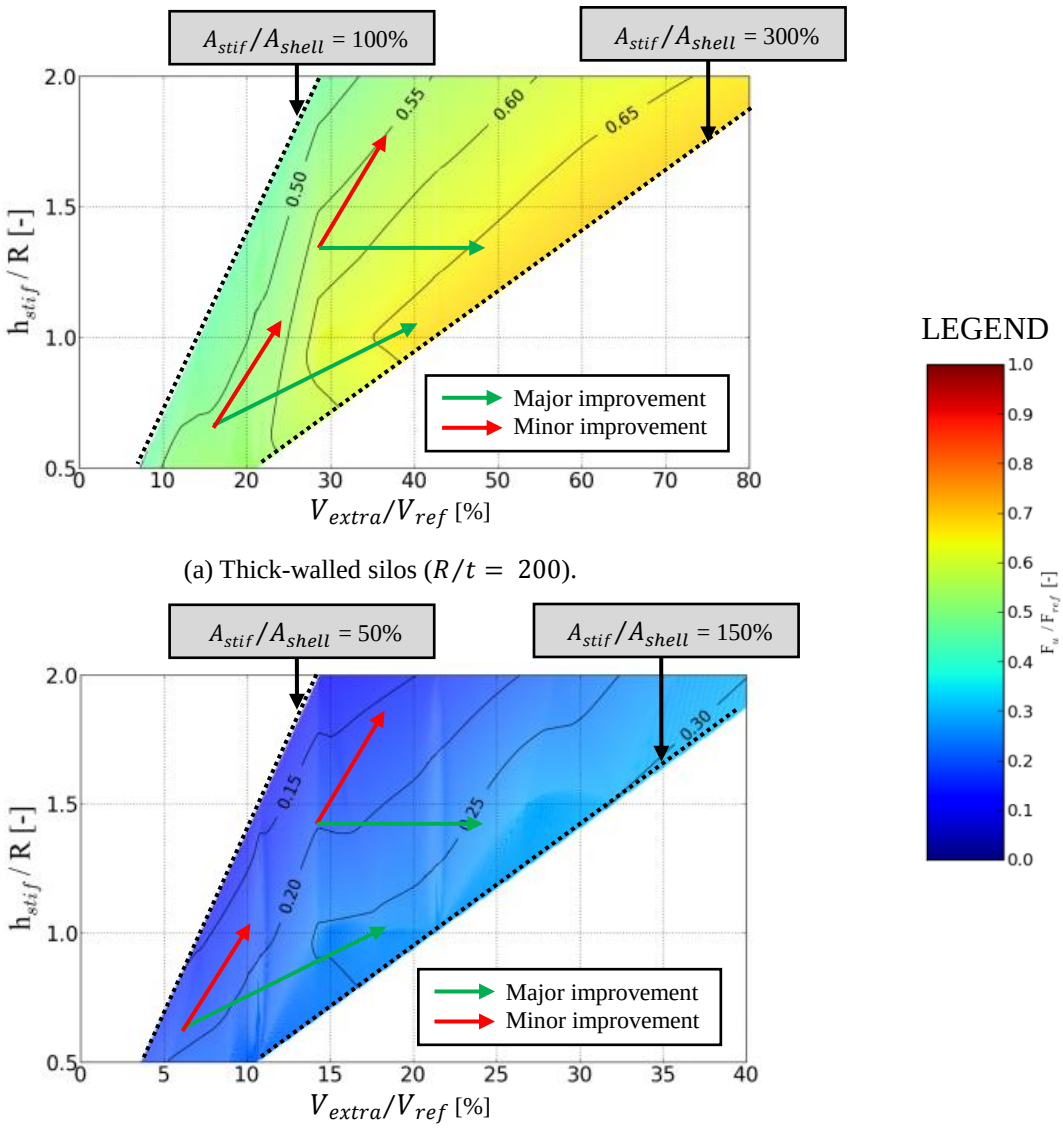

(a) Thick-walled silos ($R/t = 200$).

(b) Thin-walled silos ($R/t = 1000$).

Fig. 5-105 Dimensionless GMNA failure load F_u/F_{ref} for variable stiffener height (h_{stif}^{sup}/R) on the vertical axis and variable dimensionless material parameter (V_{extra}/V_{ref}) on the horizontal axis.

From these results, we can conclude that an increase of the attached column height to the critical height combined with an increase of the column cross-section is the most effective way to increase the failure load. A further increase of the height and/or cross-section increases

the failure load to a lesser extent. In the next paragraph, the optimal shape of the column cross-section will be determined.

8.3.2 Determination of the optimal cross-section

At first instance, the optimal shape of columns for the thick-walled silos (i.e. $R/t = 200$) are determined, and afterwards, for thin-walled silos (i.e. $R/t = 1000$) are discussed. Finally, some conclusions are drawn.

In Fig. 5-106, the results of the optimisation study (i.e. failure load) are presented. In this figure, the dimensionless GMNA failure load F_u/F_{ref} is always shown on the vertical axis, while the ratio of the radial width to the circumferential width w_{stif}/d_{stif} is plotted on the horizontal axis. Before proceeding to the discussion of the results, it is necessary to give some additional explanation on how the results are depicted in this figure. Indeed, Fig. 5-106 consists of six individual graphs, and for each graph, the column height h_{stif}^{sup}/R (0.5 or 1.0 or 1.5) and radius-to-thickness-ratios R/t (200 or 1000) are kept constant. For each graph, the dimensions of the cross-section of the column (d_{stif}, w_{stif}, and t_{stif}) are varied for well-chosen dimensionless quantities of cross-sectional material A_{stif}/A_{shell}. The latter ratios are chosen as a function of the radius-to-thickness ratio R/t of the silo.

Thick-walled silos

Fig. 5-106 (a) - (c) clearly show the favourable influence of both the quantity of cross-sectional material A_{stif}/A_{shell} and the column height h_{stif}^{sup}/R on the GMNA failure load. As previously discussed in Section 8.1.5, there is a considerable increase in failure load if the column height is increased below the critical height (i.e. $h_{stif,crit}^{sup}/R = 1.0$). Above this height, the increase in failure load is rather limited or the failure load decreases. The influence of the quantity of cross-sectional material A_{stif}/A_{shell} to the failure load is also related to the critical height. Below this height, A_{stif}/A_{shell} has a minor influence on the failure load, while the opposite is true when the column height is equal to or higher than the critical height.

As can be seen in each graph, there are always some parallel curves shown in the same colour. These curves present the variation of the column perimeter L_{stif} and the column thickness t_{stif} for a constant quantity of cross-sectional material A_{stif}/A_{shell}. The lower curve corresponds with a column with a larger thickness t_{stif} and smaller developed length L_{stif}. When the thickness t_{stif} decreases and the developed length L_{stif} increases, while A_{stif}/A_{shell} remains constant, the curve moves upward. In other words, higher failure loads are obtained with a thinner column and a larger developed length. In general, such a column increases the degree of support (i.e. larger circumferential width d_{stif}), which is beneficial for such a locally supported silo (See Sections 8.1.2 and 8.2). Furthermore, a column with a

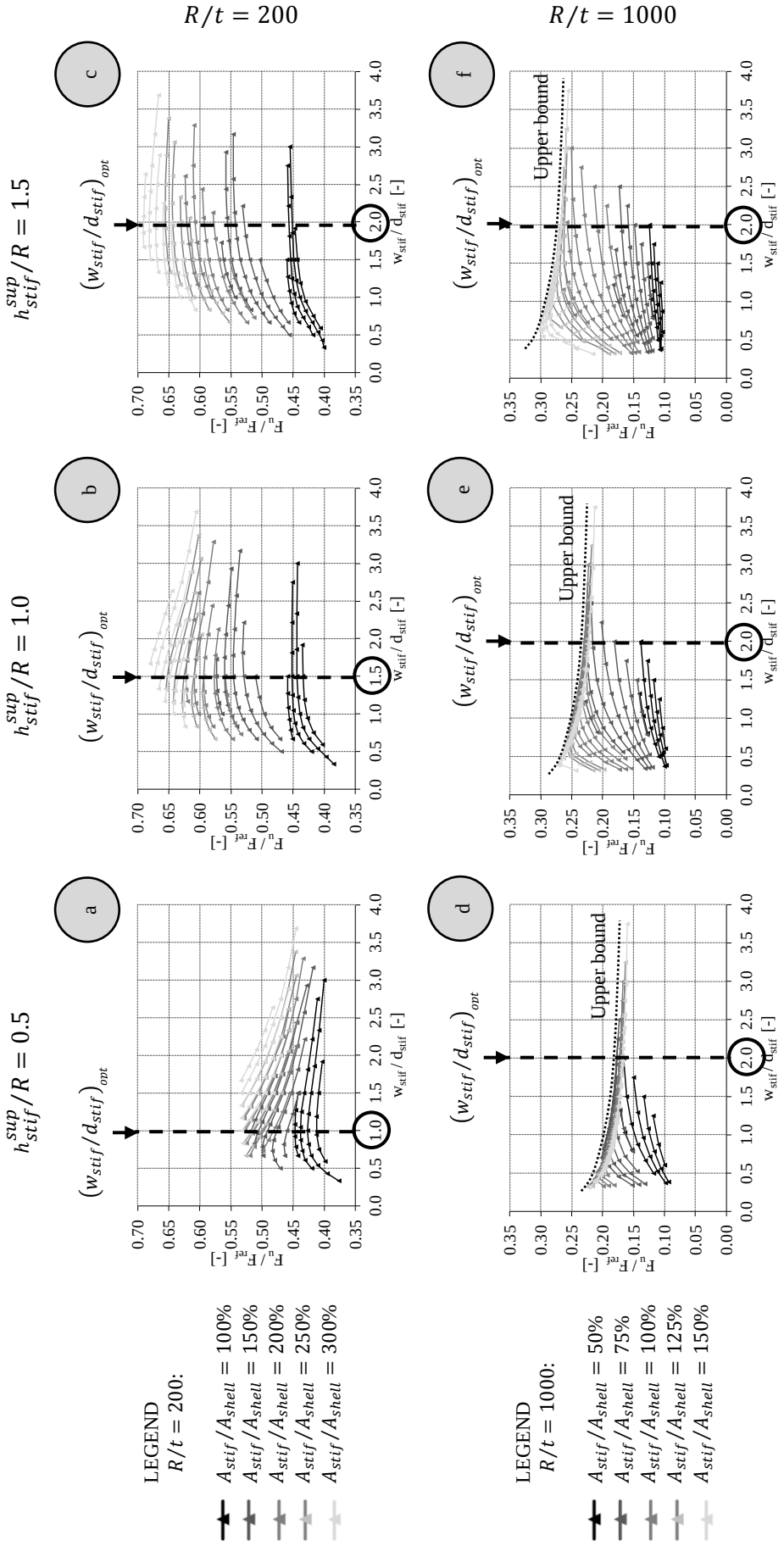

Fig. 5-106 Dimensionless GMNA failure load F_u/F_{ref} for cross-sections with variable dimensions (d_{stif}, w_{stif}, and t_{stif}) for a variable quantity of material A_{stif}/A, column height h_{stif}^{sup}/R and radius-to-thickness ratio R/t.

larger perimeter has a larger radial width w_{stif}, which is in turn advantageous for the moment of inertia of the column. As a consequence, the detrimental inwardly oriented pre-failure deformations (i.e. the flattening of the silo wall) decrease and the maximum effective yield stress is maintained (See Section 3.4), while the quantity of cross-sectional material A_{stif}/A_{shell} in the column remains constant.

Another finding is that the optimal ratio of the radial width to the circumferential width w_{stif}/d_{stif}, which corresponds with the maximal failure load, depends on a large degree on the attached column height h_{stif}^{sup}. Indeed, the best ratio of w_{stif}/d_{stif} increases as the attached column height h_{stif}^{sup} increases, as depicted in Fig. 5-106 (a) - (c) and Table 5-23. In other words, a column with a more square cross-section ($d_{stif} \approx w_{stif}$) is preferred for shorter columns, while a more slender cross-section ($d_{stif} \ll w_{stif}$) is a better solution for higher columns. This interesting finding will be explained below.

Table 5-23 The optimal ratio of the radial width to the circumferential width as a function of the attached column height.

h_{stif}^{sup}/R	$\left(w_{stif}/d_{stif}\right)_{opt}$
0.5	1.0
1.0	1.5
1.5	2.0

For less high columns, a column with a smaller ratio of w_{stif}/d_{stif} is the best solution. Such a column has a relatively small eccentricity e_{stif}, so that the supporting force has a smaller lever arm, reducing the tendency of the column to deform in inward direction. In this way, the pre-failure deformations are limited in the critical zone of the silo wall above the terminations of the column, which benefits the effective yield stress σ_y^{eff} according to the von Mises yield criterion (See Section 3.4).

However, as the height of the column increases, a column with a small ratio of w_{stif}/d_{stif}, and consequently a small eccentricity e_{stif}, no longer can prevent the larger pre-failure deformations due to its small moment of inertia I_{stif}. For that reason, it should be switched to a column with a larger moment of inertia, and consequently a larger ratio of w_{stif}/d_{stif}. Such a column with a large moment of inertia hampers the circumferential rotation of the supporting column more, reducing the pre-failure deformations. Again, these reduced deformations are advantageous for the effective yield stress according to the von Mises yield criterion (See Section 3.4).

In conclusion, for both cases, the maximum effective yield stress is obtained in the silo wall

above the terminations of the engaged columns by hampering the detrimental pre-failure deformations as much as possible. The best way to achieve this, for a constant quantity of material in the cross-section, depends on the column height, as demonstrated above. Finally, Table 5-24 presents the differences and similarities between both cases.

Table 5-24 Overview of the key characteristics between engaged columns with a variable height.

ATTACHED COLUMN HEIGHT	SMALL COLUMN HEIGHT	LARGE COLUMN HEIGHT
Optimal shape	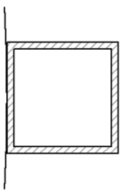	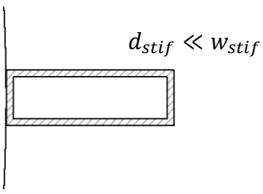
w_{stif}/d_{stif}	Small	Large
Eccentricity of the supporting columns	Relatively small	Relatively large
Circumferential rotation of the supports	Large - small moment of inertia	Small - large moment of inertia
Upper ring	No	No

Thin-walled silos

Fig. 5-106 (d) - (f) clearly demonstrate the favourable influence of both the quantity of cross-sectional material A_{stif}/A_{shell} and the column height h_{stif}^{sup}/R on the GMNA failure load. As previously discussed in Section 8.1.5, there is a considerable increase in failure load if the column height is increased below the critical height (i.e. $h_{stif,crit}^{sup}/R = 1.0$) for columns with a small quantity of cross-sectional material A_{stif}/A_{shell}. Above this height, the increase in failure load is rather limited or the failure load decreases. In contrast, for columns with a large quantity of cross-sectional material A_{stif}/A_{shell}, the failure load increases as the height of the column increases within the entire range of investigated heights (i.e. $0.5 \leq h_{stif}^{sup}/R \leq 2.0$). Indeed, this is due to the "upper bound" of the failure load increases as the column height h_{stif}^{sup} increases. The explanation for this interesting observation will be extensively discussed further, and is related to the buckling behaviour and the corresponding buckling mode. Furthermore, the influence of the quantity of cross-sectional material A_{stif}/A_{shell} to the failure load is related to the critical height $h_{stif,crit}^{sup}$. Below this height, the quantity of cross-section material A_{stif}/A_{shell} has a minor influence on the failure load, while the opposite is true when the column height is equal to or higher than the critical height $h_{stif,crit}^{sup}$.

As can be seen in each graph, there are always some parallel curves shown in the same colour.

These curves present the variation of the column developed perimeter L_{stif} and the column thickness t_{stif} for a constant quantity of cross-sectional material A_{stif}/A_{shell}. The lower curve corresponds with a column with a larger thickness t_{stif} and smaller developed length L_{stif}. When the thickness t_{stif} decreases and the developed length L_{stif} increases, while A_{stif}/A_{shell} remains constant, the curve moves upward. In other words, higher failure loads are obtained with a thinner column and a larger developed length. In general, such a column increases the degree of support (i.e. larger circumferential width d_{stif}), which is beneficial for such a locally supported silo (See Sections 8.1.2 and 8.2). Furthermore, a column with a larger perimeter has a larger radial width w_{stif}, which is in turn advantageous for the moment of inertia of the column. As a consequence, the detrimental inwardly oriented pre-buckling deformations (i.e. the flattening of the silo wall) decrease and the maximum critical buckling stress σ_{cr} is maintained (See Section 3.4), while the quantity of cross-sectional material A_{stif}/A_{shell} in the column remains constant.

Another finding is that the optimal ratio of the radial width to the circumferential width $\left(w_{stif}/d_{stif}\right)_{opt}$, which corresponds with the maximal failure load, is here always equal to 2.0, and is independent of the attached column height h_{stif}^{sup}. Note that for this choice, the "upper limit" was not taken into account. This optimal ratio is depicted in Fig. 5-106 and corresponds with a column with a more rectangular cross-section ($d_{stif} \ll w_{stif}$). In other words, such a column has a larger eccentricity e_{stif}, but more important, a larger moment of inertia I_{stif} in comparison with, for example, a column with a square cross-section. Such a column with a large moment of inertia hampers the circumferential rotation of the supporting column more. In this way, the detrimental pre-buckling deformations in the critical zone of the silo wall (i.e. in the vicinity of the top of the engaged column) are hampered more. The suppression of the flattening effect is beneficial for the critical buckling stress σ_{cr} and consequently for the buckling load (See Section 3.4).

However, if the "upper bound" is taken into account, a column with a small ratio of the radial width to the circumferential width w_{stif}/d_{stif} is preferred. This occurs only in columns with a small column height and a large cross-section.

Lastly, Table 5-25 presents an overview of the optimal shape of the cross-section of the column.

Table 5-25 Overview of the key characteristics between engaged columns with a variable height.

ATTACHED COLUMN HEIGHT	SMALL COLUMN HEIGHT AT THE "UPPER BOUND" (I.E. LARGE CROSS-SECTION)	SMALL COLUMN HEIGHT BELOW THE "UPPER BOUND" (I.E. SMALL CROSS-SECTION) LARGE COLUMN HEIGHT
Optimal shape	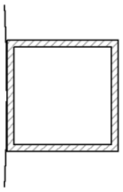 $d_{stif} \approx w_{stif}$	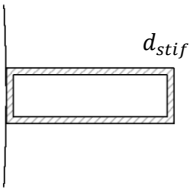 $d_{stif} \ll w_{stif}$
w_{stif}/d_{stif}	Small	Large
Eccentricity of the supporting columns	Relatively small	Relatively large
Circumferential rotation of the supports	Large - small moment of inertia	Small - large moment of inertia
Upper ring	No	No

In what follows, an explanation is given for the upper limit of the buckling load, which is clearly always present in Fig. 5-106 (d) - (f). To do this, one specific curve ($A_{stif}/A_{shell} = 100\%$; $L_{stif}/R = 0.4$) has been chosen from Fig. 5-106 (e) (i.e. $R/t = 1000$; $h_{stif}^{sup}/R = 1.0$), which reaches the "upper bound" from a certain ratio of the radial width to the circumferential width w_{stif}/d_{stif}. For reasons of clarity, the single curve is plotted again in Fig. 5-107, with the dimensionless GMNA failure load F_u/F_{ref} on the vertical axis, and the ratio w_{stif}/d_{stif} on the horizontal axis.

For the first part of the curve (i.e. $w_{stif}/d_{stif} < 1.0$), a considerable increase can be observed for the failure load as the ratio w_{stif}/d_{stif} increases. Indeed, as this ratio increases, the moment of inertia I_{stif} increases too, reducing the pre-buckling deformations, as a result of which the critical buckling stress σ_{cr} in the silo wall increases (Eq. (2-1)). Buckling will occur in the silo wall above the terminations of the engaged column (See Fig. 5-108 (a)).

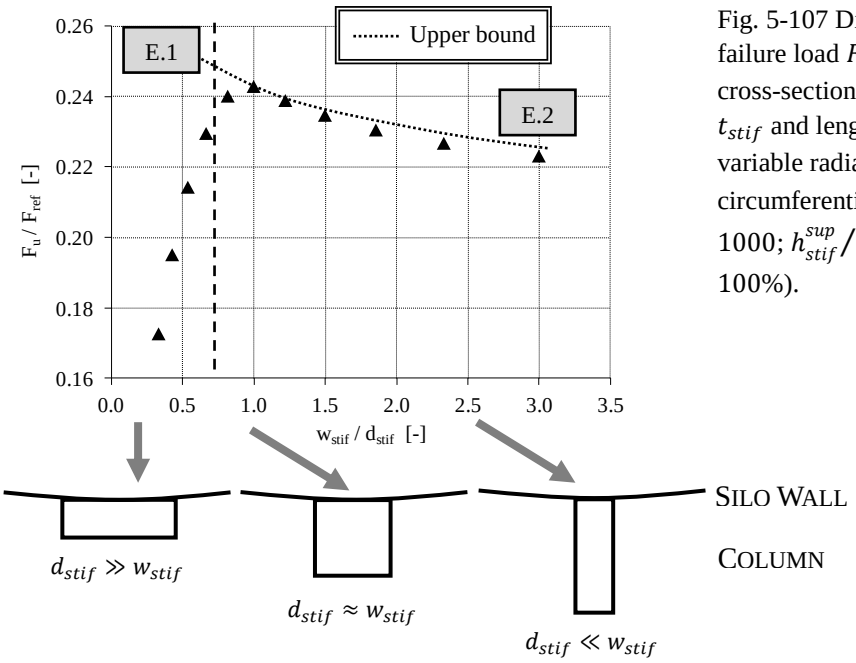

Fig. 5-107 Dimensionless GMNA failure load F_u/F_{ref} for a column cross-section with a constant thickness t_{stif} and length $L_{stif} = 0.4 \cdot R$ and variable radial width w_{stif} and circumferential width d_{stif} ($R/t = 1000$; $h_{stif}^{sup}/R = 1.0$; $A_{stif}/A_{shell} = 100\%$).

From the turning point (i.e. $w_{stif}/d_{stif} > 1.0$), the failure load starts to decrease if the ratio of the radial width to the circumferential width w_{stif}/d_{stif} increases. Furthermore, the location of buckling (i.e. the zone of highest stress concentrations) shifts to the silo wall besides the top of the engaged column, as illustrated in Fig. 5-108 (b). At that lower axial height where buckling occurs, the axial stresses are less well distributed around the circumference of the silo wall. Consequently, the critical buckling stress is reached at a lower load level.

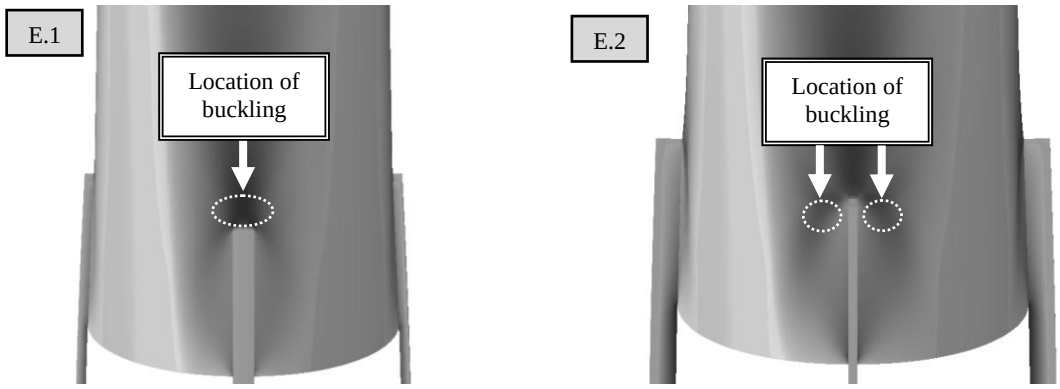

(a) For buckling mode E.1. (b) For buckling mode E.2.

Fig. 5-108 Contourplot of the axial stresses at the moment of maximum load.

Conclusions

The optimisation study has explored a wide range of engaged columns by varying all the geometrical parameters (i.e. the height and all parameters of the cross-section) to determine the optimal configuration. This study demonstrates that the choice of the dimensions of the engaged supporting columns has an important influence on the failure load and the corresponding failure behaviour. The following conclusions can be drawn:

- Within the examined range of the attached column heights ($0.5 \cdot R \leq h_{stif}^{sup} \leq 2.0 \cdot R$), this study shows that, the "attached" height has an advantageous influence on the failure behaviour, below the critical height (here: $h_{stif,crit}^{sup} = 1.0 \cdot R$). This finding is related to the better stress distribution of the axial stresses around the circumference of the silo wall. However, above the critical height ($h_{stif,crit}^{sup} > 1.0 \cdot R$), the additional column height is slightly favourable or in some cases rather unfavourable, because of the reduction of the critical stress.
- An engaged column with a height equal to the critical height and a relatively large cross-section is preferred to achieve a high failure load with a minimum amount of material.
- For all examined cases, it appears that a thin column with a large developed length is preferred over a thick column with a small developed length (for a constant quantity of material in the cross-section).
- For the thin-walled silos, a column with a large ratio of the radial width to the circumferential width (i.e. large moment of inertia) is preferred, and is independent of the column height. In contrast, in the case of thick-walled silos, the optimal shape of the cross-section of the column depends on the column height. For shorter columns, a column with a square cross-section is preferred, while a cross-section with a large ratio of the radial width to the circumferential width (i.e. large moment of inertia) is a better choice.

Finally, it is important to to notice that the above findings and conclusions are based on the range of geometrical parameters of the columns given in Table 5-22 and are not valid for engaged supporting columns with a relatively small cross-section. Such columns were excluded from this optimisation study because in these cases, premature failure occurs at relatively small load levels due to (elasto-)plastic yielding of the supporting column itself. Consequently, these supporting columns are not suitable for the engagement of locally supported cylindrical barrels.

8.4 Further explanation of the failure behaviour of column-supported silos

In fact, most of the findings deduced in Sections 8.1, 8.2, and 8.3 can be explained by the pre-failure deformations of the top of the engaged column and its vicinity in the silo wall (i.e. the critical region of failure). These inwardly oriented deformations influence the effective yield stress σ_y^{eff} for thick-walled silos (according to the von Mises criterion) or the critical buckling stress σ_{cr} for thin-walled silos (See Section 3.4), and consequently also the maximum failure load. The principle is that larger inward deformations reduce the critical stress more, both for thick-walled and thin-walled silos (and consequently also for silos with intermediate thicknesses). In other words, these disadvantageous deformations should be prevented as much as possible by application of the following measures.

- Reduction of the eccentricity of the supporting columns;
- Hampering of the circumferential rotation of the supports;
- The presence of ring stiffeners.

Engaged columns, which are for practical considerations attached to the external side of the silo wall, have a particular eccentricity relative to the silo wall. By **reducing the eccentricity** (i.e. a smaller radial width w_{stif}), two advantageous phenomena occur because of the smaller lever arm of the supporting force. Firstly, the column introduces less moments into the silo wall, which is beneficial because such silo structures are more efficient in carrying axial forces than bending moments. Secondly, the engaged column has the tendency to deform less in inward direction, because the centroid of the cross-section/supporting load is located closer to the silo wall.

The second measure is to **reduce the degree to which the circumferential rotation of the supporting columns is allowed**. This finding has already been extensively described in (Jansseune, 2013). This depends on the type of support (here: the columns are rigidly supported at the lower edge) and on the moment of inertia of the column (i.e. a larger radial width w_{stif}).

An attentive reader might have noticed that the first and second measure are contradictory. Indeed, in the case of the first measure, it is beneficial to reduce the radial width w_{stif}, while for the second measure, it is advantageous to increase the radial width w_{stif}. Depending on the silo geometry considered, a choice should be made between a column with a small eccentricity and one with a large moment of inertia. This study shows that the silo wall thickness and the column height play an important role in this choice. In general, a column with a large eccentricity is preferable for thin-walled silos and for thick-walled silo with high engaged columns. While, for thick-walled silos with engaged columns with a limited height, a column with a small eccentricity is preferred.

The third, and last, measure is the advantageous effect of **an upper ring stiffener**, which is situated just above the terminations of the engaged column. Such an intermediate ring encompasses the entire circumference and largely prevents the out-of-roundness displacements at its height. However, based on practical considerations (i.e. to reduce the costs of material and construction), it was decided only to engage the supporting columns to the silo wall, and not to provide additional ring stiffeners.

8.5 Definition of the geometrical parameters of the engaged columns for the design rule

Based on the results of the foregoing studies (Paragraphs 8.1, 8.2 and 8.3), a range is defined for all geometrical parameters of the engaged columns. The chosen values are given in Table 5-26 and Table 5-27.

Only for the range of the circumferential width d_{stif}, an additional parametric study is performed to make an appropriate choice for the final study (with $0.05 \leq d_{stif}/R \leq 0.30$). In Fig. 5-109, the influence of the ratio of the circumferential width to the cylinder radius d_{stif}/R on the dimensionless GMNA failure load F_u/F_{ref} is plotted for two different radius-to-thickness ratios R/t. Based on the magnitude of the failure load and the failure pattern, the range of d_{stif}/R is chosen for each radius-to-thickness ratio R/t separately.

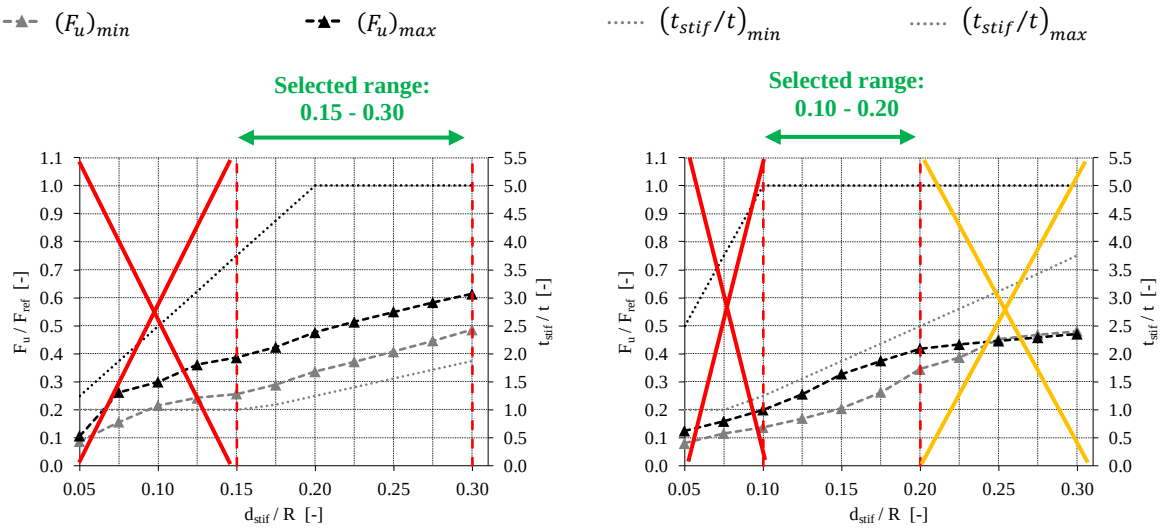

(a) $R/t = 250$. (b) $R/t = 500$.

Fig. 5-109 Dimensionless GMNA failure load F_u/F_{ref} as a function of the ratio of the circumferential width to the cylinder radius d_{stif}/R for the minimum and maximum ratio of t_{stif}/t ($n_{sup} = 4$; $w_{stif}/d_{stif} = 100\%$; $h_{stif}^{sup}/R = 2.0$; $h_{stif}^{inf}/R = 4.0$).

For small values of d_{stif}/R, premature failure will occur in the stiffened silo wall just above the local support, in the silo wall as well as in the longitudinal stiffener, which must be

avoided at all times. This range is indicated in Fig. 5-109 with red crosses and is excluded from the final study. However, very large values of d_{stif}/R are also not selected for the range of the final study (indicated with orange crosses). Indeed, when an additional increase of d_{stif}/R does not lead to an additional increase of the failure load (e.g. in $d_{stif}/R > 0.20$ in Fig. 5-109 (b)), the values of d_{stif}/R are not chosen.

Table 5-26 Geometrical parameters of the engaged columns (design rule) (part 1).

PARAMETER	VALUE(S)	DIMENSION
n_{sup}	4; 6	-
d_{stif}/R	0.05; 0.10; 0.15; 0.20; 0.25; 0.30 = f (R/t) Combinations: See Table 5-27	-
w_{stif}/d_{stif}	100; 200	%
h_{stif}^{sup}/R	0.5; 1.0; 1.5; 2.0	-
h_{stif}^{inf}/R	4.0	-
t_{stif}/t	min.; ave.; max.* = f (R/t; d_{stif}/R) Combinations: See Table 5-27	-

*: Minimum (min.), average (ave.), or maximum (max.) thickness - restrictions

Table 5-27 Geometrical parameters of the engaged columns (design rule) (part 2).

	d_{stif}/R																	
	0.05			0.10			0.15			0.20			0.25			0.30		
t_{stif}/t / R/t	min.	ave.	max.	min.	ave.	max.	min.	ave.	max.	min.	ave.	max.	min.	ave.	max.	min.	ave.	max.
100	-	-	-	-	-	-	-	-	X	X	-	X	X	-	X	X	X	X
200	-	-	-	-	-	-	-	-	X	X	X	X	X	X	X	X	-	X
250	-	-	-	-	-	-	-	X	X	X	X	X	X	X	X	X	-	X
333.3	-	-	-	-	X	X	X	X	X	X	X	X	X	-	X	X	-	X
500	-	-	-	X	X	X	X	X	X	X	-	X	-	-	-	-	-	-
666.6	-	-	-	X	-	X	X	-	X	X	-		-	-	-	-	-	-
1000	-	-	-	X	-	X	X	-		-	-	-	-	-	-	-	-	-

Remark: the average (ave.) thickness is calculated only if the difference between the minimum (min.) and the maximum (max.) thickness is sufficiently large.

9 Imperfections

This section is composed of two main sections. In Section 9.1, the influence is investigated of the orientation, the shape, and the fabrication tolerance quality class (i.e. the equivalent initial amplitude of the imperfection) to the failure behaviour and load. From this part, it will appear that **an inwardly oriented type A weld depression** generally is a relatively adverse imperfection shape. In the next section (i.e. Section 9.2), the critical meridional position will be determined of such a circumferential weld depression. Finally, some conclusions are drawn.

9.1 Imperfection sensitivity study

The purpose of the imperfection sensitivity study is to choose an appropriate imperfection shape (and orientation) which can be used during the development of the design rules. In this study, the influence of 14 different imperfections is investigated on the failure behaviour by means of GMNIA analyses. Seven different imperfection shapes (i.e. LBM, NBM, PDS - MAX, PDS - MID, PDS - MIN, WD type A, and WD type B) are considered, both inward and outward (See Table 2-14) and for three amplitudes according to the (EN 1993-1-6, 2007). For more information about the orientation, the shape, and the amplitude of equivalent imperfections, the reader is referred to Section 6 in Chapter 2.

The radius-to-thickness ratio R/t and the height h/R (high and short silos) of the cylindrical barrel were varied. All geometrical parameters of both stiffening configurations (i.e. U-shaped stiffeners and engaged columns) are mentioned in Table 5-28. The default geometrical parameters were used for the ring stiffeners. In total, 28 different geometries were examined. All parts have a standard elasto-plastic material behaviour with a yield stress σ_y equal to 235MPa.

Because the different imperfection shapes are frequently abbreviated in the following discussion, their name and abbreviation are repeated here again: the linear bifurcation mode or LBM, the non-linear bifurcation mode or NBM, the post-buckling deformed shapes or PDS, and the weld depression or WD. For the complete discussion of the different imperfection shapes, the reader is referred to Section 6.3 (Chapter 2). Finally, Table 2-14 gives an overview of the different geometrical imperfection shapes and the corresponding abbreviations. Furthermore, it is important to note that, as a simplification, only a single circumferential weld depression will be investigated, excluding possible interaction between neighbouring weld depressions.

Table 5-28 Geometrical parameters of the cylindrical barrel, the stiffening, and the supporting configuration (imperfection sensitivity study).

COMPONENT	PARAMETER	VALUE(S)	DIMENSION
SILO	R/t	$100;\ 200; 250; 333.3; 500; 666.6; 1000$	-
	h/R	$2.0;\ 10.0$	-
STIFFENERS	n_{sup}	4	-
	Type(s)	U-shaped longitudinal stiffeners (U.S.) Engaged columns (E.C.)	
	d_{stif}/R	$R/t = 100;\ 200; 250; 333.3$: 0.30 $R/t = 500; 666.6;\ 1000$: 0.20	-
	w_{stif}/d_{stif}	U.S.: 25 E.C.: 100	%
	h_{stif}^{sup}/R	$h/R = 2.0$: 1.0 $h/R = 10.0$: 1.0	-
	h_{stif}^{inf}/R	U.S.: / E.C.: 4.0	-
	t_{stif}/t	$R/t = 100;\ 200; 250; 333.3$: max. * $R/t = 500; 666.6;\ 1000$: min. *	-

*: Minimum (min.), average (ave.), or maximum (max.) thickness - restrictions

9.1.1 Influence of the imperfection orientation

In this section, the influence of the imperfection orientation is investigated by comparing the failure load of an imperfect silo with an inward imperfection shape F_{inward} with the failure load of an imperfect silo with the corresponding outward imperfection shape $F_{outward}$. In Fig. 5-110, the dimensionless ratio $F_{inward}/F_{outward}$ is plotted on the vertical axis for all imperfection shapes and for all 28 geometries, ordered on the horizontal axis according to the radius-to-thickness ratio R/t (4 cases for each thickness t).

From this figure, two trends can be identified. First, the ratio $F_{inward}/F_{outward}$ is usually smaller than the unity (only a few exceptions), indicating that inward imperfections are indeed more disadvantageous than outward imperfections. This finding is expected as mentioned in the Paragraph Orientation in Section 6.2 of Chapter 2. Secondly, a general downward trend can be noticed for the value $F_{inward}/F_{outward}$ as a function of the radius-to-thickness ratio R/t on the horizontal axis. In other words, thin-walled silos (which fail by elastic buckling) are more sensitive to the choice of the imperfection orientation than thick-walled silos (which fail by elasto-plastic buckling), because inward imperfections seem to be more detrimental than outward imperfections when the influence of plasticity decreases and elasticity becomes more important to the failure behaviour and load.

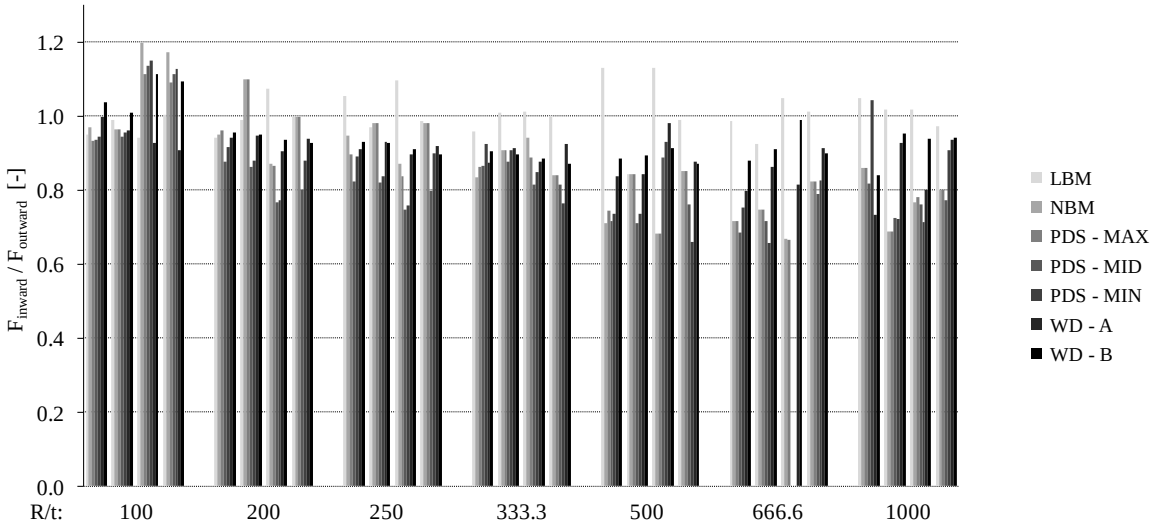

Fig. 5-110 The ratio of the failure load of an imperfect silo with an inward imperfection shape divided by the failure load of an imperfect silo with the corresponding outward imperfection shape for all imperfection shapes and for all 28 cases, ordered according to the radius-to-thickness ratio R/t (quality class A).

9.1.2 Influence of the imperfection shape

Imperfection shapes

In Fig. 5-111 and Fig. 5-112, the different imperfection shapes are illustrated for two geometries, respectively for a thick-walled (i.e. $R/t = 200$) and for a thin-walled silo (i.e. $R/t = 1000$). The contourplots show the radial deformations on a certain scale factor. Inward deformations are coloured in blue, outward deformations in red. From these two illustrative examples, the following findings can be derived.

- In most cases, the largest deformations occur in the (unstiffened) silo wall, while the stiffener configuration undergoes smaller deformations. Nevertheless, this does not mean that the deformations of the stiffeners are zero. For example in Fig. 5-111 (b), it is clearly visible that (the top of) the U-shaped stiffener is directed inwardly;
- In general, the deformations are inwardly oriented in the region above the local supports (both the silo wall and the stiffeners) and are outwardly oriented in the silo wall between the stiffeners (NBM and PDS);
- Different shapes are obtained for the linear LBM and the non-linear NBM pattern, which means that geometric non-linearity influences the deformations and the (failure) behaviour;
- For this study, three different post-buckling deformed shapes are taken into account (i.e. PDS - MAX, PDS - MID, and PDS - MIN), each time at different moment **after** failure (See Section 6.3 in Chapter 2). For these two geometries, it

can be clearly seen that the post-buckling deformed shapes are evolving after failure. In fact PDS - MAX is taken just after failure, as a result of which the deformations at that moment largely correspond with the deformations before failure. For PDS - MID and PDS - MIN, the occurring deformations are much larger than the deformations before failure (e.g. the formation of buckles) and are concentrated in more critical regions. By comparing Fig. 5-111 (c) to (e), the height of the regions of elongated deformations is decreasing after elasto-plastic collapse. From Fig. 5-112 (c) to (e), secondary buckles are developing after elastic buckling.

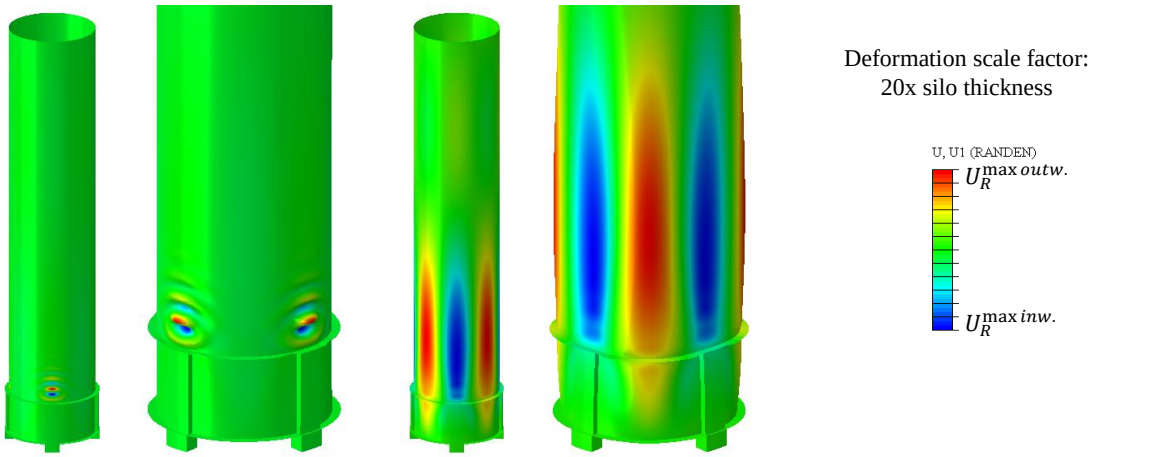

(a) LBM. (b) NBM.

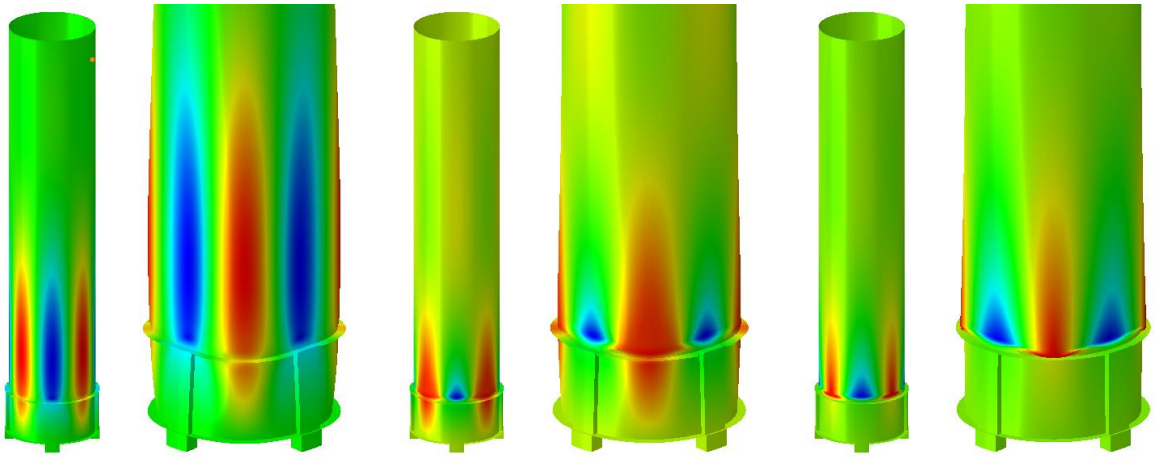

(c) PDS - MAX. (d) PDS - MID. (e) PDS - MIN.

Fig. 5-111 Plots of the different imperfection shapes ($R\ /t = 200$; $h\ /R = 10.0$; $d_{stif}/R = 0.30$; $w_{stif}/d_{stif} = 0.25$; $t_{stif}/t =$ max.; $h_{stif}^{sup}/R = 1.0$).

- For both cases, the NBM pattern (obtained from a GNA calculation just after failure) looks very similar to the PDS - MAX pattern (obtained from a GMNA calculation just after failure). For the thin-walled silo (with $R/t = 1000$), this is expected since plasticity plays no role in the failure behaviour, as a result of which a GNA and a GMNA calculation lead to very similar results, such as the buckling load but also the deformations and the stresses. For the thick-walled silo (with $R/t = 200$), plasticity plays a major role in the failure behaviour, as a result of which a GNA (with a pure elastic material behaviour, without yielding) and a GMNA calculation (with an ideal elasto-plastic material behaviour, with $\sigma_y = 235\text{MPa}$) lead to very different results, such as the failure load and the stress level. Nevertheless, the deformation patterns just after failure are very similar to each other.

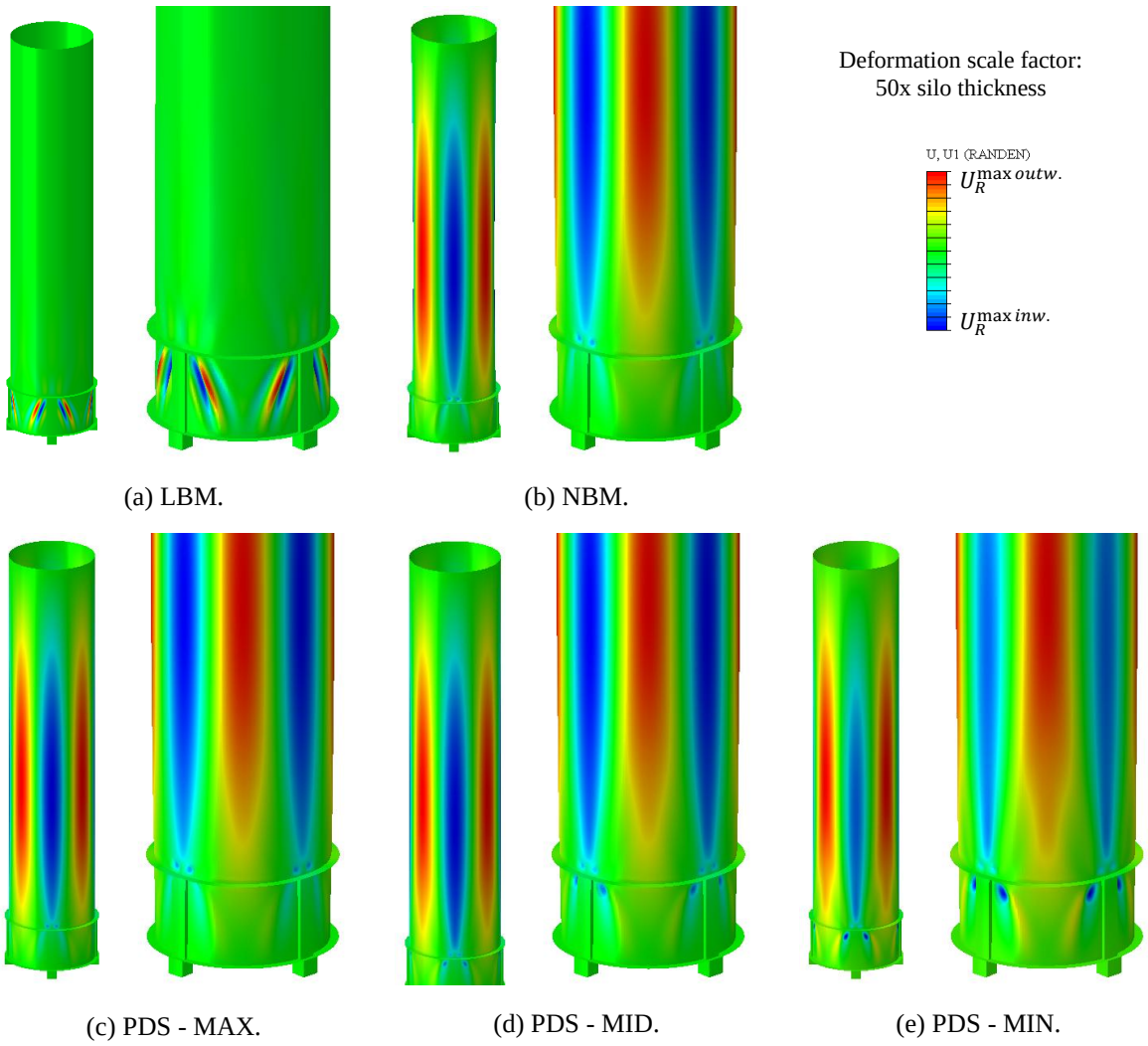

(a) LBM. (b) NBM.

(c) PDS - MAX. (d) PDS - MID. (e) PDS - MIN.

Fig. 5-112 Plots of the different imperfection shapes ($R/t = 1000$; $h/R = 10.0$; $d_{stif}/R = 0.20$; $w_{stif}/d_{stif} = 0.25$; $t_{stif}/t = \text{min.}$; $h_{stif}^{sup}/R = 1.0$).

To conclude, very different imperfection shapes are obtained for both cases. Clearly, the deformation pattern depends on many factors. Of course, the geometry of the barrel, the stiffeners, etc. will influence the deformations. Additionally, the deformation pattern (LBM, NBM, and PDS) also depends on the type of shell analysis (LBA, GNA, and GMNA, respectively) and on the considered time of the numerical simulation of which the pattern is taken (compare PDS - MAX/MID/MIN).

Since the imperfection patterns display differences in shape, they also will exhibit different responses before and during failure when they are applied as "equivalent" imperfection shape (i.e. small initial deviations perpendicular to the perfect shell wall) in a GMNIA calculation. Consequently, different responses will result in different imperfection sensitivities. However, solely on the basis of the shape, it is impossible to predict the exact impact a pattern will have on the failure behaviour and load.

In Fig. 5-113, the shapes of weld depressions type A (upper row) and type B (lower row) are illustrated for different radius-to-thickness ratios R/t (200; 500; 1000). Each time, the shape is depicted for the three tolerance quality classes (A, B, and C). On the vertical axis of each graph, the dimensionless deviation w/t is plotted which corresponds with the ratio of the deviation measured perpendicular to the perfect silo wall w to the silo wall thickness t. On the horizontal axis, the dimensionless distance x/R is plotted in which x is equal to the distance to the centre of the weld depression and R is the cylinder radius.

A WD type A (rotationally stiff during cooling; $k = 1$ in Eq. (2-44)) and a WD type B (rotationally free during cooling; $k = 0$ in Eq. (2-44)) have in common that the largest deformations occur in the middle of the imperfection (i.e. $x/R = 0$) and the deviation shrinks as a sine when the distance to the centre x/R increases. The shape of both types also displays a number of differences. The top of a type A WD is rather curved, while a type B WD has rather a sharp tip. Furthermore, the curvature near the tip is different: type A is convex and type B is concave (viewed from the upper side of the figures).

When the radius-to-thickness ratio R/t increases, two findings can be observed concerning the shape. Firstly, the ratio of the maximum deviation w_{max} to the silo wall thickness t increases. In other words, relative to the thickness of the silo wall, the deviations w are larger for thin-walled silos than for thick-walled silos (not in absolute values). Secondly, the distance between the maximum deviation at the centre and the "secondary" maximum deviations decreases.

To conclude, the shape of a weld depression is not "fixed" and depends on different parameters (See Eq. (2-44)), such as the maximum amplitude δ_{max} (related to the adopted quality class of the structure and the corresponding quality parameter Q), the shape factor k ($0 \leq k \leq 1$), and the half-wavelength λ (here: $\lambda = \lambda_b$). Furthermore, both the maximum

deviation δ_{max} (Eqs. (2-46) to (2-48)) and the half-wavelength λ (Eq. (2-45)) are dependent on the radius-to-thickness ratio R/t of the cylindrical barrel.

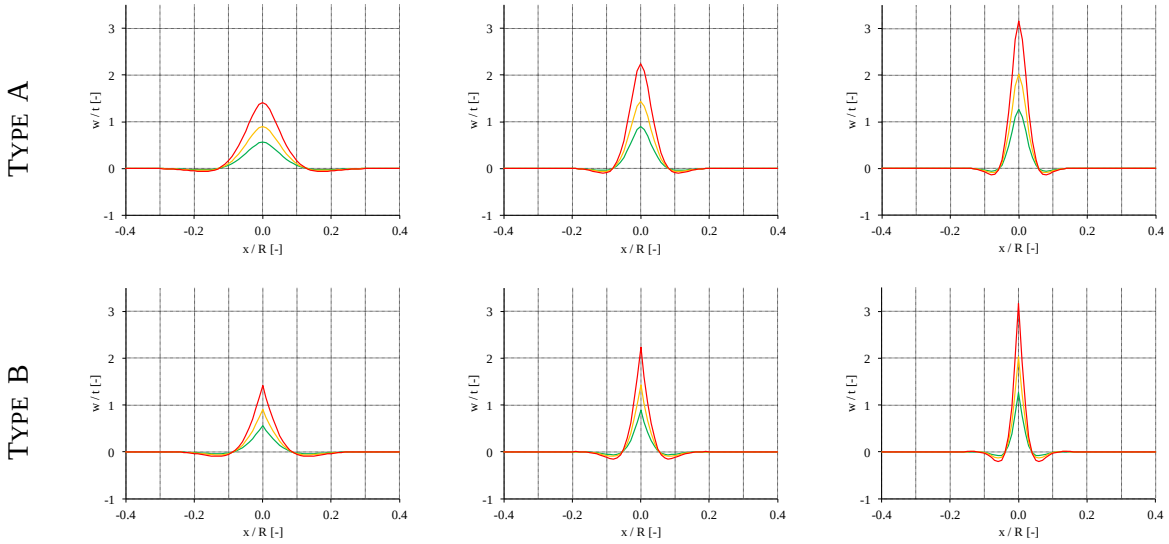

(a) $R/t = 200$. (b) $R/t = 500$. (c) $R/t = 1000$.

Fig. 5-113 The shape of a weld depression type A (upper row) and type B (lower row) for three fabrication tolerance classes defined in (EN 1993-1-6, 2007) with a variable radius-to-thickness ratio R/t.

These weld depressions will be applied over the entire circumference of the unstiffened silo wall above the top of the U-shaped stiffeners/engaged columns (See detail in Fig. 5-119).

Imperfection sensitivity study

For the previously described **inward imperfections with fabrication quality class A**, the results of the exploratory imperfection sensitivity study are depicted in Fig. 5-114. (Similar results are obtained for the imperfections with fabrication quality class B or C).

To be able to evaluate all results and to quantify the (negative) influence of an imperfection pattern, the failure load of an imperfect silo F_{GMNIA} must always be evaluated to the same reference resistance, more specifically with the failure load of the perfect silo wall F_{GMNA}. This ratio F_{GMNIA}/F_{GMNA} is plotted on the vertical axis. However, due to the large number of calculations, it is not possible to present the effective ratio of F_{GMNIA}/F_{GMNA} for each combination of geometry (28), imperfection shape (7), and amplitude (3). Therefore, an "averaged" value of the dimensionless failure load F_{GMNIA}/F_{GMNA} is plotted on the vertical axis of Fig. 5-114, which is obtained by taking the average of all effective ratios of F_{GMNIA}/F_{GMNA} for the cases which have the same radius-to-thickness ratio R/t, imperfection shape, and amplitude. On the horizontal axis, either the radius-to-thickness ratio R/t (Fig. 5-114 (a)) or the imperfection type (Fig. 5-114 (b)) is displayed.

Before proceeding to the discussion of Fig. 5-114, it may be mentioned that, for most

imperfection shapes, it is expected that the ratio F_{GMNIA}/F_{GMNA} will be smaller than the unity, meaning that the failure load of the imperfect structure is smaller than for a perfect structure (i.e. $F_{GMNIA} < F_{GMNA}$). Furthermore, the smaller the ratio F_{GMNIA}/F_{GMNA} (< 1) is for a specific imperfection pattern, the **more sensitive the structure** is for this imperfection pattern, **or** in other words, the **more detrimental the imperfection pattern** is for the structure.

From Fig. 5-114, the following findings can be derived.

- As expected, the (average) values of F_{GMNIA}/F_{GMNA} are always smaller than one, for all imperfection shapes and for all fabrication tolerance quality classes.
- In general, the ratio F_{GMNIA}/F_{GMNA} decreases and thus the imperfection sensitivity increases when the radius-to-thickness ratio R/t increases. In other words, the buckling load of a thin-walled silo (with a larger slenderness λ) is more susceptible to imperfections than the (elasto-)plastic failure load of a thick-walled silo (with a smaller slenderness λ).
- The linear buckling mode (LBM) seems to be more detrimental than the non-linear buckling mode (NBM), especially for thick-walled silos.
- The imperfection sensitivity is different for each post-buckling deformed shape (PDS). The PDS - MID is the most severe pattern, shortly followed by PDS - MIN. PDS - MAX is a less severe pattern, and its sensitivity has the same order of magnitude as the NBM pattern. The fact that both (i.e. PDS - MAX and NBM), in Fig. 5-111 and Fig. 5-112, had the same shape is thus no coincidence.
- The weld depression type A (WD - A) seems to be more severe than a weld depression type B (WD - B).

Overall, the imperfections can be arranged from less to more detrimental as follows: the non-linear buckling mode (NBM) together with the post-buckling deformed shape just after failure (PDS - MAX), the linear buckling mode (LBM), the third post-buckling deformed shape after failure (PDS - MIN), the second post-buckling deformed shape after failure (PDS - MID), a weld depression type B (WD - B), and lastly a weld depression type A (WD - A).

It is important to note that this order of importance was determined on the basis of a limited number of geometries (28) with a variable stiffening and supporting configuration (2: U-shaped stiffeners or engaged columns), a variable radius-to-thickness ratio R/t of the cylindrical barrel (7), and a variable silo height (2). To verify whether this trend also extends to other locally supported silos, GMNIA calculations with variable imperfection patterns must be done and investigated for much more stiffening configurations (variable shape of the cross-section and height of the longitudinal stiffeners/engaged columns).

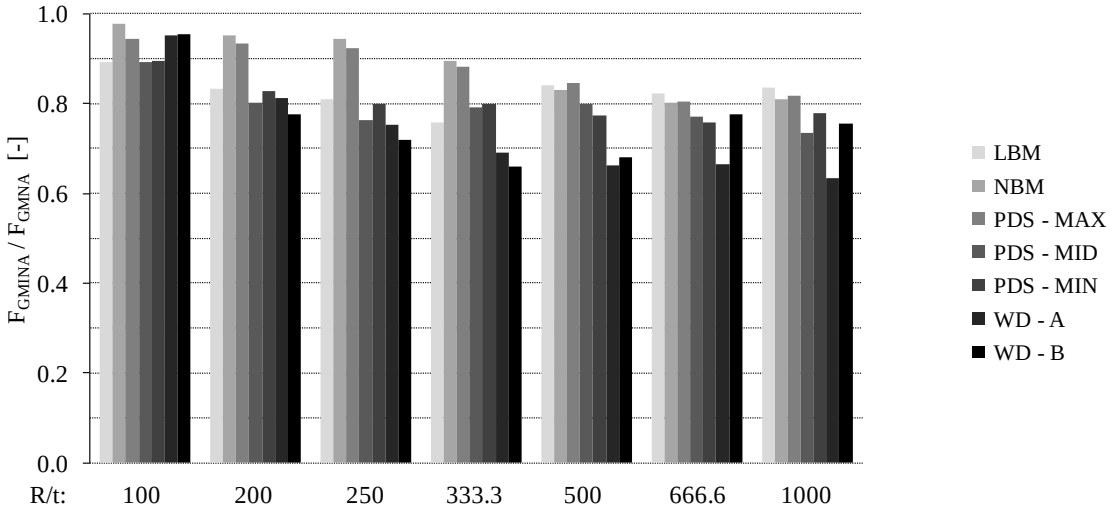

(a) Ordered according to the radius-to-thickness ratio R/t.

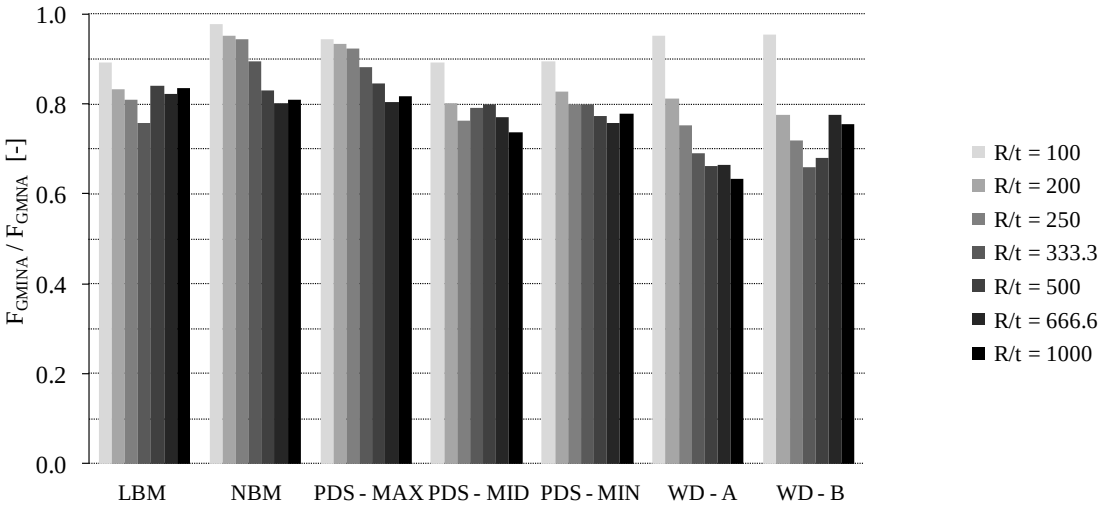

(b) Ordered according to imperfection shape.

Fig. 5-114 The averaged ratio of the failure load of an imperfect silo with an inwardly oriented imperfection shape F_{GMNIA} divided by the failure load of a perfect silo F_{GMNA} for all imperfection shapes and for all geometries (Class A).

9.1.3 General comment

Because of the large number of parameters to be investigated in this study (different shapes, orientations, and amplitudes) and in the previous numerical studies (Sections 1 to 8 in this chapter), and to keep the number of calculations within workable limits, a number of choices had to be made at the beginning of each individual study, such as which parameters are varied and which ones are kept constant, which values are given to the different parameters, etc.

In retrospect, for this imperfection sensitivity study, it might have been better to carry out calculations for even more geometries, but maybe that was at the cost of other interesting results. That said, I want to indicate that, during my PhD, I had to consider constantly how

extensive something should be investigated. Moreover, the unraveling process of the investigation to the failure behaviour of locally supported silos is complicated because a lot of different parameters influence the failure behaviour and also each other's influence on the failure behaviour. As a consequence, as the understanding to the behaviour increases, the parameters adopted in the beginning evolve during the PhD and some studies have been performed twice: a first time with the initial scope of parameters and a second time within the scope of parameters defined for the final design rule.

9.1.4 Influence of the imperfection amplitude

In the first part of this section, the influence of the initial amplitude of all **inward "equivalent" imperfection shapes** to the failure load is investigated (i.e. LBM, NBM, PDS - MAX, PDS - MID, PDS - MIN, WD type A, and WD type B). Afterwards, the influence of the amplitude of an inward weld depression (type A) to the failure behaviour is investigated more in detail.

All imperfection shapes

In Fig. 5-115, the influence of the equivalent imperfection amplitude on the failure load is presented for four geometries (4/28). The ratio of the failure loads of the imperfect and the perfect silo wall F_{GMNIA}/F_{GMNA} is plotted on the vertical axis. On the horizontal axis, the dimensionless amplitude δ_{max}/t is shown where δ_{max} is the "equivalent" imperfection amplitude (which is related to the fabrication tolerance quality class as defined in (EN 1993-1-6, 2007)) and t the silo wall thickness. Section 6.4 of Chapter 2 contains more information about the calculation of the amplitude of equivalent imperfections.

The failure load of an imperfect silo is usually less than the failure load of a perfect silo ($F_{GMNIA}/F_{GMNA} < 1$). Furthermore, the reduction of the GMNIA failure load for an arbitrary imperfection shape increases when the quality of the silo decreases and the imperfection amplitude δ_{max} increases.

The curve of a type A weld depression (indicated with a red arrow) generally lies below the curves representing the other imperfections. In other words, an inward type A weld depression appears to be relatively disadvantageous for all amplitudes.

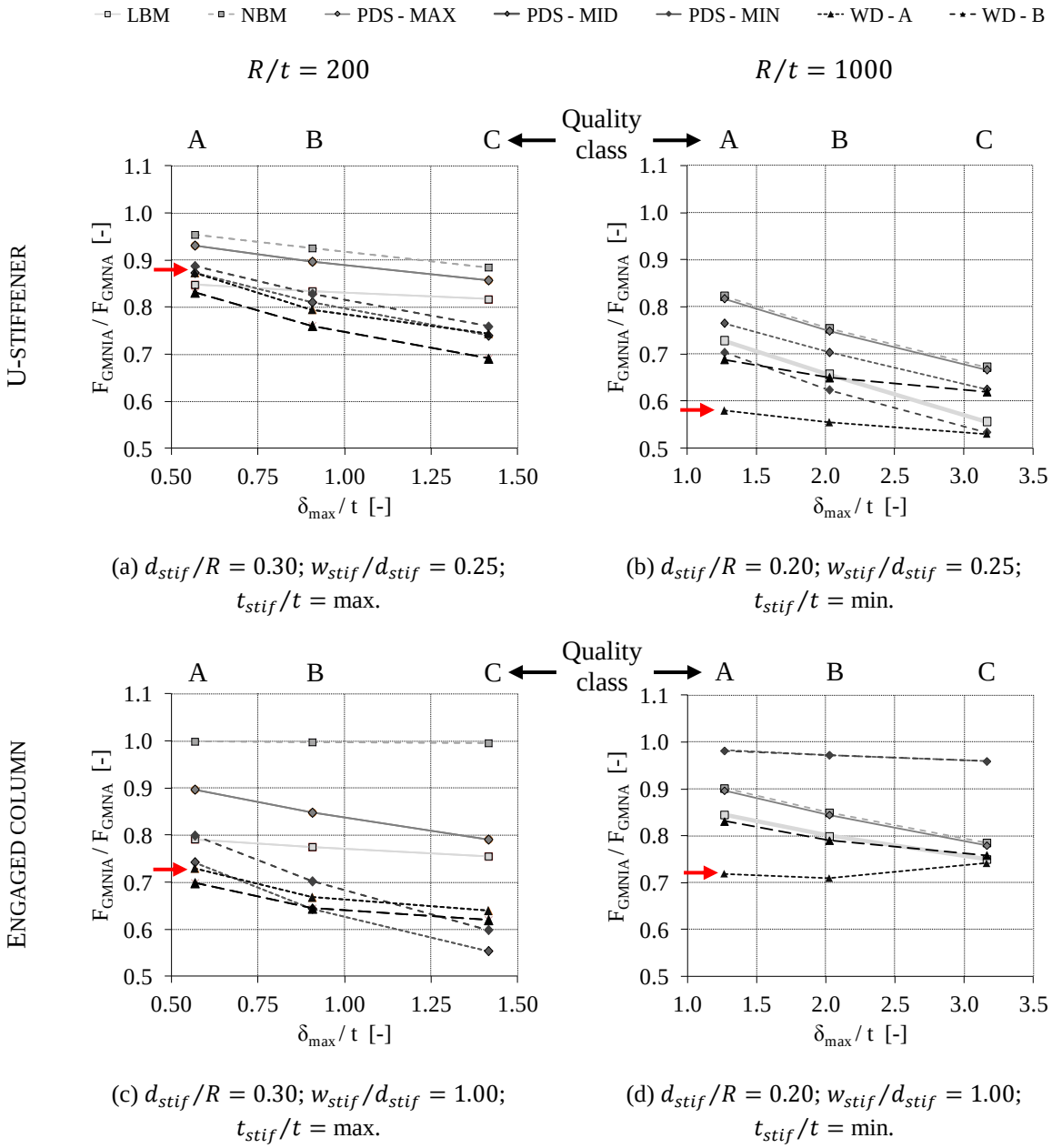

(a) $d_{stif}/R = 0.30$; $w_{stif}/d_{stif} = 0.25$; $t_{stif}/t =$ max.

(b) $d_{stif}/R = 0.20$; $w_{stif}/d_{stif} = 0.25$; $t_{stif}/t =$ min.

(c) $d_{stif}/R = 0.30$; $w_{stif}/d_{stif} = 1.00$; $t_{stif}/t =$ max.

(d) $d_{stif}/R = 0.20$; $w_{stif}/d_{stif} = 1.00$; $t_{stif}/t =$ min.

Fig. 5-115 Imperfection sensitivity for inwardly oriented imperfection shapes with a variable amplitude (quality class A, B, and C) (high silo: $h/R = 10.0$; $h_{stif}^{sup}/R = 1.0$).

Inward weld depression (type A)

In the next section, the disadvantageous effect of an inward weld imperfection (and its amplitude) will be unravelled for two specific geometries with U-shaped stiffeners, more particularly for a thick-walled silo (the geometry of Fig. 5-115 (a)) and a thin-walled silo (the geometry of Fig. 5-115 (b)). Since the weld depression largely influences the stress pattern and the location of failure, its effect is illustrated by means of (contour)plots of the axial stress σ_x distribution at the moment of maximum load.

For the perfect silo, failure occurs just above the terminations of the U-shaped stiffener. The thick-walled silo fails by elasto-plastic yielding (the yielding region corresponds with the black shaded area in Fig. 5-116 (a)), while the thin-walled silo fails by pure elastic buckling (the buckles are visible in Fig. 5-117 (a)). Furthermore, for both cases, the level of compressive stresses decreases to the meridional plane halfway between the longitudinal stiffeners, and the entire thickness of the silo wall is compressed in axial direction (i.e. $\sigma_x < 0$).

In contrast, when a weld depression is introduced in the unstiffened silo wall just above the terminations of the stiffener/column, the location of failure shifts to the axisymmetric weld depression, for the thick-walled silo (See Fig. 5-116 (b) and (c)) as well as for the thin-walled silo (See Fig. 5-117 (b) and (c)). At the centre of the WD, which is inwardly oriented, compression occurs on the exterior side (Ce), while tension occurs on the interior side of the silo wall (Ti). In the adjacent regions above and below the point of maximum inward deviation, the opposite situation is obtained: tension on the exterior side (Te), and compression on the interior side of the silo wall (Ci).

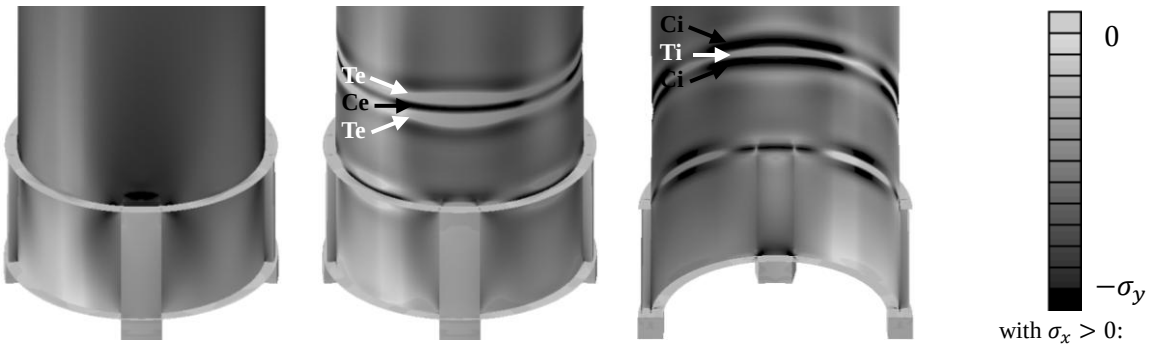

(a) Perfect silo. (b) Imperfect silo (Class C) - Exterior. (c) Imperfect silo (Class C) - Interior.

Fig. 5-116 Contourplot of the axial stresses σ_x at the moment of maximum load ($R/t = 200$; $h/R = 10.0$; $d_{stif}/R = 0.30$; $w_{stif}/d_{stif} = 0.25$; $t_{stif}/t =$ max.; $h_{stif}^{sup}/R = 1.0$).

Another finding is that, in spite of the thin-walled nature of the cylindrical barrel (i.e. $R/t = 1000$), yielding occurs in the vicinity of the weld depression (i.e. the black region in Fig. 5-117 (b) and (c)). However, this phenomenon only takes place over a part of the cross-section, namely at the exterior side at the WD centre (Ce) and the interior side in the adjacent regions just above and below the WD centre (Ci).

To conclude, Fig. 5-118 gives an overview of the sign of the axial stresses in the vicinity of an inward weld depression type A.

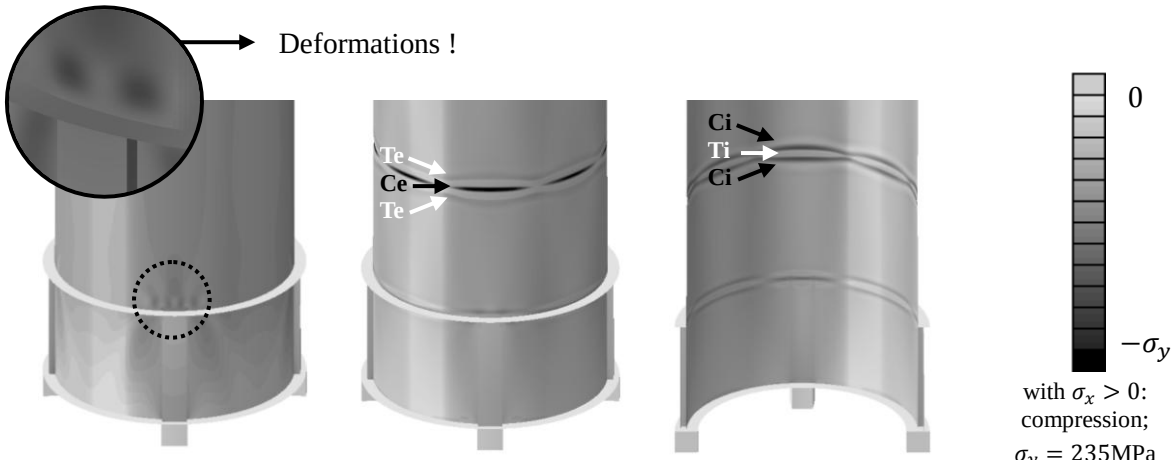

(a) Perfect silo. (b) Imperfect silo (Class C) - Exterior. (c) Imperfect silo (Class C) - Interior.

Fig. 5-117 Contourplot of the axial stresses σ_x at the moment of maximum load ($R/t = 1000$; $h/R = 10.0$; $d_{stif}/R = 0.20$; $w_{stif}/d_{stif} = 0.25$; $t_{stif}/t =$ min.; $h_{stif}^{sup}/R = 1.0$).

Next, the influence of the magnitude of the maximum inward deviation of the WD on the stress level will be discussed by means of plots of the dimensionless axial stress σ_x/σ_y at the moment of maximum load along paths in circumferential direction (See Fig. 5-120 and Fig. 5-121). The axial stress distribution is plotted along four different paths: at the centre of the point of maximum deviation (i.e. path (I) in Fig. 5-119) and just below the centre of the point of maximum deviation (i.e. path (II) in Fig. 5-119), and both on the exterior and interior side of the silo wall.

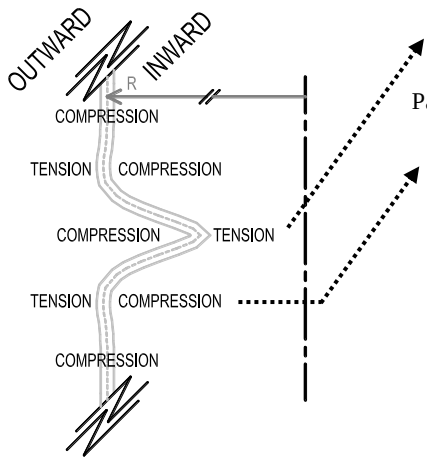

Fig. 5-118 Regions of compression ($\sigma_x < 0$) and tension ($\sigma_x > 0$) near the weld depression.

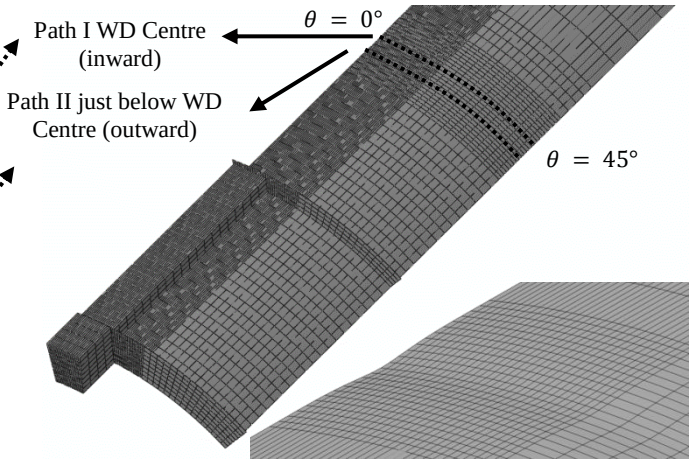

Fig. 5-119 The paths near and close-up of the weld depression.

In Fig. 5-120, the stress distribution is investigated for the thick-walled silo. Initially, if no imperfections are present, the entire thickness and circumference of the silo is compressed in axial direction (in very point: $\sigma_x < 0$).

When a type A inward weld depression Class A is introduced, the magnitude of the axial compressive stress increases at the exterior side of the WD centre (Ia) and at the interior side above and below the WD centre (IVa) to the effective yield stress σ_y^{eff}. This can be explained by the region of yielding shifts from the silo wall just above the stiffener (See Fig. 5-116 (a)) to the weld depression (See Fig. 5-116 (b) and (c)). Furthermore, the compressive axial stresses ($\sigma_x < 0$) turn into tensile axial stresses ($\sigma_x > 0$) at the interior side of the WD centre (IIa) and at the exterior side above and below the WD centre (IIIa).

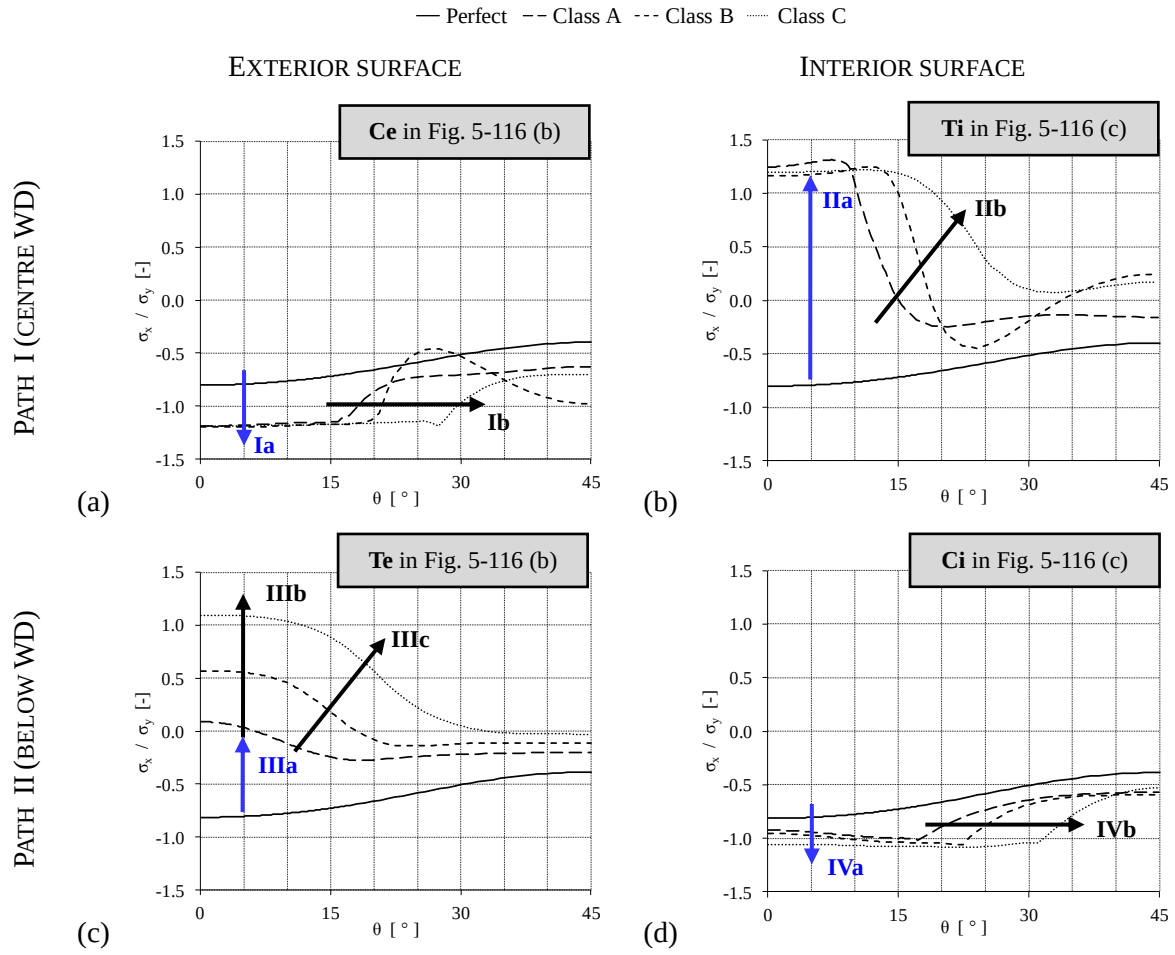

Fig. 5-120 Distribution of the dimensionless axial stress σ_x/σ_y at the moment of maximum load ($R/t = 200$; $h/R = 10.0$; $d_{stif}/R = 0.30$; $w_{stif}/d_{stif} = 0.25$; t_{stif}/t = max.; $h_{stif}^{sup}/R = 1.0$).

As the amplitude δ_{max} of the inward deviation increases further (i.e. Class A→B→C), the region of yielding in compression ($\sigma_x = \sigma_y^{eff}$) expands in circumferential direction (Ib and IVb), the amplitude of the tensile stresses increases at the exterior side above and below the WD centre (IIIb), and the region of tensile stresses expands in circumferential direction (IIb and IIIc).

In other words, due to the presence of a weld depression, the silo wall is no longer compressed over its entire thickness. Indeed, the larger the amplitude δ_{max} of the weld depression, the more the cross-section of the silo wall in its vicinity is under tension (Ti and Te in Fig. 5-116). As a result, the effective yield stress σ_y^{eff} in the compressive part (Ce and Ci in Fig. 5-116) (and thus failure) is reached sooner at a lower compressive load, despite the area of yielding in the compressive part expands (Ib and IVb).

In Fig. 5-121, the dimensionless axial stresses σ_x/σ_y are plotted for five different positions across the silo wall thickness along the paths shown in Fig. 5-119, and both for the thick-walled silo and the thin-walled silo with quality class C. In addition, the "average" axial stress $\sigma_{x,ave}$ over the silo wall thickness is calculated using formula (5-24), taking into account the axial stresses over the entire silo wall thickness.

$$\sigma_{x,ave} = \frac{1}{4} \cdot [\, 0.5 \cdot \sigma_O + \sigma_{MO} + \sigma_M + \sigma_{MI} + 0.5 \cdot \sigma_I \,] \qquad (5\text{-}24)$$

From Fig. 5-121, it can be seen that the average axial compressive stress $\sigma_{x,ave}^{C}$ of an imperfect silo is over the entire circumference smaller than the axial compressive stress σ_x^0 of a perfect silo (at the same axial height). This can be attributed to the weld depression (the only difference). In its vicinity, the cross-section of the silo wall is only partially compressed in contrast to a perfect silo wall, which is fully compressed. Because the imperfect silo wall is partially under tension, the $\sigma_{x,ave}^{imp}$ decreases due to the presence of axial tensile stresses. Moreover, it appears that, as the WD amplitude increases, both the amplitude and the region of tensile stresses increase. Furthermore, since in Fig. 5-121 only a 45 degree segment of the silo circumference is shown, the actual effect of the stress difference between a perfect and an imperfect silo will be eight times larger.

In conclusion, a WD introduces axial tensile stresses ($\sigma_x > 0$) in its vicinity of which magnitude and region largely depend on the amplitude δ_{max} of the WD (i.e. the quality class). In other words, the silo wall is only partially compressed. As a result, the critical load is reached at a smaller compression load.

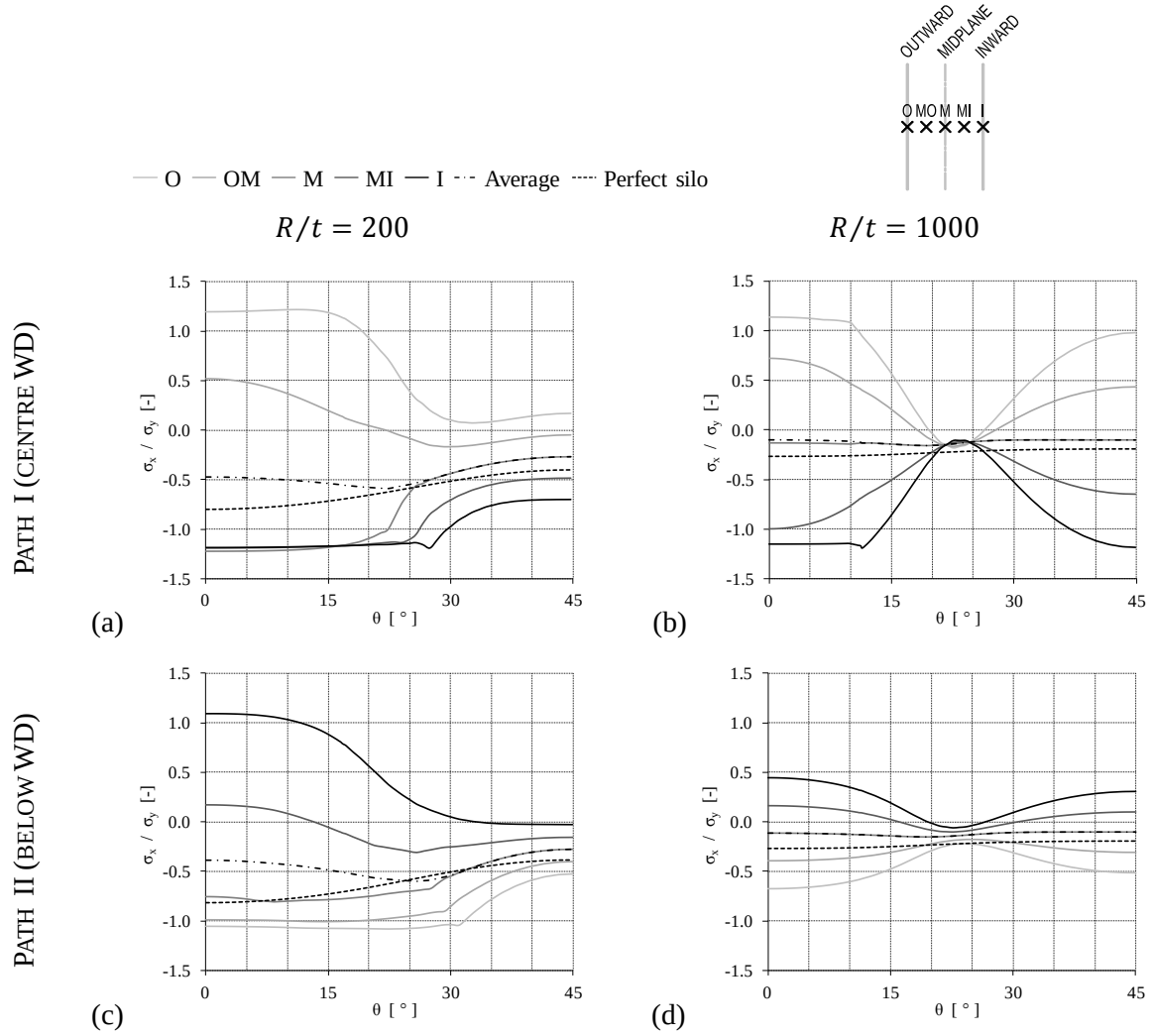

Fig. 5-121 Axial stress distribution σ_x/σ_y at the moment of maximum load (inwardly oriented weld depression type A with quality class C).

9.2 Influence of the weld depression position

Since the worst position of an inward weld depression type A with half-wavelength equal to λ_b (Eq. (2-45)) will be used in the development of a new proposal for the design rule, it is important to verify this position by means of sufficient geometries. Therefore, the critical location of the weld depression is determined by means of GMNIA analyses for about 112 cases distributed over the entire range of silos considered for the final study. In this way, a suitable choice can be made about the critical WD position.

For this study, the radius-to-thickness ratio R/t and the height h/R (high and short silos) of the cylindrical barrel were varied. Furthermore, both stiffening configurations (i.e. U-shaped stiffeners and engaged columns) were considered, taking into account the attached height h_{stif}^{sup}, and the width of the supporting columns in circumferential direction $d_{stif} = d_{sup}$.

The radius-to-thickness ratio R/t and the height h/R (high and short silos) of the cylindrical barrel were varied. All geometrical parameters of both stiffening configurations (i.e. U-shaped stiffeners and engaged columns) are mentioned in Table 5-29. The default geometrical parameters were used for the ring stiffeners. All parts have a standard elasto-plastic material behaviour with a yield stress σ_y equal to 235MPa.

Table 5-29 Geometrical parameters of the cylindrical barrel, the stiffening, and the supporting configuration (study of the position of the weld depression).

COMPONENT	PARAMETER	VALUE(S)	DIMENSION
SILO	R/t	$100;\ 200; 250; 333.3; 500; 666.6; 1000$	-
	h/R	$2.0;\ 10.0$	-
STIFFENERS	n_{sup}	4	-
	d_{stif}/R	$R/t = 100;\ 200; 250$: 0.20; 0.30 $R/t = 333.3$: 0.15; 0.30 $R/t = 500; 666.6;\ 1000$: 0.10; 0.20	-
	Type(s)	U-shaped longitudinal stiffeners (U.S.) Engaged columns (E.C.)	
	w_{stif}/d_{stif}	U.S.: 25 E.C.: 100	%
	h_{stif}^{sup}/R	$h/R = 2.0$: 0.5; 1.0 $h/R = 10.0$: 1.0; 2.0	-
	h_{stif}^{inf}/R	U.S.: / E.C.: 4.0	-
	t_{stif}/t	$R/t = 100;\ 200; 250; 333.3$: max.* $R/t = 500; 666.6;\ 1000$: min.*	-

*: Minimum (min.), average (ave.), or maximum (max.) thickness - restrictions

However, to keep the number of GMNIA analyses manageable, it was decided to limit the number of WD positions to those in the region of maximum compressive stresses, i.e. the region just above the terminations of the U-shaped stiffeners/engaged columns. In general, failure (i.e. plastic yielding and/or elastic buckling) occurs in that area.

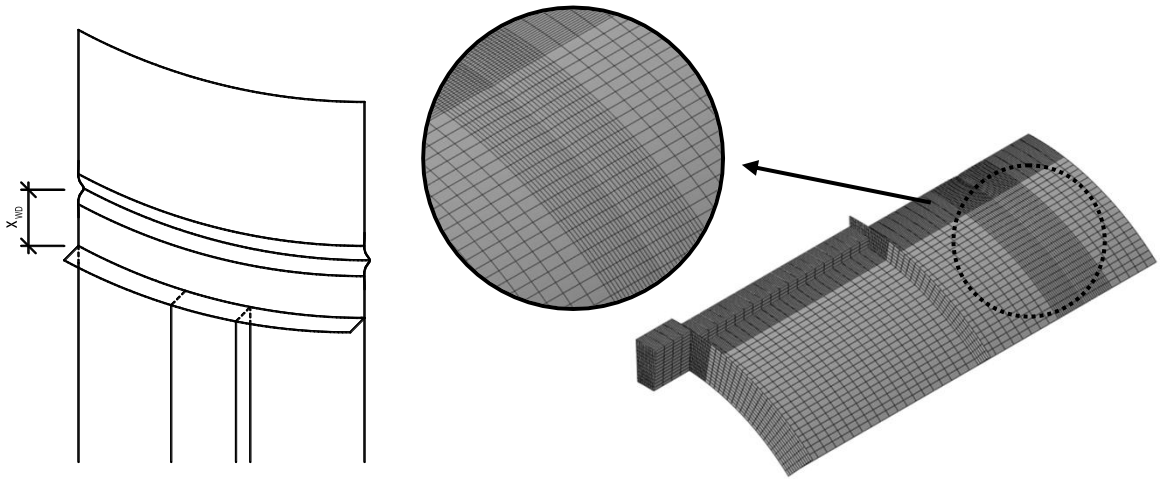

(a) WD position. (b) Refined mesh in the vicinity of the axisymmetric WD.

Fig. 5-122 Position and mesh of the weld depression.

The WD position is determined by defining the distance x_{WD} (See Fig. 5-122 (a)), which is the distance in meridional direction between the top of the U-shaped stiffeners/engaged columns and the centre of the weld depression. In this study, the values of WD position x_{WD} were chosen carefully over the entire direct vicinity of the top of U-shaped stiffeners/columns with a fixed step of $0.3 \cdot R$. A total of four WD positions x_{WD} were considered: $0.3 \cdot R$, $0.6 \cdot R$, $0.9 \cdot R$, and $1.2 \cdot R$. Furthermore, those positions were eliminated where the largest deviations (i.e. the deviations which are located at a distance less than the half-wavelength λ_b of the WD centre) are located under the top of the stiffeners/columns or above the top edge of the cylindrical barrel (in the case of less high silos). In other words, the weld depression should be completely located in the unstiffened silo wall. This restriction translates into a lower and an upper limit of the WD position x_{WD}, as presented in Eq. (5-25).

$$\lambda_b \leq x_{WD} \leq \left(h - h_{stif}^{sup}\right) - \lambda_b \tag{5-25}$$

In Fig. 5-123, the results are shown for four cases. In this figure, the dimensionless failure load F_{GMNIA}/F_{GMNA} is plotted against the WD position x_{WD} divided by the cylinder radius R. Again, it appears that an inward weld depression type A strongly influences the failure behaviour ($F_{GMNIA}/F_{GMNA} < 1$). In general, the GMNIA failure load decreases as the fabrication tolerance quality deteriorates (i.e. Class A → B → C). Now, if we look at the influence of the position of the weld depression x_{WD}, one can observe that its influence is not that significant. In general, a weld depression which is located further away from the terminations of the stiffeners/columns is more disadvantageous, within the range studied here.

For practical considerations and simplicity reasons, the starting point for the determination of the critical WD position is to couple only the most important influencing parameters to the WD position. When viewing the results of all 112 cases, it was found that the critical WD location is mainly affected by the silo thickness t (or the radius-to-thickness ratio R/t) and

silo height h (or the height-to-radius ratio h/R). Indeed, the radius-to-thickness ratio R/t clearly influences the shape of the depression, as shown in Fig. 5-113 for three different radius-to-thickness ratios. Indeed, both the maximum deviation δ_{max} (Eqs. (2-46) to (2-48)) and the half-wavelength λ (Eq. (2-45)) are dependent on the thickness of the cylindrical barrel. The silo height with its boundary conditions (preventing the out-of-roundness deformations) and loading conditions (i.e. a uniform line load) changes the distance between these end conditions at the top edge of the cylindrical barrel and the weld depression. From this, it can be concluded that both the silo thickness and the silo height influence, to a limited extent, the deformations and the stress pattern at the weld depression, and consequently their critical location.

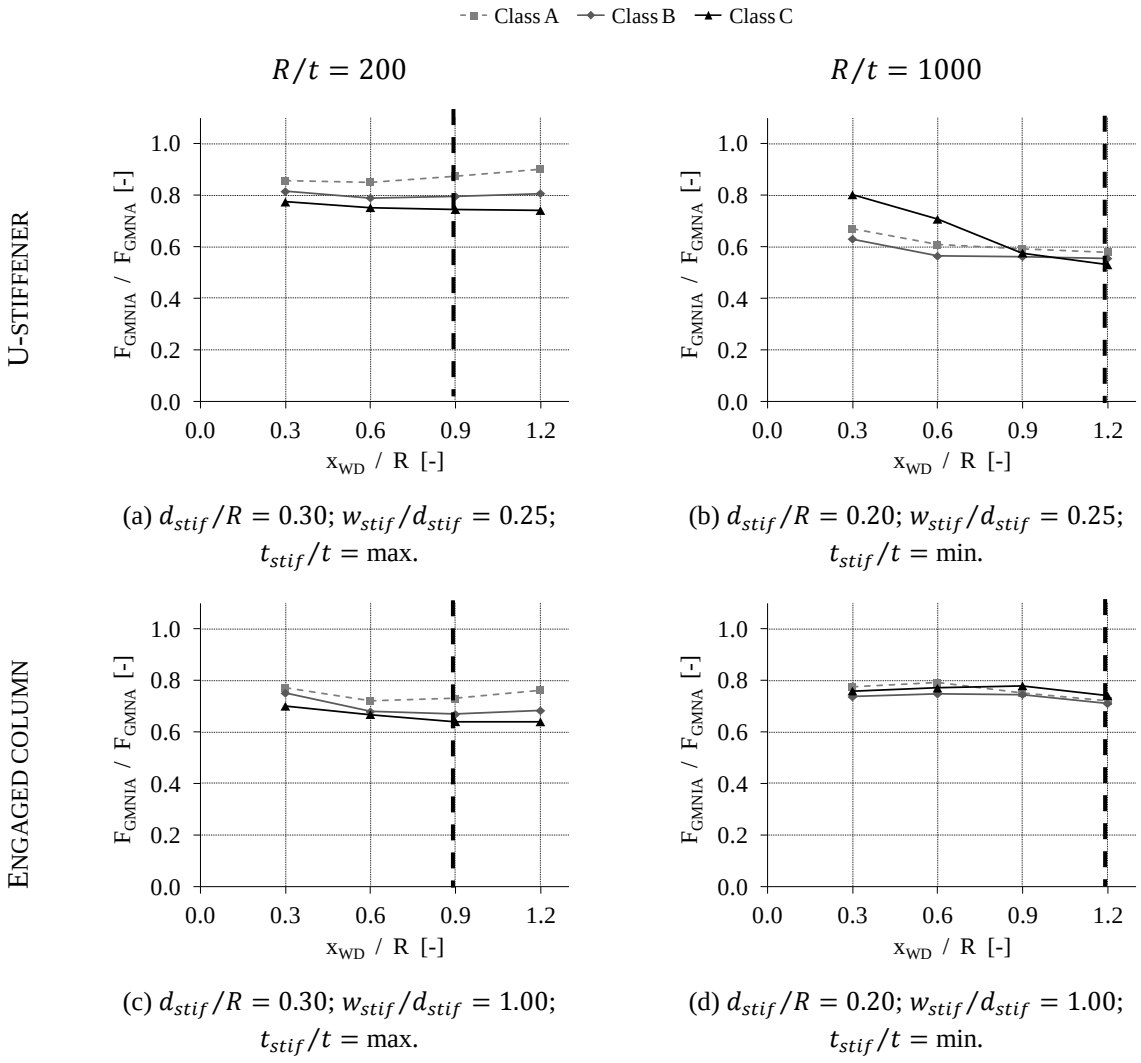

(a) $d_{stif}/R = 0.30$; $w_{stif}/d_{stif} = 0.25$; $t_{stif}/t =$ max.

(b) $d_{stif}/R = 0.20$; $w_{stif}/d_{stif} = 0.25$; $t_{stif}/t =$ min.

(c) $d_{stif}/R = 0.30$; $w_{stif}/d_{stif} = 1.00$; $t_{stif}/t =$ max.

(d) $d_{stif}/R = 0.20$; $w_{stif}/d_{stif} = 1.00$; $t_{stif}/t =$ min.

Fig. 5-123 Imperfection sensitivity for an inwardly oriented weld depression type A with a variable position x_{WD} (high silo: $h/R = 10.0$; $h_{stif}^{sup}/R = 1.0$).

Table 5-30 shows the dimensionless critical WD position x_{WD}/R as a function of the radius-to-thickness ratio R/t and the silo height (high and short silo) which will be used for the final study and the proposed design rule. The first finding is that the worst WD position is located closer to the terminations of the stiffeners/engaged columns for thick-walled silos ($R/t < 500$) than for thin-walled silos ($R/t \geq 500$). Secondly, the critical WD position moves down as the top edge of the cylindrical barrel comes closer to the weld depression.

Table 5-30 Overview of the critical weld depression position x_{WD}/R (design rule).

R/t [-]	HIGH SILO	SHORT SILO
100	0.9	0.6
200	0.9	0.6
250	0.9	0.6
333.3	0.9	0.6
500	1.2	0.6
666.6	1.2	0.9
1000	1.2	0.9

Despite the critical WD positions listed above are determined by and are in relatively good agreement with the results of all cases of the exploratory study (112), it is not certain that these positions always correspond with the 100% most disadvantageous position for all geometries. In general, it is expected that the deviation of the determined WD position and the critical WD position to the GMNIA failure load is limited.

9.3 Conclusions

From the imperfection sensitivity study, a wide range of locally supported steel silos has been investigated: both the silo geometry, the stiffening configuration, and stiffening dimensions were varied. In this way, well-founded conclusions can be drawn.

Different imperfection shapes were examined: the linear bifurcation mode, the non-linear buckling mode, three post-buckling deformed shapes of the perfect shell, and a weld depression type A and B. In addition, the amplitude (related to the Eurocode) and the orientation (inward/outward) of these equivalent imperfections were varied to investigate their influence on the failure behaviour of an imperfect structure.

This comprehensive study demonstrates that silos are very susceptible to a wide range of geometrical imperfections, and that these imperfections significantly adversely influence the failure behaviour and load compared to a perfect silo. In other words, the presence of imperfections is crucial for the prediction of the real failure load. The following conclusions can be drawn.

- Overall, the imperfections can be arranged from less to more detrimental as follows: the non-linear buckling mode (NBM) together with the post-buckling deformed shape just after failure (PDS - MAX), the linear buckling mode (LBM), the third post-buckling deformed shape after failure (PDS - MIN), the second post-buckling deformed shape after failure (PDS - MID), a weld depression type B (WD - B), and lastly a weld depression type A (WD - A).
- As expected, inward imperfections are generally more unfavourable than outward imperfections, because they reduce the curvature of the shell, resulting in a smaller (buckling) strength.
- In general, the larger the amplitude of the equivalent imperfection, the greater the adverse effect of the imperfection to the failure behaviour / strength.
- For the later proposal of the design rule, **an inward weld depression type A with half-wavelength equal to λ_b** has been chosen as equivalent imperfection shape. At first instance, such a circumferential weld depression appears to be relatively detrimental compared to the other imperfection shapes. Secondly, this shape has the advantage that it is closely related to the fabrication process of a silo, and thus can be found in a real silo.

10 Conical roof and hopper

All geometrical parameters of the silo, the stiffening and the supporting configurations (i.e. U-shaped stiffeners and engaged columns) are mentioned in Table 5-31. The radius-to-thickness ratio R/t and the height h/R (high and short silos) of the cylindrical barrel were varied. For the stiffeners/engaged columns, the width in circumferential direction d_{stif} was varied. The default geometrical parameters were used for the ring stiffeners. In total, 8 different geometries were examined. All parts have a standard elasto-plastic material behaviour with a yield stress σ_y equal to 235MPa.

Table 5-31 Geometrical parameters of the cylindrical barrel, the stiffening, and the supporting configuration (exploratory study of roof and hopper).

COMPONENT	PARAMETER	VALUE(S)	DIMENSION
SILO	R/t	200; 1000	-
	h/R	2.0; 10.0	-
STIFFENERS	n_{sup}	4	-
	Type(s)	U-shaped longitudinal stiffeners (U.S.) Engaged columns (E.C.)	
	d_{stif}/R	0.10; 0.20	-
	w_{stif}/d_{stif}	U.S.: 25 E.C.: 100	%
	h_{stif}^{sup}/R	1.0	-
	h_{stif}^{inf}/R	U.S.: / E.C.: 4.0	-
	t_{stif}/t	max.*	-

*: Minimum (min.), average (ave.), or maximum (max.) thickness - restrictions

The ranges of the geometrical parameters of the concentric conical roof and the concentric conical hopper are presented in Table 5-32. All dimensions are depicted in Fig. 3-29.

Table 5-32 Geometrical parameters of the roof and the hopper.

PARAMETER	VALUE(S)	DIMENSION
α_{roof}	0; 10; 20	°
r_{roof}/R	0.000	-
t_{roof}/t	1; 3; 5	-
β_{hop} (r_{hop}/R)	15 (0.271); 30 (0.147); 45 (0.100); 60 (0.100)	° (-)
t_{hop}/t	1; 3; 5	-

First, the roof is examined in Section 10.1, then the hopper in Section 10.2. Finally, some conclusions have been drawn (See Section 10.3).

10.1 Conical roof

In Fig. 5-124, the results are plotted for only four different silo geometries ($R/t = 200; 1000$ and $h/R = 2.0; 10.0$) with always the same U-shaped longitudinal stiffener ($d_{stif}/R =$

0.20; $w_{stif}/d_{stif} = 30\%$; $t_{stif}/t =$ max.; $h_{stif}/R = 1.0$), because identical results are obtained for all other geometries. The black bars represent the magnitude of the dimensionless GMNA failure load F_u/F_{ref} (on the horizontal axis) for the numerical models with roof (and without boundary conditions at the top edge of the cylindrical barrel). For each combination of the roof, its slope α_{roof} (relative to the horizontal) and its thickness ratio t_{roof}/t are mentioned on the vertical axis. The gray dashed vertical line is the dimensionless GMNA failure load of the standard model, thus without roof and with boundary conditions at the top edge of the cylindrical barrel. The red dotted vertical line is the dimensionless GMNA failure load of the numerical model without roof and without boundary conditions at the top edge of the cylindrical barrel.

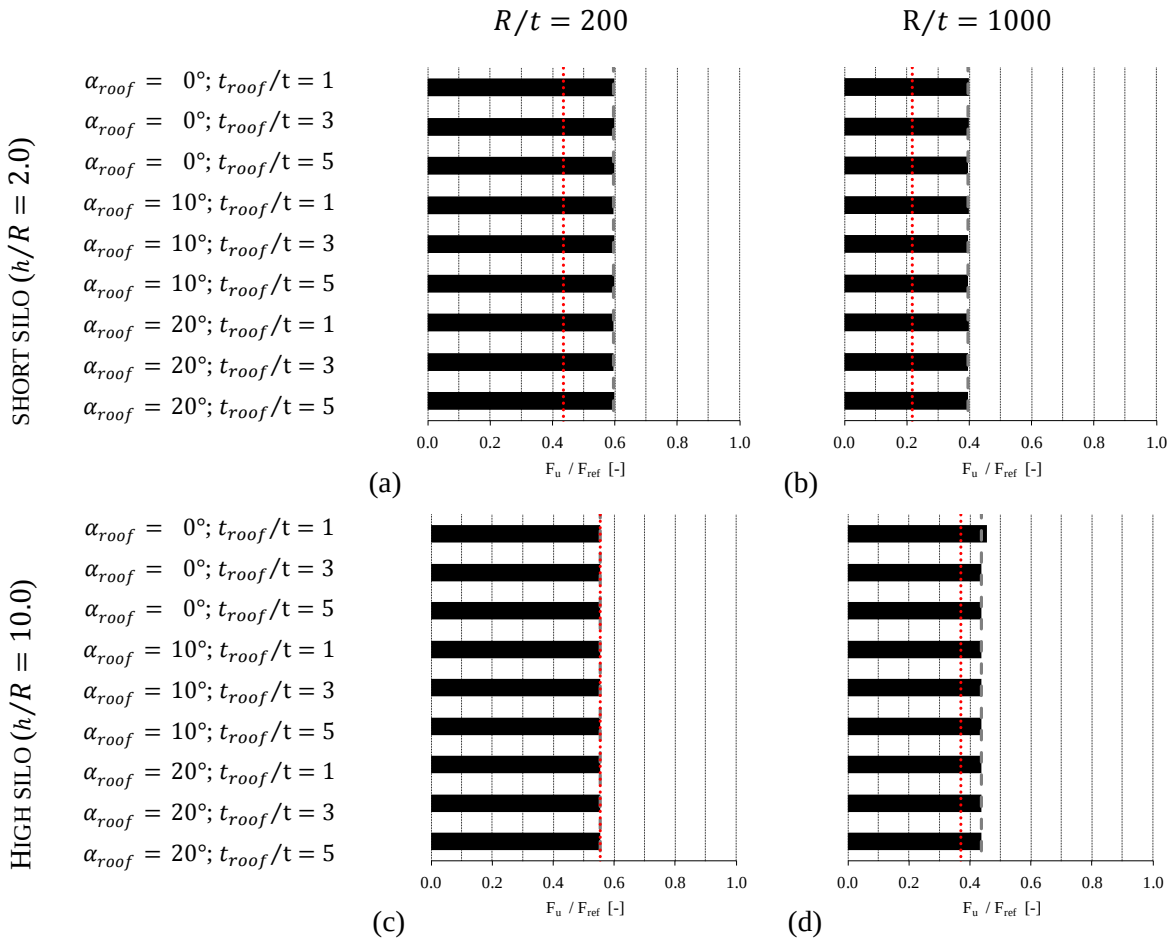

Fig. 5-124 Influence of different geometries of conical roofs (U-shaped longitudinal stiffener with $d_{stif}/R = 0.20$; $w_{stif}/d_{stif} = 30\%$; $t_{stif}/t =$ max.; $h_{stif}/R = 1.0$).

As can be seen, the same failure load is achieved for all alternatives, both for the models with roof (i.e. the black bars) as for the standard model with the boundary conditions (i.e. the gray dashed line). In other words, for the determination of the failure load of the cylindrical barrel subjected to axial compression, it is perfectly possible to replace the influence of the conical roof by boundary conditions at the upper edge of the barrel, restricting all horizontal or out-

of-roundness displacements.

By comparing the results of short silos (i.e. the upper row in Fig. 5-124) with those of high silos (i.e. the lower row in Fig. 5-124), it can be seen that the difference between the failure load of the model without roof and without boundary conditions (i.e. the red dotted line) and the other models is smaller for higher silos than for shorter silos. In other words, the influence of the conical roof and the boundary conditions on the failure load is, as expected, decreasing when the silo height increases.

10.2 Conical hopper

The different hoppers with variable hopper half angle β_{hop} (angle relative to the vertical) and radius of the outlet opening r_{hop} are illustratively depicted in Fig. 5-125.

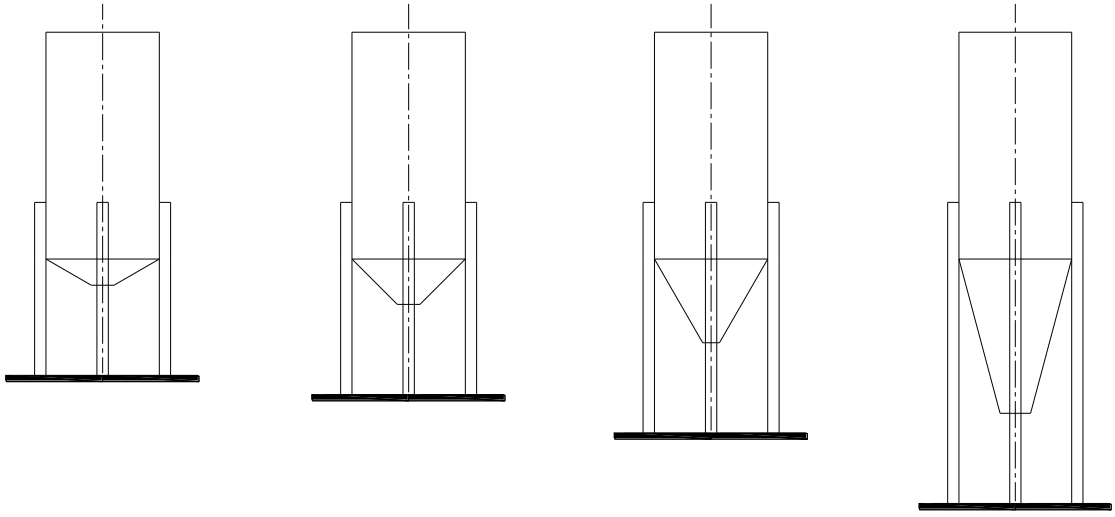

(a) $\beta_{hop} = 60°$. (b) $\beta_{hop} = 45°$. (c) $\beta_{hop} = 30°$. (d) $\beta_{hop} = 15°$.

Fig. 5-125 Different conical hopper types.

In Fig. 5-126, the results are plotted for only two geometries, because identical results are obtained for all other geometries. The black bars represent the magnitude of the dimensionless GMNA failure load F_u/F_{ref} (on the horizontal axis) for the numerical models with an additional hopper. For each combination of the hopper, its slope β_{hop} (relative to the vertical) and its thickness ratio t_{hop}/t are mentioned on the vertical axis. The gray vertical line is the dimensionless GMNA failure load of the standard model, thus without hopper and with a lower ring stiffener (U-stiffeners) or with boundary conditions (engaged columns) at the lower edge of the cylindrical barrel. From this figure, a number of observations can be made. All findings below can be explained by the same principle. **The more the horizontal or out-of-roundness deformations (mainly radial) are restricted at the lower edge of the cylindrical barrel, the larger the failure load.**

At first instance, the failure loads of the models with a hopper are systematically higher (U-shaped stiffeners) or lower (engaged columns) than the failure load of the standard model without a hopper. As already said, this can be explained by comparing the degree to which the radial deformations are restricted at the lower edge of the cylindrical barrel. In the case of U-shaped longitudinal stiffeners, the radial deformations are restricted more when the lower ring and the hopper are both attached to the lower edge, than when only the lower ring is attached to the lower edge. In other words, the presence of a hopper results in an increased restriction of the radial deformations at the lower edge of the barrel, and consequently an increased failure load. In the case of the engaged columns, the radial deformations are restricted less when only a hopper is attached to the lower edge, than when out-of-roundness boundary conditions are applied at the lower edge which restrict the deformations completely. In other words, the presence of a hopper results in a decreased restriction of the radial deformations at the lower edge of the barrel, and consequently a small decrease in failure load.

Secondly, it can be determined that the failure model of the standard model (without hopper) always best fits the failure load of the model with a lower less steep hopper (i.e. a large value of the hopper half angle β_{hop}) as depicted in Fig. 5-125 (a). This is expected since the horizontal deformations (mainly radial) in the case of a less steep hopper are restricted rather similarly as in the standard model without hopper. Furthermore, the steeper the hopper (i.e. a decreasing hopper half angle β_{hop}), the larger the difference of the failure loads between the model with hopper and the standard model without hopper (assuming that the hopper thickness t_{hop} remains constant). This is expected since a steep hopper restricts the horizontal deformations (mainly radial) less compared to a less steel hopper. In other words, the decrease of the failure load in the case of engaged columns can be explained by the decreased restriction of the radial deformations, the increase of the failure load in the case of the U-shaped longitudinal stiffeners cannot be explained at this moment with the above mentioned reasoning.

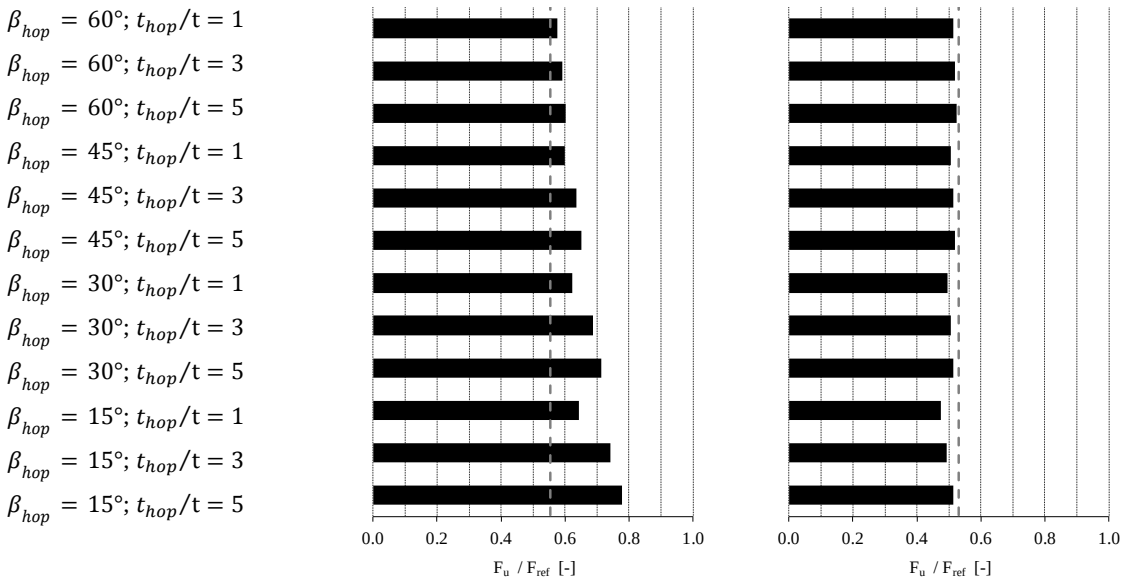

(a) U-shaped stiffener. (b) Engaged column.

Fig. 5-126 Influence of different geometries of conical hoppers (R/t = 200; d_{stif}/R = 0.20; h/R = 10).

For both geometries, the radial deformations U_R (left column) and the vertical deformations U_Z (right column) are plotted in Fig. 5-127 along the circumferential path which coincides with the lower edge of the cylindrical barrel (i.e. PC/S-h0.0 with $h_{path}/h_{stif} = 0.0$). No surprises are encountered when looking at the deformations. Indeed, the deformations of the standard model (without hopper) best fit with the deformations with a less steep hopper (β_{hop} ↑). Furthermore, when the hopper steepness increases or β_{hop} decreases, the radial deformations U_R are restricted less ((Ia) and (Ib)) and the vertical deformations U_Z are restricted more (II). When the hopper thickness t_{hop} increases, all deformations are decreasing.

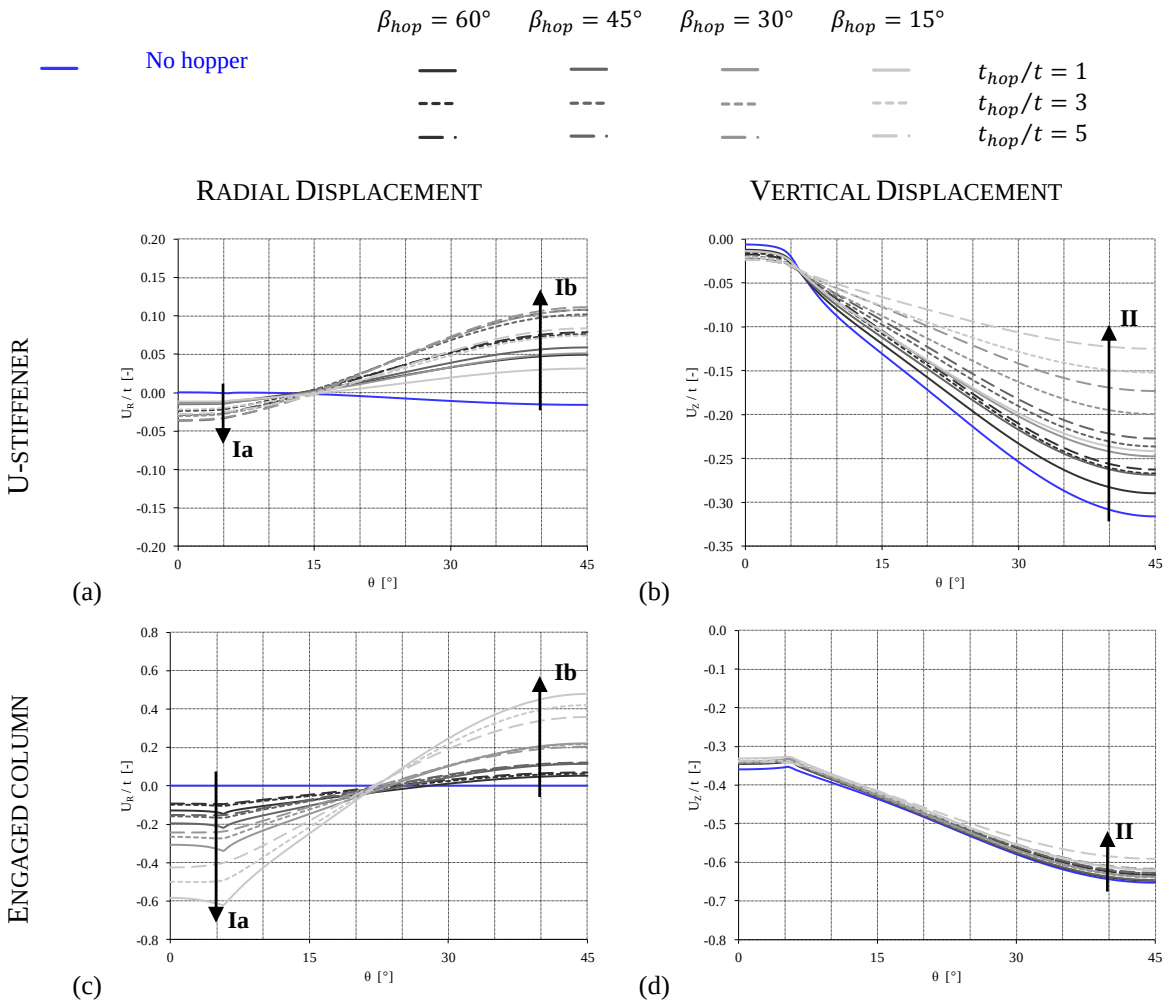

Fig. 5-127 Plot of the ratio of the radial or the vertical displacement at the moment of failure to the silo wall thickness U/t [-] against the circumferential angle θ [°] for a circumferential path PC/S-h0.0 ($h_{path}/h_{stif} = 0.0$) ($R/t = 200$; $h/R = 10$; $d_{stif}/R = 0.20$).

In Fig. 5-128, the cross-section is shown of the connection between the bottom of the silo wall and a less steel hopper (left) and a steep hopper (right) to demonstrate their different influence. The influence of the hopper can be replaced by two translational springs, one in radial direction with stiffness k_R and one in vertical direction with stiffness k_Z.

The steeper the hopper (i.e. a decrease of hopper half angle β_{hop}), the smaller the stiffness k_R and the larger the stiffness k_Z. Consequently, the radial displacement U_R increases, while the vertical displacement U_Z decreases when the hopper steepness increases. The thicker the hopper, the larger both stiffnesses (i.e. k_R and k_Z) and the smaller both displacements (i.e. U_R and U_Z).

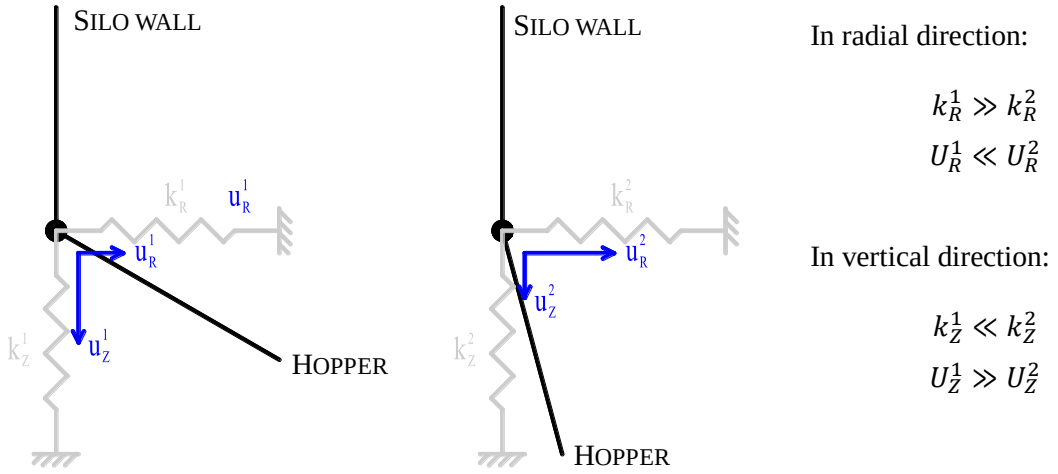

Fig. 5-128 Less steep hopper (left) versus steep hopper (right).

So far, everything can be explained, except for the increase of failure load when the hopper steepness increases in the case of U-shaped longitudinal stiffeners (See Fig. 5-126 (a)). Indeed, one would expect that the failure load decreases because the radial deformations are hampered less in the case of a steep hopper ((Ia) and (Ib) in Fig. 5-127 (a)), but the opposite trend is found.

In Fig. 5-129, the distribution of the axial stresses σ_x/σ_y in circumferential direction of the silo wall is shown along path PC/S-h0.1 (i.e. just above the lower ring: $h_{path}/h_{stif} = 0.1$) and along path PC/S-h1.1 (i.e. just above the upper ring: $h_{path}/h_{stif} = 1.1$). Just above the lower ring (i.e. Fig. 5-129 (a)), the axial stresses decrease in the silo wall just above the supporting columns ($\theta < 5.7°$) (Ia), but increase significantly in the silo wall between the supporting columns ($\theta > 5.7°$) (Ib). The latter is the consequence of the increased steepness of the hopper, which hampers the vertical deformations of the lower edge of the silo wall and the lower ring more ((II) in Fig. 5-127 (b)), as a result of which **the lower ring between the supporting columns is partially supported by the steep hopper** (i.e. a kind of elastic foundation). In other words, a part of the compressive load from the silo wall will be partially transmitted by the lower ring to the supporting columns. Consequently, the axial stresses are much better distributed in circumferential direction, which is clearly visible in Fig. 5-129 (b) (i.e. (II)), resulting in a larger failure load.

In the case of the engaged supporting columns, this effect cannot occur because no lower ring is connected to the lower edge of the cylindrical barrel.

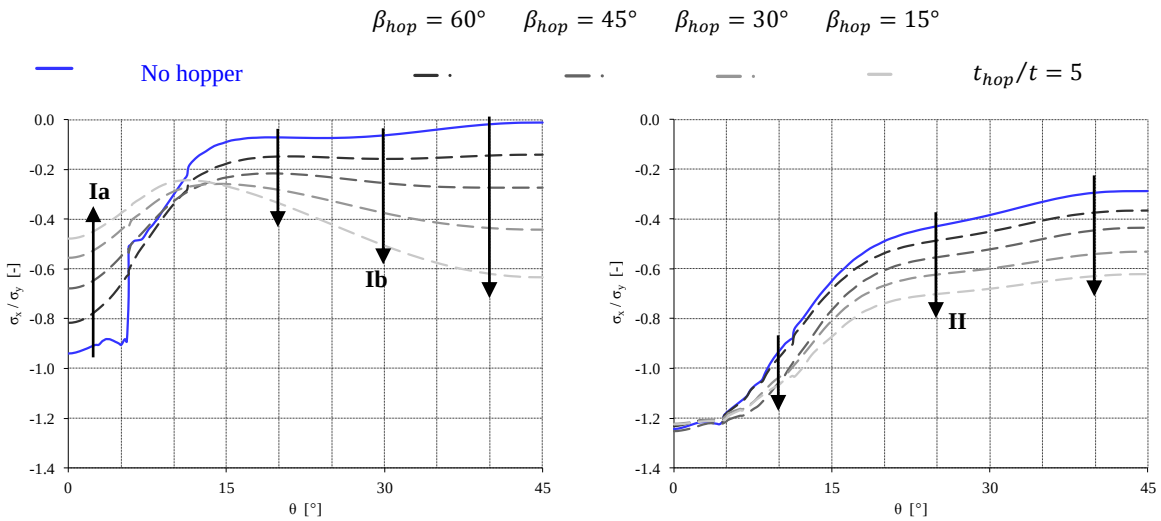

(a) In the silo wall just above the lower edge of the cylindrical barrel, i.e. along circumferential path PC/S-h0.1 ($h_{path}/h_{stif} = 0.1$).

(b) In the silo wall just above the upper ring, i.e. along circumferential path PC/S-h1.1 ($h_{path}/h_{stif} = 1.1$).

Fig. 5-129 Plot of the ratio of the axial stress at the moment of failure to the yield stress σ_x/σ_y [-] ($R/t = 200$; $h/R = 10$; U-stiffener with $d_{stif}/R = 0.20$).

10.3 Conclusions

On the basis of this exploratory study, a number of conclusions can be drawn concerning the non-modelling of the concentric conical roof above and the concentric conical hopper below the cylindrical barrel (in the standard numerical model).

For all cases considered here, the conical roof can without difficulty be replaced by horizontal out-of-roundness boundary conditions at the top edge of the cylindrical barrel, without influencing the failure behaviour and failure load.

For the engaged supporting columns, the conical hopper (and the transition ring) is replaced by default by horizontal out-of-roundness boundary conditions at the lower edge of the cylindrical barrel. In the case of U-shaped longitudinal stiffeners above the supporting columns, a lower ring stiffener is always present in the model which largely hampers the radial deformations at the lower edge of the silo wall. For both cases, the failure load of this standard model (without hopper) appears to have the largest agreement with the failure load of the numerical model with a less steep hopper. Furthermore, the steeper the hopper, the larger the deviation between the previously mentioned loads.

The failure load of the standard model is always on the safe side for the stiffening configuration with the U-shaped stiffeners (and a lower and upper ring) and is slightly on the unsafe side when eccentrically engaged supporting columns are applied. However, the author expects that these unsafe results for engaged columns become on the conservative side when, in addition to a hopper, also a transition ring in included in the model, as such transition ring

is often placed at the bottom of such light silos.

11 Loading conditions

In this section, the purpose is to map the influence of different load types on the failure load and to determine the conservatism of a uniform line load on the upper edge.

11.1 Other loading conditions

In Fig. 5-130, five load combinations are presented which will be considered in this exploratory study: (1) a uniform compressive load q, (2) a uniform compressive load q combined with a uniform internal pressure p_h, (3) a uniform frictional load p_w, (4) a uniform tensile load q_t, and (5) a uniform tensile load q_t combined with a hydrostatic pressure p_l.

The loads q and q_t are uniform line loads on the upper edge and the non-supported lower edge of the cylindrical barrel, respectively. The pressures p_h, p_w, and p_l all act on the internal side of the silo wall and represent the normal pressure, the frictional traction, and the hydrostatic pressure. The first two pressures have already been discussed for slender silos in Sections 7.3 and 7.4 in Chapter 2. The hydrostatic pressure represents the pressure distribution of fluidized solids as a consequence of entrainment of air. The hydrostatic pressure $p_l(z)$ at a distance z below the equivalent top surface of the solid (full condition) can be calculated using Eq. (5-26) where $\gamma_{fluidized}$ is equal to 80% of the upper characteristic value of the bulk unit weight γ_u (EN 1991-4, 2006).

$$p_l(z) = \gamma_{fluidized} \cdot z = 0.8 \cdot \gamma_u \cdot z \tag{5-26}$$

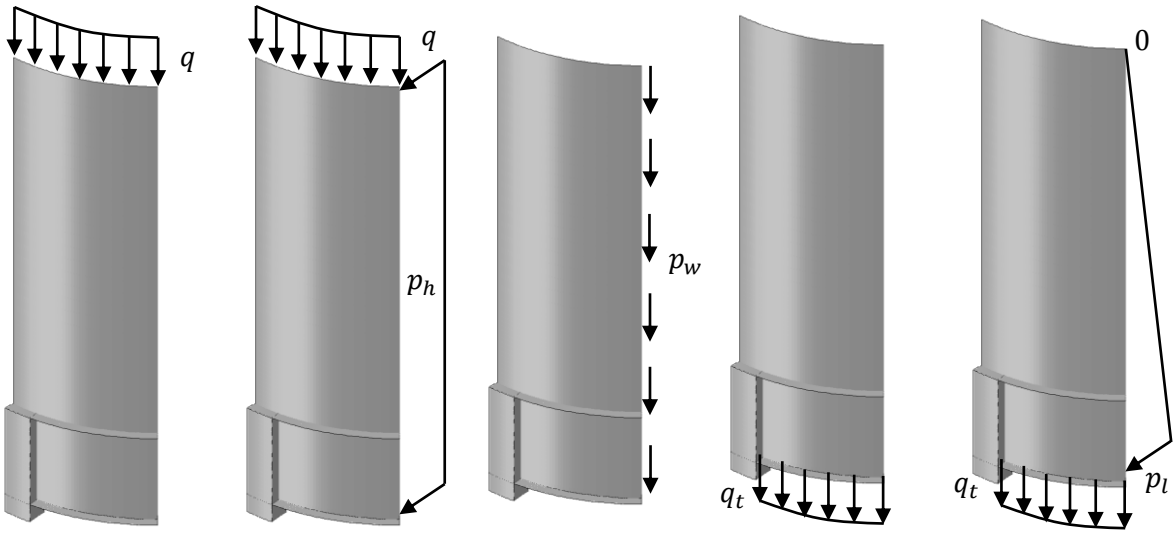

(a) Compression. (b) Compression + uniform internal pressure. (c) Uniform friction. (d) Tension. (e) Tension + hydrostatic pressure.

Fig. 5-130 Different loading conditions.

The dimensionless GMNA failure load F_u/F_{ref} is for different load combinations plotted in Fig. 5-131 (a) for a thick-walled silo (i.e. $R/t = 200$) and in Fig. 5-131 (b) for a thin-walled silo (i.e. $R/t = 1000$). Both example geometries are cylindrical barrels stiffened with U-shaped longitudinal stiffeners: $d_{stif}/R = 0.20$; $w_{stif}/d_{stif} = 25\%$; t_{stif}/t= max.; $h_{stif}/R = 2.0$. The other parameters got their default value. For the combination compression-internal pressure (See Fig. 5-130 (b)), only the maximum load ratio F_u/F_{ref} is given in Fig. 5-131 which corresponds with the maximum load ratio by varying the internal pressure $(p_h \cdot R)/(\sigma_y \cdot t)$ from zero to the unity (See Section 11.2). For the combination tension-hydrostatic pressure (See Fig. 5-130 (e)), two different values of γ_u were considered: 10kN/m³ and 20kN/m³.

Overall, very similar load levels are obtained at the moment of failure, except for the thin-walled silo subjected to tension (and hydrostatic pressure). For these cases, a value of F_u/F_{ref} larger than the unity is obtained because pure elastic buckling was replaced by extensive plastic yielding in the region above the local support. Another difference between the thick and the thin-walled silo is the difference in increase in failure load between an unpressurized compressed and a pressurized compressed silo: an increase of only 3% for the thick silo and 40% for the thin silo. This finding will be discussed more in detail in Section 11.2.

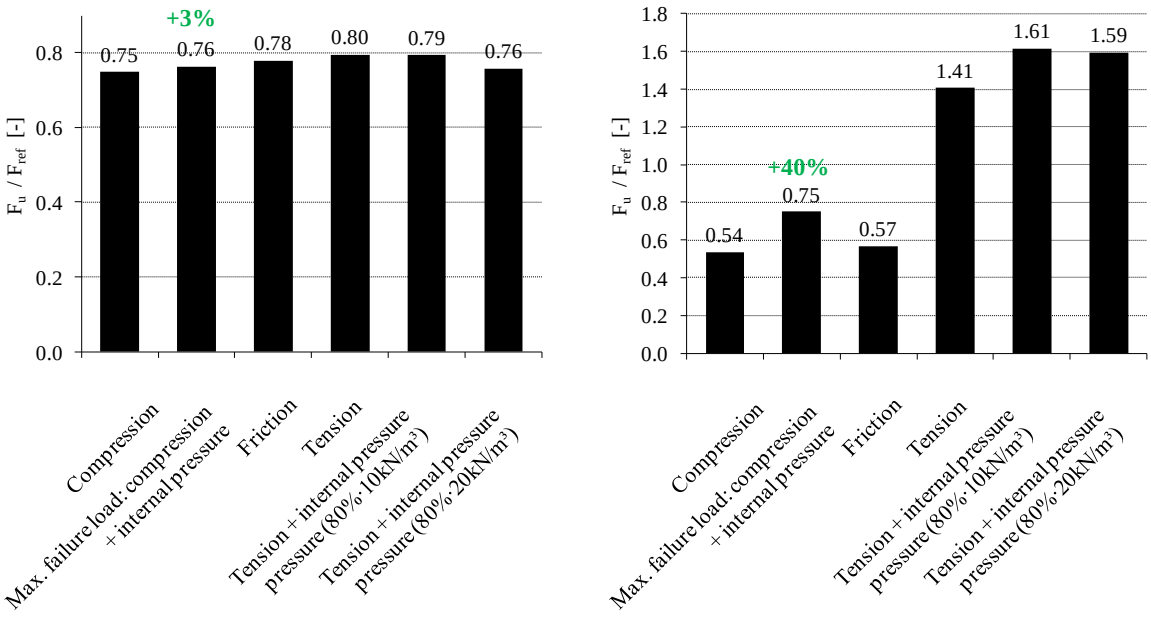

(a) $R/t = 200$. (b) $R/t = 1000$.

Fig. 5-131 Dimensionless GMNA failure load F_u/F_{ref} for different loading combinations (geometry with U-shaped stiffener with $d_{stif}/R = 0.20$; $w_{stif}/d_{stif} = 25\%$; t_{stif}/t= max.; $h_{stif}/R = 2.0$).

11.2 Compression in coexistence with internal pressures

Now, the influence of the load combination compression q - internal pressure p_h (See Fig. 5-130 (b)) on the failure load will be investigated more in detail for the same example silos used as in Section 11.1. Similar to other studies (e.g. Fig. 2-27), the ratio $(p_h \cdot R)/(\sigma_y \cdot t)$ is varied from zero to the unity, where R is the silo radius, t is the silo thickness, and σ_y is the yield stress. In Fig. 5-132, the dimensionless GMNA failure load F_u/F_{ref} is plotted as a function of the ratio $(p_h \cdot R)/(\sigma_y \cdot t)$. However, before discussing the results, it is important to notice that very large values of this ratio are far from realistic. Therefore, the range of maximum internal pressure $p_{hf,max}$ was calculated by means of Eqs. (2-50) to (2-53), by taking into account the geometry of the barrel and all bulk solids given in Table 2-2 (EN 1991-4, 2006). This calculation resulted in a range of $p_{hf,max}$ from 18.3 to 96.3kPa, which corresponds with values of $(p_h \cdot R)/(\sigma_y \cdot t)$ between 0.02-0.08 for the thick-walled silo (i.e. $R/t = 200$) and between 0.08-0.41 for the thin-walled silo (i.e. $R/t = 1000$) (when $\sigma_y = 235$MPa). In Fig. 5-132, this range is indicated with a blue double arrow.

Both graphs show a similar and expected trend: an initial increase of the pressure p_h increases the failure load (i.e. the elastic strengthening effect) and decreases again when the internal pressure p_h exceeds a certain value (due to plastic weakening). In the case of the thick-walled silo (which fails by elasto-plastic buckling), a relatively small maximum increase in failure load was found between an unpressurized compressed and a pressurized compressed silo: 3%. In contrast, a 40% increase in failure load was found for the thin-walled silo (failure by pure elastic buckling).

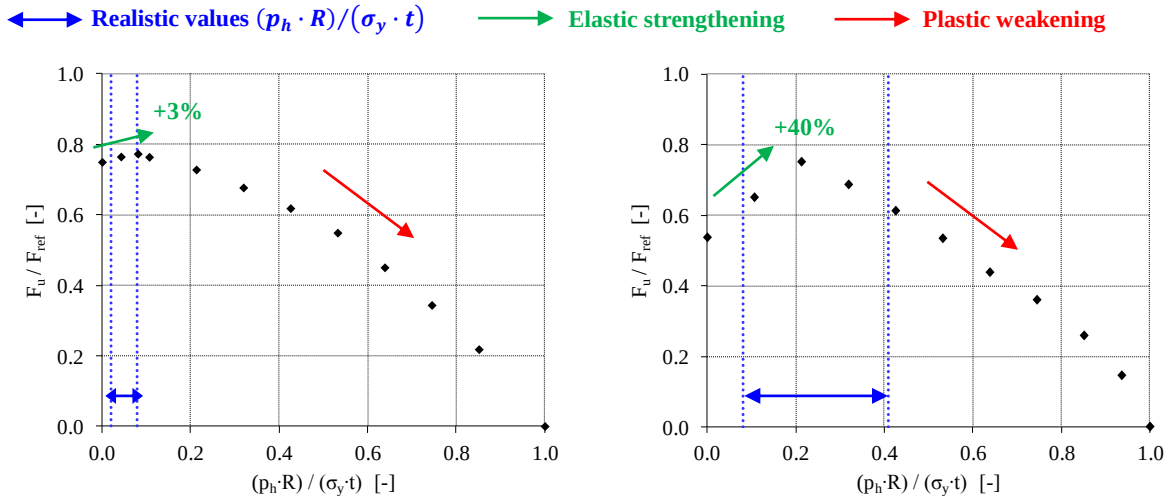

(a) $R/t = 200$. (b) $R/t = 1000$.

Fig. 5-132 Dimensionless GMNA failure load F_u/F_{ref} as a function of the internal pressure p (geometry with U-shaped stiffener with $d_{stif}/R = 0.20$; $w_{stif}/d_{stif} = 25\%$; t_{stif}/t= max.; $h_{stif}/R = 2.0$).

Flattening effect

In Fig. 5-133, the dimensionless GMNA failure load F_u/F_{ref} is plotted against the ratio of the cylinder height to the cylinder radius h/R for an unpressurized compressed silo ($(p_h \cdot R)/(\sigma_y \cdot t) = 0.00$) and a pressurized compressed silo ($(p_h \cdot R)/(\sigma_y \cdot t) = 0.05$). To compare these results with previous results, the same geometry as in Fig. 5-12 has been chosen: a silo with $R/t = 500$ and U-shaped longitudinal stiffeners with $d_{stif}/\mathrm{R} = 0.20$; $w_{stif}/d_{stif} = 25\%$; $h_{stif}^{sup}/R = 1.0$; t_{stif}/t = max..

Clearly, the increase of the internal pressure p_h has an advantageous influence on the failure load over the entire range of heights. Probably, this increase can be attributed to the internal pressures which counteract the development of deformations before failure and thus the disadvantageous effect of the flattening effect, as discussed in Sections 3.3 and 3.4 of this chapter.

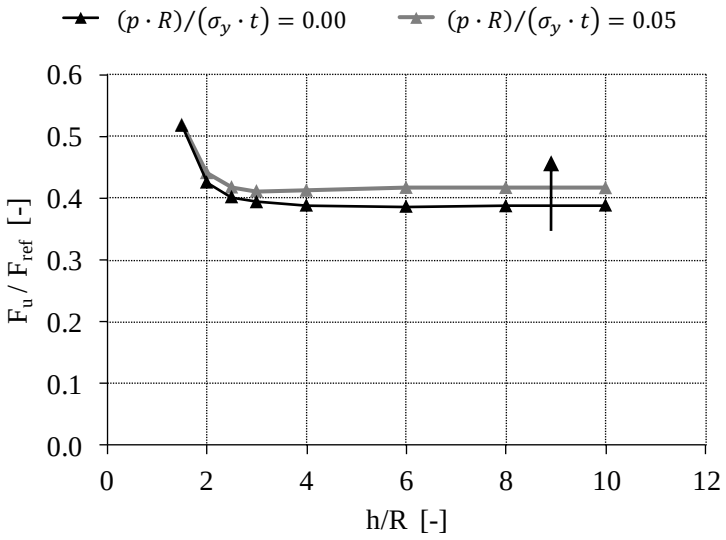

Fig. 5-133 Influence of the cylinder height to the dimensionless GMNA failure load F_u/F_{ref} witthout and with internal pressure (U-shaped longitudinal stiffener with $d_{stif}/\mathrm{R} = 0.20$; $w_{stif}/d_{stif} = 25\%$; $h_{stif}^{sup}/R = 1.0$; t_{stif}/t = max.) ($\mathrm{R}/t = 500$).

Similar as in Fig. 5-12 (b) and (c), the ratio of the radial displacements to the silo wall thickness U_R/t (Fig. 5-134 (a)) and the ratio of the axial stress at the moment of failure to the yield stress σ_x/σ_y (Fig. 5-134 (b)) are plotted along a circumferential path PC/S-h1.15 ($h_{path}/h_{stif}^{sup} = 1.15$), which corresponds with the height of elastic buckling, as depicted in Fig. 5-12 (a) for an unpressurized compressed silo. The results of the unpressurized compressed silo and the pressurized compressed silo are depicted in the upper and lower row of Fig. 5-134, respectively.

As expected, when the silo height increases, the inward deformations increase less rapidly for the pressurized compressed silo than for the unpressurized compressed silo ($\theta < 22.5°$ in Fig. 5-134 (a)). In other words, the flattening effect is less pronounced in the pressurized silo, and more important the reduction of the critical buckling stress σ_{cr} weakens by the presence of (relatively small) internal pressures, as clearly visible in Fig. 5-134 (b) ($\theta < 22.5°$).

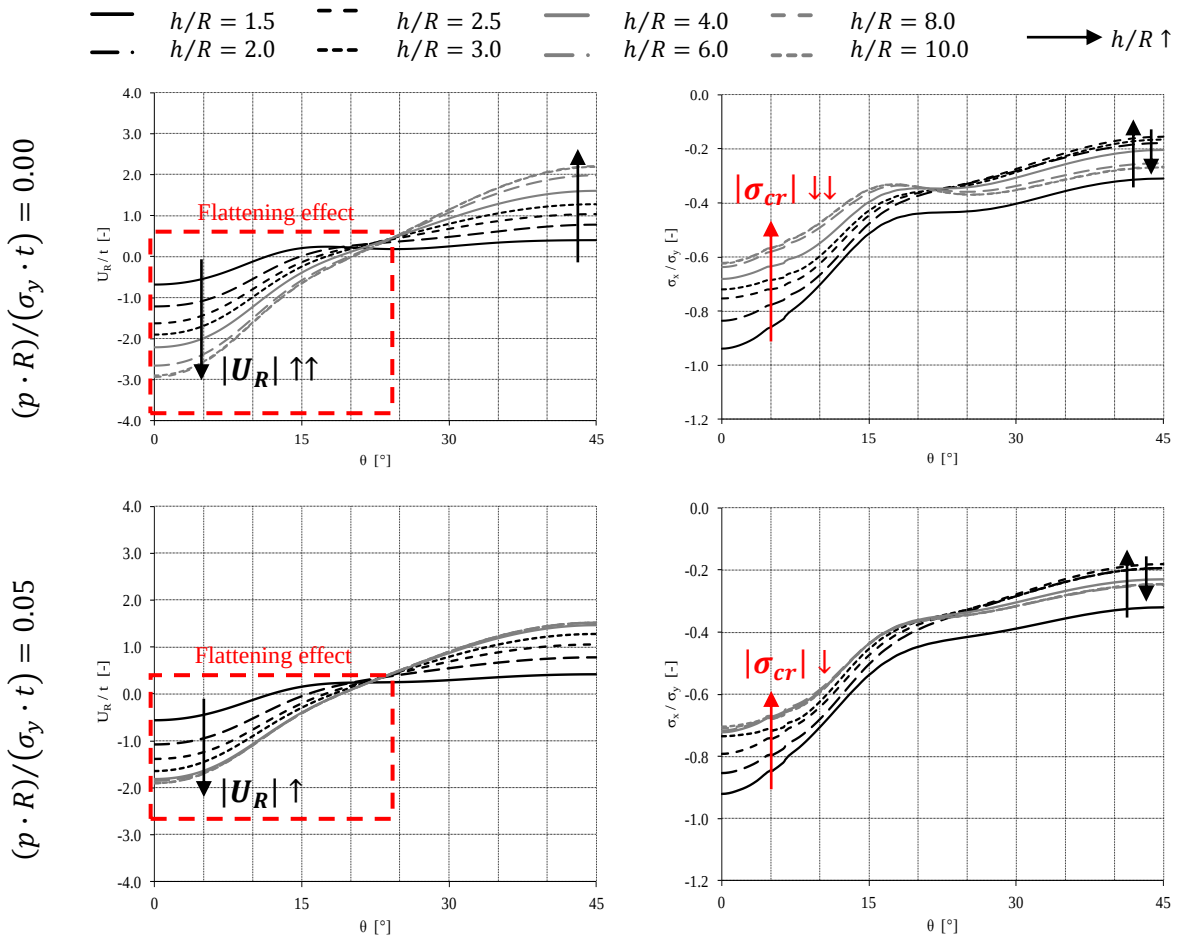

(a) Plot of the ratio of the radial displacement at the moment of failure to the silo wall thickness U_R/t [-] against the circumferential angle θ [°] for a circumferential path PC/S-h1.15 ($h_{path}/h_{stif}^{sup} = 1.15$).

(b) Plot of the ratio of the axial stress at the moment of failure to the yield stress σ_x/σ_y [-] against the circumferential angle θ [°] for a circumferential path PC/S-h1.15 ($h_{path}/h_{stif}^{sup} = 1.15$).

Fig. 5-134 Influence of the ratio of the height to the radius of the silo h/R on the failure behaviour (U-shaped longitudinal stiffener with $d_{stif}/R = 0.20$; $w_{stif}/d_{stif} = 25\%$; $h_{stif}^{sup}/R = 1.0$; t_{stif}/t = max.) without internal pressure (upper row) and with internal pressure (lower row) ($R/t = 500$).

Conclusions

As demonstrated above, neglecting the internal pressure is a conservative assumption when the failure load is determined for axially compressed cylindrical steel barrels.

12 Conclusions of the numerical research

This chapter started with two mesh studies: the influence of the shell element type and the mesh size were examined. Based on these results, it was concluded that the S8R5 shell element is suitable for the prediction of the failure load of different types of shell analyses (MNA, GMNIA, etc.). The mesh convergence study demonstrated that the default mesh is sufficiently refined and that a further reduction of the mesh size does not lead to more accurate results.

Then, the influence of the geometry of the silo barrel was investigated. In this work, all calculations (except for the validation process) are performed on 1m radius silos, while all other geometrical parameters are expressed as dimensionless parameters relative to the cylinder radius. It has been demonstrated that the failure load of a 1m radius silo can always be converted to a failure load of the corresponding silo with different cylinder radius, and that all findings derived for 1m radius silos are also valid for silos with other cylinder radii. The silo thickness is one of the most important parameters. Indeed, the radius-to-thickness ratio (together with the yield stress) determines to a large extent the failure behaviour and the occurring failure phenomenon (i.e. plastic yielding, elastic buckling, or elasto-plastic buckling). Depending on the height of the barrel, silos can be divided into three categories with different behaviour: short silos (behaviour is influenced by the boundary and loading conditions at the upper edge), intermediately high silos (transition region between short and high silos), and high silos (behaviour is independent of the silo height).

A large part of the numerical research was devoted to the influence of the U-shaped longitudinal stiffeners and the engaged columns to the failure behaviour. For both configurations, the research consisted of an exploratory study (the influence of all geometrical parameters was examined one by one) and an optimisation study (determination of the most optimal shape of the cross-section and height). From these studies, a large number of interesting findings were made making it difficult to list all of them here again. Therefore, only the most important conclusions will be formulated below. For the first configuration, a relatively high and thin U-shaped longitudinal stiffener with a large developed length (large circumferential width and smaller radial width) is preferred to maximally distribute the axial stresses in circumferential direction and consequently to maximise the failure load. For the second configuration, an intermediately high (the attached height is just below the critical height) relatively thin engaged column with a large developed length is preferred to maximise the failure load. Depending on the silo thickness and the column height, a larger or a smaller ratio of the radial width to the circumferential width is the best solution. For most cases, a large ratio of the radial width to the circumferential width is more suitable because of the increased moment of inertia. For thick-walled silos combined with short columns, a square column is preferred with a relatively small eccentricity. Moreover, for the design rule study

(i.e. Chapter 6), a range was defined for all geometrical parameters based on the results of the foregoing parametric studies.

The imperfection sensitivity study has demonstrated that axially compressed silos on local supports are susceptible for a wide range of geometrical imperfections (linear and non-linear buckling modes, post-buckling deformed shapes, and weld depressions), which all significantly reduce the elasto-plastic buckling load of a perfect structure. General speaking, inwardly oriented imperfection shapes are more disadvantageous than outwardly oriented imperfections. Furthermore, imperfections become more disadvantageous when their amplitude increases. For the design rule study, an inward weld depression type A with half-wavelength equal to linear elastic bending half-wavelength has been picked out as equivalent imperfection shape because of two reasons: (1) it is relatively detrimental compared to other imperfection shapes and (2) the shape is closely related to the fabrication process of a welded silo.

CHAPTER 6

Design rule

After the experimental part, the validation of the numerical model, and the extensive numerical research, it is time to determine capacity curves for the scope of geometries defined in Chapter 5 at the end of each parametric study. Since such capacity curves are currently not available for the configurations considered in this work, these curves will lead to new insights into the elasto-plastic failure behaviour and hopefully also to a better prediction of the elasto-plastic failure load.

The extensive dataset obtained for both configurations will be used for the following issues: (1) to compare the dataset with the design curves for buckling of unstiffened cylindrical silos under axial compression given in the Eurocode (EN 1993-1-6, 2007); (2) to develop new interaction parameters for the lower bound estimate of the entire dataset and for all individual capacity curves; (3) to link the best-fitting interaction parameters with the geometrical parameters. However, as will be seen, it is not evident to achieve this.

1 Scope of the design rule

The parametric studies and numerical work discussed in Chapter 5 have not only led to a better understanding of the failure behaviour, but at the end of each parametric study, also a range was determined for all (geometrical) parameters for which capacity curves will be drawn as a part of the final study. To keep an overview of all geometries considered, this chapter starts with a summary of the complete scope. For the parameters which are not mentioned here again, the default values have been adopted which are specified in the second part of Chapter 3 (Numerical model) and the corresponding parts of Chapter 5 (Numerical research: Parametric study).

To keep an overview of all geometries considered, the complete scope is divided into 14 "clusters". Each cluster is characterized by a configuration type (U.S. = U-shaped Stiffeners or E.C. = Engaged Columns), a constant number of local supports n_{sup}, a constant ratio of the radial width to the circumferential width w_{stif}/d_{stif}, a constant silo height h/R, and a range of attached heights h_{stif}^{sup}/R (See Table 6-1).

Table 6-1 Overview of the clusters (final study).

CLUSTER	TYPE	n_{sup} [-]	w_{stif}/d_{stif} [%]	h/R [-]	h_{stif}^{sup}/R [-]	COMBINATIONS d_{stif}/R AND t_{stif}/t		# [-]
1	U.S.	4	25	10	0.5; 1.0; 1.5; 2.0	X	X	220
2	U.S.	4	25	2	0.5; 1.0	X	X	110
3	U.S.	4	25	3	1.5; 2.0	X	X	110
4	U.S.	6	25	10	0.5; 1.0; 1.5; 2.0	X	-	56
5	U.S.	6	25	2	0.5; 1.0	X	-	28
6	U.S.	6	25	3	1.5; 2.0	X	-	28
7	E.C.	4	100	10	0.5; 1.0	X	X	110
8	E.C.	4	100	2	0.5; 1.0	X	X	110
9	E.C.	4	200	10	0.5; 1.0	X	X	110
10	E.C.	4	200	2	0.5; 1.0	X	X	110
11	E.C.	6	100	10	0.5; 1.0	X	-	28
12	E.C.	6	100	2	0.5; 1.0	X	-	28
13	E.C.	6	200	10	0.5; 1.0	X	-	28
14	E.C.	6	200	2	0.5; 1.0	X	-	28
							SUM	**1104**

The considered combinations of the circumferential width d_{stif}/R and the stiffener/column thickness t_{stif}/t depend on the radius-to-thickness ratio R/t and the number of supporting columns n_{sup} (See Table 6-2). All combinations given in this table are considered for the clusters with a default value of four supporting columns. In contrast, for the clusters with six supports, only two combinations per radius-to-thickness ratio R/t are calculated to limit the number of calculations within acceptable bounds.

Table 6-2 Combinations within each cluster of the dimensionless circumferential width d_{stif}/R and the dimensionless thickness t_{stif}/t of the U-shaped longitudinal stiffeners and the engaged columns (final study).

	d_{stif}/R														
	0.10			0.15			0.20			0.25			0.30		
t_{stif}/t / R/t	min.	ave.	max.	min.	ave.	max.	min.	ave.	max.	min.	ave.	max.	min.	ave.	max.
100	-	-	-	-	-	1.50	1.00	-	2.00	1.00	-	2.50	1.00	2.00	3.00
200	-	-	-	-	-	3.00	1.00	2.50	4.00	1.25	3.13	5.00	1.50	-	5.00
250	-	-	-	-	2.38	3.75	1.25	3.13	5.00	1.56	3.28	5.00	1.87	-	5.00
333.3	-	2.17	3.33	1.24	3.13	4.99	1.66	3.33	5.00	2.08	-	5.00	2.49	-	5.00
500	1.25	3.13	5.00	1.87	3.44	5.00	2.50	-	5.00	-	-	-	-	-	-
666.6	1.66	-	5.00	2.49	-	5.00	3.33	-	-	-	-	-	-	-	-
1000	2.50	-	5.00	3.75	-	-	-	-	-	-	-	-	-	-	-

Remark: the average (ave.) thickness is calculated only if the difference between the minimum (min.) and the maximum (max.) thickness is sufficiently large.

All combinations from Table 6-1 and Table 6-2 taken into account, amounts to 1104 different geometries!

2 Procedure

2.1 Determination of a capacity curve

Interaction curves

Four interaction curves are determined for all 1104 geometries. The first curve represents the interaction curve of the **perfect** structure (without equivalent imperfections), is always abbreviated as "--", and is coloured in black (See Fig. 6-1). The second, third, and fourth curve represent the interaction curves of the **imperfect** structure. For all cases, an inward weld depression type A with half-wavelength equal to λ_b was adopted as equivalent imperfection pattern. In Section 9 of Chapter 5, the reader can find the results of the imperfection sensitivity study and the choice for this pattern. The characteristic amplitude of the weld depression is related to the quality of fabrication classes (A, B, and C) defined in the Eurocode (EN 1993-1-6, 2007). The interaction curves of the imperfect structure are coloured in correspondence to the fabrication class: green (A), orange (B), and red (C) (See Fig. 6-1).

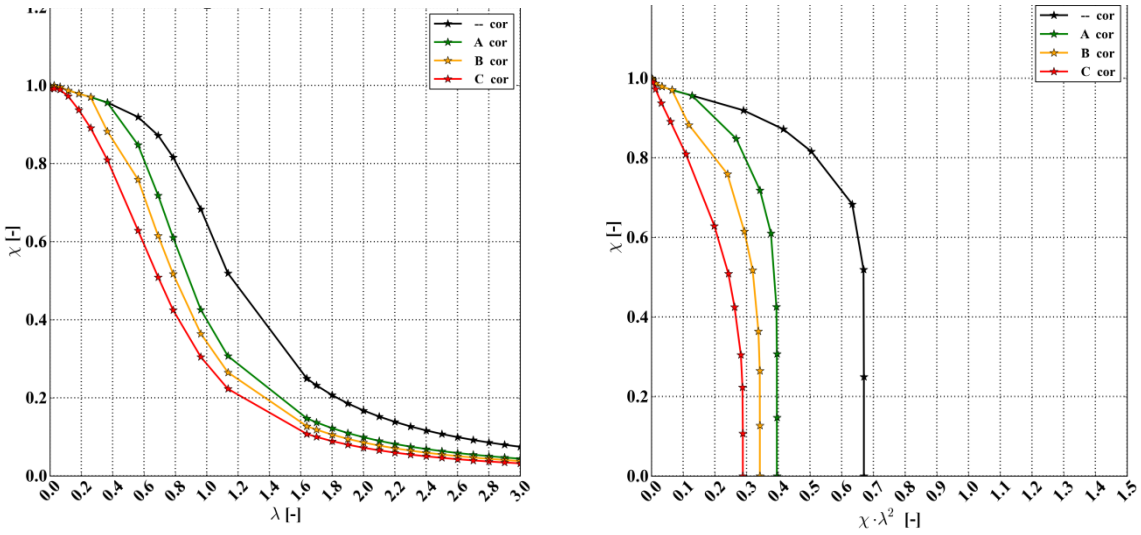

Fig. 6-1 Illustrative example of a traditional (left) and a modified capacity curve (right).

Variable yield strength

To determine an interaction curve, the overall slenderness λ of the structure is varied by changing the yield stress σ_y of (all parts of) the structure (See Section 4.2.2 of Chapter 2), as firstly proposed by Rotter (Rotter, 2003). For the numerical simulations which take into account material non-linearity (i.e. GMN(I)A and MNA), the yield stress σ_y of the ideal elasto-plastic material behaviour is varied, while the elastic material parameters (E and ν) remain constant.

For the GMN(I)A analysis, the considered values of the yield stress were determined during the initial stage of the final study on the basis of three criteria: (1) a sufficiently smooth interaction curve, (2) the calculated points are distributed along the complete interaction curve, and (3) a clear transition between the different regions of the interaction curve (i.e. fully plastic; elasto-plastic; fully elastic). To satisfy these criteria for all geometries, both realistic and fictional values were given to the yield stress σ_y and the calculated values were related to the radius-to-thickness ratio R/t. The complete matrix of yield stresses (in the first row) and the radius-to-thickness ratios R/t (in the first column) is presented in Table 6-3.

In contrast, only two yield stresses (i.e. 235 and 960MPa) were considered for the MNA calculation (with a small displacement theory), because a large number of load increments are necessary before the full plastic strain field has been developed, as is the case in silos. Furthermore, it is assumed that the plastic limit load varies linearly with the yield stress. For the ultimate curve, the MNA calculation is taken into account where yielding has developed most extensively, which corresponds with the calculation with the highest plastic limit load to yield stress ratio F_{pl}/σ_y, as mentioned in Section 6.3 of (EN 1993-1-6, 2007): *"(4) Where a MNA analysis is used, the load ratio* $r_{R,MNA}$ *may be taken as the largest value attained in the analysis, ignoring the effect of strain hardening. This load ratio is identified as the plastic*

reference resistance ratio r_{pl} in 8.7.". Afterwards, an arbitrary plastic limit load $F_{pl}(\sigma_y)$ can be determined by using Eq. (6-1).

$$F_{pl}(\sigma_y) = \sigma_y \cdot max\left(\frac{F_{pl}(235MPa)}{235MPa}; \frac{F_{pl}(960MPa)}{960MPa}\right) \quad (6\text{-}1)$$

Table 6-3 Yield stress σ_y as a function of the radius-to-thickness ratio R/t (GMN(I)A calculations).

		YIELD STRESS σ_y																				
R/t	n_y	1	3	5	10	25	50	75	100	125	150	175	235	300	355	460	550	690	960	1250	1500	2000	2500
100	12	x	-	-	x	-	x	-	x	-	-	-	x	-	x		-	x	x	x	x	x	x
200	12	x	x	-	x	x	x	-	x	-	-	-	x	-	x	x	-	x	x	-	-	x	-
250	13	x	x	-	x	x	x	-	x	-	x	-	x	-	x	x	x	x	x	-	-		-
333.3	13	x	x	x	x	x	x	-	x	-	x	-	x	-	x	x	x	x	-	-	-	-	-
500	13	x	x	x	x	x	x	-	x	-	x	x	x	x	x	-	-	x	-	-	-	-	-
666.6	12	x	x	x	x	x	x	-	x	-	x	x	x	x	x	-	-	-	-	-	-	-	-
1000	12	x	-	x	x	x	x	x	x	x	x	-	x	-	x	-	-	-	-	-	-	-	-

Calculations

For the determination of four interaction curves, $4 \cdot n_y + 7$ calculations (1 LBA, 2 MNA, 4 GN(IA), and $4 \cdot n_y$ GMN(I)A) are performed for each geometry in which n_y is equal to the variable number of yield stresses considered for the GMN(I)A analysis (See Table 6-4). This corresponds with 55 ($n_y = 12$) or 59 ($n_y = 13$) analyses per geometry and approximately 63156 analyses for the entire final study.

Table 6-4 Calculation of the number of analyses to perform for each geometry.

SHELL ANALYSIS	INTERACTION CURVE				
	PERFECT	A	B	C	ALL
LBA	1	-	-	-	1
MNA	2	-	-	-	2
GMN(I)A	n_y	n_y	n_y	n_y	$4 \cdot n_y$
GN(I)A	1	1	1	1	4
				SUM	$\mathbf{4 \cdot n_y + 7}$

2.2 Initial findings

As the slenderness λ decreases to zero, many buckling curves evolve to a value of χ smaller than the expected unity, for the perfect structure as well as for the imperfect structure (See Fig. 6-2). Further investigation for a number of randomly chosen geometries at $R/t = 200;\ 500;\ 1000$ revealed that the cause of this observation is twofold: (1) the calculated plastic limit load frequently exceeds the true plastic limit load (sometimes considerably) and (2) the presence of a weld depression (type A) in the critical region. These findings will now be discussed more in detail for three examples.

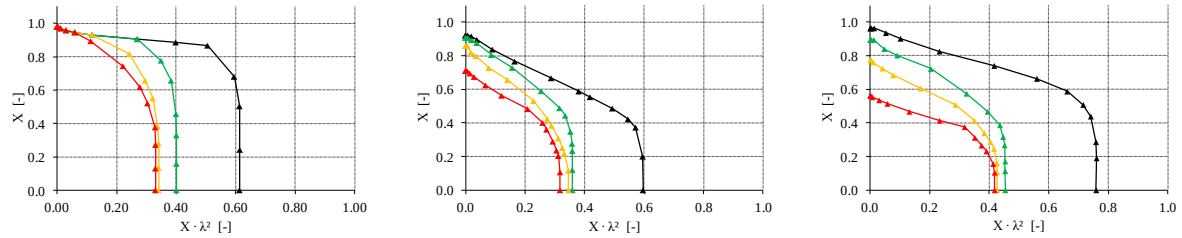

(a) Geometry 1 with $R/t = 200$. (b) Geometry 2 with $R/t = 500$. (c) Geometry 3 with $R/t = 1000$.

Fig. 6-2 Calculated modified capacity curves of three example cases.

2.2.1 Plastic limit load

Accurate determination of the plastic limit load in literature

Since the plastic limit load F_{MNA} (or F_{pl}) is used for the determination of all relative slendernesses λ (i.e. $\sqrt{F_{MNA}/F_{LBA}}$) and all dimensionless strengths χ (i.e. F_{GMNA}/F_{MNA}), it is crucial to determine this load very precisely. However, Rotter points out the danger of overestimating the "true" plastic limit load considerably (Rotter, 2005). According to Rotter, it is possible that FEA software (e.g. Abaqus) automatically invokes "fictitious" strain hardening at large strains (despite the ideal elasto-plastic material behaviour - without strain hardening) to ensure numerical stability. Because of these two reasons and the suspicion of too small values of the strength χ (remarkable at low slendernesses with $\chi < 1$), the method described by Doerich and Rotter (2011a) has been followed in this section. Instead of taking the largest value of the load at the end of a very long analysis (MNA) (EN 1993-1-6, 2007), a method was developed by Doerich (1) to provide a prediction for the plastic limit load without a close approach of that load and (2) to assess the accuracy of the prediction. In this way, it is not necessary that the complete plastic strain field is developed (by means of a long-during MNA calculation) to estimate the asymptotic load.

The first objective can be obtained on the basis of a Modified Southwell (MS) plot (See Fig. 6-3 (b)). In such a plot, the dimensionless load F/F_{ref} is plotted against the ratio of the

dimensionless load F/F_{ref} and a dimensionless displacement U/t. The latter ratio $\frac{F/F_{ref}}{U/t}$ is a measure of the secant stiffness and approaches zero as plasticity progressively increases (the load increments are decreasing, while the deformations are increasing faster). In this way, the elastic, elasto-plastic, and plastic range of a load-displacement diagram (F/F_{ref} versus U/t) (Fig. 6-3 (a)) are presented (from right to left) by a vertical line on the right part of the figure, an intermediately increasing curve, and a horizontal line on the left part of the figure. Furthermore, the hyperbolic shape of a load-displacement diagram close to the plastic limit load is transformed into a linear function. By linear extrapolation of the slope of the MS plot to the load axis (i.e. the purple dashed line in Fig. 6-3 (b)), an upper bound estimate of the plastic limit load F_{ms}/F_{ref} can be obtained. This method is based on the assumption that the slope remains unchanged as the condition $\frac{F/F_{ref}}{U/t} = 0$ is approached.

A Convergence Indicator Plot or abbreviated CIP (See Fig. 6-3 (c)) is used for an improved estimate of the collapse load F_{cip}/F_{ref} and its accuracy. This plot depicts the estimate of the plastic limit load F_{ms}/F_{ref} as a function of omega ω, which is defined as in Eq. (6-2).

$$\omega = \frac{F_{ms}/F_{ref} - F/F_{ref}}{F/F_{ref}} \tag{6-2}$$

The improved prediction of the collapse load F_{cip}/F_{ref} can be obtained by the point of intersection of the linear trend (i.e. the purple dashed line in Fig. 6-3 (c)) and the load axis. The value of ω approaches zero as the plastic limit load is reached and is thus a measure of the accuracy of that estimate.

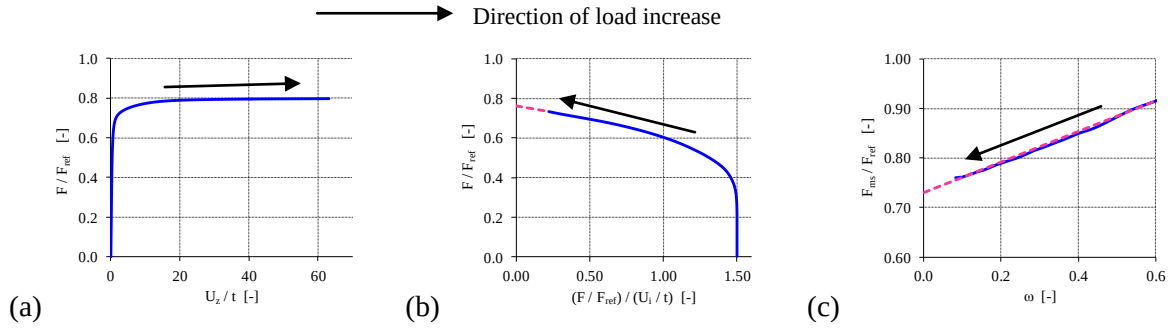

Fig. 6-3 Load-displacement diagram (a), Modified Southwell plot (b) and Convergence Indicator Plot (c).

Accurate determination of the plastic limit load for the example geometries of the final study

The above mentioned method and graphs depend on a load F and a displacement U. Here, the load F is taken equal to the total load on the upper edge of the cylindrical barrel, while the choice for a location and a direction of the displacement U is more challenging. Since this choice is surely important for the quality of the prediction, the method is applied for a wide

range of points in the region of extensive yielding (i.e. the unstiffened silo wall above the top of the U-shaped longitudinal stiffeners/engaged columns) and both the radial and the axial displacement component are every time considered. In other words, the method is applied for a large number of combinations by the use of a Python script.

For the radial and the axial displacement component in one point, the results of the method are presented below (very similar results are obtained for other points and other geometries). The four graphs represent the load-displacement diagram (upper left), the MS plot (upper right), the CIP plot (lower left), and a plot of the evolution of omega as a function of the increment number (lower right).

For both load-displacement diagrams presented in Fig. 6-4, the asymptotic plastic limit load is gradually reached, which is within expectations. In contrast, the results of the other plots are surprising. The right part of the MS plot evolves towards a certain value at the load axis, which corresponds with the upper bound estimate of the plastic limit load F_{ms}/F_{ref}). That apparent twist in the curve, the slope of the left part of the MS plot, and thus the upper bound estimate of the plastic limit load F_{ms}/F_{ref}, suddenly start to increase again. In fact, the opposite was expected: the upper bound estimate of the plastic limit load F_{ms}/F_{ref} must gradually decrease. This finding is more clearly visible in the lower figures, where the upper bound estimate of the plastic limit load F_{ms}/F_{ref} is plotted against ω and the increment number, respectively.

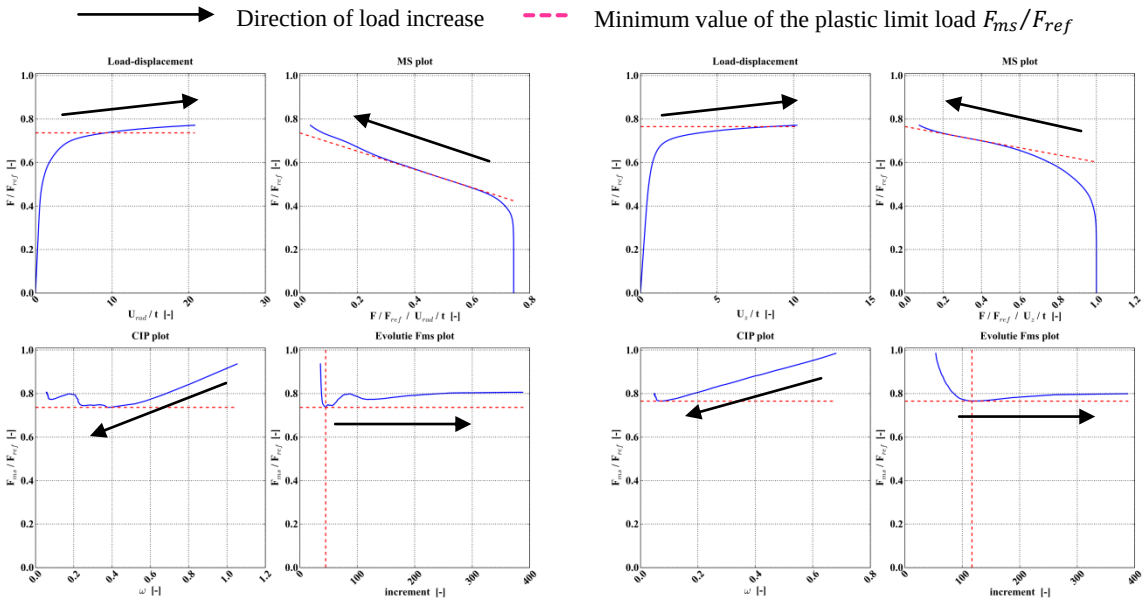

Fig. 6-4 Radial displacement (left) and axial displacement (right) for geometry 2 ($R/t = 500$).

The minimum value of the upper bound estimate of the plastic limit load F_{ms}/F_{ref} in these graphs has been adopted as the best prediction for the "true" plastic limit load. This value is systematically smaller than the calculated plastic limit load reached at the end of the load-

displacement diagram. Probably, the sudden increase of the plastic limit load estimate is caused by strain hardening at large strains invoked by Abaqus (Rotter, 2005).

In Fig. 6-5, the thousands of values of the minimum estimate of the plastic limit load are plotted for the three geometries. As can be observed, the first figure contains much less points than the other figures. This is because the plastic limit load cannot be predicted on the basis of (radial) displacements which suddenly (during the calculation) evolve in the opposite direction than the initial direction. The purple dashed horizontal line corresponds with the required value of the plastic limit load estimate in order that the dimensionless strength χ of the capacity curve of the perfect structure evolves to the unity for smaller slendernesses λ. From this figure, it can be concluded that most of the estimated values are relatively close to that value.

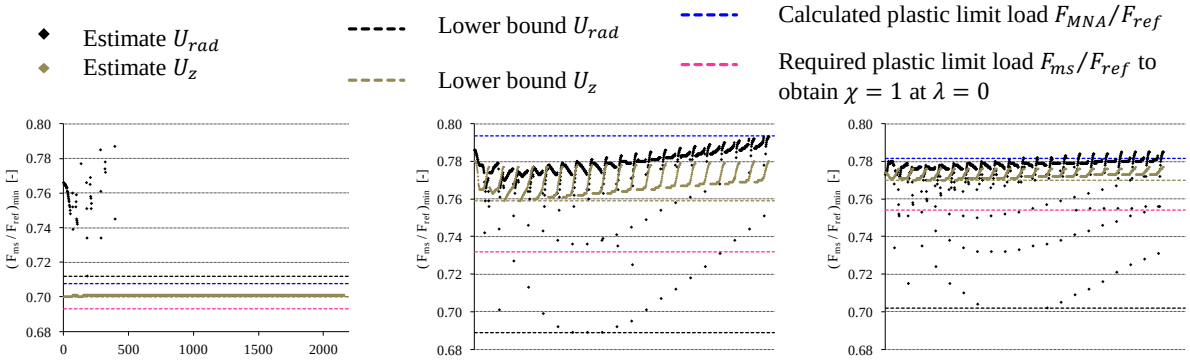

(a) Geometry 1 with $R/t = 200$. (b) Geometry 2 with $R/t = 500$. (c) Geometry 3 with $R/t = 1000$.

Fig. 6-5 Estimates of the dimensionless plastic limit load F_{ms}/F_{ref} for a large number of combinations of radial (black) and axial (brown) displacements, uniformly distributed in the shell wall above the top of the U-shaped stiffener.

Since the calculated plastic limit load is frequently (much) larger than the "true" plastic limit load, as previously demonstrated for three geometries, all capacity curves are systematically scaled so that the dimensionless strength χ of the capacity curve of the perfect structure evolves to the unity for smaller slendernesses λ. For the three cases, the modified capacity curves before and after scaling are plotted in respectively Fig. 6-2 and Fig. 6-6.

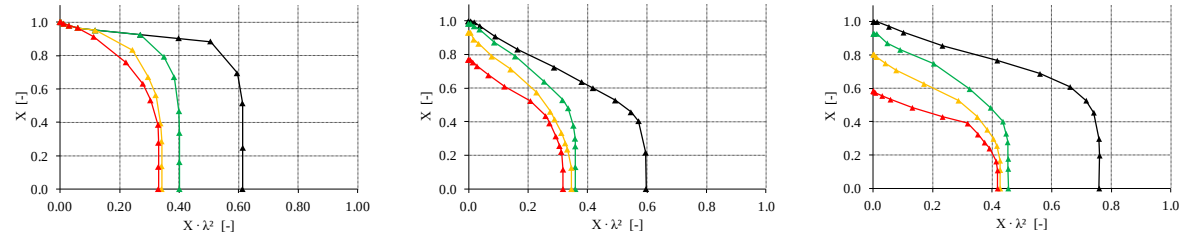

(a) Geometry 1 with $R/t = 200$. (b) Geometry 2 with $R/t = 500$. (c) Geometry 3 with $R/t = 1000$.

Fig. 6-6 Calculated modified capacity curves of three example cases (true plastic limit load).

Now, the capacity curves of the perfect structure always have the desired shape. However, the capacity curves of the imperfect structure frequently still have a different shape than may be expected, as the dimensionless strength χ evolves to a value smaller than the unity when the slenderness λ decreases (See Fig. 6-6 (b) and (c)). This deviation from the expected shape is caused by the presence of a circumferential weld depression type A in the unstiffened silo wall just above the top of the U-shaped longitudinal stiffeners/engaged columns. This finding will be discussed further in the next paragraphs.

2.2.2 Weld depression type A

The purpose of the presence of a weld depression, or generally speaking an imperfection, is to reduce the resistance against failure (due to meridional compression). In this way, the weakened structure will fail prematurely as a consequence of pure elastic buckling, plastic yielding, or a combination of both. When an imperfect collapsed silo is compared with a perfect collapsed silo, a number of things are changed due to the presence of a weld depression.

Firstly, the location of failure shifts from the unstiffened silo wall just above the top of the U-shaped longitudinal stiffeners/engaged columns to the unstiffened silo wall at the weld depression. Secondly, in the vicinity of the weld depression, both membrane and bending stresses are influencing the failure behaviour. The presence of bending stresses results in a partially compressed silo wall (over the thickness) (See Fig. 5-118) causing early yielding on one surface of the shell wall (See Fig. 5-116 and Fig. 5-117). In other words, a large difference in behaviour can be distinguished between an imperfect and a perfect structure, without any other modifications (even minor) to the structure.

Because the strength χ is defined as the ratio of the GMNIA failure load to the MNA plastic limit load, two failure loads are divided by each other with a different shell theory (non-linear versus linear), a different shell geometry (imperfect versus perfect), and consequently, due to the presence or absence of an imperfection, also a totally different (failure) behaviour. As a consequence, for smaller values of the slenderness, the GMNIA failure load (of an imperfect structure) will generally not reach the MNA plastic limit load (of a perfect structure) and the values of the dimensionless strength χ below the unity are unavoidable in the way the dimensionless strength χ is defined, also for small slendernesses (and yield stresses).

3 Study of the complete dataset

For this section, a part of the calculated dataset is compared with the current design rule mentioned in the Eurocode for meridional compression (i.e. the buckling parameters α_x, $\lambda_{x,0}$, β_x, and η_x given in Section 4.2.4 of Chapter 2) (EN 1993-1-6, 2007). For the calculated dataset, only those data points are considered which have realistic yield stresses and are used

for steel silos in practice: 235; 355; 460; 690; 960MPa. As can be seen, both conventional steel grades and high strength steels are taken into account. In contrast, neither very small nor very large values of the yield stress (e.g. 1MPa or 2000MPa) are included from the comparison, because these values are far from realistic. This comparison dataset consists of approximately 28000 points.

Both the characteristic dimensionless strength $\chi_{Rk,EC}$ and the design dimensionless strength $\chi_{Rd,EC}$ obtained with the parameters in the Eurocode are compared with the above dataset. Then, it is looked which partial coefficient on the resistance γ'_{M1} is effectively required in order that the Eurocode nearly always estimates the elasto-plastic strength $\chi'_{Rd,EC}$ safely. Afterwards, as improvement of the existing buckling parameters for meridional compression (i.e. α_x, $\lambda_{x,0}$, β_x, and η_x), a number of proposals have been suggested for these parameters, by determining the best lower bound to the above mentioned dataset.

3.1 Comparison with the Eurocode

The results of the comparison between the Abaqus dataset and the interaction curves, determined on the basis of the buckling parameters for meridional compression (EN 1993-1-6, 2007), are presented in . For clarity reasons and because the (im)perfect elastic factor α_x depends on the radius-to-thickness ratios R/t and the fabrication quality of the barrel, the results are sorted according to these parameters. In Fig. 6-7, the results are presented for $R/t = 200$ (a) and $R/t = 1000$ (b). In Appendix C, identical plots are included for all radius-to-thickness ratios R/t (i.e. $R/t =$ 100, 200, 250, 333.3, 500, 666.6, and 1000). Each figure consists of four plots: perfect structure (upper left), quality class A (upper right), quality class B (lower left), and quality class C (lower right), showing the dimensionless strength χ on the vertical axis and the relative slenderness λ on the horizontal axis.

In Fig. 6-7 and all figures given in Appendix C, the parameters $\chi_{Rk,EC}$ and $\chi_{Rd,EC}$ represent, respectively, the characteristic and the design value of the strength estimated by the Eurocode (with $\chi_{Rd,EC} = \chi_{Rk,EC}/\gamma_{M1}$), with a partial coefficient on the resistance γ_{M1} equal to 1.10 (EN 1993-1-6, 2007). This parameter reduces the characteristic value of the estimate of the elasto-plastic strength $\chi_{Rk,EC}$ (and load) by approximately 9% to its design value $\chi_{Rd,EC}$ (See Eq. (2-37) in Section 4.4.2 and Eq. (2-43) in Section 4.4.3).

The results are surprisingly good: both interaction curves (based on the buckling parameters in the Eurocode for uniformly supported unstiffened silos) are located relatively close to the lower bound of the cloud with calculated points (for locally supported stiffened silos). Generally, the points with the smallest strengths χ_{Abq} are located below the design interaction curves $\chi_{Rd,EC}$ for the perfect silos (all values of R/t) and the more thick-walled imperfect silos (i.e. $R/t < 500$), which corresponds to an unsafe situation. Indeed, for these points

(with $\lambda < 1$), the design value of the lower bound estimate of the strength $\chi_{Rd,EC}$ can be larger than the calculated value of the strength χ_{Abq}. In contrast, for the relatively thin-walled imperfect silos (i.e. $R/t \geq 500$), the points with the smallest strengths χ_{Abq} generally coincide with or are located above the design interaction curves $\chi_{Rd,EC}$, which corresponds to a safe situation. Indeed, for these points (with $\lambda > 1$), the design value of the lower bound estimate of the strength $\chi_{Rd,EC}$ is equal to or smaller than the calculated value of the strength χ_{Abq}.

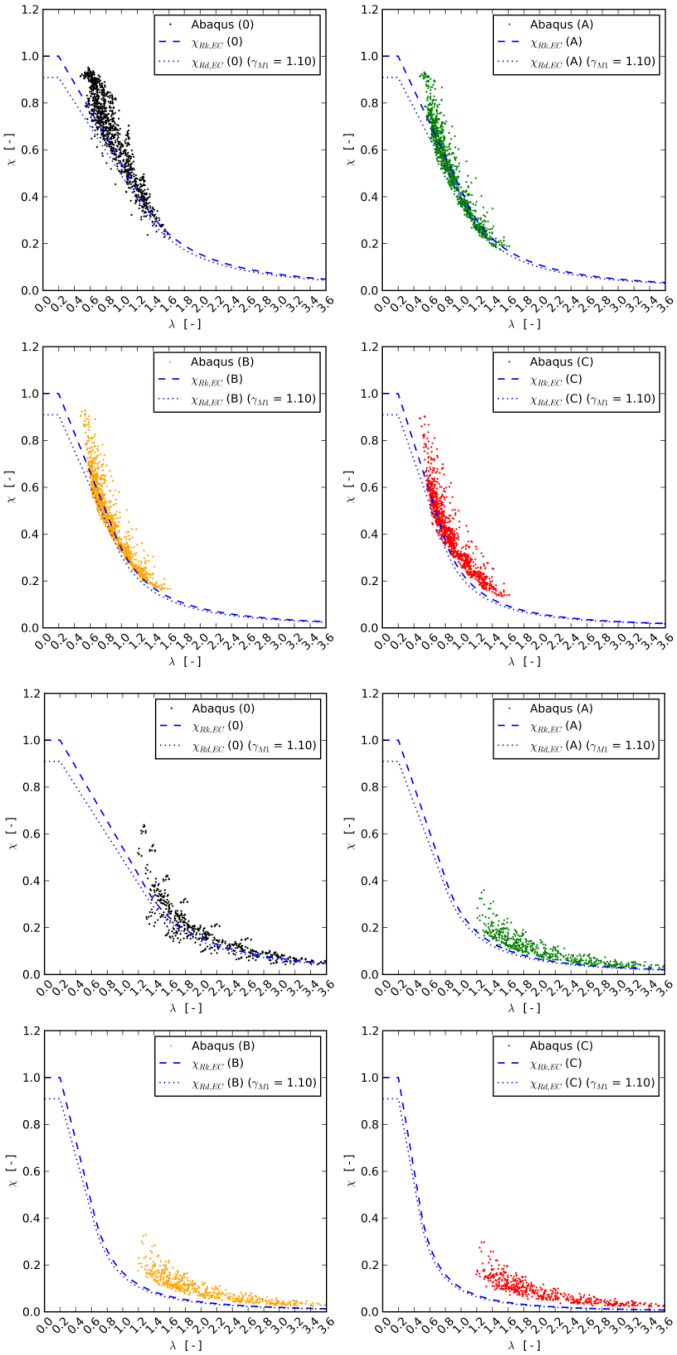

(a) $R/t = 200$.

(b) $R/t = 1000$.

Fig. 6-7 Calculated data points versus the characteristic strength $\chi_{Rk,EC}$ and the design values of the strength χ_{Rd},EC estimated with the Eurocode (with $\gamma_{M1} = 1.10$).

To conclude, the conservatism, because locally supported stiffened silos are designed based on the buckling parameters for uniformly supported unstiffened silos, seems to be better than expected from the literature (See Section 4.2.4 of Chapter 2) (EN 1993-1-6, 2007; ECCS, 2008).

3.2 Partial coefficient on the resistance

According to the expressions given in Annex D of Eurocode 0, a partial coefficient on the resistance γ_{M1} is determined for which the current buckling parameters conservatively predict the elasto-plastic buckling strength (and thus load) (EN 1990, 2002). For completeness, the used expressions are included in Appendix D. If the new value γ_{M1} is smaller or equal to the current value of γ_{M1} (1.10), then we can conclude that the Eurocode is on the safe side. In the opposite case, the current value of γ_{M1} should be increased to the new value γ_{M1}.

The value γ_{M1} was verified for (1) the complete dataset, (2) the dataset sorted by quality class, and (3) the dataset sorted by quality class and relative slenderness λ. The detailed results can also be found in Appendix D. When the complete dataset is considered (i.e. verification 1), a value of γ_{M1} equal to 1.00 is obtained. For the second verification (complete dataset is split by quality class), the obtained values of γ_{M1} are 0.97, 0.98, 0.92, 0.88 for silos without imperfections, with quality class A, B, and C, respectively. For the third verification, the results are depicted in Fig. 6-8. A decreasing trend of γ_{M1} (and thus an increased conservatism) can be found when the fabrication quality class decreases and the relative slenderness increases. Since all values are smaller than the current value of 1.10, it is not necessary to make adjustments to the current value. Finally, it is important to mention that the value of γ_{M1} should always be minimally equal to the unity.

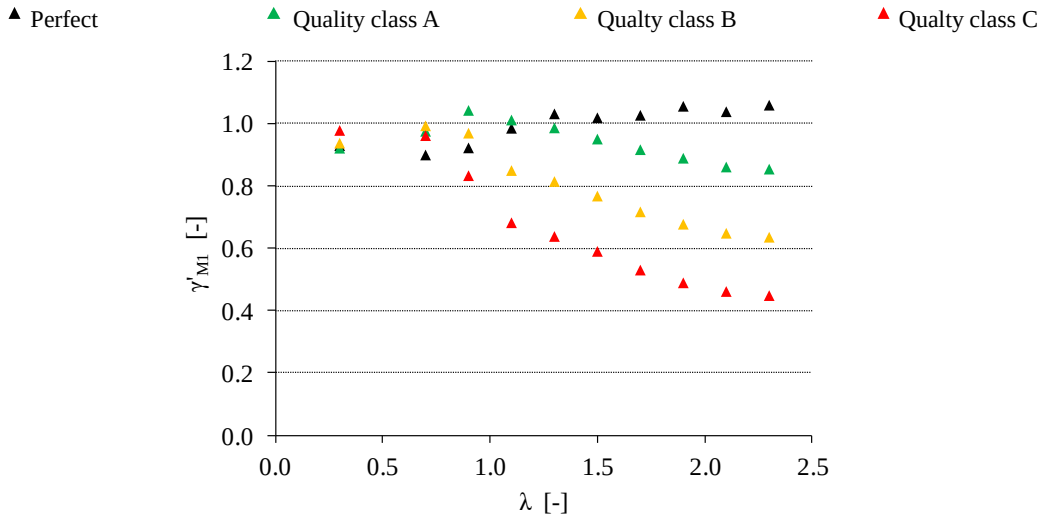

Fig. 6-8 Partial coefficient on the resistance γ_{M1}as a function of the slenderness λ, sorted by the quality class.

3.3 Development of new proposals

When the buckling parameters for meridional compression (i.e. α_x, $\lambda_{x,0}$, β_x, and η_x) and the corresponding interaction curves (EN 1993-1-6, 2007) are used for the elasto-plastic buckling load estimate, a larger value is required for the partial coefficient on the resistance γ_{M1} (See Section 3.2) because these curves do not fit precisely with the lower bound of the dataset. Therefore, an attempt is done to determine new interaction parameters (i.e. α_x, $\lambda_{x,0}$, β_x, and η_x) which are fitting better with the lower bound of the dataset.

3.3.1 Techniques for the determination of a lower bound

The attempt to determine new buckling parameters is done by fitting a wide range of interaction curves to the dataset of the final study and by taking the best fitting lower bound to the dataset as new proposal. In total, four proposals are suggested: two formulas are applied for the determination of the (im)perfect elastic factor α_x, and the interaction exponent η_x can be either constant or vary linearly in the elasto-plastic part of the capacity curve. Table 6-5 gives an overview of the applied methods.

Table 6-5 Overview of the methods applied for the lower bound fitting.

	INTERACTION CURVE	
	MERIDIONAL ELASTIC FACTOR α_x	INTERACTION EXPONENT η_x
METHOD 1	Formula 1 - Eq. (6-3)	Constant
METHOD 2	Formula 1 - Eq. (6-3)	Linear
METHOD 3	Formula 2 - Eqs. (6-4) to (6-7)	Constant
METHOD 4	Formula 2 - Eqs. (6-4) to (6-7)	Linear

3.3.2 Procedure

In short, for a large number of sets of buckling parameters (discussed in Sections 3.3.3 and 3.3.4), the value of the dimensionless strength $\chi_{fit}(\lambda_i)$ is calculated as a function of a variable relative slenderness λ_i (with $\lambda_{min} = 0.00$; $\lambda_{max} = 5.00$; $\Delta\lambda = 0.02$) by using Eqs. (2-16) to (2-18) (See scheme presented in Fig. 6-9). Afterwards, each calculated value of the dimensionless strength $\chi_{fit}(\lambda_i)$ is compared with all calculated values of the strengths $\chi_{Abq}(\lambda_i)$ with approximately the same slenderness (within the range $[\lambda_i - 0.5 \cdot \Delta\lambda;\ \lambda_i + 0.5 \cdot \Delta\lambda]$). This comparison includes the counting of the number of points and the average deviation of the calculated values of points which are located below the fitted curve. In this way, the best-fitting lower bound can be determined. This comparison and the corresponding criteria for the determination of the best-fitting curve are discussed more in detail in Section

3.3.5.

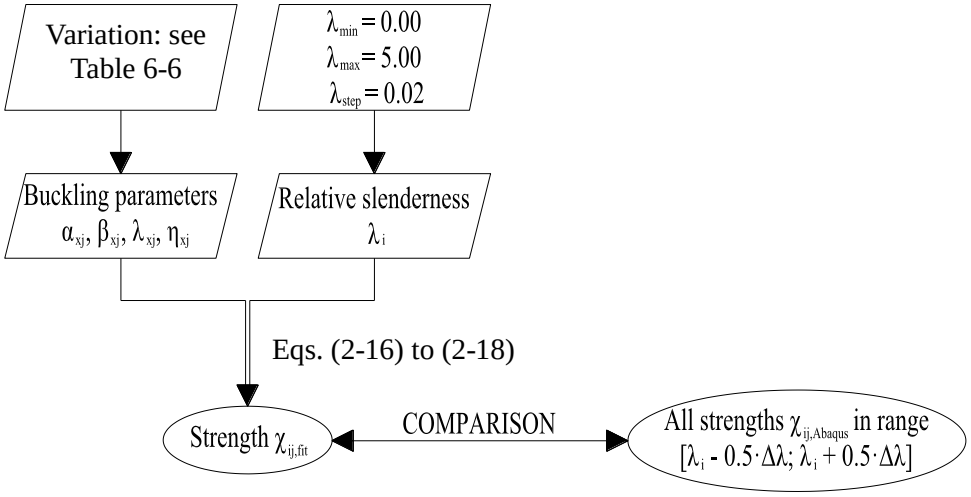

Fig. 6-9 Scheme of the procedure for the determination of the lower bound.

3.3.3 Variation of the buckling parameters

Meridional elastic imperfection reduction factor

For methods 1 and 2 (See Table 6-5), the meridional elastic imperfection reduction factor α_x is calculated using Eq. (6-3) and depends on the radius-to-thickness ratio R/t and the quality class (See Eqs. (2-31) and (2-32)). This expression is very similar to the formula given in (EN 1993-1-6, 2007) (See Eq. (2-31)), but the constant coefficients are replaced by three variable coefficients a, b, and c. The minimum value, the maximum value, and the incremental value of these coefficients are given in Table 6-6.

$$\alpha_x = \frac{a}{1 + b \cdot (\Delta w_k / t)^c} \tag{6-3}$$

For methods 3 and 4 (See Table 6-5), for each quality class, a constant value is determined for the meridional elastic imperfection reduction factor α_x (See Eqs. Eqs. (6-4) to (6-7)), and independently of the radius-to-thickness ratio R/t. The minimum value, the maximum value, and the incremental value of $\alpha_{x,0}$, d, e, and f are given in Table 6-6.

$$\alpha_{x,0} = \text{a constant value} \tag{6-4}$$

$$\alpha_{x,A} = d \cdot \alpha_{x,0} \tag{6-5}$$

$$\alpha_{x,B} = e \cdot \alpha_{x,0} \tag{6-6}$$

$$\alpha_{x,C} = f \cdot \alpha_{x,0} \tag{6-7}$$

All buckling parameters

The range of all interaction parameters is presented in Table 6-6. For all parameters, the lower limit and the upper limit were always chosen sufficiently small/large so that all possible combinations are included. A fixed step size is adopted for all parameters, except for the interaction exponents (i.e. η_x, $\eta_{x,0}$, and $\eta_{x,p}$). For these exponents, the value is interpolated linearly between a minimum step size in $\eta_{x,min}$ and a maximum step size in $\eta_{x,max}$. In this way, a more regular step size is obtained for the curvature and the dimensionless strength $\chi_{i,fit}$ in the elasto-plastic part.

Table 6-6 Overview of all varied parameters (fitting lower bound dataset).

					METHOD			
PAR.		MINIMUM	MAXIMUM	STEP	1	2	3	4
α_x [-]	a	0.40	0.80	0.05	X	X	-	-
	b	0.40	3.00	0.20	X	X	-	-
	c	0.20	2.00	0.20	X	X	-	-
	$\alpha_{x,0}$	0.30	0.45	0.01	-	-	X	X
	d	0.30	0.90	0.05	-	-	X	X
	e	0.30	0.80	0.05	-	-	X	X
	f	0.30	0.70	0.05	-	-	X	X
β_x [-]		0.40	0.98	0.02	X	X	X	X
$\lambda_{x,0}$ [-]		0.00	0.20	0.10	X	X	X	X
$\lambda_{x,p}$ [-]	Eq. (2-15) $= f(\alpha_x; \beta_x)$				X	X	X	X
η_x [-]		0.40	5.00	0.20 (at $\eta_x = \eta_{x,min}$) $\longrightarrow$ 0.80 (at $\eta_x = \eta_{x,max}$)	X	-	X	-
$\eta_{x,0}$ [-]		0.40	$\min(5.00; \eta_{x,0}^{max})$	0.20 (at $\eta_{x,0} = \eta_{x,min}$) $\longrightarrow$ 0.80 (at $\eta_{x,0} = \eta_{x,max}$)	-	X	-	X
$\eta_{x,p}$ [-]		0.40	$\min(5.00; \eta_{x,p}^{max})$	0.20 (at $\eta_{x,p} = \eta_{x,min}$) $\longrightarrow$ 0.80 (at $\eta_{x,p} = \eta_{x,max}$)	-	X	-	X

3.3.4 Restrictions to the buckling parameters

The squash limit relative slenderness $\lambda_{x,0}$ must always be smaller than the plastic limit relative slenderness $\lambda_{x,p}$:

$$\lambda_{x,0} < \lambda_{x,p} \tag{6-8}$$

Constant interaction exponent

A constant interaction exponent η_x has been adopted for methods 1 and 3 (See Table 6-5).

When the relative slenderness is equal to $\lambda_{x,p}$, the elasto-plastic part of the interaction curve must have a less negative slope than the elastic part. This limitation translates into a maximum value of the plastic range factor $\beta_{x,max}$ (Eq. (2-24)). This restriction is applied iteratively because the upper limit $\beta_{x,max}$ depends on the plastic limit relative slenderness $\lambda_{x,p}$, which in turn depends on the plastic range factor β_x:

$$\beta_x < \beta_{x,max} \quad \text{(iterative)} \tag{6-9}$$

The restrictions above are applied to all combinations. Only for relatively small and relatively large values of β_x (i.e. respectively late and early yielding), an additional restriction is applied on the interaction exponent η_x (See Eq. (6-10) or Eq. (6-11)), because the curvature of the elasto-plastic part of the interaction curve in $\lambda_{x,p}$, must be negative and positive, respectively (See capacity curve in Fig. 2-16):

$$\eta_x > 1 \qquad \text{when } \beta_x < \beta_{x,late} \tag{6-10}$$

$$0 < \eta_x < 1 \qquad \text{when } \beta_x > \beta_{x,early} \tag{6-11}$$

Where:

$\beta_{x,late} = 0.30$ the upper limit of the plastic range factor for late yielding [-];

$\beta_{x,early} = 0.70$ the lower limit of the plastic range factor for early yielding [-].

Linear interaction exponent

A linear variable interaction exponent η_x has been adopted for methods 2 and 4 (See Table 6-5). To avoid higher predicted resistances in the elasto-plastic range than under elastic conditions, the slope and the curvature of the elasto-plastic interaction curve are restricted in $\lambda_{x,p}$. At the end of the elasto-plastic part of the buckling curve (when $\lambda_x = \lambda_{x,p}$), the slope must be less negative and the curvature must be smaller than, respectively, the slope and the curvature at beginning of the elastic part of the buckling curve. The slope restriction imposes a maximum value on the plastic limit interaction exponent $\eta_{x,p}$ (Eq. (2-26)), while the curvature restriction imposes a maximum value on the squash limit interaction exponent $\eta_{x,0}$ (Eq. (2-27)). The restrictions below are applied for all combinations.

$$\eta_{x,P} < \eta_{x,p}^{max} \tag{6-12}$$

$$\eta_{x,0} < \eta_{x,0}^{max} \tag{6-13}$$

Only for relatively small and relatively large values of β_x (i.e. respectively late and early yielding), an additional restriction is applied on the squash limit interaction exponent $\eta_{x,0}$ (See Eq. (6-14) or Eq. (6-15)), because the curvature of the elasto-plastic part of the interaction curve in $\lambda_{x,p}$ must be negative and positive, respectively (see capacity curve in Fig. 2-16):

$$\eta_{x,0} < \eta_{x,0}^{lim} \qquad \text{when } \beta_x < \beta_{x,late} \tag{6-14}$$

$$\eta_{x,0} > \eta_{x,0}^{lim} \qquad \text{when } \beta_x > \beta_{x,early} \tag{6-15}$$

Eq. (2-30) gives the expression for the limit value of the squash limit interaction exponent $\eta_{x,0}^{lim}$. The same values have been adopted for the upper/lower limit of the plastic range factor for late/early yielding as used for the constant interaction exponent.

3.3.5 Determination of the "best" lower bound

For each valid combination of buckling parameters (See Sections 3.3.3 and 3.3.4), the total number $n_{smaller}$ is counted and the average deviation dev is determined of all calculated points (Abaqus) below the lower bound estimate of the interaction curve.

$$dev = \frac{1}{n_{smaller}} \cdot \sum \chi_{fit} - \chi_{Abq} \qquad \text{when } \chi_{Abq} < \chi_{fit} \tag{6-16}$$

The "best" lower bound corresponds with the curve with the smallest deviation dev and the number of point above the lower bound fit n_{larger} $(= n_{tot} - n_{smaller})$ must be smaller than 97.725% of the total number n_{tot} of calculated points (Abaqus) (i.e. the mean value minus two times the standard deviation).

3.3.6 Results

For the four methods (See Table 6-5), an overview is given in Table 6-7 of the interaction parameters corresponding to the best-fitting lower bound. The last column represents the current interaction parameters for meridional compression mentioned in the Eurocode (EN 1993-1-6, 2007) (discussed in Section 4.2.4 of Chapter 2).

The interaction curve of the characteristic value of the strength $\chi_{Rk,EC}$ obtained from the Eurocode (EN 1993-1-6, 2007), the overall best-fitting lower bound curves according to the four methods, and the Abaqus dataset are plotted in Fig. 6-10. Similar to Fig. 6-7, the results are displayed separately for each radius-to-thickness ratios R/t and the quality of the barrel. In Fig. 6-10, the results are presented for $R/t = 200$ (a) and $R/t = 1000$ (b), while identical plots are included for all radius-to-thickness ratios R/t (i.e. $R/t =$ 100, 200, 250, 333.3, 500, 666.6, and 1000) in Appendix E. Each figure consists of four plots: perfect structure (upper

left), quality class A (upper right), quality class B (lower left), and quality class C (lower right), showing the dimensionless strength χ on the vertical axis and the relative slenderness λ on the horizontal axis.

When the existing Eurocode strength estimate $\chi_{Rk,EC}$ is compared with the proposed lower bound estimates for perfect cylindrical barrels, then we can find that all proposals are systematically located below the Eurocode for all radius-to-thickness ratios R/t. However, the position of the perfect capacity curve is less relevant, because in practice, perfect silos are impossible to construct (not only geometrical imperfections) and when a designer applies the Eurocode, he/she always has to choose a fabrication quality class (A, B, or C).

For quality classes A, B, and C, all proposals are located below the Eurocode curve for the more thick-walled silos ($R/t < 500$, $R/t < 333$, and $R/t < 250$, respectively) over the entire range of slendernesses. When the radius-to-thickness ratios R/t increases, the Eurocode estimate gradually decreases and shifts downwardly, as a result of which the Eurocode interaction curve is located below all proposals for larger slendernesses ($R/t > 500$, $R/t > 333$, and $R/t > 250$, respectively), mainly in the second part of the capacity curve at larger slendernesses.

Table 6-7 Overview of the parameters of the best-fitting lower bounds to the dataset.

PARAMETER		METHOD 1	METHOD 2	METHOD 3	METHOD 4	EUROCODE
α_x [-]	a	0.5	0.5	-	-	0.62
	b	1.0	1.0	-	-	1.91
	c	1.2	1.0	-	-	1.44
	$\alpha_{x,0}$	-	-	0.45	0.43	-
	d	-	-	0.70	0.75	-
	e	-	-	0.60	0.65	-
	f	-	-	0.45	0.50	-
β_x [-]		0.64	0.74	0.56	0.62	0.60
$\lambda_{x,0}$ [-]		0.00	0.00	0.20	0.00	0.20
$\lambda_{x,p}$ [-]		Eq. (2-15) $= f(\alpha_x;\ \beta_x)$				
η_x [-]		1.082	-	1.082	-	1.0
$\eta_{x,0}$ [-]		-	1.371	-	1.697	-
$\eta_{x,p}$ [-]		-	0.600	-	1.082	-
dev [-]		0.111	0.107	0.102	0.101	-

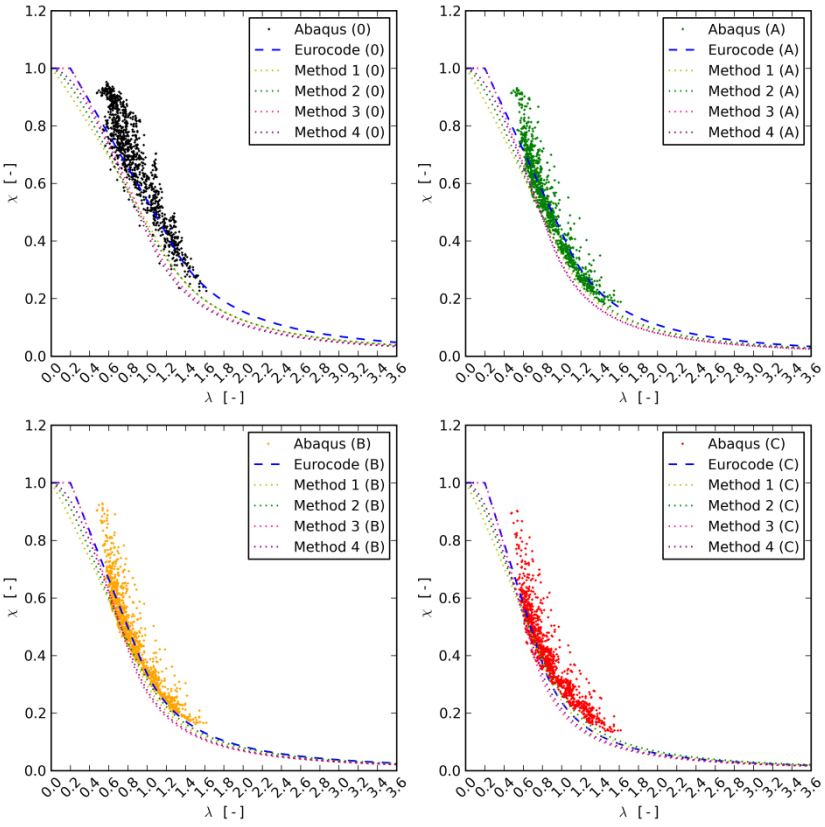

(a) $R/t = 200$.

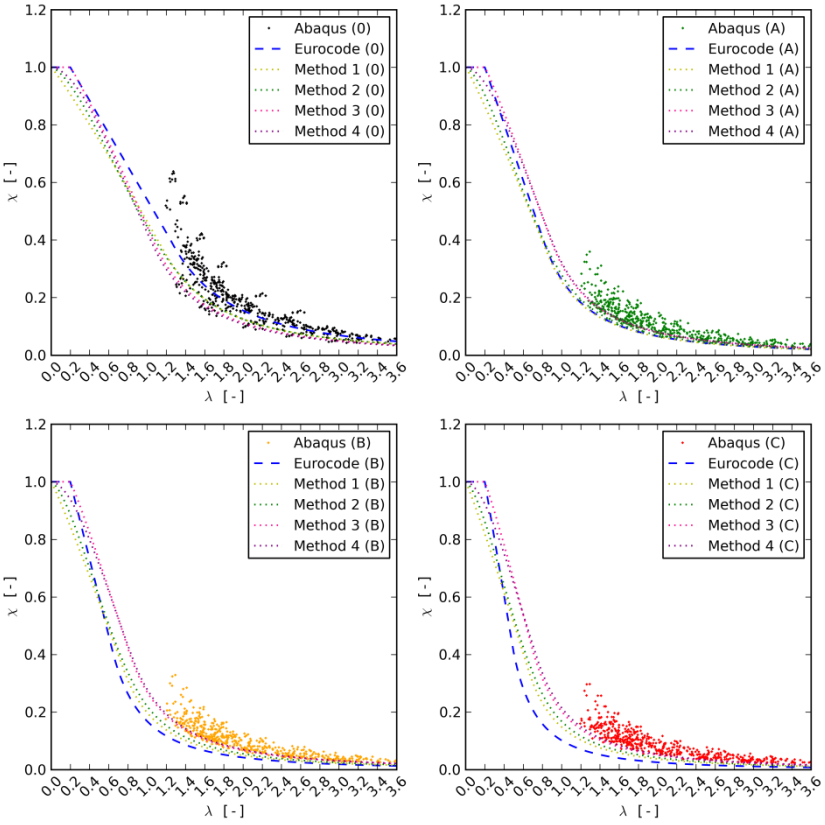

(b) $R/t = 1000$.

Fig. 6-10 Eurocode and the best-fitting lower bounds versus the data points.

4 Study of the individual capacity curves

This part focuses on the determination of the interaction parameters of the best-fitting curves for all capacity curves of the final study (See Section 4.1). Afterwards, in Section 4.2, some plots will be presented and examined of the best-fitting interaction parameters as a function of the geometrical parameters, in an attempt to find relationships between both types of parameters.

4.1 Fitting of the capacity curves

In this section, for all geometries (1104) and for all quality classes (i.e. perfect, A, B, and C), the buckling parameters (i.e. α_x, $\lambda_{x,0}$, β_x, and η_x) will be determined of the best-fitting capacity curve by fitting a large number of interaction curves on each capacity curve. In this way, the $4 \cdot n_y + 7$ failure loads (approximately 60 loads) coupled on the four capacity curves of each geometry (See Table 6-4) are converted into four times a reduced number of key parameters (i.e. α_x, $\lambda_{x,0}$, β_x, and η_x) which describe the complete capacity curve, as firstly proposed by (Rotter, 1999).

4.1.1 Techniques for the fitting of a capacity curve

Because it is not possible with the existing methods to obtain dimensionless strengths χ which are smaller than the unity at relatively small slendernesses (in particular for imperfect structures), either negative values are allowed for the squash limit relative slenderness $\lambda_{x,0}$ or the existing expressions (i.e. Eqs. (2-16) to (2-18)) for the determination of the strength χ are adapted. Furthermore, both methods are applied with a constant and linear interaction exponent η_x in the elasto-plastic part of the capacity curve. In other words, four different techniques have been applied for the fitting of the individual curves (See Table 6-8).

Table 6-8 Overview of the methods applied for the fitting of the individual capacity curves.

	INTERACTION CURVE	
	MODIFICATION COMPARED TO THE STANDARD PROCEDURE	INTERACTION EXPONENT η_x
METHOD 1	Negative squash limit slenderness $\lambda_{x,0}$	Constant
METHOD 2	Negative squash limit slenderness $\lambda_{x,0}$	Linear
METHOD 3	Modified formulas for χ	Constant
METHOD 4	Modified formulas for χ	Linear

4.1.2 Procedure

In short, for a large number of sets of buckling parameters (discussed in Sections 4.1.3 and 4.1.4), the value of the dimensionless strength $\chi_{fit}(\lambda_i)$ is calculated as a function of the relative slenderness (withλ_i $\lambda_i = \lambda_{Abq}$) by using Eqs. (2-16) to (2-18) for methods 1 and 2 and Eqs. (6-17) to (6-19) for methods 3 and 4 (See scheme presented in Fig. 6-11). Afterwards, each fitted value of the dimensionless strength $\chi_{fit}(\lambda_i)$ is compared with the calculated value of the strength $\chi_{Abq}(\lambda_i)$ with the same slenderness λ_i. This comparison includes the calculation of a weighted deviation of the fitted curve relative to the calculated curve. In this way, the best-fitting curve and the corresponding interaction parameters can be determined. This comparison and the corresponding criteria for the determination of the best-fitting curve are discussed more in detail in Section 4.1.5.

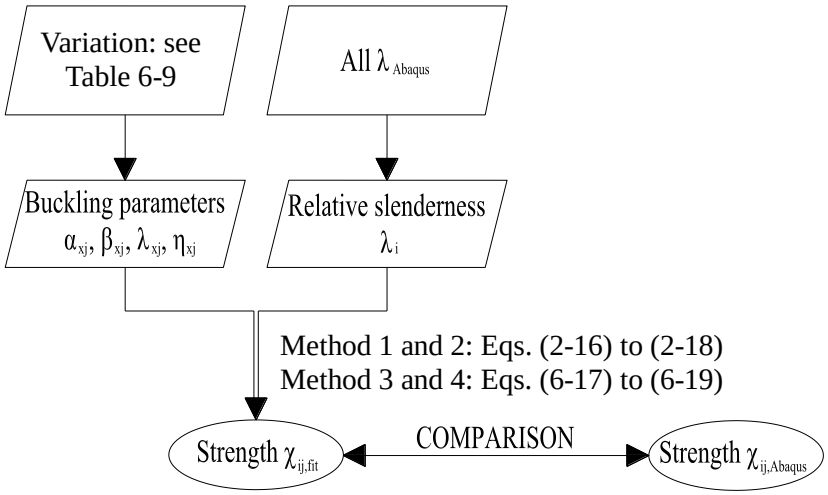

Fig. 6-11 Scheme of the procedure for the fitting of a capacity curve.

4.1.3 Variation of the buckling parameters

Negative squash limit relative slendernesses

For methods 1 and 2 (See Table 6-8), the existing expressions for the calculation of the dimensionless strength χ (i.e. Eqs. (2-16) to (2-18)) are maintained, but now, negative values are allowed for the squash limit relative slenderness $\lambda_{x,0}$. In this way, the elasto-plastic part of the interaction curve can intersect the vertical axis (at $\lambda = 0$) of the dimensionless strength χ at a value smaller than the unity.

Modified formulas for the strength χ

For methods 3 and 4 (See Table 6-8), the existing expressions for the calculation of the dimensionless strength χ (i.e. Eqs. (2-16) to (2-18)) are replaced by two new expressions:

$$\chi = \chi_0 \qquad \text{when } \lambda \leq \lambda_{x,0} \tag{6-17}$$

$$\chi = (\chi_0 - 1) \cdot \left(\frac{\lambda_{x,p} - \lambda}{\lambda_{xp} - \lambda_{x,0}}\right)^{\eta_x} + 1 - \beta_x \cdot \left(\frac{\lambda - \lambda_{x,0}}{\lambda_{x,p} - \lambda_{x,0}}\right)^{\eta_x} \text{ when } \lambda_{x,0} < \lambda < \lambda_{x,p} \tag{6-18}$$

$$\chi = \frac{\alpha_x}{\lambda^2} \qquad \text{when } \lambda_{x,p} \leq \lambda \tag{6-19}$$

In this way, the elasto-plastic part of the interaction curve evolves to a value χ_0 (which can be smaller than the unity) for smaller slendernesses λ.

All buckling parameters

The range of all interaction parameters is presented in Table 6-9. For all parameters, the lower limit and the upper limit were always chosen sufficiently small/large so that all possible combinations are included. A fixed step size is adopted for all parameters, except for the interaction exponents (i.e. η_x, $\eta_{x,0}$, and $\eta_{x,p}$). For these exponents, the value is interpolated linearly between a minimum step size in $\eta_{x,min}$ and a maximum step size in $\eta_{x,max}$. In this way, a more regular step size is obtained for the curvature and the dimensionless strength χ_{fit} in the elasto-plastic part.

Table 6-9 Overview of all varied parameters (fitting curves).

				FITTING METHOD			
PAR.	MINIMUM	MAXIMUM	STEP	1	2	3	4
α_x [-]	$= \alpha_{Abaqus}$			X	X	X	X
β_x [-]	0.05	0.95	0.01	X	X	X	X
χ_0 [-]	$= \chi_{Abaqus}(\lambda = 0)$			-	-	X	X
$\lambda_{x,0}$ [-]	-4.00	0.00	0.20	X	X	-	-
	0.00	0.20	0.05	X	X	X	X
$\lambda_{x,p}$ [-]	Eq. (2-15) $= f(\alpha_x; \beta_x)$			X	X	X	X
η_x [-]	0.40	5.00	0.10 (at $\eta_x = \eta_{x,min}$) $\longrightarrow$ 0.80 (at $\eta_x = \eta_{x,max}$)	X	-	X	-
$\eta_{x,0}$ [-]	0.40	$\min(5.00; \eta_{x,0}^{max})$	0.10 (at $\eta_{x,0} = \eta_{x,min}$) $\longrightarrow$ 0.80 (at $\eta_{x,0} = \eta_{x,max}$)	-	X	-	X
$\eta_{x,p}$ [-]	0.40	$\min(5.00; \eta_{x,p}^{max})$	0.10 (at $\eta_{x,p} = \eta_{x,min}$) $\longrightarrow$ 0.80 (at $\eta_{x,p} = \eta_{x,max}$)	-	X	-	X

4.1.4 Restrictions to the buckling parameters

The same restrictions were imposed on the interaction parameters as discussed in Section 3.3.4.

4.1.5 Determination of the "best-fitting" curve

For each valid combination of buckling parameters (See 4.1.3 and 4.1.4), a weighted deviation $wdev$ is determined which depends on the deviations $dev_{1,i}$ and $dev_{2,i}$ in each calculated point i (Abaqus) and the corresponding weighted coefficients $w_{1,i}$ and $w_{2,i}$. The subscripts indicate in which plot the parameters are determined: 1 = a traditional capacity curve and 2 = a modified capacity curve.

$$wdev = \text{average}\left(\frac{\sum_{i=1}^{i=n_y}(w_{1,i}\cdot dev_{1,i})}{\sum_{i=1}^{i=n_y} w_{1,i}}; \frac{\sum_{i=1}^{i=n_y}(w_{2,i}\cdot dev_{2,i})}{\sum_{i=1}^{i=n_y} w_{2,i}}\right) \quad (6\text{-}20)$$

The deviations $dev_{1,i}$ and $dev_{2,i}$ are equal to the distance between the fitted point i and the calculated point i in, respectively, a traditional plot and a modified plot of the capacity curve.

$$dev_{1,i} = \sqrt{\left(\chi_{fit,i} - \chi_{Abq,i}\right)^2 + \left(\lambda_{fit,i} - \lambda_{Abq,i}\right)^2} \quad (6\text{-}21)$$

$$dev_{2,i} = \sqrt{\left(\chi_{fit,i} - \chi_{Abq,i}\right)^2 + \left(\chi_{fit,i}\cdot\lambda_{fit,i}^2 - \chi_{Abq,i}\cdot\lambda_{Abq,i}^2\right)^2} \quad (6\text{-}22)$$

The weighted coefficients $w_{1,i}$ and $w_{2,i}$ are taken as half the distance between the calculated point i to the previous point $i-1$ plus half the distance between the calculated point i to the next point $i+1$ in, respectively, a traditional plot and a modified plot of the capacity curve. In this way, a point weighs less/more in regions with more/less points calculated points (Abaqus).

$$w_{1,i} = 0.5\cdot d_{1,i-1} + 0.5\cdot d_{1,i+1} \quad (6\text{-}23)$$

$$w_{2,i} = 0.5\cdot d_{2,i-1} + 0.5\cdot d_{2,i+1} \quad (6\text{-}24)$$

Where:

$$d_{1,i-1} = \sqrt{(\chi_i - \chi_{i-1})^2 + (\lambda_i - \lambda_{i-1})^2} \quad (6\text{-}25)$$

$$d_{1,i+1} = \sqrt{(\chi_i - \chi_{i+1})^2 + (\lambda_i - \lambda_{i+1})^2} \quad (6\text{-}26)$$

$$d_{2,i-1} = \sqrt{(\chi_i - \chi_{i-1})^2 + \left(\chi_i\cdot\lambda_i^2 - \chi_{i-1}\cdot\lambda_{i-1}^2\right)^2} \quad (6\text{-}27)$$

$$d_{2,i+1} = \sqrt{(\chi_i - \chi_{i+1})^2 + \left(\chi_i\cdot\lambda_i^2 - \chi_{i+1}\cdot\lambda_{i+1}^2\right)^2} \quad (6\text{-}28)$$

The "best-fitting" interaction curve corresponds with the curve with the smallest weighted deviation $wdev$.

4.1.6 Results

For a randomly chosen case of cluster 1 (with $R/t = 1000$; $d_{stif}/R = 0.10$; t_{stif}/t = max.; $h_{stif}/R = 1.0$), the results are presented in Fig. 6-12. In this figure, the stars represent the points of the capacity curves calculated with Abaqus, the solid and dashed represent the fitted capacity curves according to the four methods (See legend in Fig. 6-12; the methods are described in Section 4.1.1). It can be seen that all best-fitting curves show a relatively good agreement with their calculated curves. Similar agreement was also obtained for all other cases and for all quality classes.

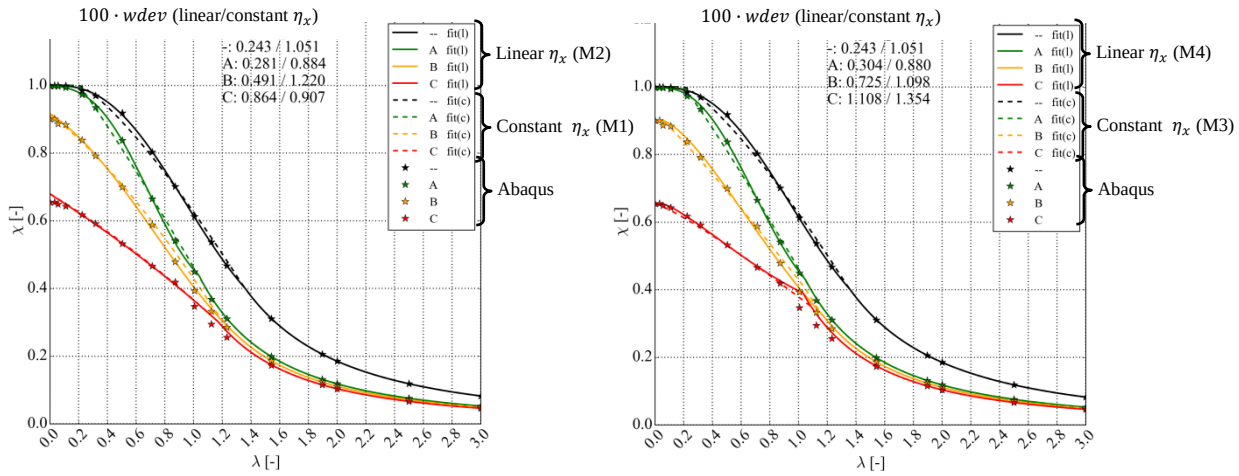

(a) Methods 1 and 2 (negative squash limit slenderness).

(b) Methods 3 and 4 (modified formulas).

Fig. 6-12 Calculated capacity curve (stars) versus the fitted capacity curves (dashed/solid lines).

In Table 6-10, the interaction parameters and the weighted deviation are given for quality class C of the same geometry as presented in Fig. 6-12. For methods 1 and 2 the squash limit slenderness $\lambda_{x,0}$ is negative, while for methods 3 and 4 a factor χ_0 smaller than the unity is taken.

Since it is difficult to discuss 1104 such plots, a figure is generated which summarizes the quality of the "best-fitting" interaction curves for all geometries (See Fig. 6-13). In this figure, the average and standard deviation of the weighted deviation $wdev$ multiplied by 100 (to limit the number of digits after the comma) are displayed for each quality class and for each method (See Table 6-8). This parameter is a measure for the quality of the fitting curve relative to the calculated curve: the smaller this number, the better the fit is with the calculated curve. From this figure, a number of general trends can be clearly noticed.

First, for all methods, the quality of the best-fitting capacity curves of the perfect structure is the best, and gradually decreases when the quality of the imperfect silo decreases. Secondly, the choice of a linear interaction exponent η_x (methods 2 and 4) significantly improves the

quality, in particular for the imperfect capacity curves, compared to a constant interaction exponent η_x (methods 1 and 3). Thirdly, when the type of the interaction exponent η_x remains the same (linear or constant), the allowance of a negative squash limit slendernesses $\lambda_{x,0}$ (methods 1 and 2) results in a better quality of the best-fitting capacity curve compared to the modified expressions for the strength χ (methods 3 and 4).

Table 6-10 Overview of the best-fitting parameters for the geometry of Fig. 6-12 (quality class C).

PARAMETER	METHOD 1	METHOD 2	METHOD 3	METHOD 4
α_x [-]	0.415	0.415	0.415	0.415
β_x [-]	0.70	0.70	0.65	0.61
χ_0 [-]	-	-	**0.65**	**0.65**
$\lambda_{x,0}$ [-]	**-2.60**	**-1.60**	0.00	0.05
$\lambda_{x,p}$ [-]	1.18	1.18	1.09	1.03
η_x [-]	2.09	-	1.08	-
$\eta_{x,0}$ [-]	-	1.28	-	1.08
$\eta_{x,p}$ [-]	-	1.51	-	0.90
$100 \cdot wdev$ [-]	0.91	0.86	1.35	1.11

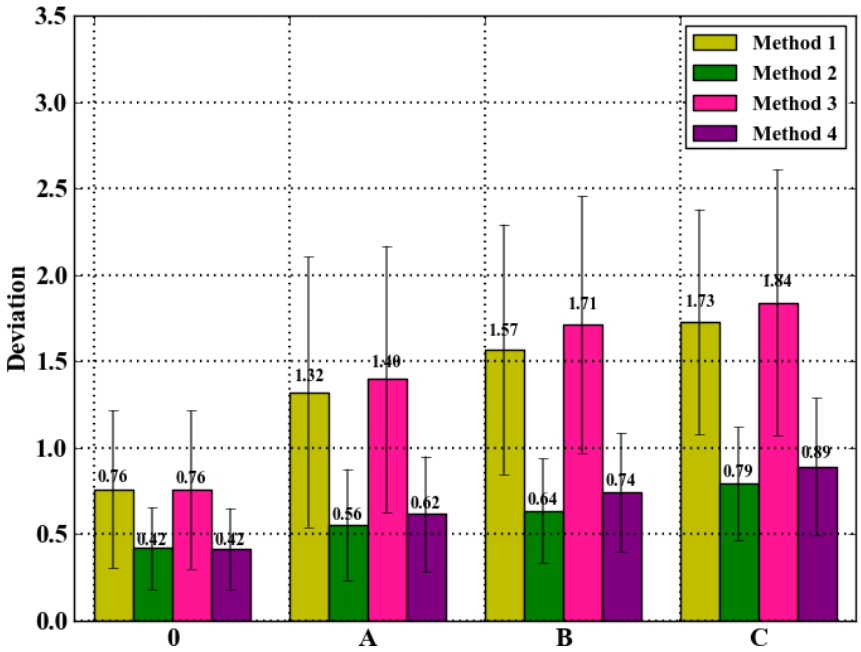

Fig. 6-13 Average and standard deviation of the weighted deviation $wdev$ as a function of the quality class and for all methods (the best-fitting curves of all 1104 geometries are taken into account) (remark: to limit the number of digits after the comma, $wdev$ is multiplied by 100).

Finally, it is important to emphasize that these findings are drawn for the entire collection of

best-fitting capacity curves (1104) and may be different when the methods are compared for individual cases.

4.2 Study of the best-fitting interaction parameters

In this part, the best-fitting interaction parameters deduced in Section 4.1 according to the method with the best performance (i.e. method 2 with a negative or a positive squash limit slenderness $\lambda_{x,0}$ and a linearly varying interaction exponent η_x in the elasto-plastic part) will be used to search for relationships with the geometrical parameters (Section 4.2.1) and with other interaction parameters (Section 4.2.2). The interaction parameters of this method are used here, because of the best agreement between the calculated capacity curve and the best-fitting capacity curve.

4.2.1 Relation between the best-fitting interaction and geometrical parameters

For this study, plots were generated of the above mentioned best-fitting interaction parameters (i.e. α_x, $\lambda_{x,0}$, β_x, $\eta_{x,0}$, and $\eta_{x,p}$) on the one hand and different geometrical parameters on the other: the number of local supports n_{sup}, the degree of circumferential support μ_{sup}, the ratio of the stiffener/column cross-section to the shell cross-section A_{stif}/A_{shell}, the ratio of the stiffener/column perimeter to the cylinder radius L_{stif}/R, the ratio of the attached height to the cylinder radius h_{stif}^{sup}/R, etc.

Some typical graphs are presented in Fig. 6-14 to illustrate the large spread between the interaction parameters (vertical axis) and the geometrical parameters (horizontal axis). Each figure consists of four plots: perfect structure (upper left), quality class A (upper right), quality class B (lower left), and quality class C (lower right). For all U-shaped longitudinal stiffeners, the elastic imperfection reduction factors α_x are depicted in Fig. 6-14 as a function of the degree of circumferential support μ_{sup}(a) and as a function of the ratio of the attached height to the cylinder radius h_{stif}^{sup}/R (b). As can be seen, it is particularly difficult to find trends and to draw firm conclusions regarding the relationship between interaction and geometrical parameters. This can be attributed to the large number of different geometries considered in the final study. Furthermore, only one "best-fitting" value is considered for each interaction parameter, while small deviations relative to the best-fitting value can still lead to a good approximation of the calculated curve. Even if there are fewer geometries considered in each plot, it is still difficult to perceive trends.

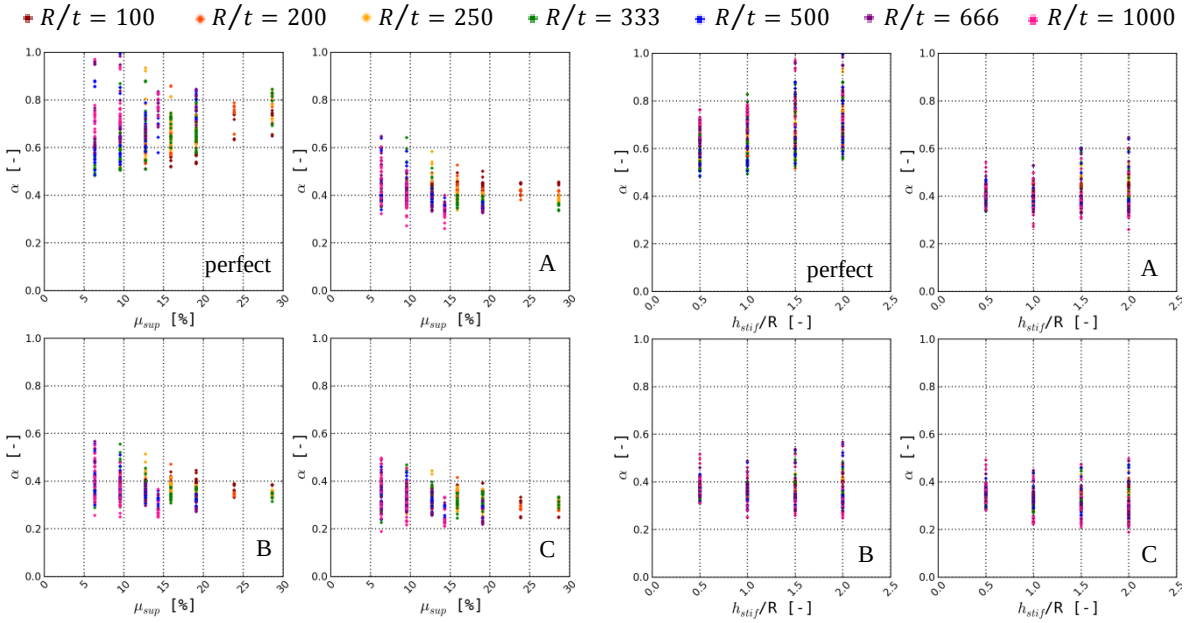

(a) As a function of the degree of support along the circumference μ_{sup}.

(b) As a function of the ratio of the stiffener's height to the cylinder radius h_{stif}^{sup}/R.

Fig. 6-14 Elastic imperfection reduction factor α_x (U-shaped longitudinal stiffeners).

For U-shaped longitudinal stiffeners, the clearest trends of all plots are found between the ratio of the stiffener cross-section to the shell cross-section A_{stif}/A_{shell} (plotted on the horizontal axis) and the elastic imperfection reduction factor α_x and the plastic range factor β_x (shown on the vertical axis of Fig. 6-15 and Fig. 6-16, respectively). In these figures, the results are sorted by the radius-to-thickness ratio R/t and quality class. In Fig. 6-15, a decreasing trend can be observed for the reduction factor α_x of imperfect silos when the value A_{stif}/A_{shell} increases. The graph of the plastic range factor β_x as a function of A_{stif}/A_{shell} consists of a scattered cloud of points in which two branches with different slope can be distinguished (See Fig. 6-16). The first branch corresponds with stiffeners with a small cross-section and is a rapidly increasing branch until a certain transition is reached where the slope changes abruptly. After the transition, the general trend is that the plastic range factor β_x slightly increases or remains constant when A_{stif}/A_{shell} increases.

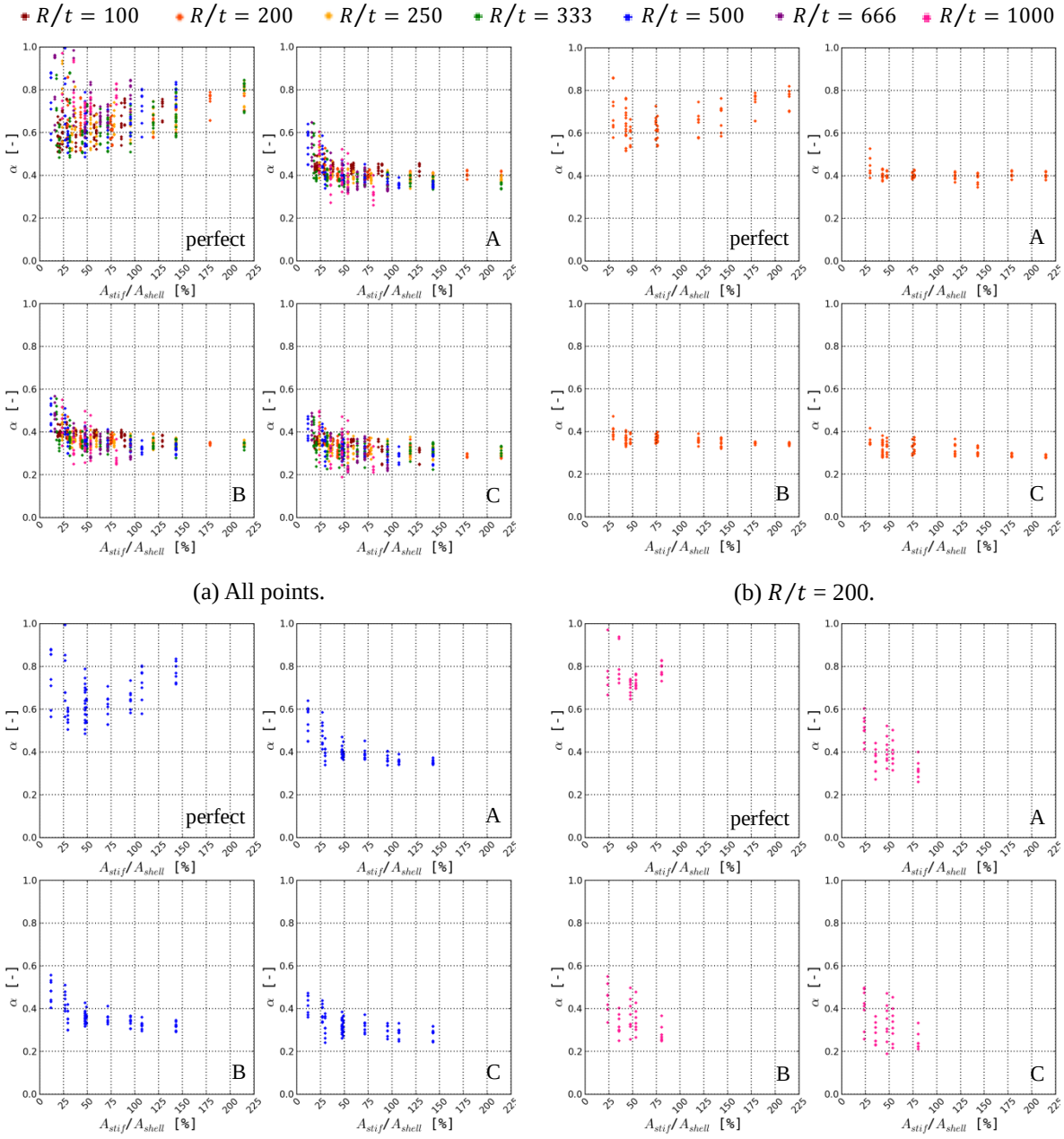

(a) All points.

(b) R/t = 200.

(c) R/t = 500.

(d) R/t = 1000.

Fig. 6-15 Elastic imperfection reduction factor α_x as a function of the ratio of the stiffener/column cross-section to the shell cross-section A_{stif}/A_{shell} (U-shaped longitudinal stiffeners).

Despite the division in Fig. 6-15 and Fig. 6-16 (R/t and quality class), a large spread is obtained for the interaction parameters α_x and β_x due to the wide range of geometries of the U-shaped stiffeners (circumferential and radial widths, thickness, and attached height) and the number of local supports. Likewise, it is valid that when fewer geometries are considered in these plots, the large spread on α_x and β_x is still present, making it difficult to accurately estimate the interaction parameters as a function of one or more geometrical parameters.

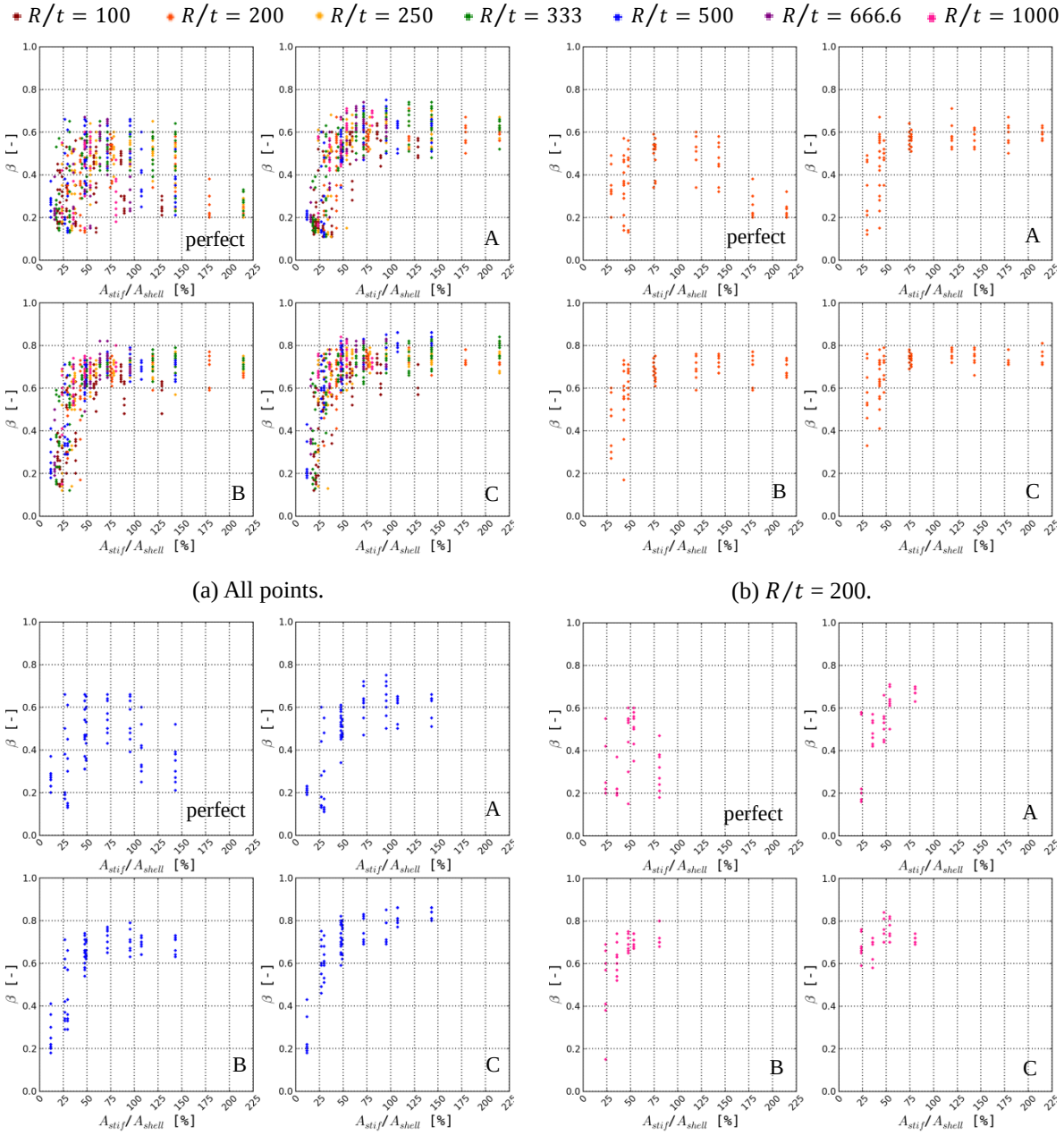

(a) All points.

(b) R/t = 200.

(c) R/t = 500.

(d) R/t = 1000.

Fig. 6-16 Plastic range factor β_x as a function of the ratio of the stiffener/column cross-section to the shell cross-section A_{stif}/A_{shell} (U-shaped longitudinal stiffeners).

From the above figures, it is clear that, due to the large scatter, further research is necessary to be able to accurately estimate the interaction parameters (for meridional compression) as a function of the geometry of axially compressed silos. However, in international coding such subdivision is generally not applied. Typical (torsional) buckling curves are not subdivided according to profile type (HEA, HEM, ...).

4.2.2 Interrelationships between the best-fitting interaction parameters

When all interaction parameters are plotted against the other interaction parameters, it is

difficult to find relationships. Only for the plastic range factor β_x and the reduction factor α_x, the scatter is relatively restricted, as depicted in Fig. 6-17. The worse the quality of fabrication (perfect → Class A → Class B → Class C), the smaller the reduction factor α_x and the larger the plastic range factor β_x. The first finding is as expected, because imperfections with an increasing amplitude are more detrimental to the (elastic) failure behaviour. The increase of the plastic range factor β_x means that plasticity will influence the failure behaviour at smaller relative slendernesses (i.e. a decrease of λ_p) for the more imperfect silos.

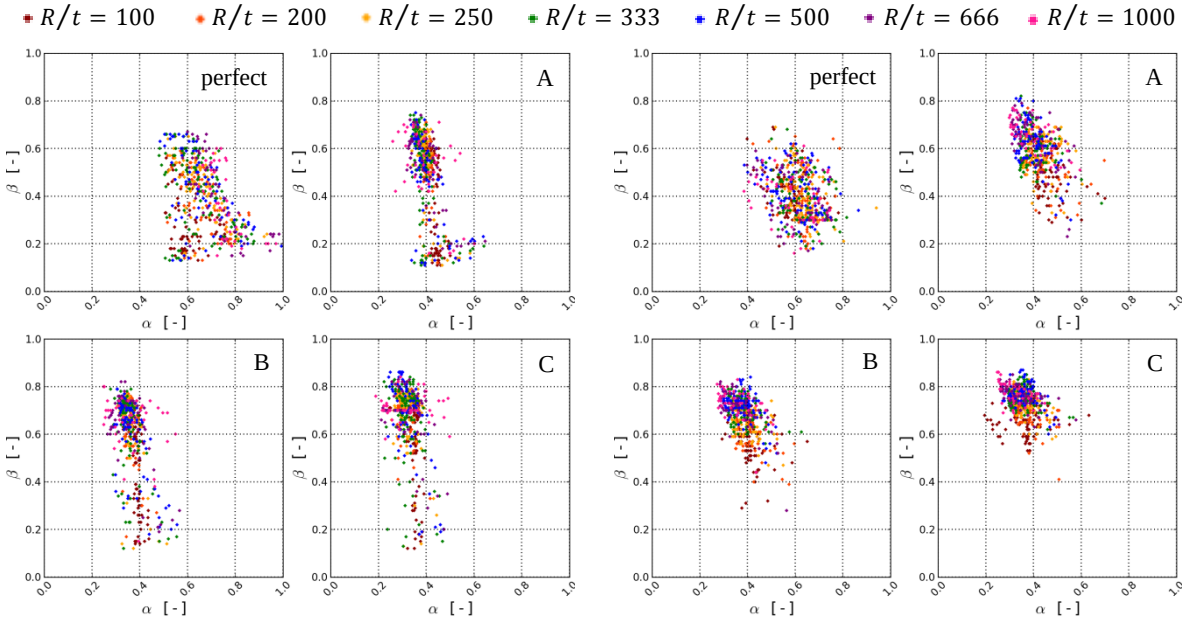

(a) U-shaped stiffeners.

(b) Engaged columns.

Fig. 6-17 Plastic range factor β as a function of the elastic imperfection reduction factor α

5 Conclusions of the design rule study

For the design rule study, capacity curves were calculated for a wide range of geometries by means of different types of shell analyses (i.e. LBA, MNA, GN(I)A, GMN(I)A) with a variable yield stress and an inward weld depression type A with different quality class.

In this chapter, the extensive dataset was compared with the present interaction parameters for meridional compression (EN 1993-1-6, 2007). Surprisingly, a relatively good agreement was found between the smallest values of the dimensionless strength χ from the calculated dataset (calculated for locally supported silos) and the estimated characteristic/design values of the dimensionless strength χ (based on the buckling parameters in the Eurocode for uniformly supported silos, taking into account a partial coefficient on the resistance γ_{M1} of 1.10). Furthermore, a number of sets of interaction parameters were developed for which the corresponding buckling curves are fitting better to the lower bound of the scatter than the current buckling curves. The determination of a lower bound fit to a scattered cloud of

calculated points in a χ- λ diagram is relatively easy to determine, but the major disadvantage is that this approach results in rather conservative results for most cases.

Subsequently, the interaction parameters of each individual capacity curve (α_x, $\lambda_{x,0}$, β_x, and η_x) were determined which best approximate the shape of each capacity curve. The best results were obtained using the approach with a linearly varying interaction exponent η_x in the elasto-plastic part and the allowance of both negative and positive squash limit slendernesses $\lambda_{x,0}$. However, it was found that it is not easy to predict the interaction parameters as a function of the geometry due to the large scatter and the (mixed) influence of different geometrical parameters. In contrast to the lower bound fit approach, it is much more difficult to accurately predict the interaction parameters for an axially compressed silo geometry and quality class. Further research will be needed to obtain an accurate design rule for the prediction of the interaction parameters. In time, this should lead to simpler and more economical design procedures, such as the MNA/LBA approach with two relatively simple shell calculations.

To conclude, a GMNIA shell calculation currently still is the most accurate (and thus the most economic) way to estimate the real elasto-plastic buckling load. Nevertheless, it is hoped that in the future, the interaction parameters (for meridional compression) can be determined more accurately as a function of the locally supported silo configuration, as a result of which the easier MNA/LBA approach is more economical to use as silo designer.

To close this chapter, the reader is referred to Appendix F where the complete scatter is plotted in a traditional χ- λ diagram and a modified χ- λ^2 diagram for the different fabrication quality classes as a function of the radius-to-thickness ratio of the cylindrical barrel. In these plots, all points are depicted with a yield stress which is used for steel silos in practice: 235; 355; 460; 690; 960MPa.

CHAPTER 7

Conclusions

1 Conclusions

In this doctoral research, (1) a numerical model was developed and validated by means of experiments, (2) numerical parametric studies were performed, and finally (3) a design rule study was conducted. The main conclusions of these three main parts will be discussed below.

Development and experimental validation of the numerical model

Steel silos which are filled with bulk solids are mainly subjected to vertical (compressive) pressure due to friction between the bulk material and the silo wall. Since the buckling limit state (and to a lesser extent the plastic limit state) is the decisive design state, it is important to accurately predict the elasto-plastic failure load. Since both hand calculations and the current calculations rules are on the conservative side (EN 1993-1-6, 2007), a major step forward for the accurate prediction of this failure load is the development of a reliable numerical model.

A FEM model was developed in Abaqus for two configurations of locally supported silos. The first configuration consists of a U-shaped partial-height longitudinal stiffener above each local support, a transition ring at the lower edge of the barrel, and an upper ring stiffener at the top of the longitudinal stiffeners. For the second configuration, the local rectangular shaped columns are engaged along a specific distance of the silo wall. In this way, the local supporting load is for both configurations gradually introduced and distributed over the entire circumference of the barrel, resulting in an increased failure load.

By means of experimental results obtained from destructive tests on scale models, the FEM model was validated by geometrically and materially non-linear shell calculations with imperfections (GMNIA) taking into account the real material behaviour (tensile tests) and the real, measured imperfections of the silo wall. To improve the agreement between the experimental and the numerical results, the influence of the connection of the bolted steel plate and the real supporting boundary conditions were considered. Furthermore, a 360 degrees model was used for the validation with a relatively fine mesh to take into account the non-symmetrical imperfections as accurately as possible in the element nodes.

Finally, after a long validation process, it can be stated that after all a satisfying agreement was obtained between the numerical model and the experimental results.

Numerical parametric studies

The failure behaviour (i.e. elastic buckling and/or plastic yielding) of axially compressed steel barrels on local supports was extensively investigated by means of numerous parametric studies using the experimentally validated FEM model.

At first instance, a mesh study was conducted to verify the suitability of S8R5 shell elements and to determine the mesh size for which the results convergence to a solution. After the mesh study, the influence of many geometrical parameters was investigated for their effects on the failure behaviour and load: the geometry of the cylindrical barrel, the U-shaped longitudinal stiffeners, the ring stiffeners, the engaged columns, etc. were explored one by one. In this way, more insight was gained into the failure behaviour of locally supported silos.

Next, an optimisation study was performed to determine the most optimal combination of the height and the cross-section of the U-shaped longitudinal stiffeners and the engaged columns to maximise the failure load with a minimal increase in material. For the first configuration, a relatively high and thin U-shaped longitudinal stiffener with a large developed length (large circumferential width and smaller radial width) is preferred to maximally distribute the axial stresses in circumferential direction and consequently to maximise the failure load. For the second configuration, an intermediately high (the attached height is just below the critical height) relatively thin engaged column with a large developed length is preferred to maximise the failure load. Depending on the silo thickness and the column height, a larger or a smaller ratio of the radial width to the circumferential width is the best solution. For most cases, a large ratio of the radial width to the circumferential width is more suitable because of the increased the moment of inertia. For thick-walled silos combined with short columns, a square column is preferred with a relatively small eccentricity.

Based on the results of the above studies, a range was defined for all geometrical parameters which were used for the design rule study.

Since the elasto-plastic buckling load of a perfect structure is significantly reduced by the presence of small imperfections in the cylindrical barrel, an imperfection sensitivity study was performed to investigate the influence of geometrical equivalent imperfections to the failure behaviour. In this work, different shapes (linear and non-linear buckling modes, post-buckling deformed shapes, and weld depressions), orientations (inwardly and outwardly oriented), and equivalent amplitudes (quality class A, B, and C) were considered. Finally, an inward weld depression type A with half-wavelength equal to the linear elastic bending half-wavelength has been picked out as equivalent imperfection shape because of two reasons: (1) it is relatively detrimental compared to other imperfection shapes and (2) the shape is closely related to the fabrication process of a welded silo.

Design rule study

For a wide range of geometries (defined by the results of numerous parametric studies), capacity curves were calculated using different types of shell analyses (i.e. LBA, MNA, GN(I)A, GMN(I)A) and an inward weld depression type A as imperfection shape. The relative slenderness of the structure was varied by changing the yield stress from very small to very large values.

Firstly, the points with realistic yield stresses (i.e. 235; 355; 460; 690; 960MPa) were plotted in a traditional χ- λ diagram (i.e. large scattered cloud of points) and compared with the current buckling curves for meridional compression mentioned in the Eurocode (EN 1993-1-6, 2007). This comparison revealed that a relatively good agreement was found between the smallest values of the dimensionless strength χ from the calculated dataset (calculated for locally supported silos) and the estimated characteristic/design values of the dimensionless strength χ (based on the buckling parameters in the Eurocode for uniformly supported silos, taking into account a partial coefficient on the resistance γ_{M1} of 1.10). Furthermore, a number of sets of interaction parameters were developed for which the corresponding buckling curves are fitting better to the lower bound of the scatter than the current buckling curves. However, all proposals have in common that, for most cases, a relatively conservative result is obtained for the strength χ (and thus load). This is the main disadvantage of the approach of a lower bound.

Secondly, for each individual capacity curve, the interaction parameters (i.e. α_x, $\lambda_{x,0}$, β_x, and η_x) were determined which best approximate the shape of the capacity curve. A linearly varying interaction exponent η_x, combined with a squash limit slendernesses $\lambda_{x,0}$ which can be both negative and positive, results in the best agreement between the fitting capacity curve and the calculated capacity curve. The next step was to develop rules for the prediction of these interaction parameters as a function of the geometry. However, due to the large scatter and the (mixed) influence of different geometrical parameters, it is not evident to relate the interaction parameters (for meridional compression) to the geometrical parameters of a silo geometry and a quality class.

2 Suggestions for further research

Numerical parametric studies

Typically, a PhD focuses on a small area in high detail, while other interesting aspects are not covered. As an example, the choice is given for a uniformly distributed line load at the top edge of the cylindrical barrel, subjecting the silo to meridional axial compression. This choice has largely influenced the results and findings in this work and has excluded many other (combinations of) loads which are also relevant for the design of a silo, such as frictional traction, whether or not combined with unsymmetrical normal pressures or local patch loads

caused by the bulk solids (internal pressures) (EN 1991-4, 2006), or wind loads (external pressures).

Additionally, the influence of imperfections on the failure behaviour of thin-walled silos should be further examined by means of imperfection sensitivity studies. Because failure behaviour is influenced by many parameters, this subject could not be fully investigated in this work. Probably, an entire PhD could be devoted to the investigation into an appropriate choice of imperfection shape which is representative for real cylindrical barrels.

Due to the development of new approaches of structural optimisation in FEM software (e.g. in the newest releases of Abaqus), it is possible to optimise the shell thickness of metal components regardless of the thickness of adjacent shell elements. In this way, it is possible to optimise the cylindrical barrel by increasing its stiffness, by minimising the stresses, by maximising the (sum of the first five) eigenvalues, etc. The optimisation of buckling is not yet included in the current release of Abaqus.

Design rule study

A GMNIA shell calculation currently still is the most accurate (and thus the most economic) way to estimate the real elasto-plastic buckling load. Nevertheless, it is hoped that in the future, the interaction parameters (for meridional compression) can be determined more accurately as a function of the locally supported silo configuration (and quality class), as a result of which the easier MNA/LBA approach is more economical to use as silo designer. To achieve this purpose, further research is certainly needed to find relationships between the interaction parameters (and thus the shape of the capacity curve) on the one hand and the geometrical parameters and fabrication tolerance quality class on the other.

References

Abaqus (2009). *ABAQUS version 6.9 documentation*. Dassault Systèmes Simulia Corp., Providence, RI (USA).

Arbocz, J. (1974). The effect of initial imperfections on shell stability. In *Thin Shell Structures*, Eds Y.C. Fung and E.E. Sechler. Prentice Hall, Englewood Cliffs, NJ*:* 205-246.

Arbocz, J. and Babcock, C.D., Jr. (1976). Prediction of buckling loads based on experimentally measured initial imperfections. In *Buckling of Structures*, Ed. B. Budiansky, Proceedings of the IUTAM Symposium, Harvard University. Springer, New York.

Arbocz, J. and Sechler, E.E. (1974). On the buckling of axially compressed imperfect cylindrical shells. *Journal of Applied Mechanics*, ASME **41**(3): 737-743.

Arcbocz, J. (1982). The imperfection databank, a mean to obtain realistic buckling loads. In *Buckling of Shells*, Ed. E. Ramm. Springer, New York.

Arbocz, J. (1983). Shell stability analysis: theory and practice. In *Collapse*, Eds J.M.T. Thompson and G.W. Hunt. Cambridge University Press, Cambridge: 43-74.

Berry, P.A. (1997). Buckling under axial compression of cylindrical shells with circumferential weld shrinkage depression. PhD Thesis, Department of Civil Engineering, University of Sydney, Sydney.

Berry, P.A., Rotter, J.M., and Bridge, R.Q. (2000). Compression tests on cylinders with circumferential weld depressions. *Journal of Engineering Mechanics*, ASCE **126**(4): 405-413.

Blachut, J. and Jaiswal, O.R. (1999). On the Choice of Initial Geometric Imperfections in Externally Pressurized Shells. *Journal of Pressure Vessel*, ASME **121**(1): 71-76.

Bornscheuer, F.W. and Häfner, L (1983). The influence of an imperfect circumferential weld on the buckling strength of axially loaded circular cylindrical shells. In *Proceedings of the 3rd international colloquium on stability and metal structures*, Paris: 407-414.

Brendel, B. and Ramm, E. (1980). Linear and nonlinear stability analysis of cylindrical shells. *Computers & structures*, Elsevier **12**(4): 549-558.

Brown, C. J. and Nielsen J. (1998). *Silos: Fundamentals of Theory, Behaviour and Design*, Ed. E & FN Spon, London.

Calladine, C.R. (1983). *Theory of shell structures*, Cambridge University Press, Cambridge.

Carson, J.W. (2001). Silo failures: Case histories and lessons learned. *Handbook of Conveying and Handling of Particulate Solids*, Eds: A. Levy and H. Kalman. Elsevier, Amsterdam **10**: 153-166.

Chen, J.F. (1996). Granular solid-structure interaction in silos. PhD Thesis, Department of Civil and Environmental Engineering, Univerity of Edinburgh, Edinburgh.

Chen, J.F., Ooi, J.Y., and Rotter, J.M. (1995). A rigorous statistical technique for inferring circular silo wall pressures from wall strain measurements. *Engineering Structures*, Elsevier **18**(4): 321-331.

Chen, L., Rotter, J.M., and Doerich, C. (2011). Buckling of cylindrical shells with stepwise variable wall thickness under uniform external pressure. *Engineering Structures*, Elsevier **33**(12): 3570-3578.

Clarke, M.J. and Rotter, J.M. (1988). A technique for the measurement of imperfections in prototype silos and tanks. Research report No. R565, University of Sydney, Sydney.

Coleman, R., Ding, X.L., and Rotter J.M. (1992). The measurement of imperfections in full-scale steel silos. In *Proceedings of the 4th International Conference On Bulk Mataterial Storage, Handling and Transportation*, 467-472.

Combescure, A. (1986). Static and dynamic buckling of large thin shells. *Nuclear Engineering and Design*, **92**(3): 339-354.

Crisfield, M.A. (1982). Variable step-lengths for non-linear structural analysis. Transport and Road Research Laboratory, Report No. 1049, Transport Research Laboratory, Wokingham (United Kingdom).

Danielson, D.A. (1974). Theoretical method to investigate the post-buckling behaviour by assuming the imperfections in the buckling mode. In *Theory of shell stability*, Eds Y.C. Fung and E.E. Sceler, Prentice Hall.

Deml, M. and Wunderlich, W. (1997). Direct evaluation of the 'worst' imperfection shape in shell buckling. *Computer Methods in Applied Mechanics and Engineering*, Elsevier **149** (1-4): 201-222.

Ding, X.L., Coleman, R.D., and Rotter, J.M. (1991). A profile measurement system and its application in precise engineering surveying. In *Proceedings of the q/58th FIG PC Meeting and lnternational Syrup*, Beijing, 87-101.

Ding, X.L., Coleman, R.D., and Rotter, J.M. (1996). Technique for precise measurement of large-scale silos and tanks. *Journal of Surveying Engineering*, ASCE **122**(1): 14-25.

Doerich, C., Holst, J.M.F.G., and Rotter, J.M. (2005). The behaviour of cylindrical steel shells supported on local brackets. In *Proceedings of the* F*ourth International Conference on Advances in Steel Structures*, ICASS, Shanghai: 377-382.

Doerich, C. (2007). Strength and stability of locally supported cylinders. PhD thesis, Institute for Infrastructure & Environment, The School of Engineering and Electronics. University of Edinburgh, Edinburgh.

Doerich, C. (2008). Effect of geometric nonlinearity of locally supported cylinders. *Structures and Granular Solids*, Taylor & Francis**:** 183-197.

Doerich, C. and Rotter, J. M. (2008). Behavior of Cylindrical Steel Shells Supported on Local Brackets. *Journal of Structural Engineering*, ASCE **134(**8): 1269-1277.

Doerich, C. and Rotter, J.M. (2011a). Accurate Determination of Plastic Collapse Loads From Finite Element Analyses. *Journal of Pressure Vessel Technology*, AMSE **133**(1): 1132-1140.

Doerich, C. and J. M. Rotter (2011b). Generalised capacity curves for stability and plasticity: Application and limitations. *Thin-Walled Structures*, Elsevier **49**(9): 1132-1140.

Dogangun, A., Karaca, Z., Durmus, A., and Sezen, H. (2009). Cause of Damage and Failures in Silo Structures. *Journal of Performance of Constructed Facilities*, ASCE **23**(2): 65-71.

Donnell, L.H. and Wan, C.C. (1950). Effect of imperfections on buckling of thin cylinders and columns under axial compression. *Journal of Applied Mechanics*, ASME **17**(1): 73-83.

ECCS (2008). *Buckling of Steel Shells: European Design Recommendations*, 5th Edition, European Convention for Constructional Steelwork, Brussels.

EN 1990 (2002). *Eurocode 0: Basis of Structural Design*, CEN, Brussels.

EN 1991-4 (2006). *Eurocode 1: Actions on Structures, Part 4: Silos and tanks*, CEN, Brussels.

EN 1993-1-1 (2005). *Eurocode 3: Design of Steel Structures, Part 1.1 General rules for buildings*, CEN, Brussels.

EN 1993-1-6 (2007). *Eurocode 3: Design of Steel Structures, Part 1.6: Strength and Stability of Shell Structures*, CEN, Brussels.

EN 1993-4-1 (2007). *Eurocode 3: Design of Steel Structures, Part 4.1: Silos*, CEN, Brussels.

Esslinger, M. and Geier, B. (1972). Gerechnete Nachbeulasten als untere Grenze der experimentellen axialen Beulasten von Kresiszylindern. (in German) *Der Stahlbau* **41**(12): 353-360.

Esslinger, M. and Ciprian J.(1982). Buckling of thin conical shells under axial loads and without internal pressure. In *Buckling of Shells*, Ed. E. Ramm. Springer, New York.

Gillie, M. & Rotter, J.M. (2002). The effects of patch loads on thin-walled steel silos. *Thin-Walled Structures*, Elsevier **40**(10): 835-852.

Greiner, R. and Derler, P. (1995). Effect of imperfections on wind-loaded cylindrical shells. *Thin-Walled Structures*, Elsevier **23**(1-4): 271-282.

Guggenberger, W. (1998). Proposal for design rules of axially loaded steel cylinders on local supports. *Thin-Walled Structures*, Elsevier **31**(1-3): 169-185.

Guggenberger, W., Greiner, R., and Rotter J.M. (2000). The behaviour of locally-supported cylindrical shells. *Journal of Constructional Steel Research*, Elsevier **56**(2): 175-197.

Hartlén, J., Nielsen, J., Ljunggren, L., Martensson, G., and Wigram, S. (1984). The wall pressure in large grain silos - Inventory, pressure measurements, material investigations. Document, Swedish Council of Building Research.

Hübner, A., Teng, J. G., and Saal, H. (2006). Buckling behaviour of large steel cylinders with patterned welds. *International Journal of Pressure Vessels and Piping*, Elsevier **83**(1): 13-26.

ISO 6892-1 (2009). *Metallic materials - Tensile testing - Part 1: Method of test at room temperature*, CEN, Brussels.

Janssen, H.A. (1895). Versuche über Getreidedruck in Silozellen. *Zeitschrift des Vereiesn Deutcher Ingenieure*. **39**(35): 1045-1049.

Knoedel, P. and Ummenhofer, T. (1996). Typical imperfections of steel silo shells in Civil Engineering. In *International Workshop on Imperfections in Metal Silos, Measurement, Characterization and Strength Analysis*, under the auspices of the BRITE/EURAM concerted action CA-SILO, Working Group 3: Metal Silo Structures, 19th: 103-118.

Koiter, W.T. (1945). On the Stability of Elastic Equilibrium. PhD thesis (in Dutch). Delft University Delft.

Koiter, W.T. (1963). The effect of axisymmetric imperfections on the buckling of cylindrical shells under axial compression. In *Proceedings, Koninklijke Nederlandse Akademie van. Wetenschappen*, Proceedings Ser. B66: 265-279.

Nielsen, J. (1983). Load Distribution in Silos Influenced by Anisotropic Grain Behaviour. In *Proceedings of the International Conference on Bulk Materials Storage, Handling and Transportation*, Newcastle, Australia: 329-334.

Nielsen, J. (1998). Pressures from flowing granular solids in silos. *Philosophical Transactions*. Royal Society of London. Series A, **356**(1747), 2667-2684.

Nielsen, J. (2008). From silo phenomena to load models. *Structures and Granular Solids*, Taylor & Francis**:** 49-57.

Nielsen, J. & Andersen, E.Y. (1981). Loads in Grain Silos. In *11th working session of the IAAS Committee of Pipes and Tanks*, Wroclaw (Poland).

von Mises, R. (1913). Mechanik der festen Körper im plastisch deformablen Zustand. *Nachrichten von der Königlichen Gesellschaft der wissenscahaften zu Göettingern.* Mathematisch-Physikalische Klasse **1913**(1): 582-592.

Pircher, M. (2000). The effects of weld-induced imperfections on the stability of axially loaded steel silos. PhD thesis, School of Civic Engineering and Environment, University of Western Sydney, Sydney.

Pircher, M., Berry, P.A., Ding, X., and Bridge, R.Q. (2001). The shape of circumferential weld-induced imperfections in thin-walled steel silos and tanks. *Thin-Walled Structures*, Elsevier. **39**(12): 999–1014.

Pircher, M. and Bridge, R.Q. (2001a). The influence of circumferential weld-induced imperfections on the buckling of silos and tanks. *Journal of Constructional Steel Research*, Elsevier **57**(5): 569-580.

Pircher, M. and Bridge, R.Q. (2001b). Buckling of thin-walled silos and tanks under axial load: Some new aspects. *Journal of Structural Engineering*, ASCE **127**(10): 1129-1136.

Rathé, J. and Greiner, R. (1996). Local Loads in Cylindrical Structures, Subproject B of ECSC Contract No. 7210–SA/208: Enhancement of ECCS Design Recommendations and Development of Eurocode 3 Parts Related to Shell Buckling. Final Report, Ghent University, Ghent.

Riks, E. (1972). Application of Newtons method to problem of elastic stability. *Journal of Applied Mechanics*, ASME **39**(4): 1060-1065.

Riks, E. (1979). An incremental approach to the solution of snapping and buckling problems. *International Journal of Solids Structures*, **15**(7): 529-551.

Riks, E. (1981). Some computational aspects of the stability analysis of nonlinear structures. In *Fenomech 81. Second International Conference on Finite Elements in Non-linear Mechanics*, Stuttgart.

Riks, E., Rankin, C.C., and Brogan, F.A. (1996). On the solution of mode jumping phenomena in thin-walled shell structures. *Computer Methods in Applied Mechanics and Engineering*, Elsevier. **136**(1): 59-92.

Roberts, A.W. (1994). Developments in silo design for the safe and efficient storage and handling of grain. In *Proceedings of the 6th International Working Conference on the Stored-product Protection*, Canberra, Australia, **1**: 259-280.

Rotter, J.M. (1983). Effective Cross-Sections of Ringbeams and Stiffeners for Bins. In *Proceedings of the International Conference on Bulk Materials Storage, Handling and Transportation*, Newcastle (Australia): 329–334.

Rotter, J. M. (1985a). Analysis and design of ringbeams. Design of steel bins for storage of bulk solids, Ed: J. M. Rotter., University of Sydney, Sydney (Australia): 164-183.

Rotter, J.M. (1985b). Buckling of Ground-Supported Cylindrical Steel Bins under Vertical Compressive Wall Loads. In *Proceedings of the Metal Structure Conference*, Institution of Engineers Australia, Melbourne: 112-127.

Rotter, J.M. (1986). The analysis of steel bins subject to eccentric discharge. In *Proceedings of the Second International Conference on Bulk Materials Storage, Handling and Transportation*, Wollongong (Australia): 264-271.

Rotter, J.M. (1987). Bending Theory of Shells for Bins and Silos. *Transactions of Mechanical Engineering*, Institution of Engineers, Australia: **12**(3) 147-159.

Rotter, J.M. (1990). Local Collapse of Axially Compressed Pressurized Thin Steel Cylinders. *Journal of Structural Engineering*, ASCE **116**(7): 1955-1970.

Rotter, J.M. (1996a). Patch load effects in unstiffened steel silos. In *Project on the Effect of Patch Loads on Metal Silos*, Ed: J.M. Rotter. CA-Silo, Edinburgh: 5-195.

Rotter, J.M. (1996b). Elastic-plastic buckling and collapse in internally pressurised axially compressed silo cylinders with measured axisymmetric imperfections: Interactions between imperfections, residual stresses and local collapse. In *Proceedings of the International Workshop on Imperfections in Metal Silos: Measurement, Characterisation, and Strength Analysis*, CA-Silo, Lyon: 119-139.

Rotter, J.M. (1997). Pressurised axially compressed cylinders. In *Proceedings of International Conference on Carrying Capacity of Steel Shell Structures*, Brno: 354-360.

Rotter, J.M. (1998). Development of proposed European design rules for buckling of axially compressed cylinders. *Advances in Structural Engineering*, Multi Science **1**(4): 273-286.

Rotter, J.M. (1999). Flow and pressures in silo structural integrity assessments. In *Proceedings of the International Symposium: Reliable Flow of Particulate Solids III*, Porsgrunn (Norway): 281-292.

Rotter, J. M. (2001a). *Guide for the Economic Design of Circular Metal Silos.* Spon Press, London; New York.

Rotter, J.M. (2001b). Pressures, Stresses and Buckling in Metal Silos Containing Eccentrically Discharging Solids. *Festschrift Richard Greiner, Celebration volume for the 60th birthday of Prof. Richard Greiner*: 85-104.

Rotter, J.M. (2002), Shell Buckling and Collapse Analysis for Structural Design: The New Framework of the European Standard. In *New Approaches to Structural Mechanics, Shells and Biological Structures*, Eds: H.R. Drew and S. Pellegrino. Kluwer Academic Publishers, London: 355-378.

Rotter, J.M. (2003). Buckling of shallow conical shell roofs for small diameter tanks and silos. In *Proceedings of the International Conference on Design, Inspection and Maintenance of Cylindrical Steel Tanks and Pipelines*, Prague, Czech Republic: 169-175.

Rotter, J.M. (2004). Buckling of cylindrical shells under axial compression. In *Buckling of thin metal shells*, Eds: J.G. Teng and J.M. Rotter. Spon Press, London: 42-87.

Rotter, J. M. (2005). The Practical Design of Shell Structures Exploiting Different Methods of Analysis. In *Proceedings of SSTA8: Eighth Conference on Shell Structures: Theory and Applications*, Eds: W. Pietraszkiewicz and C. Szymczak: 71-86.

Rotter, J.M. (2006). Elephant's foot buckling in pressurised cylindrical shells. *Der Stahlbau* **75**(9): 742-747.

Rotter, J.M. and Seide, P. (1987). On the Design of Unstiffened Cylindrical Shells Subject to Axial Load and Internal Pressure. In *Proceedings of the International Colloquium on Stability of Plate and Shell Structures*, Ghent: 539-548.

Rotter, J.M., Ooi, J.Y., Chen, J.F., Tiley, P.J., Mackintosh, I., and Bennett, F.R. (1995). *Flow pattern measurements in full scale silos.* In British Materials Handling Board, London.

Rotter, J.M. and Teng, J.G. (1989). Elastic stability of cylindrical shells with weld depressions. *Journal of Structural Engineering*, ASCE **115**(5): 1244-1263.

Rotter, J. M., Cai, M. J., and Holst, J.M.F.G. (2011). Buckling of Thin Cylindrical Shells Under Locally Elevated Compressive Stresses. *Journal of Pressure Vessel Technology-Transactions*, ASME **133**(1).

Sadowski A.J. and Rotter J.M. (2010). A study of buckling in steel silos under eccentric discharge flows of stored solids. *Journal of Engineering Mechanics*, ASCE **136**(6): 769-776.

Sadowski, A. J. and Rotter, J. M. (2011). Buckling of very slender metal silos under eccentric discharge. *Engineering Structures*, Elsevier **33**(4): 1187-1194.

Schmidt, H. (2000). Stability of steel shell structures - General Report. *Journal of Constructional Steel Research*, Elsevier **55**:159-181.

Schneider, W. (2006). Ersatzimperfektionen für den numerischen Beulsicherheitsnachweis stählerner Schalentragwerke - State of the Art (in German) (Equivalent Geometric Imperfections for the Numerical Buckling Strength Verification of Steel Shell Structures – State of the Art). *Der Stahlbau* **75**(9), 754-760.

Schneider, W., Höhn, K., Timmel, I., and Thiele, R. (2001). Quasi-collapse-affine imperfections at slender wind-loaded cylindrical steel shells. In *Proceedings of the 2nd European Conference on Computational Mechanics*, ECCM, Cracow.

Singer, J., Arbocz, J., and Weller, T. (1998). *Buckling Experiments: Experimental Methods in Buckling of Thin-Walled Structures - Basic Concepts, Columns, Beams and Plates*, Vol. 1. John Wiley & Sons, Chichester.

Song, C.Y. (2002). Buckling of shells under non-uniform stress states. PhD thesis, Department of Civil and Structural Engineering, The Hong Kong Polytechnic University, Hong Kong.

Song, C. Y., Teng, J. G., and Rotter, J.M. (2004). Imperfection sensitivity of thin elastic cylindrical shells subject to partial axial compression. *International Journal of Solids and Structures*, Elsevier **41**(24-25): 7155-7180.

Speicher, G., Saal, H., (1991). Numerical calculation of limit loads for shells of revolution with particular regard to the applying equivalent initial imperfections. In *Buckling of Shell Structures, on Land, in the Sea and in the Air*, Ed: J.F. Jullien. Elsevier Applied Science, London: 466-475.

Teng, J.G. and Rotter, J.M. (1990). A study of buckling in column-supported cylinders. In *Proceedings of the IUTAM Symposium*, Preliminary Report 1990. Also in: *Contact Loading and Local Effects in Thin-Walled Plated and Shell Structures*, Eds: V. Krupka and M. Drdacky, Academia Press, Prague: 52-61.

Teng, J.G. and Rotter, J.M. (1992). Buckling of pressurized axisymmetrically imperfect cylinders under axial loads. *Journal of Engineering Mechanics*, ASCE **118**(2), 229-247.

Timoshenko, S.P. (1910). Einige Stabilitätsprobleme der Elasticitätstheorie. *Z Math Phys* **58**: 378-385.

Topkaya, C. and Rotter, J.M. (2011). Ring Beam Stiffness Criterion for Column-Supported Metal Silos. *Journal of Engineering Mechanics*, ASCE **137**(12): 846-853.

Topkaya, C. and Rotter, J.M. (2013). Ideal Location of Intermediate Ring Stiffeners on Discretely Supported Cylindrical Shells. *Journal of Engineering Mechanics*, ASCE **140**(4): 04013001.

Tresca, H. (1864). Mémoire sur l'écoulement des corps solides soumis a de fortes pression. *Comptes Rendus hebdomedaires des Seances de l'Academie des Sciences*, C.R. Acad, Paris **59**: 754-758.

Yamaki, N. (1984). *Elastic stability of cylindrical shells*, Eds: E. Becker, B. Budiansky, H.A. Lauwerier and W.T. Koiter and J.M. Rotter. Applied Science Publishers, North-Holland.

Vanlaere, W. (2006). Buckling behaviour of stiffened cylinders on local supports. PhD thesis (in Dutch), Department of Structural Engineering, Faculty of Engineering Sciences. Ghent University, Ghent.

Wozniak, R.S. (1979). Steel tanks. In *Structural Engineering Handbook (second edition)*, Eds: E.H and C.N. Gaylord. McGraw-Hill.

Wunderlich, W. and Albertin, U. (2000). Analysis and load carrying behaviour of imperfection sensitive shells. *International Journal for Numerical Methods in Engineering*, **47**(1-3): 255-273.

Appendices

A Shell analysis

The table below gives an overview of the types of shell analysis. Afterwards, all calculation types are briefly discussed.

Types of shell analysis (EN 1993-1-6, 2007).

TYPE	SHELL THEORY	MATERIAL BEHAVIOUR	SHELL GEOMETRY
Membrane theory of shells	Membrane equilibrium	/	Perfect
Linear elastic shell analysis (LA)	Linear bending + stretching	Linear	Perfect
Linear elastic bifurcation analysis (LBA)	Linear bending + stretching	Linear	Perfect
Geometrical non-linear elastic analysis (GNA)	Non-linear	Linear	Perfect
Geometrical non-linear elastic analysis with imperfections (GNIA)	Non-linear	Linear	Imperfect
Material non-linear analysis (MNA)	Linear	Non-linear	Perfect
Geometrical and material non-linear analysis (GMNA)	Non-linear	Non-linear	Perfect
Geometrical and material non-linear analysis with imperfections (GMNIA)	Non-linear	Non-linear	Imperfect

Membrane theory of shells

The membrane theory of shells takes three membrane stress resultants into account and ignores bending moments and transverse shears. The in-plane stress resultants (i.e. the meridional n_x, the circumferential n_θ, and the shear stress resultant $n_{x\theta}$) are assumed to be in equilibrium with the external loads. This theory provides accurate results of the stress state, except in the vicinity of boundaries, load concentrations, supports, and stiffeners. Consequently, this theory is difficult to apply in this investigation.

Linear elastic shell analysis (LA)

A LA calculation goes a step further than the shell membrane theory and predicts both membrane stresses and bending stresses using a small deflection linear elastic shell bending theory. It provides a good insight into the structural behaviour, but is less accurate in

structures where large displacements occur or where regions of yielding develop. For this reason, a more advanced calculation analysis is required, including geometric non-linearity and/or material non-linearity.

Linear elastic bifurcation analysis (LBA)

A LBA calculation determines the linear bifurcation eigenvalue using a small deflection linear elastic bending theory. The smallest bifurcation load is also known as the critical buckling resistance or the limit load F_{cr}. This type of analysis cannot detect snap-through buckling.

The main purposes of a LBA calculation are:

- To identify bifurcation buckling;
- To determine the elastic limit load F_{cr} (i.e. the lowest eigenvalue) to calculate the elastic imperfection reduction factor α (Eq. (2-19)) and the relative slenderness λ (Eq. (2-14)) of the structure;
- To determine an eigenmode and to apply it as an equivalent initial imperfection shape in a GMNIA calculation.

However, it is recommended to extract not only the lowest eigenvalue and -mode. Instead, it is desirable to extract several eigenvalues (e.g. ten) and to plot the corresponding modes to determine their shape and location because of two reasons (ECCS, 2008). Firstly, when eigenvalues have the same order of magnitude and the eigenmodes occur at the same location, this could be a warning that the structure is sensitive to imperfections (i.e. a small value of the imperfection reduction factor α). Secondly, it could be possible that the higher eigenmodes are found in other more critical locations (due to the geometry or the stress distribution at this point) than the first eigenmode. Therefore it may be necessary to choose a higher eigenvalue with the consequence that the value of the imperfection reduction factor α decreases.

Geometrical non-linear elastic analysis without/with imperfections (GNA/GNIA)

A GNA calculation uses a shell bending theory, and takes into account the complete change of the geometry due to actions (i.e. a non-linear large deflection theory for the displacements). The material is assumed as linear elastic and imperfections are excluded. This type of analysis can detect both snap-through and bifurcation buckling.

A GNIA calculation is similar to a GNA analysis, except that imperfections now are explicitly included. These imperfections are modelled as small deviations relative to the shell middle surface.

The main purposes of a GNA or a GNIA calculation are:

- To identify possible snap-through buckling;
- To identify the failure behaviour due to stability only (without any interaction of plasticity);
- To determine the elastic buckling load of the (im)perfect structure to calculate the elastic imperfection reduction factor α of the (im)perfect structure (Eq. (2-19));
- To determine the buckling mode and to apply it as an equivalent initial imperfection shape in a GMNIA calculation;
- To evaluate the influence of imperfections by comparing the GNIA failure load with the GNA failure load.

Material non-linear analysis (MNA)

A MNA calculation uses a shell bending theory, and takes into account a non-linear elasto-plastic material behaviour. For the displacements, a small deflection theory has been used. Furthermore, imperfections are excluded. On the basis of this calculation, the plastic reference resistance or the plastic limit load F_{pl} can be determined.

The main purposes of a MNA calculation are:

- To identify the failure behaviour due to plasticity only (without any interaction of stability);
- To determine the plastic limit load F_{pl} to calculate the dimensionless strength parameter χ (Eq. (2-13)) and the relative slenderness λ (Eq. (2-14)) of the structure.

Geometrical and material non-linear elastic analysis without imperfections (GMNA)

A GMNA calculation uses a shell bending theory, and takes into account the complete change of the geometry due to actions (i.e. a non-linear large deflection theory for the displacements) and a non-linear elasto-plastic material behaviour. Imperfections are ignored. This type of analysis can detect both snap-through and bifurcation buckling.

The main purposes of a GMNA analysis are:

- To identify the elasto-plastic behaviour of the perfect structure;
- To determine the elasto-plastic buckling load F of the perfect structure to calculate the dimensionless strength parameter χ of the perfect structure (Eq. (2-13)).
- To determine a post-buckling mode and to apply it as an equivalent initial

imperfection shape in a GMNIA calculation;

- Comparison with the GMNIA load to evaluate the influence of imperfections.

Geometrical and material non-linear elastic analysis with imperfections (GMNIA)

A GMNIA calculation is the most advanced calculation. This calculation type is similar to a GMNA analysis, except that imperfections now are explicitly included. These imperfections are modelled as small deviations relative to the shell middle surface. However, it is difficult to find an appropriate geometric imperfection (See Section 6.1). Many different imperfection shapes must be considered, and additional choices have to be made concerning the orientation, amplitude (related to fabrication quality classes), and location of the (equivalent) geometric imperfection (See Section 6.2).

The main purposes of a GMNIA analysis are:

- To identify the elasto-plastic behaviour of the real (imperfect) structure;
- To determine the characteristic elasto-plastic buckling load F_k to calculate the dimensionless strength parameter χ of the imperfect structure (Eq. (2-13)).
- Comparison with the GMNA load to evaluate the influence of imperfections.

B Measurement of the imperfections

EU1 - first measurement (complete shell wall)

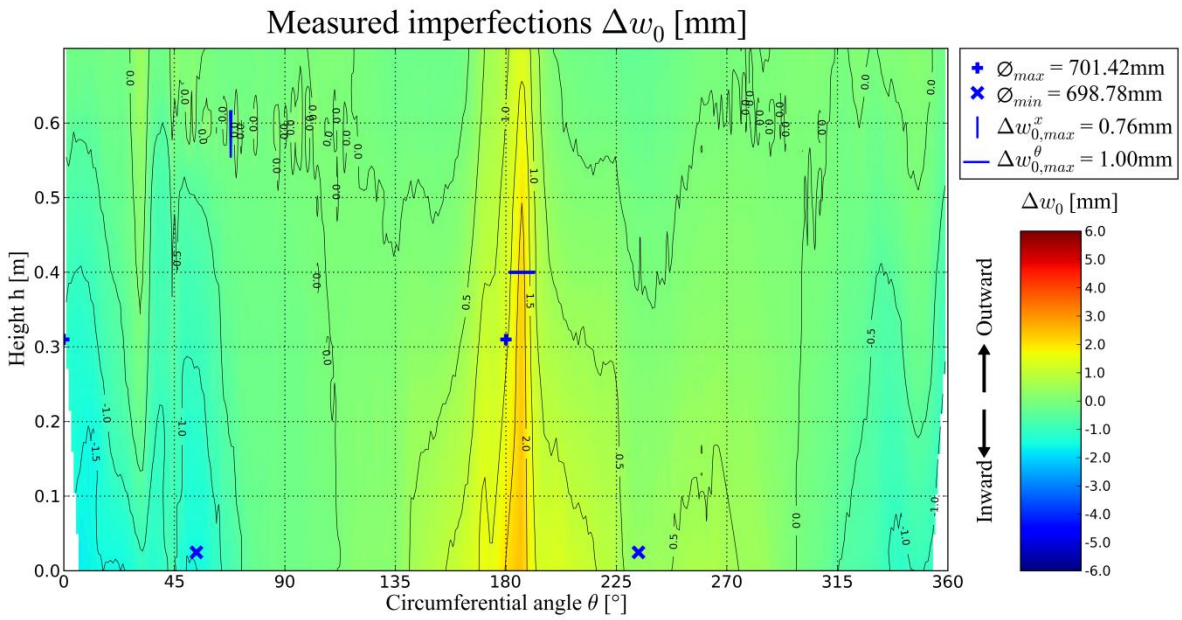

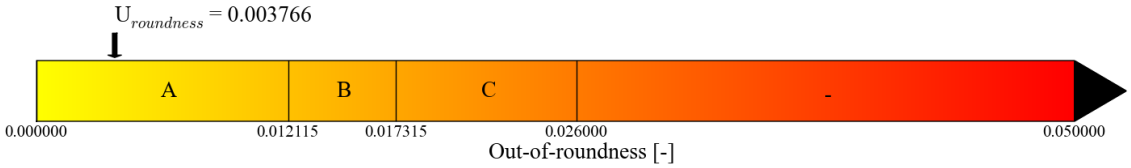

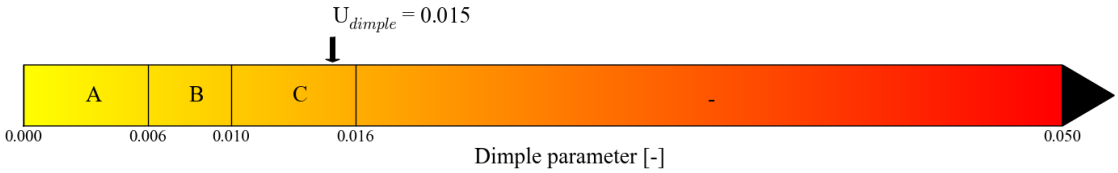

EU1 - second measurement (complete shell wall)

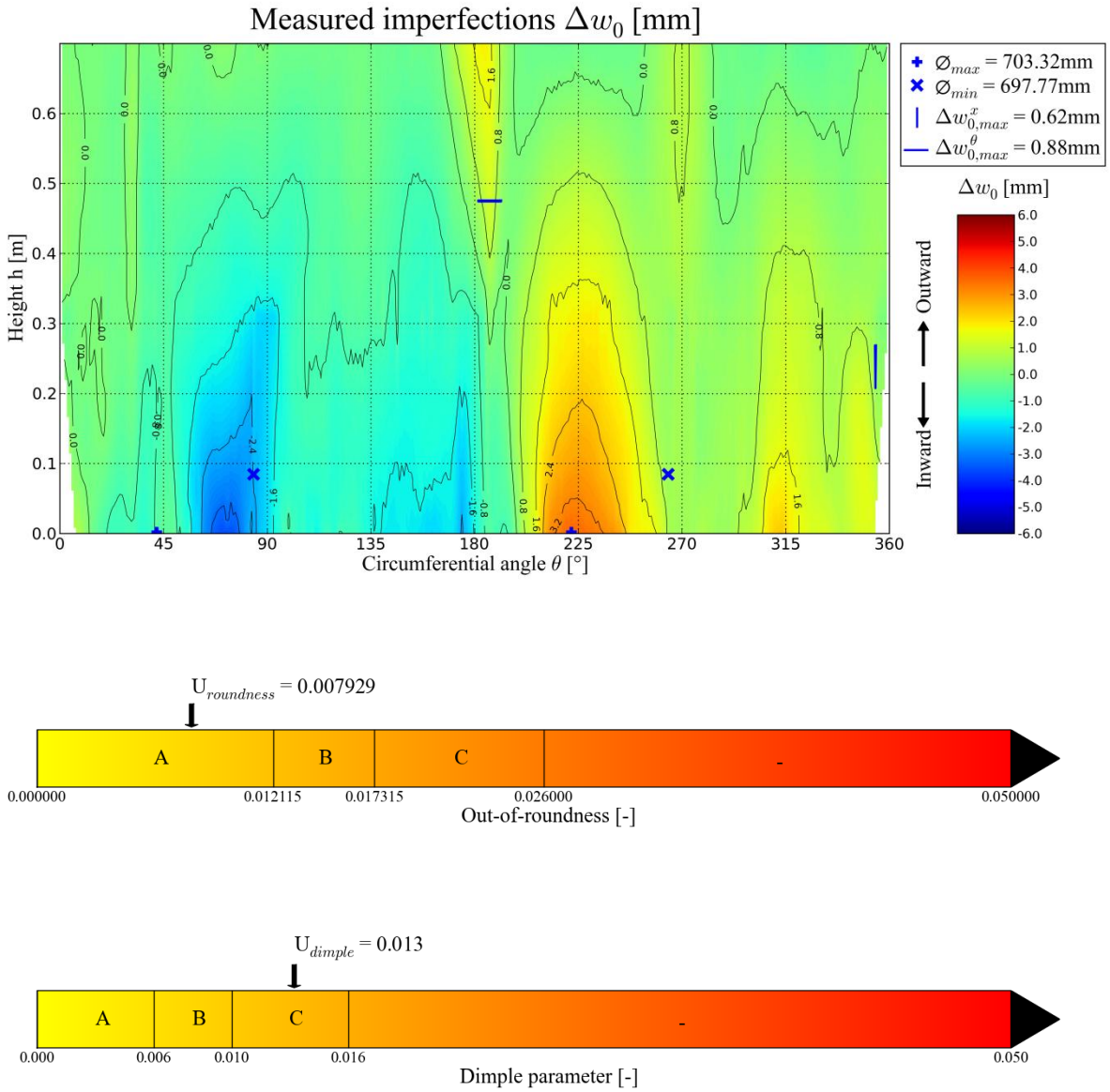

EU2 - first measurement (complete shell wall)

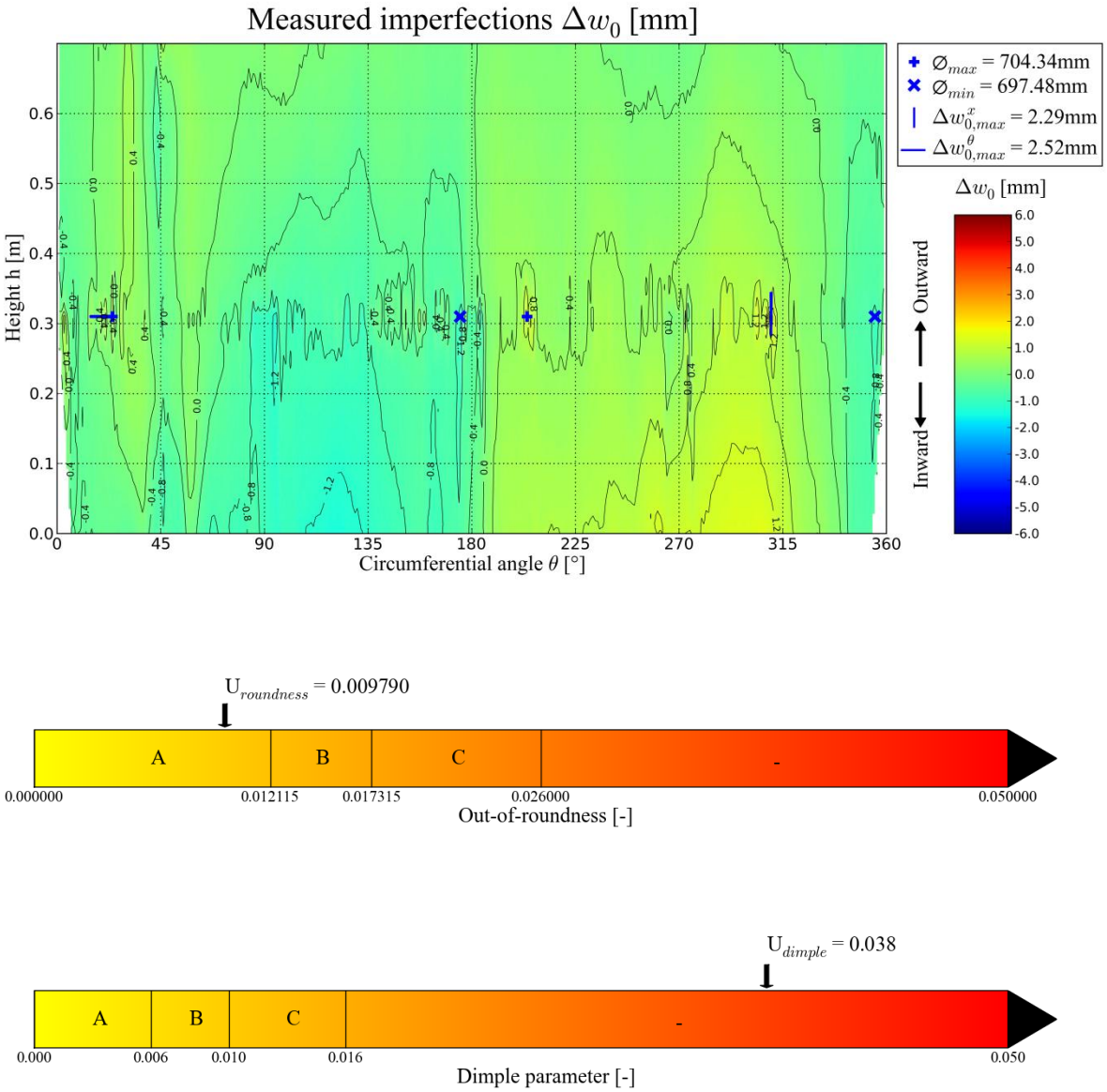

EU2 - second measurement (complete shell wall)

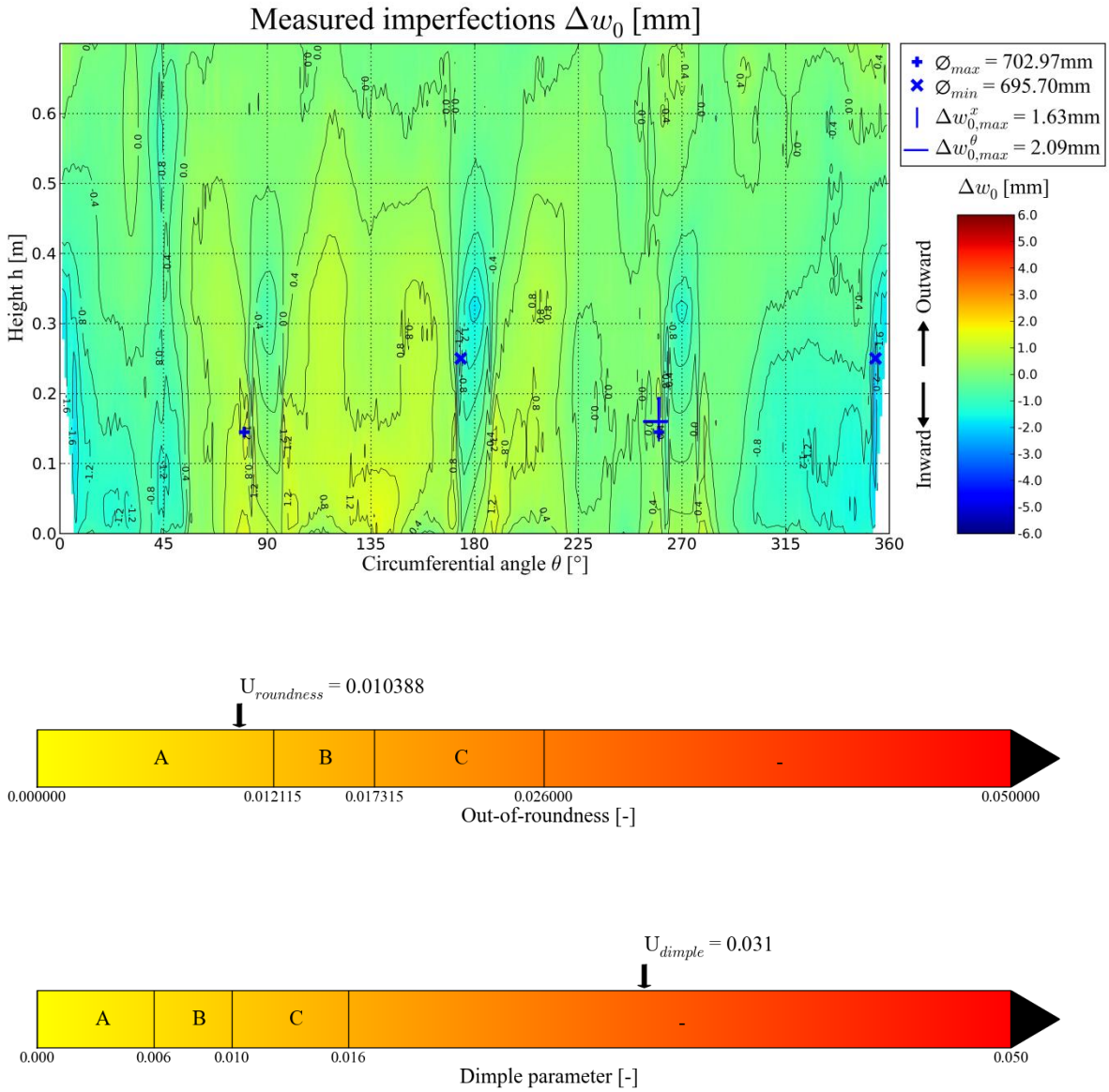

EU3 - first measurement (complete shell wall)

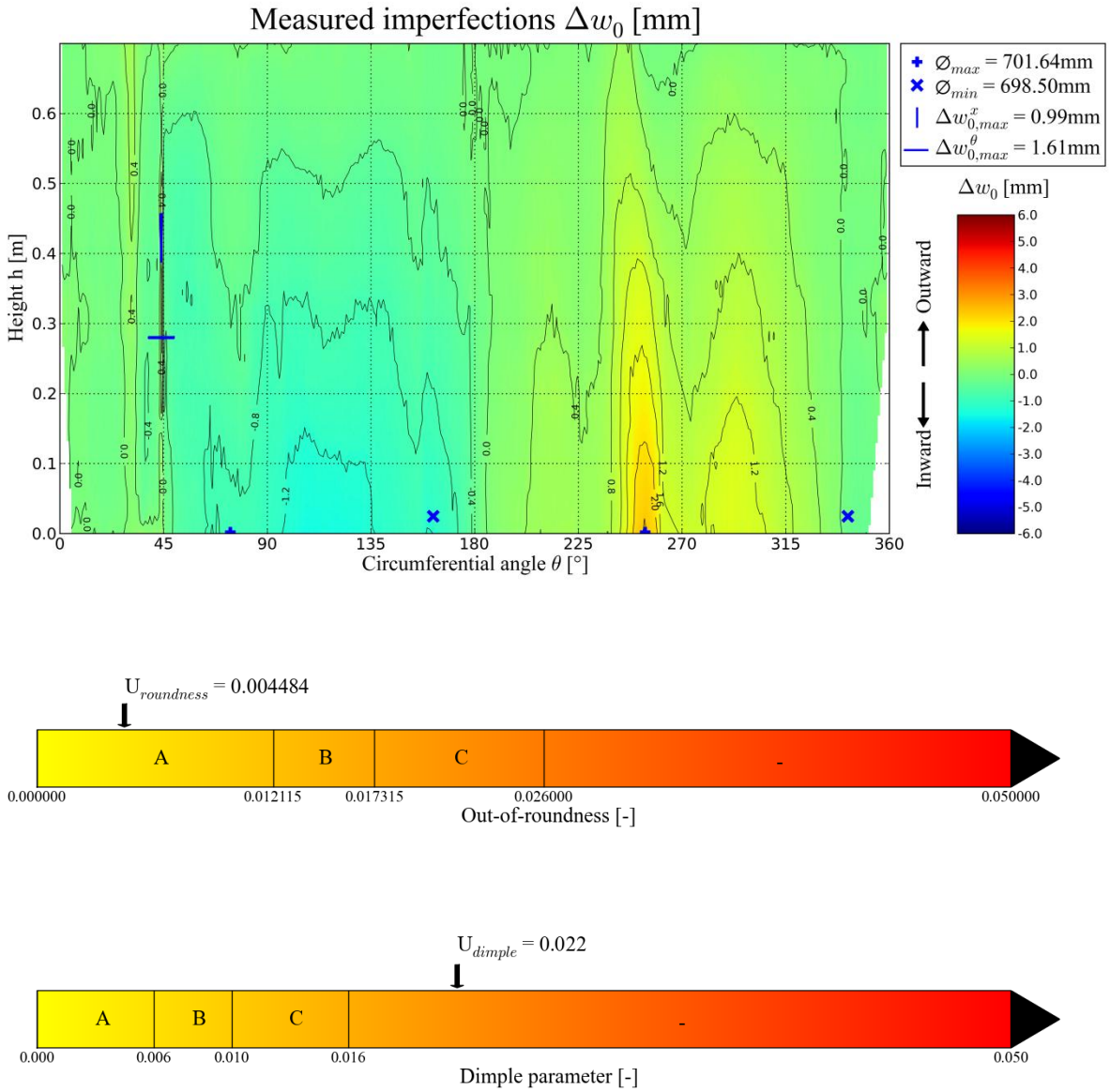

EU3 - second measurement (complete shell wall)

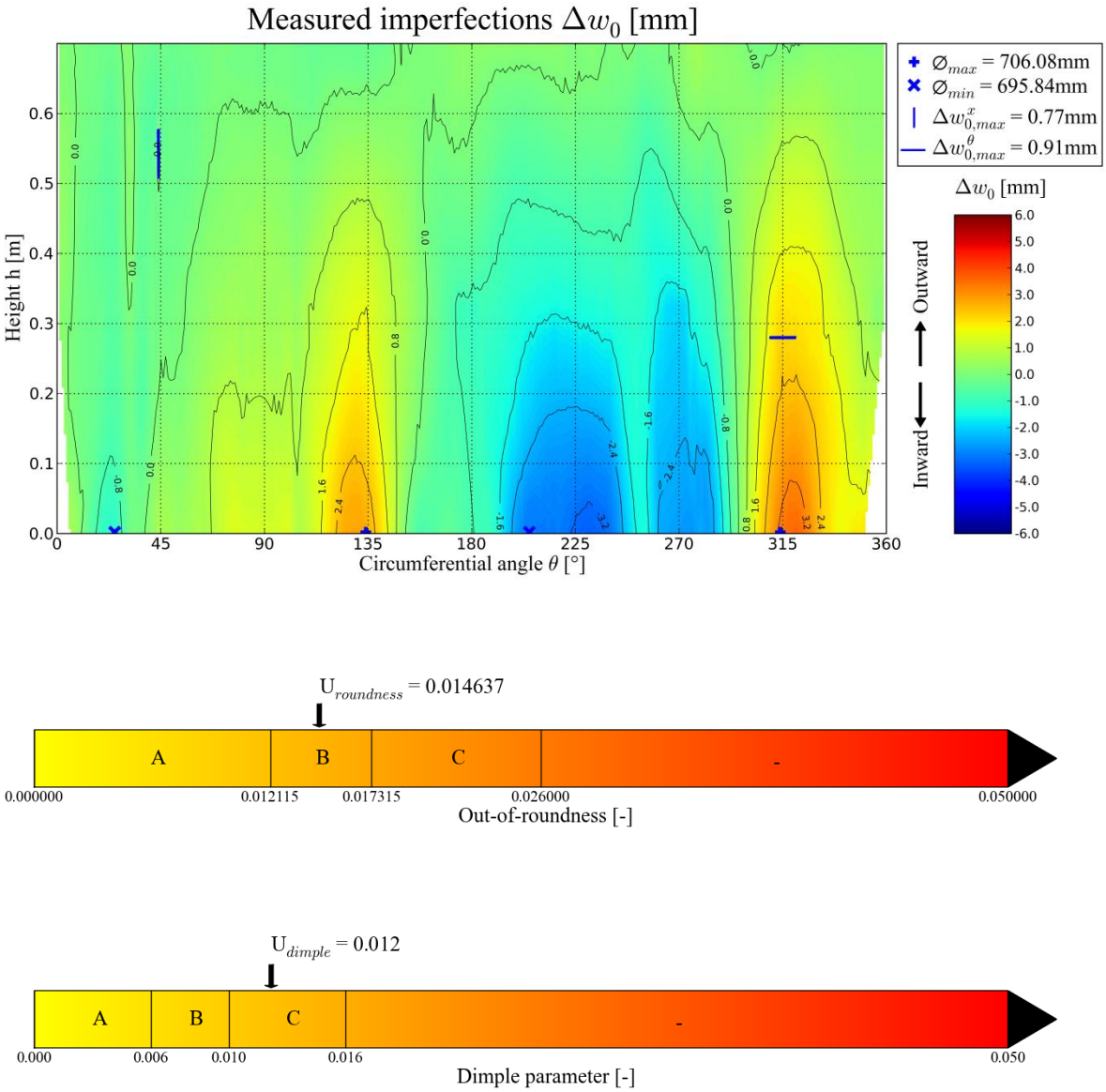

EK1 - first measurement (complete shell wall)

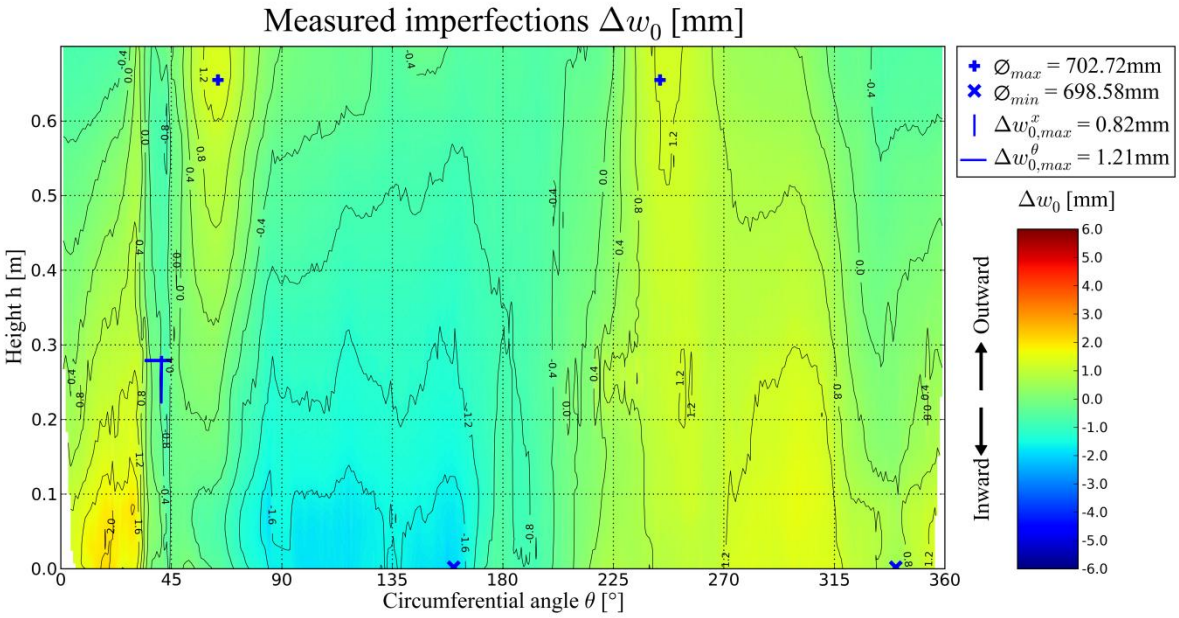

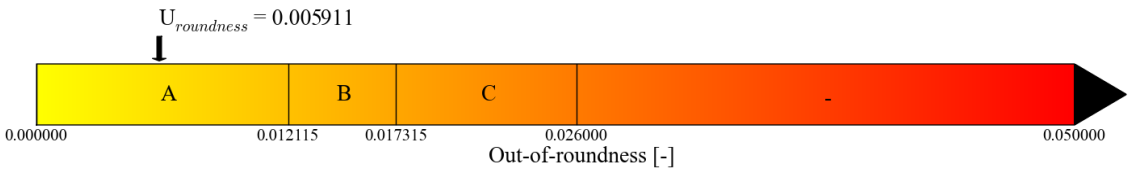

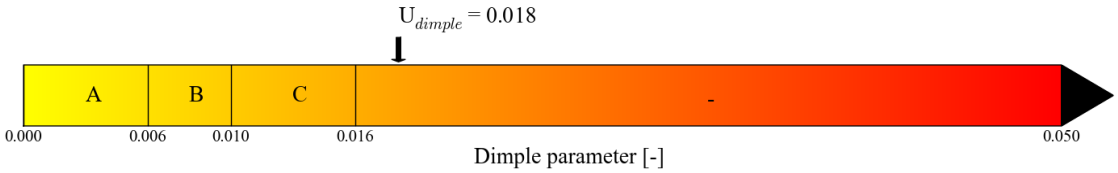

EK1 - second measurement (complete shell wall)

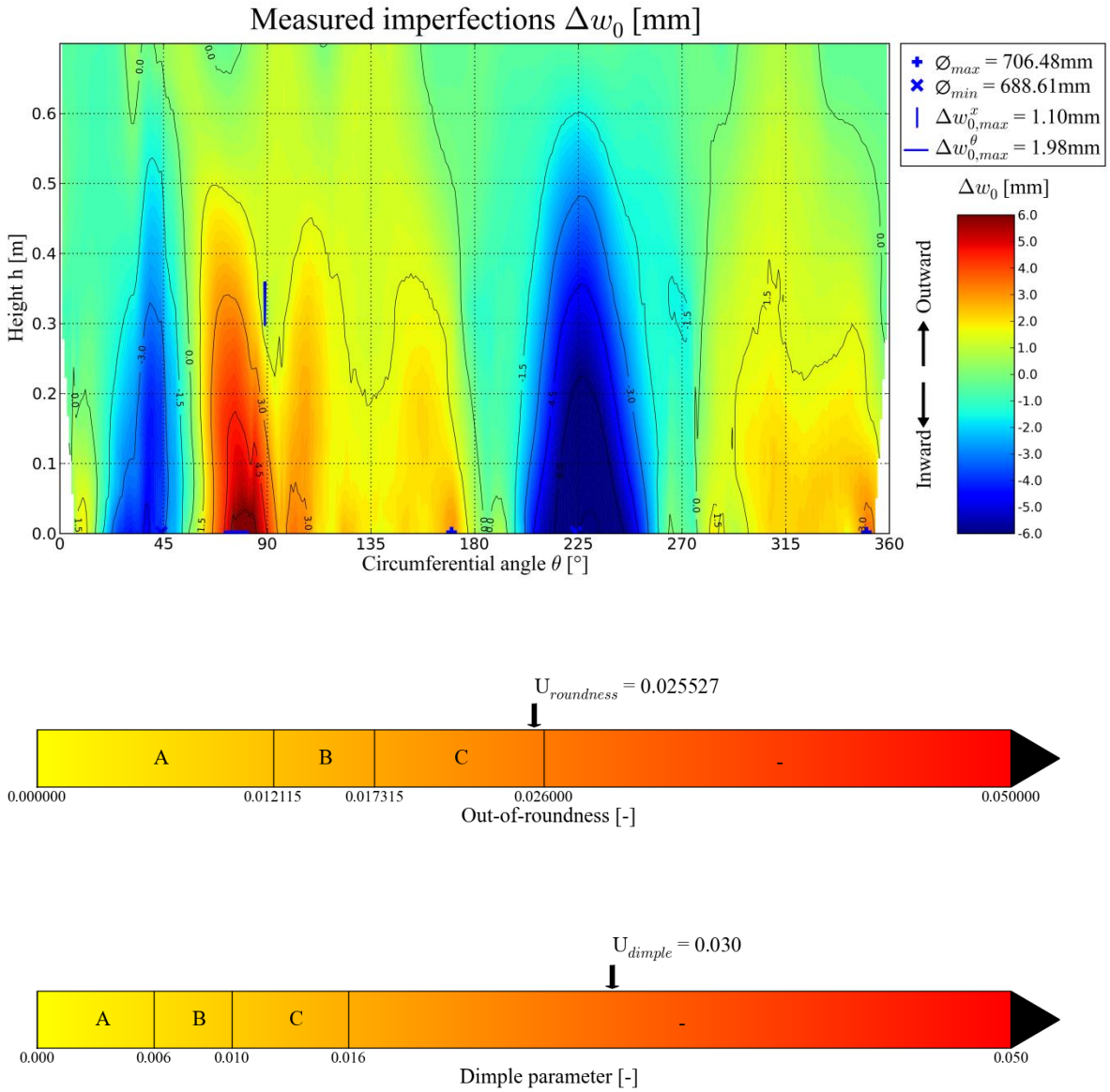

EK2 - first measurement (complete shell wall)

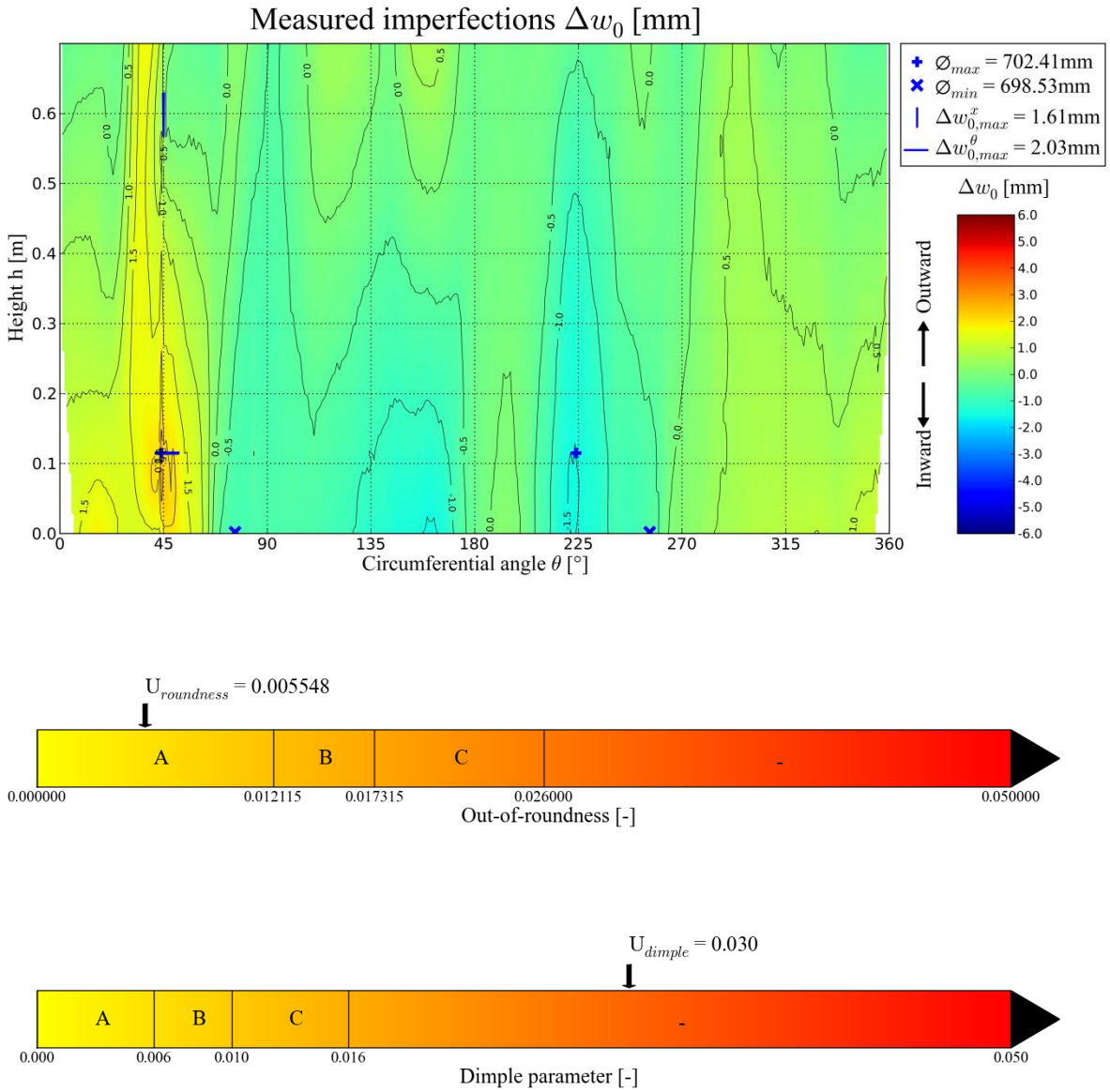

EK2 - second measurement (complete shell wall)

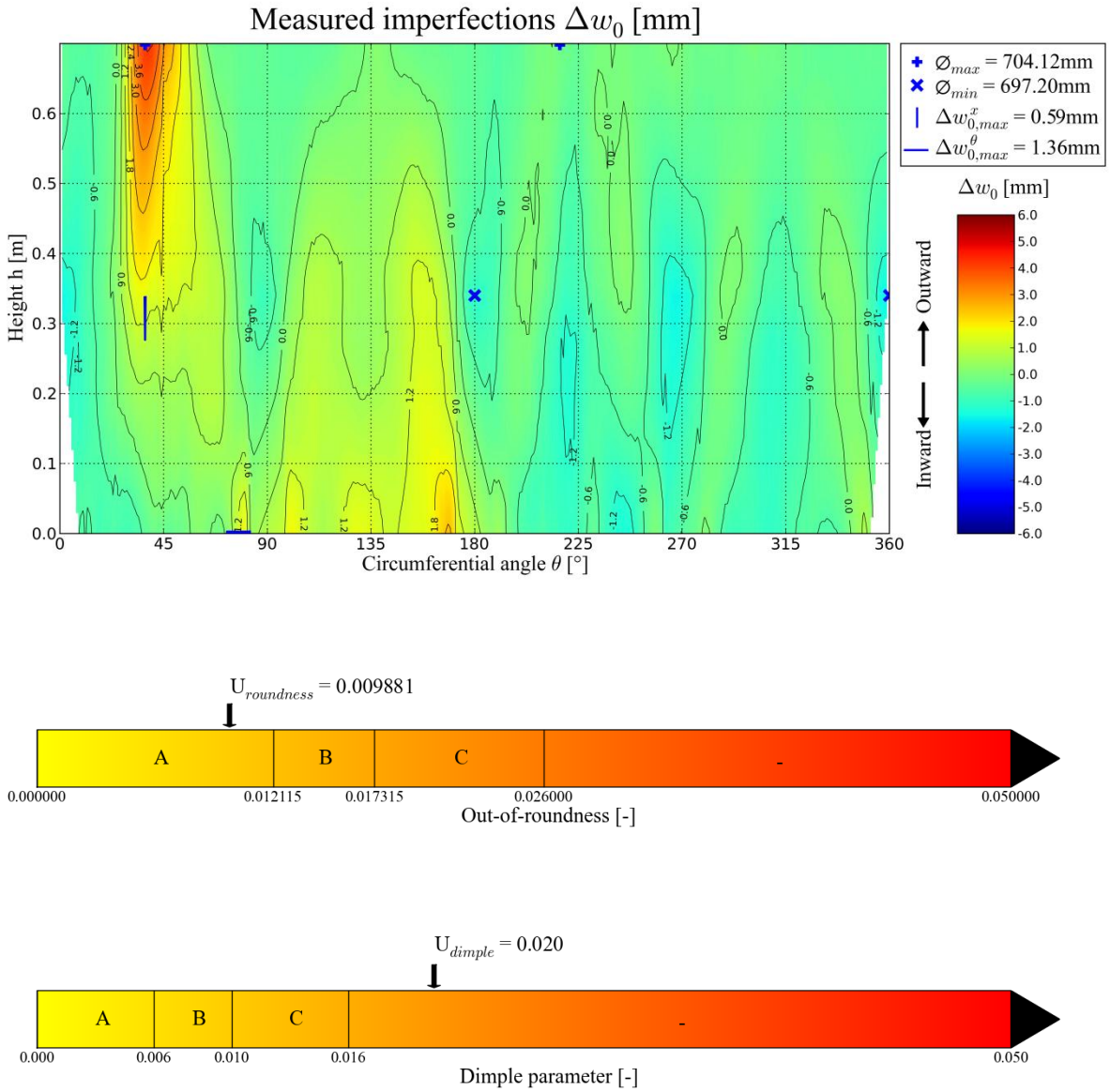

EK3 - first measurement (complete shell wall)

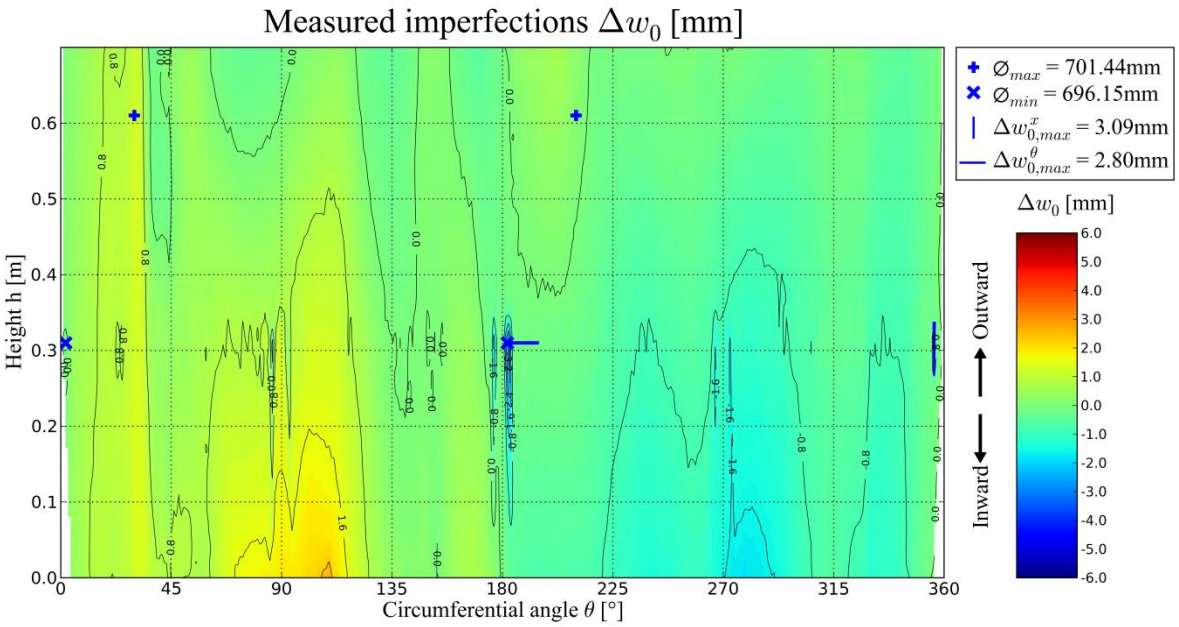

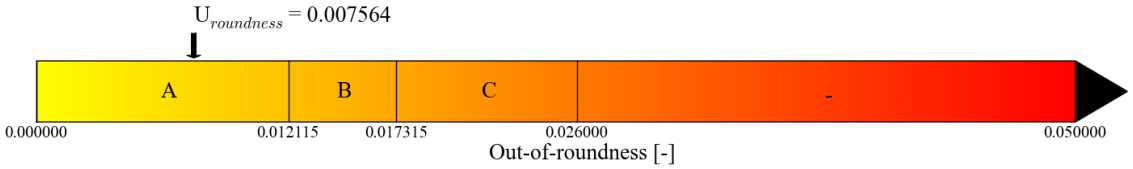

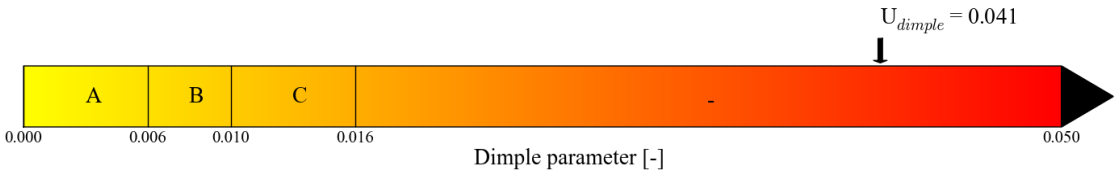

EK3 - second measurement (complete shell wall)

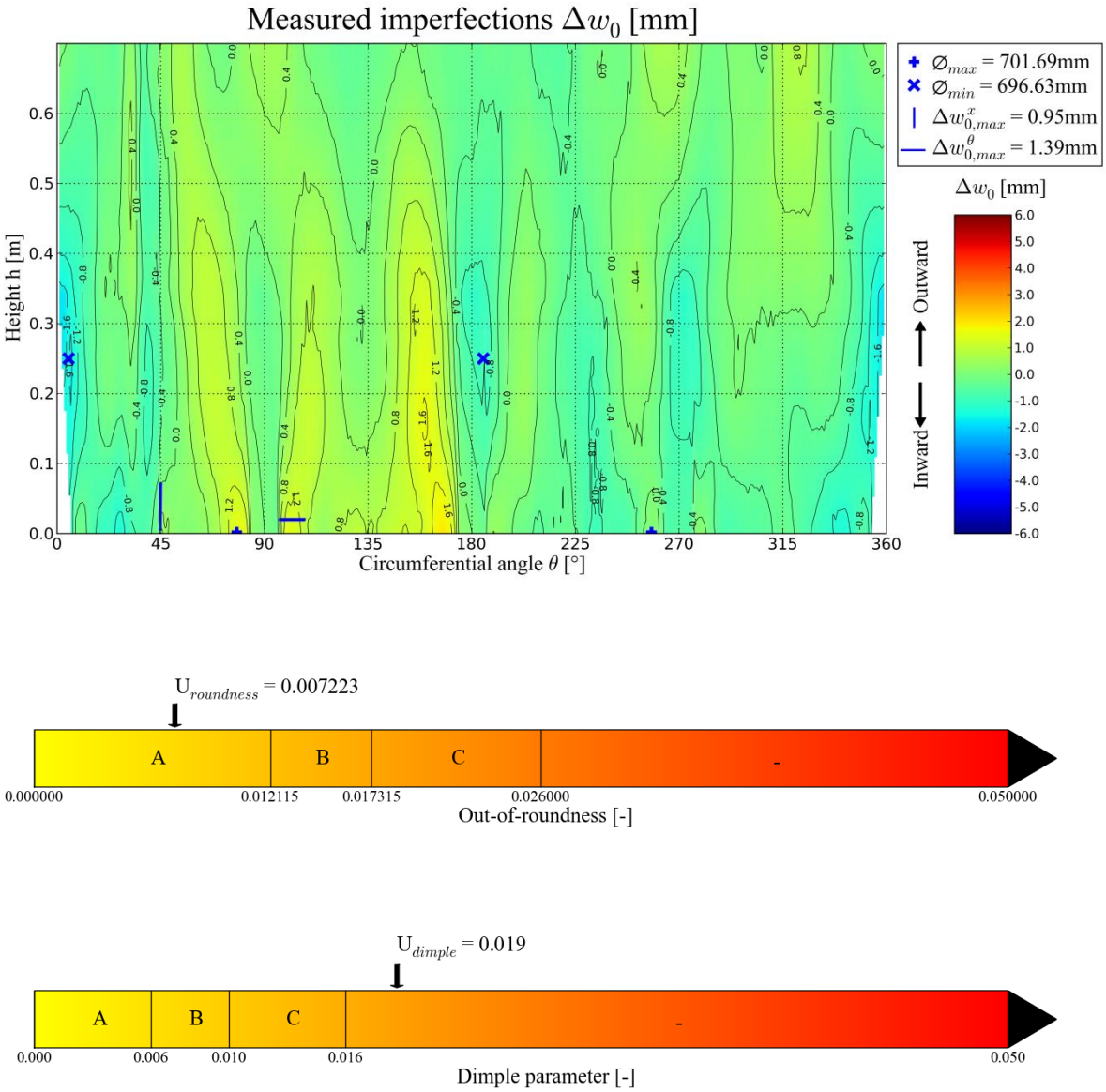

EK4 - first measurement (complete shell wall)

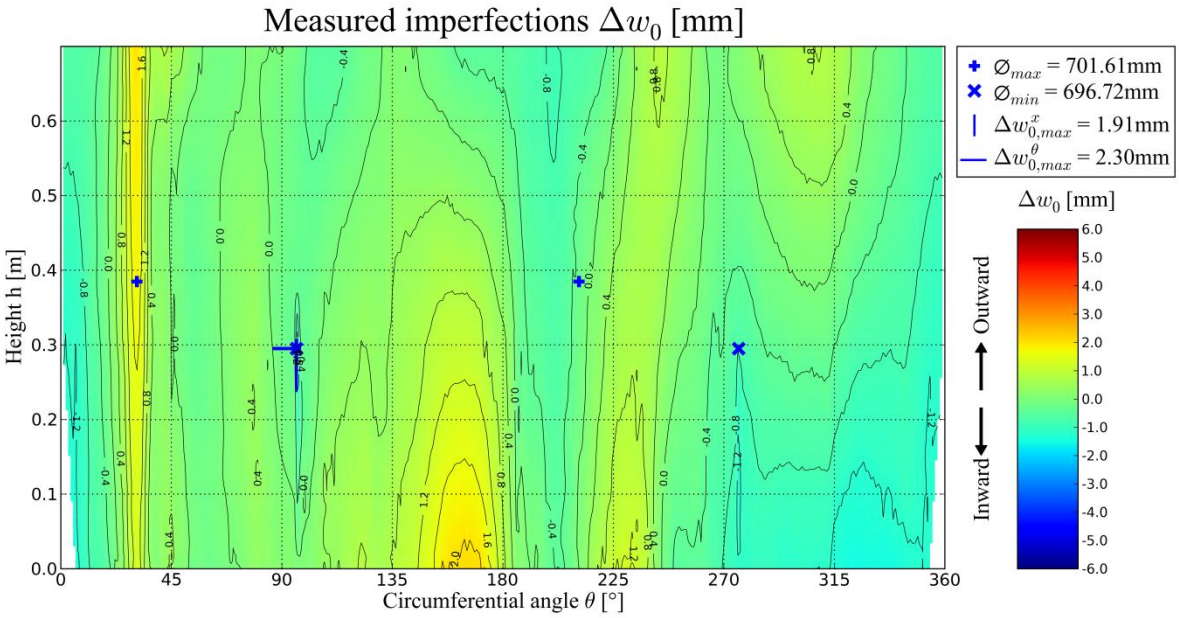

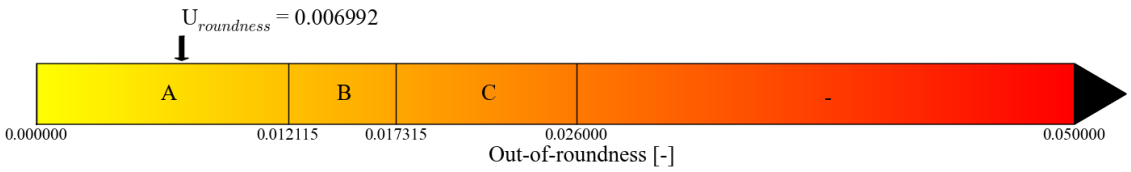

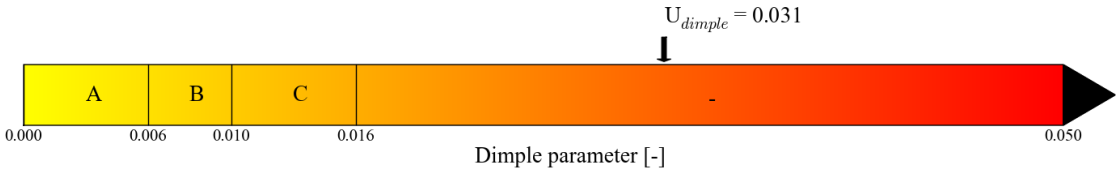

EK4 - second measurement (complete shell wall)

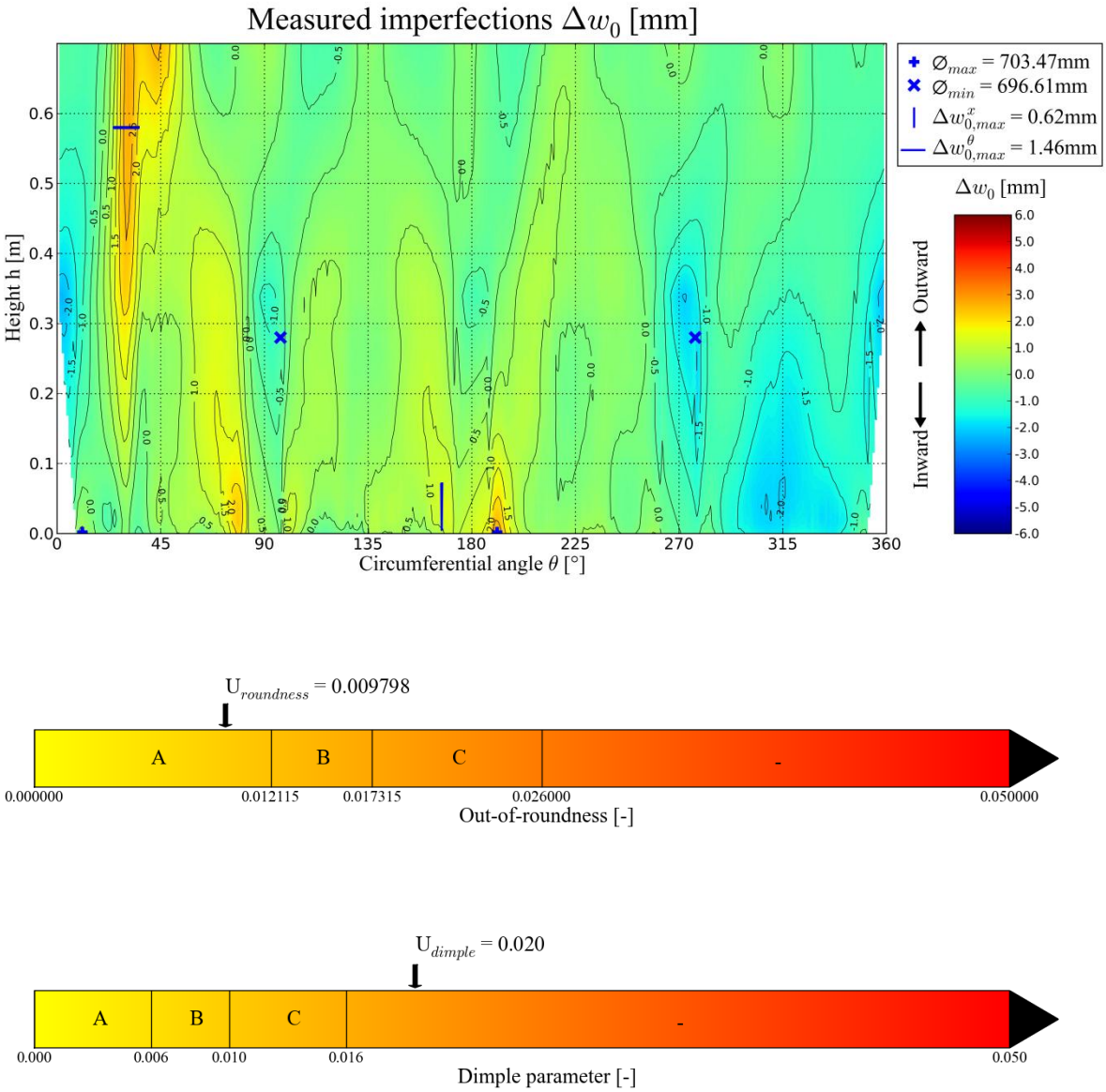

C Comparison of the final study with the Eurocode

$R/t = 100$

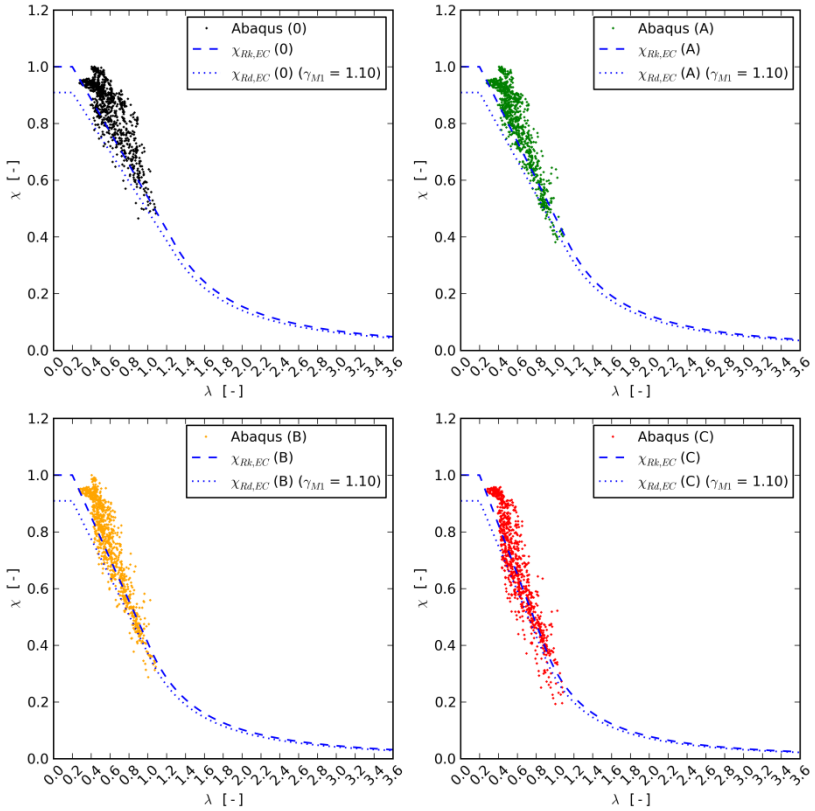

$R/t = 200$

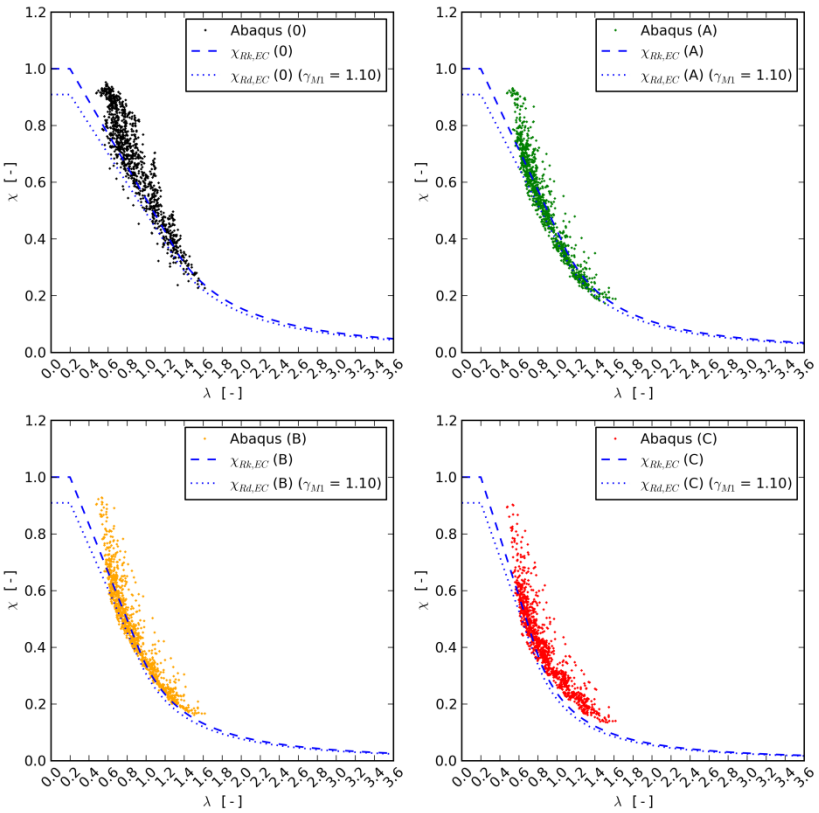

$\underline{R/t = 250}$

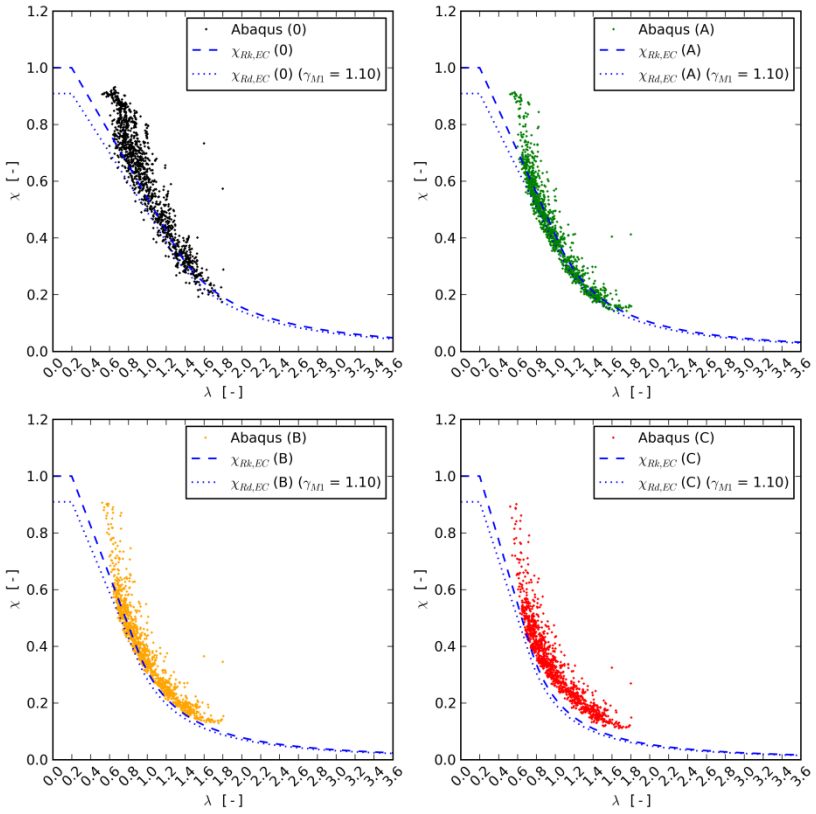

$\underline{R/t = 333.3}$

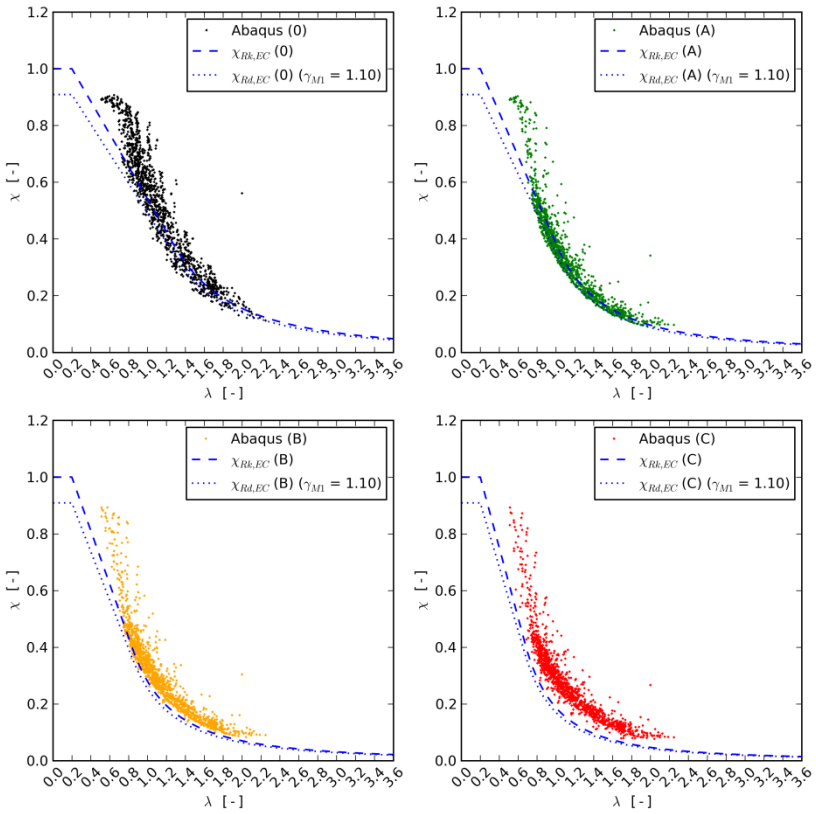

$\underline{R/t = 500}$

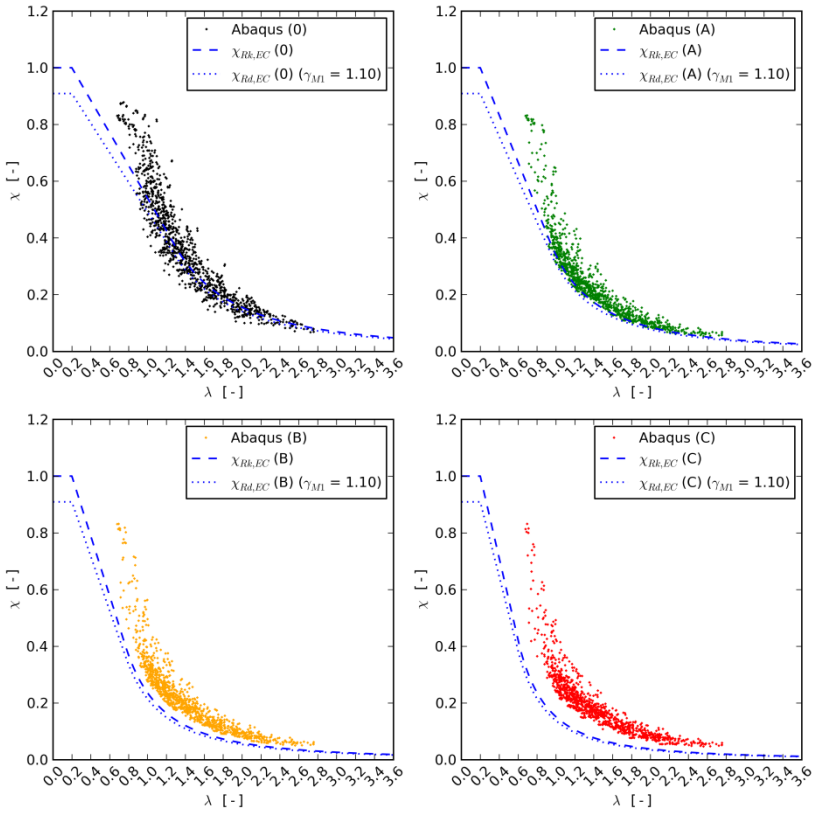

$\underline{R/t = 666.6}$

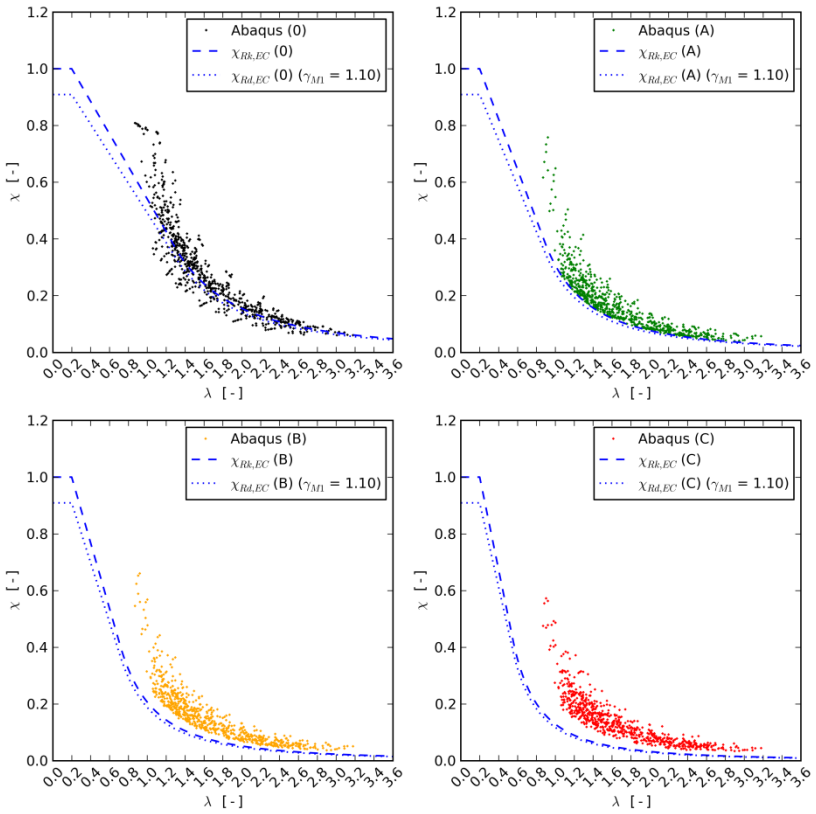

$\underline{R/t = 1000}$

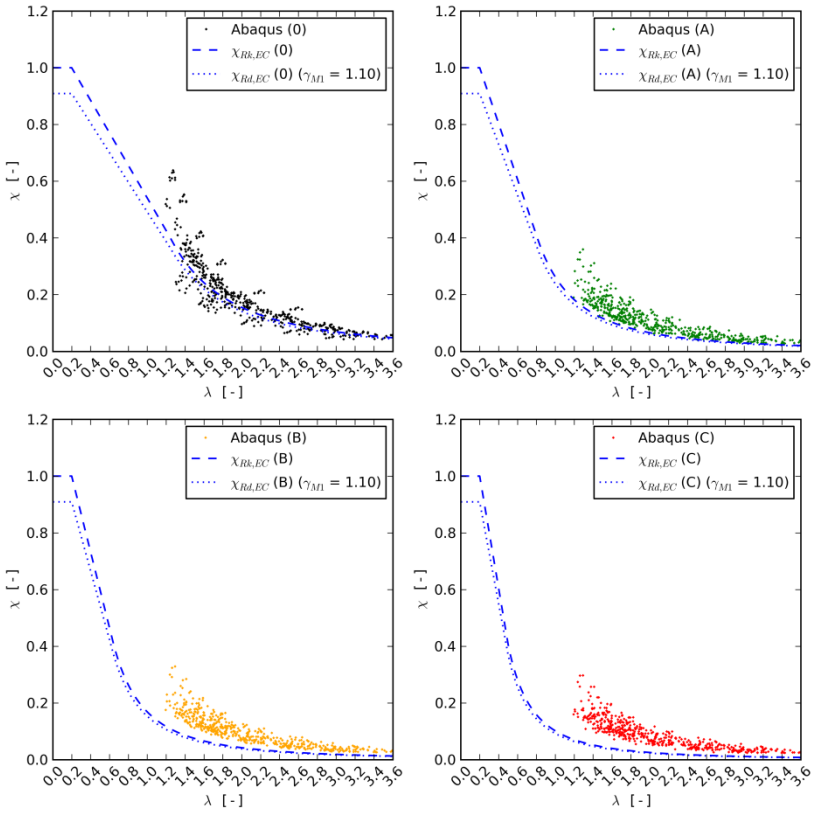

D Partial coefficient on the resistance

Used expressions

The expressions for the determination of a partial coefficient on the resistance γ_{M1} (according to Eurocode 0, annex D) and used in this work are listed below (EN 1990, 2002).

The value R_i is the ratio of the "experimental" resistance $r_{e,i}$ of a structure i (here: the dimensionless strength χ_{Abq} obtained from numerical results) to the "theoretical" resistance $r_{t,i}$ of the same structure (here: the characteristic value of the dimensionless strength $\chi_{Rk,EC}$ obtained from the design procedure in the Eurocode) (Eq. (D-1)). In general, both methods will lead to different results and R_i will be different from the unity. For an economical and reliable design, the scatter of R_i should be minimized and should not be less than the unity. The mean value R_m and the variance σ_R^2 of the value R_i can be calculated using expressions (D-2) and (D-3), respectively, where n is the sample size.

$$R_i = \frac{r_{e,i}}{r_{t,i}} \tag{D-1}$$

$$R_m = \frac{1}{n} \cdot \sum_{i=1}^{n} R_i \tag{D-2}$$

$$\sigma_R^2 = \frac{1}{n-1} \cdot \sum_{i=1}^{n} (R_i - R_m)^2 \tag{D-3}$$

The error term δ_i can be calculated using Eq. (D-4), the logarithmic transformation of the error term Δ_i with Eq. (D-5). The mean value Δ_m and the variance σ_Δ^2 of the value Δ_i can be calculated using expressions (D-6) and (D-7), respectively.

$$\delta_i = \frac{R_i}{R_m} \tag{D-4}$$

$$\Delta_i = \ln(\delta_i) \tag{D-5}$$

$$\Delta_m = \frac{1}{n} \cdot \sum_{i=1}^{n} \Delta_i \tag{D-6}$$

$$\sigma_\Delta^2 = \frac{1}{n-1} \cdot \sum_{i=1}^{n} (\Delta_i - \Delta_m)^2 \tag{D-7}$$

Consequently, the variance σ_Δ^2 is used to estimate the coefficient of variation of the error term V_δ.

$$V_\delta = \sqrt{e^{(\sigma_\Delta^2)} - 1} \tag{D-8}$$

Finally, the partial coefficient on the resistance γ_{M1} is determined using Eq. (D-9) (valid when $n > 100$), where $k_{d,n}$ is equal to 3.04 and Eq. (D-10) gives the expression for the calculation of the factor Q.

$$\gamma_{R_d} = \frac{1}{R_m \cdot e^{(-k_{d,n} \cdot Q - 0.5 \cdot Q^2)}} \geq 1.0 \tag{D-9}$$

$$Q = \sqrt{\ln\left(V_\delta^2 + 1\right)} \tag{D-10}$$

Results

	Δ_{min} [%]	Δ_{max} [%]	Δ_{mean} [%]	Δ_{med} [%]	n [-]	R_m [-]	σ_R [-]	σ_Δ [-]	γ'_{M1} [-]
Complete dataset									
	-41.7	469.8	32.5	210.9	27072	1.32	0.253	0.091	1.00
Sorted by quality class									
PERFECT	-37.7	261.8	9.2	19.1	6768	1.09	0.025	0.139	0.97
CLASS A	-20.6	255.7	12.2	52.5	6768	1.12	0.051	0.139	0.98
CLASS B	-29.3	334.2	33.9	112.6	6768	1.34	0.158	0.139	0.92
CLASS C	-41.7	469.8	74.6	210.9	6768	1.75	0.506	0.139	0.88

	Δ_{min} [%]	Δ_{max} [%]	Δ_{mean} [%]	Δ_{med} [%]	n [-]	R_m [-]	σ_R [-]	σ_Δ [-]	γ'_{M1} [-]
Sorted by slenderness, perfect									
< 0.6	-11.1	22.1	8.9	15.1	628	1.09	0.004	0.004	0.93
[0.6; 0.8 [	-15.8	34.1	13.8	7.9	1151	1.14	0.009	0.007	0.90
[0.8; 1.0 [	-24.0	49.9	12.6	14.0	1238	1.13	0.016	0.012	0.92
[1.0; 1.2 [	-35.2	68.1	8.7	20.5	1010	1.09	0.027	0.022	0.98
[1.2; 1.4 [	-37.7	72.3	5.0	20.3	853	1.05	0.030	0.026	1.03
[1.4; 1.6 [	-35.9	202.8	7.7	15.2	623	1.08	0.039	0.030	1.02
[1.6; 1.8 [	-37.7	68.0	5.4	19.1	430	1.05	0.027	0.026	1.03
[1.8; 2.0 [	-36.4	261.8	8.0	23.0	238	1.08	0.079	0.043	1.06
[2.0; 2.2 [	-37.7	62.1	5.2	19.1	207	1.05	0.030	0.029	1.04
[2.2; 2.4 [	-35.8	68.0	5.3	15.2	118	1.05	0.041	0.036	1.06
> 2.4	-37.7	68.0	4.9	19.1	272	1.05	0.034	0.033	1.05

	Δ_{min} [%]	Δ_{max} [%]	Δ_{mean} [%]	Δ_{med} [%]	n [-]	R_m [-]	σ_R [-]	σ_Δ [-]	γ'_{M1} [-]
Sorted by slenderness, quality class A									
< 0.6	-8.3	30.0	10.0	-2.9	628	1.10	0.005	0.004	0.92
[0.6; 0.8 [	-16.2	53.7	6.5	-7.8	1151	1.06	0.015	0.012	0.98
[0.8; 1.0 [	-19.2	109.3	1.5	-3.7	1238	1.02	0.026	0.019	1.04
[1.0; 1.2 [	-20.6	111.9	5.9	19.2	1010	1.06	0.031	0.023	1.01
[1.2; 1.4 [	-18.1	129.4	12.3	36.7	853	1.12	0.052	0.033	0.99
[1.4; 1.6 [	-14.8	150.7	18.9	41.7	623	1.19	0.068	0.040	0.95
[1.6; 1.8 [	-13.0	133.6	23.0	52.5	430	1.23	0.071	0.039	0.92
[1.8; 2.0 [	-10.3	255.7	29.8	57.4	238	1.30	0.109	0.047	0.89
[2.0; 2.2 [	-5.5	126.6	28.9	52.5	207	1.29	0.069	0.034	0.86
[2.2; 2.4 [	-5.5	129.6	31.8	41.7	118	1.32	0.079	0.039	0.85
> 2.4	-1.2	129.6	42.9	52.5	272	1.43	0.085	0.038	0.79

	Δ_{min} [%]	Δ_{max} [%]	Δ_{mean} [%]	Δ_{med} [%]	n [-]	R_m [-]	σ_R [-]	σ_Δ [-]	γ'_{M1} [-]
Sorted by slenderness, quality class B									
< 0.6	-16.0	38.3	8.9	-13.4	628	1.09	0.008	0.007	0.94
[0.6; 0.8 [	-17.5	101.5	6.6	-7.5	1151	1.07	0.026	0.019	0.99
[0.8; 1.0 [	-27.2	171.4	13.7	18.7	1238	1.14	0.059	0.032	0.97
[1.0; 1.2 [	-29.3	175.9	30.8	62.3	1010	1.31	0.071	0.034	0.85
[1.2; 1.4 [	-3.4	226.5	43.1	75.1	853	1.43	0.124	0.050	0.81
[1.4; 1.6 [	-1.3	236.4	55.3	103.1	623	1.55	0.165	0.057	0.77
[1.6; 1.8 [	-0.4	210.4	64.2	112.6	430	1.64	0.171	0.053	0.72
[1.8; 2.0 [	14.0	334.2	74.4	119.5	238	1.74	0.202	0.054	0.68
[2.0; 2.2 [	23.3	206.5	74.5	112.6	207	1.75	0.148	0.040	0.65
[2.2; 2.4 [	25.3	226.5	81.0	103.5	118	1.81	0.173	0.046	0.64
> 2.4	32.6	226.5	98.5	112.6	272	1.98	0.170	0.040	0.57

	Δ_{min} [%]	Δ_{max} [%]	Δ_{mean} [%]	Δ_{med} [%]	n [-]	R_m [-]	σ_R [-]	σ_Δ [-]	γ'_{M1} [-]
Sorted by slenderness, quality class C									
< 0.6	-26.2	60.0	7.1	-22.4	628	1.07	0.018	0.015	0.98
[0.6; 0.8 [	-34.3	193.9	17.7	6.7	1151	1.18	0.077	0.040	0.96
[0.8; 1.0 [	-41.7	270.7	43.0	50.6	1238	1.43	0.150	0.057	0.83
[1.0; 1.2 [	-38.0	278.7	73.3	123.2	1010	1.73	0.185	0.054	0.68
[1.2; 1.4 [	15.3	389.0	95.6	135.3	853	1.96	0.331	0.072	0.64
[1.4; 1.6 [	19.7	403.9	117.5	207.7	623	2.18	0.449	0.081	0.59
[1.6; 1.8 [	19.7	370.0	134.7	210.9	430	2.35	0.459	0.071	0.53
[1.8; 2.0 [	39.6	469.8	150.7	221.0	238	2.51	0.474	0.066	0.49
[2.0; 2.2 [	60.5	383.2	152.8	210.9	207	2.53	0.379	0.050	0.46
[2.2; 2.4 [	69.0	389.0	166.3	207.7	118	2.66	0.454	0.058	0.45
> 2.4	76.1	389.0	193.4	210.9	272	2.93	0.425	0.046	0.39

E Comparison of the final study with the lower bound fits

$\underline{R/t = 100}$

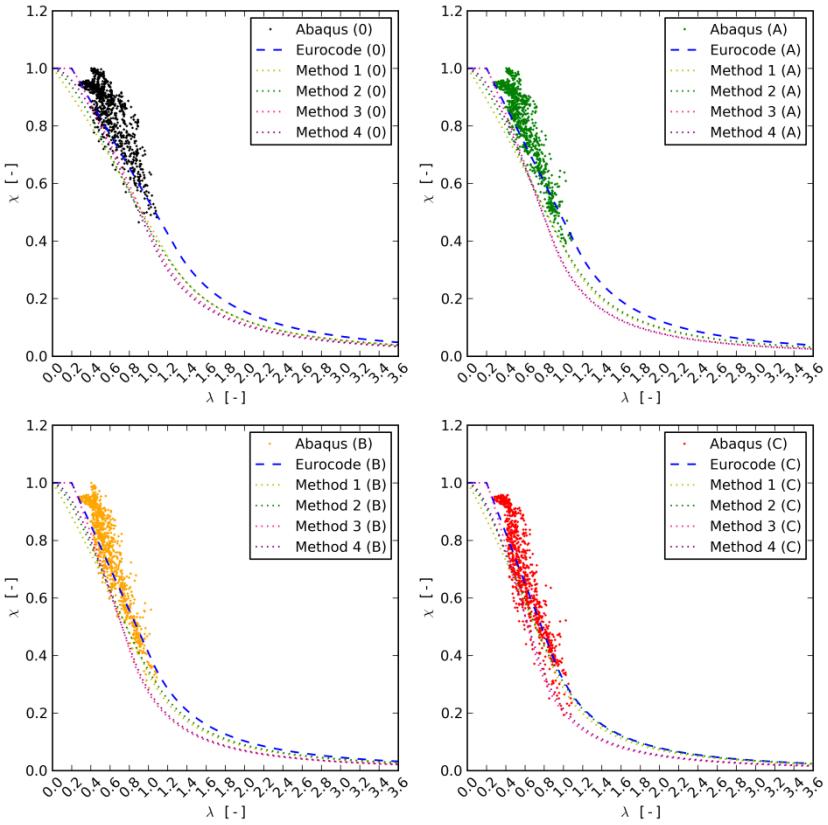

$\underline{R/t = 200}$

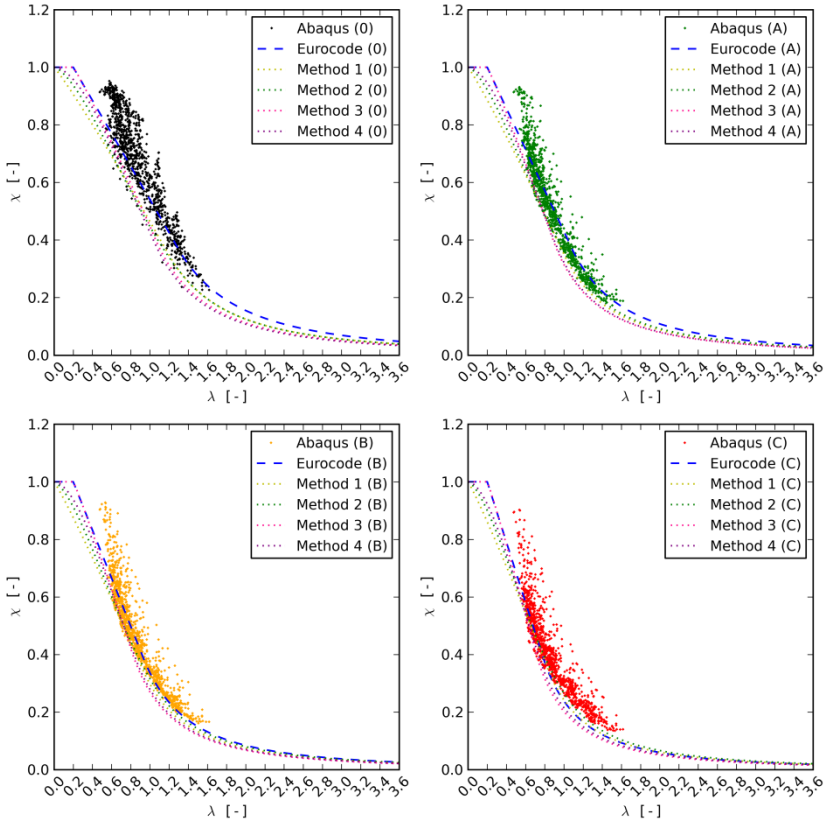

$\underline{R/t = 250}$

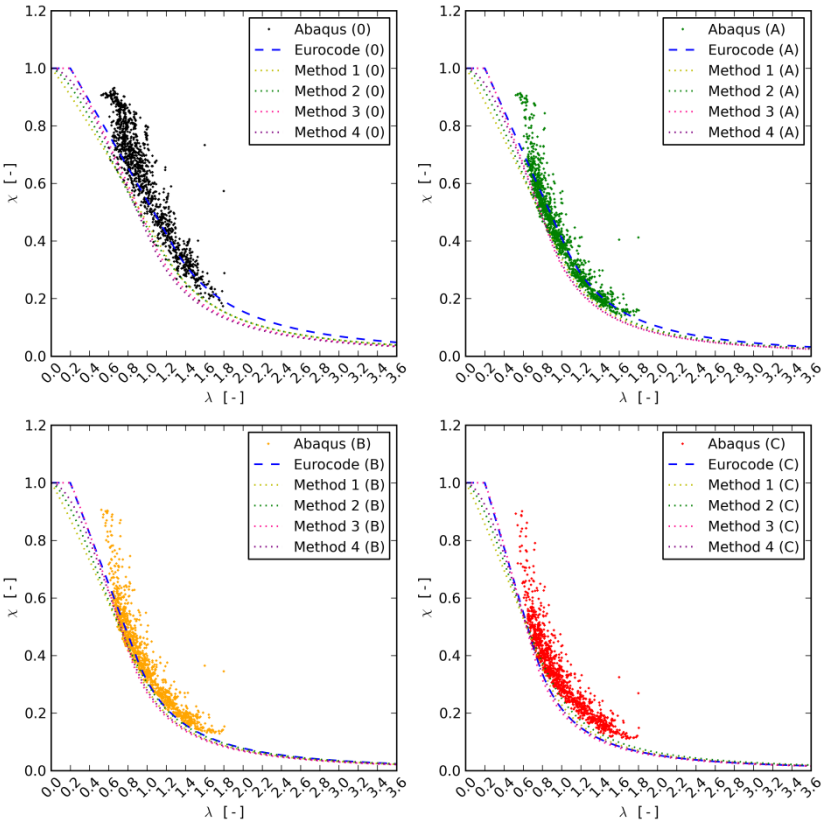

$\underline{R/t = 333.3}$

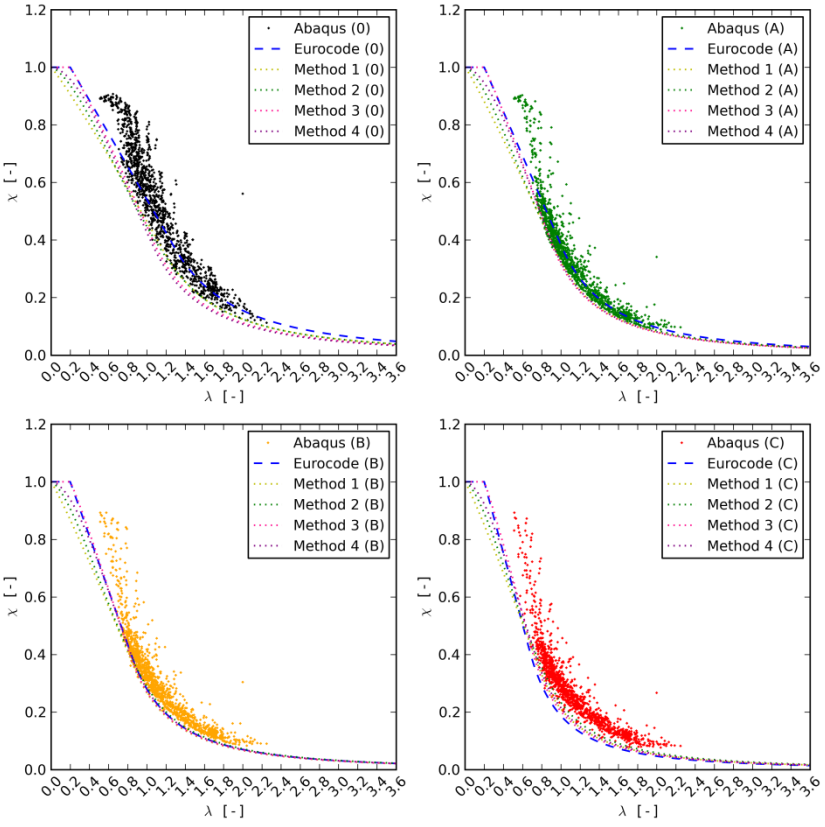

$\underline{R/t = 500}$

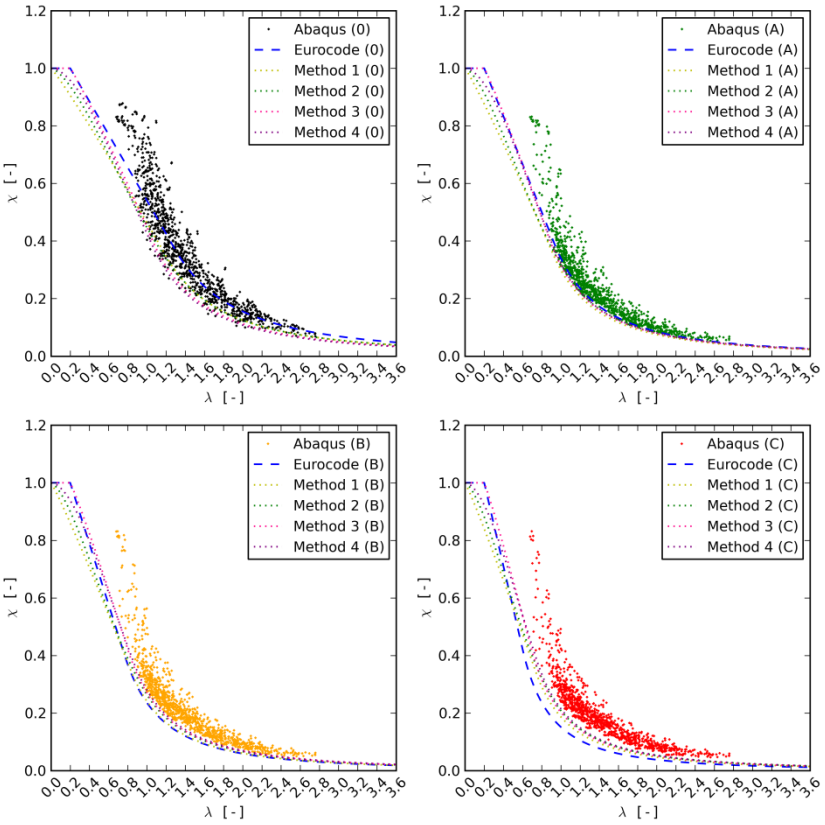

$\underline{R/t = 666.6}$

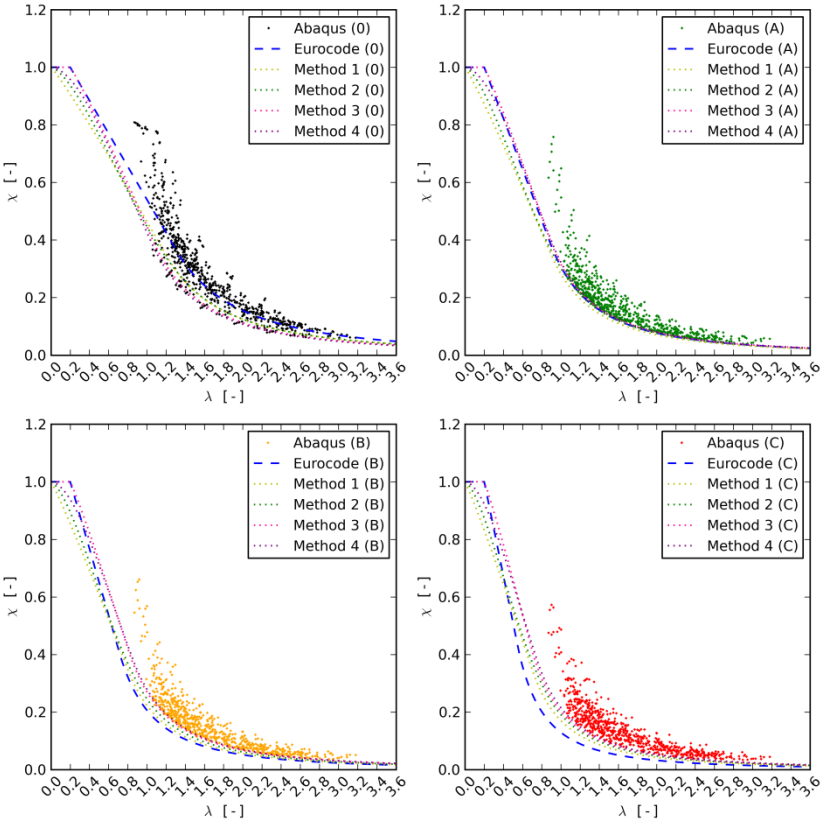

$\underline{R/t = 1000}$

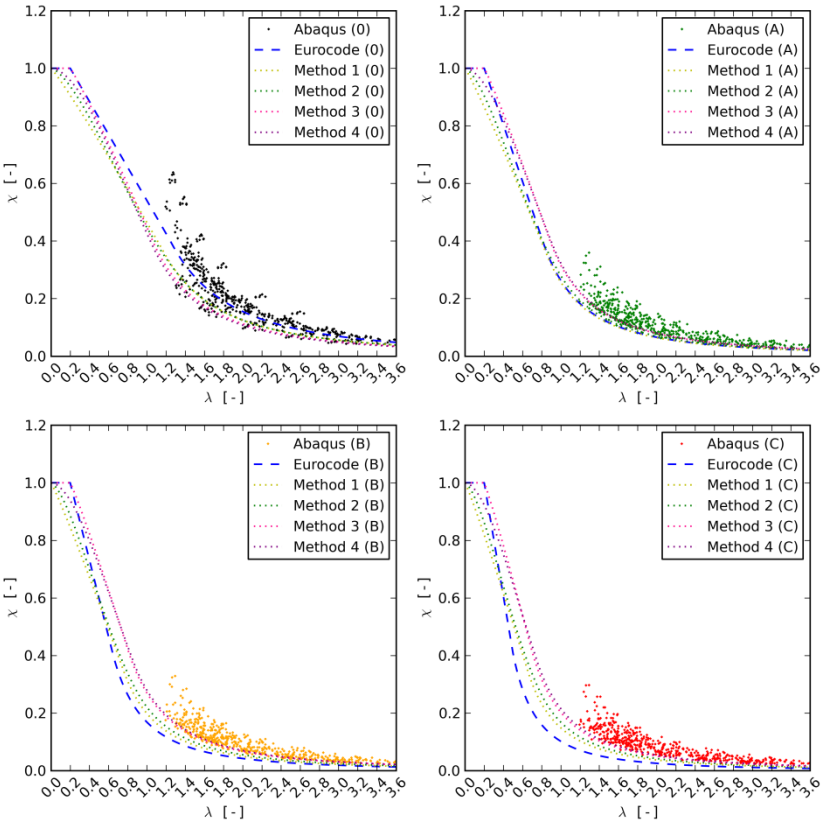

F Partial dataset of the final study

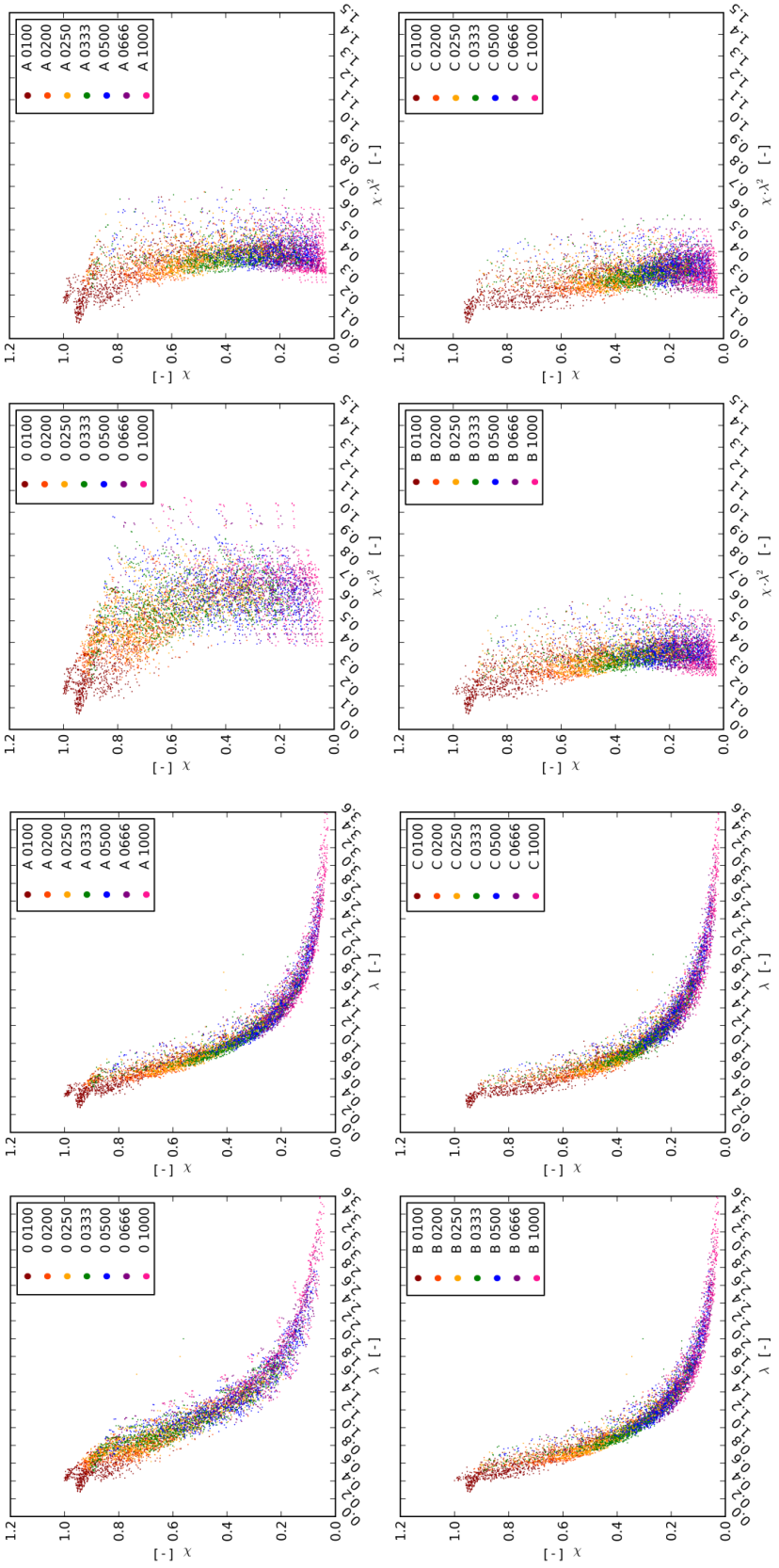

Yield stresses considered: 235; 355; 460; 690; 960MPa.